Dispersion of the elastic moduli of saturated carbonates: experimental study and modelisation

Jan V. M. Borgomano

THÈSE DE DOCTORAT

de l'Université de recherche Paris Sciences et Lettres
PSL Research University

Préparée à l'École Normale Supérieure de Paris

Dispersion des modules élastiques de carbonates saturés : étude expérimentale et modélisation.

Ecole doctorale n°560

Sciences de la Terre et de l'Environnement et Physique de l'Univers, Paris (STEP'UP)

Spécialité Sciences de la Terre et de l'Environnement

COMPOSITION DU JURY :

Dr. LYON-CAEN Hélène
École Normale Supérieure de Paris,
Présidente de jury.

Pr. STEEB Holger
Stuttgart University,
Rapporteur

Dr. BEMER Elisabeth
IFP Énergies nouvelles, Rueil-Malmaison,
Examinatrice

Pr. DAVID Christian
Université de Cergy-Pointoise,
Examinateur

Pr. GUÉGUEN Yves
École Normale Supérieure de Paris,
Directeur de thèse

Dr. FORTIN Jérôme
École Normale Supérieure de Paris,
Co-directeur de thèse

Pr. GUREVICH Boris
Curtin University, Rapporteur hors jury

M. BOISSON Michel
Total Pau, Invité

Soutenue par JAN BORGOMANO le 24 janvier 2018

Dirigée par **YVES GUÉGUEN** et **JÉRÔME FORTIN**

« Everything in the cosmos is propagated by means of waves.»

Leonardo da Vinci
Manuscript H, 67r, Institut de France, Paris.

À Alain.

REMERCIEMENTS

Je tiens à adresser tous mes remerciements à mes directeurs de thèse, Yves Guéguen et Jérôme Fortin. Merci de m'avoir fait confiance dès le début et de m'avoir tant apporté. Merci Yves d'avoir toujours été disponible lorsque j'avais besoin de votre sagesse. Merci pour les longues discussions scientifiques qui m'ont tant passionnées et inspirées. De plus, vous avez toujours eu les bons mots pour m'encourager. Merci Jérôme pour ton soutien sans faille, pour ta disponibilité, et surtout, ton optimisme naturel sur lequel je me suis souvent appuyé.

Je remercie profondément Lucas Pimienta, qui a joué le rôle d'un véritable encadrant de thèse à mes débuts, en plus d'être devenu un ami. Il m'a formé sur les presses triaxiales et sur la délicate préparation des échantillons. Je lui dois toutes mes bases en physique des roches expérimentales, et surtout sur les effets de fréquences.

Je souhaiterais remercier Boris Gurevich et Holger Steeb d'avoir accepté d'être rapporteurs de ma thèse, ainsi que Christian David, Elisabeth Bemer, Hélène Lyon-Caen et Michel Boisson, pour leur participation à mon jury.

Merci au personnel du laboratoire, sans qui tout ceci ne serait pas possible. Merci à Yves Pinquier pour toute son aide technique et Damien Deldique pour les sessions souterraines au MEB. Un grand merci également à Micheline, Angélique, Isabelle, Catherine, Delphine, Khaled, Nasser et Pierrepaolo.

J'ai une pensée profonde pour Yves Leroy, qui m'a proposé le sujet et qui a tant œuvré pour que le projet soit initié. Je le remercie pour son soutien durant toute la thèse, à la fois lorsqu'il venait à l'ENS, mais aussi lorsque je descendais au CSTJF de Pau. Par la même occasion, je remercie tous les collaborateurs de Total qui ont soutenu ce projet. Je pense d'abord à Claudine Boehm, puis à Setayesh Zandi, Michel Boisson et Jean-Paul Rolando qui en ont assuré le suivi. Je remercie également Sylviane Vernassa, Atef Onaisi et Matthieu Pellerin pour leurs contributions.

Merci à Elisabeth Bemer, Siavash Ghabezloo, Ian Jackson, Jörg Renner, Vassili Mikhaltsevitch et Ludmila Adam pour avoir partagé leurs expériences avec moi lors de leurs venues à

l'ENS. Je remercie également Christian David de m'avoir fournit des échantillons et permit d'utiliser la carotteuse de Cergy lorsque la notre était en panne.

Une grosse pensée pour les carbonatistes de Marseille avec qui j'ai beaucoup échangé, notamment François Fournier, mais aussi Jean Cochard, Quentin Villeneuve et Dawin Baden, qui en plus, ont eu la gentillesse de me transmettre des blocs/carottes d'Urgoniens.

Je remercie tous les thésards, post-docs, de l'ENS ou de l'IPGP, que j'ai côtoyés lors de ces trois années. Merci à Emilie, Audrey, Kristel, JB (merci pour le coquina), Ben, Hélène, Fred, Tim, les Christians, Xavier, Sarah, François, Aurélien, Jacques, Gianina, et Thomas. Je n'oublie pas Damian, Jérôme, Samson, Angélique, Paoline, les Cédrics, Hanjun, Li, Pierre, Kurama, Laura, Vincent, Rémi, Claire et Kanchana. Merci à vous d'avoir égayé mes journées. Merci également à mes amis Bruno, Isabelle, Paul, Arnaud, Fahd, Rémi, et les Paulines qui m'ont permis de souffler un peu.

Enfin, je tiens à remercier toute ma famille, qui malgré la distance, a toujours su m'encourager. Je remercie tout spécialement mon père et ma mère de m'avoir soutenu avec bienveillance et de m'avoir transmis leur passion des sciences et des roches. Je vous dois énormément.

RÉSUMÉ

Pour les roches saturées, la comparaison entre les mesures ultrasoniques (1 MHz) au laboratoire et les mesures sismiques (100 Hz) ou de diagraphie (10 kHz) sur le terrain n'est pas directe à cause de la dispersion des vitesses des ondes. Les mécanismes impliqués dans la dépendance en fréquence sont les écoulements de fluides à différentes échelles provoqués par le passage de l'onde. La dispersion et l'atténuation des modules élastiques de roches carbonatées ont été étudiées expérimentalement. Les calcaires étudiés sont : un Lavoux, un Indiana intact et après craquage thermique, un calcaire Urgonien de Provence (Rustrel), et un coquina pré-sel du Congo. Les mesures ont été faites sur une large gamme de fréquence, en combinant les techniques d'oscillations forcées (10^{-3} to 10^{2} Hz) et ultrasoniques (1 MHz) dans une presse triaxiale, pour différentes pressions effectives. Le forçage peut être hydrostatique pour mesurer un module d'incompressibilité, ou axial pour mesurer le module de Young et le coefficient de Poisson. Pour étudier l'effet de la viscosité, les mesures ont été faites en condition sèche, puis saturée en glycérine et en eau. Le drainage global et le mécanisme d'écoulement crack-pore ont été caractérisés, en termes d'amplitude de dispersion, d'atténuation viscoélastique, et de fréquence de coupure. Pour nos échantillons, la théorie de Biot-Gassmann s'est montrée valide pour les fréquences sismiques (10-100 Hz) sauf pour l'Indiana craqué thermiquement. La transition liée à des écoulements cracks-pores a été observé pour tous les échantillons sauf le Lavoux. Les fréquences de coupures de ceux-ci sont toutes dans la gamme des fréquences des diagraphies (10 kHz) pour des conditions de saturation en eau. Un modèle simple, combinant poroélasticité et milieux effectifs, a été développé pour prédire la dispersion des modules sur toute la gamme de fréquence, et s'est montré généralement en accord avec les résultats expérimentaux.

ABSTRACT

For fluid-saturated rocks, comparing ultrasonic measurements (1 MHz) in the laboratory and seismic (100 Hz) or logging (10 kHz) measurements in the field is not straightforward due to dispersion of the body-wave velocities. The frequency-dependent mechanisms involved are wave-induced fluid flows that occur at different scales. The dispersion and the attenuation of the elastic moduli of four fluid-saturated carbonate rocks have been studied experimentally. The selected limestones were a Lavoux, an intact and thermally cracked Indiana, a Urgonian limestone from Provence (Rustrel), and a pre-salt coquina from offshore Congo. Measurements were done over a large-frequency range, by the combination of forced oscillations (10^{-3} to 10^{2} Hz) and ultrasonic measurements (1 MHz) in a triaxial cell, at various effective pressures. The forced oscillations were either hydrostatic to deduce the bulk modulus, or axial to deduce Young's modulus and Poisson's ratio. The measurements were done in dry-, glycerin- and water-saturated conditions to investigate the effect of viscosity. For all our samples, the global drainage and the squirt-flow mechanisms were characterized experimentally, in terms of amplitude of dispersion, amount of viscoelastic attenuation, and cut-off frequencies. Biot-Gassmann's theory was found to be valid at seismic frequencies (10-100 Hz) for all the samples except the thermally cracked Indiana. Squirt-flow transitions were observed for all the samples, except the Lavoux. The cut-off frequencies were all in the range of logging frequencies (10 kHz), for water-saturated conditions. A simple model, combining poroelasticity and the non-interaction approximation effective medium, was developed to predict the dispersion of the moduli over the whole frequency range, and was generally in agreement with the experimental results.

CONTENTS

LIST OF FIGURES

LIST OF TABLES

Introduction

INTRODUCTION

Introduction générale

Pour l'exploration géophysique, les outils sismiques ou de diagraphies dans les puits sont incontournables afin d'estimer les propriétés des roches en subsurface. Ces méthodes sont utilisées pour explorer et produire les champs pétroliers, car les vitesses des ondes sismiques sont sensibles aux paramètres critiques des roches reservoirs, tels que la porosité, les lithofaciès, la saturation, le fluide de pore, ou la pression de pore. En revanche, la relation entre vitesses sismiques et ces paramètres est très complexe, et constitue l'enjeu majeur de la recherche en physique des roches actuelle (*Avseth et al.*, 2005).

La présence d'un fluide saturant dans la porosité, si l'on met de côté les effets d'intéractions chimiques, augmente la vitesse des ondes de compression (P) en conditions non-drainées, car le fluide contribue mécaniquement à augmenter la resistance à la compression du milieu. Si les modules élastiques secs sont connus, par exemple par des mesures ultrasoniques au laboratoire, la méthode standard pour évaluer les modules saturés non-drainés est la theorie de Biot-Gassmann. En revanche, les équations de Biot-Gassmann ne sont valides que pour les basses fréquences, où la pression du fluide est homogène dans toute la porosité. Les études faites par *Mavko and Nur* (1975), *O'Connell and Budiansky* (1977) ou par exemple *Mavko and Jizba* (1991), montrent que des gradients de pression peuvent exister à haute fréquence entre des pores très compressibles (fissures) et des pores peu compressibles (pores sphériques). Ce phénomène est ce que l'on nomme communément le mécanisme de "squirt-flow". Les hypothèses de Biot-Gassmann ne sont ainsi plus valides, et les vitesses d'ondes haute fréquence, en milieu saturé, apparaissent plus rapides que les prédictions.

La dépendence en fréquence des vitesses d'ondes P et S pose la question de comment comparer les mesures de terrain basses fréquences (100 Hz pour l'aquisition sismique; 10 kHz pour les diagraphies) avec les mesures conventionnelles hautes fréquences de laboratoire (1 MHz), si les hypothèses de Biot-Gassmann ne sont pas respectées. La dispersion

des vitesses d'ondes est directement liée à la dispersion des modules élastiques qui sont affectés par les écoulements de fluide à differentes échelles dans la porosité (*Batzle et al.*, 2006a; *Müller et al.*, 2010; *Sarout*, 2012). Les études expérimentales basse fréquence au laboratoire sont ainsi essentielles pour comprendre ces mécanismes. Des études ont été réalisées sur les grès (e.g., *Spencer*, 1981; *Spencer and Shine*, 2016; *Winkler*, 1985; *David et al.*, 2013; *Mikhaltsevitch et al.*, 2014; *Pimienta et al.*, 2015a,b, 2016a), mais très peu sur les roches carbonatées (e.g., *Spencer*, 1981; *Batzle et al.*, 2006a; *Adam et al.*, 2006, 2009; *Mikhaltsevitch et al.*, 2016a), alors qu'elles représentent plus de 50% des roches réservoirs d'hydrocarbures.

Les carbonates sont caractérisés par des microstructures complexes et des types poreux hétérogènes (*Lucia*, 1995). Pour une porosité donnée, les vitesses d'ondes P ou S peuvent fortement varier en fonction du type de pores en présence (*Eberli et al.*, 2003). Leurs propriétés élastiques sont affectées par le réseaux poreux et la minéralogie, qui peuvent subir des évolutions dues à la diagénèse (*Fournier and Borgomano*, 2009). Certaines études tentent de comprendre la relation entre vitesses sismiques et porosité (e.g., *Anselmetti and Eberli*, 1993; *Verwer et al.*, 2010), ou de vérifier l'applicabilité des relations de Biot-Gassmann (e.g., *Baechle et al.*, 2009; *Fabricius et al.*, 2010).

Notre étude se concentre sur la dispersion et l'atténuation en fréquence de tous les modules élastiques de quatre calcaires, composés exclusivement de calcite, sur des larges gammes de fréquences, par l'utilisation des méthodes dites d'oscillations forcées (0.01-100 Hz) et de mesures ultrasoniques dans une presse triaxiale. Les deux premiers calcaires, le Lavoux et l'Indiana, sont des roches prélevées en carrière et sont bien connues dans la bibliographie. Les effets d'un craquage thermique ont été testés sur le calcaire Indiana. Le troisième calcaire est un calcaire Urgonien de Provence qui provient de Rustrel (SE, France). L'échantillon est issu d'un faciès à rudistes, analogue à certains faciès des réservoirs pétroliers du Moyen-Orient. Le dernier échantillon est un coquina pré-sel qui provient d'un puit profond en mer au large du Congo.

Le manuscrit est organisé en trois parties. Après une introduction et une présentation du cadre théorique concernant la propagation des ondes dans les milieux poreux à différentes fréquences, la première partie présente notre système expérimental et tous les protocoles utilisés durant l'étude. La deuxième partie se focalise sur les résultats expérimentaux obtenus sur les quatre calcaires. Les dispersions et atténuations de tous les modules élastiques en conditions séche et saturée en eau ou glycérine sont présentées, avec l'effet de la pression effective. Les modules statiques et dynamiques sont également comparés. La troisième partie concerne la modélisation des mécanismes dispersifs à différentes échelles, que l'on confronte avec les résultats expérimentaux.

General introduction

Geophysical exploration with seismic methods or well logging measurements are essential to estimate the properties of the subsurface. They are extensively used to explore and develop oilfields, as the seismic-wave velocities are strongly sensitive to the critical parameters of the reservoir rock, such as porosity, lithofacies, saturation, pore fluid, or pore pressure. However, the link between seismic velocity and these rock parameters is complex, and has been the main focus of the research in rock physics (*Avseth et al.*, 2005).

The presence of fluid in the porosity, if we put aside chemical interactions that may affect the matrix, increases the P-wave velocity as the fluid contributes to mechanically increase the stiffness of the rock. If the dry properties of the rock are known, for example from ultrasonic measurements in the laboratory, the standard procedure to estimate the fluid-saturated properties is Biot-Gassmann's fluid substitution theory. However, Biot-Gassmann's relation is only valid for low frequencies, where the pore pressure is homogeneous. Studies from *Mavko and Nur* (1975), *O'Connell and Budiansky* (1977) or *Mavko and Jizba* (1991) for example, showed that wave-induced pressure gradients are possible at high frequency between compliant (e.g. cracks) and stiff pores. This phenomenon is what we refer to as the "squirt mechanism". Biot-Gassmann's assumption are therefore violated, and the high-frequency saturated velocities are greater than expected.

The frequency-dependence of the P- and S-wave velocities, and the potential violation of Biot-Gassmann's assumptions, raises questions on how to compare low-frequency field measurements (100 Hz for seismic data; 10 kHz for sonic logs) to conventional high-frequency ultrasonic measurements in the laboratory (1 MHz). The dispersion of the elastic wave velocities is directly related to the dispersion of the elastic moduli, which are affected by fluid flows occurring at different scales in the porosity (*Batzle et al.*, 2006a; *Müller et al.*, 2010; *Sarout*, 2012). Understanding the underlying mechanisms requires the ability to measure the low-frequency moduli in the laboratory. Numerous studies of such have been done on sandstones (e.g., *Spencer*, 1981; *Spencer and Shine*, 2016; *Winkler*, 1985; *David et al.*, 2013; *Mikhaltsevitch et al.*, 2014; *Pimienta et al.*, 2015a,b, 2016a), but only few on carbonate rocks (e.g., *Spencer*, 1981; *Batzle et al.*, 2006a; *Adam et al.*, 2006, 2009; *Mikhaltsevitch et al.*, 2016a), while they represent more than 60% of the reservoir rocks for hydrocarbons.

Carbonate rocks are characterized by complex microstructures and heterogeneous pore types (*Lucia*, 1995). For a given porosity, carbonate rocks were shown to exhibit a wide range of P-wave and S-wave velocities, due to the large variety of pore types (*Eberli et al.*, 2003). Their elastic properties are affected by the pore network and the mineralogy, which can be modified through diagenetic processes (*Fournier and Borgomano*, 2009). Several studies have attempted to understand the relationship between seismic wave velocity and porosity (e.g., *Anselmetti and Eberli*, 1993; *Verwer et al.*, 2010), or to verify the applicability of Biot-Gassmann's fluid substitution theory (e.g., *Baechle et al.*, 2009; *Fabricius et al.*, 2010).

In this study, we investigated the dispersion and attenuation of the elastic moduli of 4 pure calcite limestones, over a large frequency range (0.01-100 Hz) using forced oscillations and ultrasonic velocities in triaxial cells. The first two limestones, the Lavoux and the Indiana, are quarry limestones and are very well known in the bibliography. The effect of thermal cracking was investigated on the Indiana limestone. The third limestone is a Urgonian limestone from Rustrel, Provence (SE, France). The rudist-facies outcrops from which it was cored are close analogues to east-Arabic plate reservoirs. The last sample is a pre-salt coquina sample cored in a deep well offshore Congo.

The manuscript is organized in 3 main parts. After an introduction and a overview of the framework regarding wave propagation in porous-saturated media at different frequencies, the first part presents our experimental setups and all the experimental protocols used during this study. The second part focuses on the experimental results obtained for the limestones. The dispersion and attenuation of all the elastic moduli under dry-, water- and glycerin-saturated conditions are reported, with the effect of effective pressure. Static and dynamic moduli are also compared. The third part focuses on modeling the dispersive mechanisms at different scales, with a comparison with the experimental results.

CHAPTER 1

FREQUENCY DEPENDENCE AND ATTENUATION OF WAVE VELOCITIES

1.1 Résumé

Nous présentons dans ce chapitre le cadre théorique de la propagation des ondes à différentes fréquences dans les milieux poreux saturés. La propagation des ondes se résout dans le cadre de l'élasticité linéaire, où la vitesse est reliée aux modules élastiques et à la densité du milieu. Le comportement élastique linéaire des roches n'est valide que pour des petites déformations ($\epsilon < 10{-}6$). La saturation en fluide va influencer les propriétés élastiques du milieu poreux et par extension la vitesse des ondes. Le fluide contribue mécaniquement à la résistance à la compression du milieu.

La contribution du fluide à basse fréquence, lorsque la pression est homogène, se résout dans le cadre de la poroélasticité quasi-statique. Pour les roches sédimentaires, les effets inertiels dans le fluide étant négligeables en dessous de 1.2 MHz, nous pouvons ignorer le domaine dynamique de la poroélasticité. Deux conditions aux limites sont prévues par la poroélasticité, les conditions drainées où le fluide peut librement s'échapper du volume et maintenir la pression de pore constante, et les conditions non-drainées où la masse de fluide est constante dans le volume et la pression de pore augmente sous l'effet d'une contrainte extérieure. Les modules élastiques saturés, dans les conditions non-drainées, se calculent avec les équations de Biot-Gassmann. Expérimentalement, il est possible de voir une transition entre un régime drainé et non-drainé en fréquence, pour des petits échantillons à conditions de bords ouvertes. Cela dépend du temps de diffusion global dans la roche, qui est relié à la perméabilité et à la taille de l'échantillon.

Lorsque le milieu possède des fissures compressibles connectées à des pores ronds moins compressibles, un écoulement se produit des premières vers les seconds afin d'équilibrer la pression. À cause de la viscosité du fluide, il est possible que cet écoulement, dit de «

squirt-flow », n'ait pas le temps d'équilibrer la pression à haute fréquence. Le fluide est comme figé dans la porosité et des gradients de pressions importants sont maintenus dans les fissures, se qui augmente d'autant plus la résistance à la compression de la roche, et par extension la vitesse des ondes. C'est ce que l'on défini par le régime non-relaxé, qui se résout dans le cadre des milieux effectifs, où les inclusions sont considérées comme isolées. Nous pouvons ainsi définir trois régimes d'écoulements : drainé, non-drainé et non-relaxé. La transition d'un régime d'écoulement à l'autre, génère une dispersion des modules élastiques, qui s'accompagne d'une dissipation énergétique dans la viscosité du fluide. La roche peut être assimilée à un matériaux viscoélastique pour lequel on va quantifier cette dissipation par l'atténuation Q^{-1} (inverse du facteur de qualité). Ces régimes d'écoulement ont été bien identifiés expérimentalement sur les grès, tel que le grès de Fontainebleau. En revanche, peu de mesures existent sur les roches carbonatées qui présentent des microstructures bien plus complexes et hétérogènes.

En laboratoire, plusieurs techniques existent pour mesurer la dispersion des modules élastiques sur des larges gammes de fréquences, telles que les oscillations forcées, la barre résonante où les ultrasons. Chaque technique présente des avantages et des inconvénients. Les oscillations forcées permettent d'étudier les basses fréquences et les fréquences sismiques (0.01-100 Hz). La barre résonante ne donne généralement qu'une seule fréquence de résonance autour des fréquences de diagraphie (10 kHz). Enfin, les ultrasons donnent une mesure à très haute-fréquence (1 MHz), qui correspond en général à un régime non-relaxé. Au laboratoire de l'ENS de Paris, nous combinons les techniques d'oscillations forcées et d'ultrasons dans une pressure triaxiale.

1.2 Elasticity and wave propagation in isotropic media

For a purely linear elastic material, Hooke's law relates the stress and the strain by:

$$\sigma = \mathbf{C} : \varepsilon, \tag{1.1}$$

where $\mathbf{C}$ is the fourth rank tensor of the elastic moduli, or elastic stiffness tensor. $\mathbf{C}$ can be inverted to $\mathbf{S} = \mathbf{C}^{-1}$ the elastic compliance tensor. In isotropic media, $\mathbf{C}$ is completely defined with two independent elastic moduli. Equation 1.1 simplifies to:

$$\varepsilon = \frac{1+\nu}{E}\sigma - \frac{\nu}{E}\mathrm{tr}(\sigma)\mathrm{I}, \tag{1.2}$$

or with index notations:

$$\varepsilon_{ij} = \frac{1+\nu}{E}\sigma_{ij} - \frac{\nu}{E}\sigma_{ij}\delta_{ij}, \tag{1.3}$$

where E and ν are respectively the Young's modulus and the Poisson's ratio, and δ_{ij} is Kronecker's symbol ($\delta_{ij} = 1$ if $i = j$, $\delta_{ij} = 0$ if $i \neq j$). In a uniaxial loading (σ_{33}), the Young's modulus relates the axial stress to the axial strain on the sample:

$$\sigma_{33} = E\varepsilon_{33}, \tag{1.4}$$

while the Poisson's ratio relates the perpendicular (or radial) strains to the axial strain:

$$\varepsilon_{11} = \varepsilon_{22} = -\nu\varepsilon_{33}. \tag{1.5}$$

The bulk modulus (K) relates a hydrostatic stress to the volumetric strain by:

$$\frac{\sigma_{kk}}{3} = \frac{E}{3(1-2\nu)}\varepsilon_{kk} = K\varepsilon_{kk}, \tag{1.6}$$

while the shear modulus (G) relates the shear stress (σ_{ij}) to the engineering shear strain ($\gamma_{ij} = 2\varepsilon_{ij}$):

$$\sigma_{ij} = \frac{E}{2(1+\nu)}2\varepsilon_{ij} = G\gamma_{ij}. \tag{1.7}$$

It is often convenient to work with the inverse of the bulk modulus ($1/K$), which is defined as the compressibility.

In elastic media, the propagation velocity of the compressive P-wave and shear S-wave are directly related to the previous elastic moduli and the medium density. A planar wave that propagates into a medium characterized by the stiffness tensor $\mathbf{C}$ creates a deformation $\varepsilon = grad\,\overrightarrow{u}$, where $\overrightarrow{u}$ is the displacement vector of the particle. By combining Hooke's law

(Equation 1.1) and Newton's second law, $\rho\frac{\partial^2\vec{u}}{\partial t^2} = \text{div}\sigma$, we obtain:

$$\rho\frac{\partial^2\vec{u}}{\partial t^2} = \text{div}\left(\mathbf{C} : \text{grad}\vec{u}\right), \tag{1.8}$$

where ρ is the density of the medium. In a linear elastic isotropic medium, for the compressive P-wave, the direction of the propagation (Ox) and of the particle displacement are the same, and $\vec{u} = u_x(x,t)\vec{i}$. Equation 1.8 becomes:

$$\rho\frac{\partial^2 u_x}{\partial t^2} = \frac{E(1-\nu)}{(1+\nu)(1-2\nu)}\frac{\partial^2 u_x}{\partial x^2}, \tag{1.9}$$

from which we can deduce the P-wave velocity:

$$V_P = \frac{\partial x}{\partial t} = \sqrt{\frac{E(1-\nu)}{(1+\nu)(1-2\nu)\rho}} = \sqrt{\frac{K+\frac{4}{3}G}{\rho}}. \tag{1.10}$$

For the shear S-wave, the displacement of the particle is perpendicular to the direction of propagation, such that $\vec{u} = u_y(x,t)\vec{j}$. From Equation 1.8, the shear wave velocity is given by:

$$V_S = \sqrt{\frac{G}{\rho}}. \tag{1.11}$$

Elastic properties can therefore be inverted from wave velocities if the density ρ of the medium is known. This technique is generally used in laboratory by measuring the ultrasonic P- and S-wave velocities.

In porous rocks, the previous equations stand if the wavelength is larger than the grain diameters, pores or cracks. If the wavelength approaches the size of the heterogeneity, scattering effects may occur (*Sarout*, 2012). By analogy with seismic-field measurements, if the wavelength becomes even much smaller than the heterogeneity, then ray theory would apply. Our measurements are limited to ultrasonic frequencies (1 MHz). If the wave velocity is around 3000 m/s, then the wavelength at 1 MHz is of $\lambda = 3\,\text{mm}$, which is higher than the grain or pore sizes of the samples we selected for our study (maximum 500 µm). We can therefore exclude scattering effects from the scope of our study.

In dry conditions, within the small deformation hypothesis ($\varepsilon \sim 10^{-6}$), rocks behave like linear elastic media. This is the case for the body wave propagation. The elastic moduli relative to the wave propagation are the dry dynamic moduli, and the density is the density of porous medium taking in account the mineral and the porous voids. For large deformations obtained for quasi-static experiments such as triaxial loadings, the elastic moduli are the static moduli, which are generally lower than the dynamic because of nonlinear effects due to microheterogeneity (*Ide*, 1936; *Fjær*, 2009). Therefore they are not relevant moduli for the wave propagation.

1.3 Poroelasticity: fluid substitution at low frequency

Porous rocks in the field can be saturated with fluids, such as water or hydrocarbons. The extension of elasticity to porous saturated media is given by the theory of poroelasticity, which was developed by *Biot* (1956a,b) and *Gassmann* (1951), and reformulated by *Rice and Cleary* (1976). If the fluid is unable to flow in or out of the studied volume, considered as a representative elementary volume (REV) of the rock, it will contribute to increase the bulk modulus of the medium when submitted to a stress field, such as a propagating wave. This type of condition on the fluid's boundaries is called the "undrained" conditions, by opposition to "drained" conditions where the fluid is allowed to go in and out of the REV to maintain a constant pressure p_f. In the drained conditions, the case where $p_f = 0$ is equivalent to dry conditions, if chemical interactions are negligible.

1.3.1 Drained conditions

The effective dry compressibility (inverse of K_{dry}) of a porous solid is written as (*Mavko et al.*, 2009):

$$\frac{1}{K_{dry}} = \frac{1}{K_m} + \frac{\phi}{v_p}\frac{\partial v_p}{\partial \sigma_{hyd}}\bigg|_{dry}, \tag{1.12}$$

where K_m is the bulk modulus of the solid mineral material, ϕ is the porosity, v_p is the pore volume and $\partial v_p/\partial \sigma_{hyd}|_{dry}$ is the derivative of v_p with respect to externally applied hydrostatic stress σ_{hyd}. We can define the dry pore-space stiffness $K_\phi = v_p/(\partial v_p/\partial \sigma_{hyd})|_{dry}$ so that the previous equation rewrites:

$$\frac{1}{K_{dry}} = \frac{1}{K_m} + \frac{\phi}{K_\phi}. \tag{1.13}$$

The compressibility of the porous medium is equal to the intrinsic mineral compressibility plus an additionnal compressibility due to the pore space. We can also define the Biot coefficient α, such as (*Mavko et al.*, 2009):

$$K_{dry} = K_m(1-\alpha). \tag{1.14}$$

From the previous expression of K_{dry}, we can deduce that:

$$\alpha = \frac{\phi K_{dry}}{K_\phi} = \frac{\Delta v_p}{\Delta V}\bigg|_{dry}, \tag{1.15}$$

The Biot coefficient describes the ratio between pore-volume change (Δv_p) and bulk-volume change (ΔV) for the dry or drained REV.

For a given confining pressure $P_c = \sigma_{hyd}$ applied to the REV, the presence of a pressurized fluid in the porosity, of pressure p_f, will modify the effective stress state of the REV.

The notion of effective pressure P_{eff} is essential in poroelasticity, and is given by:

$$P_{eff} = P_c - \alpha p_f, \tag{1.16}$$

The effective stress state σ_{eff} of the REV is therefore:

$$\sigma_{eff} = \sigma - \alpha p_f \mathrm{I}. \tag{1.17}$$

The drained elastic moduli, which depend on the effective stress state, are given for an effective pressure. Experimentally, the comparison of dry moduli and saturated drained moduli (with a pore pressure), is only possible at equivalent effective pressure. The effective pressure should not be confused with the differential pressure P_{diff} given by:

$$P_{diff} = P_c - p_f. \tag{1.18}$$

However, since in general $K_d << K_m$, the Biot coefficient α is close to 1, and $P_{diff} \approx P_{eff}$.

1.3.2 Undrained conditions

In undrained conditions, the pore pressure build-up (dp_f) in the fluid when a hydrostatic stress increment ($d\sigma_{hyd}$) is applied on the REV are related by Skempton's coefficient B. If we assume that the pore pressure is homogeneous in the whole connected pore space, then B is given by (*Mavko et al.*, 2009):

$$B = \left.\frac{dp_f}{d\sigma_{hyd}}\right|_{undrained} = \frac{1}{1 + K_\phi \left(\frac{1}{K_{fl}} - \frac{1}{K_m}\right)} = \frac{1}{1 + \phi \left(\frac{1}{K_f} - \frac{1}{K_m}\right) \left(\frac{1}{K_{dry}} - \frac{1}{K_m}\right)^{-1}}, \tag{1.19}$$

where K_f is the fluid's bulk modulus. The hypothesis of homogeneous pore pressure, or isobaric pressure, is possible if the pore space deformation is slow enough to relax any pressure gradient in the heterogeneous pore space. This is what we can define as a relaxed regime. With respect to wave propagation, these conditions are valid for low frequencies. The bulk modulus of the undrained medium K_u is then given by Biot-Gassmann's equation (*Gassmann*, 1951):

$$K_u = K_d + \frac{K_f \left(1 - \frac{K_d}{K_m}\right)^2}{\phi + \left(\left(1 - \frac{K_d}{K_m}\right) - \phi\right) \frac{K_f}{K_m}}. \tag{1.20}$$

Since a shear stress does not change the volume of the medium, the fluid does not contribute to additional stiffness. Therefore (*Gassmann*, 1951):

$$G_u = G_d. \tag{1.21}$$

The five essential conditions of the applicability of Biot-Gassmann's equations are: (1) ϕ represents a connected pore space fully saturated; (2) the REV is in undrained conditions; (3) the fluid is isobaric within ϕ (low frequency); (4) no chemical interaction occur between the fluid and the solid; (5) the solid is monomineralic.

In fact, the Gassmann limit represents the lower frequency limit (quasi-static) of the generalized poroelasticity developed by *Biot* (1956a), which also includes dynamic (inertial) poroelasticity at higher frequencies (*Biot*, 1956b). The quasi-static and the dynamic domains of poroelasticity are separated by Biot's characteristic frequency:

$$f_b = \frac{\eta\phi}{2\pi\rho_f\kappa}, \tag{1.22}$$

where η is the dynamic viscosity of the fluid, ρ_f the fluid's density and κ the intrinsic permeability. Below f_b, the porous medium response is dominated by viscous flow, and above f_b, it is dominated by inertial drag and no flow occurs. In water saturated conditions ($\eta = 10^{-3}$ Pa.s, $\rho_f = 1000\,\mathrm{kg.m^{-3}}$), for a porosity of 7.5% and a permeability of $10^{-14}\,\mathrm{m^2}$, representing the extreme values we shall encounter in the samples of this study, Biot's characteristic frequency is at minimum of $f_b = 1.2$ MHz, which is superior to the ultrasonic frequencies. Therefore, we exclude the dynamic poroelasticity from the scope of our work, and shall consider solely the viscous driven flows.

1.3.3 Experimental drained/undrained regimes

In laboratory, the low-frequency moduli of saturated small samples ($\sim 80\,mm$ length) depend on the type of boundary condition that is at play: either drained or undrained. To measure dynamic drained moduli at low-frequency, any increase of pore pressure at the center of the sample should have time to diffuse towards the drained boundaries. Drained boundaries can be achieved by a constant-pressure regulation from a pump, or with very large dead-volumes (*Pimienta et al.*, 2016b). This diffusion of pore pressure throughout all the REVs towards the boundary conditions can be defined as a global-drainage flow. *Cleary* (1978) defined it as the global diffusion between adjacent continuum elements. This flow is a viscous-controlled flow through the permeability of the sample. Therefore, it should not be confused with the inertial global flow defined by *Biot* (1956a) relevant to static/dynamic poroelasticity, which is characterized by the cut-off frequency f_b (Equation 1.22). For a sample of characteristic length L, *Cleary* (1978) showed that the cut-off frequency of this global diffusion is given by;

$$f_{undrained} = \frac{4\kappa K_d}{\eta L^2}. \tag{1.23}$$

At low-frequency, $f_{undrained}$ separates the experimental drained regime from the undrained regime, only in the case drained boundary conditions around the sample. Pure undrained conditions can be achieved at lower frequencies if a valve is placed at the nearest of the

sample in the drainage circuit, or by sealing completely all the faces of the sample after saturating it. However, a residual dead volume between the valve and the sample will still induce a partial drainage (*Pimienta et al.*, 2016b).

1.4 Effective medium theory

Rocks are heterogeneous materials that can be composed of various minerals with different properties. Moreover, they can bear a heterogeneous pore-space that can be saturated with a fluid. Since we deal with mixtures of two or more materials, effective medium theories have been developed in order to predict the effective elastic properties. The latter do not dependent solely on the properties of the individual constituents, but also depend on geometry. If inclusions of a second material are embedded in the first material (matrix), then the orientations and the aspect ratios of these inclusions will affect the effective properties.

We can distinguish two families of effective medium theories: the bounds and the mixing laws. Bounds are a mean to find the lower and upper bounds of the effective properties considering solely the intrinsic properties of the constituents and their volume fractions. Mixing laws are a mean to give estimates of the elastic properties with the addition of the geometrical information of the constituents, their distribution and their interactions.

1.4.1 Bounds

The simplest bounds are the Voigt (upper) and Reuss (lower) bounds (*Voigt*, 1889; *Reuss*, 1929). They correspond respectively to the arithmetic and the harmonic averages of the elastic moduli of each of the N phases in presence in the medium:

$$K^{+}_{Voigt} = \sum_{i=1}^{N} f_i K_i \quad \text{and} \quad \frac{1}{K^{-}_{\mathrm{Re}uss}} = \sum_{i=1}^{N} \frac{f_i}{K_i}, \tag{1.24}$$

where f_i is the volume fraction of phase i. They do not depend upon any geometrical consideration, either for the shapes of the inclusions or their spacial distribution. They simply use the volume fractions of each phase in presence. The interval between the bounds gets smaller, only if the contrast between the N phases moduli gets smaller. *Hill* (1952) proposed to average them to give the Voigt-Reuss-Hill average to approach the effective properties.

More sophisticated bounds were developed by *Hashin and Shtrikman* (1963), which considers solely two phases (f_1 and f_2) arranged as a mixture of spheres, each sphere's core

composed by the first material and each sphere's shell composed by the second.

$$\begin{aligned} K_{HS}^{\pm} &= K_1 + \frac{f_2}{(K_2-K_1)^{-1}+f_1\left(K_1+\frac{4}{3}G_1\right)^{-1}} \\ G_{HS}^{\pm} &= G_1 + \frac{f_2}{(G_2-G_1)^{-1}+2f_1(K_1+2G_1)\Big/\left[5G\left(K_1+\frac{4}{3}G_1\right)\right]} \end{aligned} . \tag{1.25}$$

The upper and lower bounds are found by inverting the roles of the two materials in the sphere mixture. They are the sharpest possible bounds attainable for a biphasic isotropic medium, without using any geometrical information about the constituents.

1.4.2 Mixing laws

Mixing laws use geometrical information about the constituents, their distribution and their interactions, to predict more accurately the effective properties of the composite material. *Eshelby* (1957) was the first to demonstrate that the stress-tensor within an ellipsoidal inclusion is homogeneous when a homogeneous stress is applied at infinity. Because the stress-tensor is homogeneous, determining the inclusion's strain, and therefore the elastic moduli, becomes straightforward. The stiffness of a single ellipsoidal inclusion, either spherical or with a crack-like low aspect ratio, are given by:

$$\frac{1}{K_{\phi-sphere}} = \frac{1}{K_m}\frac{3(1-\nu)}{2(1-2\nu)} \quad \text{and} \quad \frac{1}{K_{\phi-crack}} = \frac{1}{K_m\xi}\frac{4(1-\nu^2)}{3\pi(1-2\nu)}, \tag{1.26}$$

where $\xi = a/c$ is the aspect ratio of the ellipsoidal crack, c being the largest diameter and a the height. *Walsh* (1965) gave the effective bulk modulus in the case of a uniform distribution of randomly oriented penny-shaped cracks:

$$\frac{1}{K} = \frac{1}{K_m}\left(1+\frac{16}{9}\frac{1-{\nu_m}^2}{1-2\nu_m}\rho\right), \tag{1.27}$$

where ρ is the crack density parameter. For n inclusions of length c_i in a volume V, the crack density is given by:

$$\rho = \sum_{i=1}^{n}\frac{{c_i}^3}{V}. \tag{1.28}$$

For higher concentration of inclusions, *O'Connell and Budiansky* (1974) developed the self-consistent approximation (SCA) scheme for randomly orientated ellipsoidal cracks to account for interactions between the inclusions. The approach uses the result of *Eshelby* (1957): the deformation of a medium containing similar ellipsoidal inclusions is considered equivalent to the deformation of a medium with one inclusion, in which the background is

replaced by the as-yet-unknown effective medium (*Mavko et al.*, 2009), which gives:

$$\frac{K_{SCA}}{K_m} = 1 - \frac{16}{9}\left(\frac{1-{\nu_{SCA}}^2}{1-2\nu_{SCA}}\right)\rho \tag{1.29}$$

$$\frac{G_{SCA}}{G_m} = 1 - \frac{32}{45}\frac{(1-\nu_{SCA})(5-\nu_{SCA})}{(2-\nu_{SCA})}\rho. \tag{1.30}$$

Berryman (1980, 1995) extended this approach to N different inclusions. One major drawback of this method, is that the predicted moduli decrease rapidly with increasing pore/crack concentration. *Cleary* (1978) stated that the SCA scheme overestimates interaction energy, resulting in a abnormally strong decrease with increasing pore/crack concentration. A differential self-consistent approach was then suggested.

The differential effective medium (DEM) model computes the effective moduli after an iteration process where the inclusions are added one by one into the matrix. At each step, the inclusion is added to a homogeneous matrix, which in turn gives a new homogeneous matrix that will host the next inclusion. The effective properties are computed at each step to serve as host to the next inclusion. This allows for a better control over the interactions between the inclusions (*Guéguen et al.*, 1997). However, the final effective moduli strongly dependent upon the order in which the inclusions were added. To counter this, it is possible to apply a Monte-Carlo simulation with the same number and type of inclusions, but added in different orders. *Le Ravalec and Guéguen* (1996) showed that just over a hundred of simulations are necessary to obtain a converging solution. They also showed that the predictions are consistent, only if the aspect ratios are not too small.

The last effective medium we shall present here is the non-interaction approximation developed by *Kachanov* (1993). *Kachanov* (1993) considers two possible interactions between two parallel inclusions: (1) an amplifying effect if the cracks are aligned; (2) a shielding effect if the cracks are facing each other. The hypothesis of non-interaction considers that for random distributions of inclusions, there should be, statistically, an equivalent proportion of amplifying and shielding effects. The two interactions would then compensate each other, so that the effective elastic properties can be calculated without considering any interaction (*Kachanov*, 1993). One major advantage compared to DEM, is that it is not restricted to randomly oriented cracks, but applies to arbitrary orientational distributions (*Kachanov*, 1993). It can therefore be used for anisotropic materials. Moreover, since interactions are ignored, the contribution of cracks (ρ) can be added to the contribution of spherical pores of porosity ϕ_p, and the contribution of a saturating fluid can be added through a fluid/solid coupling parameter δ. In the fully-saturated isotropic case, i.e., for randomly oriented cracks mixed with spherical pores, the effective moduli are given by

(*Fortin et al.*, 2007):

$$\frac{K_m}{K} = 1 + \phi_p \frac{3(1-\nu_m)}{2(1-2\nu_m)} \left(\frac{\delta_p}{1+\delta_p} \right) + \rho \frac{16(1-{\nu_m}^2)}{9(1-2\nu_m)} \left(\frac{\delta_c}{1+\delta_c} \right) \tag{1.31}$$

$$\frac{G_m}{G} = 1 + \phi_p \frac{15(1-\nu_m)}{7-5\nu_m} + \rho \left[\frac{16(1-\nu_m)}{15(1-\frac{\nu_m}{2})} + \frac{32(1-\nu_m)}{45} \left(\frac{\delta_c}{1+\delta_c} \right) \right], \tag{1.32}$$

where the fluid/solid coupling parameters for the spherical pores (δ_p) and for the cracks (δ_c) are given by:

$$\delta_p = \frac{2E_m}{9(1-\nu_m)} \left(\frac{1}{K_f} - \frac{1}{K_m} \right) \quad \text{and} \quad \delta_c = \frac{E_m \pi \xi}{4(1-{\nu_m}^2)} \left(\frac{1}{K_f} - \frac{1}{K_m} \right). \tag{1.33}$$

For dry conditions ($K_f = 0$) the ratio $\delta/(1+\delta)$ tends to 1, and if we fill the inclusions with the matrix materials ($K_f = K_m$), the ratio $\delta/(1+\delta)$ tends to 0 and we obtain $K = K_m$. *Sayers and Kachanov* (1995) and *Schubnel and Guéguen* (2003) showed that this non-interacting approximation presented very satisfactory results. *Kachanov* (1993) compared his model with SCA and DEM methods, and with a numerical simulation, for a medium with randomly distributed and oriented cracks. The numerical simulations were in better agreement with the non-interaction approach (*Kachanov*, 1993).

1.5 Dispersion and attenuation mechanisms

1.5.1 Definitions

Dispersion refers to the variation of the elastic moduli, or the seismic wave velocities, with frequency. When there is dispersion of an elastic modulus M, the rheology of the medium is similar to that of a viscoelastic material (*O'Connell and Budiansky*, 1977). One can measure a phase shift $\Delta\phi$ between the stress and the strain response related to the modulus M. Since M relates the stress and the strain, it can be written in the form of a complex number:

$$M = M_R + iM_I. \tag{1.34}$$

During stress oscillations, such as the passing of a wave, if E is the maximum elastic energy stored in one cycle, and ΔE is the dissipated elastic energy during that cycle, then by analogy to viscoelastic media, we can define the inverse of the quality factor (Q_M^{-1}) of the linear dynamic response related to the complex modulus M by (*O'Connell and Budiansky*, 1978):

$$Q_M^{-1} = \frac{1}{2\pi} \frac{\Delta E}{E} = \frac{M_I}{M_R} = \tan(\Delta\phi). \tag{1.35}$$

For a viscoelastic medium, a body wave of angular frequency ω related to the modulus M, follows the propagation equation along the x-axis:

$$u = u_0 e^{-ax} e^{i\omega(t-\frac{x}{V_0})}, \tag{1.36}$$

where V_0 is the wave velocity, $M = K + (4/3)G$ for the P-wave and $M = G$ for the S-wave. a is the attenuation coefficient. It translates the attenuation of the wave's energy during propagation: along the x-axis, the wave's energy decreases according to e^{-2ax}. Q_M^{-1} and a are related by:

$$a = \frac{Q_M^{-1}\omega}{2V_0}. \tag{1.37}$$

For the sake of comparison between different samples, the term "attenuation" will refer solely to Q_M^{-1} as it depends exclusively on the energy dissipation at a given frequency, while a also depends on the wave velocity that can vary for different rocks. For purely elastic material, there is no phase shift between the stress and the strain ($\Delta\phi = 0$), therefore there is no attenuation ($Q^{-1} = 0$). The more the material moves away from pure elasticity towards pure viscosity, the higher Q^{-1} gets. However, since the wave-induced fluid flows are within the frame of Biot's theory of poroelasticity, the analogy to a viscoelastic material to calculate the attenuation is not straightforward. *Solazzi et al.* (2016) investigated whether this analogy is valid and demonstrated, from numerical calculations in the theoritical framework of poroelasticity, that the analogy is true for low attenuation values, and slightly deviates when $Q^{-1} \geq 0.1$ (less than 5% for 0.1) in a cracked medium (*Solazzi et al.*, 2016).

Different mechanisms can lead to seismic wave attenuation and dispersion. One of the major causes of attenuation in heterogeneous porous media is wave-induced fluid flow (WIFF). A review of the different WIFF mechanisms has been presented by *Müller et al.* (2010). Effects of patchy saturation or mesoscopic fractures are out of the scope of our study, since we studied fully-saturated homogeneous samples, with heterogeneities smaller than 1 mm. Scattering can also be considered as a dispersive mechanism (*Sarout*, 2012), but it only occurs when the wavelength is comparable to the size of the heterogeneities. For the selected samples of the study, the ultrasonic wavelengths are within the range of 4-5 mm, which excludes scattering effects from our study. In fully-saturated conditions, two types of mechanisms are to be considered, the inertial and the viscous effects. The inertial effects are taken in account within the generalized poroelasticity of *Biot* (1956a). Attenuation would occur from the transition to the quasi-static limit (Biot-Gassmann) to the dynamic limit, around Biot's cut-off frequency f_b (Equation 1.22). We saw previously in Section 1.3.2 that for all the samples we shall encounter in this study, Biot's cut-off frequency is higher than 1.2 MHz in water-saturated conditions. Since we will study low frequencies (10 Hz - 10 kHz) up to the ultrasonic measurements (1 MHz), we shall ignore inertial effects and remain within the framework of the quasi-static limit of poroelasticity. Our study will focus

solely on viscous-driven fluid flows at different scales that can generate attenuation.

1.5.2 Viscous driven fluid-flow regimes in fully-saturated conditions

When the porous medium is submitted to an oscillating stress field, the deformation of the solid frame may induce a fluid pressure variation if the fluid has no time to diffuse through the pore network. In fully saturated conditions, viscous diffusion can occur at different scales (*Sarout*, 2012): global within the wavelength scale, or local within a representative elementary volume (REV). Local flow, or squirt flow, may equalize the fluid pressure between compliant cracks and rounded pores within one REV (*Mavko and Jizba*, 1991), whereas the global-drainage flow equalizes pressure through all the connected REVs. Three fluid-flow regimes can therefore be considered from this: drained, undrained and unrelaxed regimes (*Pimienta et al.*, 2016c) (Figure 1.1).

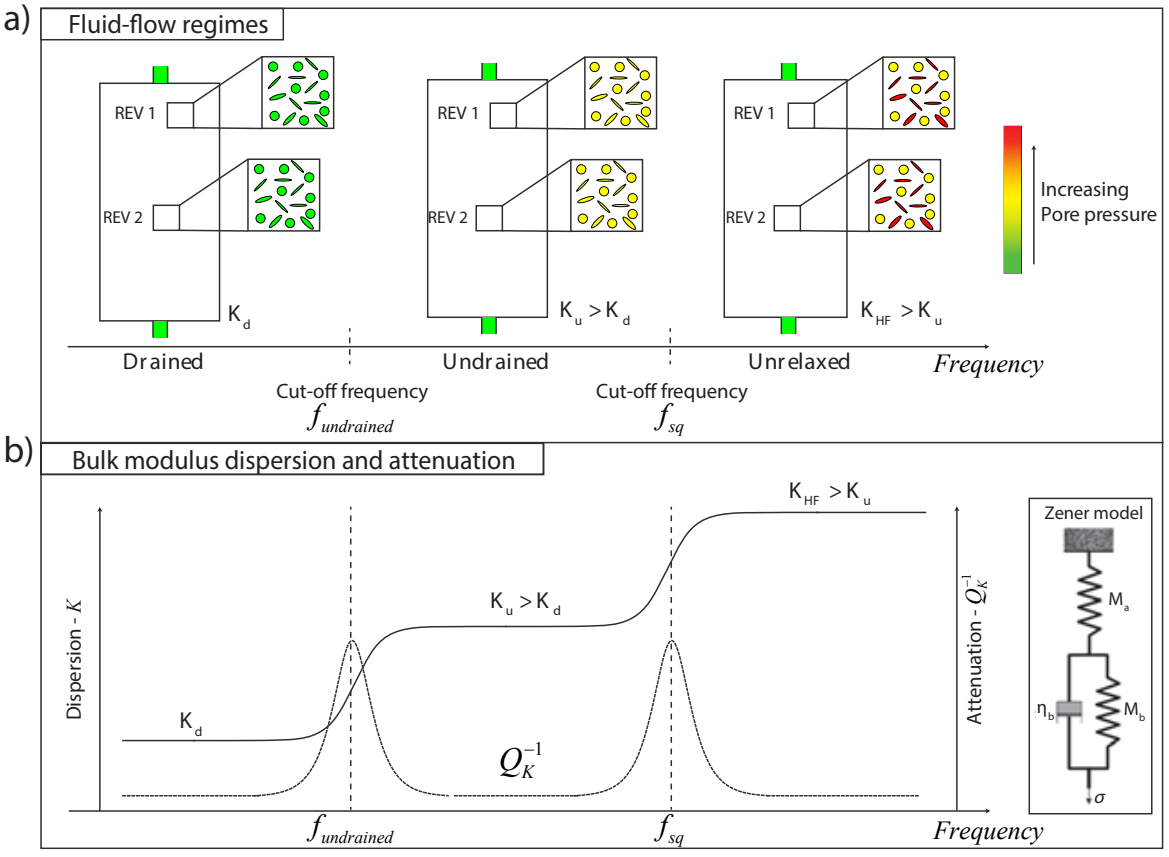

Figure 1.1: (a) Drained, undrained and unrelaxed fluid-flow regimes, and (b) related bulk modulus dispersion and attenuation. The attenuation is calculated here by Zener model. Modified after *Pimienta et al.* (2015a).

The undrained and unrelaxed regimes refer to respectively the saturated isobaric and the saturated isolated regimes described by *O'Connell and Budiansky* (1977). The drained regime occurs when the fluid has time to diffuse by local and global flow through all the

REVs, i.e., when $f < f_{undrained}$ (Figure 1.1). The elastic properties of the porous medium are similar to dry conditions if no chemical interaction occur. When the frequency increases beyond $f_{undrained}$, the fluid stops diffusing at wavelength scale, letting place to the undrained regime. In this regime, the REVs are as disconnected from each other and remain isobaric. Because of the deformation of the frame, the fluid pressure increases in the porosity, therefore increasing the stiffness of the medium (Figure 1.1). The two previous regimes are well accounted for in the quasi-static poroelasticity (*Gassmann*, 1951).

When the frequency is high enough, pressure may not equilibrate by local flow within the REVs. This is what we define as the unrelaxed regime. A pore space can be composed with compressible cracks connected to stiff rounded pores. Therefore, the volumetric deformation of the cracks will be greater than the pores, generating a flow attempting to relax the induced pressure gradient. This viscous-dominated flow is called squirt-flow. It can be assimilated to a Hagen-Poiseuille flow, and if the deformation is too rapid, a relative high pressure can be maintained in the crack because of the viscous drag. In this regime, the fluid can be considered immobile in the cracks with high pressure gradients (Figure 1.1). The unrelaxed pressure gradients will further increase the apparent stiffness of the medium (*Dvorkin et al.*, 1995; *Shafiro and Kachanov*, 1997).

Effective medium theories are possible tools to predict the elastic properties in this last regime, since the fluid is immobile and can be considered as a solid with a nil shear modulus (e.g., *Adelinet et al.*, 2011). If we model a crack with a penny-shape geometry of aspect ratio ξ (height over diameter) connected to a round pore, the characteristic diffusion time of the squirt-flow can be evaluated, which gives a squirt-flow cut-off frequency (f_{sq}) of:

$$f_{sq} = \frac{\xi^3 K_m}{\eta}. \tag{1.38}$$

Below f_{sq}, the squirt-flow has time to equilibrate the pressure between the crack and the pore, which corresponds to the relaxed regime (isobaric) accounted for in poroelasticity. Above f_{sq}, the fluid is like "frozen" within the compliant crack, which corresponds to an unrelaxed regime that violates the isobaric assumption of poroelasticity. Above f_{sq}, the fluid is like "frozen" in the pore space, and the rock is equivalent to a medium of isolated (unconnected) saturated pores and cracks. The elastic properties can therefore be predicted by effective medium theories. While the elastic properties are not frequency dependent within a specific regime, they will show dispersion in the transitions between these regimes (*Pimienta et al.*, 2015a), around the two cut-off frequencies, $f_{undrained}$ and f_{sq}, respectively for the drained/undrained transition and undrained/unrelaxed transitions. For the sake of simplicity and consistency with the discussions of the experimental results in the following chapters, the cut-off frequencies $f_{undrained}$ and f_{sq} can also be written respectively f_1 and f_2:

$$f_1 = f_{undrained} = \frac{4\kappa K_d}{\eta L^2} \quad \text{and} \quad f_2 = f_{sq} = \frac{\xi^3 K_m}{\eta}. \tag{1.39}$$

We have to distinguish two types of dissipation: (1) attenuation of the matrix, and (2) the attenuation related to fluid-flow. The attenuation of the matrix is the natural attenuation of the dry frame at every frequency. Two factors can contribute to this attenuation: the anelasticity of the matrix minerals and the frictional dissipation due to relative motions at grain contacts or in cracks (*Johnston et al.*, 1979). It is still unclear how fluid in the porosity may affect this latter. The fluid-flow attenuation is due to the viscous dissipation in the saturating fluid during the fluid-flow transitions: global-drainage and squirt-flow. Therefore, this attenuation will be localized between the different fluid-flow regimes, when the dispersion of the elastic moduli occurs (1.1). From the bulk modulus attenuation measurements on carbonate rocks done by *Adam et al.* (2009), the attenuation of the matrix corresponds to the "background" level of Q_K^{-1}, which was found to be between 0.01 and 0.02 in general, while the fluid-flow attenuation correspond to peaks that can reach 0.1 or more.

The dispersion and the attenuation are related to the same phenomenon: a viscous-controlled transition between two fluid-flow regimes when the frequency increases (Figure 1.1). Since the rock can be assimilated to a linear viscoelastic material of complex modulus M, a causality principle links the dispersion and the attenuation. This causality is expressed by the Kramers-Kronig relations, which link the real part and the imaginary part of M by:

$$M_R(\omega) = \frac{2}{\pi}\int_0^\infty \frac{\Omega M_I(\Omega)}{\Omega^2-\omega^2}d\Omega \quad \text{and} \quad M_I(\omega) = -\frac{2\omega}{\pi}\int_0^\infty \frac{M_R(\Omega)}{\Omega^2-\omega^2}d\Omega. \tag{1.40}$$

O'Donnell et al. (1981) found an approximate form of the Kramers-Kronig relations, which enables to calculate the attenuation by (*Mikhaltsevitch et al.*, 2016b):

$$Q_M^{-1}(\omega) = \frac{\pi}{2}\frac{\omega}{M_R(\omega)}\frac{dM_R(\omega)}{d\omega}. \tag{1.41}$$

From the previous equation, we can see that the amount of attenuation ($Q_M^{-1}(\omega)$) is directly related to the slope of the dispersion ($dM_R(\omega)/d\omega$). Viscoelastic relaxation models can also be used to relate dispersion and attenuation, such as the Zener model, or more generally the Cole-Cole model initially applied for dielectrics (*Cole and Cole*, 1941), given by:

$$M(\omega) = M_\infty + \frac{M_0 - M_\infty}{1+(i\omega\tau)^{1-r}}, \tag{1.42}$$

where τ is the relaxation time and r is a distribution parameter. M_0 and M_∞ are the moduli at zero and infinite frequency respectively.

1.5.3 Theoretical models of squirt-flow

We present here a brief review of theoretical squirt-flow models for the undrained/unrelaxed transition. A more extended review has been done by *Müller et al.* (2010). This latter review also presents dispersion models related to Biot's equations of dynamic poroelasticity that

we ignore here since we only focus on the quasi-static limit of poroelasticity and viscous-driven mechanisms such as squirt-flow. Two family of models can be used for squirt-flow: (1) models based on viscoelastic rheology and poroviscoelasticity or (2) models that use hydraulically communicating cavities (*Müller et al.*, 2010).

Since the dispersive phenomenon is related to a pressure-relaxation process, phenomenological models based on viscoelastic material behavior can be used to describe the evolution of the modulus from a relaxed state (M_0) to an unrelaxed state (M_∞) at a given characteristic frequency. One of the most popular viscoelastic model is the Standard Linear Solid (SLS) or Zener model (e.g., *Mavko et al.*, 2009), which will be presented in more details in Section 3.4.3 for comparison with attenuation measurements. However, the phenomenological nature of these models prevents us to interpret dispersion and attenuation in terms of rock properties.

The models based on hydraulically connected cavities attempt to forward model the dispersion of the effective elastic moduli when squirt-flow dissipation occurs locally between the cavities. Such models highly depend on the geometrical description of the cavities selected to model the rock. Some attenuation models are based on analyzing aspect-ratio distributions (e.g., *O'Connell and Budiansky*, 1977; *Mavko and Nur*, 1979; *Palmer and Traviolia*, 1980). A review of these models is given by *Jones* (1986). Other models consider the pore space to be a binary structure, with stiff pores on one side, that represent most of the porosity, and compliant cracks on the other side, responsible for the pressure dependence of the elastic moduli (e.g., *Walsh*, 1965; *Mavko and Jizba*, 1991; *Shapiro*, 2003).

A model from *Dvorkin et al.* (1995) and reformulated by *Pride et al.* (2004) even considers the medium to be a aggregate of porous grains, where the intragranular porosity is soft and the intergranular porosity is stiff. The main advantage of this latter over all the other squirt models is that it is compatible with Biot's equations of poroelasticity (*Pride and Berryman*, 2003). It is also consistent with the well established high-frequency limit of *Mavko and Jizba* (1991). However, interpretation of the parameters of these imaginary microporous grains in terms of rock properties can be difficult (*Müller et al.*, 2010; *Gurevich et al.*, 2010).

An alternative approach from *Murphy III et al.* (1986) considers the compliant pores as gaps at the adjacent grain contacts. However, this model is not consistent with the high-frequency limit of *Mavko and Jizba* (1991), because it was developed within the framework of the Hertz-Mindlin grain contact theory (*Digby*, 1981; *Winkler*, 1983) where grains are assumed rigid and the compliance of the rock is only due to the gaps. This results in an overestimation of the rocks stiffness at high-frequency. A model from *Gurevich et al.* (2010) uses the same pressure relaxation approach in the gaps as *Murphy III et al.* (1986), in conjunction with the discontinuity tensor formulation of *Sayers and Kachanov* (1995). This allows the model to be consistent with the *Gassmann* (1951) limit at low frequency, the *Mavko and Jizba* (1991) limit at high frequency, and the stress-sensitivity model of *Shapiro* (2003). Moreover, the formulation of the model is compatible with Biot's equations of

dynamic poroelasticity if needed (*Gurevich et al.*, 2010). *De Paula et al.* (2012) extented this approach with the addition of an intermediate aspect-ratio family of pores that explains the pressure-dependence of bulk modulus at high confining pressures where all the compliant cracks are closed.

Chapman et al. (2002) developed a model that can be expressed through a macroscopic parametrization, and where the microstructure consists of randomly oriented thin cracks and spherical pores. Each parameter of the model has a physical interpretation corresponding to a well-defined rock property (*Chapman et al.*, 2002). The model is consistent with Biot's theory and the dispersion amplitudes predicted by *Endres and Knight* (1997), which are the standard effective medium theory results, for distibutions of aspect ratios, in the low frequency (Gassmann limit) and the high frequency cases (unrelaxed regime where there is no fluid exchange). The frequency dependence of the full elastic tensor can be obtained and the model can be extended to include the effect of mesoscale fractures (*Chapman*, 2003, 2009).

Jakobsen et al. (2003) and *Jakobsen* (2004) developed a more general computational model that uses the T-matrix approximation. This method can take into account pores and fractures of any size and any aspect ratio. In this approach, the effects of the pores and fractures are introduced as perturbations of the solution for the elastic background. *Jakobsen and Chapman* (2009) further investigated the similarities with the approach of *Chapman* (2003).

1.6 Experimental investigation in laboratories

1.6.1 Experimental techniques

We present here a brief overview of experimental techniques to investigated the dispersion and attenuation of the dynamic elastic properties in laboratory, over a large frequency range. These experimental studies, in controlled conditions, are essential to understand the fluid-related dispersive processes that are at stake when comparing classical low-frequency field measurements, such as seismics (1-100 Hz) or well logging (10 kHz), with ultrasonic measurements in laboratory (1 MHz) (Figure 1.2). A more exhaustive overview was done by *Subramaniyan et al.* (2014). Three main laboratory techniques exist for such matter: (1) ultrasonics, (2) resonant bar, and (3) forced oscillations techniques.

(1) Ultrasonics: two ultrasonic transducer are positioned on both sides of the sample. One acts as a source and the second acts as a receiver. The transducers are piezoelectric crystals (quartz or piezoceramics) that can vary in size. The size of the crystal determines its resonant frequency. For quartz disks of 1 cm diameter and several millimeters height, the resonant frequencies for compression and shear are between 0.3 and 1 MHz (Figure 1.2). To avoid scattering effects, the size of the sample's largest heterogeneity should be lower than the wavelength, which is generally between 3 to 6 mm for sedimentary rocks.

(2) Resonant bar: the sample is mechanically excited to vibrate at its resonant frequencies. The frequencies depend on the bar's length and P-wave velocity, and gives a moduli measurement in that corresponding frequency range (e.g., *Murphy III*, 1982; *Lucet et al.*, 1991). The longer the bar, the lower the characteristic frequency. For the Hunton limestone, *Born* (1941) obtained a resonant frequency of 10.6 kHz for a 17.8 cm long bar, and 2.8 kHz for a 71 cm long bar. The attenuation can be measured either from the width of the resonant peak, or from the time constant of the resonant decay (*Murphy III*, 1982). The need for such long bars to measure lower frequencies is the main limitation of this technique, as they are difficult to core directly. Generally the long bars are fabricated by cementing short length bars together end to end (*Born*, 1941). *Nakagawa* (2011); *Nakagawa et al.* (2013) developed a method to bypass this issue, named the Split Hopkinson Resonant Bar (SHRB) technique. Instead of extending the sample with other short elements of the same rock to investigate lower frequencies, the SHRB uses metal-rod extensions. Then, numerical inversions have to be performed to invert the complex Young's modulus and shear modulus, corrected from the effects of the sample-rod interfaces.

(3) Forced oscillations: the sample is generally set in a confining cell (e.g. triaxial cell) where controlled stress oscillations are applied on it, and the resulting strains are recorded (e.g., *Spencer*, 1981; *Paffenholz and Burkhardt*, 1989; *Lienert and Manghnani*, 1990). These type of setups require: (i) a force generator with adjustable frequency, (ii) a force sensor to estimate the applied stress and (iii) strain sensors for the sample. The strain oscillation amplitudes have to be in the order of 10^{-6} to be in the linear elastic domain. This technique has gained popularity in recent years as the frequency range of the measurements corresponds to that of seismic data (e.g., *Lu and Jackson*, 1996; *Batzle et al.*, 2006a; *Tisato and Madonna*, 2012; *Madonna and Tisato*, 2013; *Mikhaltsevitch et al.*, 2014; *Fortin et al.*, 2014). Different modes of stress-oscillation are possible with this technique. The forced oscillations can be in the axial direction, from which the Young's modulus and the Poisson's ratio can be deduced if axial and radial strains are recorded (e.g., *Batzle et al.*, 2006a). Torsional oscillations were performed in the setup of *Jackson and Paterson* (1987, 1993), from which the complex shear modulus could be deduced. Hydrostatic-stress oscillations by the mean of confining pressure oscillations were performed by *Adelinet et al.* (2010), from which the complex bulk modulus can be deduced.

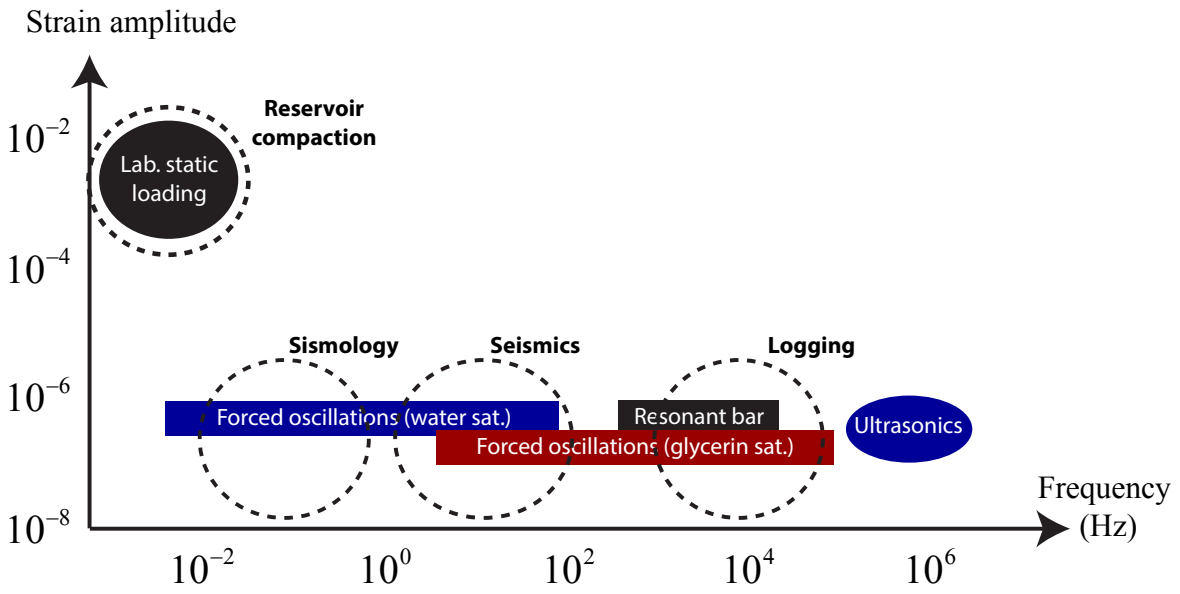

Figure 1.2: Schematic of the measurement techniques' position in the frequency-strain space. The techniques are either from laboratory or from field measurements.

For forced oscillations technique, with current technologies, the frequency of the stress oscillations can hardly go above 1 kHz (e.g., *Batzle et al.*, 2006a). Most of the setups' maximum frequency are around 100-200 Hz (*Subramaniyan et al.*, 2014). This is generally sufficient to measure the properties at seismic frequencies, however it fails to investigate the gap between seismic and ultrasonic frequencies (Figure 1.2), which would correspond to well logging ($\sim 10kHz$). In order to investigate fluid-flow related dispersion that would occur at logging frequencies, if the rock was saturated with water, is to use forced oscillations on a sample saturated with a very viscous fluid, such as glycerin (*Fortin et al.*, 2014; *Pimienta et al.*, 2016c). Since the time-scale of diffusion processes are related to the fluid's dynamic viscosity, the frequency of the measurement can be scaled by the viscosity of the fluid. If water is the reference fluid, the use of glycerin that is a thousand times more viscous, will give fluid-flow related dispersion for apparent frequencies a thousand times greater (*Pimienta et al.*, 2015a,b, 2016a) (Figure 1.2).

1.6.2 Some results on sandstones and limestones

The previous techniques to measure dispersion at seismic frequencies have been used mainly on sandstones (e.g., *Spencer*, 1981; *Spencer and Shine*, 2016; *Winkler*, 1985; *Batzle et al.*, 2006a; *Mikhaltsevitch et al.*, 2014; *Pimienta et al.*, 2015a), and more rarely on carbonates (e.g., *Spencer*, 1981; *Batzle et al.*, 2006a; *Adam et al.*, 2009; *Mikhaltsevitch et al.*, 2016a). Most of the previous studies used forced oscillations to measured Young's modulus' dispersion between 0.01 to 100 Hz. Deducing the other elastic moduli of a isotropic sample was possible by measuring both axial and radial strains. However, few studies attempted to measure di-

rectly the bulk modulus, which is expected to be the most sensible to the different fluid-flow regimes. Direct measurements of K at low-frequency using hydrostatic oscillations were done by *Adelinet et al.* (2010) and *David et al.* (2013). They compared the high-frequency (1 MHz) and the low-frequency (0.1 Hz) bulk moduli for dry and fluid-saturated rocks, but they did not investigate the transitions occurring at intermediate frequencies.

Pimienta et al. (2015a) reported the bulk modulus frequency-dependence and attenuation on a Fontainebleau sandstone (Figure 1.3). The sample was measured under dry-, glycerin- and water-saturated conditions, to scale the frequency with the viscosity of the fluid. Water is considered the reference fluid for the apparent frequency. The drained, undrained and unrelaxed fluid-flow regimes were clearly identified, with dispersive transitions between them. The first transition occurring around 40 Hz, was interpreted as the drained / undrained transition due to the experimental boundary conditions (*Pimienta et al.*, 2015a). The undrained bulk modulus, visible between 100 Hz and 1 kHz, can be consistently deduced from the drained modulus with Biot-Gassmann's theory. The ultrasonic results (1 MHz for water) exhibit a much greater bulk modulus than the undrained value, suggesting the presence of a second dispersive transition between 1 kHz and 1 MHz (Figure 1.3) interpreted as squirt-flow dispersion (*Pimienta et al.*, 2015a). Attenuation was successfully measured from the phase shift between the stress and the strain, and correlated perfectly with the dispersion (Figure 1.3).

Few analysis of such are available in carbonate rocks. *Batzle et al.* (2006a) reported P-wave and S-wave dispersion of a heavy oil-saturated Uvalde carbonate as a function of temperature for a frequency range of 1 Hz to 2.5 kHz and 0.8 MHz. The low-frequency velocities were deduced from axial oscillations up to 1 kHz. Significant dispersion was observed between 10^4 and 10^6 with an increasing effect of temperature. Because of the viscous-solid nature of the heavy oil, from which a frequency-dependent shear modulus can be measured (*Das and Batzle*, 2008), the observed dispersive transition is out of the scope of the fluid-flow regimes discussed previously.

Other measurement on carbonate-reservoir plugs have been reported by *Adam et al.* (2009) on the same experimental setup, for a frequency range of 10-1000 Hz and 0.8 MHz, and are presented Figure 1.4. The resonant bar technique adds an additional measurement at 10^4 Hz. Three of the carbonates are presented here: the samples 100, 200 and 300 (*Adam et al.*, 2009). Sample 100 and sample 200 are two very porous wackestones ($\phi \sim 30\%$) that are composed of 9% of dolomite, and the rest of calcite. Sample 300 is a porous packestone ($\phi \sim 20\%$) that is pure calcite. The samples were measured in dry condition, then were saturated with butane and brine. The differential pressure $P_{diff} = P_c - P_p$ was around 31 MPa for samples 100 and 200, and around 24 MPa for sample 300. Results of the P-wave velocities show that there is no significant difference between the dry and the butane-saturated results. The brine-saturated results however exhibits a greater P-wave velocity for every frequencies (Figure 1.4). Not much dispersion is observed between 10

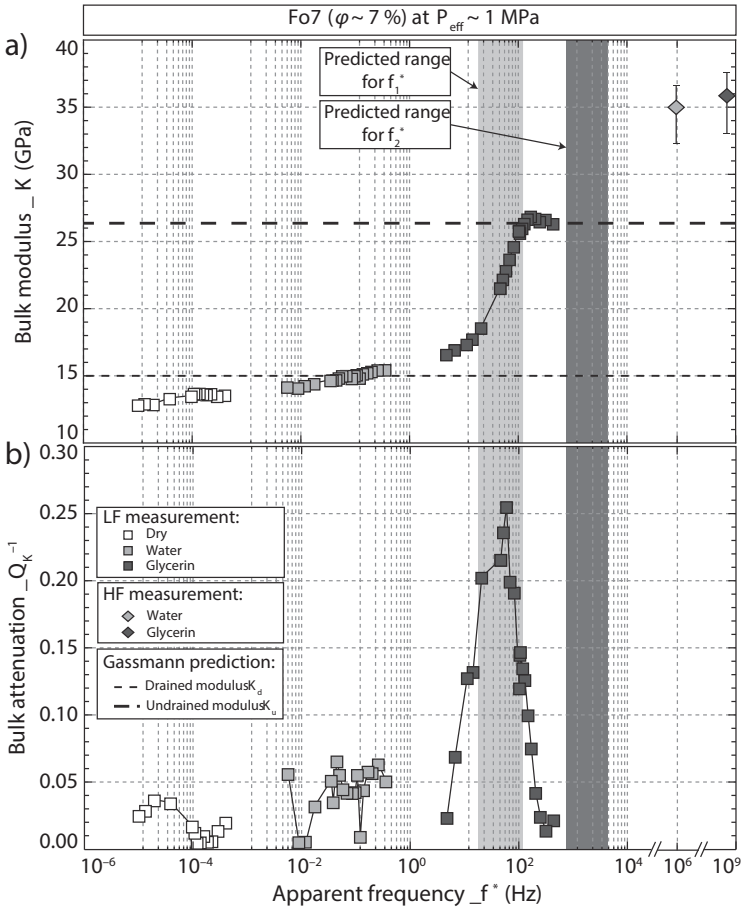

Figure 1.3: Bulk modulus dispersion (a) and attenuation (b) measured on a 7% porosity Fontainebleau sandstone obtained by *Pimienta et al.* (2015a). The drained, undrained and unrelaxed fluid-flow regimes are clearly visible, with dispersive transitions between them. The undrained regime is consistent with Biot-Gassmann, while the unrelaxed regime, visible with ultrasonic measurements, exhibits a much higher bulk modulus.

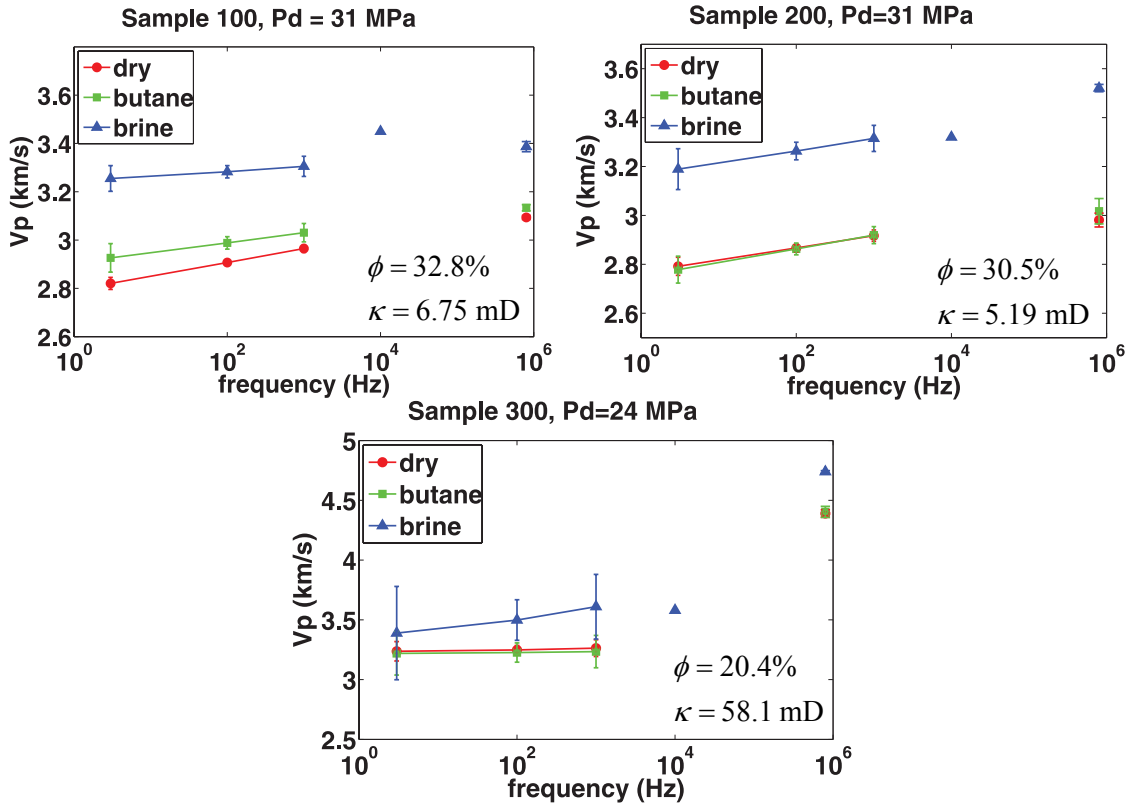

Figure 1.4: P-wave velocity dispersion of three different carbonates from *Adam et al.* (2009). The samples 100 and 200 are wackstones with 9% of dolomite, and sample 300 is a pure calcite packstone.

Hz and 0.8 MHz for the wackestones (samples 100 and 200), however, a large dispersion of at least 1000 m/s is expected for the packestone (sample 300) between 10^4 and 10^6 Hz. Because this seemed to apply also for the dry measurements, it lead to the conclusion that this dispersion may not be related to fluid-flow dispersion, but rather to a path-dependent wave propagation during the ultrasonic measurements (*Adam et al.*, 2009).

To further investigate fluid-flow related dispersion in carbonates and understand the interplay between the heterogeneous pore types and the stress-induced viscous flows, we limited our experimental study to pure calcite and homogeneous rocks with different microstructures. Moreover, we limit ourselves to fully-saturated conditions to exclude any dispersive mechanisms related to partial saturation (e.g. *White*, 1975; *Dutta and Odé*, 1979; *Toms et al.*, 2007; *Lebedev et al.*, 2009; *Tisato and Madonna*, 2012; *Chapman et al.*, 2016; *Chapman*, 2017), which would add a level of complexity and prevent us from identifying effects intrinsically due to the microstructure's heterogeneity.

Part I

Experimental setup to measure the dynamic moduli over a large frequency range.

CHAPTER 2

EXPERIMENTAL DEVICES AT THE LABORATOIRE DE GÉOLOGIE DE L'ENS

2.1 Résumé

Nous présentons ici les dispositifs expérimentaux qui ont été utilisés au cours de cette thèse. Au laboratoire de géologie de l'ENS de Paris, deux cellules triaxiales sont équipées pour faire des oscillations forcées combinées à des mesures ultrasoniques. La première presse est une cellule Géodesign équipée de pompes Sanchez Technologies, dans laquelle nous avons caractérisé le Lavoux. La seconde presse est un système complet de Top Industrie, que nous avons reçu en cours de deuxième année de thèse, et qui a permis de caractérisé l'Indiana, le Rustrel et le coquina, après un phase de calibration sur du gypse. Cette seconde presse a été dimensionnée spécifiquement pour les oscillations forcées, et est bien plus ergonomique que la première.

Les deux cellules sont capables de faire des oscillations axiales jusqu'à 100 Hz, grâce à un oscillateur piézoélectrique logé entre l'échantillon et le piston. De plus, des oscillations hydrostatiques peuvent être générées par oscillation de la pression de confinement. Pour ce dernier mode, la presse Géodesign est limitée à 0.4 Hz alors que la Top Industrie peut aller au-delà de 1.2 Hz. Les déformations radiales et axiales de l'échantillon sont mesurées par des jauges de déformations directement collées sur la surface latérale. La contrainte axiale générée durant les oscillations axiales est déduite de la déformation de l'embase en aluminium sous l'échantillon.

2.2 Introduction

At the Laboratoire de Géologie de l'ENS de Paris, two triaxial cells are able to perform forced oscillations over a wide frequency range, along with ultrasonic mesurements. The first is a Geodesign triaxial cell equipped with Sanchez Technologies pumps. The second is a triaxial cell entirely produced by Top Industrie. Both cells are designed for cores of 40 mm diameter, and about 80 mm height.

2.3 Geodesign triaxial cell

The Geodesign cell is an autonomous (integrated piston) and auto-compensated cell, which can reach 300 MPa of confining pressure (Figures 2.3a and 2.2). The axial loading and the confining pressure are regulated by two single screw pumps of from Sanchez Technologies that can go up to 100 MPa (Figure 2.3b). The volume of each pump is 300 mL and they are controlled through a FALCON software.

The sample is held between two end-platens (Figure 2.2), and is isolated from the confining oil by a neoprene jacket (visible next to the sample in Figure 2.3a). The top and bottom end-platens contain the pore pressure upstream and downstream (Figure 2.2). Moreover, they are equipped with P- and S-ultrasonic transducers of 10 mm diameter and 1 mm height from PI Ceramics (type PI255). The pore pressure is regulated by a Quizix QX-1500 dual-pump, which can reach 10 MPa and has a stroke volume of about 50 mL per cylinder (Figure 2.3c). The top and bottom drainage circuit can be closed by two valves between the Quizix pumps and the cell. This creates small dead volumes of about 3.3 mL at the top and bottom of the sample.

The cell has 34 electrical wire outputs, of which 28 can be used to connect strain gauges in quarter-bridge configuration. A total of 14 strain gauges can be monitored (2 wires per strain gauge). These wires are connected to a HBM MGCplus data acquisition system (DAQ), which is also connected to the thermocouple and the three pressure transducers for the axial loading, confining pressure, and pore pressure upstream (Figure 2.2). All the sensors connected to the DAQ are then monitored through a CATMAN data aquisition software. The sampling frequency of the DAQ can go up to 2 kHz. The strain gauges used for axial and radial measurements throughout all the experiments were 350Ω foil strain gauges (FCB-6-350-11) built by Tokyo Sokki Kenkyujo Co., Ltd.

A PI PICA piezoelectric stack actuator is mounted between the piston and the top end-platen, which can generate axial-stress oscillations up to 100 Hz (Figure 2.2). The blocking pressure of the piezo actuator is around 35 MPa. The initial signal is generated by a TTi TG1010A function generator. It is then amplified by PI high-power amplifier before reaching the piezo actuator. The top end-platen is made out of aluminium 2017A (AU4G), and two axial strain gauges are glued on it to measure the axial stress.

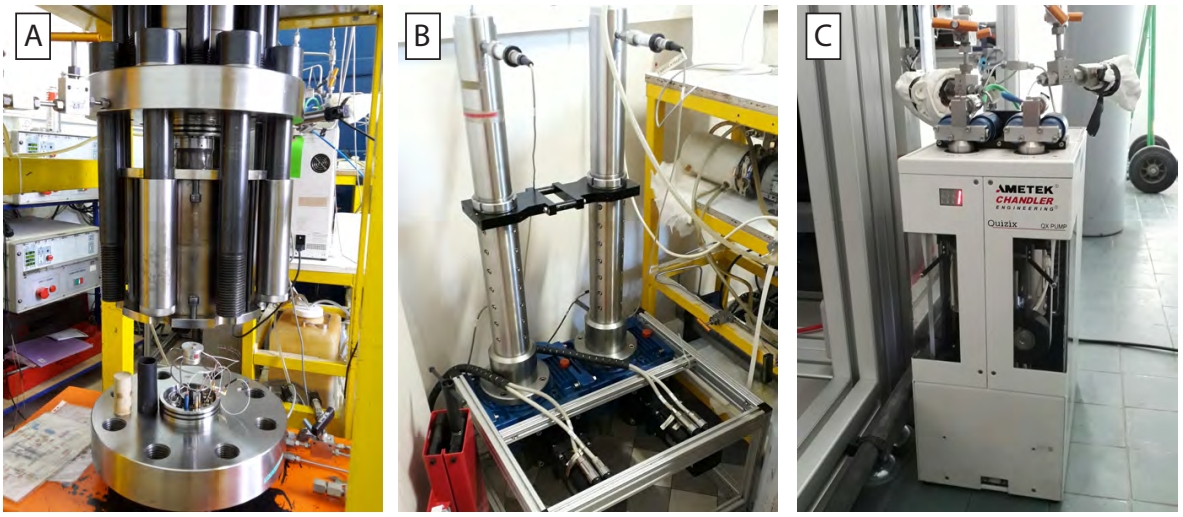

Figure 2.1: Photographs of the Geodesign triaxial cell (a), the Sanchez Technologies pumps for the axial loading and the confining pressure (b), and the Quizix dual-pumps for the pore pressure (c).

The confining pressure pump can be programmed to perform hydrostatic oscillations around a mean value. The calibration of the system from *Pimienta et al.* (2015a) show that the maximum frequency measurable is around 0.4 Hz (Figure 2.3). Because the confining pump has a limited flux and the cell has a large volume of oil, when the frequency increases above 0.1 Hz for a programmed oscillation of 0.1 MPa, the actual pressure oscillation in the cell will decrease, and eventually reach zero (Figure 2.3a). This has the effect of reducing the measured strain on the sample when the frequency increases (Figure 2.3b). For a sample of bulk modulus $K = 40$ GPa (e.g. gypsum), the volumetric strain would be just above the measurable limit of 3×10^{-7} for a frequency of 0.4 Hz (Figure 2.3b).

2.4 Top Industrie triaxial cell

The Top Industrie cell is similar to the Geodesign cell, although it has been specifically designed to measure frequency-effects. It is equipped with four single screw pumps controlling the axial load, the confining pressure, the pore presure upstream and dowstream, which are all Top Industrie made, and are integrated into a single frame (Figure 2.4). Similarly to the Geodesign, it is an autonomous triaxial cell that can reach 100 MPa of confining pressure.

The jacketed sample is held between two endplatens equipped with the similar PI255 ultrasonic transducers than the Geodesign cell (Figure 2.5). The lower endplaten is made out of aluminium 2017A (AU4G), and is bolted to the cell base. It is equipped with 4 axial strain gauges to deduce the axial stress (Figure 2.5).

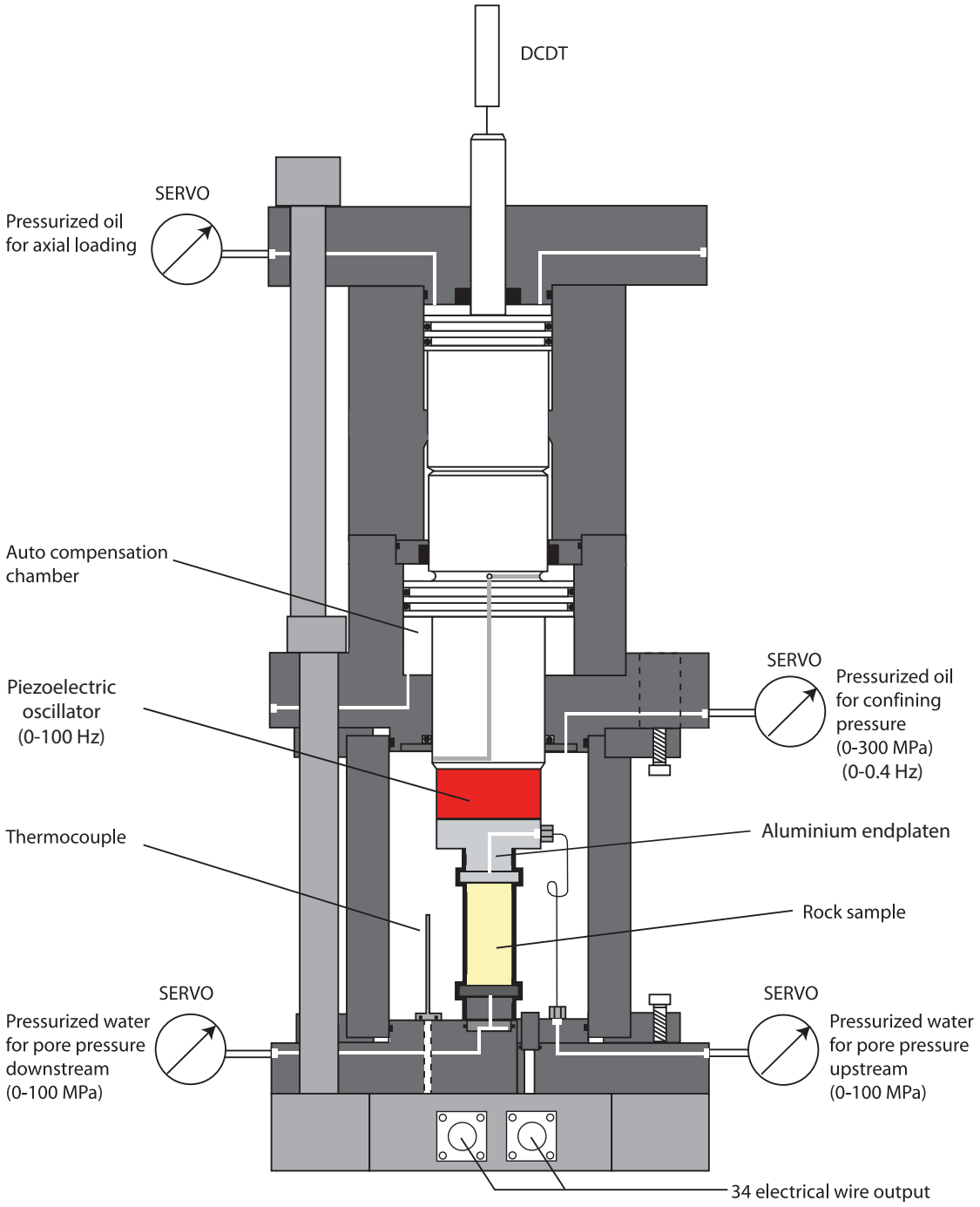

Figure 2.2: Schematic diagram of the Geodesign triaxial cell (Modified after *Fortin et al.* (2007)).

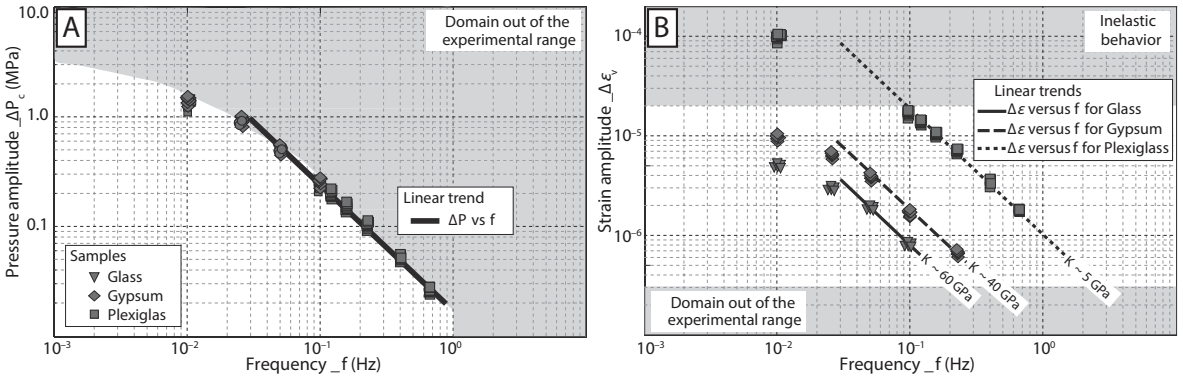

Figure 2.3: Calibration of the hydrostatic oscillations in the Geodesign cell. Measurement of the pressure amplitude (a) and the strain amplitude (b) on three reference samples: glass (triangles), gypsum (diamonds) and plexiglas (squares). The grey zone is out of the experimental range, as the strains have to be between 3×10^{-7} and 2×10^{-5}, to be above the uncertainty limit of the strain gauges, and to respect the small deformation condition of elasticity. Modified after *Pimienta et al.* (2015a).

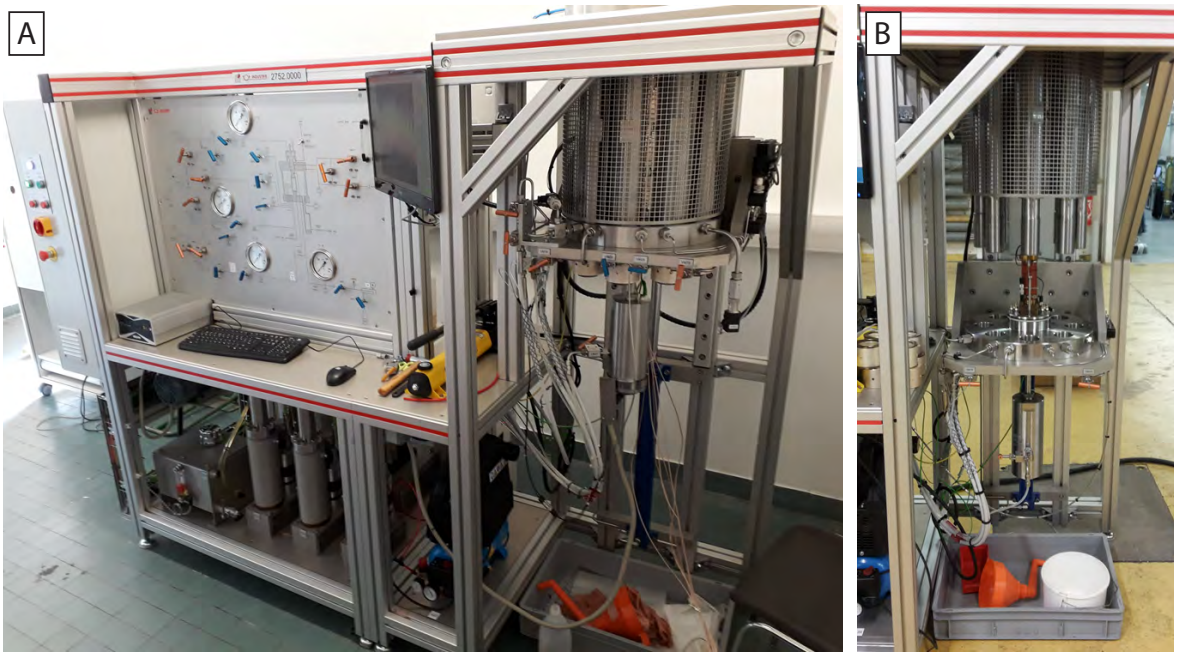

Figure 2.4: Photograph of the Top Industrie triaxial cell in the closed (a) and open (b) configuration.

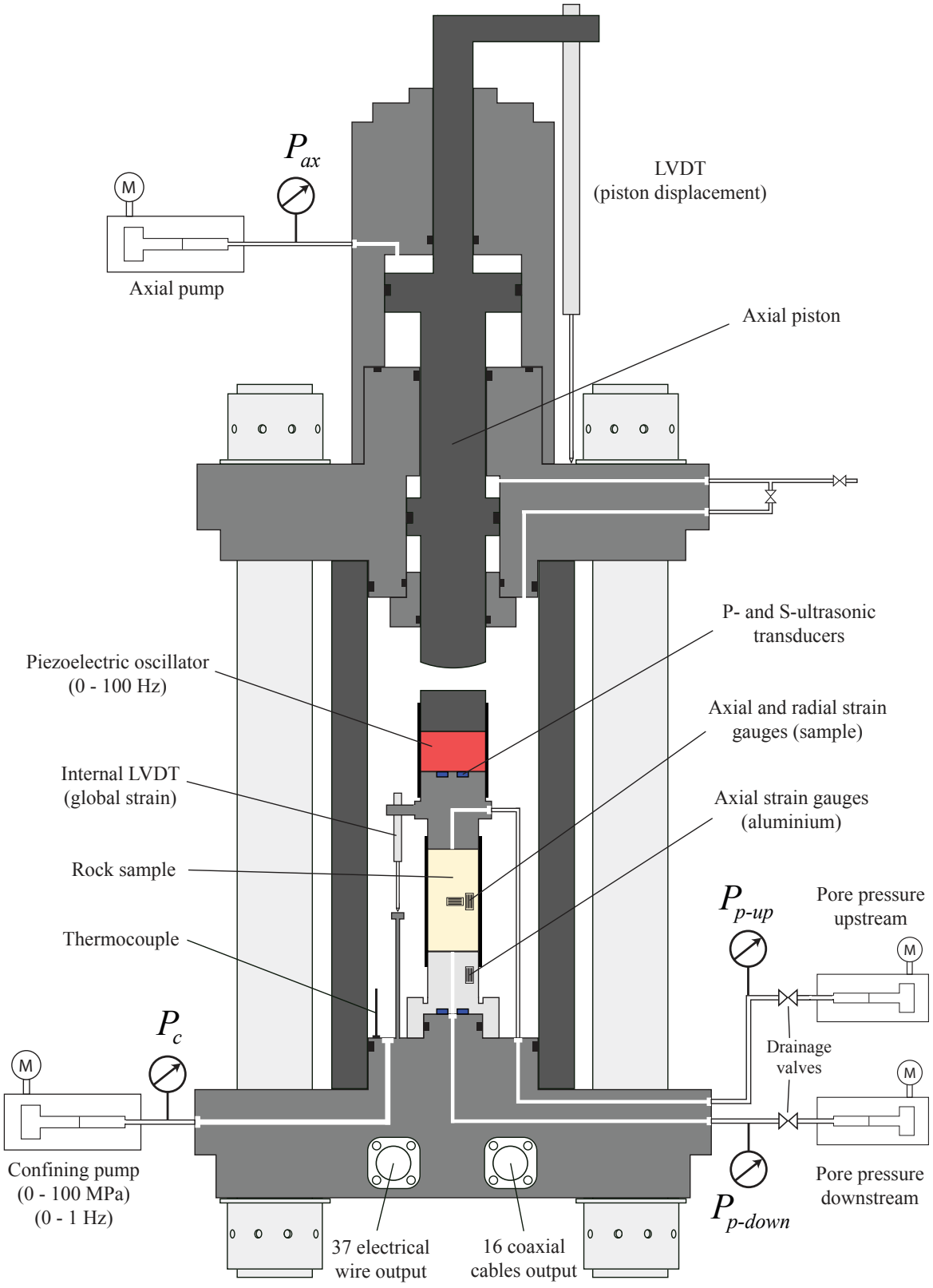

Figure 2.5: Schematic diagram of the Top Industrie triaxial cell.

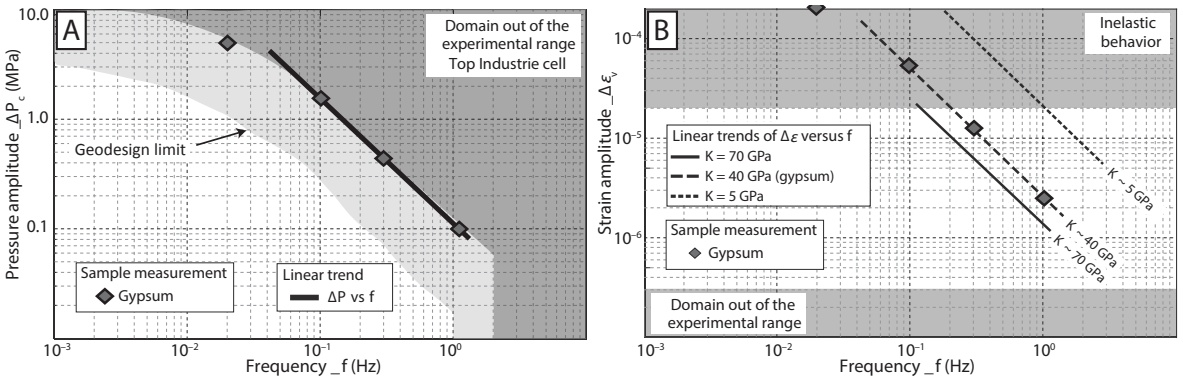

Figure 2.6: Calibration of the hydrostatic oscillations in the Top Industrie cell. Measurement of the pressure amplitude (a) and the strain amplitude (b) on a gypsum standard (diamonds). The dark grey zone is out of the experimental range, as the strains have to be between 3×10^{-7} and 2×10^{-5}, to be above the uncertainty limit of the strain gauges, and to respect the small deformation condition of linear elasticity. The light grey zone corresponds to the Geodesign cell (Figure 2.3a). Modified after *Pimienta et al.* (2015a).

The cell has 37 electrical wire output on which can be connected a total of 16 strain gauges (4 being dedicated to the aluminium endplaten). Similarly to the Geodesign cell, the strain gauges are wired in quarter-bridge configuration. The data acquisition system (DAQ) for the strain gauges and the pressure sensors is integrated in the Top Industrie's frame. The maximum sampling rate of the DAQ is 4 kHz. A unique Labview software designed by Top Industrie controls both the pumps and the data acquisition. The confining pump can be programmed through a sequencer. This enables to perform tasks, say a sequence of different frequencies, automatically. To reduce the size of the data file, the sampling frequency can be adjusted in the sequencer in accordance to the oscillation frequency.

Although the Top Industrie cell has two integrated pumps for the pore pressure, each of 200 mL volume, the complexity of the pore-fluid circuit makes it difficult to change fluid. In order to saturate the sample with a second fluid, say glycerin, the Quizix pump previously used for the Geodesign cell (Figure 2.3c) can be connected to the drainage circuit next to the sample.

The Top Industrie confining pump has similar characteristics in terms of maximum flux and pressure than the Sanchez Technology pump used for the Geodesign cell. However, the overall oil volume of the Top Industrie cell is smaller than the Geodesign, which means that the pressure amplitude will be higher for the same pump displacement. This enables the Top Industrie cell to measure higher frequencies in hydrostatic conditions. In practice, the maximum frequency measured is around 1.1 Hz (Figure 2.6). Moreover, a heating system allows for measuremtns up to 100°C.

Finally, the same piezoelectric oscillator as in the Geodesign cell is used to generate the axial-stress oscillations. The PI stack is mounted above the top endplaten (Figure 2.5). As previously, the input signal and frequency change is controlled manually on the TTi

function generator, and is then amplified before reaching the piezoelectric oscillator.

CHAPTER 3

EXPERIMENTAL PROTOCOL

3.1 Résumé

Nous présentons ici tous les protocoles expérimentaux qui ont été utilisés pour caractériser les quatre échantillons étudiés au cours de la thèse. Pour les cellules triaxiales présentées précédemment, les échantillons doivent être des cylindres de longueur 80 mm et de diamètre 40 mm. La première étape consiste à effectuer un carottage de 40 mm de diamètre dans un bloc, puis de couper la carotte à la longueur souhaitée. Les surfaces supérieure et inférieure sont rectifiées afin d'être parfaitement parallèles, et ainsi éviter de la flexion lors d'un chargement axiale. La porosité est mesurée par triple pesée, puis l'échantillon est séché dans une étuve à 60°C. Après préparation de la surface latérale, quatre paires de jauges axiales et radiales y sont collées à mi-hauteur, dans des positions diamétralement opposées. L'échantillon est enfin mis dans sa jaquette et est installé dans la cellule triaxiale.

Après quelques cycles de chargements hydrostatiques visant à supprimer tout effet irréversible, le module d'incompressibilité statique est mesuré en sec. Ensuite, pour différentes pressions effectives, les cycles d'oscillations forcées hydrostatiques (0.01-1 Hz) et axiales (0.01-100 Hz) sont effectués à différentes fréquences, suivi des mesures de vitesses ultrasoniques P et S (1 MHz). Une fois le cycle en sec terminé, l'échantillon est saturé en glycérine par drainage après avoir effectué le vide. On répète les mesures puis l'on sature avec l'eau, également par drainage. Les mesures de perméabilité par écoulement de Darcy sont effectuées avant chaque changement de pression effective.

Les oscillations hydrostatiques permettent de calculer un module d'incompressibilité pour chaque fréquence, après avoir moyenné les signaux de toutes les jauges de déformations. Le module de Young et le coefficient de Poisson sont déduits des oscillations axiales. Si la roche est isotrope, les formules de conversion entre modules élastiques permettent de calculer un module de cisaillement et un module d'incompressibilité. Ce dernier est com-

paré au module obtenu précédemment lors des oscillations hydrostatiques. L'atténuation liée à un module est déduite du déphasage entre la contrainte et la déformation correspondante. L'atténuation mesurée est également comparée au modèle viscoélastique de Zener.

3.2 Sample preparation

The sample's preparation is a delicate, yet important, step in order to obtain proper measurements. First, the sample is cored in the bloc with a diameter of 40 mm. The plug is reduced to 80 mm length, and the upper and lower surfaces are rectified to be perfectly perpendicular to the cylinder's axis. The lateral surface is locally polished and cleaned to obtain a perfectly smooth surface where the strain gauges will be glued. A first layer of glue can be locally applied in order to fix any residual dust and to create a perfectly clean surface (Figure 3.1a).

The 350Ω strain gauges are then glued on the preexisting layer, with axial and radial orientations (Figure 3.1b). The strain gauges are foil strain gauges built by Tokyo Sokki Kenkyujo Co., Ltd. (FCB-6-350-11), which combine two perpendicular elements (vertical and horizontal).

The wires welded to the strain gauges go through smalls holes in the neoprene jacket, and finish with connectors adapted to the apparatus (Figure 3.1c). After the jacket holes are sealed with epoxy glue, the sample can be installed in the cell (Figure 3.1d). The process of gluing strain gauges requires that the sample is placed into a 80°C oven for at least 4 hours in order to crystallize the glue. This process being repeated at least twice, we can assume that the sample is dry when installed in the cell.

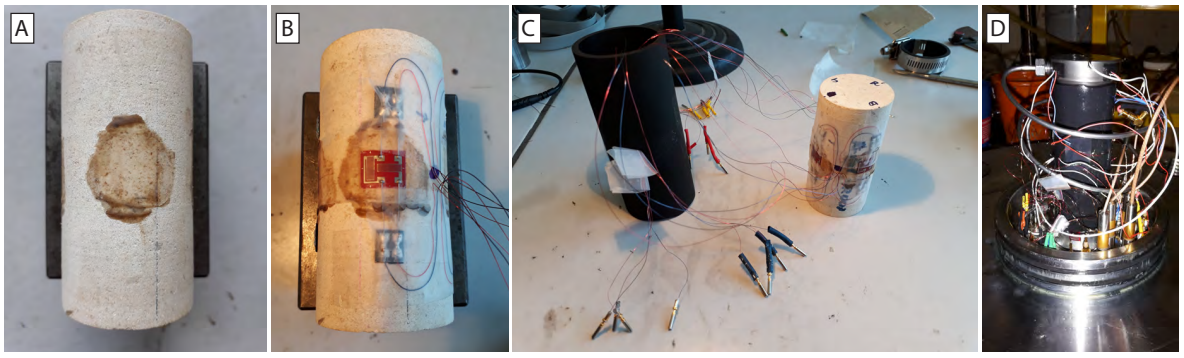

Figure 3.1: Preparation of the sample. After the plug has been cored and rectified, the lateral surface is polished and a first layer of glue is applied to create a clean surface (a). The strain gauge is glued on the preexisting layer, and the electric wires are welded (b). The wires go through two small holes in the jacket, and connectors adapted to the apparatus are welded (c). After the jacket holes are sealed with epoxy glue, the sample is installed in the apparatus (d).

3.3 Static bulk modulus

Once the sample is installed in one of the triaxial cell, it runs through a first hydrostatic seasoning cycle in order to minimize nonlinear cycling effects caused by microcracks (*Hart*

and Wang, 1995). The maximum confining pressure considered is always lower than 30 MPa, as it is the maximum pressure tolerable for the piezoelectric stack. Moreover, the studies reviewed by *Zhu et al.* (2010) suggests that the high porous limestones (between 21% and 30% in the study) have a minimal pore collapse pressure of 30 MPa. For samples of porosity superior to 20%, a maximum pressure of 20 MPa is therefore chosen.

After the seasoning cycle is done, the static modulus is deduced from the unloading of the next cycle. We consider the tangent modulus as our static measurement at a given confining pressure. All the strain gauges are average and multiplied by 3 to obtain the volumetric strain. A polynomial function, of order higher or equal than four, is fit through the stress-strain curve. The tangent modulus is then easily calculated from the derivative of the polynomial at each confining pressure.

3.4 Forced oscillation methods

To measure the dispersion and the attenuation of the dynamic elastic moduli over a large frequency range, we used the forced oscillation method (or stress-strain method), combined with ultrasonic measurements, in two different triaxial cells at the ENS of Paris (Figure 3.2) (*Fortin et al.*, 2005, 2014; *Adelinet et al.*, 2010; *David et al.*, 2013). With these type of apparatus, two types of stress oscillations can be achieved: hydrostatic (Figure 3.2a) to measure the bulk modulus (K), and axial (Figure 3.2b) to measure the Young's modulus (E) and the Poisson's ratio (ν).

To investigate the effect of the fluid's viscosity, the sample's properties were measured under dry, glycerin-saturated and finally water-saturated conditions. The glycerin used for the experiments is the Glycérol $\geq$ 98% GPR RECTAPUR provided by VWR. The advantages of glycerin is that it is a thousand times more viscous than water, and chemically inert to non-hydrous minerals. Moreover, it has three hydroxyl groups that are responsible for its high solubility in water, and its hygroscopic nature. Therefore, the samples are first measured dry, secondly with glycerin, and finally with water. The certificate of analysis provided by VWR guaranties a minimal mass content of 98% of glycerin. At room temperature (20 °C), the viscosity of glycerin and water will be taken as $\eta_{gly} = 1$ Pa.s and $\eta_{wat} = 10^{-3}$ Pa.s (Figure 3.3).

To fully saturate the sample with glycerin after the dry measurements, vacuum conditions are made in the sample and the drainage circuit. Then the glycerin is injected from the upstream in one side of the sample with a constant differential pressure ($P_c - P_p$) of 1 MPa. The confining pressure is generally set between 2 MPa and 5 MPa in order to maximize the permeability. This process can take more than 15 days for a sample of permeability 0.02 mD at room temperature. After the glycerin-saturated measurements, the similar process is repeated to saturate with water. The downstream is unconnected from the circuit and drains out of the cell at atmospheric pressure. This enables to control the mixture going out of the

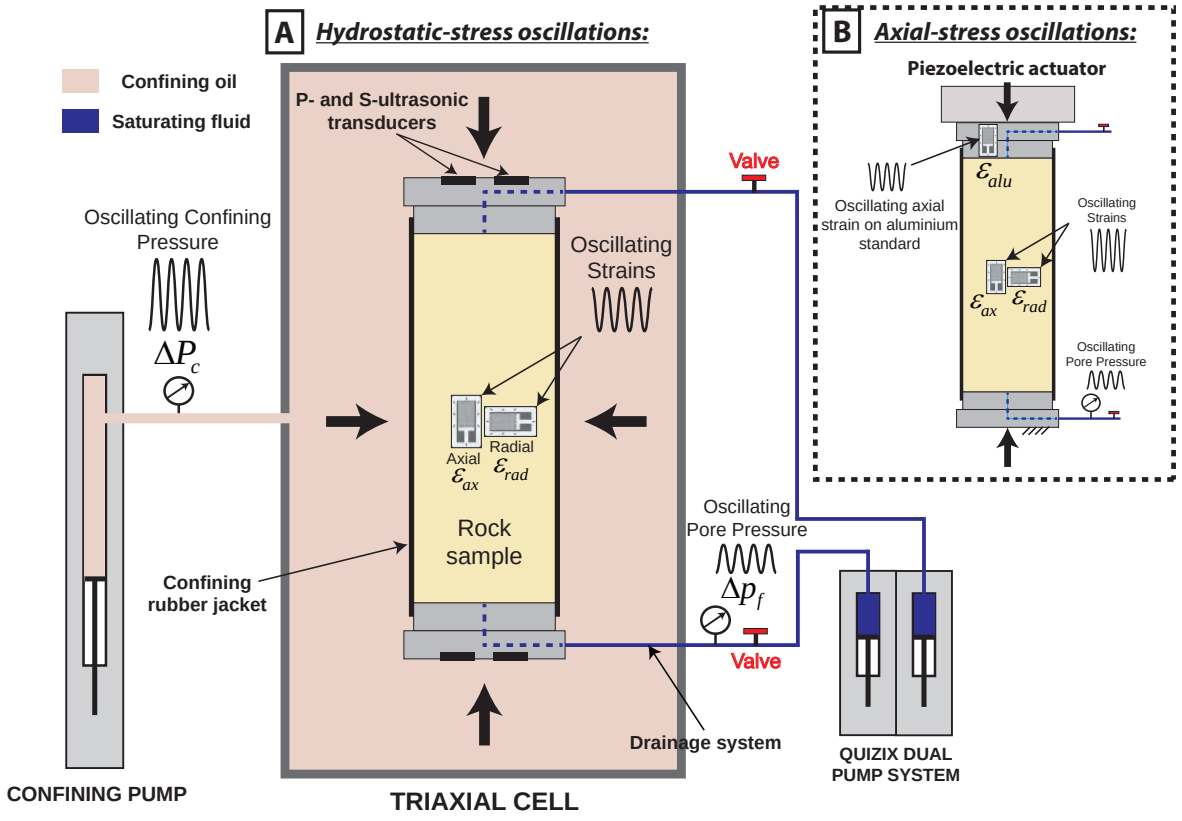

Figure 3.2: Schematics of the experimental set-up for a) hydrostatic oscillations and b) axial oscillations, in the triaxial cell at the ENS of Paris. The hydrostatic oscillations were imposed by the confining pump, in the frequency range of $[0.004; 0.4]$ Hz for the Geodesign cell, and $[0.004; 1.1]$ Hz for the Top Industrie cell. The axial oscillations are imposed by a piezoelectric actuator mounted over the top endplaten, in the frequency range of $[0.004; 100]$ Hz. Strains are measured by axial and radial strain gauges bonded on the sample at mid-height. Ultrasonic transducers are settled in the endplatens to obtain the P- and S-wave velocities at 1 MHz.

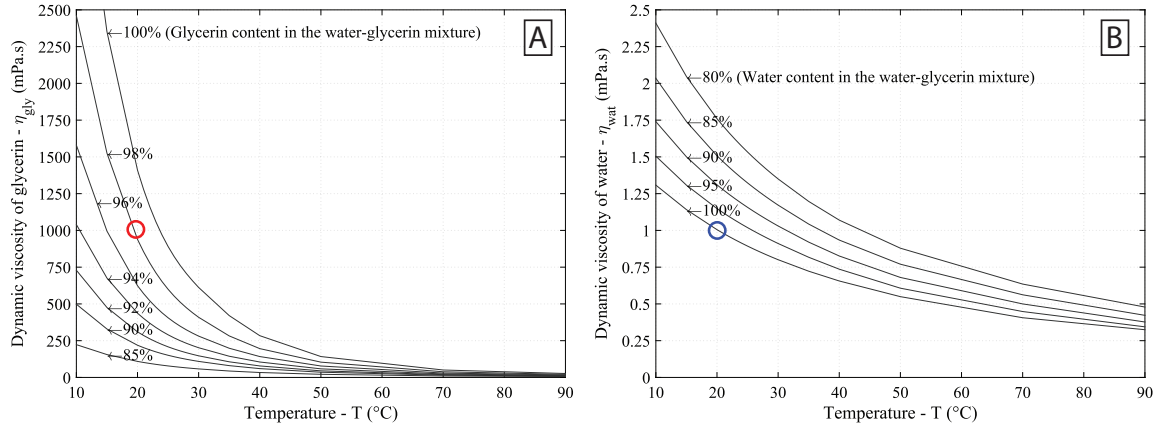

Figure 3.3: Dynamic viscosity of water-glycerin mixture as function of temperature. The source data is extracted from *Segur and Oberstar* (1951).

sample.

We also studied the effect of the boundary conditions on the measured elastic properties, with two different configurations for the drainage system: 1) open (drained conditions), and 2) closed (undrained for the system $\{sample + dead\,volumes\}$) (Figure 3.2a). *Pimienta et al.* (2016b) demonstrated that the effect of the dead volumes on the measured properties depends upon the ratio of the storage capacities of the sample and the drainage system. In the drained frequency range, the measured properties would tend to their undrained value if the dead volumes tend to zero. For example, in the Geodesign cell, the dead volumes of the closed drainage system (second case) were measured at about $V_d = 3.3\,\text{mL}$ for the top and bottom endplatens (*Pimienta et al.*, 2016b). *Pimienta et al.* (2016b) showed that if the dead volumes were 10 times greater than this volume, the measured properties would converge to the fully drained values. For our experiments, either in the Geodesign cell or the Top industrie cell, when the drainage system is open, the dead volumes are in fact much larger, and correspond to the volume of all the hydraulic tubings added to the volume of fluid in the pore-pressure pumps. During the stress oscillations, the pore pressure pumps are shut off, to avoid a fluid induced response back to the sample, and to monitor the pore pressure evolution.

The sample is 8 cm long and 4 cm diameter cylinder. To measure the strains, 4 pairs of $350\,\Omega$ metal-foil strain gauges with axial and radial orientations are glued at mid height all around the lateral surface (Figure 3.2). Axial strain (ε_{ax}) and radial strain (ε_{rad}) are averaged from all the strain gauges. The sample is under a rubber jacket that separates the pore pressure (p_f) from the confining pressure (P_c) (Figure 3.2a). When the sample is fluid saturated, the pore pressure is controlled by the pore-pressure pumps system connected to the top and the bottom of the sample through a drainage circuit (Figure 3.2a). Throughout all the experiments, the pore pressure was maintained at 2 MPa. Measurements at different

differential pressures ($P_{diff} = P_c - p_f$) were done, with a maximum confining pressure of 30 MPa, which is the blocking pressure of the axial piezoelectric actuator.

3.4.1 Hydrostatic-stress oscillations - Bulk Modulus

The hydrostatic-stress oscillations give a direct measurement of the bulk modulus K_{hyd} (*Adelinet et al.*, 2010). The oscillations are obtained from the confining pressure ΔP_c that oscillates with an amplitude of 0.2 MPa around a mean value P_c (Figure 3.4a). This amplitude value has been calibrated in order to obtain small strains on the sample ($\varepsilon \sim 10^{-6}$) to remain in the linear elastic domain (Figure 3.4a) (*Winkler and Murphy III*, 1995). The frequency of these hydrostatic oscillations is between 4×10^{-3} Hz and 4×10^{-1} Hz for the Geodesign cell, and a maximum of 1.1 Hz for the Top Industrie apparatus. The induced volumetric strain signal (ε_{vol}) is calculated by $\varepsilon_{vol} = \varepsilon_{ax} + 2\varepsilon_{rad}$. Thus, the bulk modulus K_{hyd} is obtained from the measured stress ΔP_c and the measured strain ε_{vol} such that:

$$K_{hyd} = \frac{-\Delta P_c}{\varepsilon_{vol}}, \tag{3.1}$$

with the convention $\Delta P_c = -\sigma_{ii}/3$. A linear regression of the stress signal versus the strain signal is then processed to calculate K_{hyd} (Figure 3.4b).

3.4.2 Axial-stress oscillations - Young's Modulus and Poisson's Ratio

In order to perform axial-stress oscillations (e.g., *Batzle et al.*, 2006a; *Mikhaltsevitch et al.*, 2014; *Tisato and Madonna*, 2012; *Madonna and Tisato*, 2013; *Pimienta et al.*, 2015b; *Szewczyk et al.*, 2016), we used a piezoelectric actuator that is mounted between the axial piston of the triaxial cell and the top end-platen (Figure 3.2b). A small deviatoric stress of 1 MPa is maintained on the assemblage in order to have a good contact. The frequency range of the oscillations applied on the Lavoux sample is 10^{-2} Hz to 10 Hz. The top end-platen is made out of aluminium 2017A (AU4G) and is bonded with 2 axial strain gauges acting as a axial stress sensor (Figure 3.2b). During the measurements, the two axial strains are averaged (ε_{alu}) and the axial stress is computed from $\sigma_{ax} = E_{alu}.\varepsilon_{alu}$ (Figure 3.4c), where E_{alu} is the Young's modulus of the aluminum endplaten ($E_{alu} = 72$ GPa). With the measurements of the axial strain (ε_{ax}) and the radial strain (ε_{rad}) of the sample (Figure 3.4c), we can directly obtain the Young's modulus (E) and the Poisson's ratio (ν) of the sample:

$$E = \frac{\sigma_{ax}}{\varepsilon_{ax}} \quad \text{and} \quad \nu = -\frac{\varepsilon_{rad}}{\varepsilon_{ax}}. \tag{3.2}$$

E and ν are determined by linear regression of the signals, respectively, σ_{ax} over ε_{ax} and $-\varepsilon_{rad}$ over ε_{ax} (Figure 3.4d). A bulk modulus (K_{ax}) and a shear modulus (G_{ax}) are calcu-

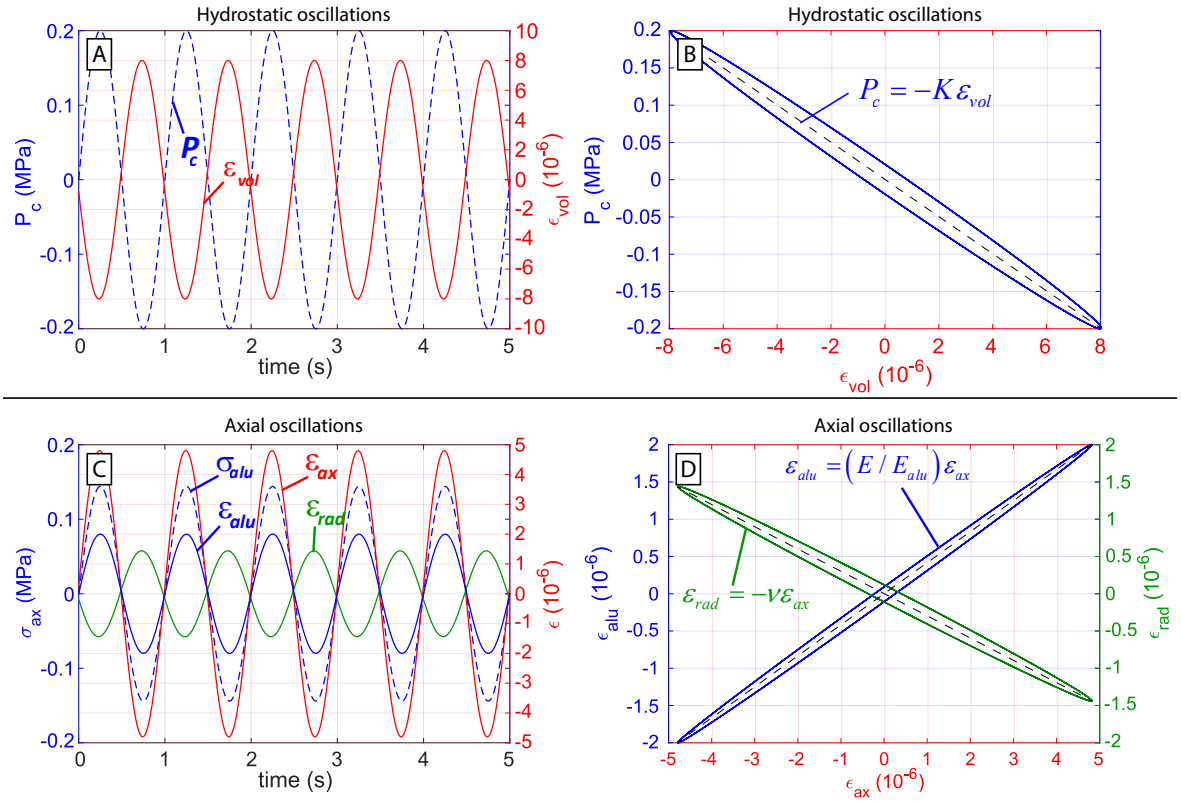

Figure 3.4: Example of stress-strain vs time recordings during a-b) hydrostatic oscillations, and c-d) axial oscillations. The elastic moduli are calculated from the linear regressions of the stress vs strain curves (b-d). The ellipse shapes (hysteresis) result from the phase shift between stress and strain when dispersion occurs, similarly to viscoelastic materials.

lated, with the assumption of an isotropic medium:

$$K_{ax} = \frac{E}{3\,(1-2\nu)} \quad \text{and} \quad G_{ax} = \frac{E}{2\,(1+\nu)}. \tag{3.3}$$

K_{ax} can then be compared to the bulk modulus K_{hyd} obtained from the hydrostatic oscillations to validate the assumption of isotropy, and to check the consistency of the results.

3.4.3 Attenuation - Q^{-1} measurements

The factor Q^{-1} measures the elastic energy dissipation within the sample. When this dissipation occurs, the rheology of the medium is similar to a viscoelastic material (*O'Connell and Budiansky*, 1977). The stress-strain curve presents an elliptic shape that clearly highlights the non elastic behavior (e.g. Figures 3.4b and 3.4d). This results from the phase shift between the stress and the strain. During a dynamic oscillation of frequency f, the complex stress can be expressed as $\bar{\sigma} = \sigma e^{i(2\pi f t + \phi_\sigma)}$ and the resulting complex strain $\bar{\varepsilon} = \varepsilon e^{i(2\pi f t + \phi_\varepsilon)}$, where ϕ_σ and ϕ_ε are the phases of $\bar{\sigma}$ and $\bar{\varepsilon}$. For each elastic modulus, the calculation of the Q^{-1} factor is based on the causality principle, where the complex modulus $\bar{M}$ relates the stress $\bar{\sigma}$ to its resulting strain $\bar{\varepsilon}$:

$$\bar{\sigma} = \bar{M}\bar{\varepsilon}. \tag{3.4}$$

The factor Q_M^{-1} of the modulus $\bar{M}$ is then defined as follows (*O'Connell and Budiansky*, 1978):

$$Q_M^{-1} = \frac{\mathrm{Im}\,(\bar{M})}{\mathrm{Re}\,(\bar{M})} = \frac{\mathrm{Im}\left(\bar{\sigma}/\bar{\varepsilon}\right)}{\mathrm{Re}\left(\bar{\sigma}/\bar{\varepsilon}\right)} = \tan\left(\phi_\sigma - \phi_\varepsilon\right), \tag{3.5}$$

In the case of the bulk modulus measured from hydrostatic oscillations, $Q_{K_{hyd}}^{-1}$ is deduced from the phase shift between the hydrostatic stress $-\Delta P_c$, with the convention $\Delta P_c = -\sigma_{ii}/3$, and the volumetric strain ε_{vol}. With the combination of Equations 3.1 and 3.5, we obtain:

$$Q_{K_{hyd}}^{-1} = \tan\left(\phi_{-\Delta P_c} - \phi_{\varepsilon_{vol}}\right). \tag{3.6}$$

The Young's modulus and Poisson's ratio factors Q_E^{-1} and Q_ν^{-1} are deduced from Equations 3.2 and 3.5:

$$Q_E^{-1} = \tan\left(\phi_{\sigma_{ax}} - \phi_{\varepsilon_{ax}}\right) \quad \text{and} \quad Q_\nu^{-1} = \tan\left(\phi_{\varepsilon_{ax}} - \phi_{\varepsilon_{rad}}\right). \tag{3.7}$$

To derive Q^{-1} for K_{ax} and G_{ax}, with the assumptions of isotropy and small strains, we combine Equations 3.2 and 3.3:

$$K_{ax} = \frac{1}{3}.\frac{\sigma_{ax}}{\varepsilon_{ax} + 2\varepsilon_{rad}} \quad \text{and} \quad G_{ax} = \frac{1}{2}.\frac{\sigma_{ax}}{\varepsilon_{ax} - \varepsilon_{rad}}. \tag{3.8}$$

For both K_{ax} and G_{ax} the stress is σ_{ax} and the resulting strains are respectively $\varepsilon_{ax} + 2\varepsilon_{rad}$ and $\varepsilon_{ax} - \varepsilon_{rad}$. After combining Equations 3.5 and 3.8, the related attenuations are:

$$Q_{K_{ax}}^{-1} = \tan\left(\phi_{\sigma_{ax}} - \phi_{\varepsilon_{ax}+2\varepsilon_{rad}}\right) \quad \text{and} \quad Q_{G_{ax}}^{-1} = \tan\left(\phi_{\sigma_{ax}} - \phi_{\varepsilon_{ax}-\varepsilon_{rad}}\right) \tag{3.9}$$

Three different methods can be used to calculate the Q^{-1} factors (e.g., *Tisato and Madonna*, 2012). The first method consists of fitting two sine functions $y = A\sin(2\pi f + \phi)$ through the stress and strain signals and extract ϕ from each signal to calculate the phase shift $\phi_\sigma - \phi_\varepsilon$. The second method consists in extracting the phases from a Fourier analysis of the signals. For this purpose a Fast Fourier Transform (FFT) algorithm is applied on the stress and strain signals. And finally, the last method is based on the definition of Q^{-1} factor that relates Q^{-1} to the dissipated elastic energy (ΔE) during a stress-strain cycle and to the average elastic energy stored (E_m) as follows (*O'Connell and Budiansky*, 1978):

$$Q^{-1} = \frac{\Delta E}{4\pi E_m}. \tag{3.10}$$

When viscous dissipation occurs in the fluid, the stress-strain curve presents an elliptic shape, similarly to viscoelastic materials (e.g. Figures 3.4b and 3.4d). The dissipated energy ΔE is equal to the surface of this ellipse, and E_m is equal to the average surface under the stress-strain curve. The surfaces that represent ΔE and E_m can be calculated from the stress versus strain curve by numerical integration (*Tisato and Madonna*, 2012):

$$\Delta E = \sum_{n=1}^{N-1} \frac{\left(\sigma_{n+1} + \sigma_n\right)\left(\varepsilon_{n+1} - \varepsilon_n\right)}{2N_c} \quad \text{and} \quad E_m = \sum_{n=1}^{N} \frac{\sigma_n \varepsilon_n}{2N}, \tag{3.11}$$

where σ_n and ε_n are all the data points of respectively $\bar{\sigma}$ and $\bar{\varepsilon}$ signals during one recording, N is the total number of sampled data and $N_c = f.t_{tot}$ is the number of cycles, f being the frequency of the oscillation and t_{tot} the total time of the sequence. For simplicity, the three methods presented above are respectively denominated as "Sines", "FFT" and "Ellipse" method in the following text. The experimental measurements presented later in the results section were calculated from the "FFT" method, and comparison between the three methods will be provided for the axial oscillations.

The relation between the dispersion and the attenuation of the complex modulus $\bar{M}$, arises from the causality principle between the stress and strain that is expressed through the Kramers-Kronig equations (*Mikhaltsevitch et al.*, 2016b). If $\bar{M} = M_R + iM_I$, with i the imaginary unit, M_R the real part and M_I the imaginary part of $\bar{M}$, an approximation of the Kramers-Kronig equations was found by *O'Donnell et al.* (1981):

$$M_I(\omega) = \frac{\pi}{2}\omega \frac{dM_R(\omega)}{d\omega}, \tag{3.12}$$

where $\omega = 2\pi f$. The major drawback of applying Equation 3.12 to experimental data, is that an accurate calculation of the derivative $dM_R/d\omega$ by finite difference requires a good resolution in ω.

The use of Kramers-Kronig relations is the most general approach to relate dispersion and attenuation for linear systems. However, because our experimental measurements did not necessarily have a proper resolution in ω, the consistency between the measured dispersion and attenuation was verified instead with a Zener viscoelastic model (*Pimienta et al.*, 2015a), since only the modulus at zero and at infinite are required. The equivalent spring-damper model is represented Figure 3.5b, and its transfer function $\bar{M}$ can be expressed with the viscoelastic parameters of the system:

$$\bar{M} = \frac{1 + i\omega\tau}{\left(\frac{1}{M_a} + \frac{1}{M_b}\right) + \frac{i\omega\tau}{M_a}}, \tag{3.13}$$

where M_a and M_b are the moduli of the two springs, $\tau = \eta_b/M_b$ where η_b is the viscosity of the dashpot element (Figure 3.5b). This model follows the assumption that only one viscous dissipation mechanism is involved. With the approximation $M_a << M_b$, the Equations 3.5 and 3.13 give:

$$Q_M^{-1} \simeq \frac{\omega\tau}{1 + \omega^2\tau^2}\frac{M_a}{M_b}. \tag{3.14}$$

If we consider a dispersive transition where the sample's modulus ($\bar{M}$) varies from M_0 to M_1 around the cut-off frequency f_c (Figure 3.5a), the elastic parameters of the Zener model become $M_a = M_1$ and ${M_b}^{-1} = {M_0}^{-1} - {M_1}^{-1}$, and the viscosity of the dashpot becomes $\eta_b = M_1/2\pi f_c$ (Figure 3.5b). Therefore, only three parameters are required to calculate the Q^{-1} factor from Zener's model: the moduli M_0 and M_1, and the cut-off frequency f_c. It is to note here that if the dispersion is related to the global-drainage flow, M_0 and M_1 would be the drained and undrained (isobaric) moduli. If the dispersion is related to squirt-flow, M_0 and M_1 would be the undrained (isobaric) and unrelaxed (isolated) moduli.

3.5 Measurements on standard materials

Dispersion and attenuation measurements on standard materials have been done in both cells to validate the experimental protocol. Measurements on gypsum, glass and plexiglas have been done in the Geodesign cell. The full data set for hydrostatic oscillations can be found in *Pimienta et al.* (2015a), and for axial oscillations in *Pimienta et al.* (2015b).

For the Top Industrie cell, the initial design of the lower aluminum endplaten was not adapted for the axial-stress oscillations. The strain gauges were glued on the 50 mm diameter shoulder at the bottom of the piece (Figure 3.6). The whole piece being bolted to cell's base, the apparent Young modulus E_{alu} was estimated around 340 GPa (Figure 3.6). The inconvenience was that the axial strain signals from the aluminium were very weak,

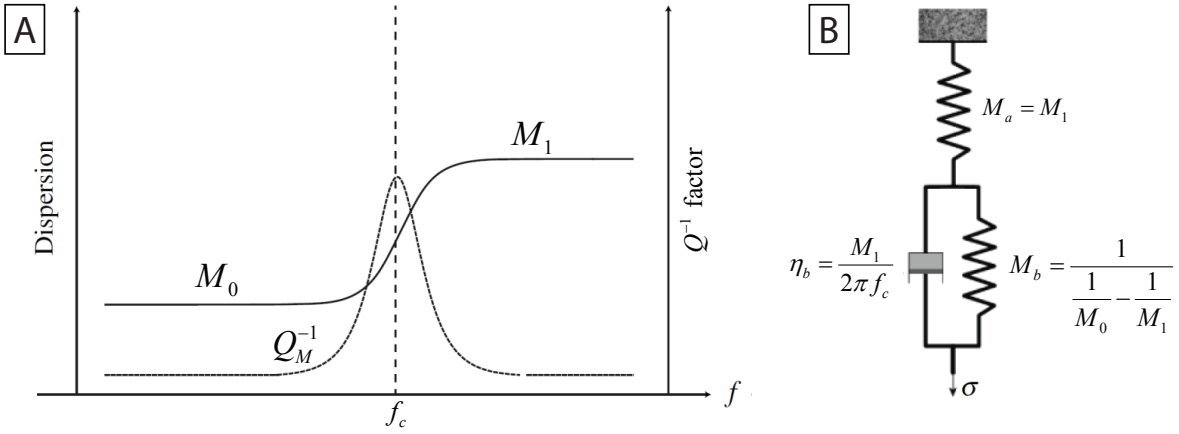

Figure 3.5: Zener's viscoelastic model used to calculate the attenuation from the dispersion. a) Model applied to the dispersion of the modulus M of relaxed value M_0 and unrelaxed value M_1. b) Spring-damper representation of Zener's model, with the relationships between the springs elastic moduli (M_a and M_b) and dispersion's relaxed and unrelaxed values (M_0 and M_1). The viscosity (η_b) of the damper is a function of M_1 and the cut-off frequency f_c: $\eta_b = M_1/2\pi f_c$.

near the uncertainty limit of the strain gauges.

A modification of the endplaten was done in order to reduce the apparent Young's modulus, and increase the amplitudes of the strain signals (Figure 3.6). The shoulder was replaced by a trench and the strain gauges were glued as high as possible on the 40 mm diameter central cylinder (Figure 3.6). The idea is to measure the strain as far as possible from the lower fixed boundary conditions, and on a smaller diameter section. A residual 13 mm had to be left above the strain gauges for the sample's jacket.

Measurements on gypsum have been done after the modification, and the results are shown Figure 3.7. The Young's modulus of the aluminum endplaten was taken to be 72 GPa. For both axial and hydrostatic oscillations, the gypsum exhibits no dispersion as expected (Figures 3.7a-c) and no attenuation accordingly (Figures 3.7d-i). Moreover, the moduli exhibit no dependence to the confining pressure. From axial oscillations, we obtain $E_{gypsum} = 41\,GPa$ (Figure 3.7a) and $\nu_{gypsum} = 0.34$ (Figure 3.7b). For the gypsum, the bulk modulus measured from hydrostatic oscillations is around $K_{gypsum} = 43$ GPa and matches the bulk modulus deduced from the axial oscillations (Figure 3.7c). The gypsum's measured moduli are in accordance with the previous calibrations of the Geodesign cell (*Pimienta et al.*, 2015a,b).

3.6 Ultrasonic measurements

In addition to the low frequency forced oscillations at different differential pressures, the apparatus enables the measurement of the high-frequency ($f = 1$ MHz) moduli from P- and

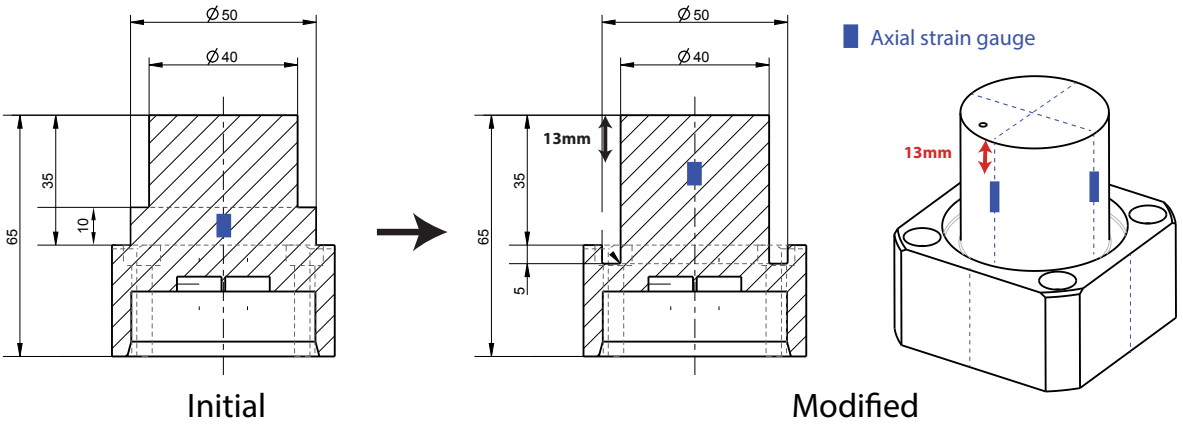

Figure 3.6: Design of the bottom aluminium endplaten acting as our stress sensor (Figure 2.5). In the initial design, the strain gauges were glued on the 50 mm diameter shoulder at the bottom of the piece. The modified design replaces the shoulder by a trench, and glues the strain gauges as high as possible on the central cylinder of diameter 40 mm, leaving a 13 mm space for the sample's jacket.

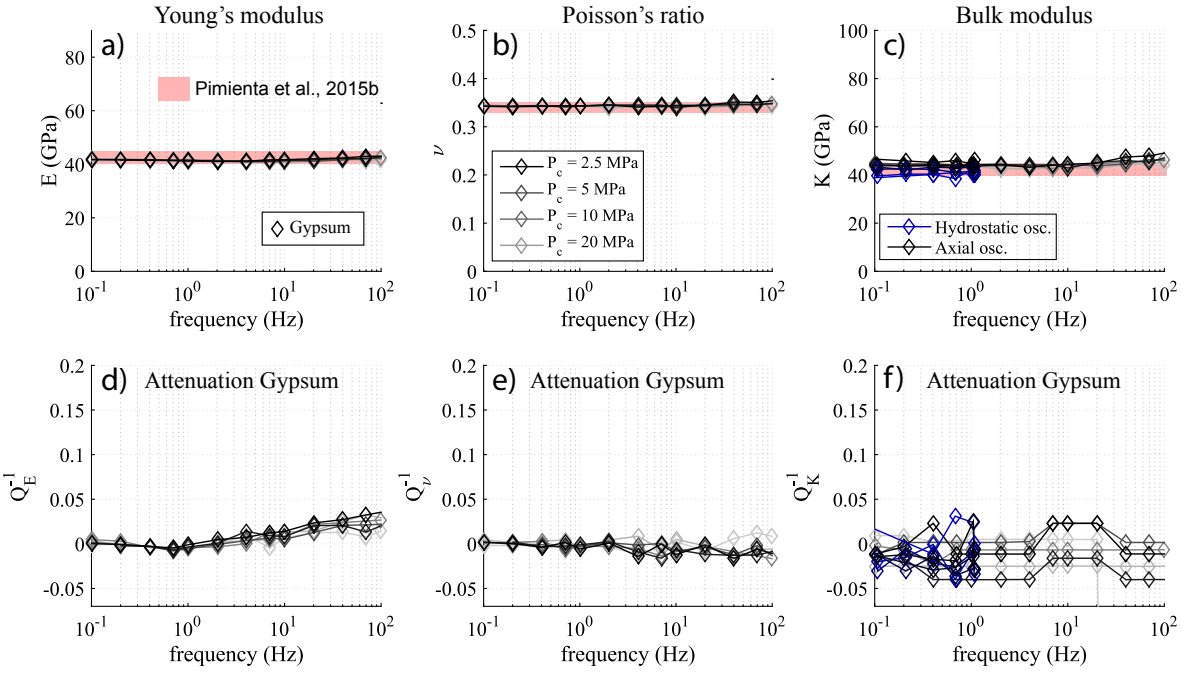

Figure 3.7: Dispersion and attenuation measurements on a gypsum standard in the Top Industrie cell, along with the results obtained from previous calibrations on the Geodesign cell by *Pimienta et al.* (2015b).

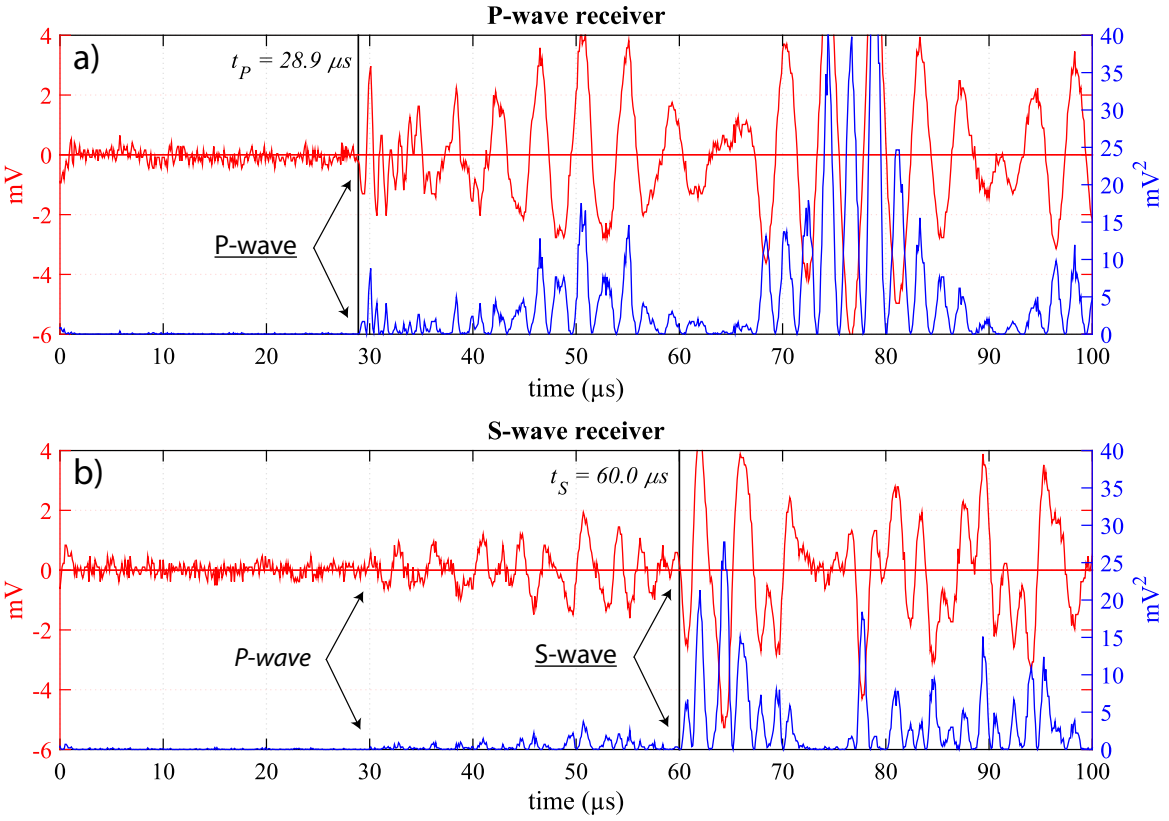

Figure 3.8: Example of ultrasonic P- and S- waves picking.

S-wave ultrasonic transducers (PI piezoceramics), glued in the end-platens at both ends on the sample (Figures 2.5 and 3.2a). The ultrasonic signals are generated by the TTi TG1010A function generator, and amplified with a FLC A400 linear amplifier. The signals are monitored and analyzed through Insite Seismic Processor software. The sampling frequency is $10MHz$. To reduce the noise, the software enables to stack signals up to 1000 times. The P- and S-waves travel times are handpicked at the first rupture of the signal (Figure).

The P- and S-wave velocities V_P and V_S are then inferred from the travel time (Δt) through the sample's length ($L = 80\,\text{mm}$), after correction of the travel time through the end-platens. The P- and S-wave travel times in the endplatens were calibrated with the aluminum sample of 80 mm length. They were found to be $t_{P-end} = 15.3\,\mu\text{s}$ and $t_{S-end} = 30.0\,\mu\text{s}$ respectively. The arrival times of the P- and S-waves are hand-picked with a maximum error of $\pm 0.1\,\mu\text{s}$. The velocity (V) is then calculated by $V = L/\Delta t$. With a maximum error on L of $\pm 0.01\,\text{mm}$, the relative uncertainty on the velocities is about $\Delta V/V = 0.5\,\%$. The high-frequency moduli K_{HF} and G_{HF} are obtained by the well known formulas:

$$K_{HF} = \rho\left({V_P}^2 - \frac{4}{3}{V_S}^2\right) \quad \text{and} \quad G_{HF} = \rho {V_S}^2, \tag{3.15}$$

where ρ_{sample} is the density of the medium, calculated from the density of the dry sample ρ_{dry}, the density of the saturating fluid ρ_{fluid} and the porosity ϕ by: $\rho_{sample} = \rho_{dry} + \phi.\rho_{fluid}$. The densities of glycerin and water are respectively $\rho_{gly} = 1250\,\mathrm{kg/m^3}$ and $\rho_{wat} = 1000\,\mathrm{kg/m^3}$ (*Bosart and Snoddy*, 1927). With a relative uncertainty on ρ estimated around 1 %, the relative uncertainty of the product ρV^2 is about 2 %. From this we can deduce the relative uncertainties $\Delta K_{HF}/K_{HF} \simeq 4\,\%$ and $\Delta G_{HF}/G_{HF} \simeq 2\,\%$ for respectively the ultrasonic bulk and shear modulus.

3.7 Permeability

In order to understand the relationship between diffusion processes and frequency effects, and especially to characterize the drained/undrained transition, it is essential to measure the permeability at different effective pressures. The permeability of medium quantifies its ability to let the fluid flow when there is a pressure gradient. This permeability can be quantified by the intrinsic permeability κ (m^2), which is an intrinsic property of the porous medium. It is defined by Darcy's law:

$$Q = \kappa \frac{A \Delta P}{\eta L}, \tag{3.16}$$

where Q ($\mathrm{m^3/s}$) is the volumetric flux through the sample, A ($\mathrm{m^2}$) the cross-sectional surface, η (Pa.s) the dynamic viscosity of the fluid, ΔP (Pa) the pressure difference between the two ends of the sample of length L (m).

To measure the permeability in the triaxial cell, the upstream and downstream pressure are regulated individually by a separate pump. A pressure difference of about $\Delta P = 1\,\mathrm{MPa}$ is imposed to the sample (Figure 3.9a), and the volumetric displacement of each pump is recorded to deduce the flux (Figure 3.9b). The volumetric flux going into the sample (here Q_{down}) and going out of the sample (here Q_{up}) are calculated from the slopes of the asymptotes (dV/dt) of the volume vs time curves, after the permanent regime is reached (Figure 3.9b). The intrinsic permeability is then calculated from Darcy's law (Equation 3.16), with $Q = (Q_{up} + Q_{down})/2$.

The permanent regime is reached when the flux becomes constant with time, i.e., when the volume variations of the pumps are linear with time. A transient regime with a higher flux is always present just after setting the pressure gradient, and its duration depends on the permeability. For low-permeability samples, the monitoring has to be long enough to be able to distinguish the permanent regime from the transient regime.

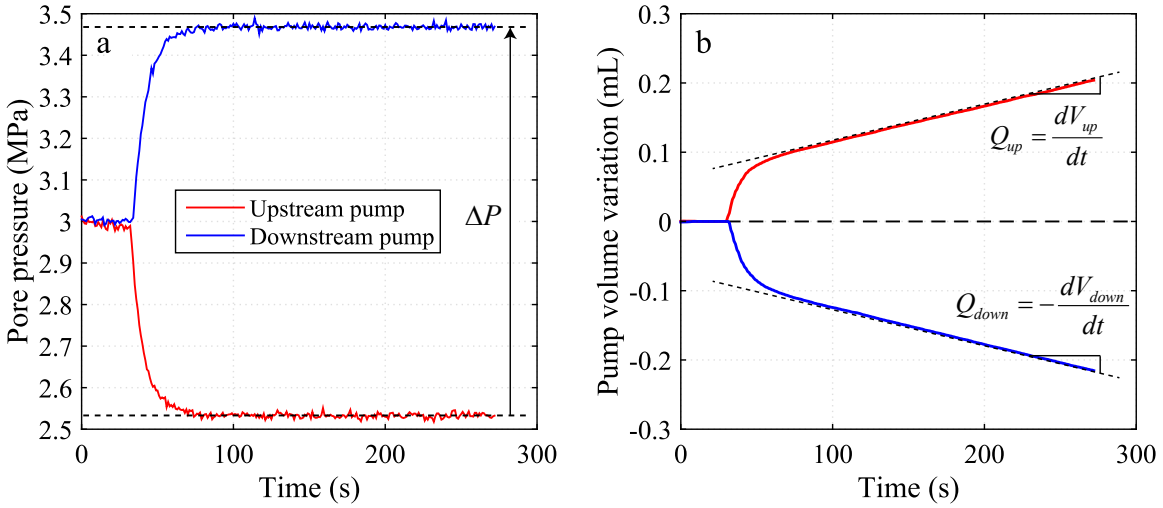

Figure 3.9: Permeability measurement by Darcy flow. A pressure gradient is imposed between the upstream and the downstream by the two pore-pressure pumps (a). The volume of each pump can be monitored as a function of time (b). The flux calculated from the upstream pump (Q_{up}) and the downstream pump (Q_{down}) are calculated from the slopes of the asymptotes (dV/dt) after the permanent regime is reached.

3.8 Sequence of a typical experiment

We present here the full experimental sequence that has been used for the different samples that will be presented in Part II.

1) Coring of the sample, and rectification of the upper and lower faces. Measurement of length and diameter.

2) Measurement of the porosity by triple-weight method. The sample is then dried in a oven around 60°C.

3) The sample is instrumented with the strain gauges and is jacketed (section 3.2).

4) The sample is installed in one of the triaxial cells, between the two endplatens, and the strain gauge wires are connected to the cell.

5) Once the cell is closed and filled with oil, a first seasoning cycle is performed. The static bulk modulus is measured from the next hydrostatic cycle.

6) Low-frequency hydrostatic and axial oscillations are performed at different frequencies around a given differential pressure (Figure 3.10).

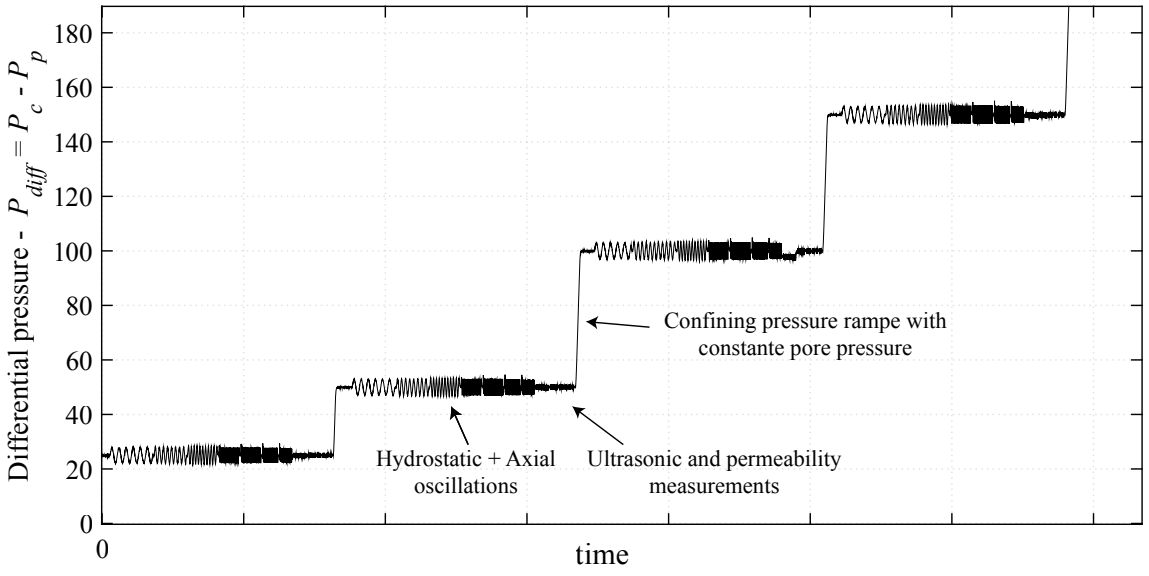

Figure 3.10: Illustration of the experimental sequence for one saturating fluid.

7) Ultrasonic measurements are done just after the low-frequency oscillations.

8) The differential pressure is changed by increasing the confining pressure to a new value, with enough time to equilibrate the pore pressure (Figure 3.10).

9) Steps 6 to 8 are repeated for each differential pressure to be characterized for the dry conditions (Figure 3.10).

10) Saturation with glycerin at a low differential pressure.

11) Steps 6 to 8 are repeated as much as necessary for the glycerin-saturated conditions.

12) Saturation with water at a low differential pressure.

13) Steps 6 to 8 are repeated as much as necessary for the water-saturated conditions, with the addition of the permeability measurement just before step 8 (Figure 3.10).

Part II

Dispersion and attenuation measurements in limestones.

CHAPTER 4

OOLITIC GRAINSTONE FROM LAVOUX

4.1 Résumé

Le calcaire Lavoux est un grainstone oolitique provenant du Dogger dans une carrière au Sud-Ouest du bassin parisien. Il est pure calcite, est a une distribution de tailles de pores bimodale, avec de la microporosité intragranulaire et de la macroporosité intergranulaire. La porosité est d'environ 23% pour une perméabilité de 10 mD. Les modules élastiques se sont montrés insensible à la pression effective entre 2.5 et 20 MPa. Seuls les résultats à 2.5 MPa seront discutés. Les fréquences sont discutées en termes de fréquences apparentes normalisées à l'eau.

La transition drainé / non-drainé est observée autour de 200 Hz, avec dispersion et atténuation des modules K, E, et ν. Le module K déduit des oscillations axiales se compare bien à celui mesuré par les oscillations hydrostatiques, en termes de disperion et d'atténuation. La théorie de Biot-Gassmann est en accord avec les résultats, d'autant plus que le module G s'est avéré non-dispersif, ce qui était prédit par la théorie.

Les mesures ultrasoniques donnent des valeurs de modules élastiques similaires aux résultats non-drainés, suggérant l'absence de toute autre transition dispersive, tel que l'écoulement crack-pore. Cela rejoint l'observation d'insensibilité à la pression effective qui suggérait l'absence de fissures. Si l'on extrapole aux mesures de terrain, cette roche serait non-dispersive car elle serait en régime non-drainé quelque soit la fréquence. Les mesures sismiques, de diagraphie ou ultrasoniques seraient ainsi équivalentes.

4.2 Indroduction

Carbonate rocks can bear multiple pore-types that depend on textural depositions and diagenetic processes (*Lucia*, 1995). It is of particular interest to identify the possible wave-induced fluid flow that might occur between different pore types, if their respective compressibilities are different and induce pressure gradients. Quarry limestones are good candidates to start investigating dispersion/attenuation effects, as they are generally monomineralic, homogeneous, and are well documented as "reference" limestones. We selected a pure calcite sample with solely two different pore types, intragranular microporosity and intergranular macroporosity, exhibiting a clear bimodal porosity distribution.

4.3 Sample description

The studied sample is a Lavoux limestone that was quarried in Paris basin, and was extensively studied in the literature (e.g., *Fabre and Gustkiewicz*, 1997; *Rasolofosaon and Zinszner*, 2002; *Youssef et al.*, 2008; *Bemer and Lombard*, 2010; *Vincent et al.*, 2011; *Zinsmeister*, 2013). It is from Dogger age and is considered as an analogue to the White Oolitic Formation of Paris basin (*Bemer and Lombard*, 2010). It is a pure calcite oolitic grainstone with intergranular macroporosity and intragranular microporosity (Figure 4.1). Mercury porosimetry measurements confirm the presence of a connected bimodal porosity distribution with pore-entry diameters around 0.6 µm and 20 µm, which corresponds respectively to the intra-oolite micropores and the inter-oolite macropores (Figure 4.2). Similar results were obtained by *Vincent et al.* (2011) or *Zinsmeister* (2013). Moreover, the NMR unimodal distribution results from *Vincent et al.* (2011) were interpreted as indicating a good connectivity between the intragranular-micropore network and the intergranular-macropore network. The study from *Zinsmeister* (2013) suggests that there are generally two families of Lavoux limestones, with small grains or with large grains. Our sample can be considered from the large grain family.

The porosity was measured around 23% from the triple-weight method, where the sample's mass is measured under three different conditions: dry, fluid-saturated and suspended in the saturant. Image analysis of the SEM photomicrograph enables to evaluate the proportion of macroporosity in the total porosity. A threshold was applied on the grayscale of the photomicrograph to turn it into a binary image showing solely the macropores (Figure 4.3). The macropores' proportion in the binary image, combined with the previous experimental porosity, gives a contribution to the total porosity of 45% and 55% for the macroporosity and the microporosity, respectively. The permeability was measured to be around 10 mD, under water-saturated conditions, and shows no dependence to differential pressure (Figure 4.4).

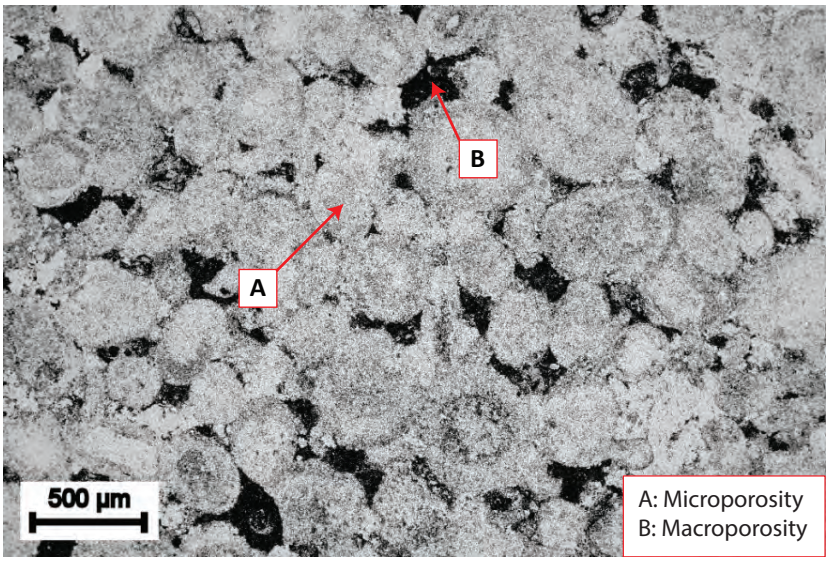

Figure 4.1: SEM photomicrograph of the Lavoux sample. The sample is a pure calcite grainstone composed of microporous oolites (marker A), surrounded by macropores (marker B). The average size of the oolites is around 300 µm.

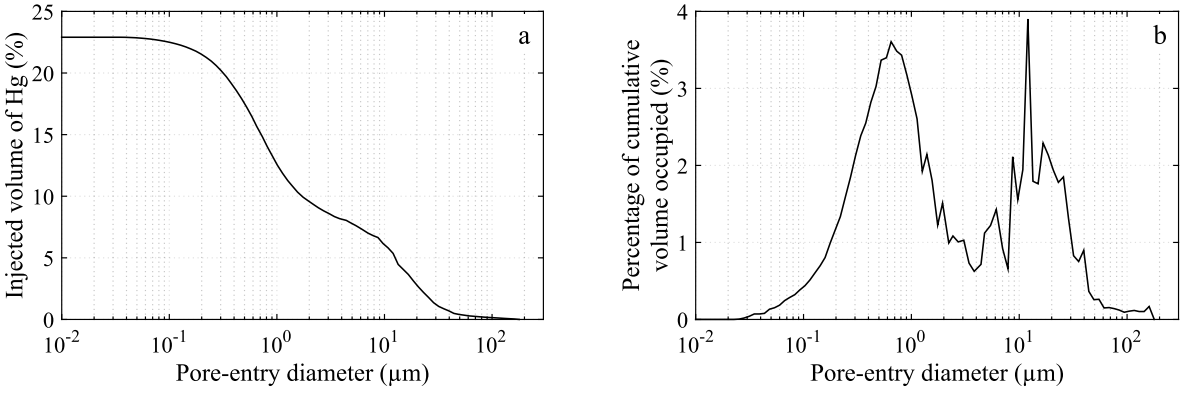

Figure 4.2: MICP analysis of a large grain Lavoux sample, exhibiting a bimodal porosity distribution.

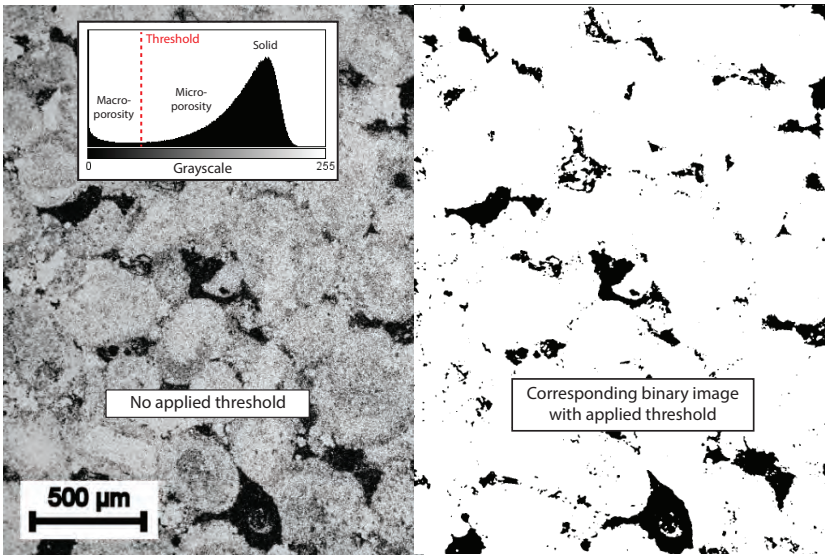

Figure 4.3: Determination of the proportion macroporosity/microporosity in the sample from the grayscale analysis of the SEM photomicrograph. A threshold is applied on the initial photomicrograph (Left), to create a binary image representing solely the macropores (Right). The porosity of the macropores is calculated from the number of black pixels over the total number of pixels of the image, evaluated at 10.35 %. With a total porosity of 23% measured experimentally, the proportion of macroporosity over microporsity is therefore around 45/55.

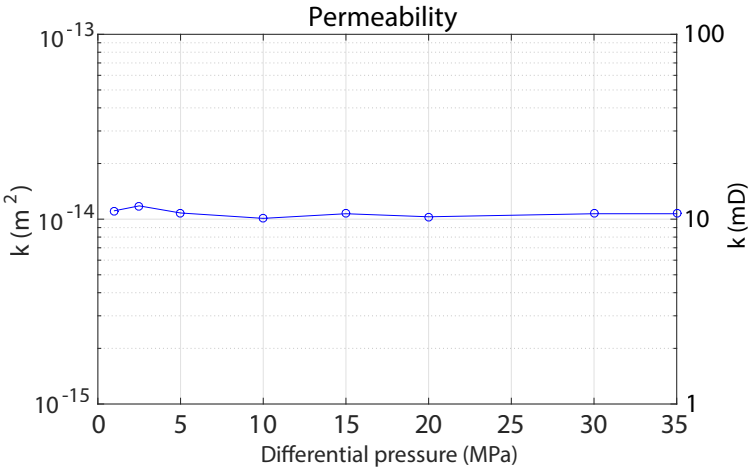

Figure 4.4: Intrinsic permeability of the Lavoux sample as a function of differential pressure. The measurements were obtained by Darcy's law under water-saturated conditions. The results show no dependence to the effective pressure.

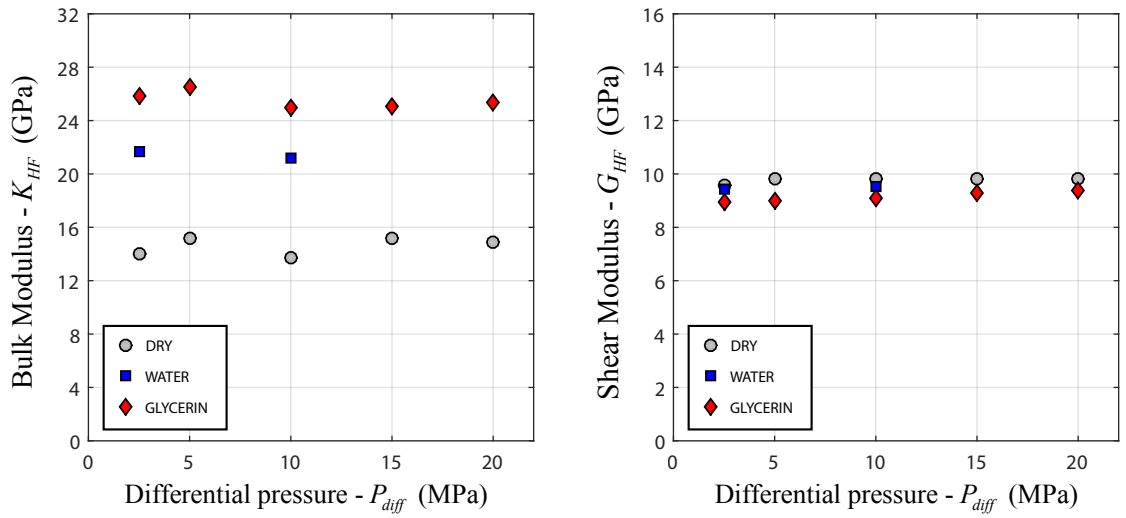

Figure 4.5: Ultrasonic results (1 MHz) at different differential pressures ($P_{diff} = P_c - p_f$) for a) the bulk modulus (K_{HF}) and b) the shear modulus (G_{HF}), for dry-, water- and glycerin-saturated conditions.

4.4 Results

4.4.1 Pressure dependence of the sample's elastic properties

Ultrasonic measurements and the axial oscillations have been performed at differential pressures from 2.5 MPa to 20 MPa, to check the pressure dependence of the elastic moduli. The travel times measured for the Lavoux limestone are reported Table 4.1, along with the deduced P-wave and S-wave velocities and high-frequency moduli K_{HF} and G_{HF} (Equation 3.15). K_{HF} and G_{HF} for dry-, water- and glycerin-saturated conditions as a function of differential pressure are represented in Figure 4.5. No variation in pressure is to be noted. K_{HF} is constant at about 14.5 GPa, 21.5 GPa and 25.5 GPa, respectively for the dry-, water- and glycerin-saturated conditions. We can see that the fluid nature strongly affects the high-frequency bulk moduli. On the other hand, G_{HF} remains constant at 9.5 GPa, with no sensitivity to the fluid nature.

For the axial oscillations at different pressures, the Young's modulus (E) and Poisson's ratio (ν) results measured at 5×10^{-2} Hz, 10^{-1} Hz and 5 Hz are presented Figure 4.6. Again, no dependence to differential pressure is observed, either for Young's modulus (Figure 4.6a) or Poisson's ratio (Figure 4.6b). Under dry conditions, no dependence to f is observed. Under glycerin-saturated conditions, nearly no dependence to f is observed on E (Figure 4.6a), but a large one is observed on ν (Figure 4.6b).

We can conclude that, similarly to the permeability, the elastic properties of the Lavoux limestone seem to not depend on the differential pressure. Therefore, in the following, all the results will be presented solely for a differential pressure of 2.5 MPa, and can be

Saturating fluid	$P_{diff}(MPa)$	t_P (µs)	t_S	V_P (m s^{-1})	V_S	K_{HF} (GPa)	G_{HF}
DRY	2.5	23.0	38.5	3520	2103	14.0	9.6
	5	22.4	38.0	3614	2131	15.4	9.8
$\rho_{sample} = 2160$ kg.m^{-3}	10	23.0	38.0	3520	2131	13.7	9.8
	15	22.4	38.0	3614	2131	15.1	9.8
	20	22.5	38.0	3598	2131	14.9	9.8
WATER	2.5	21.4	40.8	3783	1984	21.7	9.4
$\rho_{sample} = 2391$ kg.m^{-3}	10	21.5	40.6	3766	1994	21.2	9.5
GLYCERIN	2.5	20.6	42.3	3930	1914	25.9	9.0
	5	20.4	42.2	3969	1918	26.5	9.0
$\rho_{sample} = 2448$ kg.m^{-3}	10	20.8	42.0	3892	1928	25.0	9.1
	15	20.7	41.6	3911	1946	25.1	9.3
	20	20.6	41.4	3930	1956	25.3	9.4

Table 4.1: Ultrasonic measurements (1 MHz) on the Lavoux limestone under dry-, water- and glycerin-saturated conditions. The travel times t_P and t_S were corrected from the travel times in the end-platens. The length of the sample is 80 mm. K_{HF} and G_{HF} are deduced from Equation 3.15.

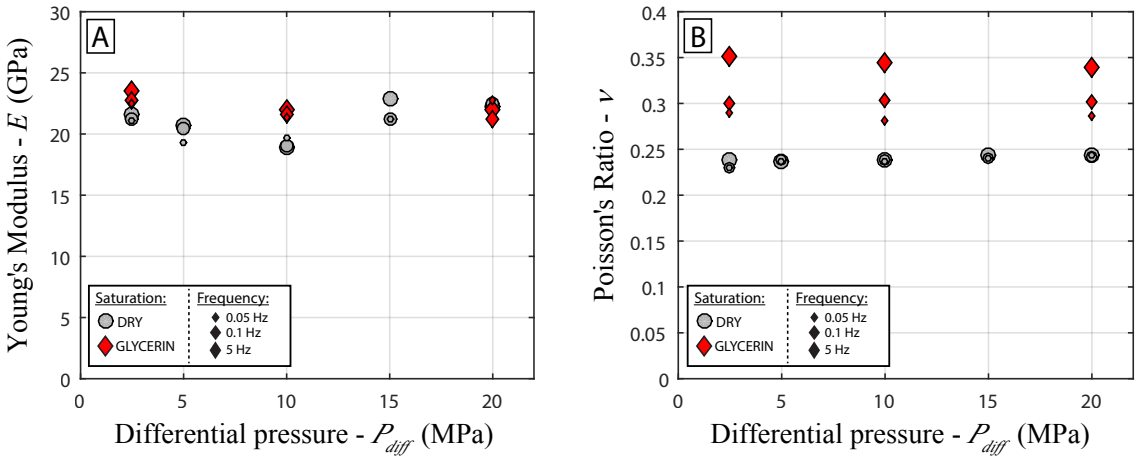

Figure 4.6: Axial oscillations results at different differential pressures ($P_{diff} = P_c - p_f$) for a) Young's modulus (E) and b) Poisson's ratio (ν). The results for dry and glycerin-saturated conditions are presented, for 0.05 Hz, 0.1 Hz and 5 Hz.

considered as independent of differential pressure.

4.4.2 Axial-stress oscillations results at $P_{diff} = 2.5\,\mathbf{MPa}$

The dispersion and attenuation results from the axial and the hydrostatic oscillations under dry-, water- and glycerin-saturated conditions are presented Figures 4.8-4.7. The results are represented as a function of an apparent frequency $f^* = f.(\eta_{fluid}/\eta_{water})$ to take into account the effect of the fluid's viscosity, with water as the reference fluid ($\eta_{water} = 10^{-3}$ Pa.s). For dry conditions, the viscosity of air is considered at about $\eta_{air} = 10^{-5}$ Pa.s. The Q^{-1} factors results are calculated from the "Ellipse" method and are systematically compared to Zener's viscoelastic model. The measurements are done with the valves of the drainage circuit open (Figure 3.2a), i.e. in drained boundary conditions, with a pore pressure of $p_f = 2$ MPa.

The Young's modulus and Poisson's ratio dispersion and attenuation results from the axial oscillations at $P_{diff} = 2.5$ MPa are presented Figure 4.8. The Young's modulus (E) is constant around 22.5 GPa between 10^{-3} Hz and 10^2 Hz, with a good agreement between the dry-, water- and glycerin-saturations (Figure 4.8a). Then, E increases slightly between 10^2 Hz and 10^3 Hz from 22.5 GPa to 24 GPa (Figure 4.8a). The factor Q_E^{-1} results are consistent with the dispersion data: no attenuation under 10^2 Hz, a small peak around $Q_E^{-1} = 0.025$ at $3\,10^2$ Hz, and no more attenuation beyond 10^3 Hz (Figure 4.8b). Moreover, the results are in good agreement with Zener's model, using the parameters $M_0 = 22.5$ GPa, $M_1 = 24$ GPa and $f_c = 220$ Hz (Figure 3.5).

Similarly to E, the Poisson's ratio (ν) below 10^2 Hz shows no dispersion, but a slight disagreement subsists between the dry- ($\nu = 0.25$), and the water- and glycerin-saturated results ($\nu = 0.275$) (Figure 4.8c). Then ν increases from 0.275 to 0.35 between $5\,10^1$ Hz and 10^3 Hz (Figure 4.8c), in correlation with a Q_ν^{-1} peak of 0.08 at around $3\,10^2$ Hz (Figure 4.8d). For this case, Zener's model seems to over predict the attenuation. The Zener peak is around 0.13 at $3\,10^2$ Hz, with the parameters $M_0 = 0.275$ and $M_1 = 0.35$. (Figure 4.8d).

Assuming isotropic conditions, the dispersion and attenuation results of the bulk modulus and the shear modulus, deduced from E and ν, are presented Figure 4.9. The bulk modulus deduced from the axial oscillations (K_{ax}) shows a large dispersion from 16 GPa to 26 GPa between $f^* = 5\,10^1$ Hz and $f^* = 10^3$ Hz, visible under glycerin-saturated conditions (Figure 4.9a). The corresponding attenuation peak reaches $Q_{K_{ax}}^{-1} = 0.225$ around $f^* = 3\,10^2$Hz with a good fit with Zener's model with the parameters $M_0 = 16$ GPa and $M_1 = 26$ GPa. The shear modulus G_{ax} shows no dispersion at all, with a constant value around $G_{ax} = 9$ GPa (Figure 4.9c). Consistently, the related attenuation $Q_{G_{ax}}^{-1}$ is nil throughout the whole frequency range (Figure 4.9d).

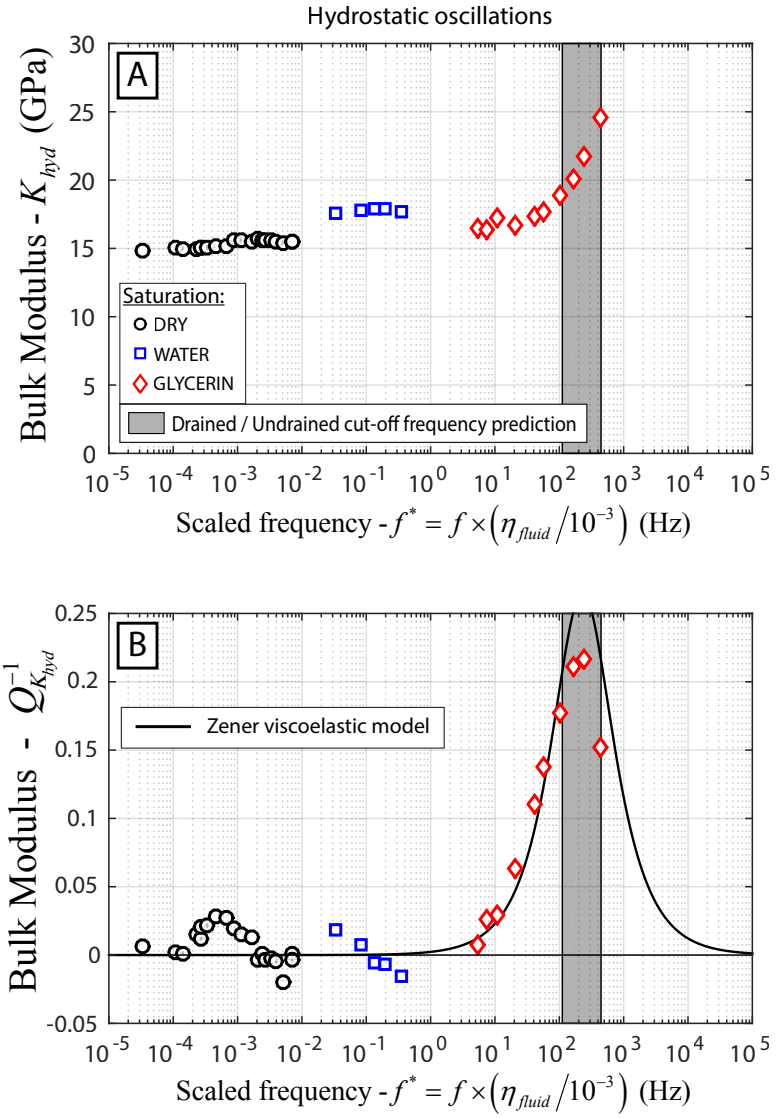

Figure 4.7: (a) Bulk modulus K_{hyd} and (b) $Q^{-1}_{K_{Hyd}}$ resulting from the hydrostatic oscillations at $P_{diff} = 2.5\,\text{MPa}$, under dry, water and glycerin-saturated conditions. The frequency is scaled with the viscosity of the saturating fluid η_{fluid}. The factor $Q^{-1}_{K_{Hyd}}$ is compared with Zener's model. The range for the drained/undrained cut-off frequency f_1^* is represented by the grey area.

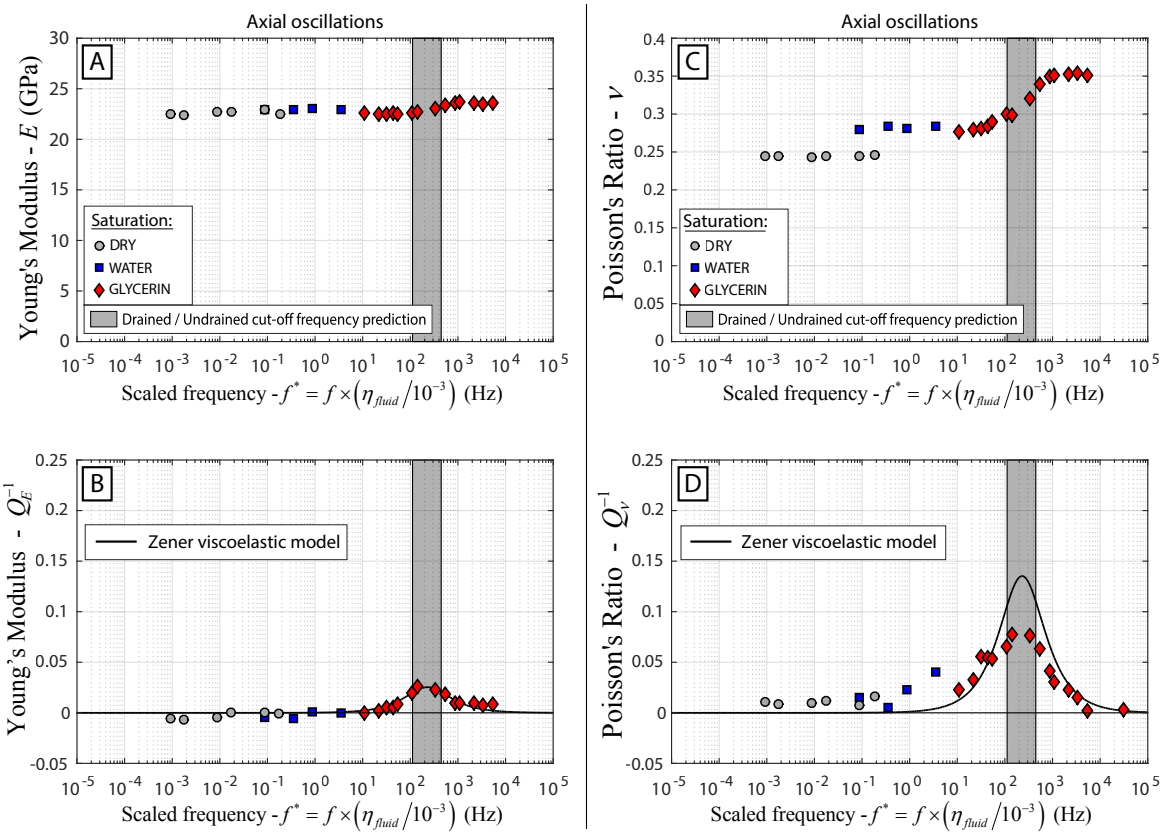

Figure 4.8: (a) Young's modulus E, (b) Q_E^{-1}, (c) Poisson's ratio ν and (d) Q_ν^{-1} resulting from the axial oscillations at $P_{diff} = 2.5\,\text{MPa}$, under dry, water and glycerin-saturated conditions. The frequency is scaled with the viscosity of the saturating fluid η_{fluid}. The factors Q_E^{-1} and Q_ν^{-1} are compared to Zener's model. The range for the drained/undrained cut-off frequency f_1^* is represented by the grey area.

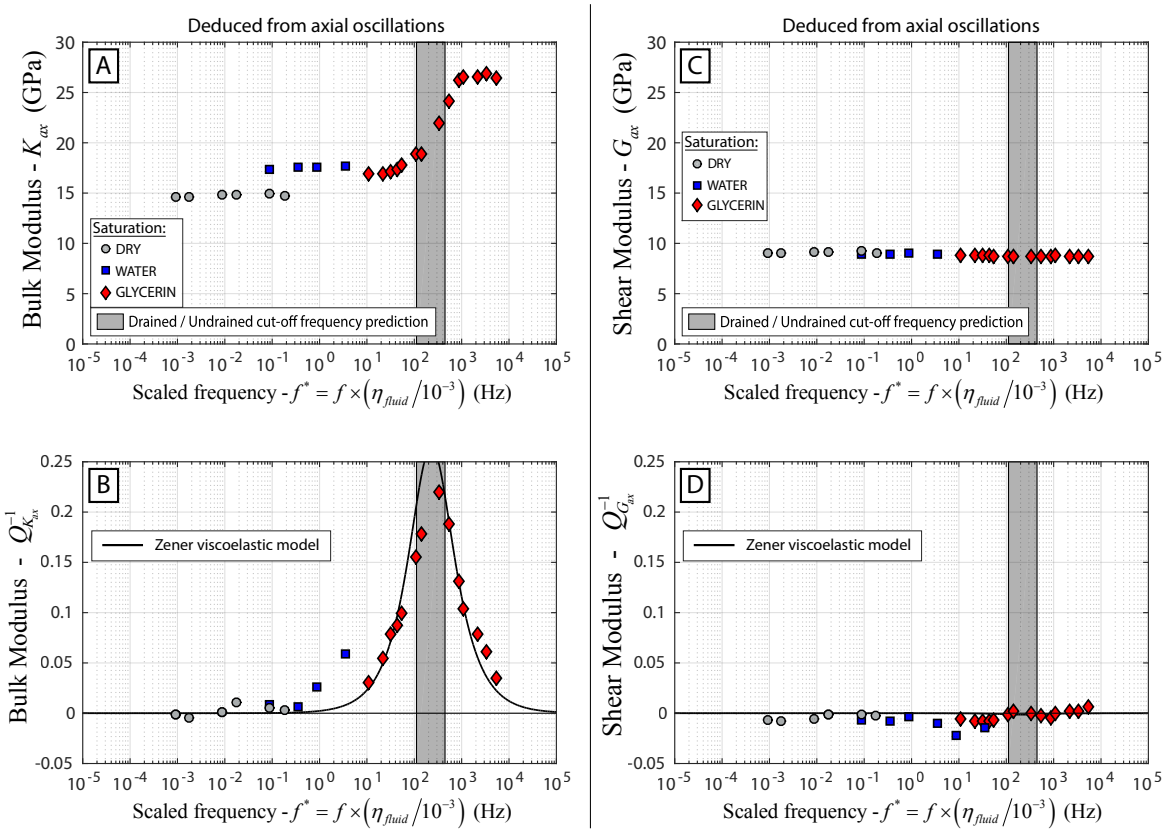

Figure 4.9: (a) Bulk modulus K_{ax}, (b) $Q^{-1}_{K_{ax}}$, (c) shear modulus G_{ax} and (d) $Q^{-1}_{G_{ax}}$ deduced from the results of the axial oscillations (Figure 4.8). K_{ax} and G_{ax} are deduced from E and ν (Equation 3.3) under the assumption of an isotropic medium. $Q^{-1}_{K_{ax}}$ and $Q^{-1}_{G_{ax}}$, deduced from Equations 3.8 and 3.9, are compared to Zener's model. The frequency is scaled with the viscosity of the saturating fluid η_{fluid}. The range for the drained/undrained cut-off frequency f_1^* is represented by the grey area.

4.4.3 Hydrostatic oscillations results at $P_{diff} = 2.5\,\mathbf{MPa}$

The results of the purely hydrostatic oscillations at $P_{diff} = 2.5\,\text{MPa}$ are presented Figure 4.7. The measured bulk modulus K_{hyd} shows a dispersion from 16 GPa to 25 GPa between $f^* = 2\,10^1$ Hz and $f^* = 4\,10^2$Hz, visible under glycerin-saturated conditions (Figure 4.7a). The related factor $Q^{-1}_{K_{hyd}}$ has a peak at about $Q^{-1}_{K_{hyd}} = 0.22$ around $f^* = 2\,10^2$ Hz and is nil elsewhere (Figure 4.7b). The attenuation seems to compare well with Zener's model with the parameters used previously for K_{ax} ($M_0 = 16\,\text{GPa}$, $M_1 = 26\,\text{GPa}$) (Figure 4.7b).

4.4.4 Uncertainty analysis

For the hydrostatic oscillations, the uncertainty on the bulk modulus measurements (δK) depends on the confining pressure uncertainty (δP), and the uncertainty of the strain measurements ($\delta\varepsilon$). From Equation 3.1, the relative uncertainty on K is given by:

$$\frac{\delta K_{hyd}}{K_{hyd}} = \frac{\delta P}{P} + \frac{\delta\varepsilon}{\varepsilon}. \tag{4.1}$$

The pressure sensor of the confining cell is capable to measure pressure with a resolution of $\delta P = 0.001\,\text{MPa}$. The amplitude of the confining pressure oscillations being around 0.2 MPa, the relative uncertainty on pressure becomes $\delta P/P = 0.005$, which can be considered negligible. Therefore, the uncertainty on the bulk modulus highly depends on the quality of the strain measurement. The higher the number of strain gauges, the lower this uncertainty becomes. A total of $n = 8$ strain gauges were used (4 axial and 4 radial). When proceeding with the oscillations, the amplitude of the strain gauges may vary slightly from one another. These variations could be related to the quality of the contact between the strain gauge and the sample, or to small heterogeneities in the sample despite being considered perfectly homogeneous. Although the orientation of the strain gauges relatively to the vertical and horizontal axis can be determinant for axial oscillations, it is irrelevant for hydrostatic oscillations on a isotropic medium. For the hydrostatic oscillations at $f = 0.004\,\text{Hz}$ and $P_{diff} = 2.5\,\text{MPa}$, the average of the 8 measured strain was $\varepsilon = 2.22\,\mu\text{m/m}$, with a standard deviation of $std = 0.266$. The error on the average strain ($\delta\varepsilon$) can be calculated from $\delta\varepsilon = std/\sqrt{n} = 0.094\,\mu\text{m/m}$. From Equation 4.1, we deduce the relative uncertainty on K_{hyd} for the hydrostatic oscillations: $\delta K_{hyd}/K_{hyd} = 4.2\%$. This corresponds to an error of about $\pm\,0.3\,\text{GPa}$ for K_{hyd}.

The similar approach can be done to calculate the uncertainties for the axial oscillations results. From Equation 3.2, we can deduce:

$$\frac{\delta E}{E} = \frac{\delta\varepsilon_{alu}}{\varepsilon_{alu}} + \frac{\delta\varepsilon_{ax}}{\varepsilon_{ax}} \quad \text{and} \quad \frac{\delta\nu}{\nu} = \frac{\delta\varepsilon_{rad}}{\varepsilon_{rad}} + \frac{\delta\varepsilon_{ax}}{\varepsilon_{ax}}. \tag{4.2}$$

With 2 strain gauges measuring ε_{alu}, 4 measuring ε_{ax} and 4 measuring ε_{rad}, the relative un-

certainties on E and ν were found to be: $\delta E/E = 12\%$ and $\delta\nu/\nu = 8\%$. These uncertainties corresponds to errors of ± 1.3 GPa for E and ± 0.01 for ν. We can then use Equation 3.3 to propagate the error to K_{ax} and G_{ax}. This gives an error of ± 1.5 GPa for K_{ax}, and ± 0.6 GPa for G_{ax}.

The presented methodology to calculate uncertainty does not take into account any systematic error that would be due to the apparatus or the protocol. As shown by the calibration measurements on a gypsum standard (Figure 3.7), it would appear that such systematic error on the gypsum appeared negligible. However, we cannot exclude that the quality of the strain gauge bounding might differ in quality depending on the rock type, and might even degrade in time with long experiments, increasing the systematic error.

4.4.5 Comparison of the three methods used to infer Q^{-1}

Q^{-1} factors of all the elastic properties deduced from the axial oscillations at $P_{diff} = 2.5$ MPa under glycerin-saturated conditions were also calculated using the "Sines" and the "FFT" method. Those are compared to the previously presented results from the "Ellipse" method (Figure 4.10). For E, K_{ax} and G_{ax} (respectively Figures 4.10a, 4.10c and 4.10d) the three methods compare well over the experimental frequency range $f \in [2\,10^{-2}\,;\,5]$ Hz. In case of ν (Figure 4.10b), the "FFT" and the "Ellipse" method are consistent with each other, but not with the "Sines" method. The results obtained with the "Sines" method for ν are unstable and give erratic results with data points off the chart (Figure 4.10b). The "Sines" method shows also some slight inconsistencies with the other methods at 10^{-2} Hz for E and K_{ax} (Figures 4.10a and 4.10c). We can therefore conclude that only the "Ellipse" and the "FFT" methods are reliable to calculate Q^{-1} in our case.

4.5 Discussion

4.5.1 The drained and undrained regimes

With respect to the cut-off frequencies (Equation 1.39), and especially the drained/undrained cut-off frequency, a viscosity contrast for the fluid results in a shift in frequency of the transition. The results presented with the three different saturating fluids show a good continuity in scaled frequency (Figure 4.11). A slight discrepancy exists between the dry and the water saturated conditions, the dry bulk modulus being about 2.5 GPa lower than the water-saturated bulk modulus (Figure 4.11a). This discrepancy is seen in both the hydrostatic and the axial oscillations and seems larger then the uncertainties of the measurements (Figure 4.11a). It is possible that this is related to a systematatic error on the strain gauges after a long experiment, since the water-saturation measurements are done after the dry- and the glycerin-saturated cycles.

The drained/undrained cut-off frequency (f_1) was experimentally measured around

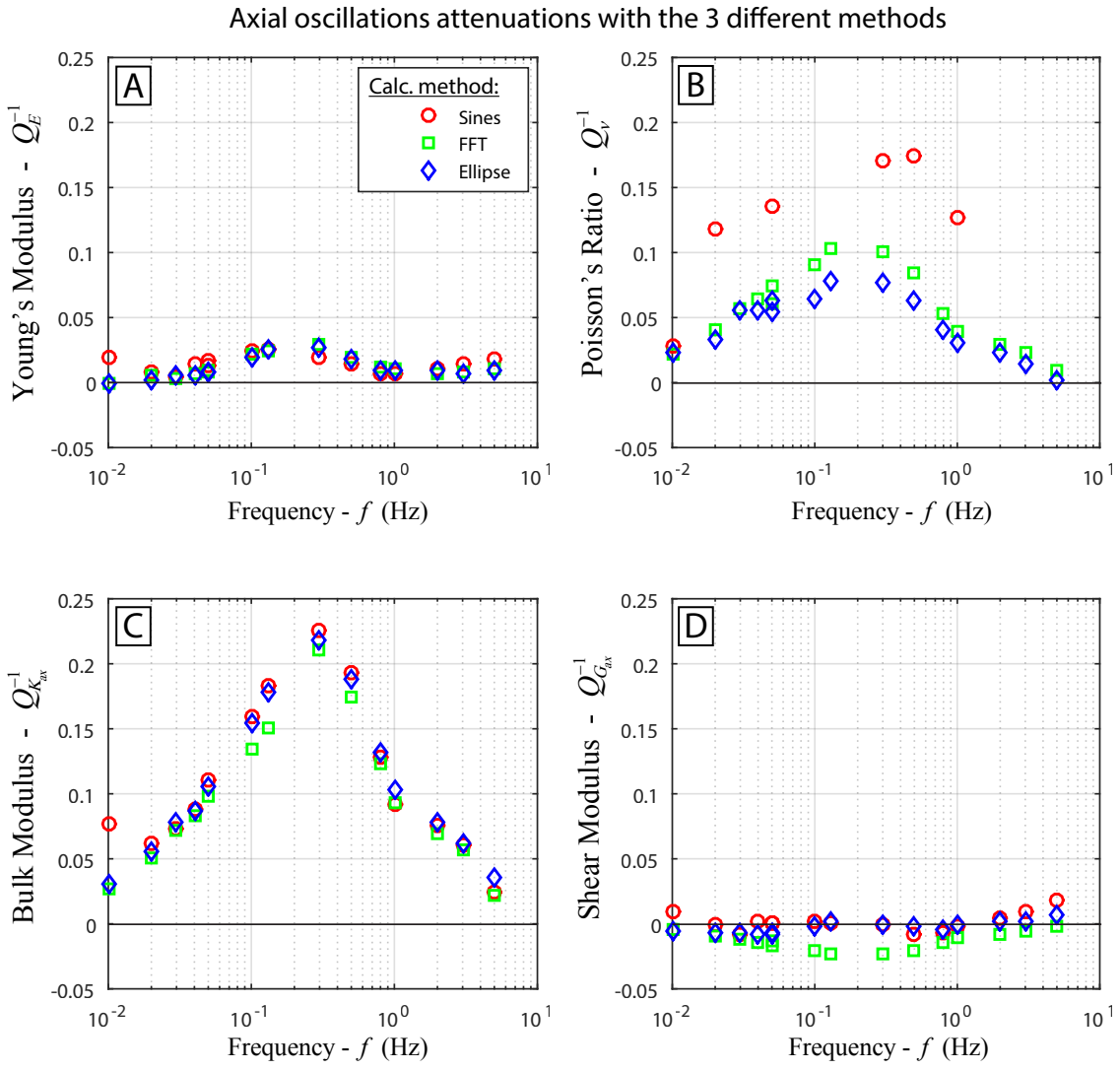

Figure 4.10: Comparison of the three methods used to calculate Q^{-1}: "Sines", "FFT" and "Ellipse" methods. Example for the axial oscillations at $P_{diff} = 2.5\,\text{MPa}$ under glycerin-saturated conditions, for (a) Young's modulus, (b) Poisson's ratio, (c) bulk modulus and (d) the shear modulus.

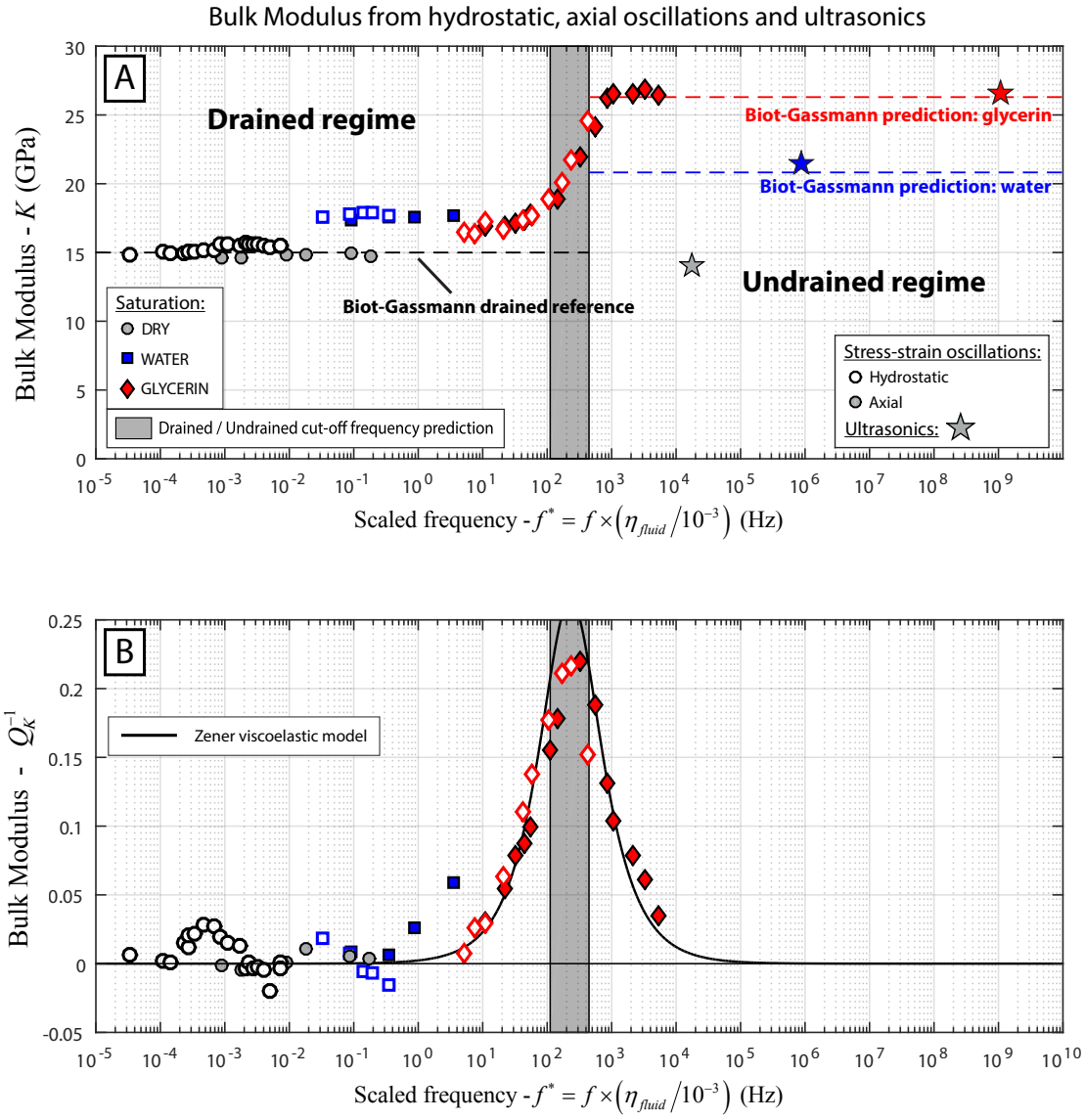

Figure 4.11: (a) Comparison of the hydrostatic, the axial and the ultrasonic measurements for the bulk modulus and (b) the bulk modulus Q^{-1} factor deduced from the hydrostatic and axial oscillations for dry, water and glycerin-saturated conditions at $P_{diff} = 2.5\,\text{MPa}$. Biot-Gassmann's predictions for water and glycerin are represented for the undrained regime in addition to the ultrasonic results (Figure 4.11a). The frequency is scaled with the viscosities of the saturating fluids.

$2\,10^{-1}$ Hz in glycerin-saturated conditions, which is a frequency that is equivalent to $2\,10^{2}$Hz in water-saturated conditions. Therefore, when studying dispersion and attenuation phenomenon related to diffusion processes at different scales, the experimental frequencies can be scaled by the dynamic viscosity of the fluid η (*Pimienta et al.*, 2015a,b, 2016c; *Spencer and Shine*, 2016). This has the major advantage to increase the apparent frequency range reachable by the experimental setup-up, in our case for the axial oscillations from $10^{-2} - 10^{1}$ Hz to $10^{-4} - 10^{4}$ Hz, and therefore characterize the dispersion of the sample over a much larger frequency band.

Elastic moduli

The common elastic modulus we can extract from the hydrostatic and the axial oscillations is the bulk modulus, respectively K_{hyd} and K_{ax} (deduced from E and ν). The comparison between the dispersion and Q^{-1} of both moduli at $P_{diff} = 2.5$ MPa is presented Figure 4.11. The hydrostatic and the axial results compare well over their overlapping frequencies, both for the dispersion (Figure 4.11a), and for Q^{-1} (Figure 4.11b). This tends to validate our hypothesis of an isotropic medium, and shows a good consistency between both forced oscillation methods, for the drained and undrained regimes.

Using the measured permeability value (i.e. $\kappa = 10^{-14}$ m^2) and the dry bulk modulus (i.e. $K_d = 15$ GPa), and assuming a diffusion length L in the sample between 40 mm and 80 mm, the expected cut-off frequency f_1^* for the drained/undrained transition is between 10^2 Hz and $4\,10^2$ Hz. All the previous dispersions and Q^{-1} results are in agreement with this frequency transition (Figures 4.8, 4.9, 4.7 and 4.11). The maximum Q^{-1} peaks for E, ν, K_{ax} and K_{hyd}, and the dispersion slopes of the elastic moduli are systematically in the expected range of f_1^* (Figures 4.8, 4.9, 4.7 and 4.11).

The undrained elastic properties of a rock are generally deduced from the drained (or dry) properties using Biot-Gassmann relations (*Gassmann*, 1951):

$$K_u = K_d + \frac{K_f\left(1 - \frac{K_d}{K_S}\right)^2}{\Phi + \left(\left(1 - \frac{K_d}{K_S}\right) - \Phi\right)\frac{K_f}{K_S}} \quad \text{and} \quad G_u = G_d, \tag{4.3}$$

where K_d and G_d are respectively the drained bulk modulus and shear modulus, Φ the porosity, K_f the saturating fluid's bulk modulus, K_S the skeleton bulk modulus, K_u and G_u respectively the undrained bulk modulus and shear modulus. The Biot-Gassmann predictions for the bulk modulus with water- and glycerin-saturated conditions are presented in Figure 4.11a, using the parameters $K_d = 15$ GPa, $\Phi = 23\%$, $K_{f-water} = 2.21$ GPa, $K_{f-glycerin} = 4.36$ GPa (*Bridgman*, 1931) and $K_S = 77$ GPa, which is the bulk modulus of calcite (*Mavko et al.*, 2009). The predictions give an undrained bulk modulus with water of $K_{u-wat} = 20.8$ GPa and with glycerin $K_{u-gly} = 25.8$ GPa. These results are consistent

with the bulk modulus results independently obtained from the forced oscillations under glycerin-saturated conditions (Figure 4.11a). Moreover, the shear modulus G_{ax} deduced from the axial oscillations is constant over the frequency range of the drained/undrained transition (Figure 4.9c), which is again consistent with Biot-Gassmann's theory.

Q^{-1} factors

The Zener viscoelastic model (Figure 3.5), used to calculate Q^{-1} from the modulus' dispersion, gives accurate results for the Young's modulus (Figure 4.8b), the bulk modulus (Figures 4.9b and 4.7b) and the shear modulus (Figure 4.9d). However, the model seems to overpredict Q^{-1} for the Poisson's ratio (Figure 4.8d), with a peak value of 0.13 instead of 0.09. These results, added to similar observations in Fontainebleau sandstones (*Pimienta et al.*, 2015a), show the general good applicability of Zener's model to the drained/undrained transition.

In an isotropic medium, we previously showed that the bulk modulus and the shear modulus can be deduced from axial solicitations, and that the bulk modulus gives consistent results with the hydrostatic measurements in the drained and undrained regimes. Therefore, the axial oscillations allows to measure all the moduli if we measure the axial and the radial strains. The Young's modulus Q_E^{-1} and Poisson's ratio Q_ν^{-1} are directly measured from the phase shifts between the output signals σ_{ax}, ε_{ax} and ε_{rad} (Equation 3.7). We presented a method to deduce the bulk modulus $Q_{K_{ax}}^{-1}$ and the shear modulus $Q_{G_{ax}}^{-1}$ from different combinations of the previous output signals (Equation 3.9). It is therefore of great interest to check the consistency of these Q^{-1} values with existing equations that give relationships between Q^{-1} of all the different moduli. Our aim is to calculate Q_K^{-1} and Q_G^{-1} from the measured Q_E^{-1} and Q_ν^{-1}. Such relationships have been given by *Winkler and Nur* (1979), but with the hypothesis of a constant Poisson's ratio ν. *Pimienta et al.* (2016a) introduced a dispersive ν into *Winkler and Nur* (1979)'s equations, and obtained the following relationship between ν, Q_ν^{-1}, Q_E^{-1} and Q_G^{-1}:

$$Q_\nu^{-1}\left[\nu + Q_G^{-1}\left((1+\nu)\,Q_E^{-1} - Q_G^{-1}\right)\right] = (1+\nu)\,Q_E^{-1} - (1+\nu)\,Q_G^{-1}. \tag{4.4}$$

For our purpose, the previous equation can be turned into a second order polynomial on Q_G^{-1}:

$$-Q_\nu^{-1}\left[Q_G^{-1}\right]^2 + (1+\nu)\left(1 + Q_\nu^{-1}Q_E^{-1}\right)\left[Q_G^{-1}\right] + \left(\nu Q_\nu^{-1} - (1+\nu)\,Q_E^{-1}\right) = 0, \tag{4.5}$$

which admits two solutions that can be numerically calculated. The order of magnitudes of these two solutions are around $Q_G^{-1} \sim 0.01$ and $Q_G^{-1} \sim 10$. The second solution being unrealistic as it would give a phase shift between the stress and the strain of nearly $\pi/2$, we keep only the first one. We then calculate the bulk modulus attenuation Q_K^{-1} with the

relationship from *Winkler and Nur* (1979):

$$Q_K^{-1} = \frac{3}{1-2\nu} Q_E^{-1} - \frac{2\,(1+\nu)}{1-2\nu} Q_G^{-1}. \tag{4.6}$$

For the axial oscillations, in the frequency range of the drained/undrained transition under glycerin-saturated conditions at $P_{diff} = 2.5\,\text{MPa}$, the results for Q_K^{-1} and Q_G^{-1} deduced from Equations 4.5 and 4.6 are reported Figure 4.12, along with $Q_{K_{ax}}^{-1}$ and $Q_{G_{ax}}^{-1}$ obtained experimentally from the output signals with the "FFT" and the "Ellipse" method (Equation 3.9, Figures 4.10c and 4.10d). The results show a general good match between the two methods to calculate Q_K^{-1} and Q_G^{-1}. Q_K^{-1} as deduced from $Q_{E_{Ellipse}}^{-1}$ and $Q_{\nu_{Ellipse}}^{-1}$ through Equations 4.5 and 4.6, seems to be a bit lower than the direct experimental result, with a value of 0.15 instead of 0.22 at $f = 0.3\,\text{Hz}$ (Figure 4.12). This error is solely related to the small difference that was measured between $Q_{\nu_{Ellipse}}^{-1}$ and $Q_{\nu_{FFT}}^{-1}$ (Figure 4.10b). Note that $Q_{E_{Ellipse}}^{-1} = Q_{E_{FFT}}^{-1}$ (Figure 4.10a). We can therefore conclude that, in an isotropic medium and for the drained/undrained transition, the axial oscillations allow to measure all moduli and their respective Q^{-1} factors, either directly calculated from σ_{ax}, ε_{ax} and ε_{rad} (Equation 3.9), or from the relationships relating ν, Q_E^{-1}, Q_ν^{-1}, Q_K^{-1} and Q_G^{-1} (Equations 4.5 and 4.6).

4.5.2 Absence of dispersion at higher frequencies

Once the drained and the undrained properties of the rock are clearly identified, one can investigate the possible existence of other dispersive transitions at higher frequencies. This concerns a possible unrelaxed (saturated isolated) regime.

No squirt-flow: absence of cracks?

Undrained/unrelaxed transitions can exist when local flows occur within the REV in the undrained regime, for instance squirt-flows from compliant cracks to rounded pores (*Mavko and Jizba*, 1991). The only high-frequency properties available to us in this study are the ultrasonic results (1 MHz) reported Table 4.1. The high-frequency bulk modulus K_{HF} for dry-, water- and glycerin-saturated conditions are reported on Figure 4.11a. In dry conditions, the ultrasonic result corresponds clearly to the drained properties. For water- and glycerin-saturated conditions, the ultrasonic results show a good correspondence with the undrained properties, or the Biot-Gassmann's predictions (Figure 4.11a). We can conclude that no distinct unrelaxed regime is expected beyond the drained/undrained transition for this dual-porosity limestone. In the Lavoux limestone, the elastic moduli are independent of the differential pressure (Figures 4.5 and 4.6), suggesting the absence of cracks. Consistently, no squirt-flow is thus possible between cracks or from cracks to rounded pores. This is corroborated by the sample's permeability that is also independent of differential pressure (Figure 4.4) (*Guéguen et al.*, 2011).

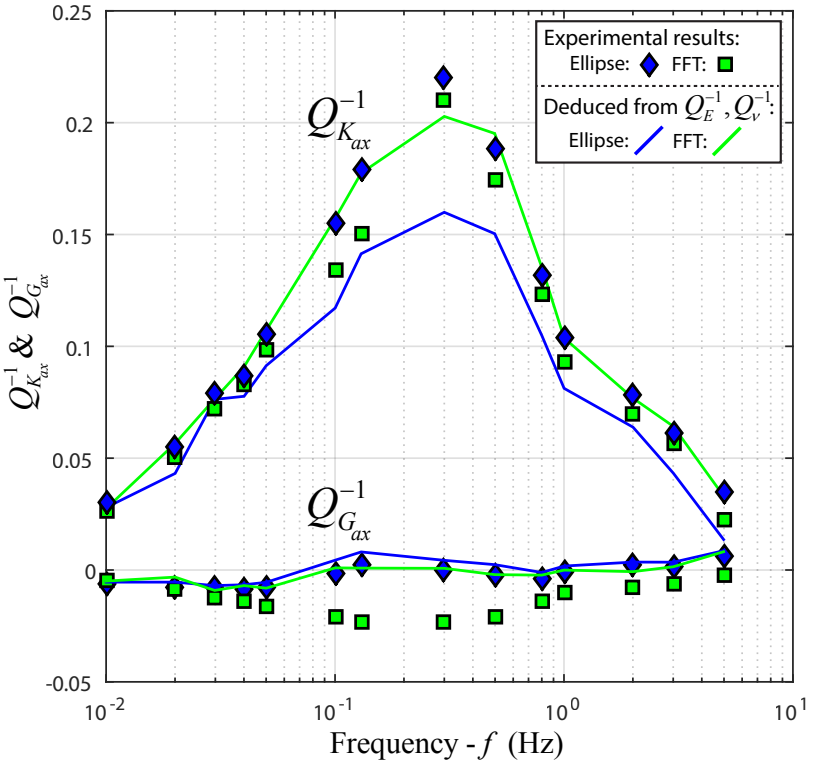

Figure 4.12: Comparison between $Q_{K_{ax}}^{-1}$ and $Q_{G_{ax}}^{-1}$ obtained experimentally (Equation 3.9) with the "FFT" and the "Ellipse" methods for the drained/undrained transition under glycerin-saturated conditions at $P_{diff} = 2.5\,\text{MPa}$ (Figures 4.10c and 4.10d), and the same factors deduced from Q_E^{-1}, Q_ν^{-1} and ν (Equations 4.5 and 4.6).

No local diffusion between the microporosity and the macroporosity.

In a bimodal-porosity medium, question rises whether there could be a local diffusion between the macroporosity and the microporosity, delayed relative to the global diffusion, due to a lower permeability of the micropores contained in the oolites. The macroporosity of the Lavoux limestone being connected independently of the microporosity, we can model this grainstone as a pile of spherical-microporous oolites, of diameters 100 µm to 500 µm, solely surrounded by macropores (Figure 4.13). The REV of the Lavoux would be a volume containing a few oolites separated by macropores, as no heterogeneity larger than the oolites seem to exist (Figure 4.1). At $f = 1\,\text{MHz}$ in saturated conditions, the ultrasonic velocities of both the P-wave or the S-wave are greater than $1914\,\text{m}\,\text{s}^{-1}$ (Table 4.1) corresponding to a minimum wavelength of approximately 2 mm. This wavelength represents a square area similar to half the area of the photomicrograph presented in Figure 4.1, containing at least a dozen of oolites. Thus, we can safely assume that, during the propagation of the ultrasonic P-wave and S-wave, the volume of the oscillating stress field is much larger than the limestone's REV. In the undrained regime, the pore-pressure is isobaric in the REV (*Gassmann*, 1951), meaning that the fluid's pressure in the macropores ($p_{f-Macro}$) equals the fluid's pressure in the oolites' micropores ($p_{f-micro}$) (Figure 4.13).

Similarly to the drained/undrained transition characterized by the cut-off frequency f_1^* (Equation 1.39) that concerns the global diffusion, a local cut-off frequency $f_{1\,oolite}^*$ could characterize the fluid flow occurring locally from the oolites to the macropores. The permeability of the oolites κ_{oolite} should be lower than the total permeability of the sample because of a much smaller pore-entry radius compared to the macropores (Figure 4.1). A 1D permeability model from *Guéguen and Dienes* (1989) can be used to have an estimation of κ_{oolite}. The oolite's microporous network is modeled as a set of pipes of variable radii r and lengths λ, isotropically distributed (Figure 4.13). If we assume that all the pipes are connected, with respect to the definition of percolation theory, *Guéguen and Dienes* (1989) showed that the permeability of the medium can be given by:

$$\kappa_{oolite} = \frac{\bar{r}^2}{32}\Phi_{oolite}. \tag{4.7}$$

The porosity of the oolite Φ_{oolite} is calculated from the proportion of microporosity in the total porosity, which was deduced from the SEM image analysis at about 55 % (Figure 4.3), and the total porosity measured experimentally at about 23 %. If we consider all the microporosity to be in the oolites and the total volume $V_{tot} = V_{Macropores} + V_{oolites}$, we can deduce $\Phi_{oolite} = 14.2\,\%$. The average radius $\bar{r}$ is taken as the pore entry radius of the micropores measured from the porosimetry measurements from *Zinsmeister* (2013), and corroborated with the SEM photomicrograph (Figure 4.1), at about $\bar{r} = 0.6\,\mu\text{m}$. Therefore, Equation 4.7 gives a permeability of $\kappa_{oolite} = 1.6\,10^{-15}\,\text{m}^2$, which is smaller than the sample's global permeability ($\kappa = 10^{-14}\,\text{m}^2$). Now if we apply the drained/undrained cut-off frequency

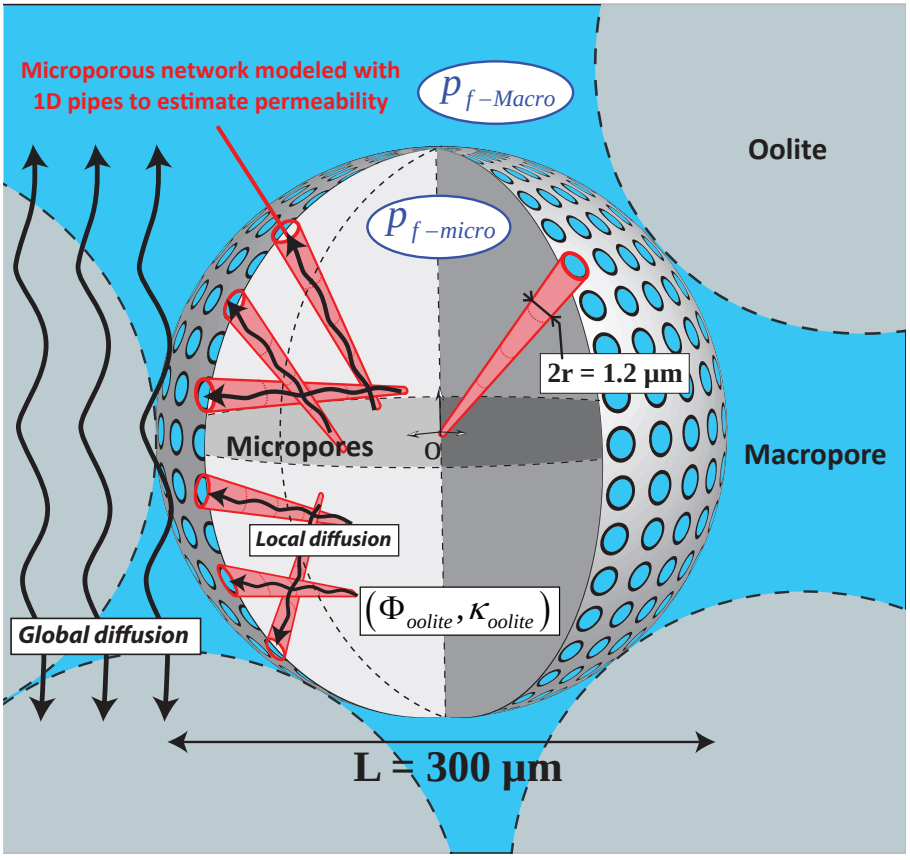

Figure 4.13: Model of the Lavoux, composed with spherical microporous oolites surrounded by macropores. The global diffusion within the REV, and the local diffusion in the oolites are represented. The oolites' porosity (ϕ_{oolite}) is deduced from the experimental total porosity (23 %), and from the ratio macroporosity/microporosity (45/55), calculated from the photomicrograph's analysis (Figure 4.3). A 1D pipe model (Equation 4.7) is used to calculate the local permeability of the oolites (κ_{oolite}). The obtained results are: $\phi_{oolite} = 14.2\,\%$ and $\kappa_{oolite} = 1.6\,10^{-15}\,\mathrm{m}^2$. The calculated local permeability of the micropores (κ_{oolite}) is smaller to the sample's permeability measured experimentally ($\kappa = 10^{-14}\,\mathrm{m}^2$).

to the oolite, with a diffusion length L of about 300 µm (Figure 4.13) and a drained bulk modulus K_d taken as 15 GPa, we obtain $f^*_{1\,oolite} = 10^6$ Hz in scaled frequency, which is far above the cut-off frequency of the global diffusion ($f^*_1 = 2\,10^2$ Hz). This frequency measures the minimum time scale that allows total diffusion in the oolite, and therefore to equilibrate the inner pore pressure $p_{f-micro}$ and the surrounding pore pressure $p_{f-Macro}$ (Figure 4.13). Above $f^*_{1\,oolite}$, no fluid exchange by diffusion is possible between the oolites and the macropores.

The only measurement we have above $f^*_{1\,oolite}$ is the ultrasonic measurement in glycerin-saturated conditions ($f^* = 10^9$ Hz). The bulk modulus and shear modulus K_{HF-gly} and G_{HF-gly} of the sample were found equal to their respective undrained values (Table 1, Figure 4.9a and 4.9c). Therefore, no dispersion is visible around $f^*_{1\,oolite}$, which suggests that there is no flow between the oolites and the macropores in the undrained regime ($f^* > f^*_1$). This is consistent with the idea that the micropores and the macropores have similar aspect ratios ($\xi = 1$), implying no pressure gradients to relax, and that the fluid is isobaric in the REV because the sample is already in the undrained regime. If $f^*_{1\,oolite}$ had been less than f^*_1, one could imagine a "partially-undrained" regime, for a frequency between $f^*_{1\,oolite}$ and f^*_1, where the oolites are undrained while the macropores are still drained. A local transition around $f^*_{1\,oolite}$ could then be expected with dispersion and attenuation.

4.6 Conclusion

The elastic moduli (E, ν, K and G) dispersion, and their associated Q^{-1} factors, have been measured on a Lavoux limestone, using forced oscillation method and ultrasonic measurements in a triaxial cell. The sample was measured under dry-, water- and glycerin-saturated conditions, which enabled to extend the apparent frequency range of our measurements. Two types of stress oscillations were performed: axial and hydrostatic.

The bulk modulus obtained from both the axial and the hydrostatic oscillations compared well over their mutual frequency range, confirming the consistency of both methods when applied on an isotropic material in the drained and undrained regimes. Therefore, the axial oscillations enable to calculate all the moduli and Q^{-1} factors. The formalized relationships between the Q^{-1} factors (*Winkler and Nur*, 1979; *Pimienta et al.*, 2016a) are in agreement with the experimental results, with the condition of a dispersive Poisson's ratio.

The drained/undrained transition has been successfully characterized, with a dispersive effect on all the elastic moduli except for the shear modulus. The Q^{-1} factors were also measured and correlate well with the measured dispersions. The dispersion on K and G are consistent with Biot-Gassmann's theory, either in the water-saturated or the glycerin-saturated sample.

No other dispersive transitions is detected above the drained/undrained cut-off frequency. We interpret this as an absence of squirt-flow due to the absence of cracks. This is

corroborated by the fact that the elastic properties and the permeability are independent of effective pressure. We conclude that both the intragranular micropores and intergranular macropores are rounded pores ($\xi_{Macro} = \xi_{micro} = 1$). The sample has a bimodal porosity distribution. Local diffusion between the oolites' micropores and the surrounding macropores is however faster than the global diffusion. In other words, the cut-off frequency of the global flow (drained/undrained transition) f_1^* is lower than the theoretical cut-off frequency of the local flow in the oolites $f^*_{1\,oolite}$.

The drained/undrained transition is measurable in the laboratory. Its critical frequency concerns a global diffusion process on a small length scale, which in our case is the size of the sample L. In the field, with seismic or sonic logs, the global diffusion process would occur within the scale of the wavelength, which is far larger than L for frequencies under 10^5 Hz. Therefore, at the seismic and sonic frequencies, the medium would always be in the undrained regime and be non dispersive. This would not be the case if an open, or drained, boundary condition would exist, for example a permeable fault.

CHAPTER 5

BIOCLASTIC GRAINSTONE FROM INDIANA: INTACT AND AFTER THERMAL CRACKING.

5.1 Résumé

Le calcaire d'Indiana est un grainstone bioclastique provenant d'une carrière de Bedford, Indiana (Etats-Unis), d'âge Mississipien. Il est composé essentiellement de fragments de fossiles, ou d'ooides, avec l'espace intergranulaire presque exclusivement rempli de ciment calcitique. Les grains sont microporeux, et peu de macropores sont visibles dans l'espace intergranulaire. Il a été sélectionné en complément du Lavoux, car d'après la bibliographie, l'Indiana est sensible à la pression effective suggérant la présence de fissures. La porosité a été mesuré à environ 11.4% pour une perméabilité d'environ 0.02 mD.

Après avoir caractérisé les effets de fréquences dans l'échantillon intact, l'effet d'un craquage thermique à 500°C sur la dispersion des modules a été étudié. Seuls les modules K et ν ont été présentés due à un défaut de mesure de contrainte axiale. Le craquage thermique a sensiblement diminué le module d'incompressibilité de la roche, tout en augmentant sa dépendance en pression, qui s'explique par la création de nouvelles fissures.

Les fréquences sont discutées en termes de fréquences apparentes normalisées à l'eau. Dans les deux cas, intact et après craquage thermique, la transition drainé / non-drainé, visible en saturation à l'eau, se situe autour de 0.1 Hz et est en accord avec Biot-Gassmann, quelque soit la pression effective. Dans le cas intact, les mesures ultrasoniques sont supérieures aux résultats non-drainés suggérant la présence d'une transition d'écoulement crack-pore entre 10^4 et 10^6 Hz. En revanche, cette dispersion n'a pu être observée directement car les oscillations forcées ont permis de mesurer une fréquence maximale de 10^3 Hz. Après le craquage thermique, la fréquence de cette seconde transition a diminué autour de 100 Hz, ce qui a permis de l'observer expérimentalement.

5.2 Indroduction

We previously observed that in the bimodal oolitic grainstone Lavoux, no dispersion is suspected to occur in the field, as the saturating-fluid, within the grain's micropores and surrounding macropores, is isobaric up to ultrasonic frequencies. The elastic properties were nearly pressure-independent up to 20 MPa, suggesting the absence of any compliant porosity that could have generated squirt-flow (*Dvorkin et al.*, 1995). The second sample we chose is an Indiana limestone, which is also originated from a quarry, but was known to presented pressure-dependent elastic properties (*Vajdova et al.*, 2004). We investigated the frequency effects first in an intact sample. Then, we decided to thermally crack the same sample to investigate a high crack-density material and compare the dispersion/attenuation results with the original sample.

5.3 Sample description

The Indiana limestone is a pure calcite bioclastic limestone that comes from Bedford, Indiana, of Mississippian age. It may also be known as the Salem or Spergen limestone (*Fossum et al.*, 1995). Its mechanical properties have been extensively studied in the literature (*Brace and Riley*, 1972; *Michalopoulos and Triandafilidis*, 1976; *Hart and Wang*, 1995; *Vajdova et al.*, 2004; *Zhu et al.*, 2010; *Ji et al.*, 2012). It is essentially composed of fossil fragments and ooids, with calcite cement between the grains (Figure 5.1). According to *Fossum et al.* (1995), the calcite distribution is about 69% of fossiliferous calcite and 31% of cement calcite, which seems consistent with the SEM photomicrograph of our own sample (Figure 5.1). The grain sizes can go up to 300 µm and are poorly sorted (Figure 5.1). The sample is assumed to be isotropic.

The total porosity of our sample has been estimated by triple-weight method to be around 11.4%. The mass density of the dry sample is around $D_{dry} = 2348\,\mathrm{kg.m^{-3}}$. It is characterized by some intergranular macroporosity and intragranular microporosity. An image analysis of the SEM photomicrograph can enable us to calculate the proportion of macropores and micropores (Figure 5.2). A threshold is applied to the grayscale of the photomicrograph to isolate the macropores as a binary image (Figure 5.2). The 2D porosity of macropores is estimated around 5.4%, which suggests a distribution between macro- and micropores of 47/53.

After the sample's elastic moduli have been fully studied, the same sample has been thermally cracked in an oven, following the procedure described by *Johnston and Toksöz* (1980). The temperature was progressively increased to 500°C and was maintained for 1 hour in order to leave sufficient time for outgassing. According to *Rodriguez-Navarro et al.* (2009), with measurements done on Iceland spar single crystals, the thermal decomposition of calcite ($CaCO_3$) into calcium oxide (CaO) and carbone dioxide (CO2) starts around 600°C

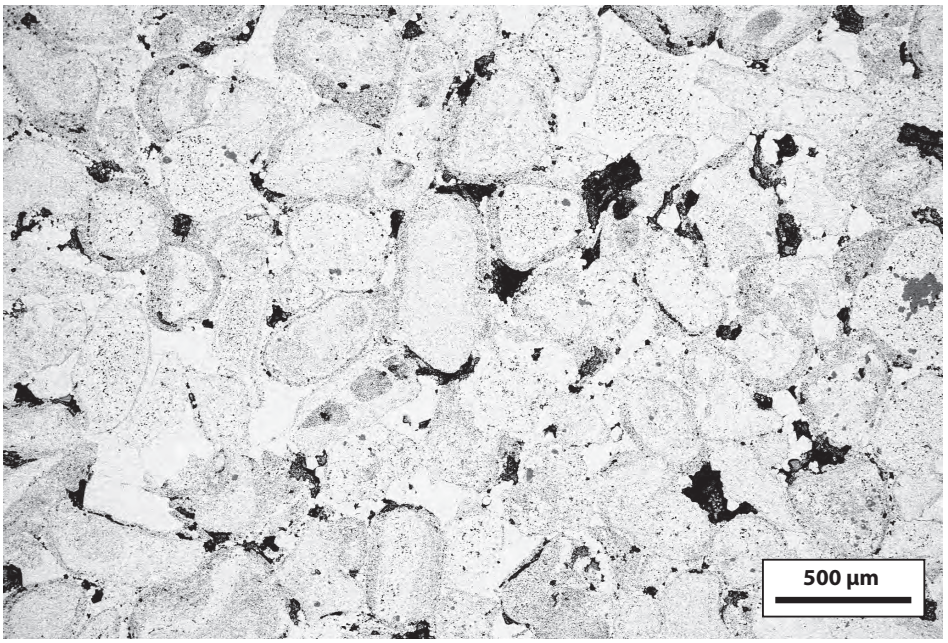

Figure 5.1: SEM photomicrograph of the Indiana limestone.

with a very low degree of conversion, and is complete after 850°C. Therefore, we assume that our thermally cracked sample has no change in mineralogy. The sample was then naturally cooled down to room temperature and re-instrumented with new strain gauges.

For both the intact and the thermally cracked sample, Mercury Injection Capillary Pressure (MICP) results exhibit a unimodal pore-entry size distribution, with a maximum peak around 0.5 µm that corresponds to the microporosity (Figure 5.3). The macropores visible in the SEM photomicrograph (Figures 5.1 and 5.2) are not detected by the MICP analysis suggesting that they do not constitute an independent connected network like in the Lavoux limestone. In other words, the fluid accesses the macropores solely by going through micropores or cracks. The measurements on the thermally cracked sample seems to detect slightly higher pore-entry diameters (Figure 5.3b), with a higher total volume injected (Figure 5.3a). This could just be due to heterogeneity between the two different fractions of the plug that were sliced out to do the measurements. The slices were 40 mm diameter for only several millimeters height. However, two small peaks seem to be distinguishable in the thermally cracked sample, which was not the case for the intact sample (Figure 5.3). This could be due to the new population of cracks.

5.3.1 Permeability

The permeability as a function of differential pressure of the two samples have been measured by Darcy flow with water. The results are presented Figure 5.4. The permeability does not substantially change between the intact sample and the thermally cracked

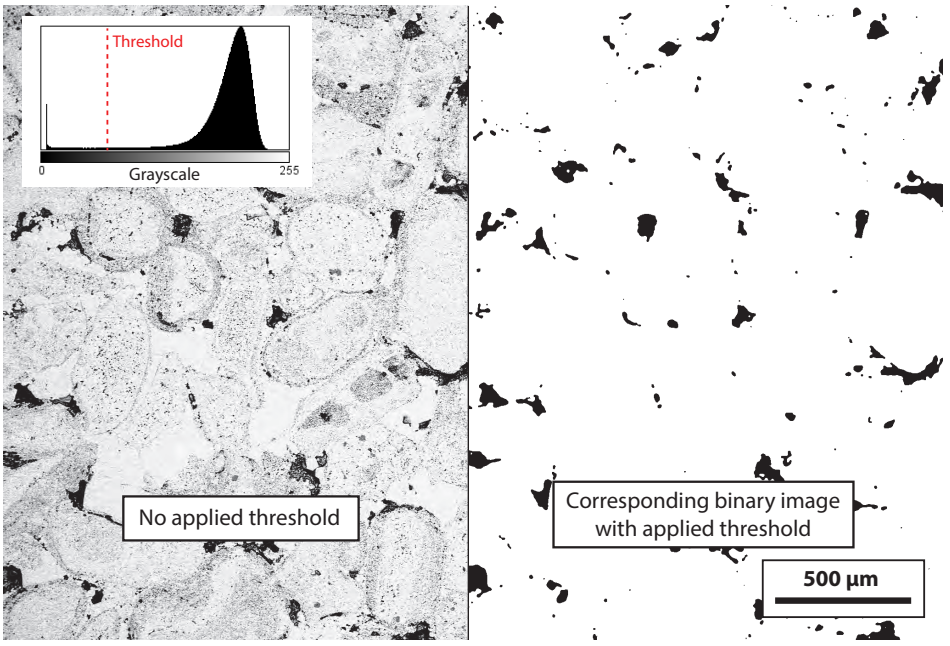

Figure 5.2: Image analysis of the SEM photomicrograph of the Indiana limestone to determine the proportion of macropores versus micropores. A threshold is applied to the grayscale of the original image (left) to obtain a binary image (right) where solely the macropores are present.

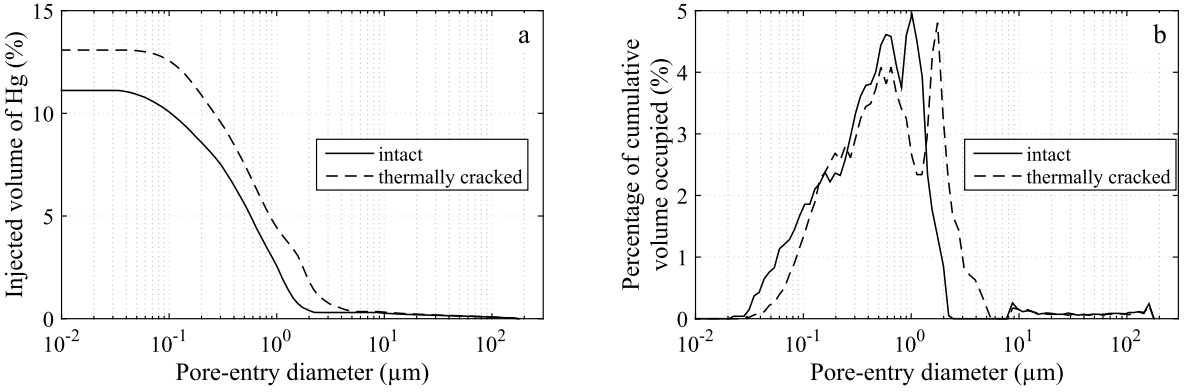

Figure 5.3: Pore-entry size distribution of the intact Indiana sample obtained from MICP.

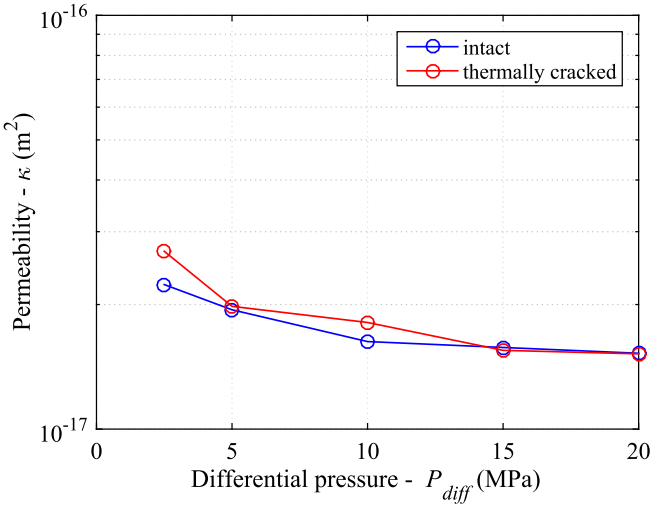

Figure 5.4: Permeability measurements of the Indiana sample intact and after the thermal cracking at 500°C for 1 hour. The measurements were done by Darcy flow under water-saturated conditions.

sample, with a difference less than 1×10^{-17} m^2 at $P_{diff} = 2.5$ MPa and no difference at $P_{diff} = 20$ MPa (Figure 5.4). Both samples' permeability show a small dependence to differential pressure that could be linked to the closure of microcracks. With the differential pressure increasing from 2.5 MPa to 20 MPa, the permeability decreased from 2.2×10^{-17} m^2 to 1.5×10^{-17} m^2 for the intact sample and from 2.7×10^{-17} m^2 to 1.5×10^{-17} m^2 for the thermally cracked sample (Figure 5.4). The samples properties are summarized in Table 5.1 for unconfined conditions.

Indiana	Intact	Thermally cracked
$\Phi(\%)$	11.4	11.4
D_{dry} (kg.m^{-3})	2348	2348
κ (m^2)	2.2×10^{-17}	2.7×10^{-17}
$\hat{\xi}$	1.8×10^{-4}	1.4×10^{-4}
ρ	0.22	0.99
K_d (GPa)	20	6
f_1^* (Hz)	0.25	0.1
f_2^* (Hz)	420	230

Table 5.1: Unconfined properties of the Indiana sample intact, and after thermal cracking. K_d is the dry dynamic moduli estimated from the hydrostatic oscillations. The drained/undrained and undrained/unrelaxed (squirt-flow) cut-off frequencies, respectively f_1^* and f_2^* (Equation 1.39), are valid for water-saturated conditions.

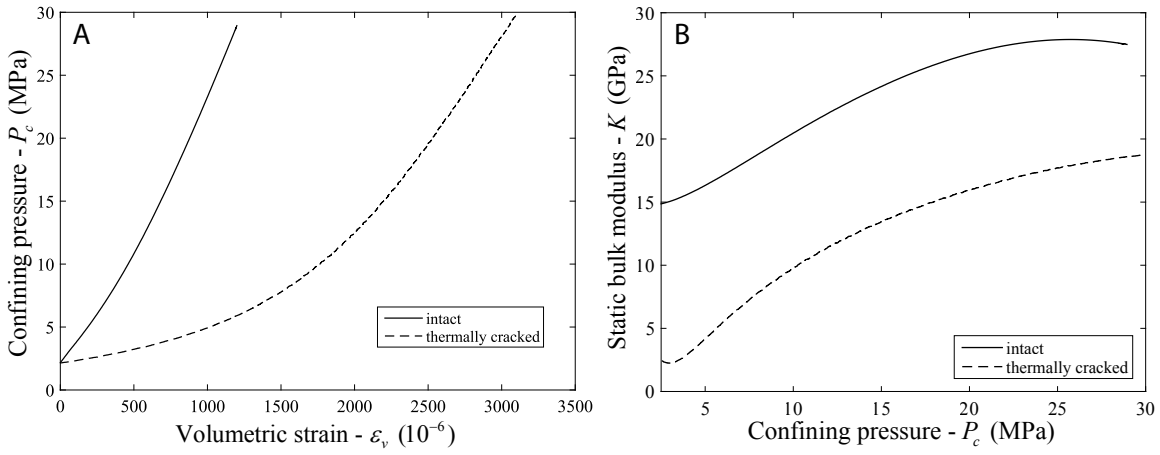

Figure 5.5: Static bulk modulus analysis of the Indiana sample intact and after thermal cracking.

5.3.2 Static bulk modulus

The hydrostatic stress-strain curve and the pressure dependence of the static (tangent) bulk modulus of the Indiana sample before and after thermal cracking are presented Figure 5.5. The pore collapse pressure P^* of a 18% porosity Indiana limestone was measured to be around 60 MPa by *Vajdova et al.* (2004). For both our samples, the maximum confining pressure was $P_c = 30$ MPa. The hydrostatic loading started at 2.5 MPa. Both samples exhibit a typical crack-closure behavior, much more pronounced for the thermally cracked sample, with a crack-closing phase at low pressure before reaching a linear elastic phase (Figure 5.5a). Therefore, the static bulk modulus of each sample, respectively K_{in} and K_{th} for the intact and thermally cracked, increases with pressure before tending to a constant maximum value (Figure 5.5b). K_{in} increased from 15 GPa to 27.5 GPa. With larger strains observed for the thermally cracked sample (Figure 5.5a), K_{th} is much lower than K_{in} at all the measured pressures, and increased from 2.5 GPa to 18 GPa (Figure 5.5b).

To deduce the crack density (ρ) and crack aspect ratio ($\hat{\xi}$) of the samples, we applied Morlier's method which consists on fitting the pressure-dependence of the dry bulk modulus in order to deduce crack aspect ratio distributions and porosities (*Morlier*, 1971; *Jaeger et al.*, 2009). This method is similar to *Walsh* (1965). The method will be very detailed in a following chapter (Chapter 10) dedicated to the effective medium approach to model frequency effects. The results obtained for the Indiana intact and after thermal cracking give respectively a crack density of 0.20 and 0.99, for crack aspect ratios of 1.8×10^{-4} and 1.4×10^{-4}. This corresponds to crack total porosities of 0.016% and 0.06% respectively (Chapter 10).

From the measurements of the permeability and the characterization of the microcracks, we can have a first estimation of the cut-off frequencies of the drained/undrained transi-

INDIANA		Intact				Thermally cracked			
	P_{diff} (MPa)	V_P (m s^{-1})	V_S	K_{HF} (GPa)	G_{HF}	V_P (m s^{-1})	V_S	K_{HF} (GPa)	G_{HF}
DRY	2.5	4061	2439	20.3	14.1	2572	1642	7.1	6.3
	5	4348	2556	24.2	15.5	2758	1785	7.9	7.5
	10	4494	2564	27.1	15.6	3065	1918	10.5	8.6
	20	4762	2658	31.5	16.8	3375	2127	12.6	10.6
	30	4878	2667	34.0	16.9	3493	2228	13.1	11.7
WAT	2.5	4848	2548	37.1	16.2	3721	1965	21.5	9.5
	5	4908	2589	37.8	16.7	3756	1999	21.7	9.9
	10	4938	2597	38.4	16.9	3864	2025	23.4	10.1
	20	4969	2606	39.1	17.0	3980	2066	25.1	10.5
GLY	2.5	4967	2548	40.6	16.4	4519	2331	32.9	13.6
	5	5031	2597	41.3	17.1	4545	2325	33.6	13.5
	10	5063	2632	41.5	17.5	4597	2345	34.5	13.7
	20	5096	2649	42.0	17.8	4651	2401	34.8	14.4

Table 5.2: Results of the ultrasonic measurements on the intact and thermally cracked Indiana limestone.

tion by $f_1^* = 4\kappa K_d/\eta L^2$, and the undrained/unrelaxed transition related to squirt-flow by $f_2^* = \hat{\xi}^3 K_S/\eta$ (Equation 1.39). With K_d taken as the dry dynamic moduli measured by the hydrostatic oscillations, and L taken as the samples' lengths (80 mm), f_1^* is estimated at 0.25 Hz and 0.1 Hz respectively for the intact and thermally cracked sample, which is in the same order of magnitude. With $K_S = 77$ GPa for the skeleton modulus (*Mavko et al.*, 2009), and $\hat{\xi}$ the aspect ratio estimated from Morlier's method (see Table 5.1) (*Morlier*, 1971), f_2^* is estimated around 420 Hz and 230 Hz respectively for the intact and thermally cracked sample.

5.3.3 High-frequency ultrasonic results

The ultrasonic P- and S-wave velocities were measured in the axial direction of the sample. The corresponding frequency is 1 MHz. The measured travel times in the apparatus are corrected from the travel times in the endplatens. The high-frequency bulk modulus (K_{HF}) and shear modulus (G_{HF}) are deduced from Equation 3.15. The obtained results are presented Table 5.2.

In dry conditions, the moduli of the intact and thermally cracked sample show a clear dependence to the differential pressure. The pressure sensitivity disappears in fluid-saturated conditions, either for the high-frequency bulk modulus (K_{HF}) or shear modulus (G_{HF}) (Table 5.2).

5.4 Low-frequency dynamic moduli

The low-frequency dynamic moduli of the Indiana sample intact and after thermal cracking have been studied under dry, glycerin-saturated and water-saturated conditions at different differential pressures. The measurements were done in the Top Industrie apparatus. The boundary conditions at both ends of the sample were drained (large dead volumes including volumes of the pumps). The attenuation were all calculated by the "FFT" method.

5.4.1 Bulk modulus from hydrostatic oscillations

Hydrostatic oscillations were performed within the frequency range of $[0.01; 1]$ Hz, at the differential pressures of $[2.5; 5; 10; 20; 30]$ MPa. The pressure amplitude of the oscillations were around 0.2 MPa, for resulting linear strains between 10^{-6} and 10^{-5}. The full set of results are presented Figure 5.6. From Equation 4.1, the uncertainty due to the averaging of strain gauges was around $\Delta K/K = 1.45\%$ for the intact sample, and $\Delta K/K = 4.35\%$ for the thermally cracked one. The apparent frequency ($f^* = f \times \eta_{fl}/10^{-3}$) is the frequency normalized by the viscosity of the fluid, taking water as the reference fluid ($\eta_{wat} \approx 10^{-3}$ Pa.s). It has the effect of shifting the glycerin-saturated measurements to higher frequencies by a factor 10^3, and the dry measurements to lower frequencies by a factor 10^{-2}. This enables to compare the glycerin-saturated and the water-saturated measurements as if they were the same fluid in terms of mobility, but with different compressibilities. The total apparent frequency range measured becomes $[10^{-4}; 10^3]$ Hz, although the shift of the dry measurements is simply a visual aid as no fluid-related dispersion can be expected from dry conditions.

From the hydrostatic oscillations, the bulk modulus of the intact sample exhibits one dispersive frequency range between 10^{-2} Hz and 1 Hz visible under water-saturated conditions (Figure 5.6a), correlated with attenuation (Figure 5.6b). As the dry bulk modulus increases from 21 GPa to 34 GPa with increasing differential pressure, the amount of dispersion decreases. The attenuation peaks decrease from 0.19 to 0.06 with increasing differential pressure, and are all centered around 0.1 Hz (Figure 5.6b). Zener's viscoelastic model adjusted to the dispersion (Equation 3.14), seems to overpredict the attenuation at low pressure but is in agreement at high-pressure (Figure 5.6b). This dispersive transition correlates well with the drained/undrained cut-off frequency $f_1^* = 0.25$ Hz of the intact sample (Table 5.1).

The bulk modulus of the thermally cracked sample exhibits two dispersive frequency ranges between 10^{-2} Hz and 1 Hz visible under water-saturated conditions, and between 10 Hz and 10^3Hz visible under glycerin-saturated conditions (Figure 5.6d). Both transitions are consistent with the attenuation measurements, with the presence of two peaks around 8×10^{-2} Hz and 10^2 Hz (Figure 5.6e). Zener model seem to apply well for the first transition, but over estimates the attenuation of the second Zener's viscoelastic model adjusted

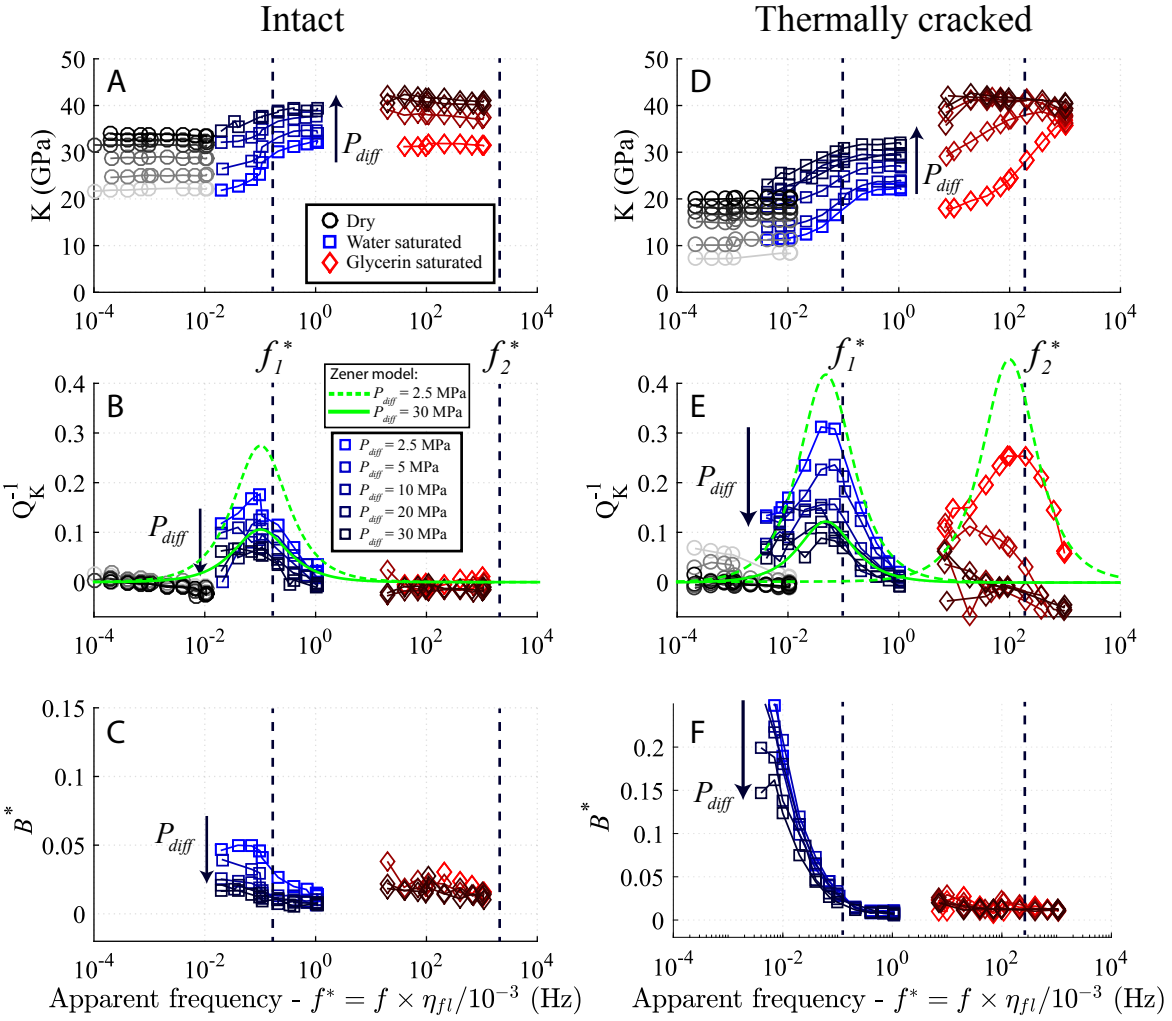

Figure 5.6: Results of the hydrostatic oscillations on the Indiana limestone before and after thermal cracking.

to the dispersion (Equation 3.14), seems to overpredict the attenuation at low pressure but is in agreement at high-pressure. With the increase of the differential pressure, the dry bulk modulus increases from 6 GPa to 20 GPa, and the amount of dispersion decreases for both transitions. With increasing differential pressure from 2.5 MPa to 30 MPa, the first attenuation peak decreases from 0.3 to 0.1, and the second peak decreases from 0.25 and tends rapidly to 0 just above $P_{diff} = 10$ MPa (Figure 5.6e). Moreover, the frequency of the second attenuation peak seem to slightly decrease with increasing differential pressure (Figure 5.6e). The first transition correlates well with the drained/undrained cut-off frequency $f_1^* = 0.1$ Hz, and the second transition with a undrained/unrelaxed cut-off frequency $f_2^* = 230$Hz related to squirt-flow.

Despite the experimental drained boundary conditions achieved with large dead volumes, a pore pressure oscillation (ΔP_p) was detectable in the drainage tubes, and a non nil "pseudo-Skempton" coefficient (B^*) could be calculated by $B^* = \Delta P_p / \Delta P_c$ for both samples (Figures 5.6c and 5.6f). For both the intact and the thermally cracked sample, B^* decreases to 0 between 0.01 Hz and 1 Hz, which is perfectly consistent with the drained/undrained transitions of both samples. Indeed, a pore pressure oscillation in the drainage system can only be detected if the sample is drained or partially drained (*Pimienta et al.*, 2016b). An undrained regime, by definition, is a closed boundary condition where the fluid cannot diffuse out of the sample, and therefore no pressure buildup can be measured by the pore pressure sensor.

5.4.2 Poisson's ratio from axial oscillations

After the hydrostatic oscillations are performed at a given differential pressure, the piston of the triaxial cell is lowered to be in contact with the piezoelectric oscillator and the axial oscillations up to 100 Hz were performed, which gives a maximum apparent frequency of 10^5 Hz for the glycerin-saturated conditions. The measurements were done prior to the modification of the aluminium endplaten (Figure 3.6), preventing us to have a proper measurement of the axial stress during the oscillations. Solely the sample's Poisson's ratio could be directly measured with the sample's remaining axial and radial strain gauges. The dispersion and attenuation of the Poisson's ratio are presented Figure 5.7. From Equation 4.2, we deduce an average relative uncertainty of $\Delta\nu/\nu = 2.7\%$ for the intact sample, and $\Delta\nu/\nu = 5.2\%$ for the thermally cracked one.

The intact sample exhibits not much dispersion at the measured frequency range, with a value around 0.28 for dry and water-saturated conditions (Figure 5.7a). A slight increase is observed in water-saturated conditions around 0.1 Hz, which is consistent with the high-frequency end of the drained/undrained transition (Figure 5.7a). The related attenuation, is consistent with the dispersion, exhibiting a peak around 0.06 at 0.1 Hz, and decreasing to 0 at higher frequencies (Figure 5.7b). The attenuation is in agreement with Zener model (Equation 3.14). The drained/undrained cut-off frequency is consistent with the observed

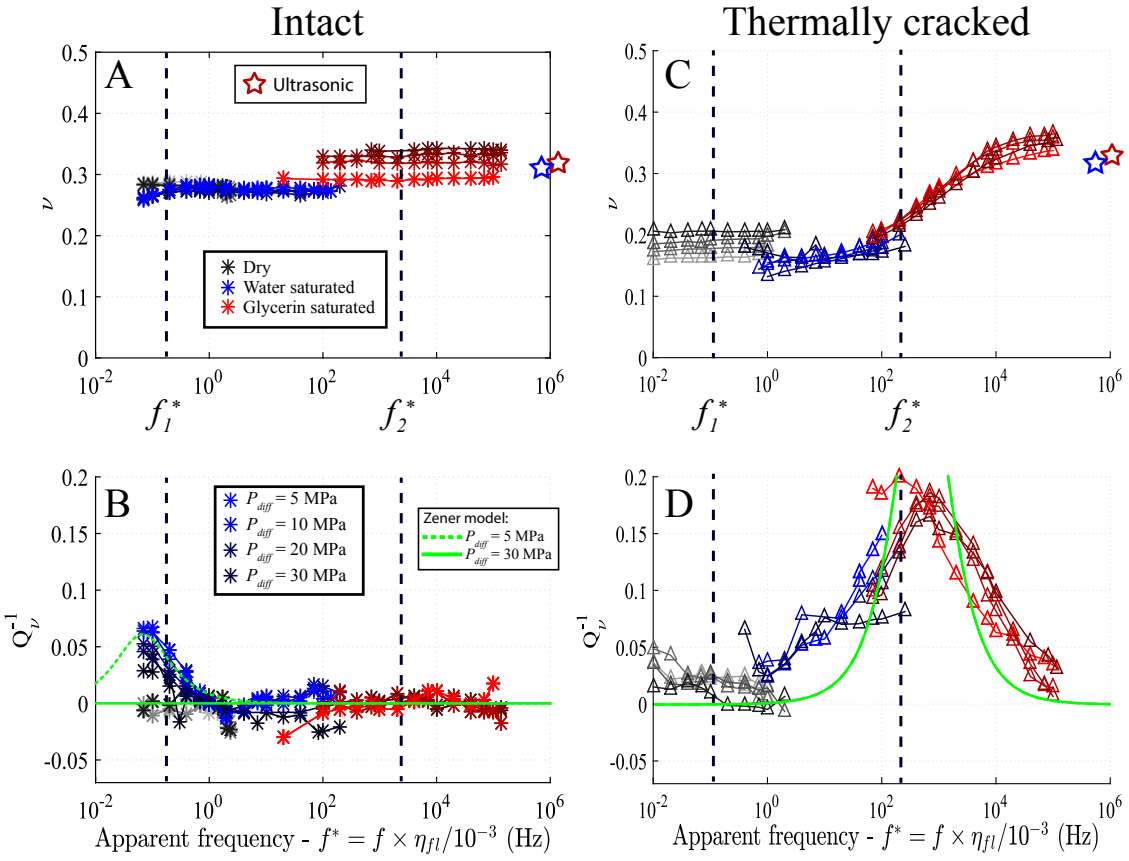

Figure 5.7: Frequency dependence of Poisson's ratio and respective attenuation measured on the intact and the thermally cracked Indiana limestone from axial oscillations.

transition (Figures 5.7a and 5.7b). In dry and water-saturated conditions, the Poisson's ratio did not seem to be sensitive to the differential pressure, going up 5 MPa to 30 MPa. On the other hand, in glycerin-saturated conditions, a slight dependence to the differential pressure was observed, with a Poisson's ratio increasing from 0.3 to 0.34 between $P_{diff} = 5$ MPa and $P_{diff} = 30$ MPa (Figures 5.7a and 5.7b). No dispersive transition is observed around the squirt-flow frequency $f_2^* = 420$ Hz deduced previously (Table 5.1).

The dispersion and attenuation of the Poisson's ratio of the thermally cracked sample are presented Figures 5.7c and 5.7d. The minimum frequency measured was around 1 Hz as our objective was to observe high-frequency effects such as squirt-flow. Therefore, the drained/undrained transition could not be observed from the axial oscillations. First, the differential pressure has nearly no effect on the observed measurements, with a slight variation of the dry Poisson's ratio from $\nu = 0.16$ at $P_{diff} = 5$ MPa to $\nu = 0.2$ at $P_{diff} = 30$ MPa. The Poisson's ratio of the thermally cracked sample exhibits dispersion from $\nu = 0.14$ to $\nu = 0.35$ between 1 Hz and 10^5 Hz, visible with water- and glycerin-saturated conditions (Figure 5.7c). This transition is consistent with attenuation, with a peak of about 0.18 around 7×10^2 Hz (Figure 5.7d). However, the Zener model predicts a much higher peak value with a more narrow frequency range. Nevertheless, this dispersive transition is centered around the squirt-flow cut-off frequency f_2^* predicted previously (Table 5.1).

5.5 Discussion

5.5.1 Frequency-dependence of the bulk modulus due to different fluid-flow regimes.

The frequency dependence of the dynamic bulk modulus over a large frequency range in dry or fully-saturated conditions, by combination of ultrasonic measurements and low-frequency oscillations with different viscous fluids, enables us to identify all the fluid-flow regimes within the medium, and characterize their frequency ranges and their effect on the elastic properties. For both the intact and thermally cracked sample, the results of the dispersion of K over the full frequency range ($[10^{-4}; 10^9]$ Hz), for differential pressures of 2.5, 5, 10 and 20 MPa, are presented Figure 5.8. The corresponding static measurements are also represented. Biot-Gassmann fluid substitution theory (Equation 4.3) is applied on the dynamic dry bulk modulus to predict the undrained bulk modulus. The skeleton bulk modulus was taken as 77 GPa (*Mavko et al.*, 2009). Biot-Gassmann's prediction was calculated for the lowest differential pressure ($P_{diff} = 2.5$ MPa).

The general observation we make is that the Indiana limestone exhibits three fluid-flow regimes: the drained, the undrained and the unrelaxed regimes, either for the intact or the thermally cracked sample (Figure 5.8).

Both samples exhibit the drained/undrained transition around the predicted cut-off

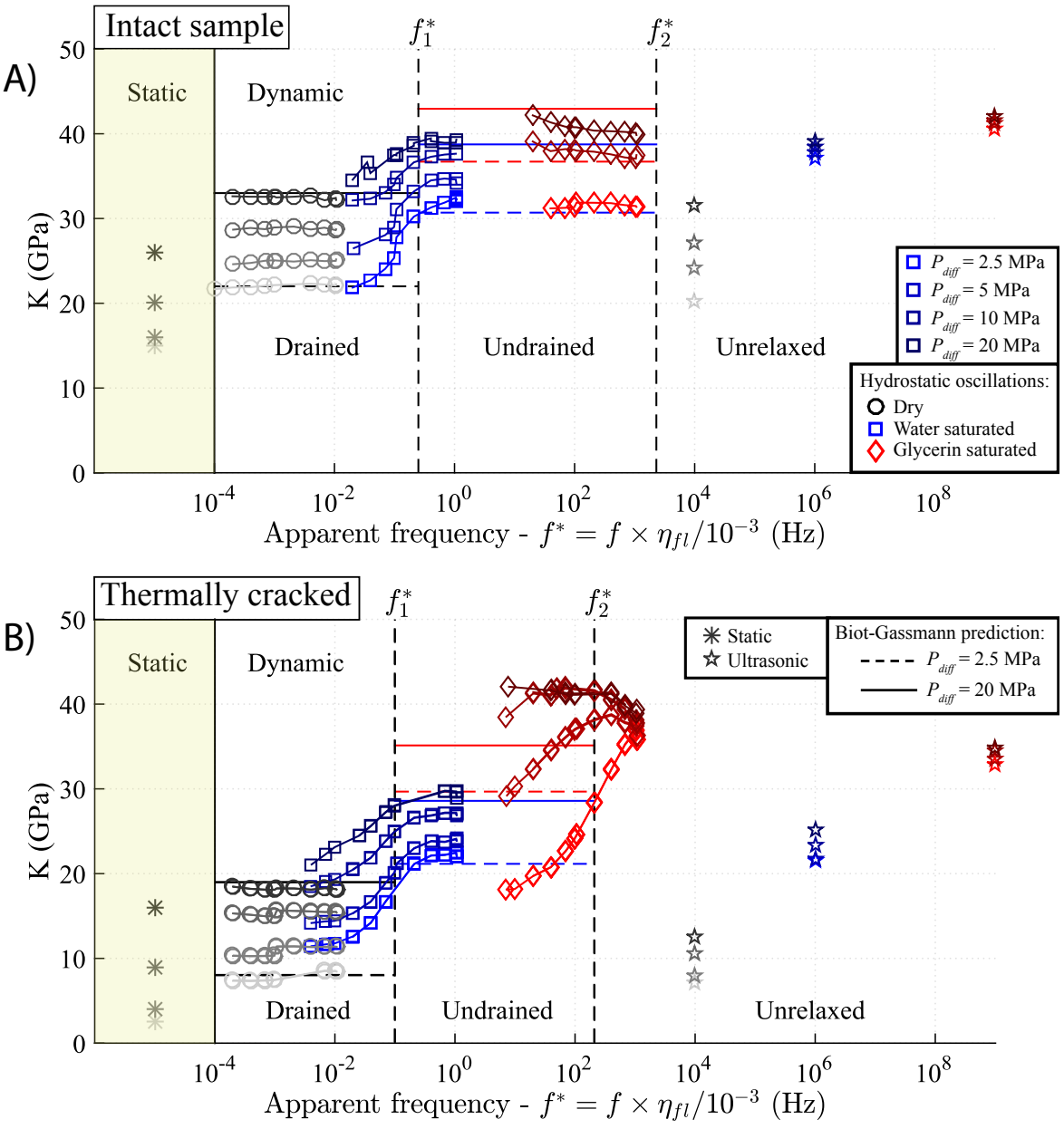

Figure 5.8: Static and frequency-dependent dynamic bulk modulus of the Indiana limestone intact (a) and after the thermal cracking (b), for four different differential pressures in fully-saturated conditions. The results combine the hydrostatic-stress oscillations results with the ultrasonic and static measurements.

frequency f_1^*, as the saturated bulk modulus tends to the dry result when decreasing the frequency. At low and high differential pressure, for both samples, the undrained regime is consistent with Biot-Gassmann's prediction in water-saturated conditions (Figure 5.8). The cut-off frequency of this transition shows no dependence to effective pressure, which is perfectly with by the permeability measurements that show almost no dependence to pressure (Figure 5.4).

For the dry intact sample, there is a good match between the ultrasonic results and the low-frequency dynamic results at every differential pressures (Figure 5.8a). The sample is non-dispersive in the absence of a saturating fluid. In fluid-saturated conditions, the ultrasonic measurements become nearly pressure-independent and fit with the undrained high-pressure bulk modulus(Figure 5.8a). This suggests, that for low effective pressures a second dispersive transition, corresponding to the undrained/unrelaxed transition, is expected between 10^4 and 10^6 Hz. In the unrelaxed regime, the saturated cracks have a similar response as filled-isolated inclusions, which increases the effective bulk modulus of the medium close to the high-pressure modulus where the cracks are closed (*Mavko and Jizba*, 1991; *Adelinet et al.*, 2011; *Pimienta et al.*, 2015a). The consistency with effective medium theory shall be developed in a following chapter.

For the thermally cracked sample, the results from the ultrasonic measurements in fluid-saturated conditions seem to always be lower than the hydrostatic-oscillation result, either in dry or fluid-saturated condition (Figure 5.8b). This could be due to a non homogeneous thermal cracking of the core, due to temperature gradients perpendicular to the surface for example. The strain-gauges, limited to the surface, and the ultrasonic waves, propagating in the center of the core, would therefore probe a different medium. However, experimental studies on pure glass from *Ougier-Simonin et al.* (2011) and *Mallet* (2014) showed that transverse isotropy is mainly due to the thermal quenching after being heated, which was not our case here. Nevertheless, similarly to the intact sample, the fluid-saturated ultrasonic measurements are weakly pressure-dependent, consistent with an unrelaxed regime (Figure 5.8b).

For the intact sample in glycerin-saturated conditions, Biot-Gassmann predictions are in good agreement with the measurements, but seems to slightly over-predict the measurements at $P_{diff} = 2.5$ MPa (Figure 5.8a). For the thermally cracked sample, the same observations can be made, but due to the low frequency-shift of the second transition with increasing differential pressure, the high-pressure results in glycerin, visible in Figure 5.8b, are to be considered in the unrelaxed regime, explaining why they are higher than Biot-Gassmann's high-pressure prediction. It would seem that the undrained regime is solely visible, for glycerin-saturated conditions, for $P_{diff} = 2.5$ MPa and $P_{diff} = 5$ MPa. The pressure-dependence of the undrained/unrelaxed cut-off frequency is noticeable, with a decrease of 2 orders of magnitude with increasing pressure from 2.5 MPa to 20 MPa.

5.5.2 Effect of the thermal cracking

The pressure dependence of the intact Indiana's bulk modulus is associated to the presence of microcracks (*Walsh*, 1965), either for the static (Figure 5.5b) or the dynamic moduli (Figure 5.6a). We attempted to observe the squirt-flow phenomenon related to these cracks, either by hydrostatic or axial low-frequency oscillations. Despite a predicted cut-off frequency of $f_2^* = 421\,\text{Hz}$, which is measurable from the axial oscillations under glycerin-saturated conditions but not for the hydrostatic oscillations, no fluid-related dispersion nor attenuation was observed on the Poisson's ratio (Figure 5.7a). The attenuation observed around 0.1 Hz (Figure 5.7b) is related to the drained/undrained transition as it is consistent with the drained/undrained cut-off frequency ($f_1^* = 0.25\,\text{Hz}$).

A clear effect of the thermal cracking was observed on the Indiana. The squirt-flow transition was observed both with the hydrostatic and the axial oscillations under glycerin-saturated conditions (Figures 5.7c and 5.8b), and exhibits more dispersion than intact. The thermal cracking reduced both the static and the dynamic bulk moduli of the limestone at every differential pressure. This reduction at low effective pressures, when the cracks are open, can be explained by a higher crack density of $\rho = 0.99$ instead of $\rho = 0.22$ (Figure 5.8), but we would have expected the high-pressure moduli to be identical if all the cracks are closed. According to the static loading, the cracks should be all closed above 25 GPa (Figure 5.5). The thermal heating might have induced some damage into the rock's matrix that cannot be simply recovered by increasing the effective pressure. SEM photomicrographs have been done on the Indiana sample before and after the thermal cracking to localize the induced cracks. We selected images that are centered on random microporous grains surrounded by cement and macropores. These images are presented Figure 5.9.

The major difference we can observe between the intact microstructure (Figures 5.9a-c) and the thermally cracked one (Figures 5.9d-f) is the presence of cracks in the cement of the latter. In the intact sample, we do not visually distinguish any cracks whatever the scale (Figures 5.9a-c). The thermally induced cracks are essentially located in the blocky calcite cement (Figures 5.9d-f), although we noticed that some grains, occasionally, possessed microcracks within (Figure 5.9d). It is noticeable that in a thin band of cement between two grains, most cracks are oriented perpendicularly to the surfaces of these grains, with a clear example visible in Figure 5.9d. On the other hand, in the center of a large intergranular space, the cracks are more randomly oriented, and may even connect to separate rounded grains of cement (Figure 5.9e). If the cement is damaged to some extent, debris might separate from the initial matrix and no longer support external stresses, similarly to cataclastic failures during a triaxial test. This would explain the systematic difference between the intact bulk modulus and the thermally cracked one, even at high pressure. Such cataclastic failures of the cement of an Indiana limestone have been observed by *Ji et al.* (2012) during a classic triaxial experiment.

Thermally induced cracking occurs when the stress exceeds the local strength of the

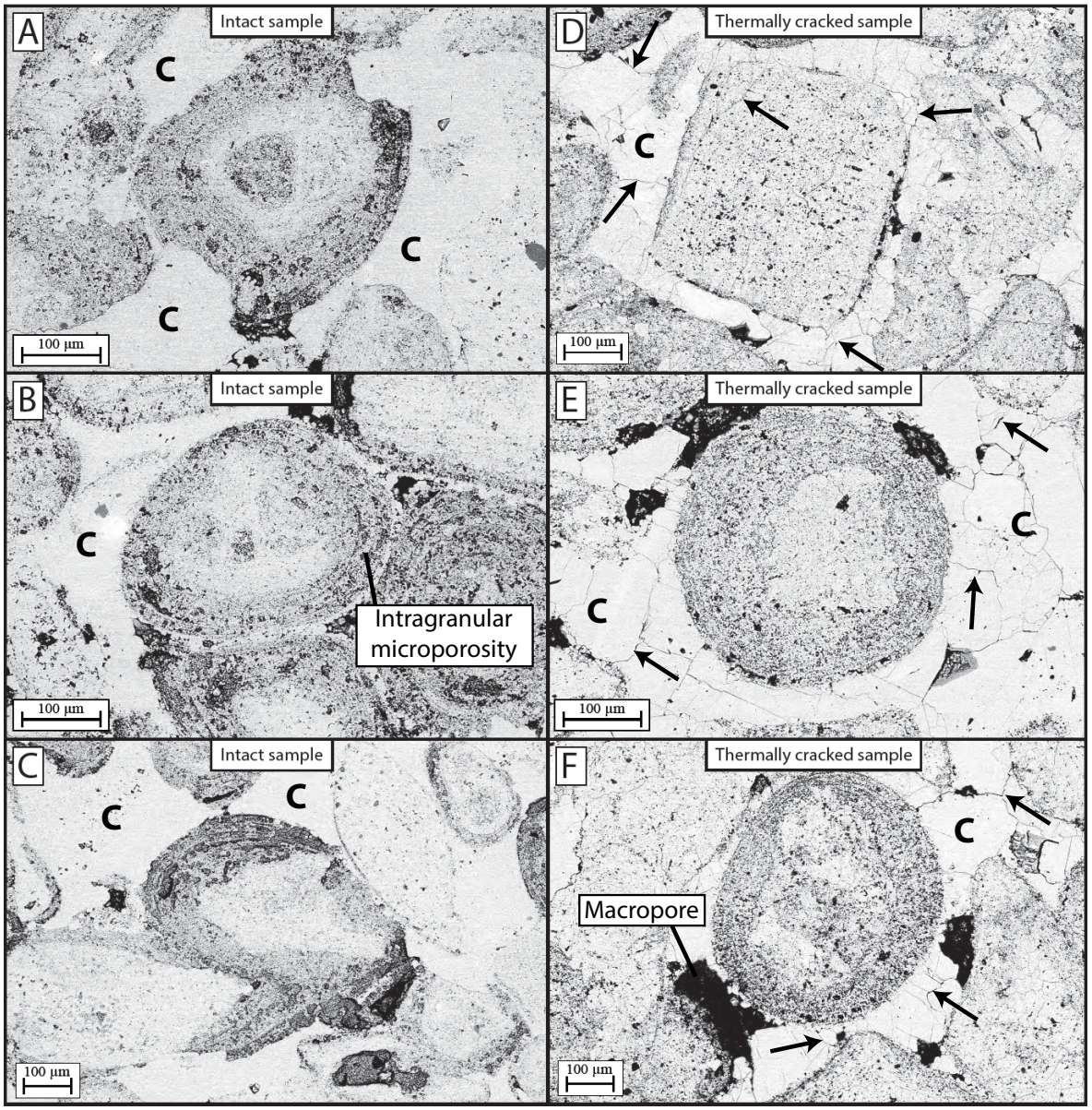

Figure 5.9: SEM images of the Indiana sample, intact (a-c) and after the thermal cracking (d-f). The intergranular space is mainly filled with blocky calcite cement (letter C), and some macropores. The thermally cracked sample exhibits microcracks (black arrows), mainly located in the blocky calcite cement.

rock (*Lu and Jackson*, 1996). Different mechanisms can lead to such stress concentration. In polymineralic rocks, like granites, each mineral possesses a different thermal expansion coefficient. This induces a thermal expansion mismatch (*Fredrich and Wong*, 1986) and create high local stresses. Thermal gradients are also known to create local stress even in homogeneous solids (*Fredrich and Wong*, 1986). The thermal expansion anisotropy of a mineral can also induce microcracks in a monomineralic rock, and calcite is known to possess such characteristic (*Fredrich and Wong*, 1986; *Lu and Jackson*, 1996). Calcite thermoelastic properties are highly anisotropic, with thermal expansion coefficients of $\alpha_{\parallel} = 26.4 \times 10^{-6}$ / °C for the c-axis direction, and $\alpha_{\perp} = -5.3 \times 10^{-6}$ / °C for any direction perpendicular to the c-axis (*Lu and Jackson*, 1996).

In addition to the previous mechanisms, one other factor that has to be taken into account is texture (*Homand-Etienne and Troalen*, 1984). Several studies, on rocks or ceramics, showed that thermal cracking can be grain-size dependent and that a minimal grain-size is required (*Evans*, 1978; *Fredrich and Wong*, 1986; *Laws and Lee*, 1989). Therefore, the thermal behavior of monomineralic carbonate rocks is conditioned by textural heterogeneity and thermal expansion anisotropy.

Clear evidences of thermally induced cracks have been observed in homogeneous marbles, such as Carrare limestone (*Homand-Etienne and Troalen*, 1984; *Lu and Jackson*, 1996), with grain sizes of at least 300 µm. The main mechanism of microcracking was thermal expansion anisotropy, which occured as soon as the temperature was increased (*Homand-Etienne and Troalen*, 1984).

The study from *Homand-Etienne and Troalen* (1984) also investigated the response to thermal heating of a heterogeneous Crepey oolitic limestone. Similarly to the Indiana limestone of this study, the Crepey limestone was composed of different crystals of calcite such as micrite in the grains and microsparites in the blocky cement. *Homand-Etienne and Troalen* (1984) concluded that the largest crystals of microsparite were clearly the most responsive to thermal cracking compared to the micrite, as they occur at the periphery of intergranular pores where they can expand.

In a study by *Lion et al.* (2005), an oolitic limestone from Anstrude, France, has been subjected to thermal heating up 250°C to study the effects on the hydraulic and poroelastic properties. Similarly to the Crepey and the Indiana limestone, the calcite is present as different forms such as micrite in the grains or sparite in the cement. However, not much thermally induced cracks were observed in the SEM photomicrographs, which might be explained by an insufficient temperature increase. *Fredrich and Wong* (1986) heated an Oakhall oolitic limestone at least up to 500°C to observe some microcracks. The general consensus between these studies is that monomineralic limestones with heterogeneous textures, such as oolitic limestones, are not very sensitive to thermal heating when compared to homogeneous textures or polymineralic rocks.

In our study case, 500°C was a sufficient temperature to create microcracks in the blocky

cement of the Indiana limestone, but no cracking was observed in the grains composed of micrite. This is in agreement with the previous conclusion, as the micritic heterogeneous texture of the bioclasts prevents the development of microcracks. The thermal expansion is likely to be accommodated within the microporosity. Some small microcracks may exist between micrite grains before the thermal treatment. Due to the random orientations and the small size of the grains ($< 5\,\mu m$), they would more likely accommodate the anisotropic thermal expansion of the individual micrite grains rather than propagate into larger cracks.

5.6 Conclusion

The frequency dependence of dynamic elastic moduli (K and ν) have been measured over a large frequency range ($[10^{-4}\ ;\ 10^{9}]\,Hz$) on an Indiana limestone at different effective pressures, before and after thermal cracking at 500°C. In both cases, the Indiana limestone exhibited three fluid-flow regimes, that correspond to the drained, the undrained and the unrelaxed regimes. The undrained regime under water-saturated conditions was consistent with Biot-Gassmann's theory, either at low or high effective pressure.

The presence of an unrelaxed regime, with a bulk modulus higher than in the undrained regime, is explained by squirt-flow between compliant cracks and more rounded pores. The thermally cracked sample exhibited a more dispersive squirt-flow transition than the intact sample, at lower frequencies. This observation was made both from hydrostatic and axial oscillations, although the squirt-flow transition from the axial oscillations seem to have a larger frequency range, but centered around the same cut-off frequency.

The additional cracks induced by the heating seem to localize essentially in the blocky calcite cement around the grains. This is explained by the homogeneous texture due to the microsparite that allowed nucleation and propagation of cracks. On the other hand, the heterogeneous textures of the microporous bioclasts composed of micrite inhibited the development of intragranular microcracks.

CHAPTER 6

RUDIST DOMINATED URGONIAN LIMESTONE FROM RUSTREL.

6.1 Résumé

Le troisième échantillon étudié est un calcaire Urgonien de Provence, qui provient d'un affleurement à Rustrel. Le bloc a été prélevé dans un faciès à rudistes. L'intérêt particulier de ces calcaires est qu'ils sont des analogues à certains réservoirs carbonatés du Moyen-Orient. Sachant que les rudistes peuvent avoir des dimensions importantes (quelques centimètres), nous nous sommes limités à un bloc homogène contenant seulement des grains fins, qui équivaux à la matrice entourant les plus gros rudistes dans ces faciès. La porosité de l'échantillon a été mesurée aux alentours de 14.9% pour une perméabilité d'environ 0.04 mD. La distribution de taille de pores est unimodale, avec principalement de la microporosité intragranulaire. L'espace intergranulaire est entièrement cimenté. En revanche, le ciment calcitique n'est pas entièrement cristallisé, ce qui laisse place à de la microporosité intercristalline.

Les fréquences sont discutées en termes de fréquences apparentes normalisées à l'eau. La transition drainé / non-drainé a été observée autour de 0.1 Hz, et est en accord avec la prédiction de Biot-Gassmann, quelque soit la pression effective. En régime non-drainé, aucune dispersion n'est observée jusqu'à 10^4 ,Hz. En revanche, les mesures ultrasoniques à basse-pression semblent donner des modules élastiques légèrement supérieurs aux valeurs non-drainées pouvant suggérer une seconde transition d'écoulement crack-pore. En revanche, tout comme l'Indiana intact, cette dispersion n'est pas observable directement, et devrait se situer au-delà de 10^5 Hz. Au vu de l'écart entre les modules non-drainés et ultrasoniques, la dispersion reste néanmoins très faible.

6.2 Indroduction

The Urgonian limestones from Monts de Vaucluse (Provence, France), are a good opportunity to study close analogues to carbonate reservoir rocks on the east part of the Arabian plate, such as the Kharaib and Shu'aiba Formations (*Alsharhan and Nairn*, 1997; *Leonide et al.*, 2012). The depositional context of the Barremian - lower Aptian carbonate platform of Provence was very similar to the east-Arabic carbonate platform. Therefore the outcrop limestone are found to be good analogues in terms of age, facies, or reservoir properties (*Borgomano et al.*, 2002; *Fournier et al.*, 2011; *Borgomano et al.*, 2013). Urgonian carbonates are an opportunity to follow the evolution of wave velocities with diagenetic evolution of the pore space, with three main categories: by increasing stiffness 1) purely microporous, 2) preserved intergranular and moldic, 3) vuggy (*Fournier et al.*, 2014). A large dataset of ultrasonic wave velocities has been done by *Fournier et al.* (2014), and showed some substantial dependence to confining pressure for the more compliant intercrystalline micropores, whereas the moldic pores were stiff and less sensible to pressure. For the study of frequency effects and potential squirt-flow related to relative compliant porosities, we selected a sample mainly microporous with pressure-dependent elastic properties.

6.3 Sample description

The sample comes from a lower cretaceous carbonate platform outcrop in SE of France, corresponding to the barremian-lower Aptian succession in the Monts de Vaucluse (*Leonide et al.*, 2012), which is part of the Urgonian Limestone Formation. The sample was cored in a block that came from Rustrel (Figure 6.1), in an outcrop identified as "Les Antennes" (N43.926516°,E5.502709°) in the studies of *Leonide et al.* (2012) and *Léonide et al.* (2014).

The block we retrieved from the outcrop "Les Antennes" presented some sparsely distributed rudists of around 1 cm size. The block's original facies is identified as the Rudist facies (FA6) in the studies of *Leonide et al.* (2012) and *Fournier et al.* (2014). The use of 5 mm strain gauges prohibits us to measure the elasticity of such large heterogeneities. We therefore cored the plug in the fine-grained homogeneous part of the block that constitutes the matrix surrounding the large rudists. A SEM photomicrograph of the sample is presented Figure 6.2. The sample is homogeneous, with poorly sorted grains of maximum size 500 µm (Figure 6.2). We can therefore assume the plug is isotropic at this scale. The microstructure is mainly composed of calcite cement surrounding micritic peloidal grains that could be fragments of rudist shells (Figure 6.2). The principal pore type is intragranular micropore within the micritic grains, and intercrystalline porosity within the calcitic cement.

The porosity was measured to be around 14.9% by triple-weight method, and the permeability was measured to be around $4 \times 10^{-17}\,\mathrm{m}^2$ (Figure 6.3). The dry density is around

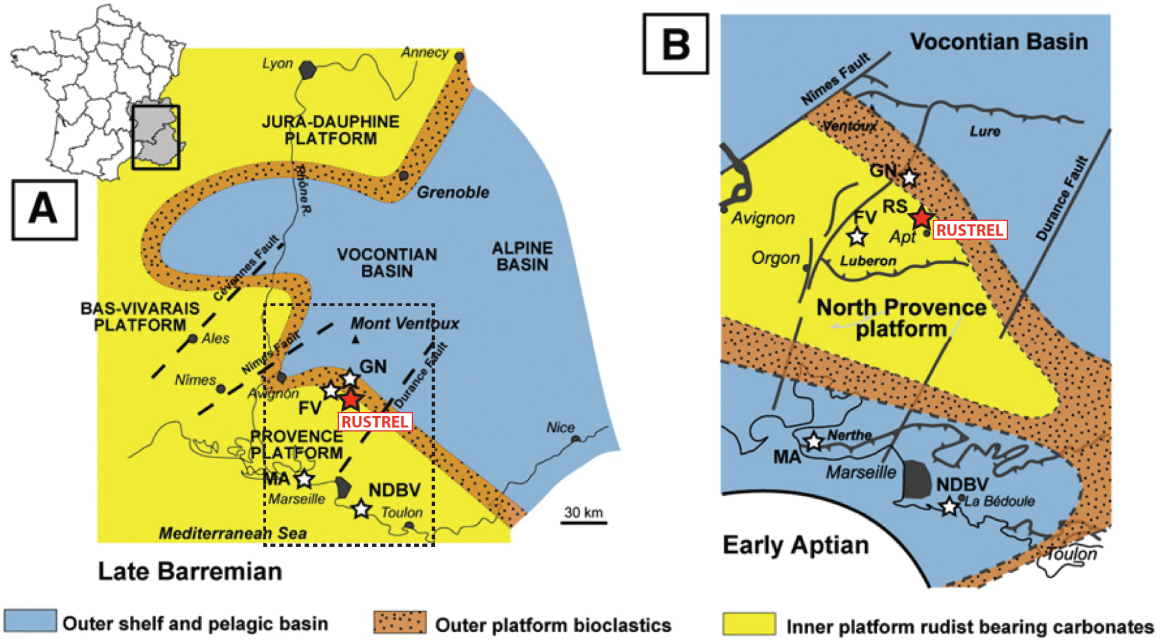

Figure 6.1: Setting of the Urgonian platform in the South-East of France during the Late Barremian (a) and the Early Aptian (b). Rustrel is located at the edge of the Provence inner platform. Modified after *Léonide et al.* (2014).

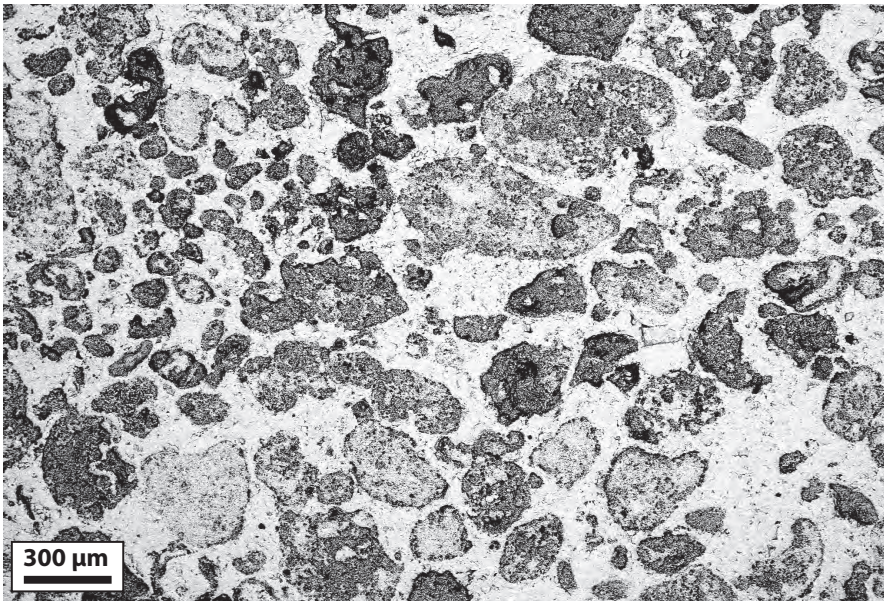

Figure 6.2: SEM photomicrograph of the Rustrel sample, showing the large amount of intergranular calcite cement in white with some intercrystalline microporosity, and the intragranular microporosity in black.

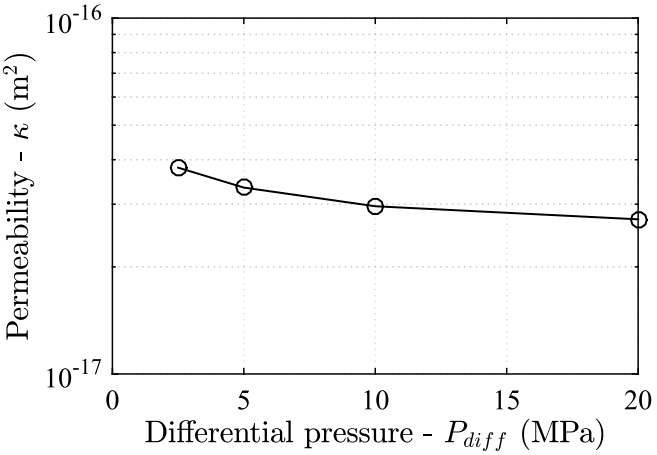

Figure 6.3: Permeability results of the Rustrel sample at different differential pressures. Measurements were done by Darcy flow under water-saturated conditions.

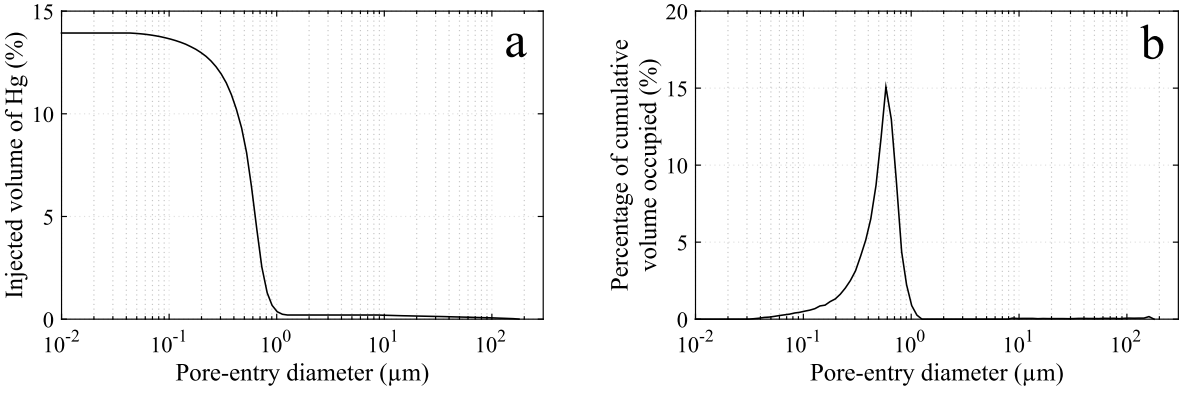

Figure 6.4: MICP results of the Rustrel sample.

$D = 2345\,\mathrm{kg.m^{-3}}$. With increasing differential pressure, the permeability slightly drops around $2 \times 10^{-17}\,\mathrm{m^2}$ (Figure 6.3). The MICP results show a clear unimodal pore-entry size distribution with a maximum peak at 0.6 µm (Figure 6.4), corresponding to the intragranular microporosity (Figure 6.2).

6.3.1 Static bulk modulus

Because no mechanical data was available concerning the pore-collapse pressure, we decided to limit the measurements to a maximum effective pressure of 20 MPa. The hydrostatic loading stress-strain curve, up to 18 MPa, is shown Figure 6.5a. After a polynomial fit, we can deduce the static bulk modulus by derivation of the stress-strain curve (Figure 6.5b). Results show a static bulk modulus that increases from 5 GPa at $P_c = 2.5$ MPa to 23 GPa at $P_c = 18$ MPa (Figure 6.5b). A typical crack closure behavior is observed between 2.5 MPa and 18 MPa, with an increase of the bulk modulus, but the high-pressure asymptote was

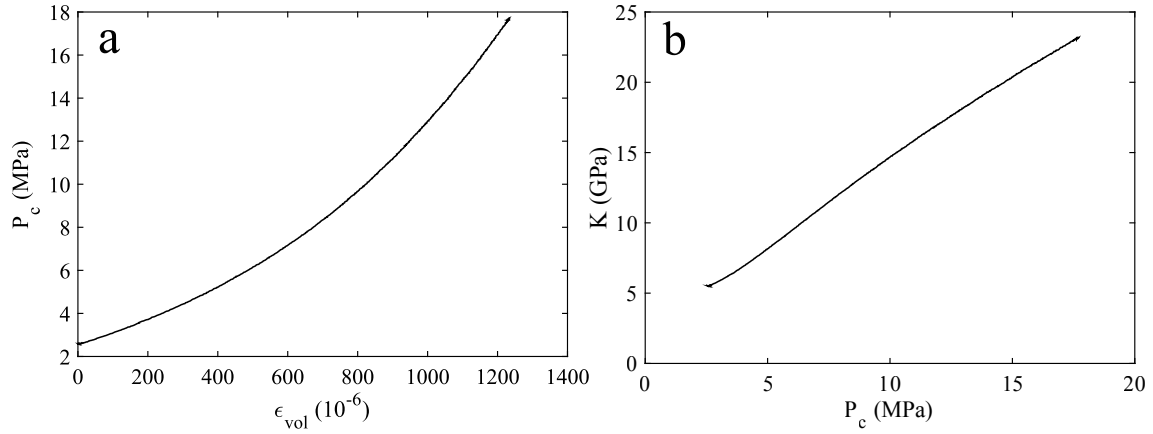

Figure 6.5: Static loading results obtained on the Rustrel sample.

not reached.

6.3.2 High-frequency ultrasonic results

The ultrasonic results at different effective pressures under dry-, water- and glycerin-saturated conditions are presented Table 6.1. All four elastic moduli (K, G, E and ν) are calculated, with the assumption of isotropy. In dry conditions, the high-frequency bulk

RUSTREL							
	P_{diff} (MPa)	V_P (m s^{-1})	V_S	K_{HF} (GPa)	G_{HF}	E_{HF}	ν_{HF}
DRY	2.5	3545	2185	14.5	11.2	26.7	0.19
	5	3762	2265	17.1	12.0	29.3	0.22
	10	4008	2395	19.7	13.4	32.9	0.22
	15	4111	2484	20.3	14.5	35.1	0.21
	20	4198	2548	21.0	15.2	36.8	0.21
WAT	2.5	4111	2104	27.3	11.0	29.0	0.32
	5	4265	2197	29.2	12.0	31.6	0.32
	10	4506	2366	31.8	13.9	36.4	0.31
	20	4583	2431	32.6	14.7	38.2	0.30
GLY	2.5	4748	2215	40.2	12.3	33.6	0.36
	5	4776	2265	40.2	12.9	35.0	0.35
	10	4805	2366	39.3	14.1	37.7	0.34
	15	4863	2453	39.3	15.1	40.2	0.33
	20	4893	2467	39.8	15.3	40.7	0.33

Table 6.1: Results of the ultrasonic measurements on the Rustrel sample.

modulus (K_{HF}) is pressure-dependent and increases from 14.5 GPa to 21.0 GPa between $P_{diff} = 2.5$ MPa and $P_{diff} = 20$ MPa (Table 6.1). G_{HF} and E_{HF} both seem to be pressure-dependent, but ν_{HF} seems to be relatively constant with pressure, around 0.21.

Rustrel	$P_{diff} = 2.5\,\text{MPa}$
$\Phi(\%)$	14.9
$D_{dry}\,(\text{kg.m}^{-3})$	2345
$\kappa\ (\text{m}^2)$	4×10^{-17}
$\hat{\xi}$	1.8×10^{-4}
ρ	0.52
$K_d\,(\text{GPa})$	14.5
$f_1^*\,(\text{Hz})$	0.36
$f_2^*\,(\text{Hz})$	477

Table 6.2: Properties of the Rustrel sample for a differential pressure of 2.5 MPa. K_d is the dry dynamic moduli estimated from the ultrasonic measurements. The drained/undrained and undrained/unrelaxed (squirt-flow) cut-off frequencies, respectively f_1^* and f_2^* (Equation 1.39), are valid for water-saturated conditions.

In fluid-saturated conditions, K_{HF} is only slightly pressure-dependent with water, but completely pressure-independent with glycerin (Table 6.1). The Poisson's ratio ν_{HF} decreases with increasing pressure, while the Young's modulus E_{HF} continues to increase. The shear modulus, and its pressure-dependence, doesn't appear to be fluid sensitive.

From the permeability measurement (κ), the sample's length (L), and the measurement of the dry K_{HF} considered as the drained modulus (K_d), we can have a first estimation of the drained/undrained cut-off frequency ($f_1^* = 4\kappa K_d/\eta L^2$). At $P_{diff} = 2.5\,\text{MPa}$, the drained/undrained cut-off frequency would be around $f_1^* = 0.36\,\text{Hz}$.

We obtain from Morlier's method (*Morlier*, 1971), applied on the pressure-dependence of the dry bulk modulus obtained from hydrostatic oscillations (see Chapter 10), a characteristic crack aspect ratio $\hat{\xi} = 1.8 \times 10^{-4}$ with a crack density of $\rho = 0.52$. If we take $K_S = 77\,\text{GPa}$, the squirt-flow cut-off frequency of these cracks would be $f_2^* = K_S\hat{\xi}^3/\eta = 477\,\text{Hz}$ for water saturated conditions. A synthesis of the sample's properties at $P_{diff} = 2.5\,\text{MPa}$ can be found Table 6.2.

6.4 Low-frequency dynamic moduli

The low-frequency axial and hydrostatic oscillations were performed under drained boundary conditions (large dead volumes).

6.4.1 Young's modulus, Poisson's ratio and shear modulus deduced from axial oscillations

The Top Industrie apparatus was used for the experiments, with the modified aluminium endplaten (Figure 3.6). This enabled us to have a proper measurement of the axial stress during the oscillations, and therefore deduce the dynamic Young's modulus in addition to the Poisson's ratio. A small deviatoric load of 1 MPa was applied with the piston

in order to maintain the piezoelectric oscillator. The dispersion and attenuation of the Young's modulus and the Poisson's ratio are presented respectively Figures 6.6a-b and Figures 6.6c-d, for dry-, water- and glycerin-saturated conditions, at differential pressures $[2.5, 5, 10, 20]$ MPa. From Equation 4.2, the average relative uncertainties found on E and ν was around $\Delta E/E = 2.4\%$ and $\Delta\nu/\nu = 3.4\%$.

The Young's modulus, obtained from the low-frequency axial oscillations, exhibits dispersion around 0.05 Hz (Figure 6.6a), correlated with attenuation (Figure 6.6b), visible under water-saturated conditions. Q_E^{-1} has a maximum peak around 0.1 for $P_{diff} = 2.5$ MPa and decreases with increasing pressure, consistently with Zener's model (Equation 3.14). This transition seems to correspond to the drained/undrained cut-off frequency (f_1^*), although the prediction f_1^* seems to overestimate the experimental results of nearly one order of magnitude. No dispersion, nor attenuation, is detected for higher apparent frequencies with glycerin, although the measurements cross the predicted squirt-flow cut-off frequency f_2^* (Figures 6.6 and 6.6b). The dry results are consistently non-dispersive. The Young's modulus in water- and glycerin-saturated conditions at $P_{diff} = 2.5$ MPa seem to be inferiour to the dry Young's modulus (Figure 6.6a). At higher differential pressures, the results between dry and fluid-saturated moduli seem consistent.

The Poisson's ratio exhibits the similar dispersive transition around 0.05 Hz (Figure 6.6), which is related to the drained/undrained transition. Q_ν^{-1} peaks at a higher value than Q_E^{-1} as predicted by Zener's model (Figure 6.6d). At frequencies lower than f_1^* (drained regime), ν seems to slightly increase with increasing pressure (Figure 6.6c). On the other hand, at frequencies greater than f_1^* (undrained regime), we observe the opposite: ν decreases slightly with increasing pressure (Figure 6.6c). Similarly to E, the Poisson's ratio does not exhibit any dispersive transition around the predicted squirt-flow cut-off frequency f_2^*.

The dispersion and attenuation of the shear modulus can also be obtained from the axial oscillations, with the condition of an isotropic medium (Equations 3.3 and 3.9). No dispersion nor attenuation is observed for the shear modulus (Figure 6.7). The relative uncertainty on G was found to be around $\Delta G/G = 3.3\%$ (Equations 3.3 and 4.2). Similarly to E, the water- and glycerin-saturated shear moduli are lower than in the dry conditions, at $P_{diff} = 2.5$ MPa. This could be some shear-weakening due to chemical fluid/rock interaction, although it is similarly observed both with water and with glycerin.

6.4.2 Bulk modulus deduced from hydrostatic and axial oscillations

The bulk modulus dispersion and attenuation can be obtained from both hydrostatic (Equations 3.1 and 3.6) and axial oscillations (Equations 3.3 and 3.9). The results at different differential pressures under fully saturated conditions are presented Figure 6.8. The relative uncertainties on K_{hyd} and K_{ax} were found to around $\Delta K_{hyd}/K_{hyd} = 2\%$ (Equation 4.1) and $\Delta K_{ax}/K_{ax} = 6.5\%$ (Equations 3.3 and 4.2). For both stress-oscillation type, the drained/undrained transition is detected at the same frequency, between 0.05 and 0.1 Hz.

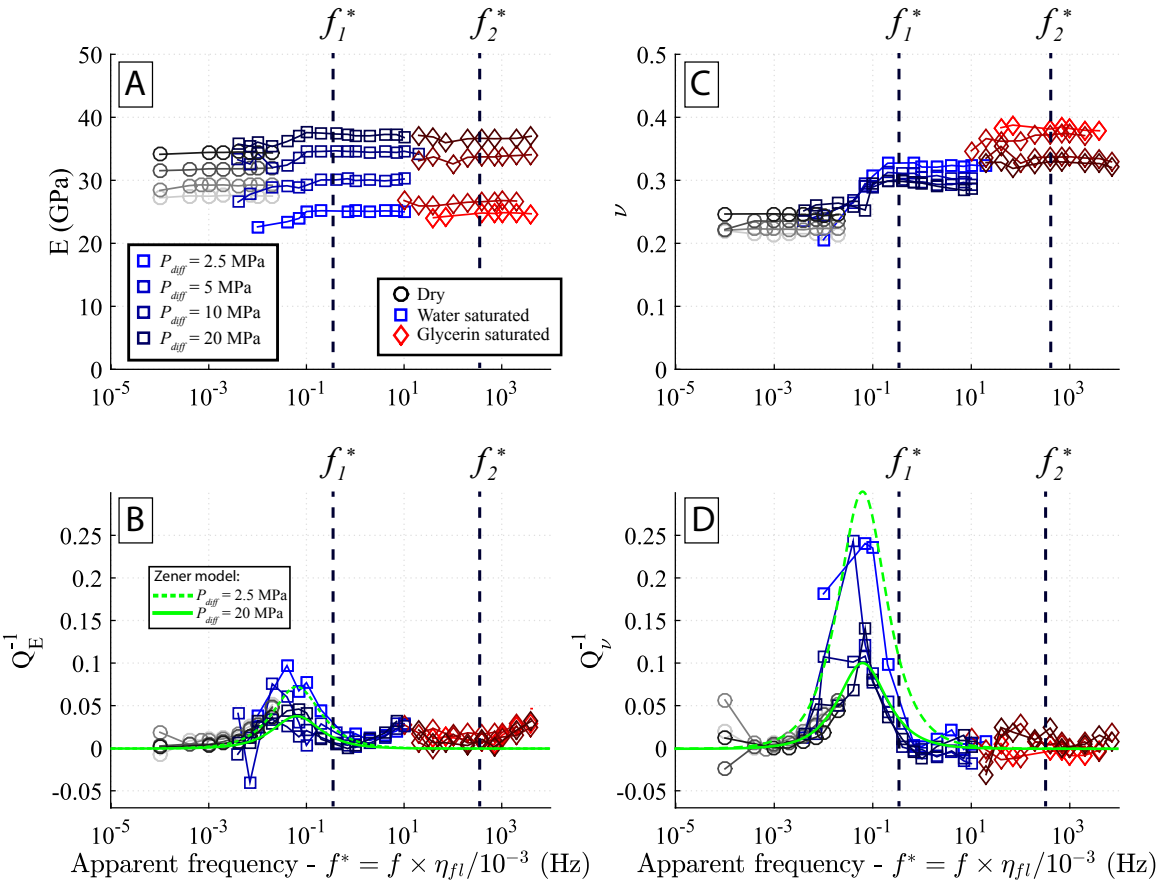

Figure 6.6: Results of Young's modulus (a-b) and Poisson's ratio (c-d) dispersion and attenuation obtained from axial oscillations at different differential pressures on the Rustrel sample.

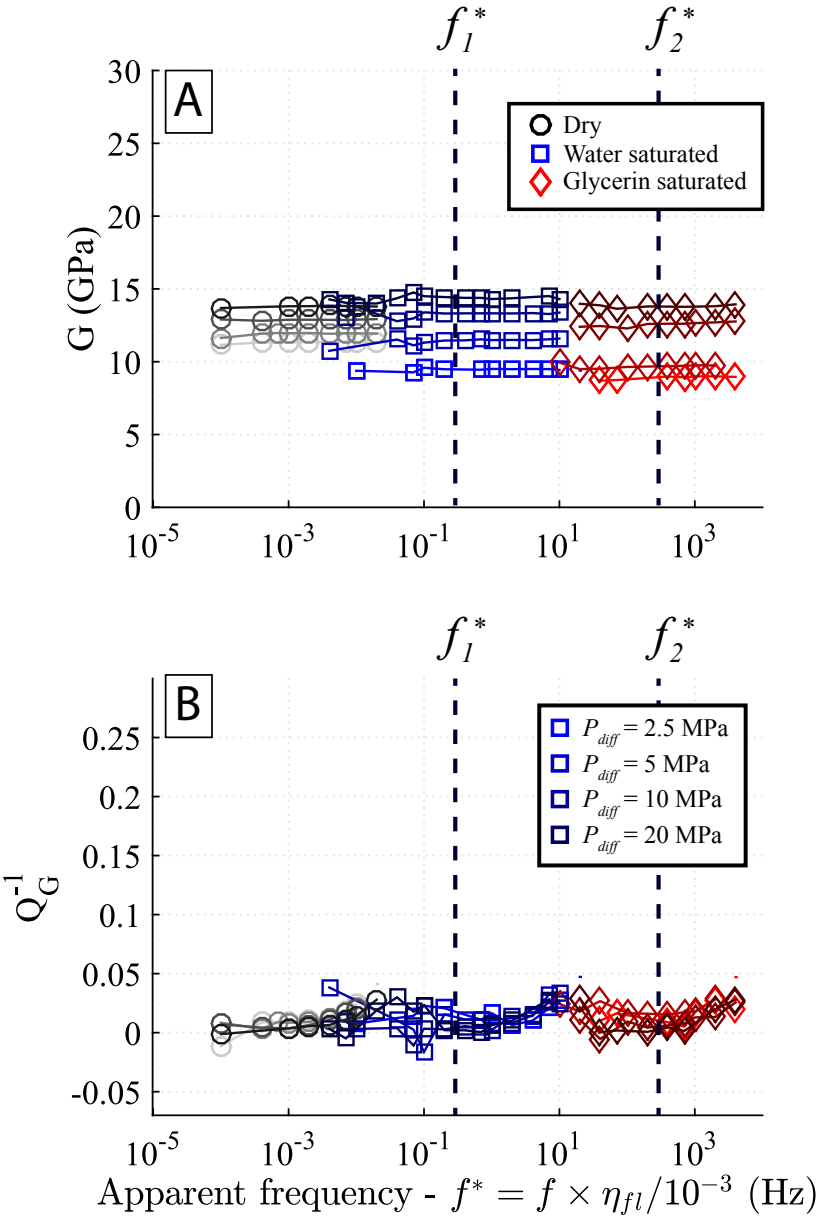

Figure 6.7: Results of the shear modulus dispersion (a) and attenuation (b) obtained from axial oscillations at different differential pressures on the Rustrel sample.

No dispersive transition is detected for frequencies higher than f_1^*, in glycerin-saturated conditions (Figure 6.8). The bulk modulus obtained from the hydrostatic oscillations (K_{hyd}) seems to be slightly more sensitive to differential pressure than the bulk modulus obtained from the axial oscillations (K_{ax}) (Figures 6.8a and 6.8b). In dry conditions, K_{hyd} increases from 11 GPa to 25 GPa, while K_{ax} increases from 15 GPa to 23 GPa (Figures 6.8a and 6.8b). Similar observation can be made for the bulk modulus results in glycerin-saturated conditions (undrained regime), K_{hyd} is pressure sensitive while K_{ax} shows less dependence to differential pressure.

The attenuation related to K_{hyd} at $P_{diff} = 2.5$ MPa has a higher peak than for K_{ax}, respectively 0.62 and 0.42 (Figures 6.8b and 6.8e), which is consistent with the higher amount of dispersion measured for the hydrostatic oscillations in water-saturated conditions (Figures 6.8a and 6.8d). No attenuation is detected elsewhere. The attenuation peaks at low and high-pressures are consistent with Zener's model.

Despite the sample being with drained boundary conditions achieved with large dead volumes, a small pore pressure oscillation was detected in the drainage circuit, either for hydrostatic or axiual oscillations, similarly to the Indiana samples. The ratio between this pore pressure oscillation amplitude (ΔP_p) and the hydrostatic stress oscillation ($\sigma_{ii}/3$) are reported Figures 6.8c and 6.8f for the hydrostatic and the axial oscillations respectively. We recall that for the hydrostatic oscillations $\sigma_{ii}/3 = \Delta P_p$, and for the axial oscillations $\sigma_{ii}/3 = \sigma_{ax}/3$. When the frequency increases, we see that for both stress-type oscillations, the ratio $3\Delta P_p/\sigma_{ii}$ tends to 0 around 0.05 Hz, which is consistent with a drained/undrained transition (Figures 6.8c and 6.8f). The ratio decreases with increasing differential pressure, which is consistent with an increasing bulk modulus that, in the frame of poroelasticity, generates less pressure build-up in the fluid for a given stress oscillation (Figures 6.8c and 6.8f).

6.5 Discussion

6.5.1 The drained/undrained transition

The results of the bulk modulus obtained from the static-loading, the ultrasonic measurements, and the low-frequency axial and hydrostatic oscillations are compared Figure 6.9. The drained/undrained transition was observed around 0.1 Hz in water-saturated conditions, which is in goood agreement with the predicted cut-off frequency of 0.36 Hz. For the hydrostatic and the axial bulk modulus results, Biot-Gassmann equation was applied on the low-pressure ($P_{diff} = 2.5$ MPa) and the high-pressure ($P_{diff} = 20$ MPa) drained results in water-saturated conditions (Figure 6.9). The skeleton bulk modulus was taken equal to the calcite's bulk modulus $K_S = 77$ GPa. For the hydrostatic oscillations (Figure 6.9a), Biot-Gassmann prediction seems to slightly underestimate the experimental undrained re-

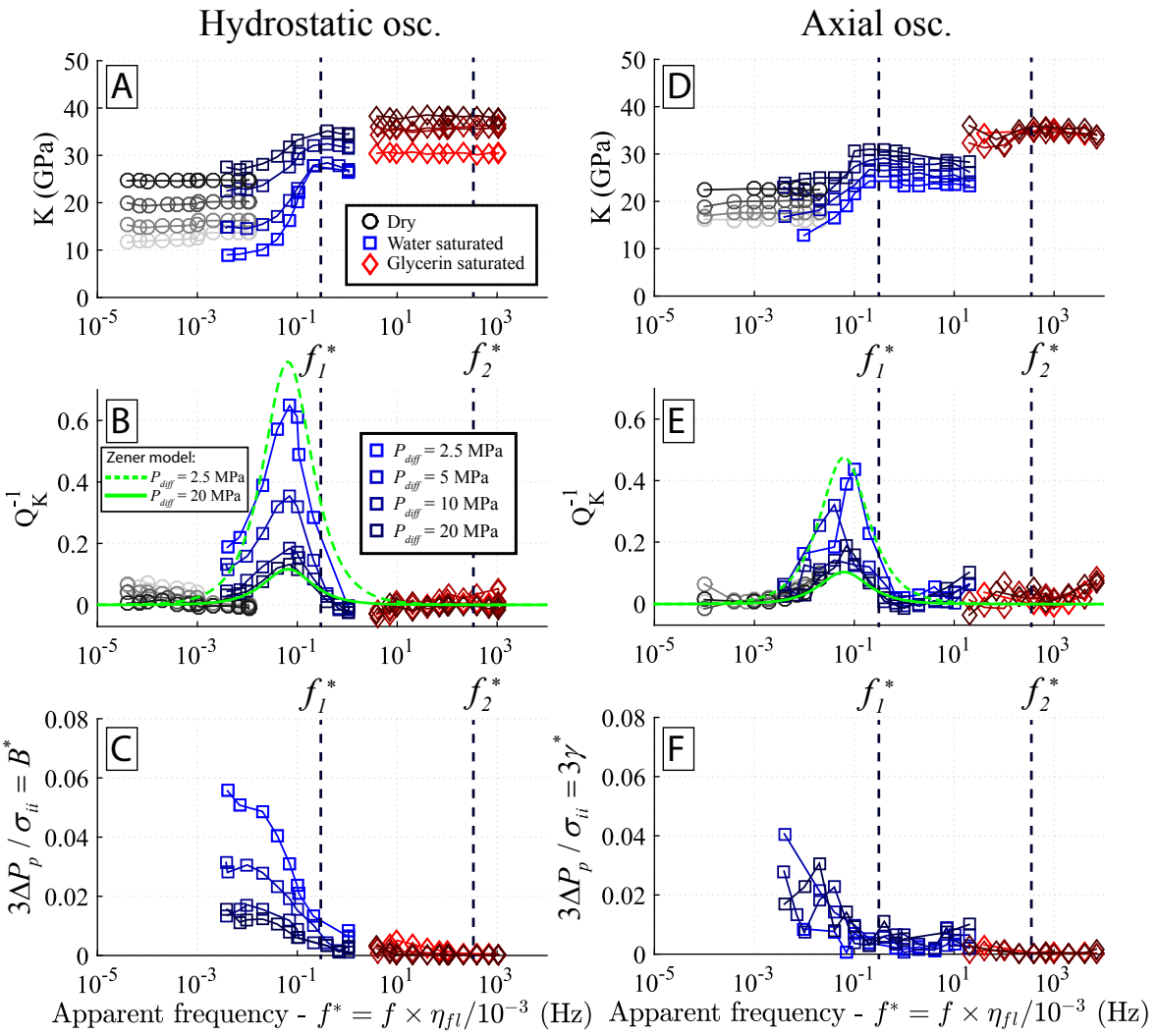

Figure 6.8: Results of the bulk modulus dispersion and attenuation obtained from hydrostatic (a-b) and axial oscillations (d-e) at different differential pressures on the Rustrel sample. The pore pressure variation in the drainage circuit over the hydrostatic stress variation are respectively presented in (c) and (f).

sults in water-saturated conditions, and is consistent with the glycerin-saturated undrained results (Figure 6.9a). For the axial oscillations (Figure 6.9b), Biot-Gassmann's prediction is consistent with the water-saturated undrained results, but slightly underestimated the low-pressure ($P_{diff} = 2.5\,\text{MPa}$) glycerin-saturated undrained results, although the latter seem not to be much pressure-sensitive.

6.5.2 Unrelaxed regime?

In water-saturated conditions, K_{HF-wat} at $P_{diff} = 20\,\text{MPa}$ is in agreement with Biot-Gassmann's prediction, while K_{HF-wat} at $P_{diff} = 2.5\,\text{MPa}$ overestimates the prediction from at least 7 GPa (Figure 6.9), which could suggest a small dispersion at low effective pressures. Despite the fact that K_{HF} seem to fit well with the undrained values of K_{hyd} (Figure 6.9a), even at low pressures, the bulk moduli deduced from axial oscillations (K_{ax}) are all lower than K_{HF} for all pressures (Figure 6.9b). Moreover, the ultrasonic results in glycerin-saturated conditions show nearly no dependence to differential pressure, and are consistent with the high-pressure prediction of Biot-Gassmann (Figure 6.9). This suggests that there could be a small amount of dispersion due to squirt-flow above $10^4\,\text{Hz}$. If we invert the expression $f_2^* = \hat{\xi}^3 K_S/\eta$, the corresponding crack aspect ratios would be at least 5×10^{-4}. The predicted cut-off frequency from Morlier's method gave $f_2^* = 477\,\text{Hz}$ with the microcracks parameters $\hat{\xi} = 1.8 \times 10^{-4}$ and $\rho = 0.52$, which underestimates the experimental observations.

The comparison of the low-frequency and the ultrasonic results for the Young's modulus, Poisson's ratio and the shear modulus are presented Figure 6.10. We recall that the drained/undrained transition is visible for both E and ν consistently with f_1^* (Figures 6.10a and 6.10b), and that the shear modulus is constant throughout this transition, which is consistent with poroelasticity. We note that all these moduli are pressure-dependent. E and G increase with increasing differential-pressure, either in drained or undrained regime (Figures 6.10a and 6.10c). The pressure-dependence of Poisson's ratio is different, ν increases with pressure in the drained regime but decreases with pressure in the undrained regime (Figure 6.10b).

For both the hydrostatic (Figure 6.9a) and the axial oscillations (Figure 6.9b) the static bulk modulus is lower than the dynamic one, except for $P_{diff} = 20\,\text{MPa}$. The axial and hydrostatic oscillations results compare well over the frequency range, as they detected the drained/undrained transition at exactly the same frequency (Figure 6.9). A slight difference subsists regarding the sensitivity to differential pressure: the hydrostatic results are more sensible than the axial results in the drained regime, visible under dry- and water-saturated conditions (Figure 6.9).

For E and G, the ultrasonic results in glycerin-saturated conditions seem to be slightly higher than the undrained moduli, similarly to K, especially for the low differential pressures (Figures 6.10a and 6.10c). Not much difference is visible for water-saturated condi-

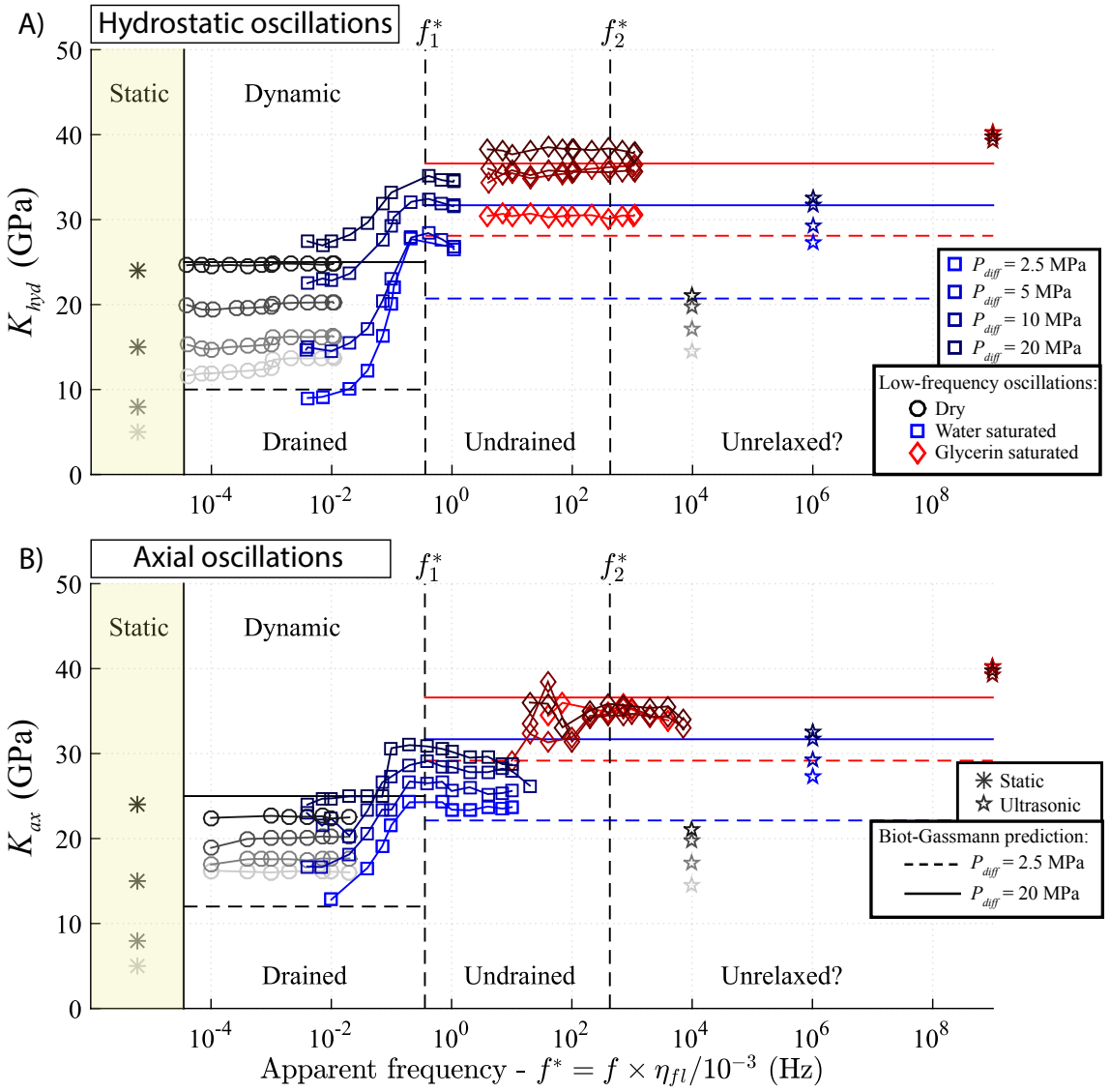

Figure 6.9: Static and frequency-dependent dynamic bulk modulus obtained from the hydrostatic (a) and axial oscillations (b) of the Rustrel sample, for four different differential pressures in fully-saturated conditions. The results combine the low-frequency results with the ultrasonic and static measurements. The drained and undrained regimes are clearly identified, however, it is difficult to conclude if there is any unrelaxed regime.

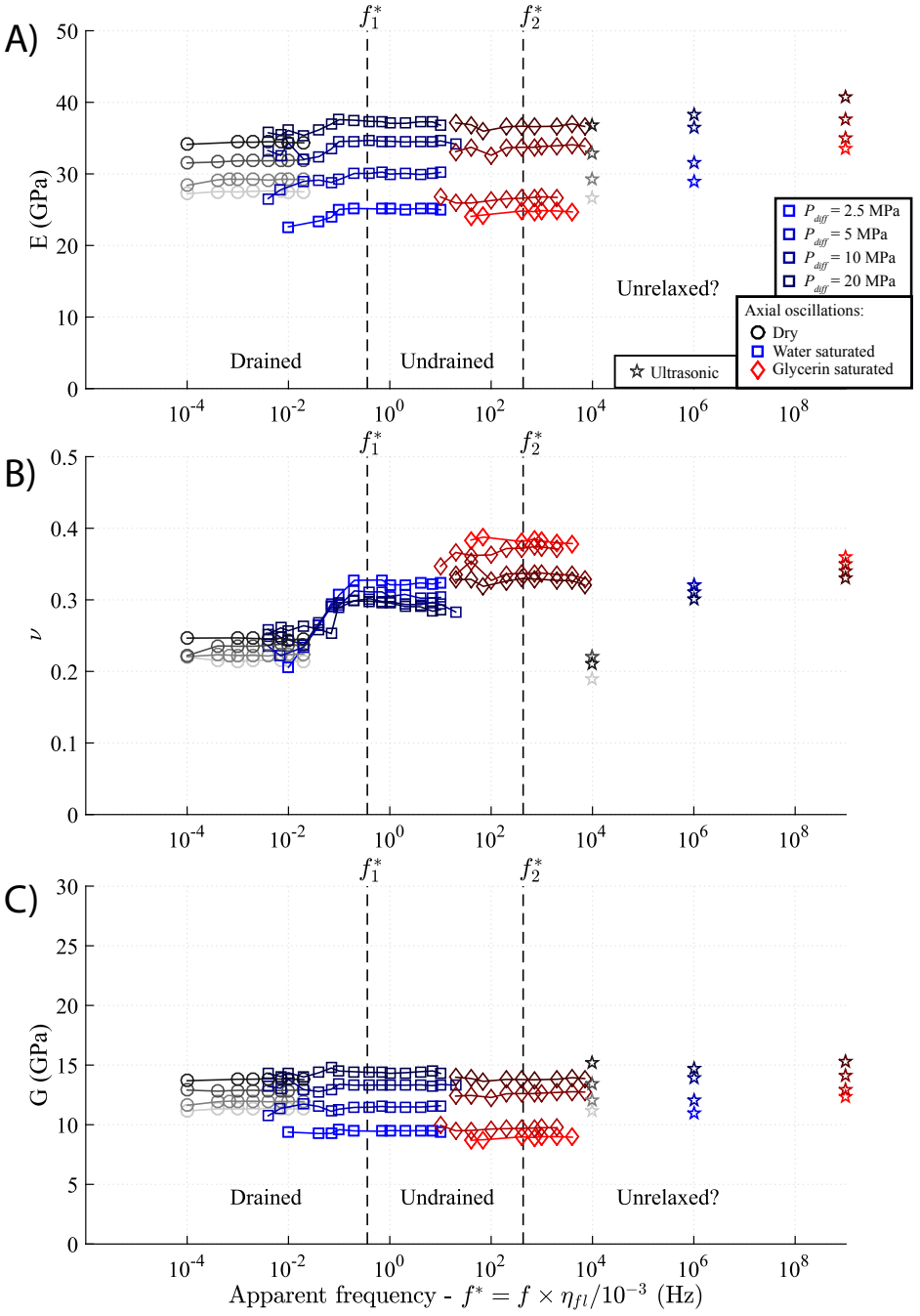

Figure 6.10: Frequency-dependent dynamic Young's modulus (a), Poisson's ratio (b) and shear modulus (c) obtained from the low-frequency axial oscillations and the ultrasonic measurements on the Rustrel sample, for four different differential pressures in fully-saturated conditions.

tions. For ν, there is nearly no difference between the ultrasonic and the undrained results (Figure 6.10b) in fluid-saturated conditions. This confirms that the squirt-flow dispersion is overall very small for this sample.

Previously, for the Indiana limestone, we evoked the key role the intergranular blocky cement might play into hosting microcracks able to generate squirt-flow. A comparison of SEM photomicrographs of the Rustrel sample and the Indiana sample (intact and thermally cracked) is presented Figure 6.11. Our main observation is the microstructural difference between the blocky calcite cement of the Rustrel and the Indiana limestones. The Rustrel sample is not fully cemented. Its cement still bears intercrystalline microporosity (Figures 6.11a-c). On the other hand, the cement of the Indiana is fully composed of large homogeneous crystals (Figures 6.11d-f). Question rises whether this incomplete cementation of the Rustrel sample could explain a pressure-dependent behavior, but still not generate much squirt-flow dispersion due to leak-off in the intercrystalline microporosity of the blocky calcite cement. We can suspect a similar behavior if the pressure-dependence originates from microcracks located in the micriticized grains. As comparison, the thermally cracked Indiana (Figure 6.11f) that exhibited substantial squirt-flow dispersion, bears neat microcracks within the homogeneous cement.

6.6 Conclusion

The frequency dependence of all the dynamic elastic moduli have been measured over a large frequency range ($[10^{-4}$; $10^{9}]$ Hz) on a rudist-dominated facies limestone from Rustrel, at different effective pressures. The drained and the undrained regime were clearly identified for all the elastic moduli, and were consistent with Biot-Gassmann theory within the uncertainty of the measurements. The transition was also consistent with the predicted cut-off frequency f_1^*, and by extension with the measured permeability of the sample.

Similarly to the intact Indiana, the presence of an undrained/unrelaxed transition was not directly observed, but was inferred from the comparison of the undrained moduli, obtained from forced oscillations, and the ultrasonic measurements that are expected to be in the unrelaxed regime. Only a small amount of squirt-flow dispersion is expected, equivalent to the intact Indiana despite a higher crack density. The main difference between the Rustrel and the Indiana was found to be the texture of the calcite cement. The Indiana bears a homogeneous cement with large crystals, while for the Rustrel sample the cement is not fully crystallized and bears extensive intercrystalline porosity resulting in a overall weaker frame, but not generating substantial squirt-flow. The consistency with effective medium theory shall be discussed in an other chapter.

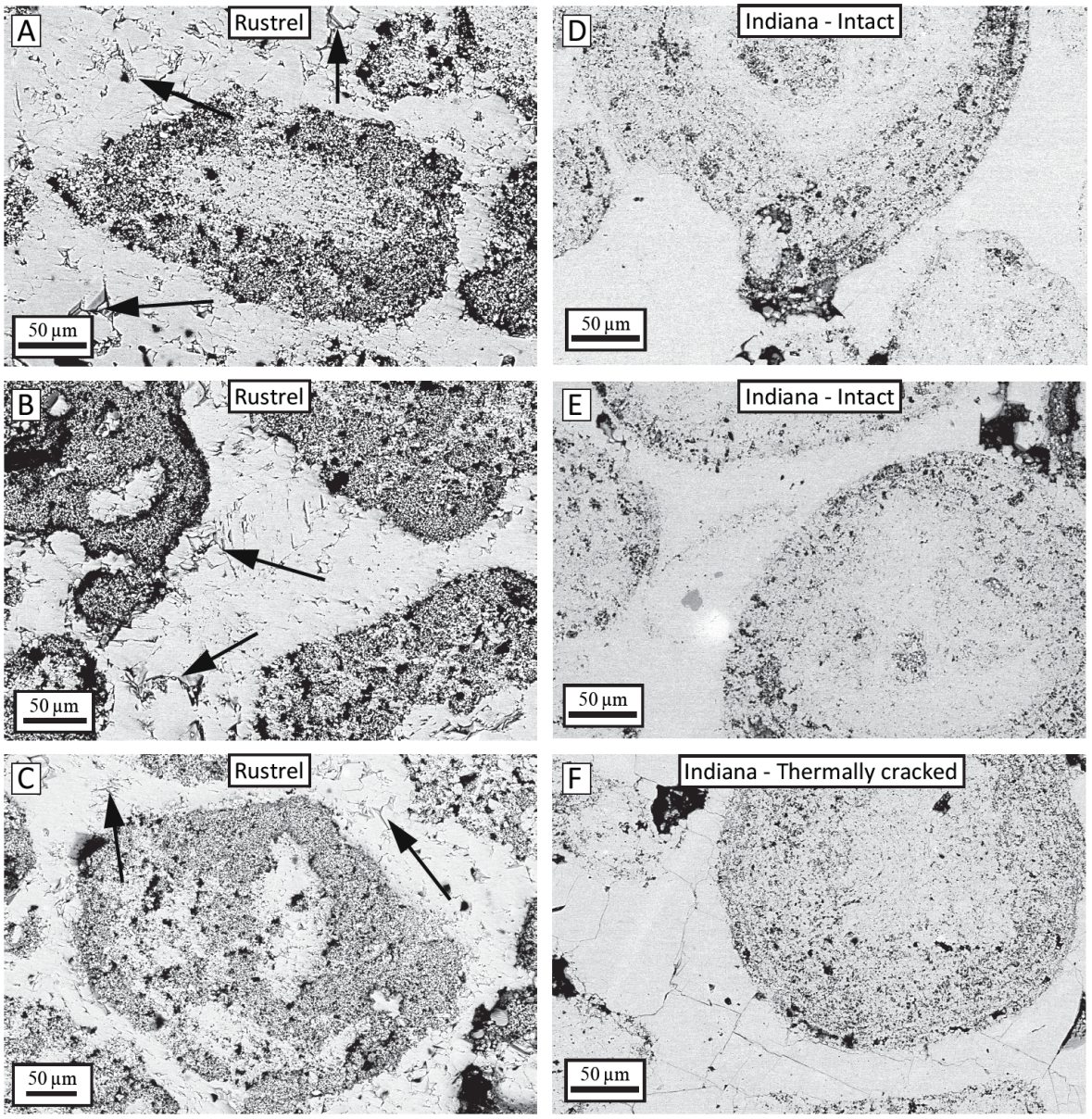

Figure 6.11: SEM photomicrographs of the Rustrel sample (a-c), compared to photomicrographs of the intact (d-e) and thermally cracked (f) Indiana samples. The arrows indicate some examples of intercrystalline microporosity embedded in the calcite cement of the Rustrel limestone. As comparison, the Indiana's calcite cement is more homogeneous with no intercrystalline porosity.

CHAPTER 7

PRE-SALT COQUINA FROM OFFSHORE CONGO.

7.1 Résumé

Le dernier échantillon étudié est un coquina pré-sel, provenant d'un puits profond en mer (4000 m) au large du Congo. Ce coquina est un calcaire lacustre détritique, composé essentiellement de fragments de coquilles. Il a été déposé dans les grands lacs qui se sont formés au crétacé inférieur en marge de l'ouverture de l'océan Atlantique. Le sel s'est ensuite déposé par-dessus, à mesure que les lacs s'asséchaient. On retrouve ces coquina pré-sel de part et d'autre de l'Atlantique, dans les marges continentales au large du Congo mais également du Brésil. Ils constituent une grande partie des roches réservoirs des champs pétroliers découverts au large du Brésil. Les coquinas du Congo peuvent potentiellement être des analogues à ceux du Brésil, bien que les conditions de dépôts furent différentes. La porosité de notre échantillon est d'environ 7.5% pour une perméabilité d'environ 0.05 mD. Les grains du coquina ne sont pas microporeux, et la porosité est essentiellement intergranulaire. De plus, la roche ne semble pas du tout cimentée.

Les fréquences sont discutées en termes de fréquences apparentes normalisées à l'eau. La transition drainé / non-drainé a été observée autour de 0.2 Hz, et est en parfait accord avec Biot-Gassmann, quelque soit la pression effective. Une seconde transition a été observée autour de 10^4 Hz, qui correspond à l'écoulement crack-pore. Cette seconde dispersion est nettement plus importante que les échantillons précédents, mis à part l'Indiana craqué thermiquement. Elle a été observée sur les modules E, G et K. Ce ne sont pas forcément que des fissures qui peuvent générer ce type d'écoulement, mais également les contacts entre les grains qui peuvent avoir un comportement analogue. Ce raisonnement est en général applicable aux grès, et par extension au roches détritiques.

Ainsi, pour les mesures sismiques sur le terrain (100 Hz), un tel coquina saturé à l'eau serait en régime non-drainé et les prédictions de Biot-Gassmann seraient valides. En re-

vanche les mesures de diagraphies (10 kHz) seraient exactement dans la gamme fréquentielle de la seconde transition (écoulement crack-pore), avec des atténuations importantes. Les mesures ultrasoniques sont dans le régime non-relaxé.

7.2 Indroduction

In the South Atlantic, number of offshore hydrocarbon reservoirs are pre-salt lacustrine carbonates, and more specifically coquinas. These coquina reservoirs are located in the Brazilian and West African continental margins, and were deposited on shallow lacustrine platforms created during the break-up of West Gondwana in the Early Cretaceous (*Thompson et al.*, 2015). Coquinas are detrital rocks that are mainly composed of calcitic shell debris. They can also be composed with a large amount of siliciclastic or other carbonate components such as pellets (*Thompson et al.*, 2015). Few experimental studies on Coquinas have been published because of the limited availability of well-cores. We present here our results of the effect of frequency on the elastic properties of a West-African pre-salt coquina.

7.3 Sample description

The sample is a pre-salt coquina that comes from offshore of the Republic of Congo (Figure 7.1), around 60 km off the West African Atlantic Margin. The Congo-Angola margin is a passive continental margin that resulted from the opening of the South Atlantic Ocean in the Early Cretaceous (*Marton et al.*, 2000). Three main units can be distinguished in the sedimentary series of the lower Congo basin, which are related to three tectonic phases: pre-rift continental deposits (Jurassic), syn-rift fluvio-lacustrine deposits and sag phase (Lower Cretaceous), and post-rift unit with large accumulation of salt (Middle Aptian) covered by thick marine succesions (Albian to present) (*Savoye et al.*, 2009).

The margin hosts one of the largest deep-sea fan in the world (Figure 7.1), with a maximum thickness of 5 km (*Anderson et al.*, 2000), which bears important activity in terms of sedimentary processes due to active turbidity currents (*Wonham et al.*, 2010). Oligocene and Miocene turbidite systems are particularly studied by the oil industry due to oil and gas reservoirs discoveries in the Tertiary series (*Savoye et al.*, 2009).

Beneath the fan, there is the Middle-Aptian Salt (Loeme Formation) that covers the Lower-Cretaceous lacustrine deposits (*Wonham et al.*, 2010), from which our sample originates. The pre-salt coquinas of this latter deposites are of major interest as they could be analogues to the pre-salt lacustrine deposites of the Brazilian offshore fields, although the deposition conditions were slightly different. The west african coquinas deposited on distally steepened ramps and rimmed platforms, whereas the Brazilian coquinas were deposited on low angle ramps, resulting in different facies (*Thompson et al.*, 2015).

The coquina sample measured here did not bear any large clasts of large moldic pores as frequently observed for coquinas. The texture of our selected plug was homogeneous and fined grained, so that the strain gauges are larger than the REV. A SEM photomicrograph of the coquina sample is presented Figure 7.2a. The microstructure seems poorly cemented, with extensive intergranular or intercrystalline porosity (Figure 7.2a). The EDX analysis

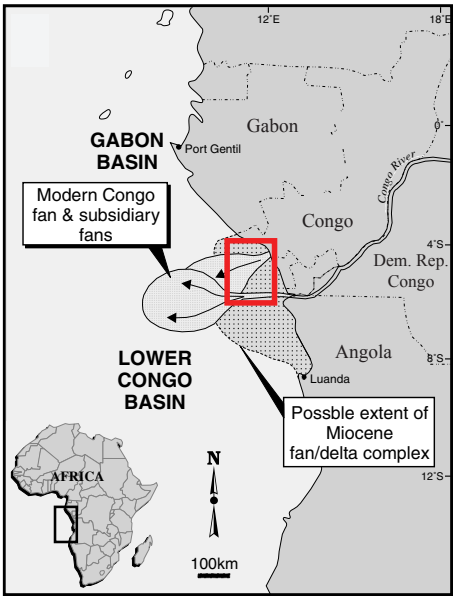

Figure 7.1: The Coquina sample was cored in the pre-salt deposits beneath the fan, at approximately 4 km depth, in Offshore Republic of Congo (red rectangle). Modified after *Anderson et al.* (2000).

shows that the sample is mainly composed of calcite (>97%) (Figure 7.2b). Some traces of quartz and solid bitumen was also detected (< 1%) and can be visualized in the element mapping Figure 7.2c. Some pores seem to be filled by the solid bitumen (Figure 7.2c). The porosity was measured to be around 7.5% by triple-weight method, and the dry mass density is around $D_{dry} = 2540\,\mathrm{kg.m^{-3}}$.

The pressure-dependence of the permeability is given Figure 7.3. A clear decrease with pressure is visible, with a variation from $5.0 \times 10^{-17}\,\mathrm{m^2}$ at $P_{diff} = 2.5\,\mathrm{MPa}$ to $2.5 \times 10^{-17}\,\mathrm{m^2}$ at $P_{diff} = 20\,\mathrm{MPa}$. The MICP results are presented Figure 7.4. The obtained results show a large distribution of pore-entry diameters, with a relatively constant plateau between 0.5 µm and 5 µm (Figure 7.4), which should correlate with intercrystalline microporosity. Moreover, a small peak is visible around 10 µm that decreases slowly up to 30 µm (Figure 7.4), which should correlate with the intergranular pore space (Figure 7.2). the visible grains in the microstructure do not seem to be micriticized, and therefore, do not seem to bear much intragranular microporosity (Figure 7.2).

7.3.1 Static bulk modulus

Because we only possessed one plug of this low-porosity coquina ($\phi = 7.5\%$), and no mechanical data was available, the measurements were limited to a maximum effective pressure of 25 MPa to avoid pore-collapse. The results of the static loading stress-strain curve, up to 25 MPa, is shown Figure 7.5a. After a polynomial fit, we can deduce the static

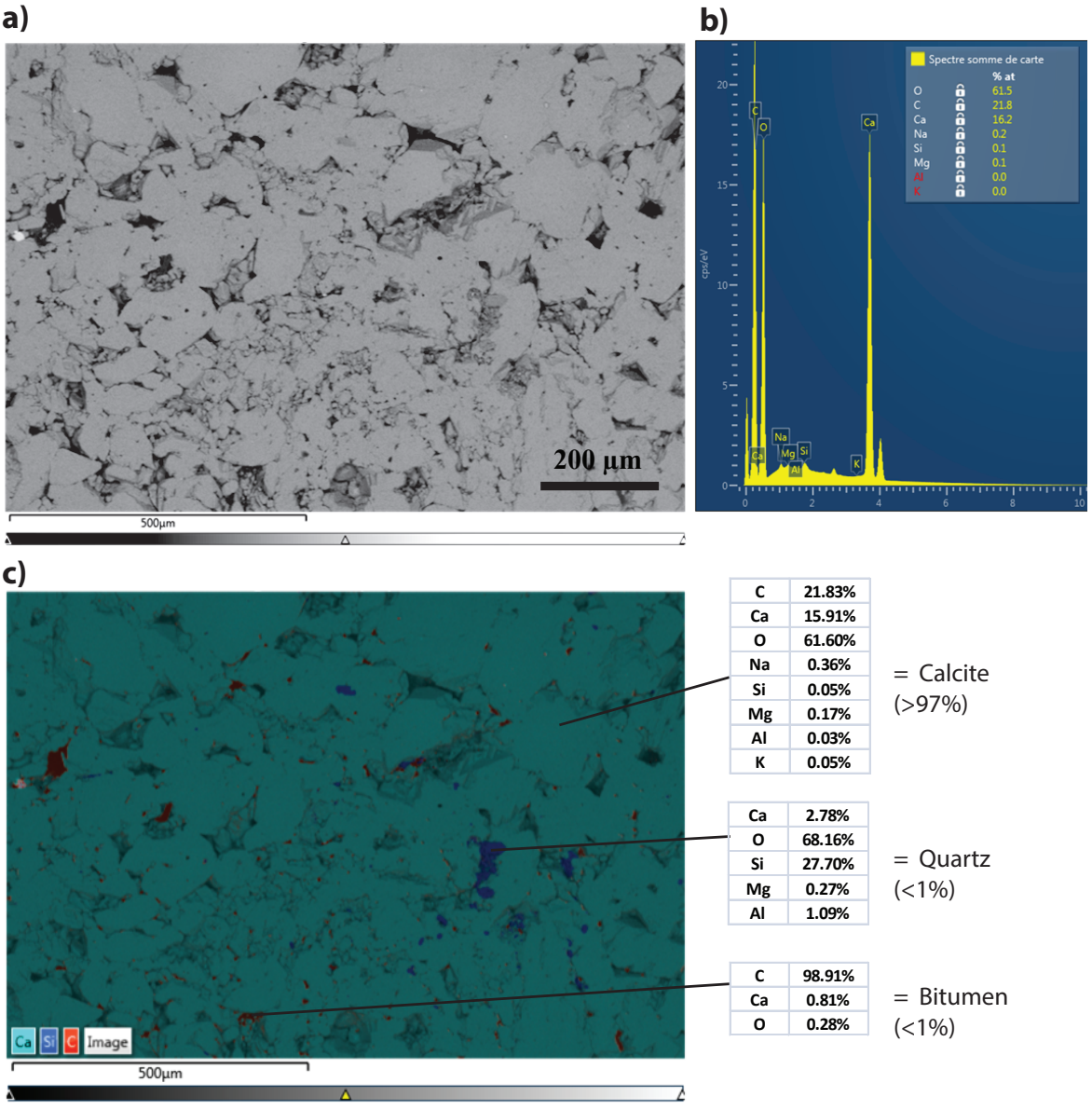

Figure 7.2: (a) SEM photomicrograph, (b) EDX bulk spectrum and (c) element mapping of the elements calcium (Ca), silicium (Si) and carbon (C) of the Coquina sample.

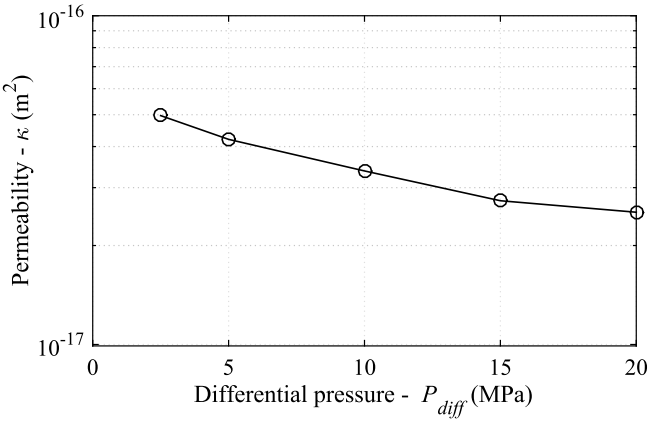

Figure 7.3: Permeability results of the Coquina sample at different differential pressures. Measurements were done by Darcy flow under water-saturated conditions.

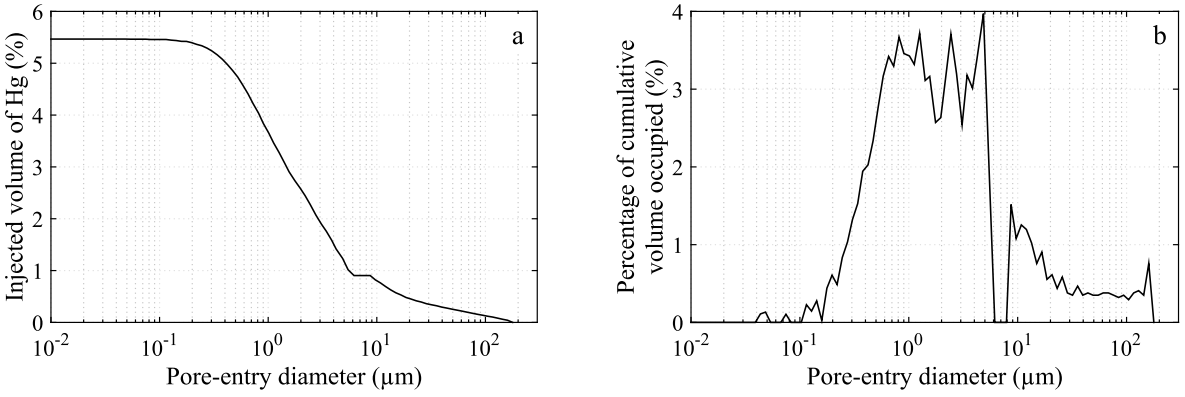

Figure 7.4: MICP results of the Coquina sample.

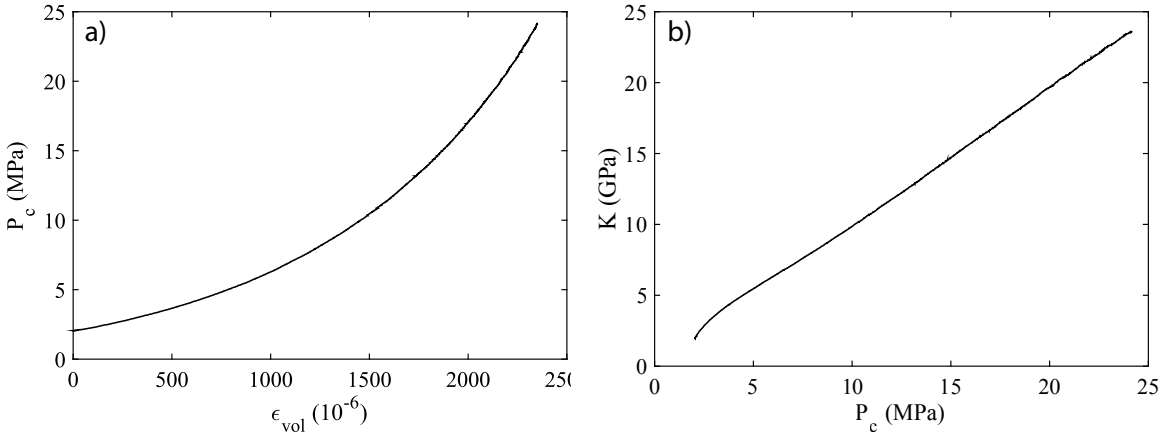

Figure 7.5: Static loading results obtained on the Coquina sample.

bulk modulus by derivation of the stress-strain curve (Figure 7.5b). Results show a static bulk modulus that increases from 2 GPa at $P_c = 2.5$ MPa to 23 GPa at $P_c = 25$ MPa (Figure 7.5b). A rather exotic behavior is observed between 2.5 MPa and 25 MPa, with nearly a perfectly linear increase of the static bulk modulus with increasing pressure (Figure 7.5b). It could suggest that the high-pressure asymptote is reached at much higher pressures than 25 MPa. But because we do not know the pore-collapse pressure of the sample, and that this unique plug had to be kept intact, we decided not to investigate the high-pressure limit.

7.3.2 High-frequency ultrasonic results

The ultrasonic results at different effective pressures under dry-, water- and glycerin-saturated conditions are presented Table 7.1. All four elastic moduli (K, G, E and ν) are calculated, with the assumption of isotropy. In dry conditions, the high-frequency bulk modulus (K_{HF}) is pressure-dependent and increases from 12.2 GPa to 26.8 GPa between $P_{diff} = 2.5$ MPa and $P_{diff} = 20$ MPa (Table 6.1). Similarly, all the other moduli (G_{HF}, E_{HF} and ν_{HF}) all increase with increasing pressure (Table 7.1).

In fluid-saturated conditions, K_{HF} remains pressure-dependent, with an increase from 32.8 GPa to 38.6 GPa in water-saturated conditions, and an increase from 45.3 GPa to 48.9 GPa in glycerin-saturated conditions (Table 6.1). The Poisson's ratio ν_{HF} seems rather pressure-independent in fluid-saturated conditions, with a values between 0.27 and 0.29 for water- and between 0.32 and 0.34 for glycerin-saturated conditions. The fluid-saturated shear moduli are higher than the dry shear moduli at every pressure, with an average increase of 6 GPa (Table 6.1).

From the permeability measurements (κ), the sample's length (L), and the measurement of the dry K that is measured to be around 5 GPa from hydrostatic oscillations at $P_{diff} = 2.5\,MPa$, we can have a first estimation of the drained/undrained cut-off frequency ($f_1^* =$

COQUINA							
	P_{diff} (MPa)	V_P (m s^{-1})	V_S	K_{HF} (GPa)	G_{HF}	E_{HF}	ν_{HF}
DRY	2.5	3174	1985	12.2	10.0	23.6	0.18
	5	3545	2148	16.3	11.7	28.4	0.21
	10	3890	2312	20.3	13.6	33.3	0.23
	15	4191	2400	25.1	14.6	36.7	0.26
	20	4335	2486	26.8	15.7	39.4	0.25
WAT	2.5	4626	2571	32.8	17.2	43.9	0.28
	5	4741	2597	35.1	17.6	45.1	0.29
	10	4863	2661	37.0	18.4	47.4	0.29
	15	4958	2718	38.3	19.2	49.4	0.29
	20	5057	2840	38.6	21.0	53.3	0.27
GLY	2.5	5057	2495	45.3	16.3	43.7	0.34
	5	5196	2562	47.8	17.2	46.0	0.34
	10	5268	2689	47.4	18.9	50.1	0.32
	20	5380	2778	48.9	20.2	53.3	0.32

Table 7.1: Results of the ultrasonic measurements on the Coquina sample.

Coquina	$P_{diff} = 2.5$ MPa
$\Phi(\%)$	7.5
κ (m^2)	5×10^{-17}
$\hat{\xi}$	2.8×10^{-4}
ρ	1.3
K_d (GPa)	5
f_1^* (Hz)	0.16
f_2^* (Hz)	1600

Table 7.2: Properties of the Coquina sample for a differential pressure of 2.5 MPa. K_d is the dry dynamic moduli estimated from the hydrostatic oscillations. The drained/undrained and undrained/unrelaxed (squirt-flow) cut-off frequencies, respectively f_1^* and f_2^* (Equation 1.39), are valid for water-saturated conditions.

$4\kappa K_d/\eta L^2$). At $P_{diff} = 2.5$ MPa, the drained/undrained cut-off frequency would be around $f_1^* = 0.38$ Hz, and for $P_{diff} = 20$ MPa, the cut-off frequency gives $f_1^* = 0.16$ Hz, which includes the increase of the drained bulk modulus .

From the hydrostatic loading stress-strain curve (Figure 7.5), we cannot know the high-pressure limit after which the bulk modulus becomes constant. A first estimation can be given, if we assume that the high-pressure value of the static bulk modulus is equal to $K_{HF} = 35$ GPa at $P_{diff} = 30\,MPa$, we obtain from Morlier's method (*Morlier*, 1971) a characteristic crack aspect ratio $\hat{\xi} = 2.8 \times 10^{-4}$ with a crack density of $\rho = 1.3$ (see Chapter 10). If we take $K_S = 77$ GPa, the squirt-flow cut-off frequency of these cracks would be $f_2^* = K_S\hat{\xi}^3/\eta = 1600$ Hz for water saturated conditions. A synthesis of the sample's properties at $P_{diff} = 2.5$ MPa can be found Table 7.2.

7.4 Low-frequency dynamic moduli

The low-frequency axial and hydrostatic oscillations presented in this section were performed under drained boundary conditions (large dead volumes), in the Top Industrie apparatus, for differential pressures of $[2.5; 5; 10; 20; 25]$ MPa, in dry- and water-saturated conditions, and $[2.5; 5; 10]$ MPa for glycerin-saturated conditions.

7.4.1 Young's modulus, Poisson's ratio and shear modulus.

In this section we present the results of the low-frequency axial oscillations, along the ultrasonic results, for E, ν and G. A small deviatoric load of 1 MPa was applied to the piston to maintain the piezoelectric oscillator. The dispersion and attenuation of the Young's modulus, the Poisson's ratio, and the deduced shear modulus, are presented respectively Figure 7.6, Figure 7.7, and Figure 7.8, for dry-, water- and glycerin-saturated conditions at different differential pressures. The low-frequency measurements are compared with the respective ultrasonic results (Table 7.1). The relative uncertainties on E, ν and G_{ax} were found to be around $\Delta E/E = 6.7\%$, $\Delta\nu/\nu = 4.2\%$ and $\Delta G_{ax}/G_{ax} = 6.4\%$ (Equations 3.3 and 4.2).

The Young's modulus seems to exhibit only one dispersive-frequency range, visible in glycerin-saturated conditions above 10^3 Hz (Figure 7.6a), correlated with a peak in attenuation around $Q_E^{-1} = 0.25$, consistently with Zener's prediction (Figure 7.6b). Only a small quantity of dispersion is visible around the predicted drained/undrained cut-off frequency (Figure 7.6a). The low-frequency dry measurements are consistent with the ultrasonic results (Figure 7.6a). The water-saturated and glycerin-saturated ultrasonic results are nearly equal to each other, and seem to correspond to the high-frequency limit (10^5 Hz) of the Young's modulus measured by forced oscillations (Figure 7.6a). The dispersive phenomenon could be related to squirt-flow, as it is within one order of magnitude from the cut-off frequency $f_2^* = 1600$ Hz. The attenuation peaks in glycerin-saturated conditions seem to decrease very slightly with increasing pressure (Figure 7.6b).

The Poisson's ratio exhibits dispersion and attenuation around the drained/undrained cut-off frequency f_1^*, but none around the squirt-flow predicted cut-off frequency f_2^* (Figure 7.7). The effect of the differential pressure is inverted from one side of the drained/undrained transition to the other: in the drained regime ($f^* < f_1^*$), ν increases with pressure, while in the undrained regime ($f^* > f_1^*$), ν decreases with pressure (Figure 7.7a). With the increase of frequency from 10^{-2} Hz to 1 Hz, ν varies from 0.21 to 0.34 for $P_{diff} = 2.5$ MPa, and varies from 0.26 to 0.3 for $P_{diff} = 20$ MPa. The crossing point that sees no effect of the differential pressure is located precisely at $f_1^* = 0.16$ Hz (Figure 7.7a). The drained/undrained dispersion of ν is well correlate to attenuation (Q_ν^{-1}) with peaks centered around f_1^*Hz that decrease with increasing pressure (Figure 7.7b). The attenuation peaks are in agreement with Zener's model. No more attenuation is visible at higher frequencies (Figure 7.7).

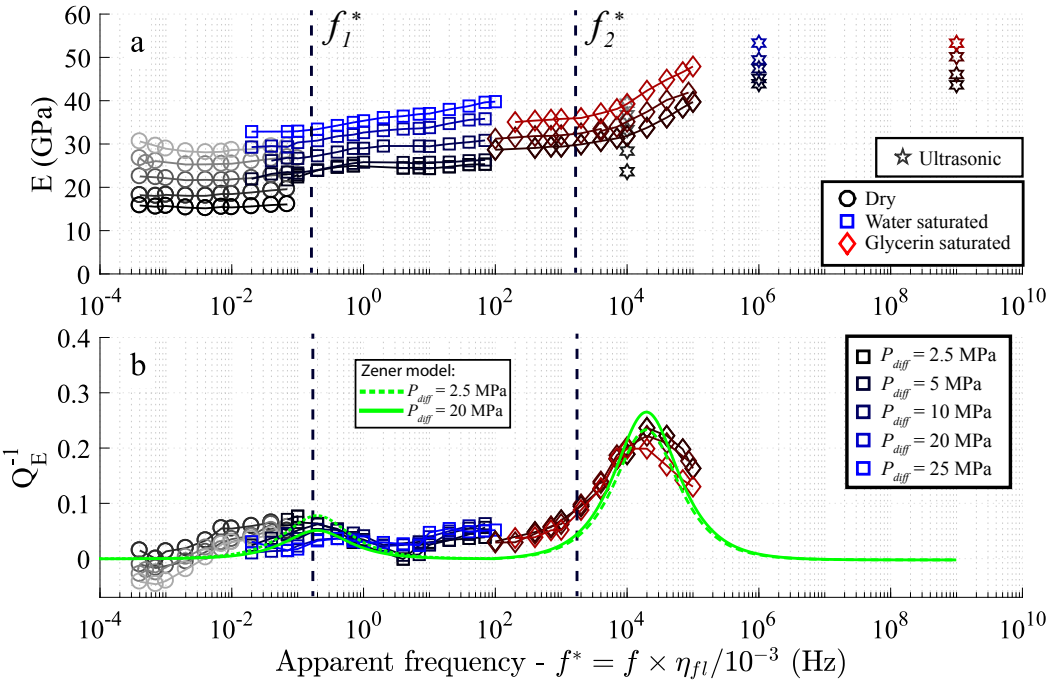

Figure 7.6: Results of Young's modulus dispersion (a) and attenuation (b) obtained from axial oscillations and ultrasonic measurements at different differential pressures on the Coquina sample.

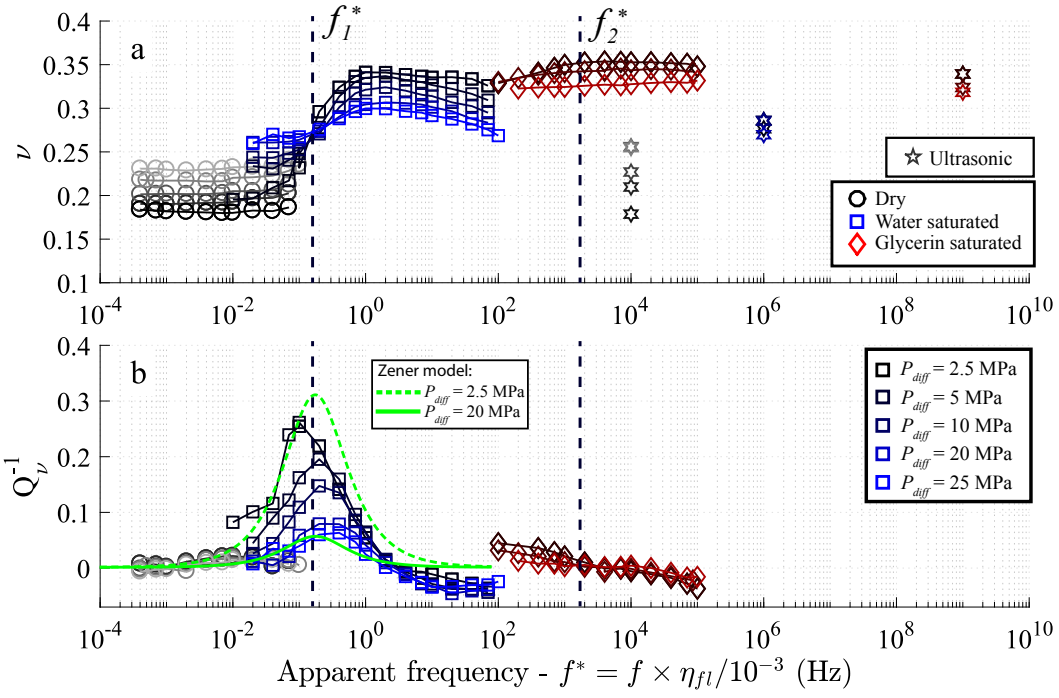

Figure 7.7: Results of Poisson's ratio dispersion (a) and attenuation (b) obtained from axial oscillations and ultrasonic measurements at different differential pressures on the Coquina sample.

For dry conditions, the ultrasonic results are consistent with the low-frequency measurements, and for glycerin-saturated conditions, the ultrasonic results seem consistent with the low-frequency undrained values (Figure 7.7a). In water-saturated conditions, across the drained/undrained transition, ν increases much higher than ν_{HF}. A slight decrease of ν is then visible between 1 Hz and 100 at every pressures (Figure 7.7), suggesting that ν tends to ν_{HF}. Similar phenomenon has been observed for the Poisson's ratio of a Fontainebleau sandstone (*Pimienta et al.*, 2016a), but with a much larger decrease than seen here. The phenomenon was correlated to the undrained/unrelaxed regime of the sandstone, and was equally visible for water- and glycerin-saturated conditions (*Pimienta et al.*, 2016a). In our case, the glycerin-saturated results do not see the effect above 10^2 Hz (Figure 7.7a), and are consistent with the ultrasonic results. The phenomenon might have been observed in glycerin-saturated conditions at much lower experimental frequencies ($0.001 - 0.01$ Hz).

The results of the shear modulus, obtained from the ultrasonic and the low-frequency axial oscillations, are presented in Figure 7.8. We observe a very similar behavior than the Young's modulus (Figure 7.6), except for the drained/undrained transition that exhibits no dispersion/attenuation (Figure 7.8) around f_1^*, consistently with Biot-Gassmann (*Gassmann*, 1951). Similarly to E a dispersive transition that could be related to squirt-flow is visible above 10^3 Hz (figure 7.8a), consistent with attenuation peaks around 0.25 as predicted by Zener's model (Figure 7.8b). The dry ultrasonic results are consistent with the low-frequency results, and the fluid-saturated ultrasonic results seem to be consistent with the high end of the dispersive transition visible with glycerin (Figure 7.8a). The effect of the differential pressure is analogue to E, with a constant pressure-dependence throughout the whole frequency range (Figure 7.8).

7.4.2 Bulk modulus deduced from hydrostatic and axial oscillations

The bulk modulus obtained from the low-frequency hydrostatic (K_{hyd}) and axial oscillations (K_{ax}) are presented Figure 7.9. Both K_{hyd} and K_{ax} consistently exhibit dispersion around the drained/undrained cut-off frequency f_1^* in water-saturated conditions (Figures 7.9a and 7.9d), with associated attenuation peaks (Figures 7.9b and 7.9e). The relative uncertainty on K_{hyd} and K_{ax} were found to be around $\Delta K_{hyd}/K_{hyd} = 3.2\%$ (Equation 4.1) and $\Delta K_{ax}/K_{ax} = 8.6\%$ (Equations 3.3 and 4.2).

K_{hyd} seems to be more pressure-sensitive than K_{ax}. For dry conditions, from $P_{diff} = 2.5$ MPa to $P_{diff} = 20$ MPa, K_{hyd} increases from an average value of 7 GPa to 28 GPa, and K_{ax} increases from an average value of 10 GPa to 19 GPa (Figures 7.9a and 7.9d). The undrained values of K_{hyd} and K_{ax}, above 1 Hz, seem consistent with each other. For each pressure, the amount of dispersion for K is slightly higher for the hydrostatic oscillations than for the axial oscillations (Figures 7.9a and 7.9d), and accordingly, the related attenuation peaks for K_{hyd} are slightly higher than for K_{ax} (Figures 7.9b and 7.9e), with a maximum value

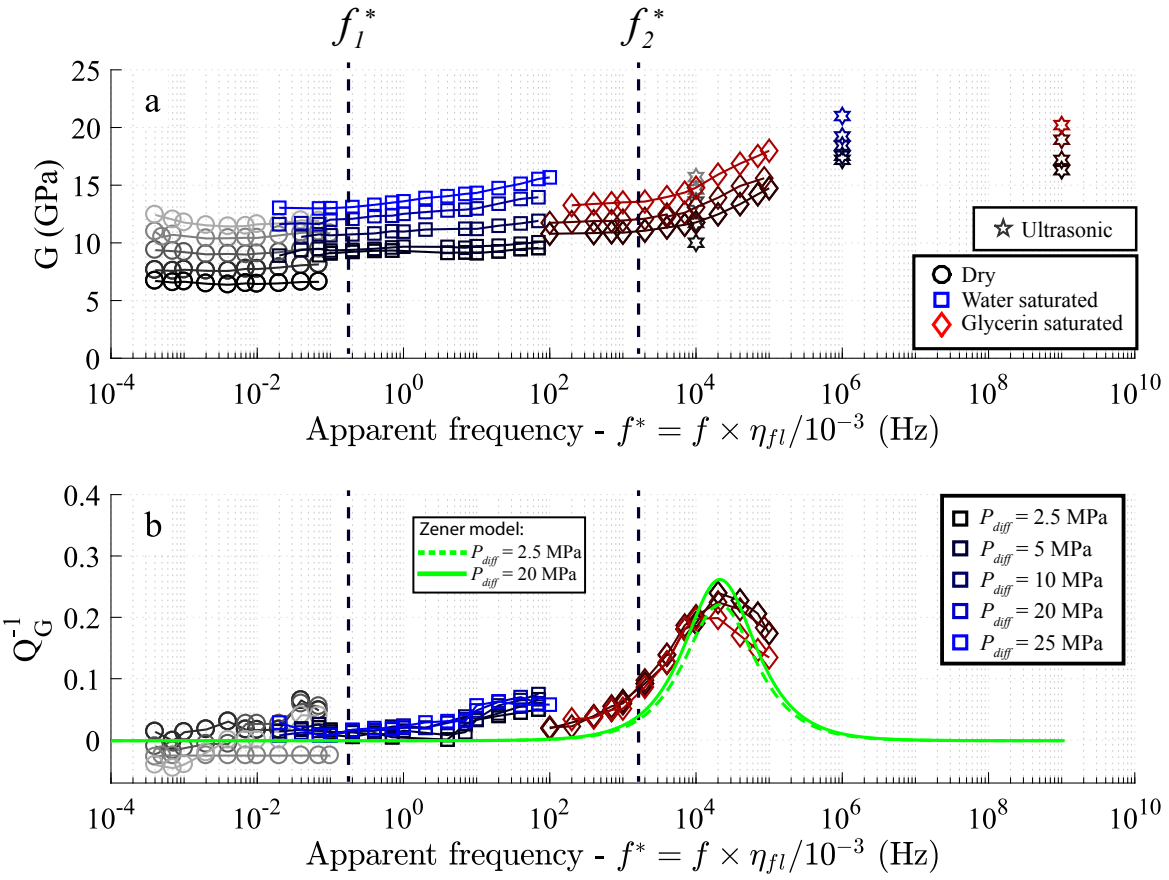

Figure 7.8: Results of the shear modulus dispersion (a) and attenuation (b) obtained from axial oscillations and ultrasonic measurements at different differential pressures on the Coquina sample.

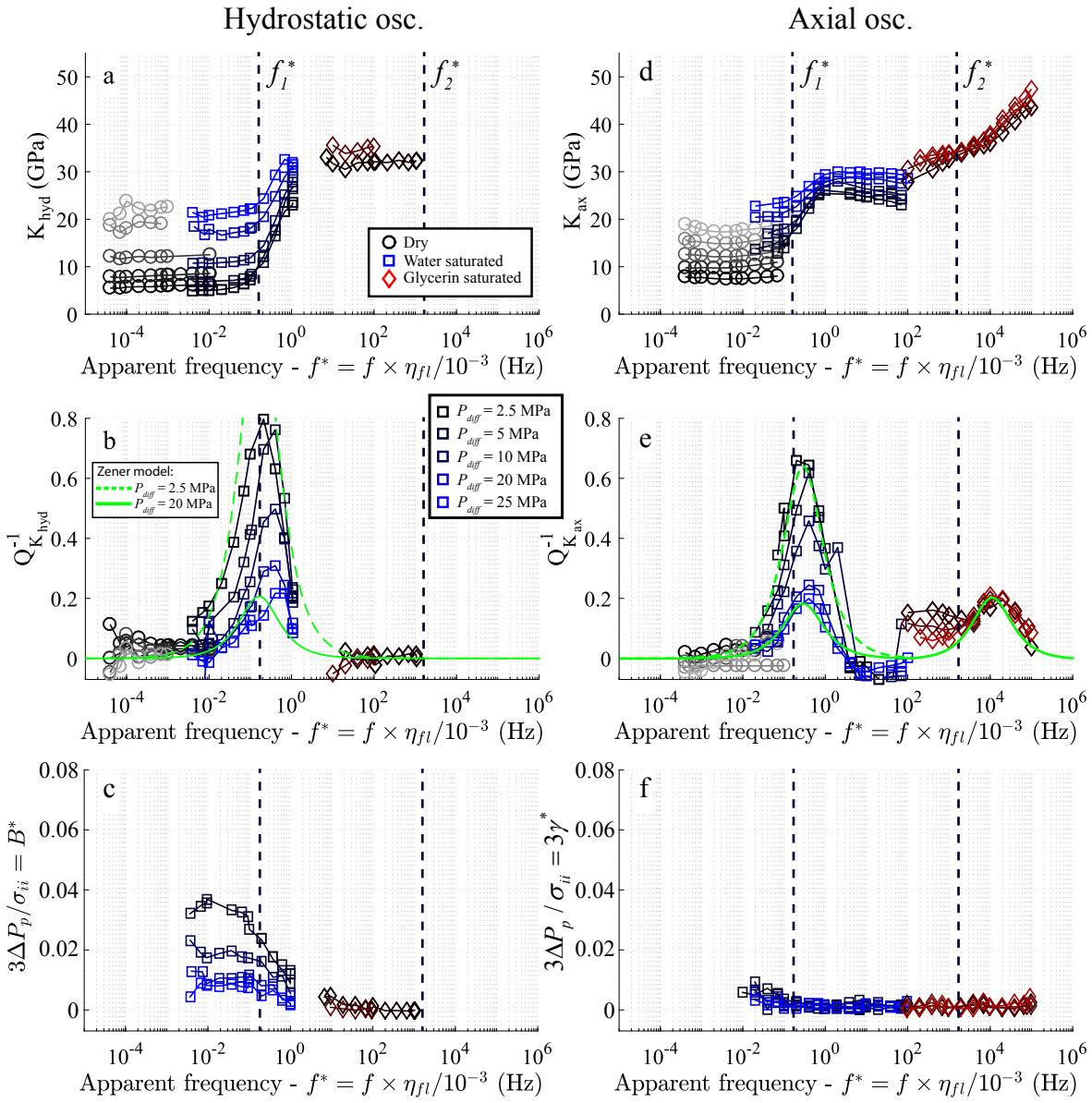

Figure 7.9: Results of the bulk modulus dispersion and attenuation obtained from hydrostatic (a-b) and axial oscillations (d-e) at different differential pressures on the Coquina sample. The pore pressure variation in the drainage circuit over the hydrostatic stress variation are respectively presented in (c) and (f).

of $Q^{-1}_{K_{hyd}} = 0.8$ and $Q^{-1}_{K_{ax}} = 0.65$ for $P_{diff} = 2.5\,\text{MPa}$, which are in agreement with Zener's model.

Similarly to E and G, a dispersive transition is observe above 10^3 visible under glycerin-saturated conditions that could be explained by squirt-flow. K_{ax} seems rather pressure-independent in glycerin-saturated conditions, and increases from around 30 GPa to 45 GPa between 10^2 Hz and 10^5 Hz. The corresponding attenuation peak has a maximum value of 0.2 at 10^4 Hz and seems also pressure-independent.

Despite being in experimental drained conditions (large dead volumes), similarly to the previous samples, the pore pressure sensor in the drainage circuit was able to detect a small fluid-pressure oscillation when applying the forced oscillations on the sample. The ratio $3\Delta P_p/\sigma_{ii}$ is reported Figure 7.9c for the hydrostatic oscillations ($3\Delta P_p/\sigma_{ii} = B^*$), and Figure 7.9f for the axial oscillations ($3\Delta P_p/\sigma_{ii} = 3\gamma^*$). For the Coquina sample, it would seem that a pore pressure oscillation in the drainage circuit was detected only during the hydrostatic oscillations experiment (Figure 7.9c), as $3\gamma^*$ was nearly nil for all the frequencies during the axial oscillations (Figure 7.9f). Nevertheless, for the hydrostatic oscillations, B^* decreases to 0 consistently with the drained/undrained transition.

7.5 Discussion

7.5.1 Drained and undrained regimes.

The results of the bulk modulus obtained from the static-loading, the ultrasonic measurements, and the low-frequency axial and hydrostatic oscillations are compared Figure 7.10. The static bulk modulus is lower than the dynamic bulk modulus, obtained either by the hydrostatic oscillations (Figure 7.10a) and the axial oscillations (Figure 7.10b), for differential pressures between 2.5 and 20 MPa. The axial and hydrostatic oscillations results compare well over the frequency range, as they detected the drained/undrained transition at exactly the same frequency, and the difference between K_{hyd} and K_{ax} is at most of 5 GPa (Figure 7.10). A slight difference regarding the sensitivity to differential pressure was noted: the hydrostatic results are more sensible than the axial results in the drained regime, visible under dry- and water-saturated conditions (Figure 7.10).

For K_{hyd} and K_{ax}, Biot-Gassmann equation was applied on the low-pressure ($P_{diff} = 2.5\,\text{MPa}$) and the high-pressure ($P_{diff} = 20\,\text{MPa}$) drained results in water-saturated conditions (Figure 7.10). The skeleton bulk modulus was taken equal to the calcite's bulk modulus ($K_S = 77\,\text{GPa}$). For the hydrostatic oscillations, Biot-Gassmann prediction is consistent with the experimental results, both for water- and glycerin-saturated conditions (Figure 6.9a). For the axial oscillations, Biot-Gassmann's prediction is consistent with the water-saturated undrained results, but slightly overestimated the glycerin-saturated undrained results (Figure 6.9b).

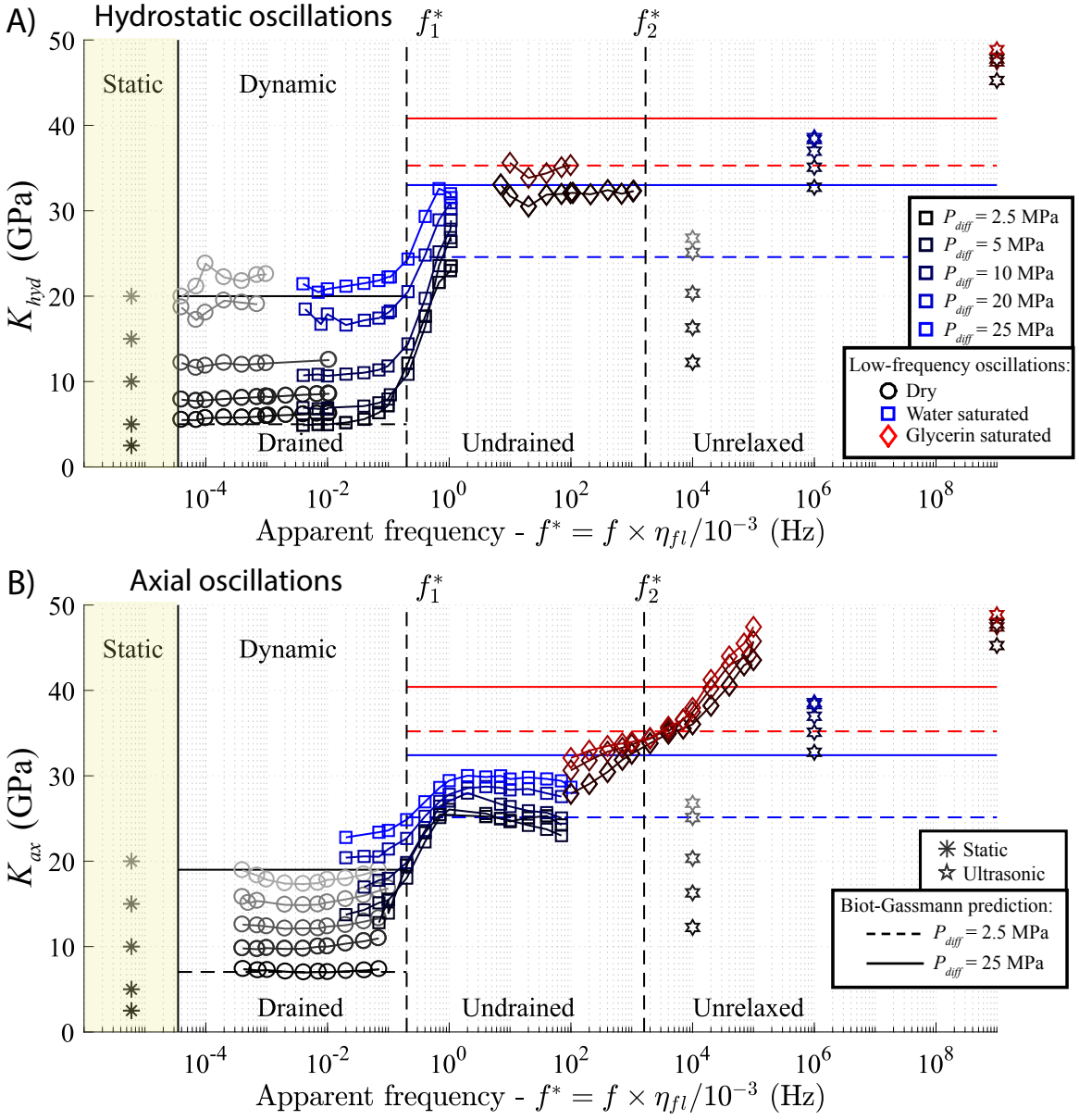

Figure 7.10: Static and frequency-dependent dynamic bulk modulus obtained from the hydrostatic (a) and axial oscillations (b) of the Coquina sample, for different differential pressures in fully-saturated conditions. The results combine the low-frequency results with the ultrasonic and static measurements. The drained and undrained regimes are clearly identified, and an undrained/unrelaxed transition that seems related to squirt-flow is visible under glycerin-saturated conditions.

7.5.2 Unrelaxed regime

The sample exhibits a clear second dispersion range visible from the axial oscillation results under glycerin-saturated conditions (Figure 7.10b). The bulk modulus, which doesn't vary so much with differential pressure, increases from the undrained value around 30 GPa to the ultrasonic values around 45 GPa (Figure 7.10b). We saw previously that attenuation was consistent with this dispersion, with a maximum peak around $Q_K^{-1} = 0.2$ (Figure 7.9e), and was not correlated to fluid drainage out of the sample (Figure 7.9f). The cut-off frequency of squirt-flow, deduced from the characteristic crack aspect ratio calculated from Morlier's method, was expected to be around 1600 Hz, which is within one order of magnitude of our observed transition. We can therefore interpret this observed transition as squirt-flow between compliant grain contacts and intergranular pores, as we would find for sandstones (*Pimienta et al.*, 2015a).

These observations also hold for the other elastic moduli, where the Young's modulus and the shear modulus exhibit a large dispersion and attenuation (Figures 7.6 and 7.8). The Poisson's ratio however did not vary much during this undrained/unrelaxed transition, with no attenuation visible, in agreement with the ultrasonic results (Figure 7.7).

7.5.3 Conclusion

The frequency dependence of all the dynamic elastic moduli at different effective pressures have been measured over a large frequency range ($[10^{-4}\,;\,10^{9}]$ Hz) on a coquina originating from a deep well in offshore Congo. The three fluid-flow regimes, drained, undrained and unrelaxed, were clearly identified for all the elastic moduli. The transition between the undrained and unrelaxed regime by squirt-flow affected mainly K, E and G but not ν. The drained/undrained transition, visible under water-saturated conditions, was consistent with Biot-Gassmann theory, and was consistent with the predicted cut-off frequency f_1^*. It mainly affected K and ν.

The pressure-dependence of the elastic moduli suggested the presence of microcracks with aspect ratios around 2.8×10^{-4}. The related squirt-flow was observed but at frequencies one order of magnitude greater than the cut-off frequency, for any moduli. One explanation could be the fact that not one crack aspect ratio is expected in reality, but a more widespread distribution, especially if they result from contacts between grains of different sizes. Moreover, these contact may not be perfectly planar, with rugosity or punctual contacts, which would therefore increase the squirt-flow frequency of the remaining open space around such contact. We can say that the detrital nature of the coquina, with non-porous grains and low cementation, explains the analogies with sandstones.

CHAPTER 8

SYNTHESIS OF THE EXPERIMENTAL RESULTS

8.1 Résumé

Nous synthétisons ici les résultats de dispersions et atténuations de tous nos échantillons, en termes d'ondes P et S. Lorsque nécessaire, une correction poroélastique est appliquée aux résultats en glycérine afin d'être comparés aux données en l'eau. De plus, pour chaque échantillon et chaque pression effective, le modèle viscoélastique de Zener est ajusté aux données de dispersions afin de comparer les atténuations obtenues. L'objectif principal du chapitre est de corréler les observations de dispersions/atténuations avec les microstructures des roches. Une discussion supplémentaire est apportée en lien avec la comparaison des modules statiques et dynamiques.

Les résultats sur le Lavoux nous indiquent que la microporosité intragranulaire ne génère pas nécessairement une dépendance en pression et un comportement mécanique similaire aux fissures. L'Indiana intact et le Rustrel nous indique que, bien que cimenté, un grainstone peut être sensible à la pression effective. Il est en revanche difficile de localiser les fissures (ou pores) qui sont à l'origine de cette dépendance en pression. Cela pourrait être les contacts entre grains ou le contact grain/ciment, voir même, pour le Rustrel, la porosité intercristalline dans le ciment. Dans tous les cas, la dispersion liée à l'écoulement crack-pore est relativement faible (maximum 400 m/s pour l'onde P), et se situe à des fréquences supérieures à 10^5 Hz.

Dans l'Indiana craqué thermiquement et le coquina, la dispersion liée à l'écoulement crack-pore s'est montrée beaucoup plus significative. Dans le premier cas, les cracks thermiques à l'origine de la dispersion autour de 100 Hz se sont essentiellement créés dans les gros cristaux du ciment. Dans le second cas, il semblerait que ce soit les contacts en grains qui généreraient l'écoulement type crack-pore, autour de 10^4 Hz. Ce comportement semble similaire à celui des grès. Dans les carbonates non-détritiques, la cimentation semble être

un paramètre clé, permettant la présence ou non de fissures susceptibles de générer des écoulements locaux.

8.2 Indroduction

In this chapter, we resume our observations of dispersion and attenuation of the elastic moduli of our carbonate samples, and discuss what is the effect on the P- and S-wave velocities and attenuation. Possible correlations of the dispersion with the observed microstructures will be discussed, followed by a discussion on the discrepancy between static and dynamic bulk moduli.

	ϕ (%)	κ (m^2)	D_{dry} (kg/m^3)
Lavoux	23.0	1×10^{-14}	2100
Indiana intact	11.4	2×10^{-17}	2348
Indiana th. cracked	11.4	3×10^{-17}	2348
Rustrel	14.9	4×10^{-17}	2345
Coquina	7.5	5×10^{-17}	2540

Table 8.1: Porosity, permeability and dry density of the carbonate samples

8.3 Dispersion/attenuation associated to microstructure

The dispersion and attenuation of the elastic moduli can be converted into velocity dispersion and attenuation, to see the implications of field measurements versus ultrasonic laboratory measurements. For isotropic medium, the velocity dispersions of the P- and S-waves are given by:

$$V_P(\omega) = \sqrt{\frac{K(\omega) + \frac{4}{3}G(\omega)}{D}} \quad \text{and} \quad V_S(\omega) = \sqrt{\frac{G(\omega)}{D}}, \tag{8.1}$$

where D is the density of the medium.

The attenuation of the P-wave and S-wave (respectively Q_P^{-1} and Q_S^{-1}) are defined by:

$$Q_P^{-1}(\omega) = \frac{\mathrm{Im}\left(\bar{K} + \frac{4}{3}\bar{G}\right)}{\mathrm{Re}\left(\bar{K} + \frac{4}{3}\bar{G}\right)} \quad \text{and} \quad Q_s^{-1}(\omega) = \frac{\mathrm{Im}\left(\bar{G}\right)}{\mathrm{Re}\left(\bar{G}\right)}, \tag{8.2}$$

where $\bar{K} = K(\omega) + iK_I(\omega)$ and $\bar{G} = G(\omega) + iG_I(\omega)$ represent the bulk and shear complex moduli. Since by definition $Q_K^{-1} = K_I(\omega)/K(\omega)$ and $Q_G^{-1} = G_I(\omega)/G(\omega)$, we can deduce from Equation 8.2:

$$Q_P^{-1}(\omega) = \frac{1}{1 + \frac{4}{3}\frac{G(\omega)}{K(\omega)}} Q_K^{-1}(\omega) + \frac{1}{1 + \frac{3}{4}\frac{K(\omega)}{G(\omega)}} Q_G^{-1}(\omega), \tag{8.3}$$

and

$$Q_S^{-1}(\omega) = Q_G^{-1}(\omega). \tag{8.4}$$

In order to have an idea of the velocity dispersion over a large frequency range (10^{-3} Hz to 10^{6} Hz), we can put side by side our experimental results from hydrostatic and axial forced-oscillations and ultrasonic results under water- and glycerin-saturated conditions. But in order to have a frequency profile for V_P or V_S that would apply for a single fluid saturation, we have to correct either the water-saturated moduli or the glycerin-saturated moduli to take into account the difference in fluid bulk modulus ($K_{wat} = 2.24$ GPa and $K_{gly} = 4.34$ GPa), and calculate the velocities with the common medium density $D = D_{dry} + \phi D_{fluid}$.

As a first approximation, we could apply a poroelastic correction to the either the water- or the glycerin-saturated bulk moduli results, to obtain their equivalent in the other fluid saturation, similarly to *Spencer and Shine* (2016). In theory, a poroelastic correction would be valid only for undrained moduli and cannot be applied for the drained or partially drained moduli. Since most samples (except Lavoux) exhibit the drained/undrained transition in water-saturated conditions, we choose to correct eventually the glycerin-saturated results. With the use of Biot-Gassmann equation, if K is the glycerin-saturated bulk modulus we want to correct into its equivalent water-saturated bulk modulus K_{corr}, one can obtain:

$$\frac{1}{\frac{1}{K_{corr}} - \frac{1}{K_m}} = \frac{1}{\frac{1}{K} - \frac{1}{K_m}} + \frac{1}{\phi\left(\frac{1}{K_{wat}} - \frac{1}{K_m}\right)} - \frac{1}{\phi\left(\frac{1}{K_{gly}} - \frac{1}{K_m}\right)}. \tag{8.5}$$

Moreover, we keep note that this poroelastic correction does not apply completely for unrelaxed moduli if squirt-flow occurs. In the unrelaxed regime, effective medium theory applies, representing saturated-isolated inclusions. Therefore, the hypothesis of isobaric REV are violated and poroelasticity cannot apply.

For the Lavoux sample, since the drained/undrained transition is visible under glycerin-saturated conditions, no corrections are needed as the drained modulus is common to all dry, water- and glycerin-saturations. We therefore keep the moduli as they are, and calculated the velocities with a glycerin-saturated density. Since the Indiana intact sample and the Rustrel sample glycerin-results do not exhibit squirt-flow and are solely undrained, the poroelastic correction can fully apply, and the final results will all be expressed in terms of water-saturated conditions.

Only the thermally cracked Indiana sample and the Coquina sample exhibit squirt-flow visible under glycerin-saturated conditions. The maximum error, due to the correction, would occur for a purely unrelaxed bulk modulus, i.e., at ultrasonic frequencies (K_{HF}). We can therefore apply the poroelastic correction on K_{HF-gly}, and compare it with the measured K_{HF-wat}. Our maximum error on the bulk modulus due to the correction can be taken as $dK = |K_{corr} - K_{HF-wat}|$. Since the poroelastic correction does not apply to the shear modulus $G = G_{HF-gly}$ at ultrasonic frequencies, the maximum error on the shear modulus can be taken as $dG = |G_{HF-gly} - G_{HF-wat}|$. If we neglect the uncertainty on D, the maximum relative uncertainty on the corrected-glycerin V_P at ultrasonic frequencies is

given by (Equation 8.1):

$$\frac{dV_P}{V_P} = \frac{1}{2}\frac{dK}{\left(K_{corr} + \frac{4}{3}G_{HF-gly}\right)} + \frac{2}{3}\frac{dG}{\left(K_{corr} + \frac{4}{3}G_{HF-gly}\right)}. \tag{8.6}$$

For the coquina, from Equations 8.5 and 8.6 and the ultrasonic results Table 7.1, we deduce $dV_P/V_P = 4.2\%$ at $P_{diff} = 2.5\,\text{GPa}$ and $dV_P/V_P = 4.6\%$ at $P_{diff} = 20\,\text{GPa}$. For the Indiana thermally cracked sample, the bulk modulus results under-glycerin saturation at $P_{diff} = 2.5\,MPa$ were abnormally lower than Biot-Gassmann's prediction and the undrained bulk modulus in water-saturated conditions (Figure 7.10b). For the sake of the illustration, we prefer to apply the correction solely on the results for $P_{diff} = 5\,\text{GPa}$ and $P_{diff} = 20\,\text{GPa}$, as the corrected results for $P_{diff} = 2.5\,GPa$ would be un-physical. For the thermally cracked Indiana, from Equations 8.5 and 8.6 and the ultrasonic results Table 5.2, the maximum relative uncertainties on V_P are $dV_P/V_P = 6.9\%$ at $P_{diff} = 5\,\text{GPa}$ and $dV_P/V_P = 8.6\%$ at $P_{diff} = 20\,\text{GPa}$. It might seem counter-intuitive the fact that the uncertainty increases with pressure, since the squirt-flow effect decreases. This in fact due to the poroelastic correction applied on K (Equation 8.5): the more K increases, the closer it gets to K_m, and therefore the lower the effect of the correction, which then increases dK.

We present Figure 8.1 the corrected (scaled to a single fluid) P- and S-wave dispersions and attenuations for the Lavoux (glycerin-saturated), the Indiana intact and the Indiana thermally cracked (water-saturated) at differential pressures of 5 MPa and 20 MPa, along with a schematic drawing of the characteristic elements of their microstructures. The same plots for the Rustrel and Coquina samples at differential pressures of 2.5 MPa and 20 MPa under water-saturated conditions are presented Figure 8.2. The poroelastic correction is only applied on the low-frequency forced oscillations results in glycerin-saturated conditions, except for the Lavoux. The corrected results, either from axial of hydrostatic oscillations are then merged with the water-saturated results. For Figures 8.1 and 8.2, no correction was applied on the attenuation results: the P- and S-attenuations were directly calculated on the uncorrected data with Equations 8.3 and 8.4. A Zener model (Figure 3.5) was fitted each for the drained/undrained and for the undrained/unrelaxed transition of V_P and V_S. The Zener models are fitted on the elastic moduli (see Equation 3.14) to be then converted into velocities by Equation 8.1. Since the attenuations are uncorrected, the attenuation deduced from Zener's model were calculated from fitting the uncorrected moduli before and after the dispersive transition. Only then, for illustration purposes, the Zener model for V_P corresponding to undrained and unrelaxed frequencies in glycerin-saturated condition was corrected by Equation 8.5, without correcting the attenuation.

The Lavoux limestone is an oolitic grainstone, with principally uniform intragranular microporosity in the oolites, and an equivalent volume of intergranular macropores (Figure 8.1a). A very low amount of calcitic cement was observed. The total porosity is 23%, with a relatively large permeability of 10^{-14}m^2. Only one dispersive transition was observed for

this type of microstructure, which corresponds to the drained/undrained transition (Figure 8.1b). The absence of any squirt-flow can be linked to the rather pressure-independent bulk modulus up to $P_{diff} = 20\,\text{MPa}$. This transition is an experimental artifact, as an increase of the sample's size would shift the observed drained/undrained transition to lower frequencies. We can see Figure 8.1a that the Zener model approaches well the P-wave attenuation. In the field, the characteristic length of diffusion would be theoretically the wavelength $\lambda = V/f$, instead of the sample's length in our experiments. Therefore, for seismic frequencies we are in no doubt in undrained condition. Since no squirt-flow is visible at higher frequencies, then we can deduce that this microstrucuture is non dispersive along the full frequency (Figure 8.1b). The ultrasonic laboratory measurements and the seismic field measurement would be equivalent. We concluded here that the micropores and the macropores had both very large aspect ratios, close to 1.

The Indiana limestone is a bioclastic grainstone, which also bears some microporosity within the grains, and very few macropores (Figure 8.1c). The distribution of micropores in the some grains such as oolites was uniform, while in the bioclasts it seemed to be more rimmed (Figure 8.1c). The intergranular pore space is nearly entirely filled with a homogeneous (large crystals) calcite cement (Figure 8.1c), in which we didn't visually see any cracks from the SEM images. The bulk modulus showed a small dependence to effective pressure, suggesting that a few amount of cracks or complaint pores are present. We suspect that the pressure-dependence provides mainly from the micriticized grains or the grain contacts, as the calcitic cement was found to be very homogeneous in the SEM analysis (Figure 5.9). The dispersion results of this sample exhibited the drained/undrained transition in agreement with the predictions, but nearly no squirt-flow (Figure 8.1d). Since we do not have the shear modulus measurements for the Indiana limestone, we used G_{HF-dry} for the drained shear modulus and G_{HF-wat} for the unrelaxed shear modulus. G is considered constant while crossing the drained/undrained transition, and a Zener model was used to estimate the dispersion between the undrained and the unrelaxed regime. Again, for the P-wave velocities, the Zener model seems in agreement with the drained/undrained transition. We suspect a little squirt-flow dispersion to occur at low pressure around $10^5\,\text{Hz}$ since the ultrasonic velocity is slightly higher than the undrained velocities (Figure 8.1d). But this would induced a maximum change in P-wave velocity of about $200\,\text{m/s}$ in water-saturated conditions. The shear wave shows no significant dispersion nor attenuation (Figure 8.1c). A good agreement between the glycerin-corrected results and the water-saturated results is observed, as the velocity profiles show a good continuity in frequency (Figure 8.1d).

After we thermally cracked the same Indiana sample at 500°C during 1 hour, we could observe on the SEM images the extensive amount of microcracks that developed in the homogeneous calcitic cement (Figure 8.1e). We did not observe much cracks developing in the microporous areas. We suspect that the crystal sizes, and therefore the texture, are the main reason for this. Microcracks can only develop in sufficiently large homogeneous

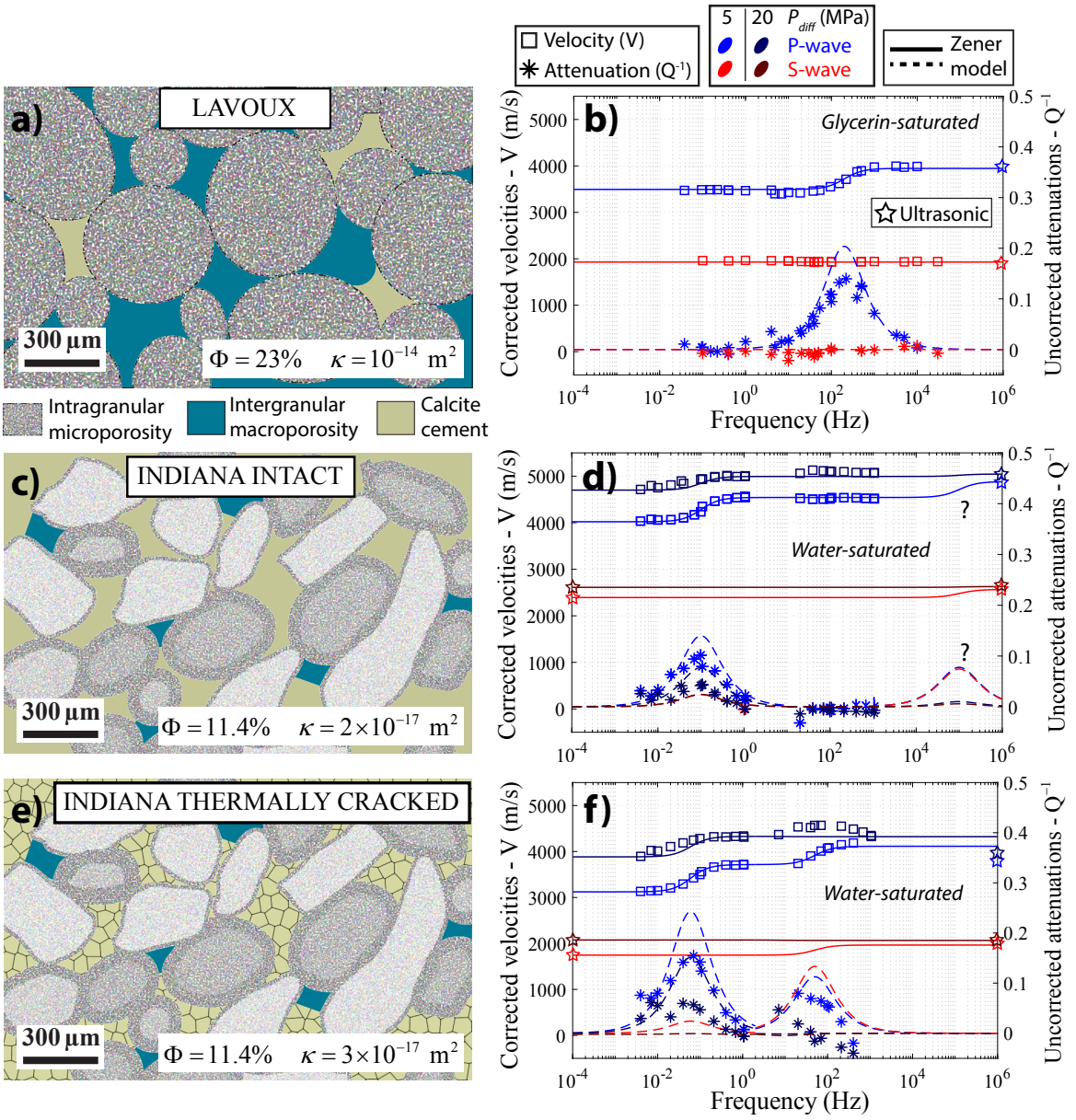

Figure 8.1: Microstructure and body wave dispersion/attenuation in the fluid-saturated Lavoux (a-b), and the Indiana limestone intact (c-d) and after thermal cracking (e-f). For overlapping frequencies between the axial and the hydrostatic oscillations, the bulk modulus from the latter is used.

grains. The microporous heterogeneous textures, like the intragranular microporosity, are not a favorable medium for cracks to propagate. Similarly to the intact sample, we decided to consider solely G_{HF-dry} for the drained and undrained shear modulus, and G_{HF-wat} as the unrelaxed shear modulus. For this microstructure, two dispersive transitions were clearly observed, the expected drained/undrained transition and the squirt-flow transition around 100 Hz (Figure 8.1f). For $P_{diff} = 5$ MPa, the P-wave dispersion in the field, between the frequency ranges of seismic acquisition and logs, would be around 500 m/s with an attenuation peak around $Q_P^{-1} = 0.1$. For the S-wave, the dispersion would be of 200 m/s with a similar attenuation peak of 0.1 (Figure 8.1f). However, above 20 MPa of effective pressure, no more squirt-flow is expected (Figure 8.1f). This transition seems consistent with Zener's model, but this latter overpredicts the attenuation peak for the drained / undrained transition (Figure 8.1f). Again, a good agreement between the glycerin-corrected results and the water-saturated results was observed, for $P_{diff} = 5$ MPa and $P_{diff} = 20$ MPa.

The Rustrel limestone is a grainstone that was cored in a rudist dominated facies surface outcrop. The observed grains or pelloides, are possibly fragments of larger rudist's shell and are extremely micriticized. The sample is essentially microporous, with the micropores located in the grains (Figure 8.2a). We do not observe any macropores, as the intergranular pore space is completely filled by calcitic cement. This latter is not completely crystallized and homogeneous like in the Indiana limestone. The SEM images revealed a substantial amount of intercrystalline porosity within the cement (Figure 8.2a), which could play the role of the pressure-dependent compliant porosity. The pressure-dependence could also originate from the micritic microporosity in the grains. The experimental results do not show much dispersion related to squirt-flow at high-frequency, despite a noticeable effect of the differential pressure on V_P and V_S (Figure 8.2b). After the drained/undrained transition, the amount of dispersion of V_P is of maximum 200 m/s for $P_{diff} = 2.5$ MPa, and is nil for $P_{diff} = 20$ MPa. The S-wave shows a dispersion less than 100 m/s. This low amount of squirt-flow dispersion is expected to occur between 10^4 Hz and 10^6 Hz. For both pressures, only the drained/undrained transition seems to exhibit large dispersion, in perfect agreement consistent with Zener's model (Figure 8.2b). A good consistency of the poroelastic correction was also observed (Figure 8.2b).

Finally, the Coquina sample is a grainstone originated from a deep well in offshore Congo, in the pre-salt sequence at least at 4 km depth. The homogeneous matrix is mainly constituted of what seems to be abraded fragments of shells, with grains less than 100 µm that are poorly sorted (Figure 8.2c). These grains are not micriticized at all, and do not bear much microporosity (Figure 8.2c). The porosity is mainly of intergranular or intercrystalline origin. No calcitic cement was found, and the grain contacts were found to be poorly cemented, making it a rather unconsolidated rock very compliant at low pressures (Figure 8.2c). The P-wave velocity at $P_{diff} = 2.5\,MPa$ was found to be less than 2800 m/s in the drained regime. This drained velocity rises to nearly 4000 m/s at $P_{diff} = 20$ MPa.

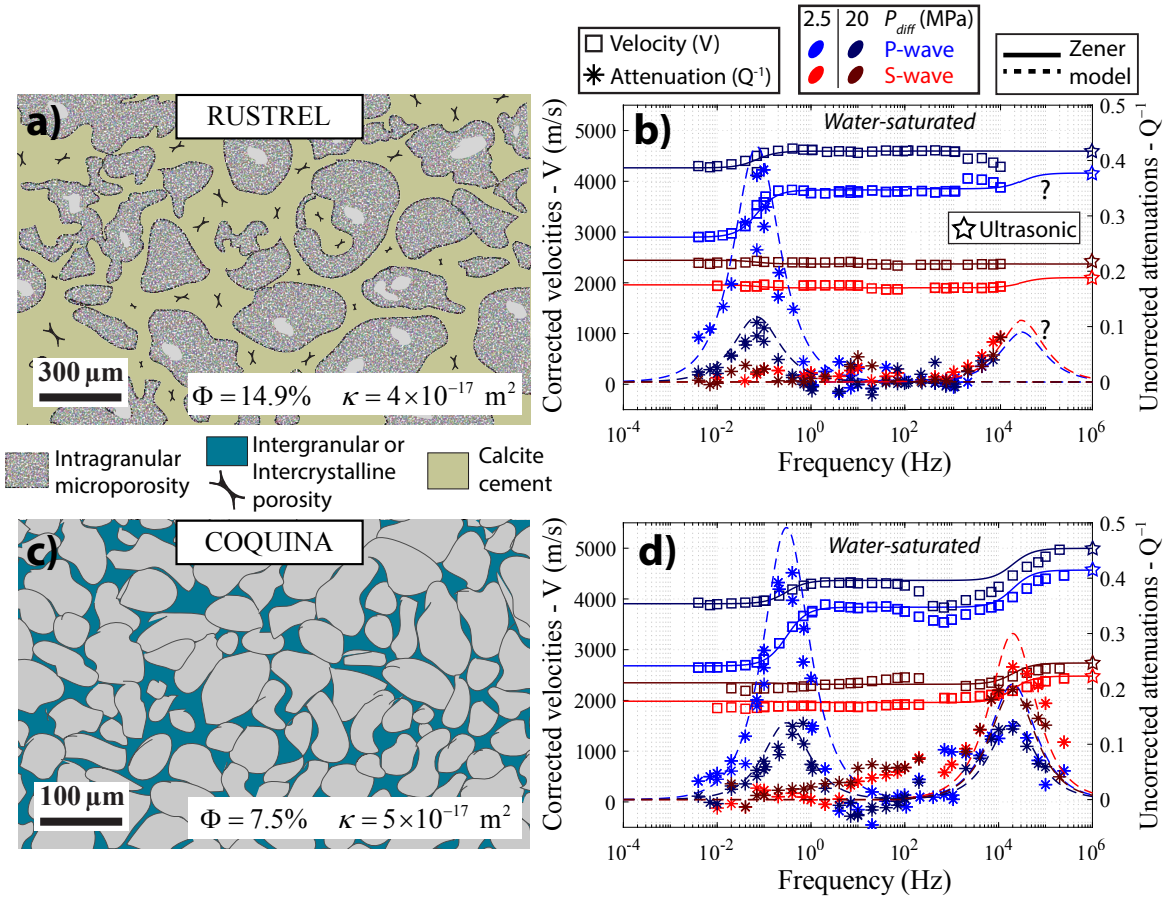

Figure 8.2: Microstructure and body wave dispersion/attenuation in the fluid-saturated Rustrel (a-b) and Coquina samples (c-d). For overlapping frequencies between the axial and the hydrostatic oscillations, the bulk modulus from the latter is used.

The compliant porosity seems to be the grain contacts, similarly to sandstones. After the drained/undrained transition, a substantial amount of dispersion related to squirt-flow was observed around 2×10^4 Hz (Figure 8.2d). At $P_{diff} = 2.5$ MPa, V_P increases by more than 600 m/s and V_S increases by 400 m/s (Figure 8.2d). The crack closure pressure was not reached during the experiments, but we can say it is expected to be greater than 40 MPa of differential pressure, as the pressure-dependence of the static bulk modulus, increases linearly with pressure up to 25 MPa (Figure 7.5). The poroelastic correction on the glycerin results seem to underestimate the water-saturated undrained results between 2×10^2 Hz and 3×10^3 Hz as we can see a little discontinuity (Figure 8.2d), which seems within our calculated relative uncertainty of 4.2% for $P_{diff} = 2.5$ MPa, but slightly greater than the relative uncertainty of 4.6% expected for $P_{diff} = 20$ MPa.

8.4 Static versus dynamic bulk modulus

We would like to investigate here if there is any correlation between the static/dynamic behavior of a rock, and the presence of dispersion/attenuation related to fluid flow. We presented Figure 8.3, the evolution with confining pressure of the static (K_{stat}) and dynamic (K_{dyn}) dry bulk modulus of all the samples, and the evolution of the ratio K_{stat}/K_{dyn} with pressure. K_{dyn} is the bulk modulus obtained from hydrostatic oscillations. We recall that the static bulk modulus is the tangent modulus of the static loading curve, calculated after a polynomial fit.

The first observation we can make, is that the ratio K_{stat}/K_{dyn} tends to 1 with increasing pressure for all our sample, which correlates well with the closure of cracks (Figure 8.3). This does not come as a surprise, since open cracks are known to induce non-linear effects during large deformations ($\varepsilon > 10^{-3}$) (*Simmons and Brace*, 1965; *King*, 1969; *Cheng and Johnston*, 1981; *Fjær*, 2009), that do not appear for the small deformations ($\varepsilon < 10^{-5}$) induced by the dynamic measurements. A linear function was fitted through the pressure dependence of K_{stat}/K_{dyn} for each sample (Figure 8.3). A rather similar trend was found between the thermally cracked Indiana, the Rustrel and the Coquina samples, with a common slope of 0.03 (Figures 8.3d, 8.3f and 8.3h) and initial ratios inferior to 0.5. The Lavoux and the intact Indiana exhibited lower slopes of respectively 0.02 and 0.01 with much higher initial ratio greater than 0.65.

Cheng and Johnston (1981) and *Fjær* (2009) both agreed that the strain amplitude is the key factor to explain the difference between the static and dynamic modulus. *Fjær* (2009) suggested that frictional sliding inside the cracks was a possible mechanism to explain this. This mechanism would be only activated if large strains occur, i.e., in the static measurements. *Fjær* (2009) even found that, in sandstones, the static and dynamic bulk moduli were always different except immediately after beginning the unloading cycle.

In our carbonate rocks, if we suppose that frictional sliding in cracks is the acting mech-

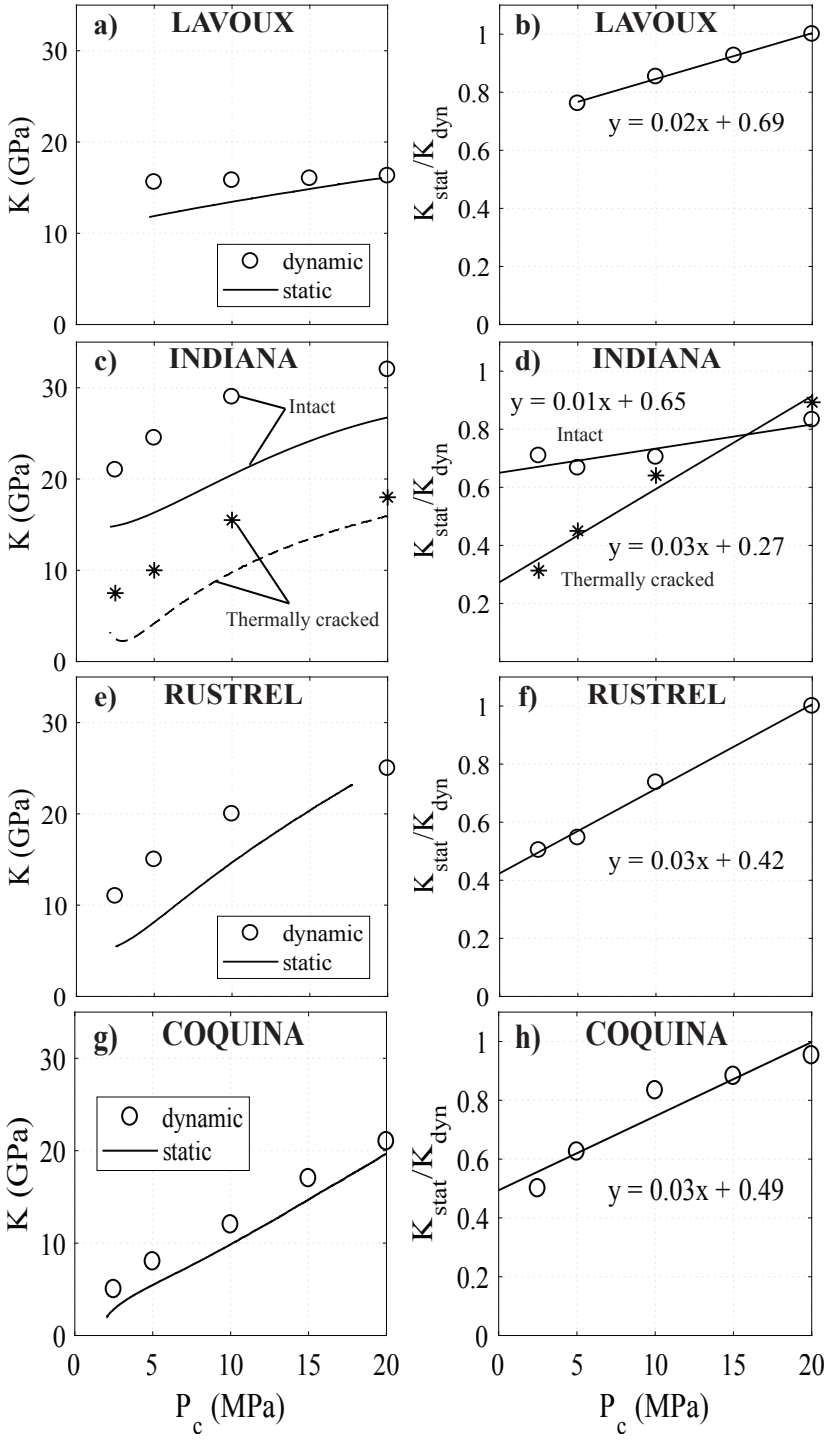

Figure 8.3: Comparison of the static and dynamic bulk moduli at different pressures for all the samples (left column). The ratio static over dynamic bulk modulus (K_{stat}/K_{dyn}) is calculated for each experimental point (right column).

anism, then the Lavoux and intact Indiana wouldn't exhibit much of it, contrary to the thermally cracked Indiana, the Rustrel and the Coquina. Interstingly, we observed cracks, or potential compliant pores, between large homogeneous crystals in the thermally cracked Indiana (cement), the Rustrel (intercrystalline porosity in the cement) and the Coquina (grain contacts), and did not observe any for the Lavoux and intact Indiana. We can only speculate that there could be a correlation between the cracks locations and the static versus dynamic behavior. Since the frictional sliding would be related to the crack's inner planes' texture or rugosity, we can only suppose that the cracks located in the heterogeneous microporous grains (Lavoux + intact Indiana) exhibited less frictional sliding than the cracks surrounded by larger homogeneous crystals (thermally cracked Indiana, Rustrel and Coquina). More experimental work would have to be done to assess this.

To the state of our understanding, a low K_{stat}/K_{dyn} is clearly correlated to the presence of cracks, but fails to discriminate potential squirt-flow from these cracks, since the Rustrel sample, which exhibited a low amount of squirt-flow dispersion, shared similar static vs dynamic trend than the cracked Indiana and the Coquina samples.

8.5 Conclusion

The investigation of the squirt-flow between compliant cracks and stiff pores is of major importance as it results in discrepancies between the elastic properties deduced from ultrasonic velocities and from seismic field measurements. The squirt-flow in Sandstones correlate well with the presence of microcracks and compliant grain boundaries and analysis of effective medium theories (*Pimienta et al.*, 2015a). However, wave induced fluid flows at microscale within the complexe pore spaces of carbonate rocks are much more difficult to predict.

For all the samples, the drained/undrained transitions in our carbonate samples were perfectly characterized and were in agreement with Biot-Gassmann predictions, either for the bulk modulus and the shear modulus measurements, and in agreement with the cut-off frequency $f_1 = 4\kappa K_d/\eta L^2$. We did not see substantial shear weakening due to fluid-saturation in our samples, except for the Rustrel sample. We recall that this transition is an experimental artifact that would dependent on the size of the sample. In laboratory measurements, characterizing this transition is essential to distinguish the drained/undrained regimes, from any potential unrelaxed regime. In our experimental setups, since the samples are relatively small (80 mm) and the boundary conditions are never perfectly undrained, it may occur that the drained/undrained transition (or partial drainage) occur at the same frequency than the squirt-flow dispersion, provided the sample has a high permeability with low aspect ratio cracks (e.g. *Pimienta et al.*, 2015a). Besides for the Lavoux limestone, the permeability range of the samples was sufficiently low (10^{-17} m2) so that the drained/undrained transition would be visible at low frequencies for the water-saturated

results, so that the glycerin-saturated measurements started in undrained conditions.

We attempted to correlate our dispersion observations with characteristic features of the rock's microstructure. The samples exhibiting pressure-dependent moduli did show squirt-flow (all except the Lavoux), but in different proportions. In general, the P-wave is the most affected by the wave-induced-fluid-flow dispersions. For all samples, effective pressures greater than 20 MPa would nearly cancel all squirt-flow dispersion. At low-pressure, the squirt-flow dispersion was much larger for the thermally cracked Indiana and the coquina, than for the intact Indiana and the Rustrel samples. This suggests that this phenomenon is more important for cracks in large homogeneous crystals or for grain contacts in detritic-type rocks such as the coquina. The compliant pores or cracks originating from the more heterogeneous micritized grains or at the grain boundaries with the cement will exhibit much less squirt-flow dispersion. The S-wave only exhibits dispersion for the squirt-flow transition. Only the coquina sample had a significant S-wave dispersion of maximum 400 m/s at an effective pressure of 2.5 MPa. The others samples showed very little S-wave dispersion with a maximum amount of 200 m/s. The presence of cracks, and therefore squirt-flow, correlates well with a low K_{stat}/K_{dyn}. With the closure of cracks with increasing pressure, K_{stat}/K_{dyn} tends consistently to 1. However, it is still difficult to find a clear correlation between the low-pressure value of K_{stat}/K_{dyn}, and the amount of squirt-flow, since the Rustrel (low amount of squirt-flow) and the coquina (large amount of squirt-flow) have nearly identical K_{stat}/K_{dyn} profile.

Part III

Modelling the frequency dependence of elastic properties over the drained / undrained / unrelaxed regimes.

CHAPTER 9

MODELLING THE DRAINED/UNDRAINED TRANSITION: EFFECT OF THE MEASURING METHOD AND THE BOUNDARY CONDITIONS.

Geophysical Prospecting, 2016.

Pimienta, L., J.V.M. Borgomano, J. Fortin and Y. Guéguen.

9.1 Résumé

La dépendance en fréquence des modules élastiques des roches saturées est liée aux écoulements de fluides à différentes échelles. Dans la gamme de fréquence $[10{-}3; 10^6]$ Hz, pour les roches saturées, deux phénomènes ont été mis en évidence expérimentalement : (i) la transition drainé / non-drainé (i.e. diffusion globale) ; et (ii) la transition non-drainé / non-relaxé (i.e. diffusion local). Lorsque l'on mesure ces phénomènes en laboratoire, ou lorsque l'on veut comparer différentes mesures sur une roche, les conditions aux limites et la méthode de mesure utilisée doivent être prises en compte. Un modèle poroélastique 1D est présenté, et vise à calculer la réponse poroélastique attendue lors d'une expérience d'oscillations. Ce modèle est utilisé pour tester différentes conditions aux limites ainsi que la méthode de mesure de déformation : locale avec des jauges, ou globale avec des LVDT. Quatre propriétés sont prédites et comparées aux données expérimentales, i.e., le module K, son atténuation, un coefficient de « pseudo-Skempton », et le déphasage de la pression de pore. Pour la transition drainé / non-drainé, puisque la pression de fluide n'est pas nécessairement homogène sur tout l'échantillon, les mesures locales et globales peuvent être différentes. De plus, on démontre que l'existence de volumes morts à chaque extrémité de l'échantillon peut fortement influencer les résultats. La relation entre la capacité

de stockage de l'échantillon et des volumes morts va déterminer l'amplitude et la dépendance en fréquence de mesures de dispersions et d'atténuations. Le modèle se compare bien avec des mesures effectuées sur des grès poreux et très compressibles. Des comparaisons supplémentaires ont été effectuées sur les calcaires.

9.2 Abstract

The dependence of fluid-saturated rocks' elastic properties to the measuring frequency is related to fluid flow phenomena at different scales. In the frequency range of $[10^{-3}, 10^{6}]$ Hz, for fully-saturated rocks, two phenomena have been experimentally documented: (i) the drained/undrained transition (i.e. global flow); and (ii) the relaxed/unrelaxed transition (i.e. local flow). When investigating experimentally those effects or comparing different measurements in rocks, one needs to account for both the boundary conditions involved and the method of measurement used. A 1D poroelastic model is presented that aims at calculating the expected poroelastic response during an experiment. The model is used to test different sets of boundary conditions as well as the role of the measuring set-up, i.e. local (strain gauges) or global (LVDT) strain measurement. Four properties are predicted and compared to the measurements, i.e. bulk modulus, bulk attenuation, pseudo-Skempton coefficient and pore pressure phase shift. For the drained/undrained transition, because fluid pressure may not be homogeneous in the sample, local and global measurements are predicted to differ. Furthermore, the existence of a dead volume at both sample's ends is shown to be important. Owing to the existence of the dead volume, an interplay between sample's and dead volumes' storage capacity determines both the magnitudes and the frequency dependence of the dispersion/attenuation measurements. The predicted behaviours are shown to be consistent with the measurements recently reported on very compressible and porous sandstone samples. Additional comparisons are done on the limestones.

9.3 Introduction

Dispersive elastic properties in porous fluid-saturated rocks originate from the presence and mechanical effect of fluid (e.g. *Biot*, 1956a; *O'Connell and Budiansky*, 1974). The characteristic frequency of those effects are related to fluid pressure equilibration during the passing of the seismic wave (e.g. *O'Connell and Budiansky*, 1974; *Cleary*, 1978). Two complementary methods have been proposed to investigate experimentally rocks' dispersive elastic properties, i.e. the resonant-bar and the stress-strain method. The resonant-bar method relies on fixing one side of a sample, applying a small displacement to the other side and observing the resonance modes of the rock sample (e.g. *Winkler and Nur*, 1979; *Bourbie and Zinszner*, 1985). Depending on the sample's length and diameter, the frequency range investigated is of about 10 kHz. However, the method often implies for the sample to be unbounded so that investigating the confining pressure effect is challenging. The stress-strain, or sub-resonance, method is promising as it allows for measurements over wide frequency ($f \in [10^{-2}; 10^{3}]$ Hz) and pressure ranges (e.g. *Subramaniyan et al.*, 2014). Depending on the apparatuses' specificity, different elastic properties can be precisely investigated

such as the bulk modulus (e.g. Adelinet et al., 2010; David et al., 2013; Pimienta, Fortin and Gueguen, 2015a), the shear modulus (e.g. *Jackson and Paterson*, 1987), Young's modulus (e.g. Batzle, Han and Hofmann, 2006; Adam et al., 2009; Takei, Fujisawa and McCarthy, 2011; Tisato and Madonna, 2012; Madonna & Tisato, 2013; Mikhaltsevitch, Lebedev and Gurevitch, 2014; Pimienta, Fortin and Gueguen, 2015b) or Poisson's ratio (Pimienta, Fortin and Gueguen, 2016).

When measuring these dispersive properties experimentally, one however needs to properly account for the specific boundary conditions brought by the measuring apparatus and method. For the resonant-bar method or stress-strain experiments under ambient pressure (e.g. *Paffenholz and Burkhardt*, 1989; *Lienert and Manghnani*, 1990; *Takei et al.*, 2011), the sample is unbounded so that fluid is allowed to flow laterally. For such experiments, *Dunn* (1987) has shown that the lateral boundary condition could affect the dispersive properties by creating a lateral fluid flow out of unjacketed samples, the so-called Biot-Gardner effect. On the contrary, the stress-strain method under confining pressure implies a lateral bounding of the sample by using either epoxy sealing (e.g. *Batzle et al.*, 2006b; *Adam et al.*, 2006, 2009), copper (e.g. *Tisato and Madonna*, 2012; *Madonna and Tisato*, 2013) or rubber (e.g. *Adelinet et al.*, 2010; *David et al.*, 2013; *Fortin et al.*, 2014; *Mikhaltsevitch et al.*, 2014; *Pimienta et al.*, 2015a,b, 2016a) jacketing. Most of the existing apparatuses have been designed to measure properties on assumed undrained samples, by not allowing for axial fluid flow through the end-platens (e.g. *Tisato and Madonna*, 2012; *Madonna and Tisato*, 2013; *Mikhaltsevitch et al.*, 2014). However, because the saturating procedure might not be optimum with such set-ups, and because the drained/undrained transition is of interest, a different set-up/methodology has been used at ENS (e.g. *Pimienta et al.*, 2015a). The drained conditions have been approached by creating large dead volumes in the drainage system, at the sample's ends, allowing to precisely measure both cause (fluid flow) and consequence (dispersion/attenuation) of the drained/undrained transition (e.g. *Pimienta et al.*, 2014a).

To check experimental data against predictions for this drained/undrained transition, a 1D poroelastic model has been derived from solving the pore pressure diffusion equation with different sets of boundary conditions. The technique used for the measurement (i.e. local or global) has also been taken into account. The predictions have been compared to measurements on two porous and compliant sandstone samples.

9.4 General 1D poroelastic model

Within the framework of linear isotropic poroelastic theory for an homogeneous medium, using the poroelastic relations, the mechanical equilibrium equation and the mass balance equation, one gets the partial derivative equation satisfied by the pore fluid pressure (p_f)

(e.g. *Rice and Cleary*, 1976; *Zimmerman*, 2000; *Guéguen and Boutéca*, 2004):

$$\frac{\partial p_f}{\partial t} - \frac{\kappa B K_d}{\eta \alpha (1 - \alpha B)} \nabla^2 p_f = \frac{B K_d}{1 - \alpha B} \frac{\partial \epsilon_v}{\partial t}. \tag{9.1}$$

Where κ, K_d, B and α are respectively the rock's permeability, drained bulk modulus, Skempton coefficient and Biot coefficient. η is the fluid's intrinsic viscosity, and ϵ_v is the volumetric strain.

Noting that the volumetric strain is $\epsilon_v = K_d^{-1}(P - \alpha p_f)$, Equation (9.1) is a diffusion equation with a source term that depends on the condition of stress solicitation P. Two cases of stress solicitation could be considered. The confining pressure oscillations (e.g. *Adelinet et al.*, 2010) can be considered as an *"isotropic solicitation"*, i.e. a stress solicitation equal in all directions. The uniaxial stress oscillation (e.g. *Batzle et al.*, 2006b) can be considered as a *"deviatoric solicitation"*. Although we focus in the following on the *"isotropic solicitation"* case, the case of a *"deviatoric solicitation"* can be shown to give very similar results.

9.4.1 Model derivation : Isotropic solicitation

An oscillating confining pressure is applied so that $P(t)$ is a source term that is time-dependent. Equation (9.1) is solved in 1 dimension (1D model) by assuming p_f to vary as a function of z only. Finally, the equation rewrites (*Zimmerman*, 2000):

$$\frac{\partial p_f}{\partial t} - \frac{\kappa B K_d}{\eta \alpha} \frac{\partial^2 p_f}{\partial z^2} = B \frac{\partial P}{\partial t}. \tag{9.2}$$

Noting that the rock's storage coefficient is $S_s = \alpha / (B K_d)$ (*Kümpel*, 1991), the equation rewrites:

$$\frac{\partial p_f}{\partial t} - \frac{\kappa}{\eta S_s} \frac{\partial^2 p_f}{\partial z^2} = B \frac{\partial P}{\partial t}, \tag{9.3}$$

which is similar to the heat equation with a heat source.

In case of no source term (i.e. $P = const$), this equation is that used in the *"oscillating pulse"* method (e.g. *Brace et al.*, 1968; *Lin*, 1977; *Hsieh et al.*, 1981; *Song and Renner*, 2006, 2007). If $P(t)$ is variable, the source term exists. Here, the applied confining pressure $P(t)$ is supposed to be small variations around a nil value of a sinusoidal form such that $P(t) = \Delta P_0 \, e^{i\omega t}$. Accounting for this time dependence, assuming a steady-state solution, and using the method of variables separation with $p_f(z,t) = f(z) e^{i\omega t}$, the partial derivative equation simplifies to:

$$f(z) + i \left(\frac{D}{\omega} \right) \frac{d^2}{dz^2} \left[f(z) \right] = B \Delta P_0, \tag{9.4}$$

with $D = \kappa / (S_s \eta)$ being the fluid hydraulic diffusivity in the sample. The equation being simplified to a typical differential equation of second order, steady-state solutions can be

found analytically. These are of the form:

$$p_f(z,t) = \left[B\Delta P_0 + p_0^{\pm} e^{\pm(1+i)\sqrt{\frac{\omega}{2D}}z}\right] e^{i\omega t}, \tag{9.5}$$

with p_0^+ and p_0^- two constants that are obtained from the chosen problem's boundary conditions. Knowing $p_f(z,t)$ (Eq. 9.5), the volumetric strain is obtained such that $\epsilon_v(z,t) = K_d^{-1}(P(t) - \alpha p_f(z,t))$.

9.4.2 Solution for undrained and drained boundary conditions

9.4.2.1 Theoretical derivation

In the undrained condition, fluid is not allowed to flow out of the sample so that:

$$\left(\frac{\partial p_f}{\partial z}\right)_{z=L} = \left(\frac{\partial p_f}{\partial z}\right)_{z=0} = 0. \tag{9.6}$$

The undrained boundary condition leads to a solution of $p_f(t) = B\,P(t)$, i.e. an immediate, position- and frequency-independent response of the pore fluid to the oscillating pressure. Under drained boundary conditions, pore pressure is maintained to the sample upper (i.e. $z = L$) and lower (i.e. $z = 0$) ends so that no overpressure can occur, and:

$$p_f(0,t) = p_f(L,t) = 0. \tag{9.7}$$

In the drained boundary condition, the sample's behaviour depends on the frequency of the applied stress oscillation.

Owing to the simple drained boundary condition, of nil pore overpressure at both ends, an analytical solution can be found such that:

$$p_f(z,t) = B\Delta P_0 e^{i\omega t}\left[1 - \frac{sinh(a(L-z)) + sinh(az)}{sinh(aL)}\right], \tag{9.8}$$

with the parameter $a = (1+i)\sqrt{\omega/2D}$. As shown from this solution, any value of $p_f(z,t)$ corresponds to the *"local"* fluid overpressure created by the stress oscillation $P(t)$. Finally, a *"local"* volumetric strain can be calculated such that:

$$\epsilon_v(z,t) = \frac{B\Delta P_0}{K_d} e^{i\omega t}\left[(\frac{1}{B} - \alpha) + \alpha\frac{sinh(a(L-z)) + sinh(az)}{sinh(aL)}\right]. \tag{9.9}$$

Parameter a depends on ω so that, at a given z, both p_f and ϵ_v depend on ω. Moreover, because a is a complex number, p_f and ϵ_v are complex-valued functions. In the following these are characterized by their amplitude and phase.

Table 9.1: Parameters values used for the model predictions. The rock parameters and dead volume values are those reported from *Pimienta et al.* (2015a).

Parameter	Estimated value
Sample length	$L = 80\,\text{mm}$
Sample diameter	$d = 40\,\text{mm}$
Sample's porosity	$\phi = 7\,\%$
Sample's drained bulk modulus	$K_d = 14\,\text{GPa}$
Sample's permeability	$\kappa = 4\,10^{-15}\,\text{m}^2$
Confining oscillation amplitude	$\Delta P = 0.2\,\text{MPa}$
Lower Dead volume (1)	$V_1 = 3.4\,\text{mL}$
Upper Dead volume (2)	$V_2 = 3.2\,\text{mL}$
Glycerine bulk modulus	$K_{gly} = 4.36\,\text{GPa}$
Glycerine viscosity	$\eta_{gly} = 1.087\,\text{Pa.s}$
Lower (1) storage capacity	$S_1 = 7.80\,10^{-4}\,\text{L.GPa}^{-1}$
Upper (2) storage capacity	$S_2 = 7.34\,10^{-4}\,\text{L.GPa}^{-1}$
Sample's storage capacity	$S_s = 5.86\,10^{-2}\,\text{GPa}^{-1}$
Sample's hydraulic diffusivity	$D_{gly} = 6.28\,10^{-5}\,\text{m}^2.\text{s}^{-1}$
Water bulk modulus	$K_{wat} = 2.25\,\text{GPa}$
Water viscosity	$\eta_{wat} = 0.89\,10^{-3}\,\text{Pa.s}$
Lower (1) storage capacity	$S_1 = 1.51\,10^{-3}\,\text{L.GPa}^{-1}$
Upper (2) storage capacity	$S_2 = 1.42\,10^{-3}\,\text{L.GPa}^{-1}$
Sample's storage capacity	$S_s = 7.36\,10^{-2}\,\text{GPa}^{-1}$
Sample's hydraulic diffusivity	$D_{wat} = 6.10\,10^{-2}\,\text{m}^2.\text{s}^{-1}$

9.4.2.2 Discussion of the analytical 1D solution

Values of the different physical parameters: The different parameters used (Table 9.1) are chosen to be the ones measured experimentally (e.g. *Pimienta et al.*, 2015a). The rock's drained bulk modulus varies with confining pressure. Its value is $K_d \sim 14\,\text{GPa}$ at lowest confining pressure (i.e. $P_{eff} = 1\,\text{MPa}$). The sample's Skempton (B) and Biot-Willis (α) coefficients and storage capacity (S_s) are calculated, assuming the skeleton bulk modulus to be the one of quartz (i.e. $K_{qtz} = 37\,\text{GPa}$), from usual relations of poroelastic theory (*Detournay and Cheng*, 1993). Finally, the hydraulic diffusivity (D) is directly deduced from the measured sample's permeability (i.e. $\kappa = 4\,10^{-15}\,\text{m}^2$) and storage capacity (i.e. S_s), and the fluid's viscosity (η).

The behaviours of the fluid saturated rock depend on two fluid's intrinsic properties. Viscosity affects the hydraulic diffusivity, thus modifying parameter a and introducing a frequency dependence of p_f (Eq. 9.5) and ϵ_v (Eq. 9.9). On the other hand, the fluid's compressibility affects the saturated sample's compressibility, the storage capacity and the Skempton coefficient B, thus affecting the magnitude of the frequency effect (Eqs. 9.8 & 9.9).

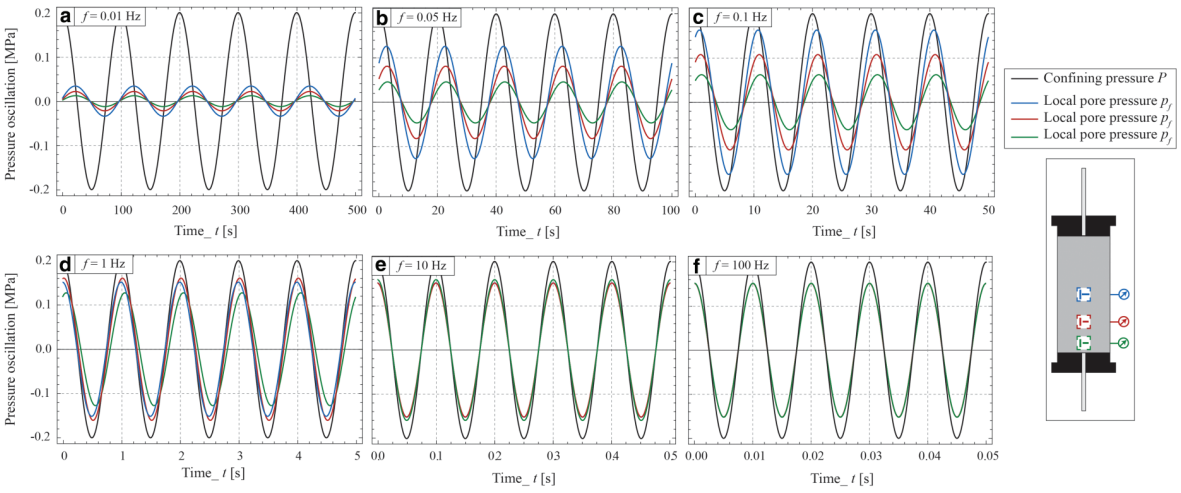

Figure 9.1: Time dependence of the applied confining pressure oscillations and predicted pore pressure response for different frequencies in the range of $f \in [10^{-2}; 10^{2}]$ Hz. The parameters values are the ones from Table 9.1 in case of glycerine saturation.

Time dependence : Using the same parameters values as above, the time-dependence of p_f for a given oscillating $P(t)$ is reported (Fig. 9.1). The local p_f is predicted for different frequencies ($f \in [10^{-2}; 10^{2}]$ Hz) and for three sensors' positions using the constants from Table 9.1 in case of glycerine saturation.

The amplitudes of the induced p_f oscillations increase with increasing frequency, up to $f \sim 10$ Hz (Fig. 9.1e) where they become independent of frequency. Beyond this frequency, the maximum amplitude of p_f is 0.15 MPa, which consistently relates to case of $B = p_f/P_c = 0.75$. The pore pressure response is initially shifted in time (i.e. phase shift) with respect to $P(t)$, by about $\pi/2$ at lowest frequency of $f = 10^{-2}$ Hz (Fig. 9.1a). The phase shift decreases, down to zero beyond $f \sim 10$ Hz (Fig. 9.1e).

The frequency-dependent variation occurs over a very large frequency band, of about $f \in [10^{-2}; 10^{1}]$ Hz. Owing to the boundary conditions, a large dependence to the position of the strain (or pore pressure) sensor is observed. This point is further investigated below.

Spatial dependence The position (z) dependence of both amplitude and phase of the *"local"* pore pressure (i.e. p_f) and strain (i.e. ϵ_v) is reported in Fig. 9.2. The properties are calculated for different frequencies of the applied P in the range of $f \in [10^{-2}; 10^{2}]$ Hz. Consistently, p_f amplitudes are low and ϵ_v are high (i.e., low bulk modulus), at lowest f. For the fluid pressure p_f, amplitude and phase show a similar monotonous behaviour. As frequency increases, the amplitude (Fig. 9.2a) increases and the phase (Fig. 9.2b) decreases. The volumetric strain ϵ_v amplitude is also monotonous (Fig. 9.2c), but the phase is not (Fig. 9.2d). At low frequency, the amplitude decrease and phase increase as frequency increases. However, there exists a critical frequency (i.e. $f \sim 0.1$ Hz) beyond which the strain phase decreases when frequency keeps increasing.

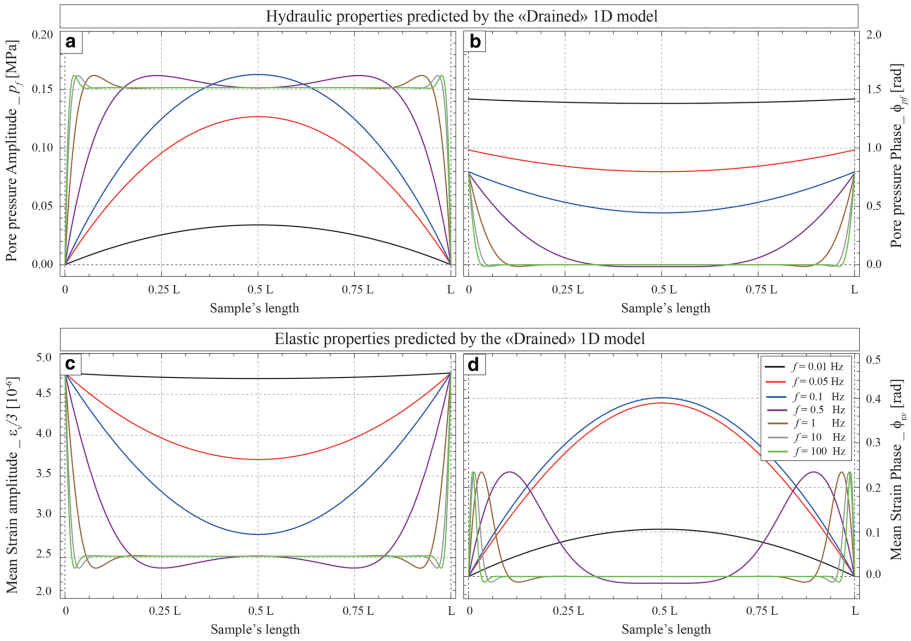

Figure 9.2: Position dependence of the predicted (a-b) pore pressure and (c-d) mean strain (i.e. $\epsilon_v/3$) response to the applied confining pressure oscillations for different frequencies in the range of $f \in [10^{-2}; 10^{2}]$ Hz. Both signals' amplitudes and phases are investigated. The properties for the prediction are the ones from Table 9.1 in case of glycerine saturation.

At low f, the largest amplitude is observed at the sample's center. As frequency increases, almost all of the sample shows the same response. Because of the symmetry chosen for the boundary conditions, the variations are symmetric with respect to the sample's center. Note that, for each position, it exists a frequency at which the signal (e.g. p_f or ϵ_v) exceeds the maximum value obtained at highest frequency. This observation was also reported by *Dunn* (1987) and *Wang* (2000).

***"Local"* versus *"Global"* predictions** As in *Pimienta et al.* (2015a), a local pseudo-Skempton coefficient B^* is defined. Similarly, a local pseudo-bulk modulus K^* may be directly deduced from the complex volumetric strain:

$$B^*(z,\omega) = \frac{p_f(z,\omega)}{P(\omega)}, \quad \& \quad K^*(z,\omega) = -\frac{P(\omega)}{\epsilon_v(z,\omega)}. \tag{9.10}$$

The parameters depend on the intrinsic properties (i.e. B and K) of a given rock sample for the specific conditions of the experiment. But, because both parameters bear a dynamic information, those are addressed as *"pseudo"*-properties. The locally calculated K^* and B^* can be averaged over the sample's length L to get global (or volume-averaged) properties

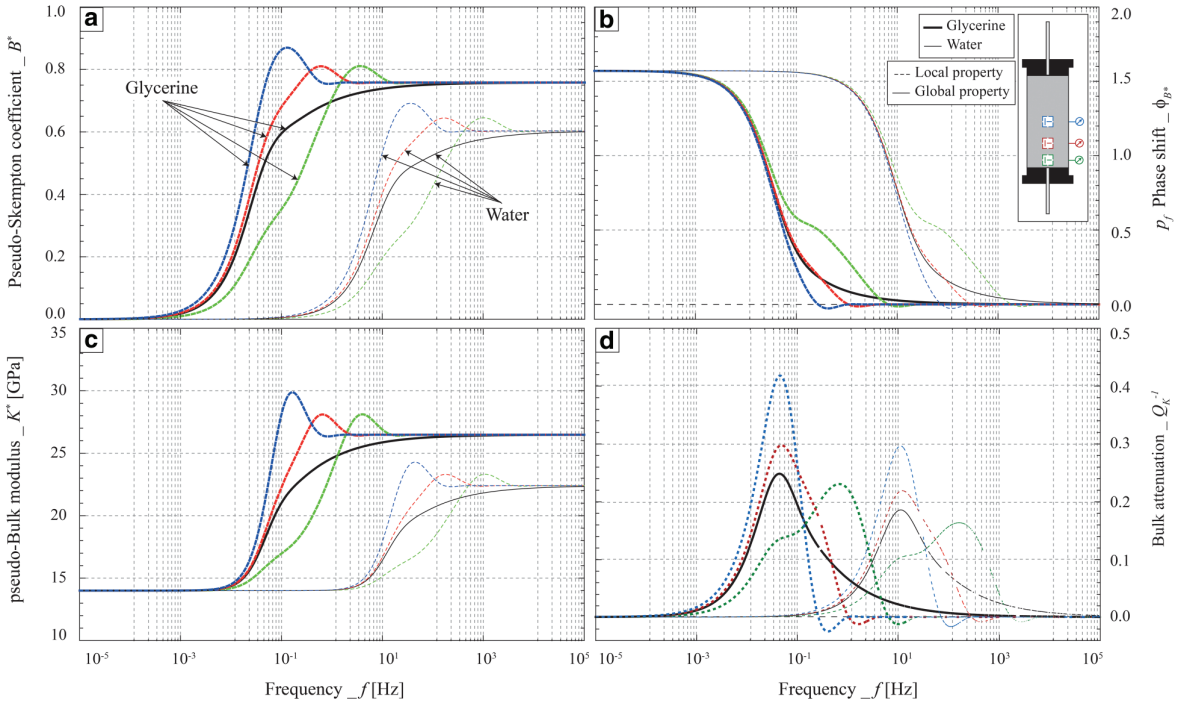

Figure 9.3: Predicted drained to undrained transition of the frequency-dependent (a-b) hydraulic and (c-d) elastic properties of a representative sandstone sample saturated by water (i.e. thin curves) or glycerine (i.e. thick curves). Both *"local"* (i.e. dashed colour curves) and *"global"* (i.e. continuous black curves) predictions are compared. The two cases of water and glycerine saturating conditions are tested.

of the rock (i.e. K_g and B_g) such that:

$$B_g(\omega) = \frac{\frac{1}{L}\int_0^L p_f(z,\omega)\,dz}{P(\omega)}, \quad \& \quad K_g(\omega) = -\frac{P(\omega)}{\frac{1}{L}\int_0^L \epsilon_v(z,\omega)\,dz}. \tag{9.11}$$

Both B_g and K_g also bear a dynamic information and are *"pseudo"*-properties.

Again, the *"local"* and *"global"* predictions can be characterised by their amplitudes (e.g. $\|B^*\|$ and $\|K^*\|$) and phases (e.g. ϕ_{B^*} and ϕ_{K^*}). The amplitudes are related to the material constants, i.e. K_d and B. The phase ϕ_{B^*} describes the shift in fluid pressure as compared to the applied confining pressure, and depends on the sample hydraulic diffusivity. The phase ϕ_{K^*} is the phase shift between the applied confining pressure and volumetric strain, and $Tan(\phi_{K^*})$ is the bulk modulus attenuation (i.e. Q_K^{-1}).

Both *"local"* and *"global"* hydraulic (Figs. 9.3a & 9.3b) and solid (Figs. 9.3c & 9.3d) responses to the applied confining pressure oscillation are predicted as a function of frequency using the parameters from Table 9.1. Three positions have been chosen along the sample's length at $z = [L/2; L/4; L/10]$. Overall, (i) $\|B^*\|$ (Fig. 9.3a) and $\|K^*\|$ (Fig. 9.3c) show a consistent increase from drained to undrained domain; (ii) the phase shift ϕ_{B^*} shows

large decrease with frequency, from $\pi/2$ down to zero; and (iii) a large Q_K^{-1} peak is observed. For all properties, owing to the water intrinsic viscosity, the transition is shifted to higher frequency in comparison to the glycerine saturation.

Consistently, the *"local"* predictions show no frequency dependence at either very high (i.e., $f > 10^2$ Hz for glycerine) or very low (i.e., $f < 10^{-3}$ Hz) frequencies, i.e. corresponding to the undrained and drained regimes respectively. In the characteristic frequency domain of the drained/undrained transition, a clear dependence to the position is predicted for all properties.

9.4.3 *"Experimentally undrained"* boundary condition

The two typical boundary conditions most often considered are the *"drained"* (Fig. 9.4a) and *"undrained"* (Fig. 9.4b) conditions (e.g. *Dunn*, 1986, 1987). They correspond to the extremal cases of fluid either fully blocked or fully unblocked in the sample. A third boundary condition should be addressed, which combines the purely *"drained"* and *"undrained"* conditions: the *"Experimentally undrained"* condition described below (Fig. 9.4c). This last condition is the most realistic one because (i) it is often difficult to attain experimentally the purely *"undrained"* (e.g. *Ghabezloo and Sulem*, 2009) experimental conditions ; and (ii) it has been shown (e.g. *Pimienta et al.*, 2015a) that measuring precisely attenuations under purely *"drained"* conditions was technically challenging.

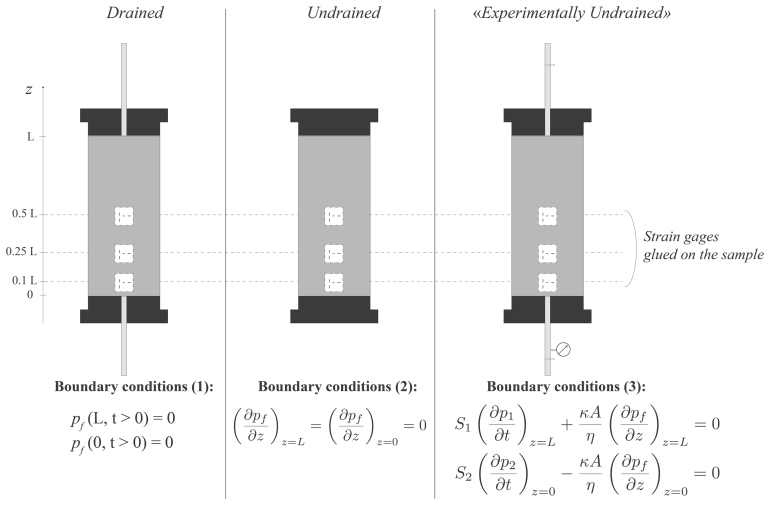

Figure 9.4: Schematic view of the sample associated with the three possible boundary conditions. The theoretical (a) *"drained"* and (b) *"undrained"* boundary conditions are complemented with the more realistic (c) *"experimentally undrained"* boundary condition, which in fact combines the two theoretical ones.

9.4.3.1 Role of the dead volumes

The *"experimentally undrained"* boundary condition consists in an undrained system not only constituted of the sample but also of a dead volume at both sample's upper and lower ends. Such boundary condition is also that considered for the *"oscillating pulse"* technique (e.g. *Brace et al.*, 1968; *Lin*, 1977; *Hsieh et al.*, 1981; *Song and Renner*, 2006, 2007). Fluid mass continuity at both ends of the sample is imposed, i.e. the change of fluid mass in the sample equals the fluid mass change in the dead volume. Following earlier studies, these boundary conditions are found to be (*Brace et al.*, 1968; *Lin*, 1977):

$$\begin{cases} S_1 \left(\frac{\partial p_1}{\partial t}\right)_{z=L} + \frac{\kappa A}{\eta} \left(\frac{\partial p_f}{\partial z}\right)_{z=L} = 0, \\ S_2 \left(\frac{\partial p_2}{\partial t}\right)_{z=0} - \frac{\kappa A}{\eta} \left(\frac{\partial p_f}{\partial z}\right)_{z=0} = 0. \end{cases} \tag{9.12}$$

Where S_1 and S_2 are respectively the storage capacities of downstream and upstream dead volumes, and $p_1 = p_f(0,t)$ and $p_2 = p_f(L,t)$ are the fluid pressures in the downstream and upstream dead volumes. A is the sample's cross-sectional area through which Darcy flow takes place.

From Equation (9.12), the dead volumes contribute through their overall storage capacity. Owing to the very low pressure variations applied (i.e. $\Delta P = 0.2\,\text{MPa}$), leading to even lower pore pressure variations, the tubing's compressibility can consistently be neglected so that only the compressibility of the fluid in the dead volume needs to be accounted for. Knowing the values of lower (i.e. V_1) and upper (i.e. V_2) dead volumes, and the fluid bulk modulus K_f, S_1 and S_2 are obtained such that $S_{1,2} = V_{1,2}\,K_f^{-1}$. The sample's storage capacity is reached from the theoretical relations (e.g. *Kümpel*, 1991). All required parameters are listed in Table 9.1.

The general solution can be obtained for example by solving the Equation (9.5) using ***Mathematica*** software. Solving $p_f(z,t)$ for this realistic set of boundary conditions would lead to a complex solution that cannot be reported in a simple formula. However, a simple analytical solution is found if $S_1 = S_2$ (i.e. $V_1 \sim V_2$). In the case of the set-up used in *Pimienta et al.* (2015a), such assumption can consistently be made as $V_1 = 3.4\,\text{mL}$ and $V_2 = 3.2\,\text{mL}$. Using this assumption, one gets the system:

$$\begin{cases} p_0^-(b+1) = p_0^+(b-1) - B\Delta P_0, \\ p_0^+(b+1)e^{aL} = p_0^-(b-1)e^{-aL} - B\Delta P_0, \end{cases} \tag{9.13}$$

with $b = (1-i)A(S_s/S)\sqrt{2D/\omega}$, and $S = S_1 + S_2$ is the dead volume storage capacity. Subtracting the two above equations, one gets:

$$(p_0^- - p_0^+ e^{aL}) \left[(1+b) - \frac{(1-b)}{e^{aL}}\right] = 0. \tag{9.14}$$

This implies that $p_0^- = p_0^+ e^{aL}$, because a, b and L have fixed values so that the second term differs from zero. Further solving the System (9.13) and replacing the constants in Equation (9.5) leads to the general solution:

$$p_f(z,t) = B\Delta P_0 e^{i\omega t}\left[1 - \frac{cosh(a(\frac{L}{2}-z))}{bsinh(a\frac{L}{2}) + cosh(a\frac{L}{2})}\right], \tag{9.15}$$

Interestingly, recalling that $a \propto \sqrt{\omega}$ and $b \propto (1/\sqrt{\omega})$, the limiting quasi-static case (i.e. zero frequency) can be reached from Equation (9.15) using the Taylor expansion of *cosh* and *sinh* to the first order in ω. Further noting that $a\,b\,(L/2) = (2AS_s/S)(L/2) = V_s(S_s/S)$, the limiting quasi-static case is:

$$\left(\frac{p_f(z,t)}{P(t)}\right)_{\omega=0} = B_0 = B\frac{V_s S_s}{V_s S_s + S}. \tag{9.16}$$

Where $V_s = AL$ is the sample's total volume and B is the Skempton coefficient. The general result (i.e. with $V_1 \neq V_2$) can further be found from introducing $S = S_1 + S_2$ in Equation (9.16). This solution under quasi-static conditions is consistent with the results from *Ghabezloo and Sulem* (2010), and implies that the measured B_0 is equal to the Skempton coefficient B only if $S_1 = S_2 = 0$ (i.e. $V_1 = V_2 = 0$). As shown by previous authors (e.g. *Ghabezloo and Sulem*, 2010), the idealistic condition of $V_1 = V_2 = 0$ can seldomly be reached experimentally so that the above result needs to be applied.

9.4.3.2 *"Global"* predictions

In order to apply the present model in a simple way to the experiment reported in *Pimienta et al.* (2015a), the two dead volumes are assumed to be equal (i.e. $V_1 = V_2$) so that the total dead volume is $V_{meas} = 6.6$mL. As a consequence, following Equation (9.15), the problem is symmetric with respect to $L/2$. The model's *"global"* predictions, averaged over the entire sample's length, are first investigated. They are noted K_g and $Q_{K_g}^{-1}$ for the predicted elastic response, and B_g and ϕ_{B_g} for the hydraulic response. The frequency-dependent hydraulic (Figs. 9.5a & 9.5b) and elastic (Figs. 9.5c & 9.5d) model's responses are predicted using the parameters from table (9.1). In order to check the sensitivity to the total dead volume value, a theoretical dead volume V_{th} is introduced. This parameter is varied from V_{meas} to values of 0, $10\,V_{meas}$ and $10^3\,V_{meas}$, and even to $10^6\,V_{meas}$ for the p_f phase shift.

A zero dead volume (i.e. $V_{th} = 0$) corresponds to the *"undrained"* boundary condition. In that case, for all frequencies (i) the predicted B_g equals Skempton coefficient B; (ii) there is no phase shift for p_f; and (iii) $K_g = K_{ud}$ (i.e. undrained bulk modulus) and $Q_{Kg}^{-1} = 0$. A very high dead volume (i.e. $V_{th} \geq 10^3\,V_{meas}$) corresponds to the *"drained"* boundary condition (Fig. 9.3). In that case, (i) at frequencies low enough, there is no Skempton coefficient (i.e. $B_g = 0$) and $K_g = K_d$; and (ii) a critical frequency f_c exists at which the

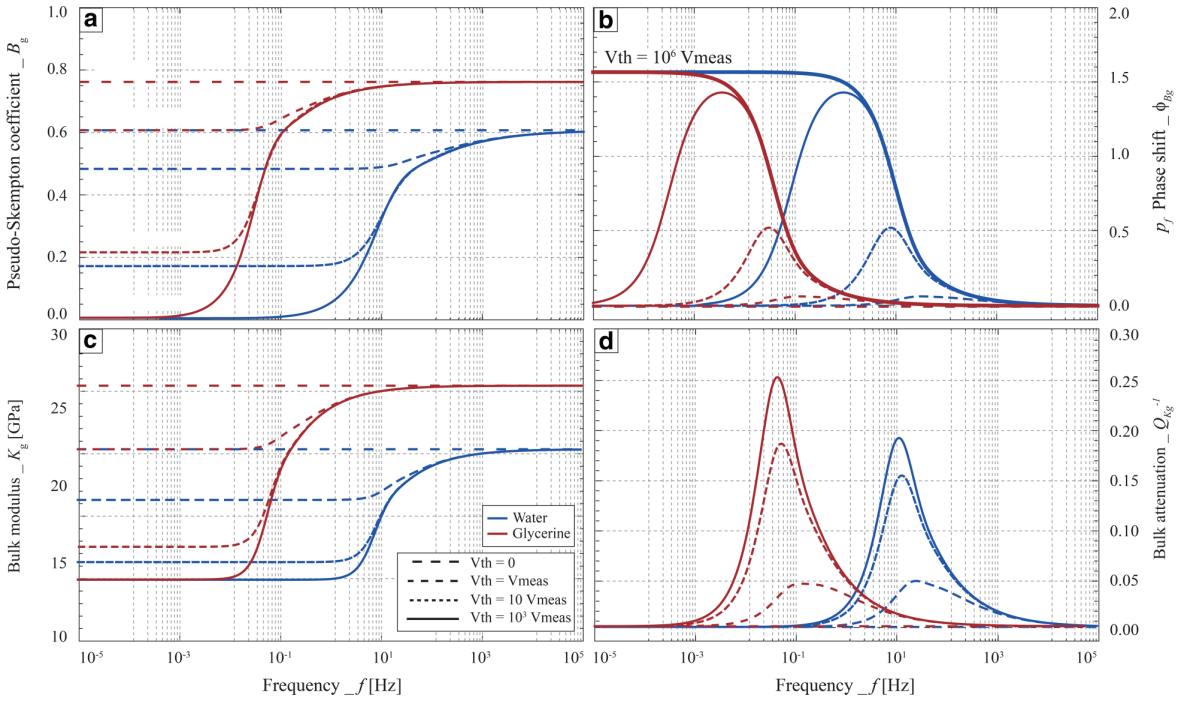

Figure 9.5: Predicted frequency dependence of the (a-b) hydraulic and (c-d) elastic response of the fluid-saturated sandstone sample. The *"global"* prediction are reported, i.e. the response averaged over the sample's length.

regime switches from *"drained"* to *"undrained"*. At f_c, a maximum in Q_{Kg}^{-1} is predicted.

The intermediate dead volumes (i.e. $V_{th} = V_{meas}$ and $V_{th} = 10\,V_{meas}$) lead to an intermediate case scenario, in between *"drained"* and *"undrained"* boundary conditions. In that final case, at frequencies low enough, (i) B_g exists but is below B (Fig. 9.5a); (ii) $K_d < K_g < K_{ud}$ (Fig. 9.5c); and (iii) a dependency to the fluid bulk modulus K_f is observed (Figs. 9.5a, 9.5c & 9.5d). Moreover, as for the *"drained"* boundary condition, a critical frequency f_c exists at which a maximum in Q_{Kg}^{-1} is predicted (Fig. 9.5d). Beyond f_c, B_g and K_g reach respectively the undrained B and K_{ud}. As V_{th} decreases, the magnitudes of the variations between drained and undrained regime decrease, and, consistently, the maximum in Q_{Kg}^{-1} decreases. Note finally that, as V_{th} decreases, the value for f_c slightly increases.

9.4.3.3 *"local"* and *"locally averaged"* predictions

The *"locally averaged"* predictions can be calculated by averaging over the strain gauge length (i.e. 6 mm) at the sample's center, i.e. $(L/2) \pm 3$ mm. They are noted K_{la} and B_{la}. In case of the pseudo-Skempton coefficient, a second *"local"* prediction B_l is investigated at a position infinitely near to the boundary, so that the frequency-dependent variations measured experimentally in the dead volume (*Pimienta et al.*, 2015a) can be approached. The frequency-dependent variations predicted for K_{la}, B_{la} and B_l under glycerine saturation

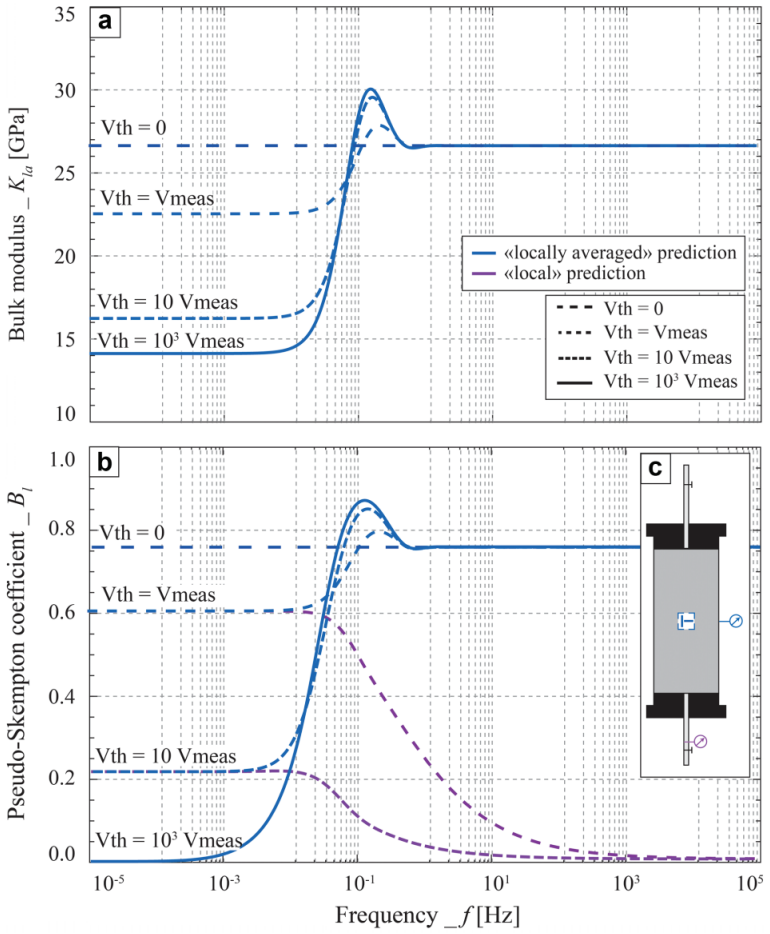

Figure 9.6: Predicted frequency dependence of K_{la}, B_{la} and B_l for the glycerine-saturated sandstone sample. Different values of dead volume V_{th} are chosen, starting from zero, up to a value a thousand times higher than the one measured ($V_{th} = V_{meas}$).

are reported (Figs. 9.6a & 9.6b).

A strong effect of the dead volume is again predicted. At lowest and highest frequencies, the values equal the ones of the *"global"* predictions. However, a sharper increase is predicted for the transition of K_{la} and B_{la}, which is similar to a characteristic transition of a viscoelastic Zener-like material. Interestingly, B_l decreases as frequency increases (Fig. 9.6b). It indicates that fluid can less and less flow out of the sample as frequency increases, i.e. the sample becomes undrained.

9.4.4 Transient regime & Numerical solution

The analytical solution obtained (Eq. 9.8), corresponds to the steady-state response of the pore pressure to an oscillating confining pressure. However, considering the time $t_0 = 0$ to be the beginning of the oscillation, a transition exists between the initial static state (at $t_0 < 0$) and the steady-state oscillation. In order to investigate this transient regime, a 1D

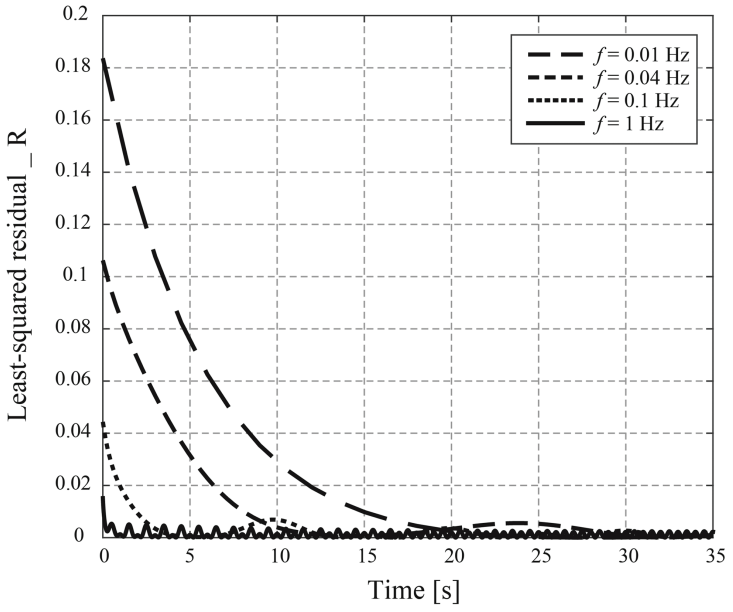

Figure 9.7: Comparison of the differences quantified by R (sum of squared residuals through the sample's length), between the analytical and the numerical solutions of the pore-fluid pressure oscillations at different frequencies. The parameters used are the ones of Table 9.1 in the case of glycerine saturation, under drained boundary conditions.

finite difference scheme, with imposed initial conditions (i.e. $P(t_0) = 0$ and $p_f(z, t_0) = 0$), is used to solve numerically the diffusion equation (Eq. 9.1). A first-order backward difference for time and a second-order central difference for space has been chosen. The grid used is uniform, with a constant mesh spacing of Δz for space and a constant time increment of Δt. The boundary conditions tested correspond to the drained regime, which are taken into account with the two Dirichlet boundary conditions (i.e., $p_f(0, t) = 0$ and $p_f(L, t) = 0$) at both ends of the space grid. For the initial conditions, the pore pressure is zero throughout all the sample (i.e., $p_f(z, 0) = 0$).

A parameter R is introduced to compare analytical and numerical solutions, respectively p_f and $\widetilde{p_f}$. R is defined as the sum of the squared residuals through the sample's length, i.e. of the difference between analytic and numerical solution for a particular position $z_i = i\Delta z$. For each time step $t_j = j\Delta t$, R is defined as:

$$R(j) = \sum_i \left| p_f(z_i, t_j) - \widetilde{p_f}_i^j \right|^2 \tag{9.17}$$

The solutions are compared as a function of time for different oscillating frequencies (Fig. 9.7). For simplicity, the drained 1D model (Fig. 9.4a) is used.

For each frequency, the sum of squared residuals R is maximum at the initial conditions ($t = 0$), then decreases with time to reach a steady-state where the difference between the

analytical and numerical solution is negligible. The transient behaviour observed for R relates to the transient behaviour accounted for in the numerical solution. As frequency increases, R decreases. The duration of this transient behaviour is always less than one oscillation period for any frequency. Therefore, the analytical solution can be considered valid after one oscillation.

9.5 Comparison with the measurements

The above model predictions are used to discuss the measurements on two sandstone (i.e. Fontainebleau and Berea) samples. The dead volume is set to 6.6 mL, with $V_1 = V_2$. The other required parameters are (i) the drained (i.e. dry) bulk modulus; (ii) the sample's porosity and permeability; and (iii) the fluid's viscosity. All these parameters are known. Finally, Biot-Willis, Skempton, and storage coefficients are derived from the poroelastic relations. The skeleton bulk modulus is taken as 37 GPa for both rocks.

The model's predictions are calculated for the appropriate experimental conditions,i.e. what has been defined as the *"experimentally undrained"* boundary condition. Moreover, the strains have been recorded at the sample's center, and the pore pressure measurement has been taken in the dead volume. Accordingly, the *"locally averaged"* K_{la} and $Q_{K_{la}}^{-1}$ are predicted at the sample center, and the *"local"* B_l is calculated very close to the dead volume. In the following, an apparent frequency parameter (i.e., $f^* = f\,(\eta/\eta_0)$, with $\eta_0 = 10^{-3}$ Pa.s) is introduced to account for the fluid's viscosity.

9.5.1 Results for a Fontainebleau sandstone

9.5.1.1 *"Experimentally undrained"* boundary conditions

The data are those of *Pimienta et al.* (2015a), measured on a Fontainebleau sandstone sample of 7% porosity. All parameters for the predictions are the ones of Table 9.1. Measurements at an effective pressure of $P_{eff} = 1$ MPa and model's predictions are compared as a function of apparent frequency f^* (Fig. 9.8). Three properties are investigated: (i) bulk modulus K (Fig. 9.8a), (ii) bulk modulus dissipation Q_K^{-1} (Fig. 9.8b), and (iii) pseudo-Skempton coefficient B^* (Fig. 9.8c). The model's predictions are calculated for two extreme values of K_d, of 5 and 13 GPa respectively.

Note first that the frequency range for the transition predicted by the model is very consistent with the measurements, and occurs at $f^* \sim 10$ Hz. A strong effect of the *"experimentally undrained"* boundary condition is predicted so that, for a K_d of 13 GPa, the values of (i) K_{la} at lowest f^* overestimates the measurements (Fig. 9.8a); (ii) $Q_{K_{la}}^{-1}$ underestimates the measured Q_K^{-1} peak (Fig. 9.8b); and (iii) B_l at lowest f^* underestimates the values of B^* measured (Fig. 9.8c).

Comparisons between measurements and model predictions thus add up and imply

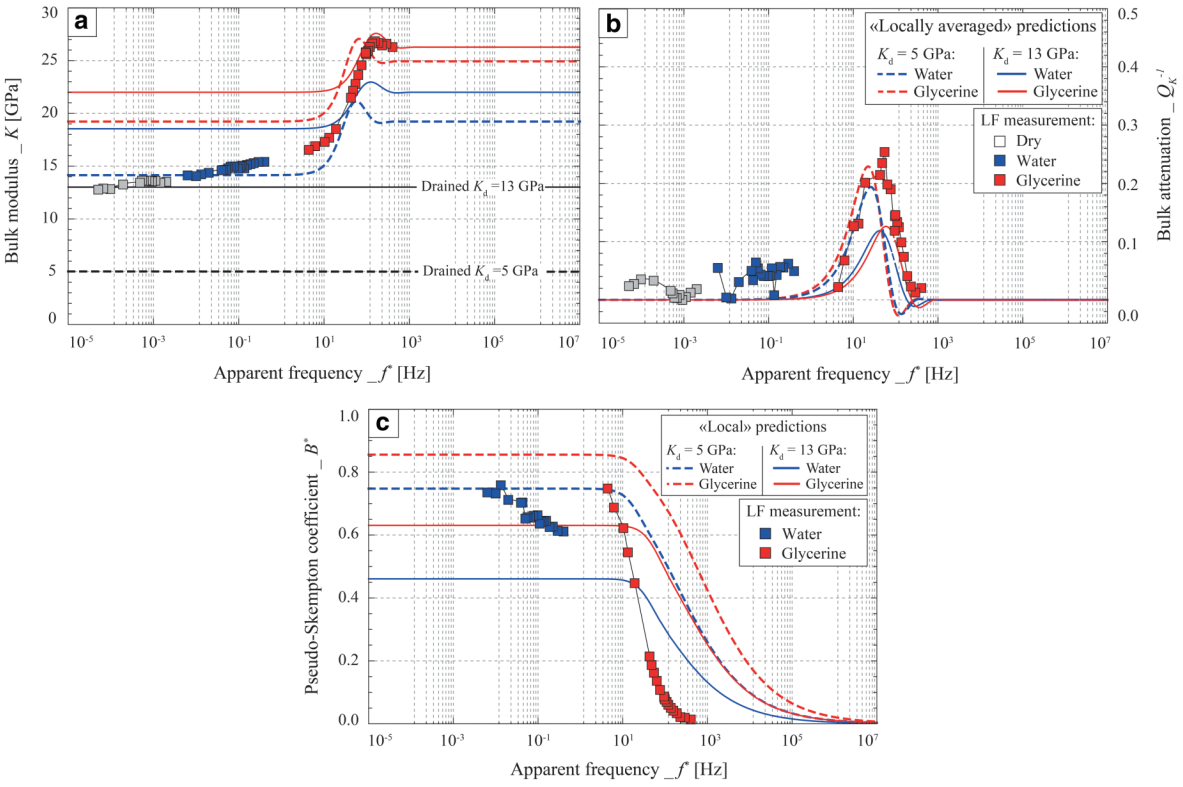

Figure 9.8: Comparison between predicted and measured frequency-dependent properties for a 7% porosity Fontainebleau sandstone. The measured (a) bulk modulus and (b) attenuation have been measured locally at the sample center, and (c) the pseudo-Skempton coefficient has been measured in the dead volume. These data are compared to the corresponding model predictions with *"experimentally undrained"* boundary conditions. Two values of K_d of 5 GPa (i.e. dashed curves) and 13 GPa are chosen for the predictions.

that measurements under liquid saturation relate to an initial K_d much lower than 13 GPa. A second prediction is thus tested with $K_d = 5\,\text{GPa}$. The predicted properties are consistent with the measurements under fluid-saturated conditions. For all properties, under water saturation, a good fit is obtained between measurements and model predictions. Under glycerine saturation, both K_{la} (Fig. 9.8a) and B_l (Fig. 9.8b) gain in consistency with the measurements. Moreover, the peak in $Q^{-1}_{K_{la}}$ is at about 0.25 (Fig. 9.8c), which is precisely what has been measured.

9.5.1.2 Role of the confining cycle

As the measured value under dry conditions is of $13 - 14\,\text{GPa}$ (Fig. 9.8a), it implies that K_d is lower under fluid-saturated conditions. Because glycerine is not a polar fluid and this sample is well cemented, a possible fluid-related elastic weakening (e.g. *Pimienta et al.*, 2014b) may be ruled out. Noting that this K_d value was measured after cycling the sample up to high pressure and back (*Pimienta et al.*, 2015a), the effect of cycling is tested on a sample from the same block (Fig. 9.9a).

For this rock sample, at pressures lower than $P_{eff} = 10\,\text{MPa}$, the K_d values after the loading stage are higher than the ones before (Fig. 9.9a). For the particular case of $P_{eff} = 1\,\text{MPa}$, the cycling introduces a variation from $K_d = 5\,\text{GPa}$ (before cycling) to $K_d = 13\,\text{GPa}$ (after cycling). After unloading the sample, glycerine then water are injected in the sample, and the drained bulk modulus is measured again under purely drained boundary conditions (Fig. 9.9b). Under both water and glycerine saturation, the value at 1 MPa is of 5 GPa, which equals the value measured during the (first) loading stage under dry conditions. This is precisely this value of $K_d = 5\,\text{GPa}$ that has been chosen for the 1D model predictions (Fig. 9.8), under fluid-saturated conditions. It implies that, for this sample and this experimental protocol, the hysteresis seems to disappear when measuring again (after cycling) under fluid saturation. This hysteresis effect under dry conditions may be caused by grain-grain or cracks internal friction (e.g. *David et al.*, 2012) that indeed largely reduces when fluid is present and pressurized.

9.5.2 Results for a Berea sandstone

9.5.2.1 Berea sandstone

Berea sandstone has been extensively used in experimental rock physics (e.g. Sayers, Van Munster and King, 1990; Seipold, Mueller and Tuisku, 1998) as a reference rock. As detailed by *Pimienta et al.* (2014c), it is characterized by (i) a porosity in the range of $\phi \in [17; 22]\,\%$; (ii) a permeability in the range of $\kappa \in [1; 10^3]\,\text{mD}$; (iii) a variable mineralogy, with mean (over 19 Berea sandstone samples) quartz and clay contents of $\sim 75\%$ and $\sim 11\%$ respectively. As shown through microstructural observation (e.g. *Prasad and Manghnani*, 1997), Berea sandstone's pore network is composed of (i) relatively equant pores; and (ii) intergranular

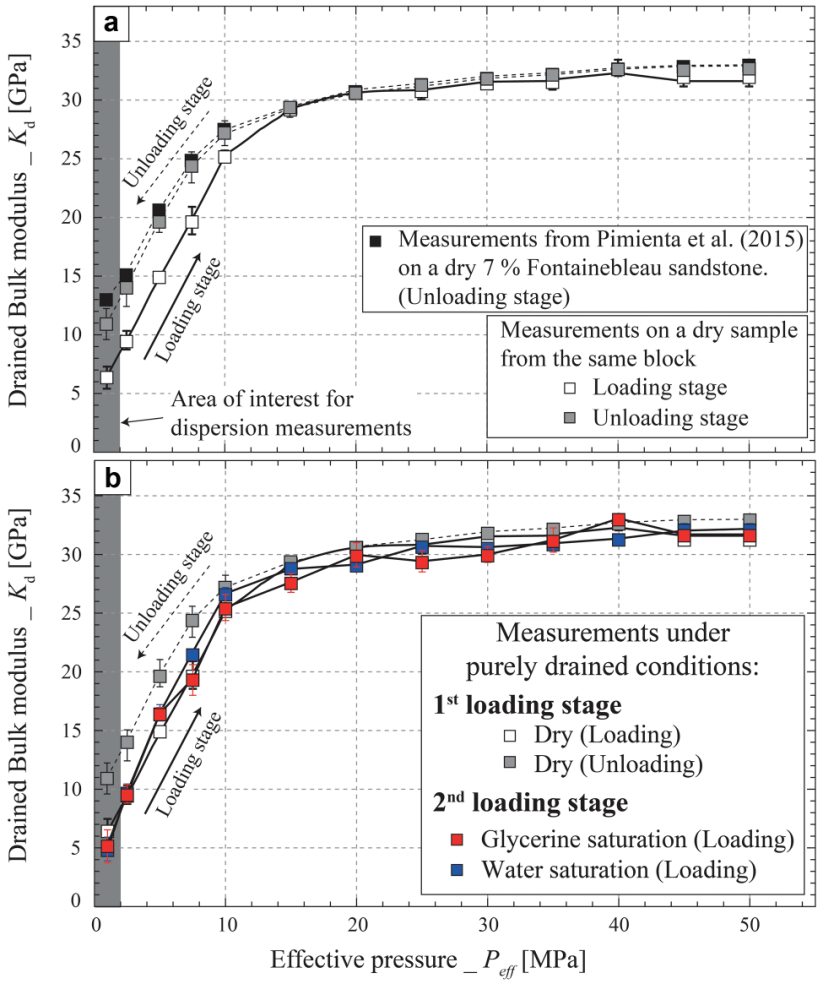

Figure 9.9: (a) Measured dry bulk modulus as a function of effective pressure for two Fontainebleau sandstone samples of 7% porosity. K_d is measured under both loading and unloading stages. (b) Measured drained bulk modulus under loading stage for the three fluid-saturated conditions. The first *"loading stage"* is the one under dry conditions, where the sample is measured under loading then unloading. The second *"loading stage"* comes after. During this stage, the rock is fully-saturated by glycerine then water. For each saturating fluid, the rock is measured under loading only. Note the greyish area corresponding to the effective pressure at which the frequency effects are investigated.

thin discontinuities (flat geometry at two-grain junctions). The latter type of feature is known to be the major contributor to the observed stress sensitivity of various physical properties such as elastic wave velocities (e.g. *Christensen and Wang*, 1985; *Sayers et al.*, 1990; *Seipold et al.*, 1998).

The Berea sandstone sample chosen has a porosity of $\phi = 19.3\,\%$ and a permeability of $\kappa \sim 10\,\text{mD}$ (i.e. $10^{-14}\,\text{m}^2$). The experimental measurements are similar to that for Fo7 (*Pimienta et al.*, 2015a), except that the data for the dry sample have also been obtained under loading conditions. This has been done to discard any possible hysteresis effect (Fig. 9.9a). The parameters used as model input are essentially very similar to that of Table 9.1. The sample's length and diameter are the same, and porosity ($\phi = 19.3\,\%$), permeability ($\kappa = 10^{-14}\,\text{m}^2$) and drained bulk modulus ($K_d \sim 6.5\,\text{GPa}$) differ. As for before, ϕ, κ and K_d are used to calculate the other properties/parameters using the theory of poroelasticity.

9.5.2.2 *"Experimentally undrained"* boundary conditions

Again, predictions are made according to the experimental conditions. The 1D model with *"experimentally undrained"* boundary conditions is used, and the *"locally averaged"* K_{la} and $Q_{K_{la}}^{-1}$ and the *"local"* B_l are predicted. The dependence to f^* of the measured and modelled elastic (Fig. 9.10a & 9.10b) and hydraulic (Fig. 9.10c) responses are compared for an effective pressure of $P_{eff} = 1\,\text{MPa}$.

At lowest frequencies, the measured K (Fig. 9.10a) under fluid saturation is much higher than K_d. This is precisely what is predicted by K_{la}. This difference results from the interplay between dead volume's and sample's storage capacity, and is theoretically expected. Although the measurement under water saturation remains higher than the model's predictions, an overall good fit is obtained between measurements and predictions for all properties. As f^* increases, both predicted and measured K slightly increase, by about 2 GPa, to reach the value of K_{ud}. A good fit is observed under glycerine saturation. Because the experimental dead volume V_{meas} is small as compared to the Berea pore volume, the measured dispersion/attenuation is much lower than the one expected in case of the transition from K_d to K_{ud}.

The attenuation is strongly controlled by the dead volume effect. Both measurements and predictions indicate a peak of 0.1 (Fig. 9.10b). A good fit is also obtained between B^* and predicted B_l (Fig. 9.10c) at lowest frequencies. The magnitude of the measured B^* is well predicted by the model for both water and glycerine saturations. Yet, the frequency-dependent variations of the *"local"* prediction are spread out as compared to the measurements. These results further indicate that, even for dead volumes much smaller than the one of the present experiment, the drained/undrained transition may be *"seen"* experimentally for highly porous and compressible rocks.

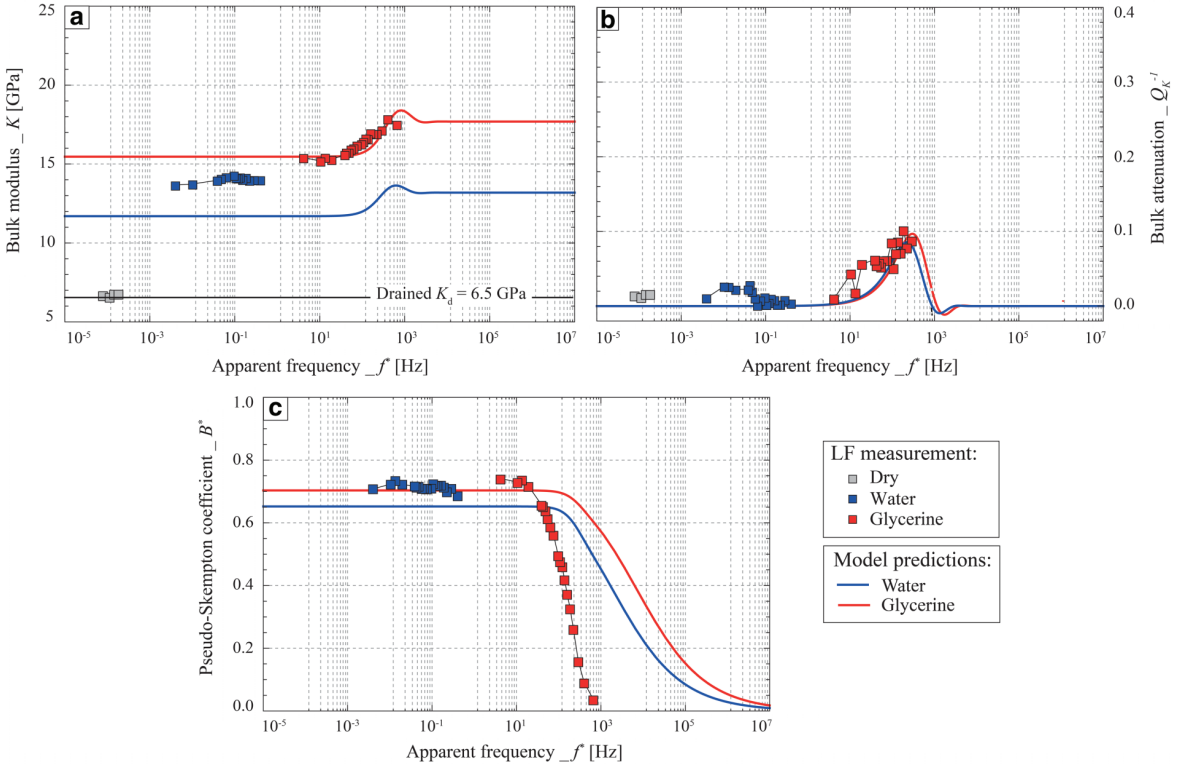

Figure 9.10: Comparison between predicted and measured (a-b) elastic and (c) hydraulic properties as a function of apparent frequency for the Berea sample saturated by different fluids. The *"experimentally undrained"* model is used for the predictions, with the measured dead volume.

9.6 Conclusion

To better understand the experimental conditions involved in the measurement of the drained/undrained transition, a 1D model has been developed by solving analytically the partial derivative equation for pressure diffusion. Different boundary conditions have been analysed. The *"undrained"* and *"drained"* boundary conditions assume that fluid is either locked in or free to flow out of the sample. A more realistic *"experimentally undrained"* boundary condition has been investigated by assuming that a dead volume is present at both ends of the sample. Four properties may be predicted by the model, i.e. the pseudo-Skempton coefficient B^*, the pore pressure phase shift ϕ_{B^*}, the bulk modulus K, and the attenuation Q_K^{-1}.

The 1D model is used to test two main aspects, i.e. the the role of the measuring condition and the role of the dead volume. Interestingly, the frequency range for the drained/undrained transition is expected to strongly differ if the measuring method is global (e.g. LVDT) or local (e.g. strain gage). Furthermore, the position of the local measurement is also expected to play a dominant role. Finally, introducing a dead volume at both sample's ends appears to strongly affect the drained/undrained transition. The measured dispersion/attenuation for this effect are expected to be strongly damped if the dead volume is small in comparison with the rock pore volume. Because it originates from an interplay between dead volume's and sample's storage capacity, this effect increases as the rock's compliance and porosity increases.

Comparison between the model's predictions and measurements on a Fontainebleau and a Berea sandstone shows a good fit and an overall consistency. The rock's storage capacity has an important effect. It could result in a non-negligible attenuation even with a very small dead volume if the storage capacity is high.

End of article

9.7 Comparison with the experimental results on the limestones

We wish to present here complementary results to the previous article, obtained for the studied carbonate samples. In addition, a 2D and a 3D numerical model were used to investigate a possible effect of the boundary geometry that can not be accounted for in 1D.

The effect of the boundary conditions on the elastic properties has been studied for the carbonate samples. The two different configurations for the drainage system, (i) open (assimilated to drained conditions), and (ii) closed (undrained conditions for the system $\{sample + dead\,volumes\}$) (Figure 3.2a) have been tested at $P_{diff} = 2.5\,\text{MPa}$ for the Lavoux, the Rustrel and the Coquina samples. The Indiana sample, intact and thermally cracked were only measured with the open drainage system. We recall that all the dispersion/attenuation results presented in the previous chapters were obtained in the open configuration. Because the dead volumes were very large in that case (at least 45 mL), the boundary conditions could be assimilated to drained boundary conditions (*Pimienta et al.*, 2016b).

Lavoux limestone in the Geodesign cell

The Lavoux limestone was measured in the Geodesign cell (Figure 2.2). The small dead-volumes at each end of the sample when the valves are closed were measured to be around 3.3mL each for this cell. The bulk modulus results during the drained/undrained transition, visible under glycerin-saturated conditions, at $P_{diff} = 2.5\,\text{MPa}$ are compared with the 1D model in Figure 9.11, for the two boundary configurations. The results for the hydrostatic and the axial oscillations are used. With dead volumes (Figure 9.11b), the drained/undrained transition is visible around the same cut-off frequency as in the drained case (Figure 9.11a), but the amplitude of dispersion is smaller. In the drained frequency range, the bulk modulus measured in the second case is higher than in fully drained conditions. Its value is 22 GPa (Figure 9.11b) instead of 16 GPa (Figure 9.11a). In the undrained frequency range, the bulk modulus of the sample is independent of the boundary conditions, with a value of 26 GPa in both configurations (Figure 9.11a and 9.11b), which is consistent with the definition of the undrained regime.

In the second configuration, the pore pressure in the drainage circuit (${p_f}^*$) was monitored during the stress oscillations. In order to have a non zero measurement, ${p_f}^*$ has to be measured in a closed volume to allow for pressure build-up when fluid drains out of the sample. The volumetric strain (ε_{vol}), induced by hydrostatic stress oscillations ($\sigma_{ii}/3$), generates a flux of fluid going in and out of the sample, into the dead volumes. This volumetric strain is defined as:

$$\varepsilon_{vol} = \frac{1}{K}\left(\frac{\sigma_{ii}}{3} - \alpha \Delta p_f\right), \tag{9.18}$$

where α is the Biot coefficient and Δp_f is the oscillation amplitude of the pore pressure in

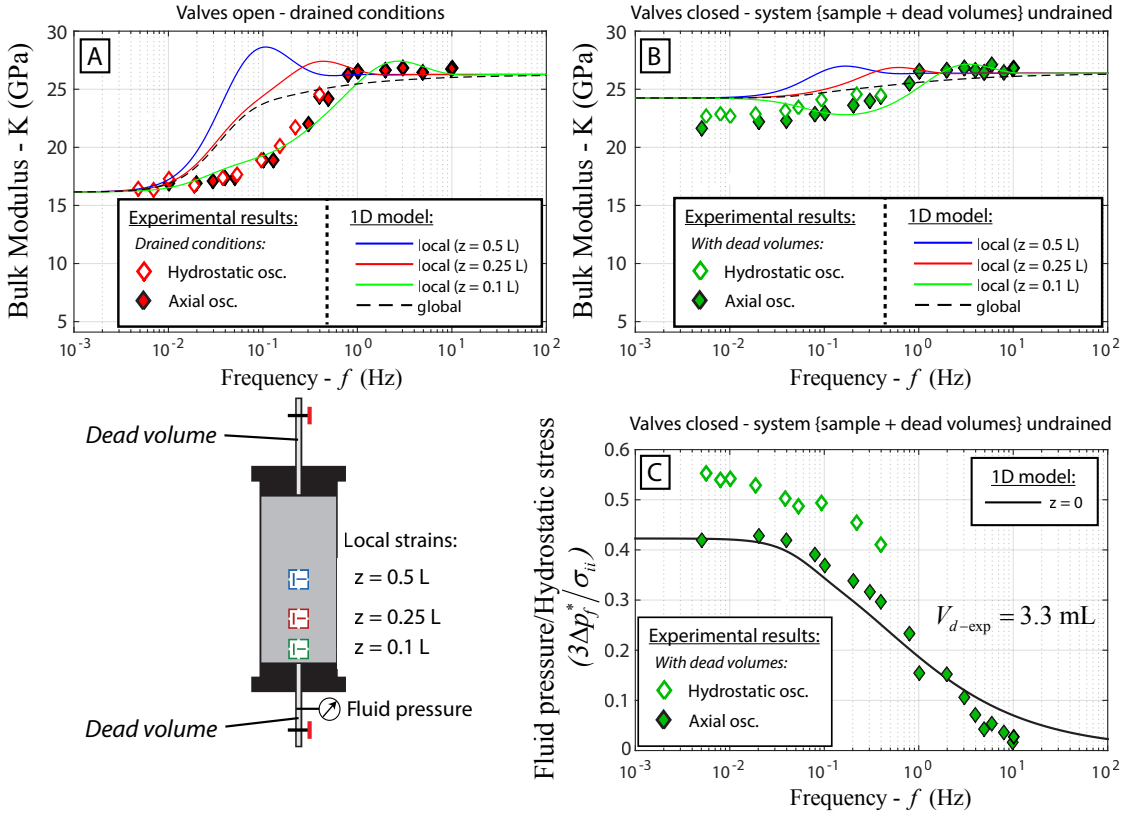

Figure 9.11: Effect of the two types of experimental boundary conditions on the measured bulk modulus and comparison with the 1D diffusion model: (a) drained conditions and (b) system $\{sample + dead\,volumes\}$ undrained. The experimental results are from the hydrostatic and the axial oscillations in glycerin-saturated conditions at $P_{diff} = 2.5\,\text{MPa}$. The model is calculated from local strains at different positions ($0.5\,L$, $0.25\,L$ and $0.1\,L$), and from global strain. The experimental results are from strains measured at $z = 0.5\,L$. (c) Measurements of the ratio pore pressure over hydrostatic stress ($3p_f^*/\sigma_{ii}$) in the second type of boundary conditions are compared to the 1D model, at the limit $z = 0$. For the hydrostatic oscillations $\sigma_{ii}/3 = \Delta P_c$, and for the axial oscillations $\sigma_{ii}/3 = \sigma_{ax}/3$.

the medium. Experimentally, when we apply the hydrostatic oscillations on the sample, we have $\sigma_{ii}/3 = \Delta P_c$. This pressure induces the volumetric strain ε_{vol}. On the other hand, when we apply the axial oscillations in an isotropic medium, the equivalent hydrostatic stress to obtain the same volumetric strain ε_{vol} is $\sigma_{ii}/3 = \sigma_{ax}/3$ (Equation 9.18). Here we assume that the stress σ is positive in compression and represents the amplitude of oscillation, and that the radial stress is constant during the axial stress oscillations ($\sigma_{rad} = 0$). For both stress oscillations at $P_{diff} = 2.5\,\text{MPa}$ on glycerin-saturated sample, the ratio between the amplitude of the oscillating fluid pressure $\Delta {p_f}^*$ and the amplitude of the equivalent hydrostatic stress oscillation $\sigma_{ii}/3$ is equal to $3\Delta {p_f}^*/\sigma_{ii}$. This ratio is reported Figure 9.11c as a function of frequency. For both hydrostatic and axial oscillations, the ratio tends to zero as the frequency crosses the drained/undrained transition range ($[5\,10^{-2}; 1]\,\text{Hz}$). In the drained frequency range ($f < 5\,10^{-2}\,\text{Hz}$), the ratio measured with hydrostatic measurements is slighly higher than with the axial oscillation, respectively 0.55 and 0.41 (Figure 9.11c). This ratio was defined as the "pseudo-Skempton" coefficient $B^* = \Delta {p_f}^*/\Delta P_c$ by *Pimienta et al.* (2015a) in the case of hydrostatic oscillations, or the "pseudo-consolidation" parameter $\gamma^* = \Delta {p_f}^*/\sigma_{ax}$ in case of axial oscillations in *Pimienta et al.* (2015b). This hydraulic parameter cannot be considered as the real Skempton coefficient (B) of the sample, because B is solely defined for an undrained REV, and ${p_f}^*$ doesn't measure the pore pressure p_f inside the sample, unless the sample is fully drained.

The model's predictions in both configurations for a glycerin-saturated sample are presented Figure 9.11. The model has been calculated for local strains at 3 different positions ($0.5\,L$, $0.25\,L$ and $0.1\,L$) and for the global strain. We recall that the experimental results are deduced from local strains measured at $z = 0.5\,L$. The parameters used for the model predictions were $L = 80\,\text{mm}$, $A = \pi(20)^2 = 1257\,\text{mm}^2$, $K_d = 16\,\text{GPa}$, $K_S = 77\,\text{GPa}$, $K_f = 4.36\,\text{GPa}$, $\eta = 1.083\,\text{Pa.s}$, $\Phi = 24\,\%$, $\kappa = 10^{-14}\,\text{m}^2$, and $V_{dead\,vol.} = 3.3\,\text{mL}$. Concerning the bulk modulus in the drained frequency range, the model predicts $K_{model} = 24\,\text{GPa}$ for the second configuration (Figure 9.11b). This is slightly above the experimental result of 23 GPa (Figure 9.11b). The bulk modulus K_{model} is 16 GPa in fully drained conditions (Figure 9.11a). In the undrained frequency range, the model predicts $K_{model} = 26\,\text{GPa}$ (Figure 9.11a), which by construction of the model corresponds to Biot-Gassmann's prediction. For the ratio $3{p_f}^*/\sigma_{ii}$, the model predicts a value of 0.41 in the drained frequency range, which corresponds to the experimental measurement done with axial oscillations (Figure 9.11c). For the drained/undrained transition, the ratio $(3{p_f}^*/\sigma_{ii})_{model}$ decreases down to 0 consistently with the axial experimental results (Figure 9.11c).

When comparing the model and the experimental results both deduced from local strain at $z = 0.5\,L$, we can see a frequency shift of nearly one order of magnitude (Figure 9.11a and 9.11b). The predicted cut-off frequency is around 0.04 Hz for the model, and the experimental value is 0.2 Hz (Figure 9.11a and 9.11b). The model calculated from local strain at $z = 0.1\,L$ seems to fit better the experimental results. However, no shift in frequency ap-

pears for the ratio $(3{p_f}^*/\sigma_{ii})$ (Figure 9.11c). The position of the local strain mainly affects the measured cut-off frequency of the transition: the closer to the boundary, the higher the cut-off frequency. In other words, when the frequency of the stress oscillations increases, the REVs at the center of the sample become undrained before the REVs close to the open boundaries. However, the amplitude of the dispersion is unchanged. *Pimienta et al.* (2016b) compared the model to experimental results on Fontainebleau sandstones, and found that the cut-off frequency of the bulk modulus was in their case consistent with the experimental results. However, in their case, it was the ratio $3\Delta{p_f}^*/\sigma_{ii}$ that had a frequency shift of one order of magnitude compared to the experimental results.

Indiana, Rustrel and Coquina sample in the Top Industrie cell

The Indiana, Rustrel, and Coquina limestones were measured in the Top Industrie cell. The dead volumes in the closed configuration were measured to be around 4.4 mL for this cell. For the open configuration, symmetry of the dead volumes (upper and lower) is insured by a hydraulic short-circuit between the up-stream and the down-stream before reaching the pumps. In that case, the dead volume (seen from one side of the sample) is therefore the total volume (tubings + the two pumps) divided by 2. Each of the previous samples exhibited the drained/undrained transition under water-saturated conditions. The frequency-dependent bulk modulus obtained from the hydrostatic oscillations at $P_{diff} = 2.5$ MPa will be used for the comparisons with the model. The model is calculated for a local strain at mid-height ($z = 0.5L$), which corresponds in theory to our experimental measurement, and for a global strain of the sample. For the sake of simplicity, we designate by K the bulk modulus obtained experimentally, K_{1D} the model's bulk modulus obtained from the local strain ($z = 0.5L$), and K_{1D-g} the model's bulk modulus obtained from global strain.

The comparisons of the 1D model and the experimental results for the Indiana limestone, intact and thermally cracked, are presented Figure 9.12. Results on the intact sample show a good match between K and K_{1D} up to 0.4 Hz corresponding to maximum peak level of the model at about 31 GPa (Figure 9.12a). Above 0.4 Hz, while K_{1D} decreases after the peak to a level of 29.5 GPa, K seems to remain at the peak level at about 32 GPa (Figure 9.12a). As evoked in the previous chapters, despite having large dead volumes, a small pore pressure oscillation was detected during the forced oscillations. The "pseudo-Skempton" coefficient (B^*) in the drainage circuit is therefore non nil (Figure 9.12b), and the model (calculated with the dead volumes conditions) can be adjusted to fit it. This gives an estimated dead volume (one at each end) of $V_d = 44$ mL, which seems reasonable since the volume of each pore-fluid pumps is 200 mL. In order to obtain a drained $K = 21$ GPa with such a dead volume, the model was calculated with a purely drained bulk modulus of $K_d = 20$ GPa, which is solely a difference of 1 GPa. For the thermally cracked sample, K seem to follow more a trend that lies between K_{1D} and K_{1D-g}, with no evidence of peak

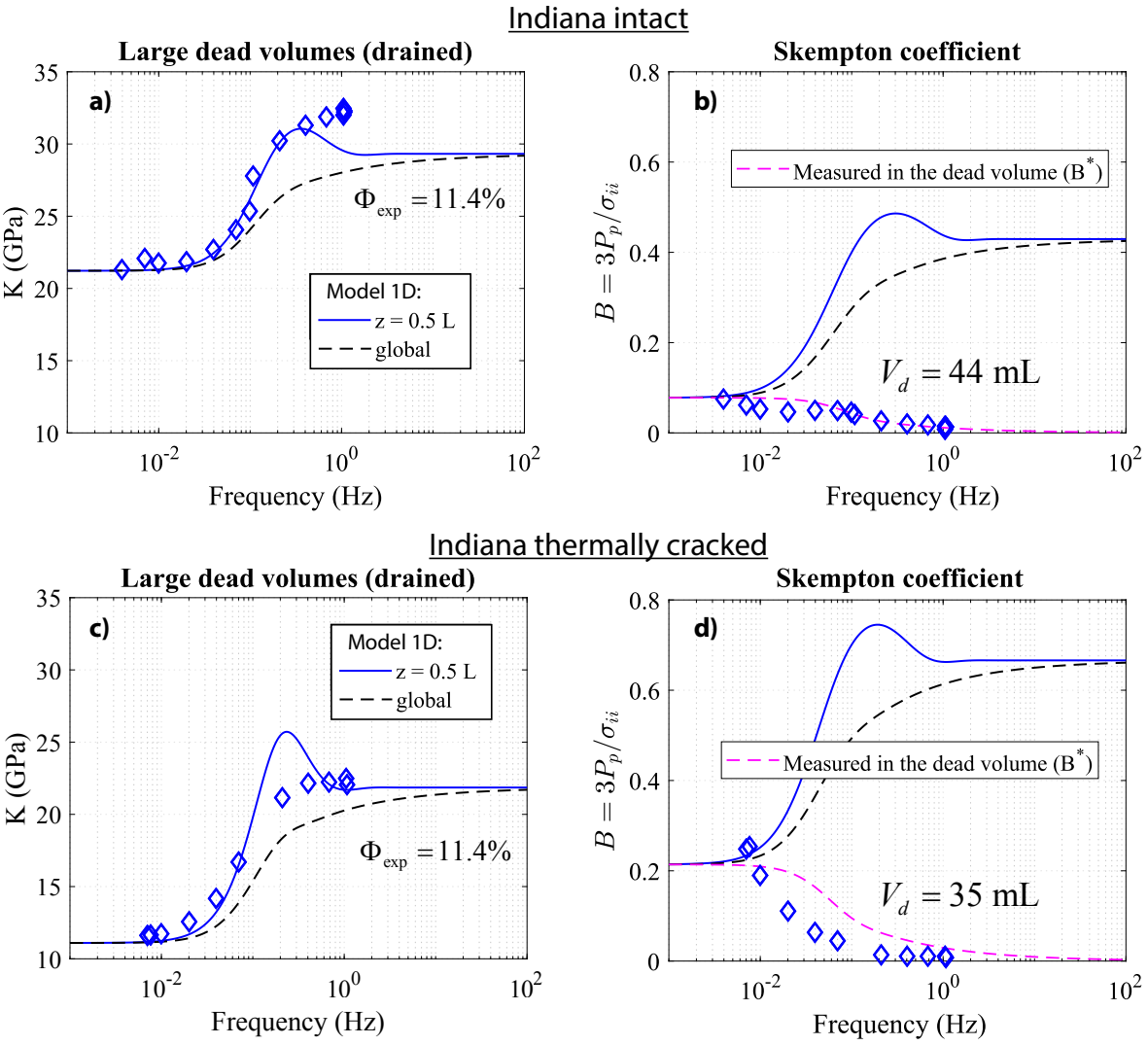

Figure 9.12: Comparison of the bulk modulus, and the pore pressure oscillation, obtained from the 1D drained/undrained model and the experimental hydrostatic oscillation, for the Indiana limestone, intact (a-b) and after thermal cracking (c-d). The experimental results and the model are compared for water-saturated conditions at $P_{diff} = 2.5$ MPa.

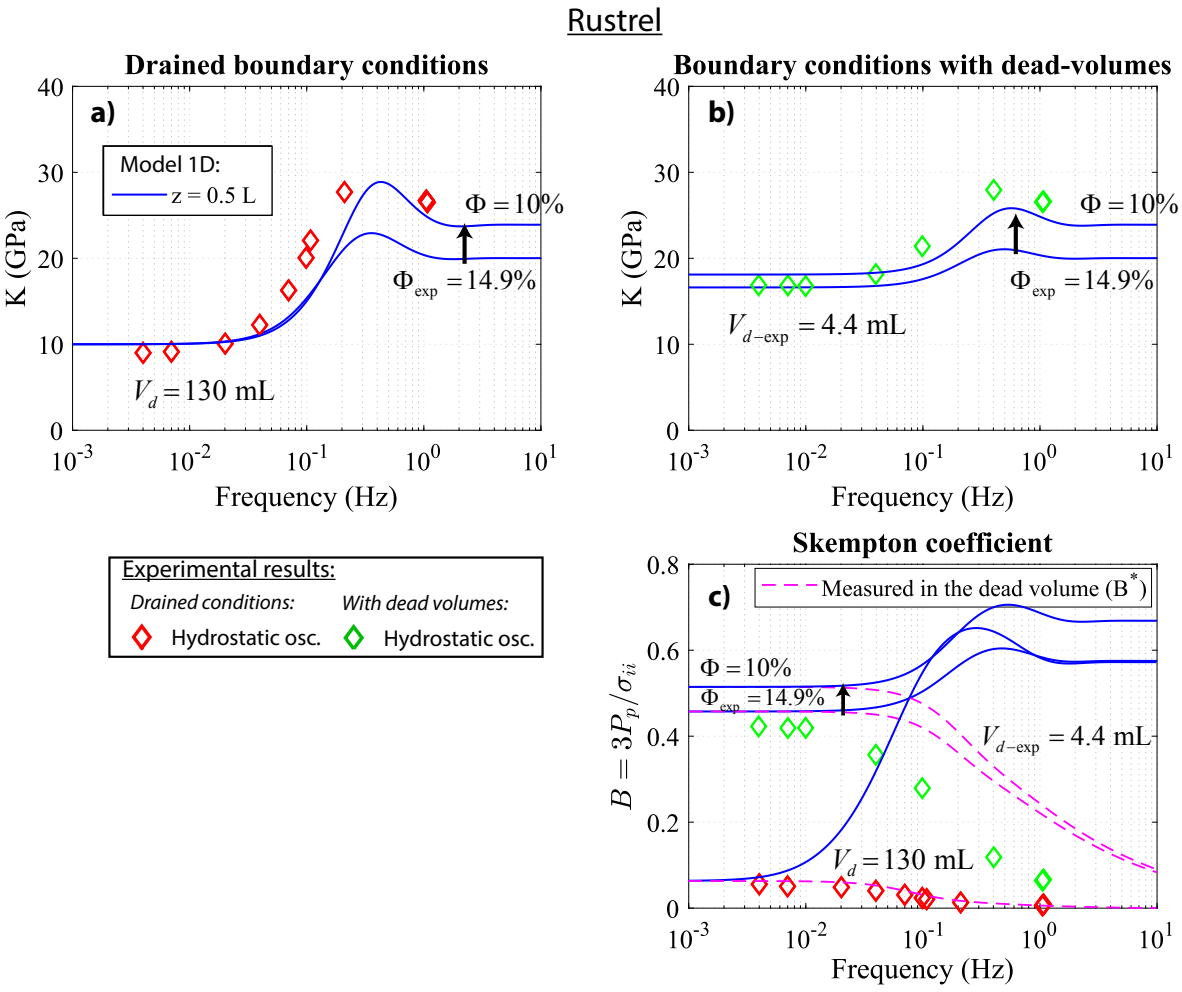

Figure 9.13: Comparison of the bulk modulus obtained from the 1D drained/undrained model and from the experimental hydrostatic oscillations obtained for the Rustrel limestone under drained boundary conditions (a) and small dead volumes (b), along with the pore pressure oscillations (c). The experimental results and the model are compared for water-saturated conditions at $P_{diff} = 2.5\,\text{MPa}$.

(Figure 9.12c). Again, after adjusting the pseudo-Skempton coefficient of the model to fit the experimental measurements, the dead volume was found to be around 35 mL, and the purely drained K_d used to calculate the adjusted model was of 9 GPa, which represents a difference of 2 GPa with the experimental result (Figure 9.12c).

The results for the Rustrel sample are presented Figure 9.13. The sample was measured with the two different boundary configurations. In both cases, when the model is calculated from the measured porosity $\phi_{exp} = 14.9\%$, K_{1D} underestimates the experimental results K (Figures 9.13a and 9.13b). However, in the closed configuration, the model's pseudo-Skempton is consistent with the experimental measurements (Figure 9.13c). Adjusting the porosity to $\phi = 10\%$ would make the model fit perfectly with the measurements, in both

the open and the closed configurations (Figures 9.13a and 9.13b). However, the pseudo-Skempton would deviate from the measurements (Figure 9.13c). This could be explained by local heterogeneity of the pore space that would affect the REV measured by the strain gauge. This would not affect the pseudo-Skempton measurement, as the volume of fluid ejected out of the sample is related to the volumetric deformation of the whole pore space, and therefore gives an average measurement for the whole sample. The discrepancy on the undrained bulk modulus is of maximum 4 GPa. The adjustement of the model for the drained configuration to fit the pseudo-Skempton (Figure 9.13c), gives a dead volume of 130 mL, with a purely drained bulk modulus of 9 GPa.

The results for the Coquina sample are presented Figure 9.14. The drained configuration was perfectly adjusted with a large dead volume of 176 mL and a pure drained bulk modulus of $K_d = 5$ GPa. For such a low drained bulk modulus, the 1D model exhibits a very large peak over 40 GPa (Figure 9.14a). The experimental results do not follow that peak, which is related to the analytical formulation, but follow a more smoothed trend corresponding to K_{1D-g} (Figure 9.14a). In the case of the closed configuration, the model calculated with dead volumes of 4.4 mL seems to overpredict the measurements solely in the drained regime, either for the bulk modulus and for the pseudo-Skempton (Figures 9.14b and 9.14c). Using a dead volume of 14 mL is the only way to perfectly adjust the model to these two measurements, as it concern solely the drained regime with dead volumes (Figures 9.14b and 9.14c). We do not have a proper explanation for such an adjustment. Nevertheless, since it doesn't seem to involve any parameter of the rock, we can conclude that for the drained conditions, K_{1D-g} perfectly predicts the measurements, the peak done by K_{1D} being too high to be physical.

9.8 Comparison of the 1D analytical model with 2D and 3D numerical models

The drained / undrained model presented here makes the assumption of solely vertical flow in the sample, between the upstream and downstream, in order to solve analytically the pore pressure diffusion equation in one dimension (z). Question rises whether this is a limiting assumption for the model, and what would be the impact of radial flow. If we consider the permeability to be isotropic and homogeneous in the whole sample, this question directly relates to the geometry of the boundary conditions (in our case lower and upper surfaces). In our experimental setups, for both the Geodesign and the Top Industrie cell, each endplaten (top and bottom) deliver the pore-fluid through a small drain of 2 mm diameter. Because the samples' diameters are always 40 mm, this necessarily induces a radial flow at the boundary. Question is whether this radial flow occurs within the sample (through a permeability κ), or is the planar contact rock/endplaten permeable enough to homogenize the fluid pressure radially before entering the sample, which would be

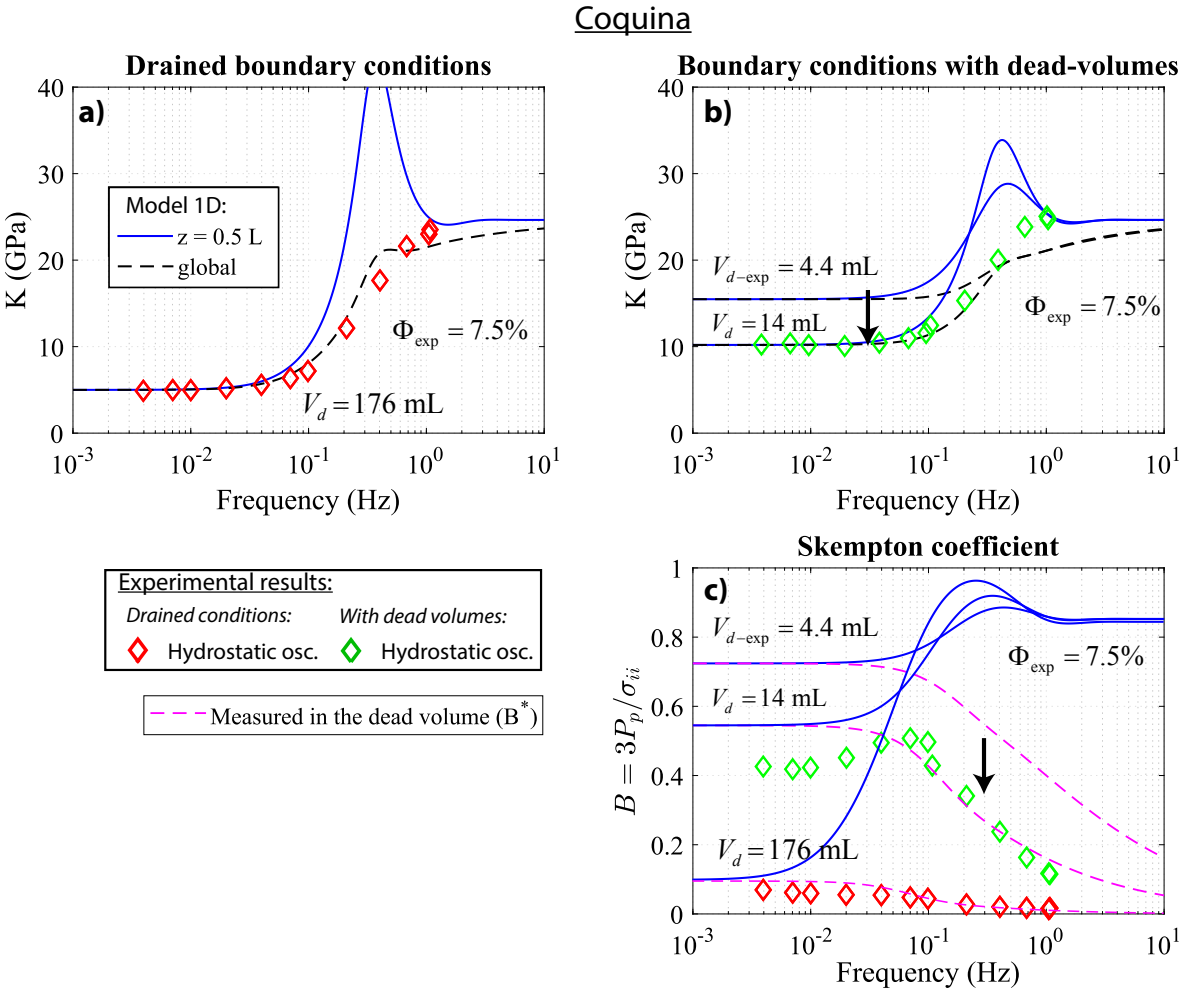

Figure 9.14: Comparison of the bulk modulus obtained from the 1D drained/undrained model and from the experimental hydrostatic oscillations obtained for the Coquina sample under drained boundary conditions (a) and small dead volumes (b), along with the pore pressure oscillations (c). The experimental results and the model are compared for water-saturated conditions at $P_{diff} = 2.5$ MPa.

equivalent to the 1D assumption.

To investigate this, we solved the diffusion equation (Equation 9.15) in 2D and 3D using numerical models, which were tested with purely drained boundary conditions (Dirichlet condition $P_p = 0MPa$). The sample is represented by a cylinder of 80 mm length and 40 mm diameter and is meshed with an unstructured grid (triangles in 2D, tetrahetra in 3D). We used the open-source ONELAB software, which combines the mesh generator Gmsh (*Geuzaine and Remacle*, 2009) and the finite element solver GetDP (*Dular et al.*, 1998). For each model, we considered the contact rock/endplaten to be perfect, so that the permeability of the contact is similar to the rock. This will enforce radial flow within the rock, and we can investigate its possible effect on the measurements of virtual strain gauges on the lateral surface of the sample. The Dirichlet condition ($P_p = 0$) applies only for a small section representing the endplaten drain of 2 mm diameter. We designate by D_b the diameter of this section, as it can be used as a adjusting parameter for the radial flow. The boundary conditions for the lateral jacketed surface, and the endplaten surface around the drain tube are defined with Neumann conditions ($dP/dr = 0$).

The calculation of the frequency dependent bulk modulus from the numerical models follows the same sequence as the 1D analytical model. First, we numerically simulate an oscillation of the confining pressure ($P(t) = \Delta P sin(\omega t)$) over a few periods, and numerically solve the pore pressure oscillation at every point M in the sample's volume (Ω). This is achieved by solving the 2D or 3D diffusion equation followed by the pore pressure p_f:

$$\frac{\partial p_f(M,t)}{\partial t} = D\nabla^2 p_f(M,t) + B\frac{dP(t)}{dt}, \tag{9.19}$$

where D is the hydraulic diffusivity, ∇ the gradient operator, and B the Skempton coefficient (calculated here for a skeleton bulk modulus of 77 GPa). The weak formulation of the diffusion equation (Equation 9.3), necessary for the finite element solver (GetDP), is given by:

$$\int_\Omega \frac{dp_f}{dt}\varphi d\Omega + D\int_\Omega \nabla p_f.\nabla\varphi d\Omega - B\int_\Omega \frac{dP}{dt}\varphi d\Omega = 0, \tag{9.20}$$

where φ is a test function. An example of a full script code for GetDP, implementing Equation 9.20, is given in Annexe D. In a second, we convert the pore pressure numerically solved at each point and time step $p_f(M,t)$ into a local volumetric strain by:

$$\varepsilon_v(M,t) = \frac{P(t) - \alpha p_f(M,t)}{K_d}, \tag{9.21}$$

where α is the Biot coefficient. The local bulk modulus $K^*(M,\omega)$, for these simulated

oscillations of angular frequency ω, is then calculated by:

$$K^*(M,\omega) = \frac{\Delta P}{\Delta \epsilon_v}, \tag{9.22}$$

where ΔP and $\Delta \epsilon_v$ are the amplitudes of the oscillations $P(t)$ and $\varepsilon_v(M,t)$. Like for the experimental measurements, we have to do one oscillating simulation to obtain the bulk modulus for one frequency.

Illustrations of the 2D and 3D pore pressure solution at a maximum peak of a pressure oscillation, calculated for $D_b = 2\,\text{mm}$, are given Figures 9.15 and 9.16 respectively. The frequency was chosen to have a partially undrained sample. For the 2D solution, when radial flow occurs near the top and bottom of the sample, the pore pressure profile along the vertical-central axis is clearly different than the profile on a vertical-lateral axis where the strain gauges are glued (Figure 9.15). The central-vertical p_f profile is drained ($P_p = 0\,\text{MPa}$) at both extremities, while the lateral-vertical p_f and is not drained at the extremities (Figure 9.15). The similar observation can be made for the 3D model (Figure 9.16) where only the central-vertical axis sees drained conditions at its top and bottom end.

The 2D model was tested with $D_b = 2\,\text{mm}$ to enforce radial flow, and $D_b = 40\,\text{mm}$ to verify the consistency with the 1D model. The 3D model was tested solely for $D_b = 2\,\text{mm}$. The dispersion of the bulk modulus obtained from two virtual strain gauges on the lateral surface of the sample, one at mid-height ($z = 0.5L$), and one close to the boundary conditions ($z = 0.1L$), are presented Figure 9.17, and are compared with the 1D analytical model. The input parameters correspond to the Lavoux limestone under glycerine saturation, with $K_d = 16\,\text{GPa}$, $K_S = 77\,\text{GPa}$, $\kappa = 10^{-14}\,\text{m}^2$, $\phi = 24\%$, $K_{fl} = 4.36\,\text{GPa}$ and $\eta = 1.083\,\text{Pa.s}$.

The results from all models show consistent values for the drained and the undrained bulk modulus for both strain gauges, only the drained/undrained cut-off frequencies seems to differ (Figure 9.17). We first note that the 2D model calculated with $D_b = 40\,\text{mm}$ is consistent with the 1D model for both strain gauges, with a large effect of the vertical position, but doesn't exhibit the 1D model's peak before reaching the undrained value (Figure 9.17). When $D_b = 2\,\text{mm}$, the cut-off frequencies are all lower, and the vertical position of the strain gauge has nearly no effect, either for the 2D and the 3D model (Figure 9.17). We observe that the cut-off frequency of the 3D model is even lower than for the 2D model when $D_b = 2\,\text{mm}$. This is due to the accumulation of two radial flux components near the endplaten drains in 3D, instead of only one radial flux component in 2D. In order words, the 2D model is simply infinite in the third direction.

9.9 Final conclusions

The 1D analytical model for the drained / undrained transition proved to be a powerful tool to determine the poroelastic parameters of the sample, not only by adjusting the elastic

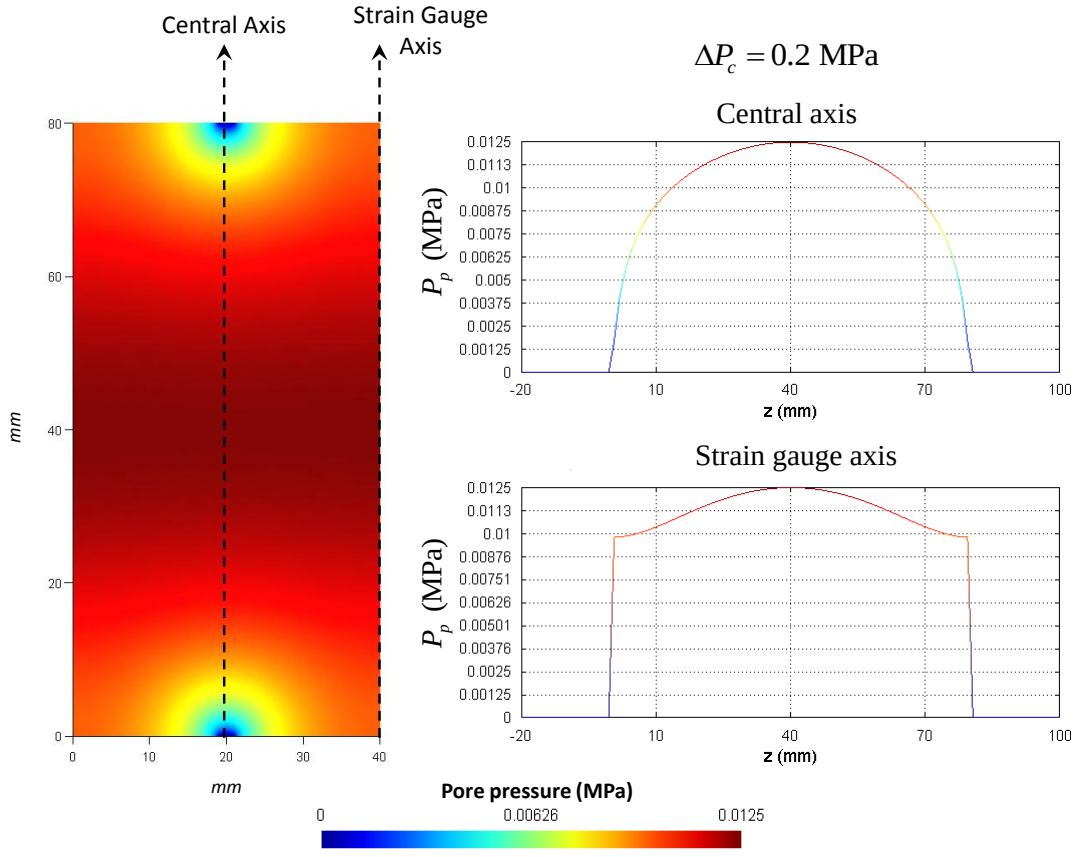

Figure 9.15: Example of a numerical calculation in 2D, with the hypothesis of Dirichlet boundary conditions only in front of the drainage tubes of diameter 2 mm in the upper and lower endplatens.

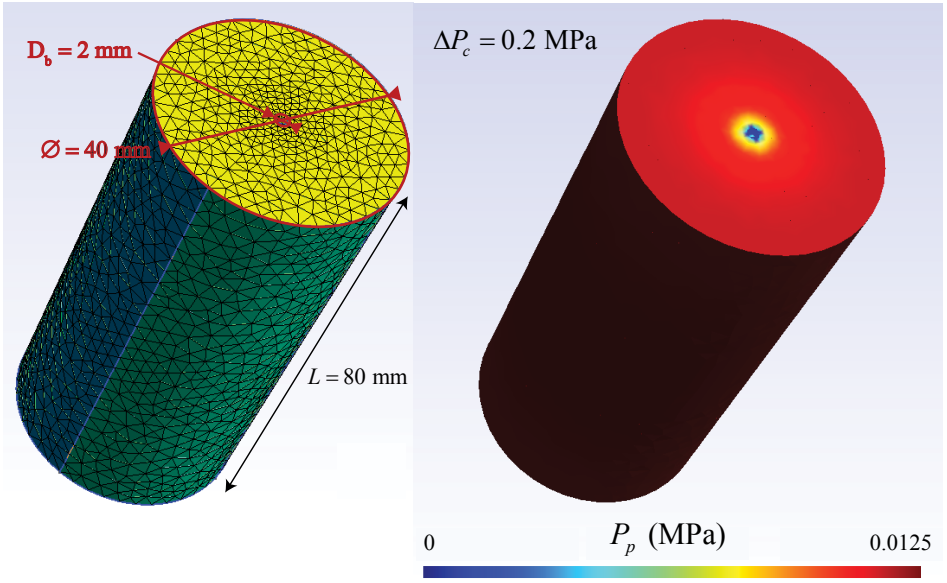

Figure 9.16: Example of a numerical calculation in 3D, with the hypothesis of Dirichlet boundary conditions only in front of the drainage tubes of diameter 2 mm in the upper and lower endplatens.

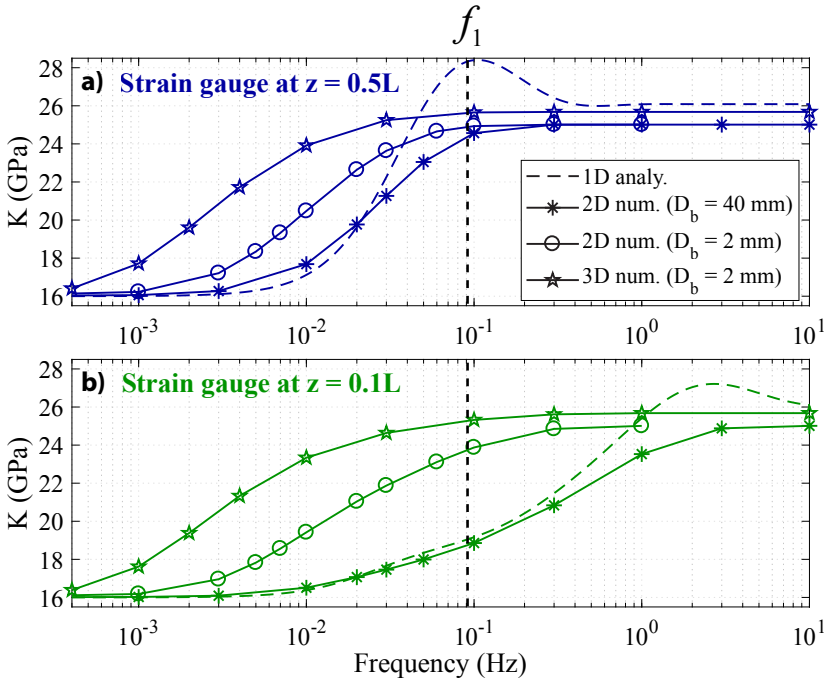

Figure 9.17: Comparison of the 1D analytical model with 2D and 3D numerical models for two virtual strain gauges, one glued at mid-height ($z = 0.5L$) (a), and the other glued near a boundary condition ($z = 0.1L$) (b). The input parameters correspond to the Lavoux limestone under glycerin-saturated conditions at $P_{diff} = 2.5\,\text{MPa}$ ($K_d = 16\,\text{GPa}$, $K_S = 77\,\text{GPa}$, $\kappa = 10^{-14}\,\text{m}^2$, $\phi = 24\%$, $K_{fl} = 4.36\,\text{GPa}$ and $\eta = 1.083\,\text{Pa.s}$).

properties, but also by adjusting the pore pressure output in a boundary dead volume. The confrontation of the model with the carbonate samples, gave general good results since the undrained bulk moduli were consistent with Biot-Gassmann's equations.

Most importantly, the cut-off frequencies of the experimental results were consistent with the 1D model. This suggests that there is little radial flow occurring within the sample in our experimental setups, as the numerical models proved that a radial flow would lower the cut-off frequency. Some complementary results confirming this matter can be found in the Figure 10 of the Appendix B, where the drained/undrained transition of the Poisson's ratio of a sandstone was measured with strain gauges glued at different vertical positions (one mid-height, one close to the boundary). The results are in agreement with our conclusions.

CHAPTER 10

EFFECTIVE MEDIUM APPROACH TO MODEL THE ELASTIC DISPERSION RELATED TO FLUID-FLOWS AT DIFFERENT SCALES: SQUIRT FLOW AND GLOBAL DIFFUSION.

10.1 Résumé

Dans ce chapitre, nous présentons un modèle simple qui permet de prédire la dispersion de tous les modules élastiques, en conditions isotropes, pour les transitions drainé / non-drainé et non-drainé / non-relaxé. Tous les paramètres d'entrées sont directement ou indirectement mesurables. Il n'y a donc pas de paramètre libre d'ajustement. Le modèle est basé sur les milieux effectifs de fissures orientées aléatoirement avec l'hypothèse de non-interaction entre les inclusions. Les avantages de ce milieu effectif est la simplicité du formalisme, notamment pour inclure l'effet du fluide, et la possibilité d'être étendue à l'anisotropie.

La première étape consiste à déterminer la distribution de facteurs de forme et des densités de cracks. La méthode de Morlier est une technique pour faire ceci, en exploitant la dépendance en pression du module K en sec. Le milieu effectif est simplifié pour être limité à un unique facteur de forme. Le milieu est assimilé à des fissures incluses dans une matrice d'arrière plan poreuse. Par des séquences d'homogénéisations, on peut résoudre l'écoulement crack-pore comme si les pores étaient drainés dans une matrice modifiée. Cela permet de calculer la contribution du fluide dans les cracks. Pour résoudre l'équation de diffusion de l'écoulement crack-pore, un modèle micromécanique simplifié est utilisé. Enfin, on utilise la poroélasticité pour rajouter la contribution du fluide dans les pores précédemment drainés. Cette dernière étape utilise le modèle poroélastique 1D développé dans le chapitre précédent.

Les comparaisons du modèle avec les résultats sur les calcaires ont montré que, en règle générale, les amplitudes de dispersions sont bien prédites, mais prédire la fréquence

de coupure de la seconde transition se révèle plus délicat. En effet, la prédiction s'est montrée convenable pour l'Indiana après craquage thermique et le coquina, mais a sensiblement sous-estimée la seconde fréquence de coupure pour l'Indiana intact et le Rustrel. Ceci peut s'expliquer par la simplicité du modèle micromécanique de crack, qui semble bien s'appliquer à des fissures générés thermiquement dans des gros cristaux ou des contacts entre grains homogènes. Les textures plus hétérogènes dans les zones microporeuses semblent avoir une relation différente entre les propriétés mécaniques et hydrauliques.

10.2 Introduction

The dispersion of the elastic properties are related to the fluid flows occurring at different scales in the porosity. Two scales are considered here: the global flow between REVs, and the squirt flow within the REV that equalizes the fluid's pressure between the compliant cracks and the stiff pores. Three regimes are generally considered when considering these two scales: the drained, the undrained, and the unrelaxed regimes (*Pimienta et al.*, 2015a; *Borgomano et al.*, 2017). The undrained and the unrelaxed regimes refer to respectively the saturated isobaric and the saturated isolated regimes described by *O'Connell and Budiansky* (1977). The drained regimes occurs at low frequency where the global diffusion has time to equalize the fluid between all the REVs. The undrained regime occurs at intermediate frequencies when there is no time for global diffusion: the REVs are disconnected from each other, but squirt flow has still time to equalize pressure within the REV. The unrelaxed regime occurs at high frequency when both the global and the squirt flow have no time to diffuse, and the inclusions are like isolated from one another.

The objective is to have an unique model, derived from a simple squirt-flow model and the previous 1D drained/undrained model, to predict the elastic dispersion related to both mechanisms, starting from a microstructural description of the sample, which in theory could be deduced from the pressure dependence of the dry bulk modulus. We choose to derive the squirt-flow model of *Gurevich et al.* (2010), since its formulation is rather simple and the general approach is compatible with *Gassmann* (1951) low-frequency and *Mavko and Jizba* (1991) high-frequency limits. The microstructure will therefore be considered binary, with compliant cracks responsible for the pressure-dependence of the elastic moduli, and stiff pores that correspond to the rest of the porosity.

The first step is to translate the mechanical response of the sample into an equivalent effective medium of equant pores and spheroidal cracks, which will give the microstructural parameters of the representative elementary volume (REV). The second step is to consider the global diffusion and how it affects the overall pore pressure in the REV. The third step is to consider the squirt-flow occurring between the cracks and the pores within the REV with the same approach of *Gurevich et al.* (2010) and combine it with 1D poroelastic model for the drained/undrained transition. The squirt-flow diffusion and the global diffusion are solved in parallel in order to be representative of the experimental measurements.

10.3 Characterization of the microstructure for different confining pressures

We want to characterize the effective medium, composed of randomly orientated cracks embedded in a porous background matrix, which has the equivalent elastic properties of our sample. It is essential to determine the aspect ratios of the cracks as this controls the

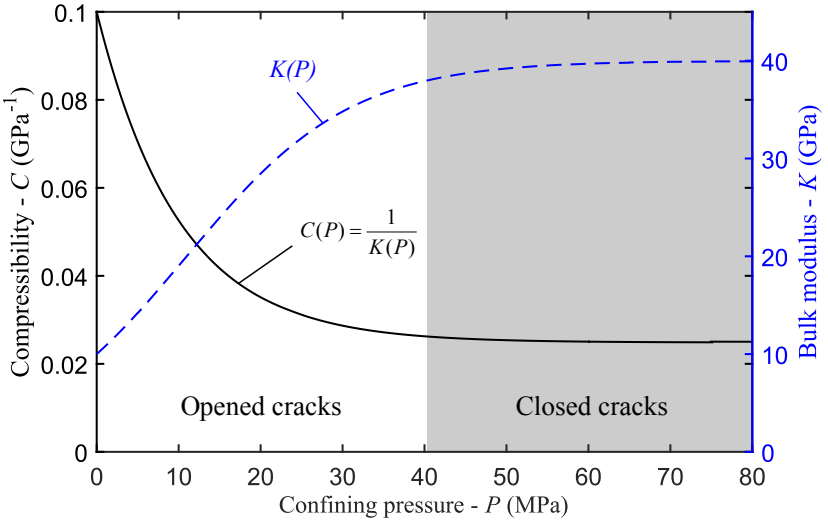

Figure 10.1: Typical pressure dependence of the compressibility (black) or bulk modulus (blue) of a cracked medium. While undergoing a hydrostatic compression, the bulk modulus increase as the cracks are progressively closing, then reaches a maximum when all the cracks are closed.

relaxation time of squirt-flow we want to model. In the approach of *Gurevich et al.* (2010), the crack aspect ratio is considered as an adjustement parameter. In our case, we want to constrain it by analyzing the pressure dependence of the bulk modulus. Similarly to the method from *Walsh* (1965), a crack porosity and the aspect ratios of the cracks can be extracted from the trend of this pressure dependence. When the confining pressure increases, the typical evolution of a rock's bulk modulus is an increase in the first phase, with the closure of cracks, before reaching a maximum value where the bulk modulus becomes independent of pressure (Figure 10.1).

A method first presented by *Morlier* (1971) enables to determine the distribution of initial aspect ratios of the cracks present in the medium. Details of the method have been presented by *Jaeger et al.* (2009). As presented previously (Equation 1.27), for a low concentration of penny-shape cracks, we have the compressibility of the effective medium given by (*Walsh*, 1965):

$$C(\rho) = C_S + \rho \frac{16(1-{\nu_S}^2)}{9(1-2\nu_S)} C_S, \tag{10.1}$$

where ρ is the crack density, C_S and ν_S are respectively the compressibility and Poisson's ratio of the skeleton. The addition of equant (spherical) pores to the medium that are non-closable would contribute to an additional compressibility term that is independent of pressure. This term could be incorporated in C_S without changing the following analysis. The closure pressure of a penny-shape crack of initial aspect ratio ξ is given by (*Jaeger et al.*,

2009):

$$P(\xi) = \frac{3\pi}{4}\frac{(1-2\nu_S)}{(1-{\nu_S}^2)}\frac{\xi}{C_S} \tag{10.2}$$

If we assume that the sample is at a pressure P, the crack density ρ represents the cracks whose aspect ratios were initially higher than $P \times 4(1-\nu_S^2)C_S/(3\pi(1-2\nu_S))$ (Equation 10.2). With the use of the chain rule, the aspect ratio distribution function $\gamma(\xi)$ is given by:

$$\gamma(\xi) = -\frac{d\rho}{d\xi} = -\left(\frac{d\rho}{dC}\right)\left(\frac{dC}{dP}\right)\left(\frac{dP}{d\xi}\right). \tag{10.3}$$

From Equation 10.1 we have $d\rho/dC = 9(1-2\nu_S)/(16(1-\nu_S^2)C_S)$, and from Equation 10.2 we have $dP/d\xi = 3\pi(1-2\nu_S)/(4(1-\nu_S^2)C_S)$. Equation 10.3 can be written as:

$$\gamma(\xi) = \frac{-3}{4\pi}\left(\frac{3\pi(1-2\nu_S)}{4(1-{\nu_S}^2)C_S}\right)^2 \frac{dC}{dP}\bigg|_{P=P^*} \tag{10.4}$$

where dC/dP has to be evaluated at the crack closing pressure P^* corresponding to the aspect ratio ξ (Equation 10.2). This derivative is obtained from the experimental results of the hydrostatic compression. An exponential function of the form:

$$C(P) = (C_i - C_S)\exp(-P/\hat{P}) + C_S, \tag{10.5}$$

can be adjusted to the data, where C_i is the initial compressibility (at $P = 0\,\text{MPa}$) where all the cracks are open, C_S is the final compressibility (when $P \to \infty$) where all the cracks are closed, and $\hat{P}$ is the characteristic pressure of the crack closure (Figure 10.2a). Although this should be applied to the hydrostatic loading, which by definition gives the evolution of a static bulk modulus with pressure, we will apply this method to adjust the pressure dependence of the dry dynamic bulk modulus obtained from hydrostatic oscillations, since we attempt to model the effective dynamic properties.

To take into account the real porosity of the sample, additional porosity ϕ_S can be embedded in the background C_S. This aspect will be considered in the next section. From Equation 10.4 and 10.5 we obtain:

$$\gamma(\xi) = \frac{3}{4\pi}\left(\frac{3\pi(1-2\nu_S)}{4(1-{\nu_S}^2)C_S}\right)\frac{(C_i - C_S)}{\hat{\xi}}\exp\left(\frac{-\xi}{\hat{\xi}}\right), \tag{10.6}$$

where $\hat{\xi}$ is related to $\hat{P}$ by Equation 10.2. The initial crack density of cracks whose aspect ratios are initially between ξ and $\xi + d\xi$ is $d\rho = \gamma(\xi)d\xi$. If all the cracks are assumed to have the same radius, $d\rho$ corresponds to a crack porosity of $d\phi = (4/3)\pi\xi d\rho$ if we consider spheroidal cracks. Therefore, the crack porosity distribution function (Figure 10.2b) is given by:

$$\tilde{c}(\xi) = \frac{d\phi}{d\xi} = \frac{4\pi\xi}{3}\gamma(\xi) = \frac{3\pi(1-2\nu_S)}{4(1-{\nu_S}^2)}\frac{(C_i - C_S)}{C_S}\frac{\xi}{\hat{\xi}}\exp\left(\frac{-\xi}{\hat{\xi}}\right), \tag{10.7}$$

and the total crack porosity can be calculated by (*Jaeger et al.*, 2009):

$$\phi_{crack} = \int_0^1 \tilde{c}(\xi) d\xi \approx \hat{P}(C_i - C_S). \tag{10.8}$$

The microstructure given by Equation 10.7 describes all the cracks that are open when $P = 0\,\text{MPa}$. Because, we want to characterize the elastic dispersion related to fluid flow at different effective pressures, we need to have the distribution of open cracks of the same sample at these given pressures. A simple way to do this is to shift the origin of the hydrostatic compression at the pressure P_0 we want to describe, and to repeat the analysis done previously (Figure 10.2a). Because the pressure sensitivity is unchanged, $\hat{\xi}$ and C_S remain constant (if we keep using the exponential function), and the term C_i changes with the change of P_0, with $C_i = C(P_0)$ (Equation 10.5). The crack porosity distribution of the open cracks at P_0 becomes (Equation 10.7):

$$\tilde{c}(\xi, P_0) = \frac{3\pi(1-2\nu_S)}{4(1-{\nu_S}^2)} \frac{(C(P_0) - C_\infty)}{C_S} \frac{\xi}{\hat{\xi}} \exp\left(\frac{-\xi}{\hat{\xi}}\right). \tag{10.9}$$

Moreover, the total porosity becomes $\phi_{crack}(P_0) = \hat{P}(C(P_0) - C_S)$ (Equation 10.8). Illustration of the procedure is presented in Figure 10.2, for $\nu_S = 0.1$, $K_i = 10\,\text{GPa}$, $K_S = 40\,\text{GPa}$, and $\hat{P} = 15\,\text{MPa}$. The distribution of cracks calculated at pressures $P_0 = [0\,;10\,;20\,;30\,;40]\,\text{MPa}$ are presented Figure 10.2b. The total crack porosity for each pressure are respectively $\phi_{crack}(P_0) = [1.13\,;0.58\,;0.30\,;0.15\,;0.08] \times 10^{-3}$ (Equation 10.8). For $P_0 = 40\,\text{MPa}$, the analysis of the compression curve with a change of origin is represented Figure 10.2a. The distribution $\tilde{c}(\xi, P_0)$ is calculated from the segment of $C(P)$ that is above P_0 (Figure 10.2a), with P_0 now considered the initial state of the medium. The porosity of the crack families decrease with the increase of pressure (Figure 10.2b), and the distributions remain centered around the same characteristic aspect ratio $\hat{\xi} = 0.2 \times 10^{-3}$ (Equation 10.2). This would not necessarily be the case if $C(P)$ couldn't be fitted by an exponential function (Equation 10.5), for example if multiple curvatures are present in the pressure trend.

Note here that the equation for $\tilde{c}(\xi, P_0)$ (Equation 10.9) is greatly simplified by the use of the exponential fit for $C(P)$ (Equation 10.5). The use of this function might not always be adapted for the experimental trend of the bulk modulus with pressure, for example if a second family of larger cracks keep influencing the compressibility of the rock at greater pressures (e.g., *De Paula et al.*, 2012). The use of this function forces the distribution to be centered around one family of cracks, which shall be used for the purpose of the squirt-flow modelling.

A more general approach was proposed by *David and Zimmerman* (2012) to describe the evolution of the crack aspect ratios with pressure. Their method demonstrates that the relation between the closure pressure and the aspect ratio of a crack is not necessarily

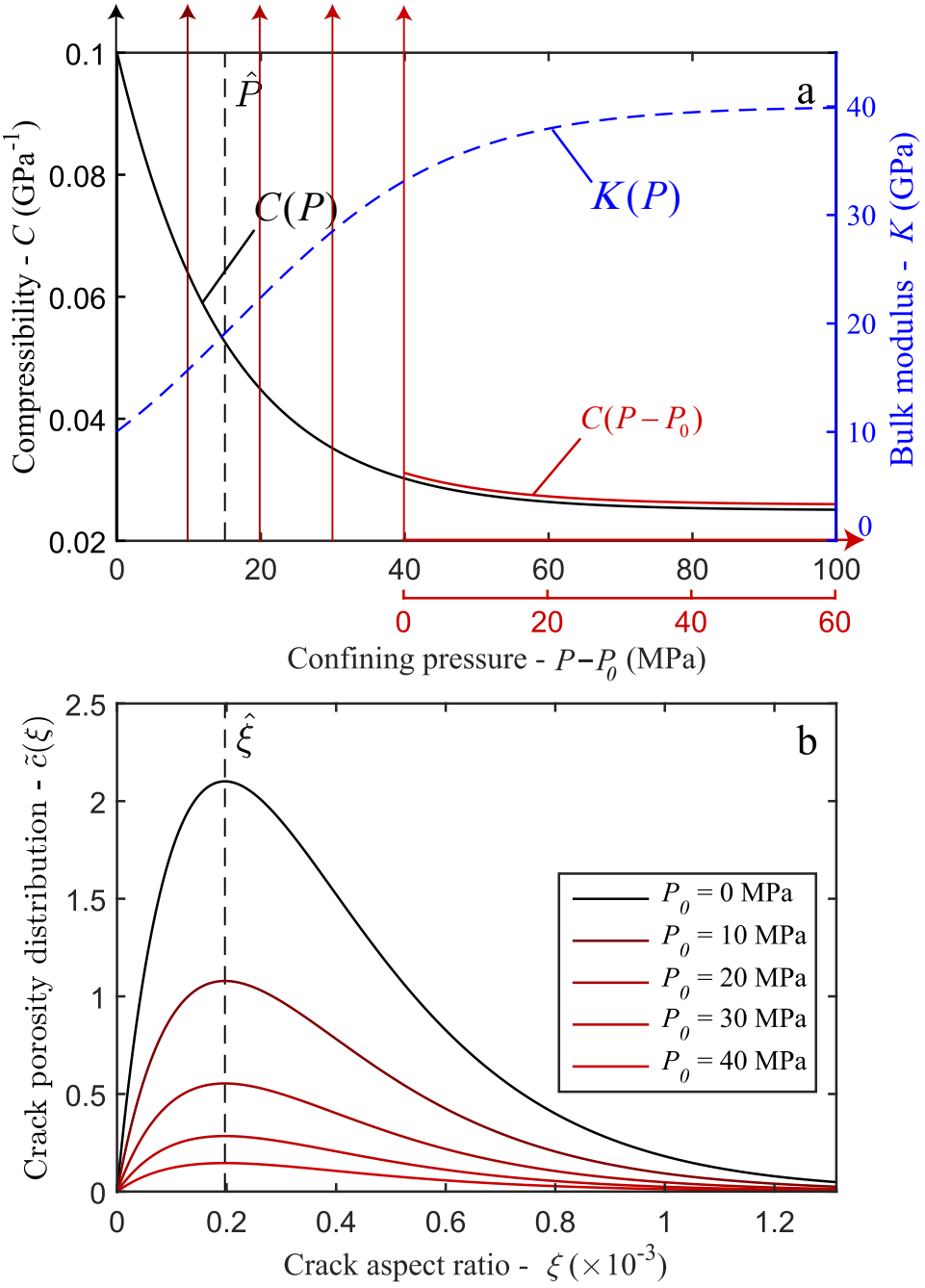

Figure 10.2: (a) Compressibility $C(P)$ of the sample as a function of pressure P (black), fitted by an exponential function with the parameters $K_i = 10\,\text{GPa}$, $K_S = 40\,\text{GPa}$, $\nu_S = 0.1$, and $\hat{P} = 15\,\text{MPa}$ (Equation 10.5), and the corresponding bulk modulus $K(P)$ (blue). (b) Deduced crack porosity distribution functions $\tilde{c}(\xi, P_0)$ at different pressures $P_0 = [0\,;10\,;20\,;30\,;40]\,\text{MPa}$ from Morlier's method (Equation 10.11). At a pressure P_0, the crack distribution is deduced from the function $C(P)$ as if the initial pressure was P_0. The characteristic aspect ratio $\hat{\xi} = 0.2 \times 10^{-3}$, and the respective total crack porosities $\phi_{crack}(P_0) = [1.13\,;0.58\,;0.30\,;0.15\,;0.08] \times 10^{-3}$.

linear, as presented here with Equation 10.2. Instead of using the hydrostatic compression, they invert the compressibilities from the ultrasonic velocities, and calculate a crack closure function depending on the pressure increment. They show that the decrease of aspect ratio with pressure is independent of the aspect ratio of the crack considered. In other words, all crack aspect ratios decrease by the same amount between two pressure stages (*David and Zimmerman*, 2012).

10.4 Effective medium: cracks in a porous matrix

Let us consider the case where the pressure dependence of the bulk modulus can be fitted by an exponential function (Equation 10.5). We assume here that the aspect ratio distribution of all the families of cracks are centered around $\hat{\xi}$. The compressibility at $P = 0\,\text{MPa}$ is C_i and the compressibility at infinite pressure is C_S. The solution of crack aspect ratio distribution, and by extension the total crack porosity, given by Equation 10.9 is valid for cracks in a background matrix of compressibility C_S. For simplification, the effective medium of randomly orientated cracks (Equation 10.1) shall be described by the characteristic family of aspect ratio $\hat{\xi}$ solely, and the total porosity of cracks $\phi_{crack}(P_0)$, which depends on the confining pressure. The crack density used in the effective medium, given by Equation 10.1, is calculated by (Equations 10.6 and 10.8):

$$\rho(P_0) = \int_0^1 \gamma(\xi) d\xi = \frac{\phi_{crack}(P_0)}{\frac{4}{3}\pi\hat{\xi}}, \tag{10.10}$$

as $\int_0^1 \exp(-\xi/\hat{\xi}) d\xi \approx \hat{\xi}$ for $\hat{\xi} \ll 1$. We therefore have (Equation 10.1):

$$C(P_0) = C_i = C_S + \frac{\phi_{crack}(P_0)}{\frac{4}{3}\pi\hat{\xi}} \frac{16(1-{\nu_S}^2)}{9(1-2\nu_S)} C_S. \tag{10.11}$$

Although the matrix compressibility C_S should be taken as equal to the mineral compressibility C_m when modeling the real samples, it is very rare to experimentally reach $C_S = C_m$ during a hydrostatic compression (Figure 10.3). The bulk modulus found at high pressure ($K_S = 1/C_S$) when the compressibility becomes independent of pressure, is generally lower that $K_m = 1/C_m$ (Figure 10.3). This can be explained by additional compressibility that is not related to the previous cracks, but related to the rest of the sample's porosity (ϕ_S), which is much less compressible and relatively pressure independent. K_S is also affected by the stiffness of the grain contacts.

For the purpose of modelling a real sample of total porosity $\phi_{tot} = \phi_S + \phi_{crack}$, the crack distribution is calculated in a background matrix of bulk modulus K_S. This matrix contains the residual porosity ϕ_S that is considered stiff, relatively incompressible when compared to the cracks, and pressure independent. ϕ_S explains the difference between K_S and K_m

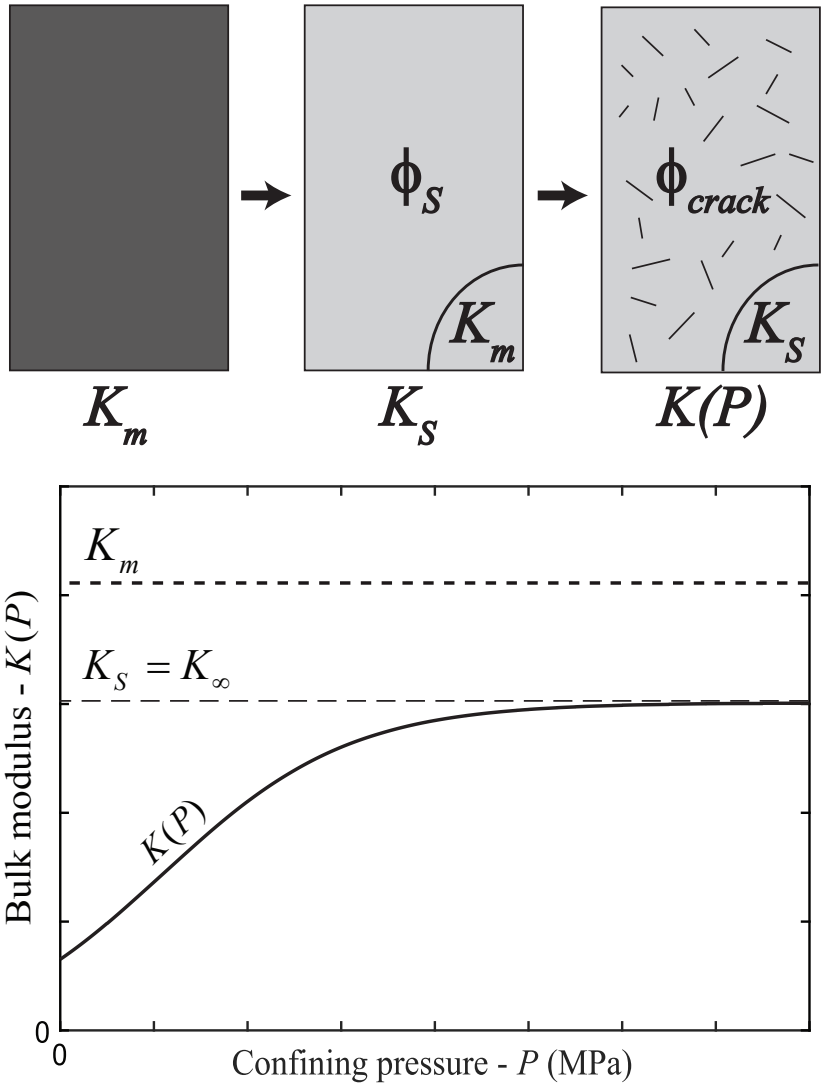

Figure 10.3: Sketch of the effective medium model, and pressure dependence of the bulk modulus. A porosity ϕ_S is embedded in a mineral of modulus K_m, and gives a homogeneous matrix of modulus K_S. The cracks are then embedded in this latter matrix. Relatively to cracks, ϕ_S is considered incompressible, as its effect on the elastic properties is accounted for in K_S. Moreover, K_S is considered pressure independent, and equal to the bulk modulus of the medium when all the cracks are closed. The pressure dependence of $K(P)$ is therefore solely due to the cracks.

(Figure 10.3). Although ϕ_S is considered stiff, it will still be sensible to the presence of an undrained fluid. The calculation of the effective compressibility of the saturated medium, which includes the cracks and the porous background, will require to apply poroelasticity to the background pores (ϕ_S).

It was demonstrated by *Adelinet et al.* (2011) that the effective compressibility in fluid-saturated conditions of a cracked medium (C_{cr}), of crack density ρ, in the case of isolated and randomly oriented inclusions of aspect ratio $\hat{\xi}$, is given by:

$$C_{cr} = C_S + \rho \frac{16(1-{\nu_S}^2)}{9(1-2\nu_S)} C_S \left(\frac{\delta_c}{1+\delta_c} \right), \tag{10.12}$$

with δ_c, a parameter used to characterize the coupling between matrix compliance (C_S), fluid compressibility (C_{fl}) and crack geometry ($\hat{\xi}$). It corresponds to an effective medium developed by *Kachanov* (1993), based on ellipsoids in the framework of non-interaction approximation. This parameter is equal to (*Adelinet et al.*, 2011):

$$\delta_c = \frac{3\pi(1-2\nu_S)}{4(1-{\nu_S}^2)} \frac{\hat{\xi}}{C_S} \left(C_{fl} - C_S \right). \tag{10.13}$$

We can note that $C_{cr} = C$ when $C_{fl} \to +\infty$ (dry cracks), and $C_{cr} = C_S$ when $C_{fl} = C_S$ (absence of cracks) (Equations 10.12 and 10.13). *Adelinet et al.* (2011) also demonstrated that the shear modulus of such medium is given by:

$$\frac{1}{G_{cr}} = \frac{1}{G_S} + \frac{\rho}{G_S} \left[\frac{16(1-\nu_S)}{15\left(1-\frac{\nu_S}{2}\right)} + \frac{32(1-\nu_S)}{45} \left(\frac{\delta_c}{1+\delta_c} \right) \right], \tag{10.14}$$

where G_S is the shear modulus of the matrix. The dry shear modulus G is obtained from Equation 10.14 when $C_{fl} \to +\infty$, i.e., when $\delta_c \to \infty$ (Equation 10.13).

The porosity ϕ_S is embedded in the mineral background K_m (Figure 10.3). Similarly to Gurevich's model, the effective compressibility of the whole medium that includes the cracks and the background porosity in undrained conditions, will then be calculated by applying poroelasticity to ϕ_S.

10.5 Frequency dependent fluid-flow at different scales

Our objective is to model the drained/undrained and the undrained/unrelaxed transitions, in a single formalism, for the microstructure characterized in Section 3. For this, the frequency dependence of the local and the global diffusions will be solved separately. Then, their effect on the elastic properties will be combined to obtain a single formalism that accounts for local and global diffusion.

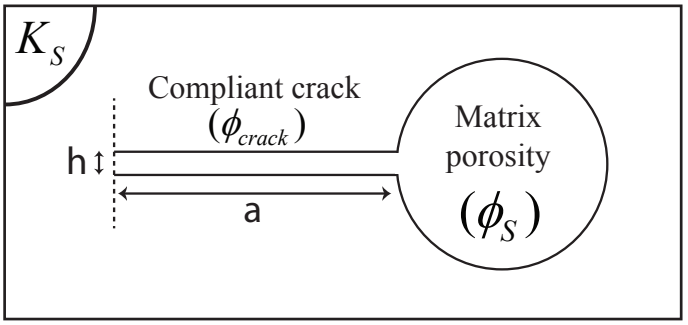

Figure 10.4: Sketch of the model configuration (*Murphy III et al.*, 1986; *Gurevich et al.*, 2010). The compliant crack forms a disc-shaped gap in the matrix of modulus K_S, and its edge opens into the matrix porosity ϕ_S, which is considered here incompressible.

10.5.1 Squirt-flow from the cracks to the drained matrix porosity

The squirt-flow model here follows the logic of the squirt-flow model presented by *Gurevich et al.* (2010), but uses a different formalism. The results are expected to be analogue, and the use of this formalism will be discussed at the end of the section.

We study here the squirt flow occurring between the saturated compliant cracks and the matrix porosity ϕ_S considered drained (or dry). We assume here a particular geometry that was used by *Murphy III et al.* (1986) and *Gurevich et al.* (2010). The compliant crack forms a disc-shaped gap in the matrix of modulus K_S, and its edge opens into the matrix porosity ϕ_S (Figure 10.4). The height of the crack is h, and its radius is a (Figure 10.4).

For a sinusoidal loading $\Delta h \exp(i\omega t)$ of frequency $f = \omega/2\pi$, *Murphy III et al.* (1986) and *Gurevich et al.* (2010) showed that the fluid pressure p in the crack can be obtained as a solution of the differential equation:

$$\frac{d^2p}{dr^2} + \frac{1}{r}\frac{dp}{dr} + k^2 p = H, \tag{10.15}$$

where r is the radial coordinate, $H = i\omega D \Delta h$ where Δh is the displacement amplitude of the crack, $D = 12\eta/h^3$ is the viscous resistance, η being the dynamic viscosity of the fluid, and k is the wavenumber given by:

$$k^2 = \frac{-i\omega h D}{K_{fl}}. \tag{10.16}$$

The inertial terms were all ignored here, as they are much smaller than the viscous resistance terms, for the small gaps and for the studied frequency range. *Murphy III et al.* (1986) showed that in a worse case scenario, the ratio of inertial to viscous terms is 0.1 for a gap of 100 nm at 10 MHz.

When the REV is drained, the solution of Equation 10.15 is given by (*Gurevich et al.*, 2010):

$$p(r,t) = -K_{fl}\frac{\Delta h}{h}\left(1 - \frac{J_0(kr)}{J_0(ka)}\right), \tag{10.17}$$

where J_0 and J_1 are Bessel's functions of the first kind of order 0 and 1. For a crack aspect ratio $\hat{\xi} = h/(2a)$, we have (Equation 10.16):

$$ka = \frac{1}{\hat{\xi}}\sqrt{\frac{-3i\omega\eta}{K_{fl}}}. \tag{10.18}$$

The equivalent force ΔF on the crack's surface is given by:

$$\Delta F = 2\pi\int_0^a p(r,t)rdr = -\pi a^2 K_{fl}\frac{\Delta h}{h}\left(1 - \frac{J_1(ka)}{\frac{ka}{2}J_0(ka)}\right), \tag{10.19}$$

and the additional effective stiffness K^* it gives to the crack, can be calculated by (*Gurevich et al.*, 2010):

$$K^* = \frac{\Delta F}{-\Delta h} = \frac{\pi a^2}{h}K_{fl}\left(1 - \frac{J_1(ka)}{\frac{ka}{2}J_0(ka)}\right). \tag{10.20}$$

We can observe here that in the limit of high frequency ($\omega \to \infty$), Equation 10.20 becomes:

$$K^* = \frac{\Delta F}{-\Delta h} = \frac{\pi a^2}{h}K_{fl}, \tag{10.21}$$

which corresponds to an isolated inclusion. Therefore, for all the frequencies, we can define a virtual fluid, of frequency-dependent bulk modulus $K^*_{fl}(\omega)$, which would give the same additional stiffness to the crack K^*, but as if the crack was isolated (e.g., *Gurevich et al.*, 2010). From Equations 10.20 and 10.21, we can deduce:

$$K^*_{fl}(\omega) = K_{fl}\left(1 - \frac{J_1(ka)}{\frac{ka}{2}J_0(ka)}\right). \tag{10.22}$$

This virtual fluid is valid for a drained REV, isolated inclusions. It can be used in the formulation of the saturated effective compressibility and effective shear modulus given by Equations 10.12 and 10.14, through the parameter δ_c. The frequency-dependent compressibility ${C_{cr}}^*(\omega)$ is given by (Equation 10.12):

$${C_{cr}}^*(\omega) = C_S + \rho\frac{16(1-{\nu_S}^2)}{9(1-2\nu_S)}C_S\left(\frac{{\delta_c}^*(\omega)}{1+{\delta_c}^*(\omega)}\right), \tag{10.23}$$

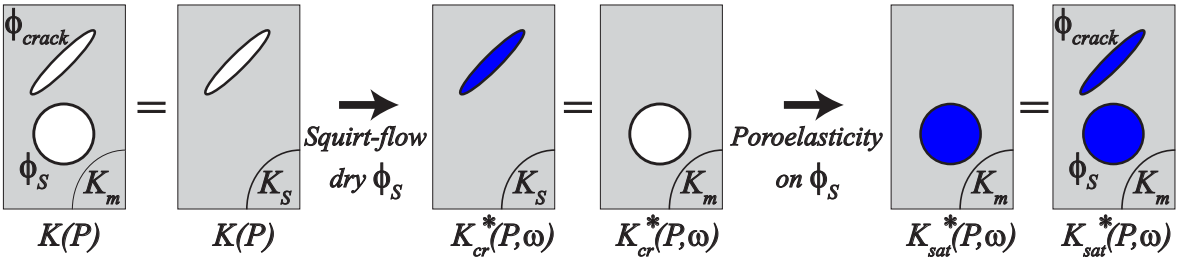

Figure 10.5: Sequence of homogenizations used by to model the squirt-flow of cracks in an undrained porous background ϕ_S.

with the new coupling parameter being (Equation 10.13):

$$\delta_c{}^*(\omega) = \frac{3\pi(1-2\nu_S)}{4(1-\nu_S{}^2)}\frac{\hat{\xi}}{C_S}\left(C_{fl}{}^*(\omega) - C_S\right), \tag{10.24}$$

where $C_{fl}{}^*(\omega) = 1/K_{fl}{}^*(\omega)$. The saturated effective shear modulus G_{cr}, given by Equation 10.14, can be calculated with the new parameter $\delta_c{}^*(\omega)$:

$$\frac{1}{G_{cr}{}^*(\omega)} = \frac{1}{G_S} + \frac{\rho}{G_S}\left[\frac{16(1-\nu_S)}{15\left(1-\frac{\nu_S}{2}\right)} + \frac{32(1-\nu_S)}{45}\left(\frac{\delta_c{}^*(\omega)}{1+\delta_c{}^*(\omega)}\right)\right]. \tag{10.25}$$

The sequence of the different homogenizations are presented Figure 10.5. C^*_{cr} is the compressibility of the saturated cracked medium embedded in an homogeneous background C_S, which is still composed of dry pores at this stage. By homogenization, C^*_{cr} equals the compressibility of the medium composed by the residual dry pores (ϕ_S) embedded in the mineral matrix C_m (Figure 10.5). Because $\phi_{cr} << \phi_S$, saturating the whole pore space is now equivalent of saturating the background pores ϕ_S of dry compressibility C^*_{cr} in the mineral skeleton C_m (Figure 10.5). The fluid-substitution in ϕ_S is given by Biot-Gassmann's equation:

$$C_{sat}{}^*(P,\omega) = C_m + \frac{1}{\frac{1}{C_{cr}{}^*(P,\omega)-C_m} + \frac{1}{\phi_S(C_{fl}-C_m)}}, \tag{10.26}$$

where $C_{sat}{}^*$ is the compressibility of the undrained saturated medium, which includes the effect of squirt-flow. Since this last fluid-substitution does not affect the shear modulus, according to Biot-Gassmann's theory, we directly have:

$$G_{sat}{}^*(P,\omega) = G_{cr}{}^*(P,\omega). \tag{10.27}$$

The only differences between this model and the model done by *Gurevich et al.* (2010) resides in Equations 10.23 and 10.25. Because the cracks are randomly oriented and have similar aspect ratio, they are isobaric under loading, therefore allowing *Gurevich et al.* (2010)

to use a poroelastic formulation to do the fluid substitution in the cracks. This gives the modified frame compressibilty C_{mf} (*Gurevich et al.*, 2010):

$$C_{mf}(P,\omega) = C_S + \frac{1}{\frac{1}{C(P)-C_S} + \frac{1}{\phi_{cr}(P)\times(C_{fl}{}^{*}-C_g)}}, \tag{10.28}$$

which plays the role of C^*_{cr} (Equation 10.23) in our model. The modified frame shear modulus is given by (*Gurevich et al.*, 2010):

$$\frac{1}{G_{mf}(P,\omega)} = \frac{1}{G(P)} - \frac{4}{15}\left(C(P) - C_{mf}(P,\omega)\right). \tag{10.29}$$

$G(P)$ can be measured independently using for example the pressure dependence of the ultrasonic S-wave velocities. For the sake of comparison with our model, $G(P)$ will be calculated from Equation 10.14 in dry conditions ($\delta_c/(1+\delta_c) = 1$). Similarly to $C_{sat}{}^{*}$ and $G_{sat}{}^{*}$ (Equations 10.26 and 10.27), the partially relaxed moduli of the medium are then calculated from Biot-Gassmann's equations (*Gurevich et al.*, 2010):

$$\tilde{C}^*_{sat}(P,\omega) = C_m + \frac{1}{\frac{1}{C_{mf}{}^{*}(P,\omega)-C_m} + \frac{1}{\phi_S(C_{fl}-C_m)}}, \tag{10.30}$$

and

$$\frac{1}{\tilde{G}^*_{sat}(P,\omega)} = \frac{1}{G(P)} - \frac{4}{15}(C(P) - C_{mf}(P,\omega)). \tag{10.31}$$

When $\omega = 0$, since $\phi_S \approx \phi_{tot}$ and $C^*_{cr} = C_{mf} = C$, both models are compatible with Biot-Gassmann's undrained prediction.

10.5.2 Combination of the squirt-flow and the global diffusion through the REV

The frequency dependence of the global flow connecting the REVs has yet to be included in the squirt-flow model. $C_{sat}{}^{*}(\omega)$ and $G_{sat}{}^{*}(\omega)$ (Equations 10.26 and 10.27) are valid for an undrained REV. We now want to include the effect of the global drainage of the REV, which occurs in our experimental set up when the sample has open boundary conditions.

The 1D poroelastic model for the drained/undrained transition presented in the previous chapter will be used. We recall that the principle of the model is to solve the 1-D diffusion equation related to the vertical global flow in the jacketed sample. When a hydrostatic stress oscillation $P_c(t) = \Delta P_c e^{i\omega t}$ is applied on the sample, the steady-state solution for the REV's pore pressure at the center of the sample, is given by Equation 9.15. The drained boundary conditions can be obtained for $S \to +\infty$, i.e., $b = 0$. The volumetric strain of the REV can be calculated from $\varepsilon_v(t) = {K_d}^{-1}\left(P_c(t) - \alpha p_f(t)\right)$ where $K_d = 1/C$ is the drained bulk modulus, and α is the Biot coefficient. The frequency dependent compressibility of

the REV is then calculated from $C_{REV}(\omega) = |\varepsilon_v| \,/\, |P_c|$. This gives:

$$C_{REV}(\omega) = C\left(1 - \alpha B + \alpha B \frac{\sinh(az) + \sinh(a(L-z))}{\sinh(aL)}\right). \tag{10.32}$$

For experimental drained conditions around the sample ($b = 0$), when $\omega \to 0$ we have $a \to 0$, which leads to $C_{REV}(0) = C$ (Equation 10.32). On the other hand, regardless of the boundary conditions, when $\omega \to +\infty$, $\left|p_f\right| \to B\Delta P_c$ (Equation **??**), which gives from the definition of the Skempton coefficient (B), $C_{REV} = C_{undrained}$. This model gives consistent results when compared to experimental data on sandstones (Section 9.5) or on limestones (Section 9.8). It allows to predict the cut-off frequency of the drained/undrained transition, and to evaluate the effect of the experimental dead volumes around the sample on the measured elastic properties.

$C_{REV}(\omega)$ is the compressibility of the REV that has open boundary conditions, and is connected to the neighbor REVs. Similarly to the previous subsection, we can define a virtual fluid, that would give the similar compressibility $C_{REV}(\omega)$, but as if the REV was closed or unconnected. Because the REV is now closed, and the porosity ϕ_{tot} within the REV is perfectly connected, the compressibility of this virtual fluid (${C_{fl-REV}}^*(\omega)$) has to be compatible with Biot-Gassmann's equations applied to ϕ_{tot}. $C_{REV}(\omega)$ being now, virtually, an undrained compressibility, Biot-Gassmann's equation gives:

$$\frac{1}{C_{REV}(\omega) - C_m} = \frac{1}{C - C_m} + \frac{1}{\phi_{tot}({C_{fl-REV}}^*(\omega) - C_m)}. \tag{10.33}$$

We deduce that:

$${C_{fl-REV}}^*(\omega) = C_m + \frac{1}{\phi_{tot}} \frac{1}{\left(\frac{1}{C_{REV}(\omega) - C_m}\right) - \left(\frac{1}{C - C_m}\right)}. \tag{10.34}$$

This virtual fluid compressibility can now be included in Equation 10.26 (respectively Equation 10.30 for Gurevich's model) to calculate the compressibility of the saturated medium with partially drained pores. This gives:

$${C_{sat}}^{**}(P, \omega) = C_m + \frac{1}{\frac{1}{{C_{cr}}^*(P,\omega) - C_m} + \frac{1}{\phi_S({C_{fl-REV}}^* - C_m)}}. \tag{10.35}$$

The shear modulus remains unchanged:

$${G_{sat}}^{**} = {G_{cr}}^*. \tag{10.36}$$

The attenuations Q^{-1} related to the different moduli can be calculated from the extraction of the imaginary parts of ${C_{sat}}^{**}$ and ${G_{sat}}^{**}$ (or the isotropic combinations for E and ν), and dividing them by the respective real parts (Equation 1.35).

For the crack distributions presented Figure 10.2b, predictions of the bulk and shear moduli dispersions, and their related attenuations, are presented Figure 10.6. The model is applied here to a laterally jacketed sample that is 8 cm long, with experimental drained conditions on the top and bottom. The matrix porosity is set to $\phi_S = 0.15$. We recall that the characteristic aspect ratio of the cracks is $\hat{\xi} = 0.2 \times 10^{-3}$ for all pressures, the high-pressure (crack closed) dry bulk modulus $K_S = 40\,\text{GPa}$. For the sake of illustration, the mineral bulk modulus is taken as $K_m = 77\,\text{GPa}$. The permeability of the sample is set to $\kappa = 10^{-16}\,\text{m}^2$ and is saturated with water ($K_{fl} = 2.24\,\text{GPa}$ and $\eta = 10^{-3}\,\text{Pa.s}$). The dispersions of the moduli can be compared to the cut-off frequency predictions for both the drained/undrained and the squirt flow transitions, which are respectively given by (*O'Connell and Budiansky*, 1977; *Cleary*, 1978):

$$f_{undrained} = \frac{4\kappa K}{\eta L^2} \quad \text{and} \quad f_{squirt} = \frac{K_S \xi^3}{\eta}. \tag{10.37}$$

In this configuration, two dispersive transitions are observed for ${K_{sat}}^{**}(\omega)$, in the ranges $[10^{-1}\,;10^{0}]\,\text{Hz}$ and $[10^{2}\,;10^{4}]\,\text{Hz}$ (Figure 10.6a), related to two attenuation peaks (Figure 10.6b). The first transition, consistent with $f_{undrained}$, corresponds to the drained/undrained transition that is compatible with Biot-Gassmann's prediction. The second transition corresponds the undrained/unrelaxed transition related to the squirt flow. The frequency range of this transition is consistent with the cut-off frequency f_{squirt}, although there seems to be a pressure dependent frequency shift of the attenuation peaks (Figure 10.6b). This undrained/unrelaxed transition is the only one seen for the shear modulus (Figures 10.6c and 10.6d), the undrained regime being equivalent to the drained regime consistently with Biot-Gassmann (*Gassmann*, 1951). The attenuation peaks are perfectly consistent with f_{squirt} and no pressure dependence of the frequency ranges is seen. For both ${K_{sat}}^{**}(\omega)$ and ${G_{sat}}^{**}(\omega)$, the amplitude of dispersions and the attenuation peaks decrease with the increase of pressure P_0, as more cracks are closed.

The corresponding virtual fluid moduli as a function of frequency are given Figure 10.7. The dispersion of ${K_{fl-REV}}^{*}$ begins around $10^{-1}\,\text{Hz}$ and is related to the drained/undrained transition (Figure 10.7). After $10^{0}\,\text{Hz}$, the REV can be considered undrained with ${K_{fl-REV}}^{*} = K_{fl}$. Above $10^{2}\,\text{Hz}$, ${K_{fl}}^{*}$ increases due to the increasing viscous dragging in the crack's squirt-flow. At the high-frequency end, the fluid is considered immobile, and ${K_{fl}}^{*} = K_{fl}$ as if the inclusions were isolated.

From Equations 10.35 and 10.36, we respectively obtain the frequency dependent bulk modulus and shear modulus, in isotropic conditions. Therefore the frequency-dependence of E and ν can simply be calculated from the relationships relating the elastic parameters for isotropy:

$$E^*_{sat}(P,\omega) = \frac{9K^*_{sat}G^*_{sat}}{3K^*_{sat} + G^*_{sat}} \quad \text{and} \quad \nu^*_{sat}(P,\omega) = \frac{3K^*_{sat} - 2G^*_{sat}}{2(3K^*_{sat} + G^*_{sat})}. \tag{10.38}$$

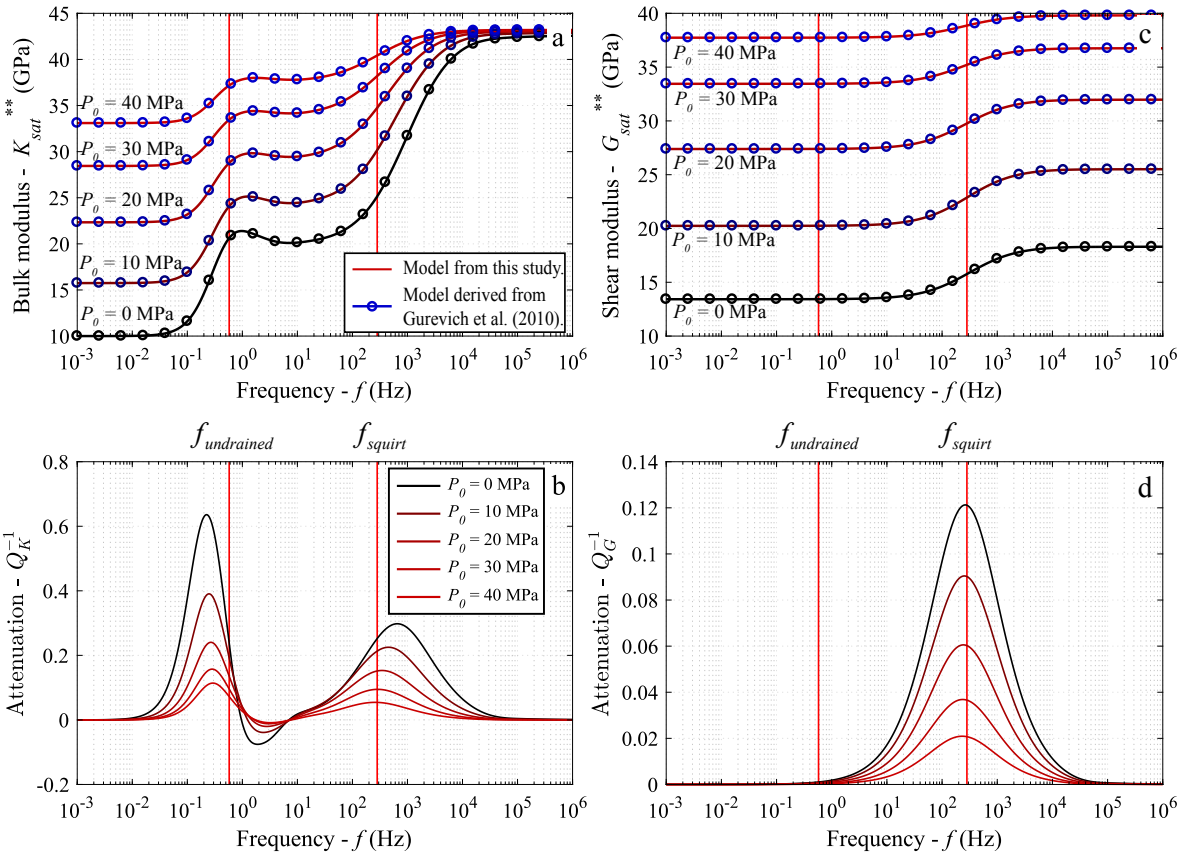

Figure 10.6: (a) Frequency dependence of the bulk modulus $K_{sat}{}^{**}$ of sample with drained boundary conditions, calculated from the model of this study (red lines) (Equation 10.35) and compared with Gurevich's model (blue circles) (Equation 10.30). (b) Related attenuation $Q_K{}^{-1}$ calculated from Equation 1.35. (c) Frequency dependence of the shear modulus $G_{sat}{}^{**}$ (Equation 10.36) and (d) its related attenuation $Q_G{}^{-1}$. The dispersions and attenuations were calculated for the crack distributions presented Figure 10.2b, at effective pressures $P_0 = [0\,;10\,;20\,;30\,;40]$ MPa. The model is calculated with $\phi_S = 0.15$, $K_S = 40$ GPa, $\nu_S = 0.1$, $K_m = 77$ GPa, $\kappa = 10^{-16}$ m^2, and with water as saturating fluid ($K_{fl} = 2.24$ GPa and $\eta = 1$ mPa.s).

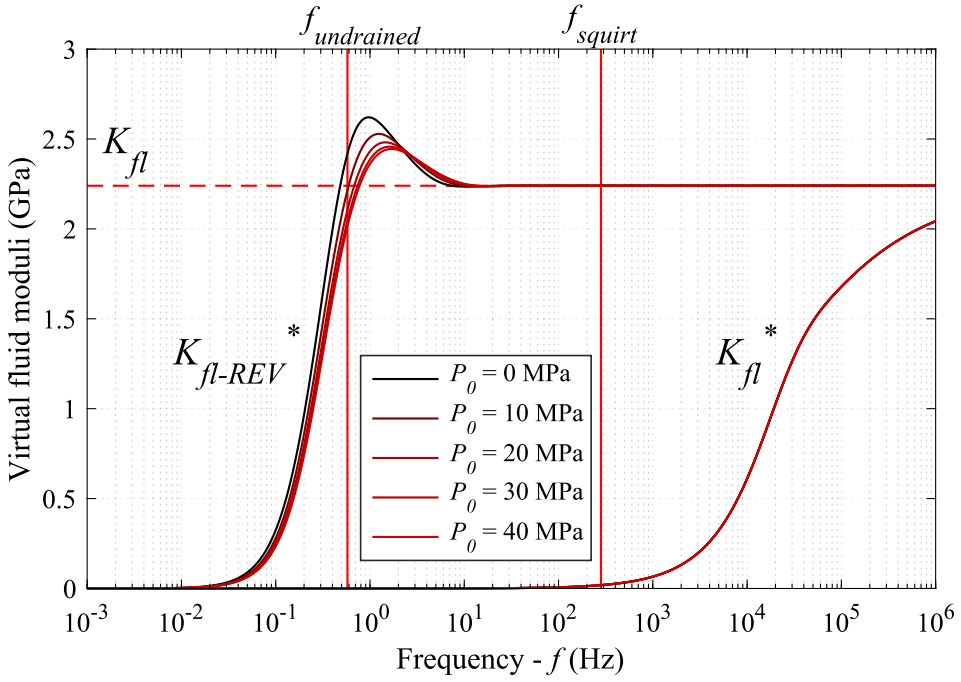

Figure 10.7: Virtual fluid moduli ${K_{fl-REV}}^{*}$ and ${K_{fl}}^{**}$ as function of frequency, corresponding to the dispersion in bulk modulus ${K_{sat}}^{**}$ (Figure 10.6a). The dispersion of ${K_{fl-REV}}^{*}$ beginning around 10^{-1} Hz is related to the drained/undrained transition. After 10^{0} Hz, the REV can be considered undrained with ${K_{fl-REV}}^{*} = K_{fl}$. After 10^{2} Hz, the increase of ${K_{fl}}^{*}$ with frequency is related to the squirt flow between the cracks and the matrix porosity, with ${K_{fl}}^{*} = K_{fl}$ when $f \to \infty$.

The corresponding attenuations Q^{-1} are deduced from Equation 1.35.

10.5.3 Extension to anisotropy

The model presented here, which combines the drained, undrained and unrelaxed fluid-flow regimes, is valid solely for isotropic conditions, that is, for randomly oriented cracks of same aspect ratio. One important point of the non interaction approximation (NIA) formalism (Equation 10.12) is the compatibility with Biot-Gassmann's poroelastic formalism in the low-frequency limit. This was well illustrated by the perfect match with Gurevich's model (*Gurevich et al.*, 2010).

The similar NIA formalism can be extented to an anisotropic medium (*Guéguen and Sarout*, 2009, 2011). The effective compliances are therefore given by (*Guéguen and Sarout*, 2011):

$$S_{ijkl} = S^S_{ijkl} + \Delta S_{ijkl}, \tag{10.39}$$

where S^S_{ijkl} are the matrix material compliances. We can assume from this point that the background matrix is an isotropic medium defined by the parameters K_S and ν_S. If we assume that all the cracks embedded in the isotropic matrix are planar, and with circular shape of same radius a, the additional compliances ΔS_{ijkl} for the general case of non-randomly oriented cracks, in the dry case, is given by (*Kachanov*, 1993; *Guéguen and Sarout*, 2009):

$$\Delta S_{ijkl} = h\left[\frac{1}{4}\left(\delta_{ik}\alpha_{jl} + \delta_{il}\alpha_{jk} + \delta_{jk}\alpha_{il} + \delta_{jl}\alpha_{ik}\right) - \frac{\nu_S}{2}\beta_{ijkl}\right], \tag{10.40}$$

where:

$$h = \frac{32(1-{\nu_S}^2)}{3(1-\nu_S)E_S}. \tag{10.41}$$

α is the second rank crack density tensor defined as:

$$\alpha_{ij} = \left(\frac{Na^3}{V}\right) < n_i n_j >, \tag{10.42}$$

with N the total number of cracks in a volume V, and n is the unit vector normal to a crack. The brackets represent a statistical angular average of the orientations of the cracks (*Guéguen and Sarout*, 2011). The fourth-rank tensor β is given by:

$$\beta_{ijkl} = \left(\frac{Na^3}{V}\right) < n_i n_j n_k n_l > . \tag{10.43}$$

Because $-\nu_S/2$ is a relatively small factor in Equation 10.40, the tensor β plays little role in the dry case. However, in fluid-saturated conditions, the β-terms get more important. The presence of the saturating fluid, which stiffens the cracks, transforms Equation 10.40

into (*Shafiro and Kachanov*, 1997; *Guéguen and Sarout*, 2011):

$$\Delta S_{ijkl} = h\left[\frac{1}{4}\left(\delta_{ik}\alpha_{jl} + \delta_{il}\alpha_{jk} + \delta_{jk}\alpha_{il} + \delta_{jl}\alpha_{ik}\right) + \left(\left(1 - \frac{\nu_S}{2}\right)\frac{\delta_c}{1+\delta_c} - 1\right)\beta_{ijkl}\right], \tag{10.44}$$

where δ_c is exactly the same solid/fluid coupling parameter defined previously in isotropic conditions (Equation 10.13).

The same squirt-flow modeling done through Equations 10.15 to 10.22, which defines a virtual fluid modulus K^*_{fl} seen by the cracks, can still be applied as it is a generic elastic response to an oscillatory stress-field normal to the crack, regardless of its orientation. Similarly to the isotropic case, K^*_{fl} is injected in the parameter δ_c, which gives the frequency dependent fluid/solid coupling parameter δ^*_c (Equation 10.24). Following the same sequence as previously, δ^*_c can be injected into Equation 10.44 to give a frequency-dependent additional compliances tensor ${\Delta S_{ijkl}}^*$, which, from Equation 10.39, gives the frequency-dependent effective compliances ${S_{ijkl}}^*$ in saturated conditions of the anisotropic cracked medium.

We propose here to follow the same homogenization sequence as proposed for the isotropic case (Figure 10.5). We consider cracks of similar aspect ratios with anisotropic orientations, embedded in a homogenous matrix S^S_{ijkl} that contains a porosity ϕ_S. S^S_{ijkl} corresponds to the compliances of the medium at high confining pressure when all the cracks are closed. The squirt-flow model gives the solution ${S_{ijkl}}^*(\omega)$ for saturated cracks embedded in a dry homogeneous matrix S^S_{ijkl}. As previously in the isotropic case, the compliances $S^*_{ijkl}(\omega)$ are homogenized, and now correspond to the compliances of the dry background matrix S^S_{ijkl} of porosity ϕ_S embedded in a mineral of compliances S^m_{ijkl}. S^m_{ijkl} can also be considered isotropic and be defined solely from K_m and ν_m. Poroelasticity can be finally used to do the fluid substitution in ϕ_S, taking $S^*_{ijkl}(\omega)$ as the dry compliances. For anisotropic mediums, this is achieved by Brown and Korringa equation (*Brown and Korringa*, 1975), which, with the assumption of homogeneity, gives (with Voigt notations):

$${S^{sat}_{ijkl}}^*(\omega) = {S_{ijkl}}^*(\omega) + \frac{\left({S_{ij}}^*(\omega) - {S_{ij}}^m\right)\left({S_{kl}}^*(\omega) - {S_{kl}}^m\right)}{\phi_S\left(K_{fl} - K_m\right) + \left({S_{ii}}^*(\omega) - K_m\right)}, \tag{10.45}$$

where ${S^{sat}_{ijkl}}^*$ is the frequency-dependent saturated compliances of the effective medium, when the REV is undrained. If we focus on TI medium, the results could then be converted to frequency dependent Thomsen parameters (*Thomsen*, 1986) for practical purposes and be compared to the anisotropic squirt-flow model developed by *Collet and Gurevich* (2016), who extented the formalism of Gurevich's model (*Gurevich et al.*, 2010) to anisotropic media. For TI symmetry (x_3 considered as the symmetry axis), 5 elastic constants are required instead of 2 in the isotropic case. The tensors α and β are simplified, with $\alpha_{11} = \alpha_{22}$, $\beta_{1111} = \beta_{2222}$ and $\beta_{1133} = \beta_{2233}$.

Experimentally, the crack density tensors (α and β) could be deduced from ultrasonic

P- and S-waves velocities in different directions, with different stress configurations in a triaxial cell. If we assume that the anisotropy of the effective medium is solely due to the orientations of the cracks, S^S_{ijkl} can be characterize at high confining pressure, where the ultrasonic P- and S-waves show no more anisotropy and no more dependence to pressure. The forced-oscillation technique could be used (axial+hydrostatic) for a TI rock, but would require 3 samples cored in different directions relatively to the bedding planes (e.g. *Szewczyk et al.*, 2016) to be able to determine the 5 independent compliances.

Similarly to the isotropic case, if we want to consider a global drainage that is unidirectional due to the external boundary conditions (vertical for a jacketed sample in a triaxial cell), the drained/undrained transition could be incorporated in the anisotropic squirt-flow model. The 1D poroelastic diffusion model presented in the previous chapter would have to be solved for an anisotropic medium, allowing for the definition of a REV frequency-dependent virtual fluid modulus K^*_{fl-REV} that will be injected into Equation 10.45 to cumulate the effects of squirt-flow and global drainage.

10.6 Comparison of the model with experimental results on the carbonate samples, in the isotropic case

The fluid-flow model at different scales (squirt-flow + global diffusion) in the isotropic case has been compared to the experimental results obtained by forced-oscillations in saturated-conditions presented in the previous part of the manuscript. The model is solely compared to the samples that presented pressure-dependent bulk moduli, which are, the Indiana limestone, intact and after thermal cracking, the Rustrel sample and finally the Coquina sample. The first step consists of characterizing the crack distributions of the samples for different confining pressures by applying Morlier's method (Equations 10.5 to 10.9). Because we want the NIA effective medium formulation (Equation 10.12) to be perfectly consistent with the measured frequency-dependent dynamic moduli, the exponential compressibility function $C(P)$ (Equation 10.5) is adjusted on the dynamic dry bulk moduli obtained from hydrostatic oscillations, rather then on the static moduli (as initially required from the method).

One parameter that still needs to be adjusted is the frequency-independent ν_S. In some cases, the experimental axial oscillations in dry conditions, from which ν can be calculated, were not done at sufficiently high pressure. One method we propose to define it with relatively good precision, is to observe the pressure dependence of the drained/undrained transition of ν in saturated conditions (water saturation for the 4 samples). We previously noted from our experimental results the presence of a crossing point at the drained/undrained cut-off frequency, which was independent of pressure (Figures 5.7, 6.6 and 7.7). This point is the consequence of an increase of the drained ν and a decrease of the undrained ν with effective pressure. From the isotropic relationships relating the elastic moduli, if $G = cst$,

which is the case for the drained/undrained transition, ν increases with K. Since K_u can only be greater than K_d, the same applies for ν. The high pressure value ν_S is therefore bounded by ν_d and ν_u and should be independent of pressure (and frequency). This corresponds to the crossing point. However, this can only apply if this crossing point exists, that is, if the variations of ν_d and ν_u are opposite with pressure, which is not necessarily the case for every rock as it depends on the combined pressure-dependence of the bulk and the shear modulus. Moreover, the drained/undrained cut-off frequency, which is related to the permeability, should be relatively constant with pressure.

The results of the crack distributions of the 4 carbonate samples are presented Figure 10.8. The crack distributions are all plotted on the same scale (Figure 10.8). The fitting parameters for each sample are presented Table 10.1. The 4 samples exhibit crack aspect ratios in the range $[1.44; 2.75] \times 10^{-4}$ (Figure 10.8, Table 10.1). We can see that the thermal cracking had a large impact on the Indiana limestone: the crack density substantially increased from 0.22 to 0.99. It was concluded from the analysis of the SEM photomicrographs that the thermally induced cracks were mainly created in the large calcitic crystals of the blocky cement. The Indiana limestone is well cemented and no cracks were observed in the cement of the intact sample. The Rustrel sample exhibits a high crack density of 0.52 for $\hat{\xi} = 1.84 \times 10^{-4}$, which could be related to the extensive intercrystalline porosity observed within the calcite cement. The microporous grains or the grain/cement contacts could also generate the pressure-dependence of the elastic properties.

	K_i	K_S (GPa)	ν_S	$\hat{P}$ (MPa)	$\hat{\xi}(\times 10^{-4})$	ρ	ϕ_{crack} (%)	f_{sq} (Hz)
Indiana intact	19	34	0.27	7	1.76	0.22	0.016	421
Indiana th. cr.	5	20	0.22	4	1.44	0.99	0.060	230
Rustrel	9.5	26	0.25	6	1.84	0.52	0.040	477
Coquina	5	28	0.27	9	2.75	1.28	0.15	1600

Table 10.1: Fitting parameters for Morlier's method, and obtained results for the characteristic crack aspect ratio ($\hat{\xi}$), the unconfined crack density (ρ), the total crack porosity (ϕ_{crack}) and the squirt-flow cut-off frequency (f_{sq}) for water-saturated conditions.

For the Coquina sample, the lack of data at high-pressure forced us to make an adjustment for K_S. We were able to define $\nu_S = 0.27$ from the crossing point in Figure 7.7). Since K_i is also known from the experimental results, we adjusted K_S so that the high-frequency end of the model fits with the ultrasonic bulk modulus in glycerin-saturated conditions. We obtained $K_S = 28\,\text{GPa}$. A very high crack density of 1.28 is obtained for the Coquina sample (Table 10.1). From the SEM photomicrographs, this probably relates to the grain contacts that can act like microcracks, as the sample is poorly cemented and doesn't bear much intragranular microporosity.

Once the characteristic aspect ratio and the pressure-dependence of the crack density are defined, the model can be calculated for the whole frequency range. We focus here on

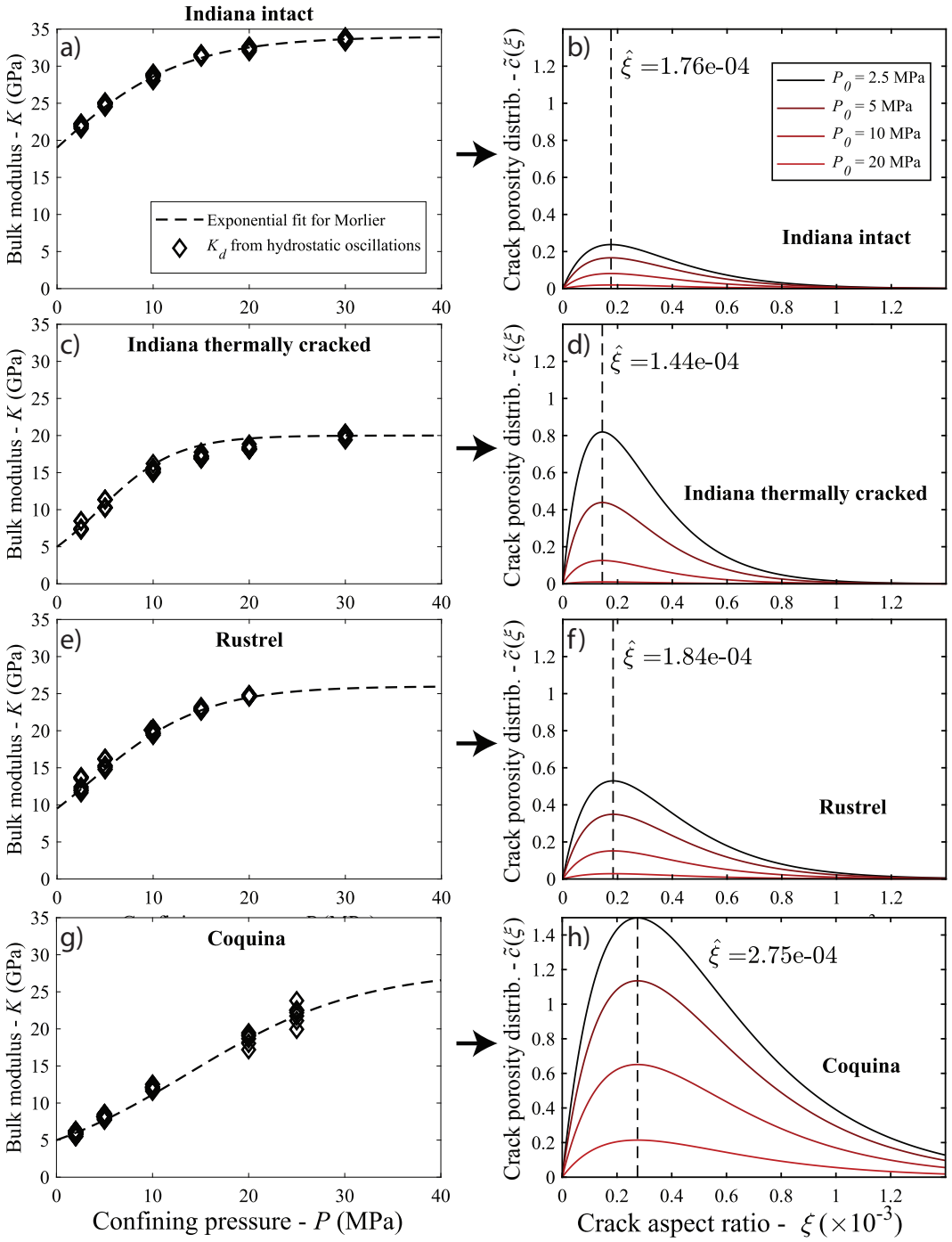

Figure 10.8: Pressure dependence of the bulk modulus and deduced crack distributions at different differential pressures for the intact Indiana (a-b), the thermally cracked Indiana (c-d), the Rustrel (e-f) and the Coquina samples (g-h). We use the pressure-dependence of the dynamic bulk modulus K_d obtained from hydrostatic oscillations in dry conditions to adjust the crack distributions with Morlier's method. For a given pressure, K_d is plotted for all the measured frequencies. The fitting parameters for each sample are presented Table 10.1.

K^*_{sat} (Equation 10.35), but the results for G^*_{sat} (Equation 10.36) and the deduced E^*_{sat} and ν^*_{sat} (Equation 10.38) compared to the ultrasonic and axial oscillations results are presented in Appendix E. Since the experimental bulk moduli obtained from hydrostatic and axial were in general consistent with each other, the data used for the comparison with K^*_{sat} is the hydrostatic oscillations results as they correspond to a direct measurement, and therefore bear less uncertainty. One exception is made for the glycerin-saturated data of the Coquina sample, where we used the axial oscillations to present higher-frequency results.

For the intact Indiana limestone (Figure 10.9), the model fits perfectly the drained / undrained transition visible under water saturation (Figure 10.9a) for the different pressures. The high-frequency end is consistent the ultrasonic results (Figure 10.9a). The attenuation seem to slightly over-predict the experimental results, with a maximum peak of 0.3 instead of 0.2 at $P_{diff} = 2.5\,\text{MPa}$ (Figure 10.9b). For the glycerin saturation (Figures 10.9c and 10.9d), the model predicts squirt-flow dispersion and attenuation between 10 Hz and 10^3 Hz but the experimental data show no dispersion nor attenuation in this range. The undrained values of the model (between 1 Hz and 10) seem consistent with the experimental results for $P_{diff} >= 5\,\text{MPa}$. For $P_{diff} = 2.5\,\text{MPa}$, the hydrostatic results are much lower than what the model predicts. The high-frequency end remains consistent with ultrasonic results. This suggests that some squirt-flow dispersion is expected to occur at frequencies greater than 10^3 Hz.

For the thermally cracked Indiana sample in water-saturated conditions (Figure 10.10a-b), the model's prediction for the drained / undrained transition fits the amplitude of dispersion, but seems to have a higher slope than the data (Figure 10.10a). Consequently, the model's attenuation over-predicts greatly the experimental results, with a peak at 0.95 instead of 0.35 for the attenuation results at $P_{diff} = 2.5\,\text{MPa}$ (Figure 10.10b). The water-saturated ultrasonic results are lower than model as they were also found to be lower than the undrained experimental results (Figure 10.10a). For the glycerin-saturated conditions (Figure 10.10c-d), the model does predict dispersion and attenuation at the same frequency range than the experimental data, but with far less amplitudes. However, the high-frequency end of the model corresponds well with the ultrasonic results (Figure 10.10c). Somehow, the experimentally undrained value of K_{gly} at $P_{diff} = 2.5\,\text{GPa}$ is much lower than what Biot-Gassmann would predict, and is equivalent to the undrained K_{wat}. Interestingly, this was also observed for the intact sample (Figure 10.9), which was a completely different set of experiments (other strain-gauges) following the same experimental protocol, making this a reproducible observation. At this stage, we do not have a proper explanation for this. These observations have to put in parallel with the Poisson's ratio experimental results, which fail to be adjusted by the model (see Appendix E). For the thermally cracked Indiana sample, the squirt-flow dispersion seen by ν seems to differ in frequency range: when K should be undrained above 1 Hz, ν seems to be still equal to the drained value, and only increase to the unrelaxed value after 10^2 Hz. Anisotropy of the thermally induced

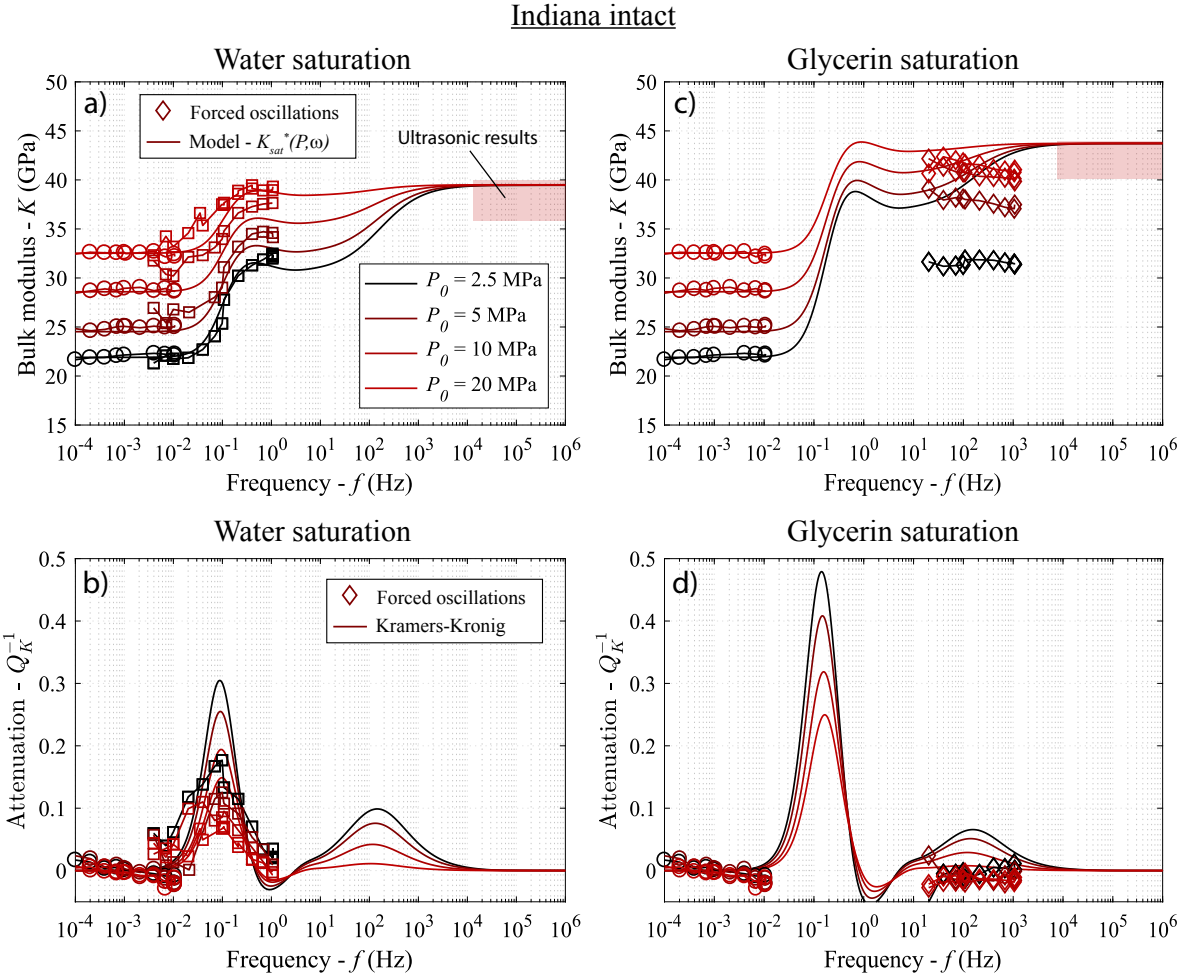

Figure 10.9: Drained/Undrained/Squirt-flow model compared to the experimental bulk modulus results of the intact Indiana limestone. The ultrasonic results under water-saturated and glycerin-saturated conditions are within the red rectangles (Table 5.2).

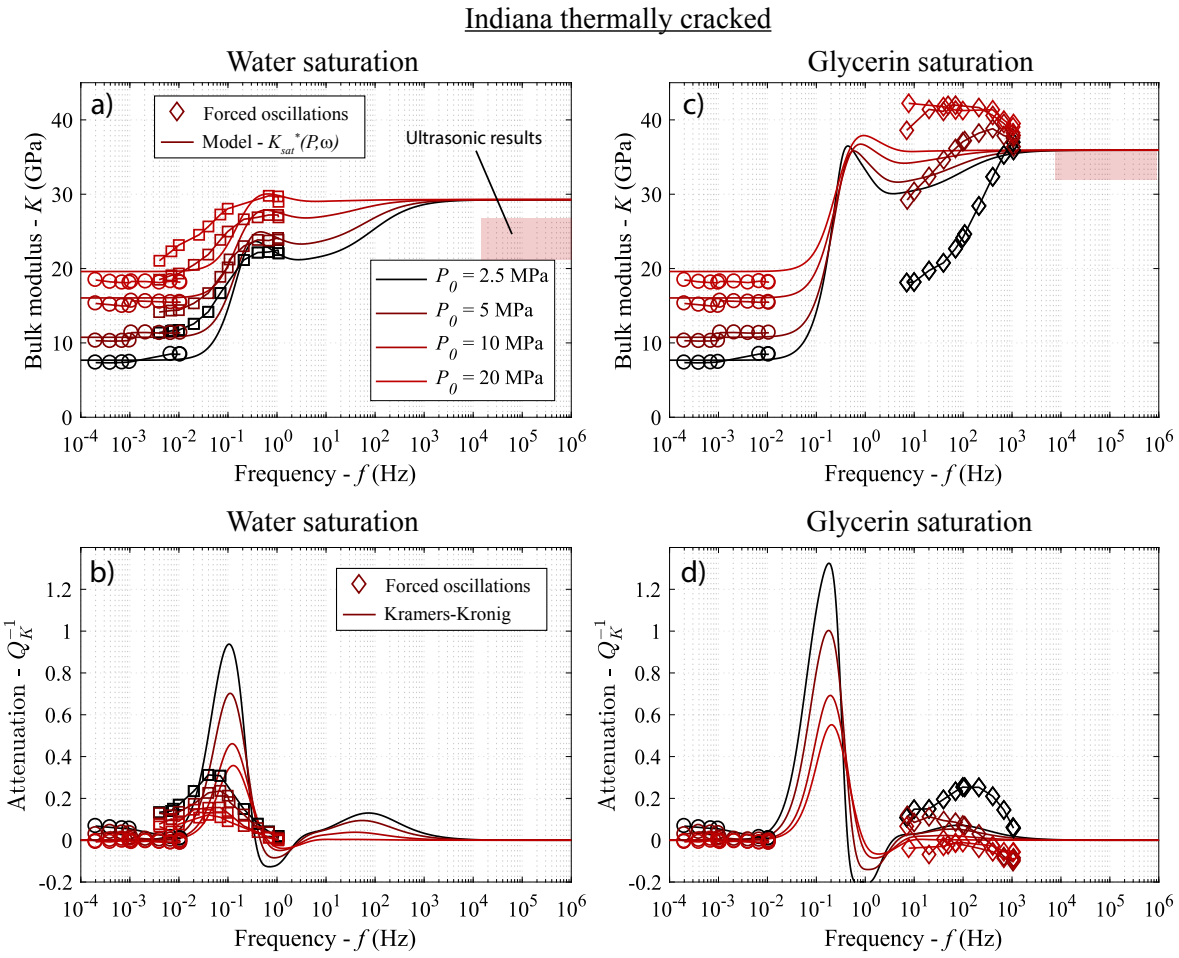

Figure 10.10: Drained/Undrained/Squirt-flow model compared to the experimental bulk modulus results of the thermally cracked Indiana limestone. The ultrasonic results under water-saturated and glycerin-saturated conditions are within the red rectangles (Table 5.2).

cracks orientations could explain this, but this fails to explain why the same phenomenon appeared in the intact sample. A chemical interaction seems unlikely as it would have to be specific to the glycerin, since the water-saturated results do not exhibit this weakening, and the high-frequency unrelaxed bulk modulus would also be affected, which doesn't seem to be the case. Unfortunately we do not have the shear modulus results to see if there is any shear weakening. The hypothesis of non-interaction between cracks could also be violated at low-pressure, but this would still not explain why the undrained value is much lower than Biot-Gassmann's prediction.

For the Rustrel sample in water-saturated conditions (Figure 10.11a-b), the model seems generally consistent with the experimental results of the drained/undrained transition, and with the high-frequency ultrasonic results (Figure 10.11a). The amplitude of dispersion of

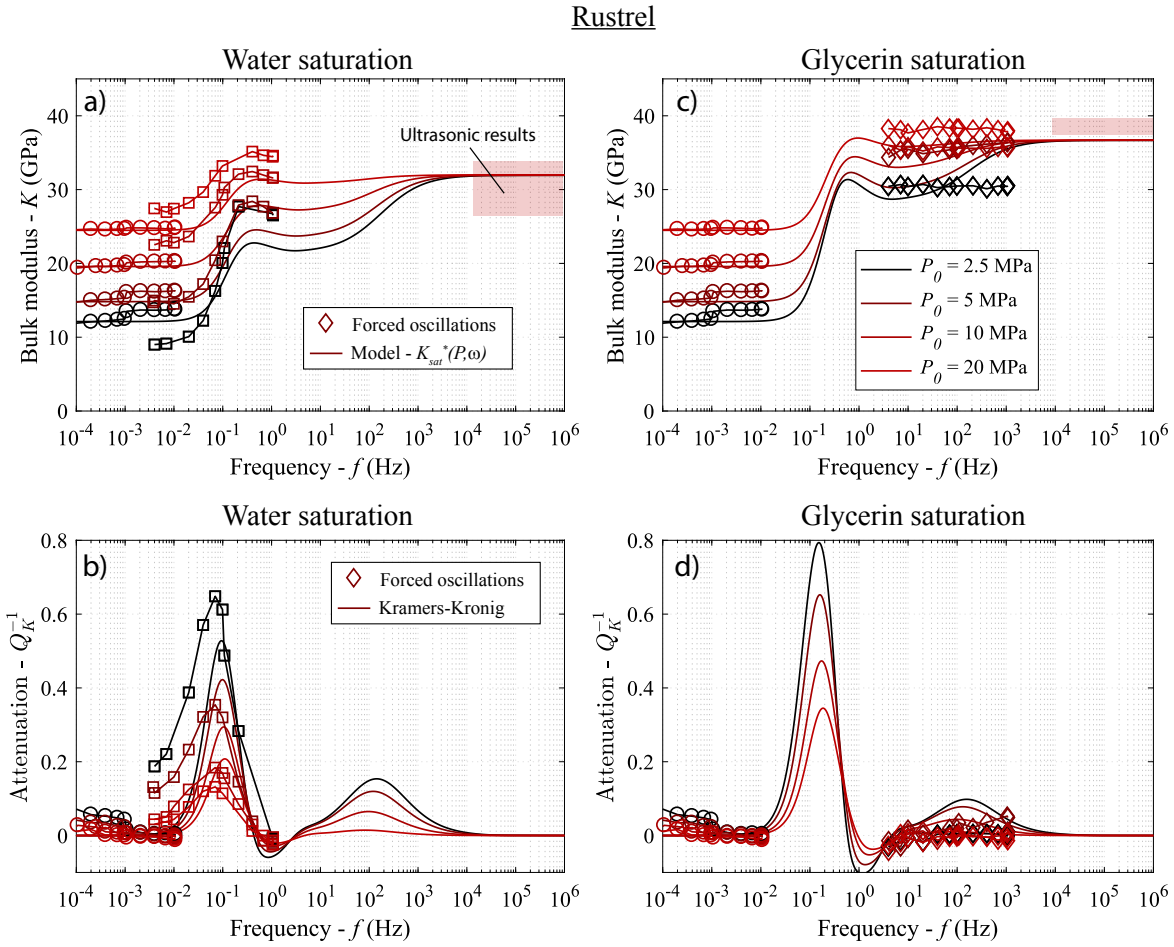

Figure 10.11: Drained/Undrained/Squirt-flow model compared to the experimental bulk modulus results of the Rustrel sample. The ultrasonic results under water-saturated and glycerin-saturated conditions are within the red rectangles (Table 6.1).

the experimental results seem greater than what the model predicts (Figure 10.11a), which results in greater attenuation than the models prediction (Figure 10.11b). In the glycerin-saturated case, the undrained values (around 1 Hz) of the model and the experimental data are consistent. However, similarly to the intact Indiana sample, the experimental data show no dispersion nor attenuation where the model predicts it (Figure 10.11c-d). The model being consistent with the unrelaxed ultrasonic results, it suggests that the squirt-flow dispersion should occur at frequencies greater than 10^3 Hz. The results for E, ν and G (see Appendix E) are in agreement with these observations.

Finally, for the Coquina sample under water saturation (Figure 10.12a-b), the model is in very good agreement with the experimental results of the drained / undrained transition, either for dispersion (Figure 10.12a) and attenuation (Figure 10.12b) at every differential pressure. The ultrasonic results are in agreement with what the models predicts

at high frequency (Figure 10.12a). In glycerin-saturated conditions (Figure 10.12c-d), the model predicts squirt-flow at slightly lower frequencies than the experimental results (Figure 10.12c). The high-frequency values of the model are consistent with the unrelaxed ultrasonic results (Figure 10.12c). The amplitude of the dispersion predicted by the model seem lower than the experimental results (Figure 10.12c), and consistently the attenuation was found to be lower also (Figure 10.12d). The experimental undrained values (visible around 100 Hz, seem to be slightly lower than what Biot-Gassmann, and therefore the model, would predict, explaining the differences in dispersions (Figure 10.12c). To a less extent, this is what we observed for the Indiana sample, i.e., a lower undrained bulk modulus with glycerin, and a higher cut-off frequency for the squirt-flow. These observations have to be put in parallel with the results of the other elastic moduli obtained from axial oscillations (see Appendix E). The results on E, ν and G seem to confirm these observations, and the small mismatch between the model and the experimental results could be related to inconsistencies between the bulk modulus obtained from the hydrostatic and the axial oscillations, as the crack determination uses solely the pressure-dependence of the hydrostatic oscillations results in dry conditions.

10.7 Conclusions

The combination of a squirt-flow model similar to *Gurevich et al.* (2010) and the 1D drained / undrained poroelastic model (*Pimienta et al.*, 2016b) proves to be a useful tool to interpret and discuss the experimental results of dispersion and attenuation over large frequency ranges. The model can be extended to anisotropic media, but has yet to be compared to experimental results (e.g. *Szewczyk et al.*, 2016). The model was here compared to results obtained with drained boundary conditions, but it can also take into account the effect of possible small dead volumes at the boundaries of the sample. One of the major application of the model would be to predict the whole frequency behavior of the elastic properties of a rock by simply measuring a static loading curve.

The general observations we can make when the model is confronted to the experimental results on the carbonate samples are: (i) the water-saturation results were always consistent with Biot-Gassmann and the 1D drained/undrained model, and (ii) the amplitude of squirt-flow is consistent but the cut-off frequency of the model is often lower than observed experimentally, except for the thermally cracked Indiana. For the coquina sample, the cut-off frequency is only slightly underpredicted. The first point confirms observations done by *Adam et al.* (2006), although we did not observe much shear weakening due to fluid saturation. The second point could be related to the micromechanical model used to model the squirt-flow between cracks and rounded pores (Figure 10.4).

One major simplification of the model is the use of a single crack family of aspect ratio $\hat{\xi}$, instead of the full distribution of crack aspect ratios determined by Morlier's method.

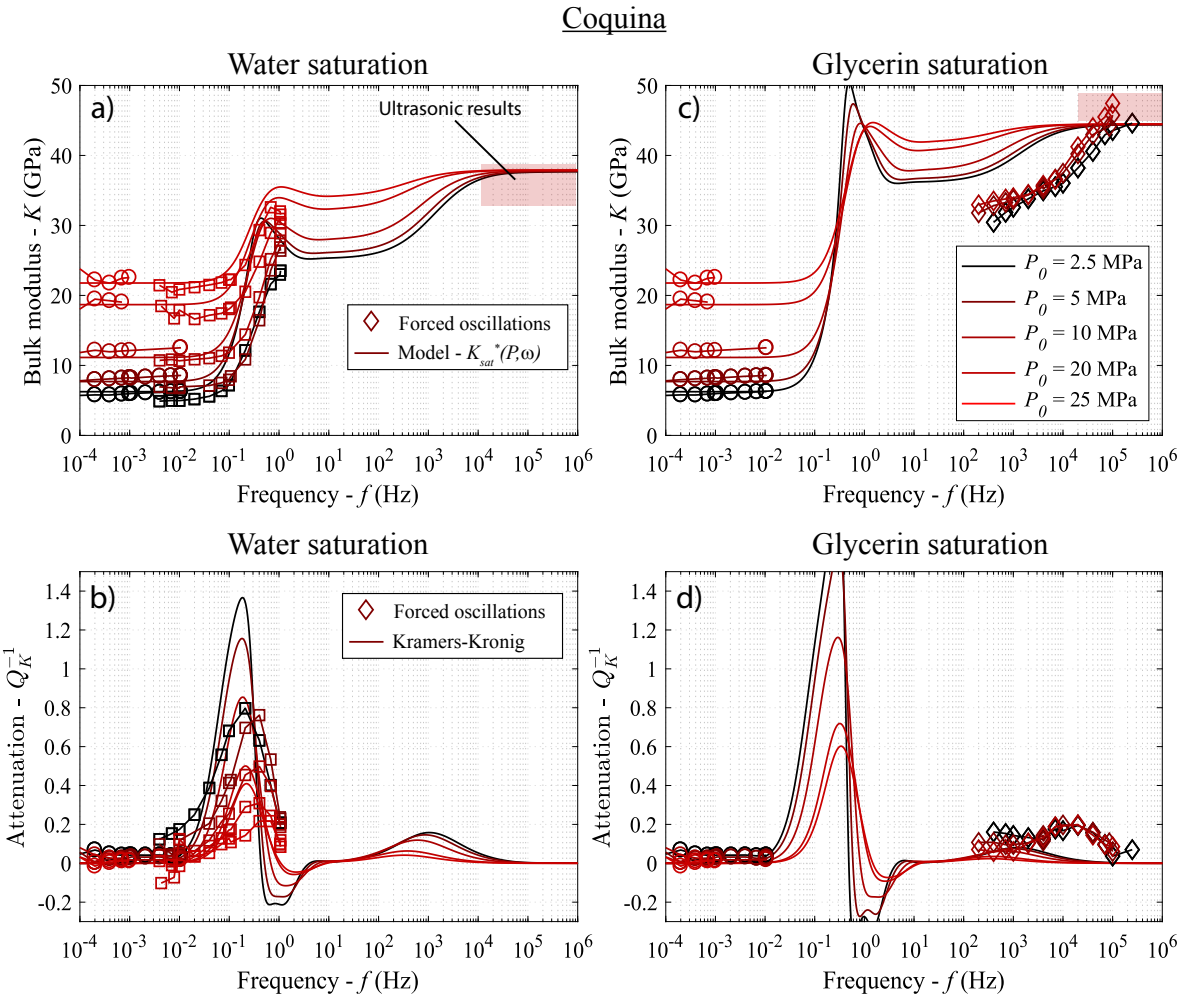

Figure 10.12: Drained/Undrained/Squirt-flow model compared to the experimental bulk modulus results of the Coquina sample. The ultrasonic results under water-saturated and glycerin-saturated conditions are within the red rectangles (Table 7.1).

This would surely broaden the frequency range of the squirt-flow dispersion. However, the characteristic crack aspect ratio $\hat{\xi}$ being the dominant family with the other crack aspect ratios distributed around it, the squirt-flow transition will not be shifted in frequency, but rather broaden around the cut-off frequency corresponding to $\hat{\xi}$. Such distribution is in fact intrinsically related to the effective medium that was used to deduce it in the first place, and therefore, by definition, is not a geometrical description of the rock. A small difference in $\hat{\xi}$ would imply a large difference in the squirt-flow cut-off frequency since $f_{sq} = \hat{\xi}^3 K_S/\eta$.

The general microporous nature of carbonate rocks may imply that the fluid in a crack does not simply flow radially between two mineral planes like in the present model, but these planes in question could bear micropores that would leak-off part of the fluid. In contrast, the thermally induced cracks in the homogeneous cement of the Indiana limestone seem not to have this issue. Although the compliance of the whole dry crack would not be changed, the presence of micropores could add drained or partially drained boundary conditions within the crack, and not simply at the circumference. For a same crack aperture h, the same differential equation followed by the fluid pressure (Equation 10.15) would be solved locally between the distance separating two drained micropores, i.e., on a diffusion length smaller than the crack radius. Locally, the fluid would see a crack of similar compliance, but with a smaller radius (distance between two micropores acting as boundary conditions). The local virtual fluid modulus defined Equation 10.22 would be calculated with a higher apparent crack aspect ratio (h is constant). This would therefore increase the cut-off frequency of the squirt-flow.

Conclusions

CONCLUSIONS AND PERSPECTIVES

Conclusions

The dispersion and the attenuation of the elastic moduli of fully-saturated limestones have been characterized experimentally using forced oscillations in a new triaxial cell at ENS of Paris, in addition to ultrasonic measurements. The limestones presented different microstructures characteristic of carbonate rocks, and the full set of dispersion and attenuation results of all the elastic moduli were obtained, either for seismic, logging, and ultrasonic frequencies. The main guideline of the study was to correlate any fluid-flow related dispersion, to microstructure observations in SEM. Five main conclusions can be emphasized.

1) - For all the samples, the drained/undrained transition was characterized to clearly identify the different fluid-flow regimes. The resulting dispersion was in good agreement with Biot-Gassmann's predictions and the frequency of the transitions were perfectly predictable from the permeability measurements. A 1D poroelastic model, solving the vertical diffusion in the sample, was developed to model this transition and include the effects of different boundary conditions, such as small dead volumes.

2) - For the bimodal-porosity Lavoux limestone, no squirt-flow dispersion was detected beyond the undrained regime, which was expected as the bulk modulus is pressure-independent up to 20 MPa of effective pressure. This suggests that the equivalent aspect ratios of intergranular macropores and intragranular micropores are relatively similar. For the Indiana sample, the results show that a small amount of squirt-flow is expected between 10 kHz and 1 MHz for water-saturated conditions. The thermal cracking increased substantially the amount of squirt-flow dispersion, with a much lower cut-off frequency measured around 100 Hz. The results for the Rustrel sample suggest that a small amount of squirt-flow dispersion is expected between 20 kHz and 1 MHz, and the coquina sample exhibited a sandstone-like behavior due to its detritic nature, with a large squirt-flow dispersion detected around 10 kHz.

3) - Except for the thermally induced cracks, it would seem that most of the ob-

served squirt-flow dispersions in water-saturated conditions were at the logging frequencies. Therefore, we can state that Biot-Gassmann's fluid substitution is generally valid for the seismic frequencies. Only thin cracks in large homogeneous crystals, such as the thermally induced cracks in the Indiana, would induce dispersion at seismic frequencies. The velocities would then be underestimated by Biot-Gassmann equation. The ultrasonic measurements seem to fall systematically within the unrelaxed regime. The previous statements apply solely for water-saturated conditions. The presence of a much more viscous fluid will shift the squirt-flow frequency to much lower frequencies. The logging measurements would fall within the unrelaxed regime, while the seismic measurements could either be undrained or unrelaxed. However, we found that for the samples of this study, the undrained and unrelaxed relaxed properties become equivalent for effective pressure higher than 20 MPa.

4) - The pressure-dependence of the dry bulk modulus enables to determine a crack distribution of the rock, susceptible to generate squirt-flow. We found that cracks in homogeneous large crystal, such as the thermally cracked Indiana or the coquina sample (grain contacts), are susceptible to generate squirt-flow at the predicted cut-off frequency applicable to sandstones. On the other hand, the results from the intact Indiana and the Rustrel limestones, showed that the squirt-flow mechanism is at higher frequencies than expected. A simple squirt-flow model was developed and is in agreement with the previous observations. Since no cracks were visible in the calcitic cements in the SEM images for both samples, we suspect that the "microcracks" (or the pressure-dependent compliant porosity) were located within the microporous grains or at the grain boundaries, resulting in a different hydraulic response.

5) - The non-interaction approximation effective medium was adapted to model both the drained/undrained transition and the squirt-flow phenomenon from penny-shaped cracks randomly oriented. The crack distribution is determined by Morlier's method from the pressure dependence of the dry, or drained, dynamic bulk modulus. The forward procedure attempts to predict the full dispersion and attenuation profiles with a limited number of measurable input parameters, and excluding any free adjustable parameter. In principle, the model can be easily extended to anisotropic crack orientations. The comparison with the experimental results on the carbonates shows that the amplitudes of dispersions are generally well predicted, but in some cases, the underlying micro-mechanical model is not appropriate, and predicts a much lower squirt-flow cut-off frequency.

Perspectives

Four main perspectives can be outlined.

1) - The experimental investigations in laboratory prove to be essential to characterize the dispersion and attenuation mechanisms in controlled conditions. However, the major

limitation of the current experiments is the requirement of small homogeneous samples, from which we can only characterize the dispersive effects of heterogeneities less than several millimeters size. In the field, dispersive effects from larger heterogeneities, such as fractures, are likely to occur and their effects would add to the dispersion at small scale. We can expect an additional flow from the fracture to the porous background that will depend on the permeability. Such upscaling problems regarding frequency effects were investigated numerically (*Quintal et al.*, 2012, 2014, 2016; *Rubino et al.*, 2014), but these models could not be confronted to experimental results obtained in laboratory. We propose here a new experiment to investigate the effect of a larger fracture using forced oscillations procedures as previously, and a cylindrical sample with one preexisting fracture, either vertical or horizontal. In a first approach, the fracture could be created by saw-cut in a known limestone. The main challenge is the strain measurement. Strain gauges could be glued far from the fracture as background references, and next to the fracture to observe fluid-flow related dispersion in the vicinity of the fracture. If the fracture is vertical, a radial extensiometer could be used to measure the radial strain of the fracture.

2) - We have found that thermal cracking (500°C) in the Indiana limestone, generates randomly oriented cracks in the cement, which were responsible for extensive dispersion due to squirt-flow. However, the subsurface reservoir rocks are more susceptible to have cracks generated by previous tectonic deformations or by compaction during production as the pore pressure drops. The squirt-flow mechanism of these mechanically induced cracks could be studied in the triaxial cell, after the sample was loaded near the yield envelops, either in the dilatant brittle failure domain, or in the compactant domain (Figure 10.13). Note that mechanical cracks orientation distribution is expected to anisotropic, especially in the dilatant domain with vertical cracks (Figure 10.13). In the compactant domain, the orientation distribution is expected to be more isotropic (Figure 10.13).

3) - One important field that requires more study is the comparison between the static and the dynamic moduli. The static moduli is essential as it is relevant for well-bore stability and reservoir compaction problems. Only few studies attempt to find correlations between static and dynamic measurements in rocks (e.g. *Fjær*, 2009). The principal mechanism proposed to explain the static/dynamic difference is the frictional sliding in closing cracks, occurring for large amplitudes of deformation. We propose here a new experiment using hydrostatic oscillations around a mean confining pressure, at low-frequency (e.g. $f \in [0.004; 0.02]$ Hz), where the frequency is kept constant but the amplitudes of the oscillations increases. For each amplitude, several cycles are performed to exclude any seasoning effects and to calculate the modulus using Fourier transform. The strain amplitude would start in the linear elastic domain ($\epsilon \sim 10^{-6}$) and progressively be increased step by step to large amplitudes ($\epsilon \sim 10^{-3}$) corresponding to the conventional static measurements. The effect of saturation on the possible frictional sliding could be investigated by doing the same cycles in dry and in drained-saturated conditions. The frequency should be low

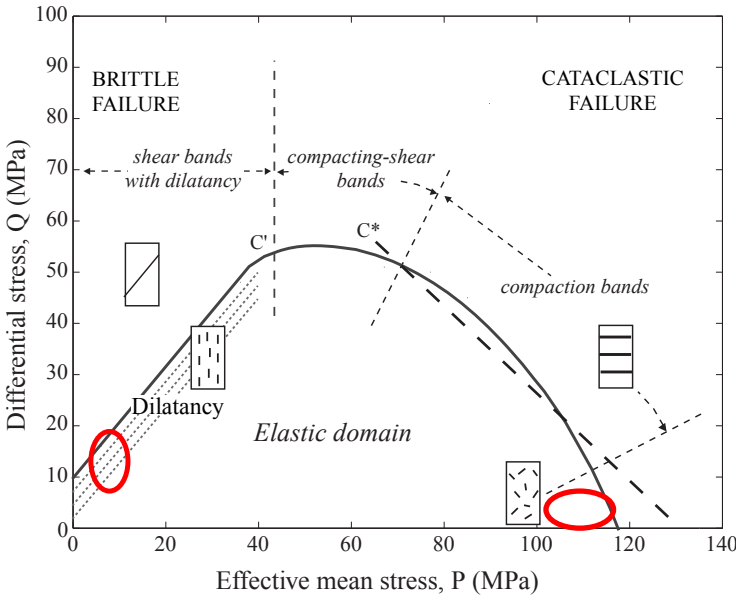

Figure 10.13: Example of the deformation map in the principle stress space for sandstones. Vertical cracks develop near the dilatancy envelop prior to brittle failure (left ellipse), while randomly oriented cracks may develop prior to the pore collapse failure with no deviatoric stress (right ellipse). Modified after *Fortin* (2005).

enough to ensure the drained conditions. Preliminary results were obtained on the water-saturated Rustrel limestone and are presented Figure 10.14. We observe the hysteresis loops in the stress-strain domain, which seem to exhibit a non-linear viscoelastic response as the amplitude increases due to the asymmetry between the loading and the unloading phase. For comparison, the endplaten aluminium remained in the linear elastic domain whatever the amplitude of deformation (Figure 10.14). The dissipated energy due to the frictional sliding in a cycle, represented by the surface of the loop in the stress-strain domain (Figure 10.14), can be calculated by numerical integration, and could give the estimation of an intrinsic "non-linear attenuation" that would be dependent on the strain amplitude, and would help to quantify the difference between static and dynamic measurements. However, Kramers-Kronig relations do not apply here as the viscoelasticity is not linear.

4) - Finally, one promising perspective would be the measurements of the frequency dispersion on well cores in the laboratory, for which seismic and log data are available on the field. The samples should be representative in terms of pore type or facies. This study would constitute a major step in order to integrate the frequency measurements in laboratory with the field observations.

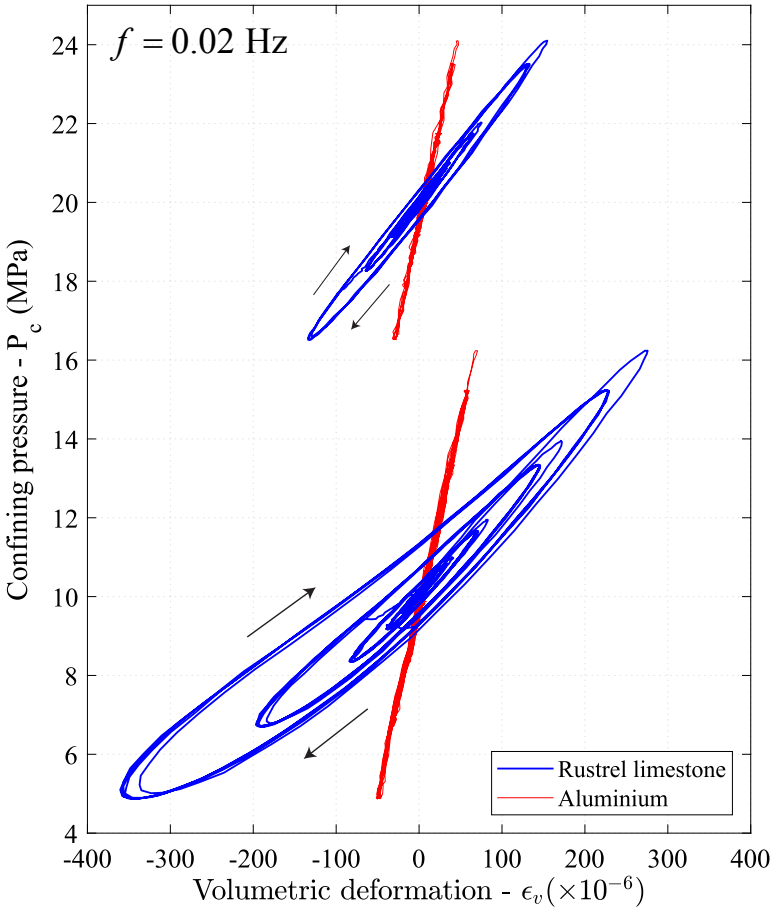

Figure 10.14: Preliminary results of hydrostatic oscillations at 0.02 Hz around 10 MPa and 20 MPa confining pressure, with increasing amplitude, on the water-saturated Rustrel limestone. The hysteresis increases with increasing amplitude, but is not comparable to a linear viscoelastic material that would give symmetrical ellipses. Instead, we observe non-linear viscoelasticity (asymetric) with a larger dissipation in the low-pressure part of the loop. The phenomenon is more pronounced at a mean pressure of 10 MPa than at 20 MPa, which could be correlated to the crack closure. The aluminum standard (endplaten strain gauge) exhibits a linear elastic response whatever the amplitude of oscillations.

CONCLUSIONS ET PERSPECTIVES

Conclusions

Les dispersions et atténuations des modules élastiques de calcaires saturés ont été caractérisées expérimentalement par l'utilisation d'oscillations forcées combinées à des mesures ultrasoniques, dans une nouvelle presse triaxiale à l'ENS de Paris. Les calcaires présentaient des microstructures différentes mais caractéristiques des roches carbonatées, et nous avons obtenu de nombreux résultats de dispersion et d'atténuation de tous les modules élastiques, pour les fréquences sismiques, de diagraphie et ultrasoniques. Le fil directeur de cette étude était de corréler la dispersion d'un écoulement local à une observation sur la microstructure observable au MEB. On peut mettre en avant cinq conclusions principales.

1) - Pour tous les échantillons, la transition drainé/non-drainé a été complètement caractérisée pour bien identifier les différents régimes d'écoulements. Cette transition s'est montrée en accord avec les équations de Biot-Gassmann, et sa fréquence de coupure est parfaitement prévisible si l'on mesure la perméabilité. Un modèle poroélastique 1D, qui résout l'équation de diffusion dans la direction verticale, a été développé pour modéliser cette transition et y inclure les effets de différentes conditions aux limites, tels que les petits volumes morts du système experimental.

2) - Pour le calcaire à porosité bimodale Lavoux, aucune dispersion d'écoulement crack-pore n'a été détecté au-delà du régime non-drainé, ce qui se corrèle bien avec l'insensibilité des modules élastiques à la pression effective, en dessous de 20 MPa. Cela suggère que les facteurs de forme des micropores intragranulaires et des macropores intergranulaires sont très similaires. Pour le calcaire Indiana, les résultats montrent qu'une faible dispersion liée aux écoulements cracks-pores est attendue entre 10 kHz et 1 MHz pour des conditions saturées en eau. Le craquage thermique a significativement augmenté cette dispersion, tout en diminuant sa fréquence de coupure autour de 100 Hz. Les résultats sur le Rustrel suggère également qu'une faible dispersion est attendue entre 20 kHz et 1 MHz, pendant que le coquina semble lui se comporter comme un grès due à sa nature détritique, avec une

large dispersion d'écoulement crack-pore observée autour de 10 kHz.

3) - A part pour les fissures induites thermiquement dans l'Indiana, il semblerait que les dispersions liées aux écoulements locaux soient systématiquement dans la gamme de fréquence des diagraphies en conditions saturées à l'eau. Ainsi, la théorie de Biot-Gassmann est en général valide pour les fréquences sismiques. Seuls des cracks à faible facteur de forme dans de larges cristaux, tels que dans l'Indiana craqué thermiquement, peuvent induire une dispersion aux fréquences sismiques. Les vitesses prédites par l'équation de Biot-Gassmann seraient alors sous-estimées. Les mesures ultrasoniques semblent être systématiquement dans le régime d'écoulement non-relaxé. Les observations précédentes ne sont valides que pour des saturations à l'eau. La présence d'un fluide beaucoup plus visqueux décalerait les transitions entre régimes d'écoulements vers de plus basses fréquences. Les diagraphies pourraient être dans le régime non-relaxé, et les mesures sismiques pourraient être en régime non-drainé ou non-relaxé. En revanche, pour l'ensemble des roches étudiées dans cette thèse, les propriétés non-drainées et non-relaxées deviennent équivalentes pour des pressions effectives supérieures à 20 MPa.

4) - La dépendance en pression du module d'incompressibilité en sec permet de déterminer une distribution de fissures dans la roche, susceptible de générer de la dispersion. Nous avons observé que des fissures dans de larges cristaux homogènes, telles que l'Indiana après craquage thermique ou le coquina (contacts entre grains), étaient susceptibles de générer une dispersion importante autour de la fréquence de coupure prédite f_{sq}, qui semblait en général bien s'appliquer aux grès. D'un autre côté, les résultats sur l'Indiana intact et le Rustrel montrent que cette dispersion à lieu à des fréquences bien plus élevées que la prédiction. Le modèle simple de dispersion est en accord avec ces observations. Puisque qu'aucune fissure n'était vraiment visible dans le ciment, sur les photomicrographies au MEB de ces deux échantillons, nous suspectons que la porosité compressible se trouve au sein de la microporosité des grains ou en périphérie, se qui pourrait modifier la réponse hydraulique.

5) - Le modèle effectif de non-interaction a été adapté pour modéliser la dispersion drainé / non-drainé et la dispersion d'écoulement crack-pore, pour des géométries de cracks proche de disques aplatis (penny-shaped), avec des orientations et distributions aléatoires dans l'espace. Les distributions des facteurs de formes et des densités de cracks sont calculées par la méthode de Morlier qui s'appuie sur la dépendance en pression du module K dynamique en sec, ou drainé. La procédure permet de simuler la dispersion des modules élastiques sur toute la gamme de fréquence, avec un nombre limité de paramètres d'entrée mesurables. Aucun paramètre libre d'ajustement n'est présent. En principe, ce modèle peut être étendu à des orientations anisotropes de cracks. La comparaison avec les données expérimentales montrent que les amplitudes de dispersion sont bien prédites, mais que parfois le modèle micromécanique utilisé sous-estime la fréquence de coupure de la transition d'écoulement crack-pore.

Perspectives

Quatre grandes perspectives peuvent être proposées.

1) - Les études expérimentales au laboratoire sont essentielles pour caractériser les mécanismes de dispersions et d'atténuations dans des conditions contrôlées. En revanche, une limitation majeure de nos expériences est qu'elles nécessitent de petits échantillons homogènes, pour lesquels on peut étudier les phénomènes dispersifs à une échelle d'hétérogénéité inférieure à quelques millimètres. Sur le terrain, des phénomènes dispersifs d'hétérogénéités beaucoup plus larges peuvent exister, par exemple liés aux fractures. Leurs effets viendraient s'additionner aux effets dispersifs à petite échelle. On pourrait s'attendre à un écoulement de la fracture vers la porosité du milieu environnant, qui dépendrait de la perméabilité. Les problèmes de changement d'échelle, liés aux effets de fréquences, peuvent être étudiés numériquement (*Quintal et al.*, 2012, 2014, 2016; *Rubino et al.*, 2014), mais ces modèles n'ont pas de données expérimentales de laboratoire sur lesquelles s'appuyer. On propose ici une nouvelle expérience pour comprendre l'effet d'une fracture, qui utilise les mêmes procédures d'oscillations forcées que précédemment, mais appliquées sur un échantillon qui aurait une fracture préexistante, soit verticale ou horizontale. En première approche, cette fracture pourrait être artificiellement sciée dans un calcaire homogène connu. Le défi réside dans la mesure de déformation. Des jauges de déformations pourraient être collées loin de la fracture pour servir de référence d'arrière plan, et près de la fracture pour voir son influence sur les dispersions des zones en marge. Si la fracture est verticale, un extensiomètre radial pourrait être utilisé pour mesurer la déformation intrinsèque de la fracture.

2) - Nous avons montré que le craquage thermique, à 500°C dans l'Indiana, a produit de larges populations de cracks isotropes dans le ciment calcitique qui génèrent de fortes dispersions. En revanche, les roches réservoir en subsurface sont plus susceptibles d'être fissuré à cause de mouvement tectoniques ou de compaction des réservoirs lors de la production, à mesure que la pression de pore diminue. Les phénomènes dispersifs liés à ce type de fissures, générées mécaniquement, peuvent être étudiés dans nos presses triaxiales, après que la roche soit emmenée près de son enveloppe limite. On note que la distribution d'orientation des fissures est suscéptible d'être anisotrope. Dans le domaine dilatant, des fissures verticales seraient générées, alors que dans le domaine compactant, les fissures auraient des orientations isotropes (Figure 10.13).

3) - Un domaine d'étude essentiel est la comparaison entre modules statiques et dynamiques. Les modules statiques sont les modules pertinents dans les études de stabilité des puits ou de compaction des réservoirs. Très peu d'études proposent des corrélations entre modules statiques et dynamiques dans les roches (e.g. *Fjær*, 2009). Le mécanisme principal qui expliquerait les différences entre modules statiques et dynamiques est le glissement frictionnel dans les fissures qui se ferment, se qui ne se produit que pour des larges amplitudes de déformation. On propose ici un nouveau protocole expérimental qui utiliserait

les oscillations hydrostatiques à basse fréquence ($f \in [0.004; 0.02]$ Hz) autour d'une pression moyenne, à fréquence constante, et en augmentant progressivement l'amplitude des oscillations. Pour chaque amplitude, les oscillations dureraient quelques périodes afin de pouvoir calculer un module K dans le domaine de Fourier, et de vérifier la réversibilité des cycles. L'amplitude de déformation commencerait dans le domaine linéaire élastique ($\epsilon \sim 10^{-6}$), et augmenterait étape par étape aux larges déformations proche des mesures statiques ($\epsilon \sim 10^{-3}$). L'effet d'un fluide saturant sur le glissement frictionnel dans les fissures pourrait être étudié, en comparant les résultats de ces oscillations en sec et saturé, sous condition que la fréquence soit suffisamment basse pour que la roche soit totalement drainée. Des résultats préliminaires ont déjà été obtenus sur le Rustrel saturé en eau, et sont présentés Figure 10.14. On peut clairement observer les cycles d'hystérésis dans l'espace contrainte-déformation, qui semble tendre vers un comportement viscoélastique non-linéaire à mesure que l'amplitude augmente due à l'asymétrie prononcé entre chargement et déchargement. En comparaison, l'aluminium del'embase est resté dans le domaine élastique linéaire pour toutes les amplitudes de déformations (Figure 10.14). L'énergie dissipée par friction interne pourrait être évaluée en calculant numériquement la surface de ces boucles d'hystérésis. Cela donnerait une estimation d'atténuation intrinsèque qui serait dépendante de l'amplitude, et permettrait de quantifier l'écart entre statique et dynamique. En revanche, les relations de causalités de Kramers-Kronig ne peuvent pas s'appliquer ici car la viscoélasticité est non-linéraire.

4) - Finalement, une perspective prometteuse serait de mesurer les effets de fréquence sur des échantillons de puits en laboratoire, pour lesquels des données sismiques et de diagraphie de terrain sont disponibles. Les échantillons devront être représentatif d'un type poreux ou d'un faciès. Cette étude serait une grande étape pour intégrer les effets de fréquence mesurés au laboratoire avec des données de terrains.

Appendices

Appendix A

Dispersion and attenuation measurements of the elastic moduli of a dual-porosity limestone.

Article published in **Journal of Geophysical Research: Solid Earth**.

Borgomano, J.V.M., L. Pimienta, J. Fortin and Y. Guéguen.

Published 22 April 2017

AGU PUBLICATIONS

JGR

Journal of Geophysical Research: Solid Earth

RESEARCH ARTICLE
10.1002/2016JB013816

Special Section:
Rock Physics of the Upper Crust

Dispersion and attenuation measurements of the elastic moduli of a dual-porosity limestone

J. V. M. Borgomano[1], L. Pimienta[1], J. Fortin[1], and Y. Guéguen[1]

[1]Laboratoire de Géologie de l'ENS, PSL Research University, Paris, France

Key Points:
- Elastic moduli dispersion and attenuation have been measured on a limestone, using stress-strain oscillations and ultrasonic measurements
- The drained/undrained transition has been measured for all moduli and is consistent with Biot-Gassmann's predictions
- There is no dispersive transition beyond the undrained regime, meaning no squirt flow or local diffusion between the micropores and macropores

Correspondence to:
J. V. M. Borgomano,
borgomano@geologie.ens.fr

Citation:
Borgomano, J. V. M., L. Pimienta, J. Fortin, and Y. Guéguen (2017), Dispersion and attenuation measurements of the elastic moduli of a dual-porosity limestone, *J. Geophys. Res. Solid Earth*, *122*, 2690–2711, doi:10.1002/2016JB013816.

Received 1 DEC 2016
Accepted 26 MAR 2017
Accepted article online 7 APR 2017
Published online 22 APR 2017

Abstract The dispersion and the attenuation of the elastic moduli of a Lavoux limestone have been measured over a large frequency range: 10^{-3} Hz to 10^{1} Hz and 1 MHz. The studied sample comes from a Dogger outcrop of Paris Basin and has the particularity to have a bimodal porosity distribution, with an equal proportion of intragranular microporosity and intergranular macroporosity. In addition to ultrasonic measurements, two different stress-strain methods have been used in a triaxial cell to derive all the elastic moduli at various differential pressures. The first method consists of hydrostatic stress oscillations ($f \in [0.004;\ 0.4]$ Hz), using the confining pressure pump, from which the bulk modulus was deduced. The second method consists of axial oscillations ($f \in [0.01;\ 10]$ Hz), using a piezoelectric oscillator on top of the sample, from which Young's modulus and Poisson's ratio were deduced. With the assumption of an isotropic medium, the bulk modulus (K) and the shear modulus (G) can also be computed from the axial oscillations. The sample was studied under dry, glycerin- and water-saturated conditions, in order to scale frequency by the viscosity of the fluid. Results show a dispersion at around 200 Hz for water-saturated conditions, affecting all the moduli except the shear modulus. This dispersion is related to the drained/undrained transition, and the bulk modulus deduced from the axial and hydrostatic oscillations are consistent with each other and with Biot-Gassmann's equations. No dispersion has been detected beyond that frequency. This was interpreted as the absence of squirt flow or local diffusion between the microporous oolites and the macropores.

1. Introduction

In fluid-saturated porous media, the dependence to frequency of the body wave velocities (V_P and V_S) rises questions on how to compare low-frequency field measurements (100 Hz for seismic data and 10 kHz for sonic logs) to conventional high-frequency measurements in the laboratory (1 MHz for ultrasonic). These dispersions in elastic wave velocities are related to the dispersion of the elastic moduli, which can be affected by fluid flows occurring at different scales in the porosity [*Batzle et al.*, 2006; *Muller et al.*, 2010; *Sarout*, 2012].

When the porous medium is submitted to an oscillating stress field, the deformation of the solid frame may induce a fluid pressure variation if the fluid has no time to diffuse through the pore network. In fully saturated conditions, this fluid diffusion can occur at different scales [*Sarout*, 2012]: global within the wavelength scale or local within a representative elementary volume (REV). Local flow, or squirt flow, may equalize the fluid pressure between compliant cracks and rounded pores within one REV [*Mavko and Jizba*, 1991], whereas global flow equalizes pressure through all the connected REVs. Three fluid flow regimes can be considered from this: drained, undrained, and unrelaxed regimes [*Pimienta et al.*, 2016a]. The undrained and unrelaxed regimes refer to, respectively, the saturated isobaric and the saturated isolated regimes described by *O'Connell and Budiansky* [1977]. The drained regime occurs when the fluid has time to diffuse by local and global flow through all the REVs. The elastic properties of the porous medium are similar to dry conditions. Then, when the frequency increases, the fluid stops diffusing at wavelength scale, letting place to the undrained regime. In this regime, the REVs are as disconnected from each other and remain isobaric. Because of the deformation of the frame, the fluid pressure increases in the porosity, therefore increasing the stiffness of the medium. The two previous regimes are well accounted for in quasi-static poroelasticity [*Gassmann*, 1951]. Finally, when the frequency is high enough, pressure may not equilibrate by local flow within the REVs. This is the case, for example, of squirt flow between cracks and stiff pores, leading to the unrelaxed regime [*Dvorkin et al.*, 1995; *Shafiro and Kachanov*, 1997]. In this regime, the fluid can be considered immobile, and higher pressure gradients are

maintained in the cracks. This increases further the stiffness of the medium. Effective medium theories are possible tools to predict the elastic properties in this last regime [e.g., *Adelinet et al.*, 2011].

While the elastic properties are not frequency dependent within a specific regime, they show dispersion and attenuation in the transitions between these regimes [*Pimienta et al.*, 2015a]. The two cutoff frequencies, f_1 and f_2, respectively for the drained/undrained transition and undrained/unrelaxed transition, can be expressed as follows [*O'Connell and Budiansky*, 1977; *Cleary*, 1978]:

$$f_1 = \frac{4kK_d}{\eta L^2} \quad \text{and} \quad f_2 = \frac{K_s \xi^3}{\eta}, \tag{1}$$

where k is the permeability, K_d is the drained bulk modulus, K_s is the skeleton's bulk modulus, ξ the average crack aspect ratio, η the fluid's dynamic viscosity, and L the wavelength. At low frequencies in the laboratory, the corresponding wavelength is generally larger than the sample's length, in which case L is taken equal to the sample's length. When there is dispersion of an elastic modulus M, in other words, when there is viscous dissipation in the fluid, the rheology of the medium is similar to that of a viscoelastic material [*O'Connell and Budiansky*, 1977]. One can measure a phase shift $\Delta\phi$ between the stress and the strain response. The dissipation related to M is usually quantified from the inverse of the quality factor Q_M^{-1}, such that [*O'Connell and Budiansky*, 1978]:

$$Q_M^{-1} = \tan(\Delta\phi). \tag{2}$$

Carbonate rocks are characterized by complex microstructures and heterogeneous pore types [*Lucia*, 1995]. For a given porosity, carbonate rocks were shown to exhibit a wide range of *P* wave and *S* wave velocities, due to the large variety of pore types [*Eberli et al.*, 2003]. Their elastic properties are affected by the pore network and the mineralogy, which can be modified through diagenetic processes [*Fournier and Borgomano*, 2009]. Several studies have attempted to understand the relationship between seismic wave velocity and porosity [e.g., *Anselmetti and Eberli*, 1993; *Verwer et al.*, 2010] or to verify the applicability of Biot-Gassmann's fluid substitution theory [e.g., *Baechle et al.*, 2009; *Fabricius et al.*, 2010]. Very few studies aimed at characterizing the dispersion and the attenuation at seismic frequencies in carbonate rocks, due to the interplay between microstructure and fluid flow [e.g., *Adam et al.*, 2006, 2009; *Mikhaltsevitch et al.*, 2016a]. This is, however, essential in hydrocarbon exploration and reservoir characterization, to improve the inversion of the rock properties using seismic data. In this study, we present our first measurements of dispersion and attenuation of the elastic moduli of a pure calcite oolitic limestone from Lavoux (France).

2. Experimental Setup

To measure the dispersion and the attenuation of the elastic moduli over a large frequency range, we used the stress-strain method, combined with ultrasonic measurements, in a triaxial cell at the ENS of Paris (Figure 1) [*Fortin et al.*, 2005, 2014; *Adelinet et al.*, 2010; *David et al.*, 2013]. The detailed experimental protocol and the calibration of the apparatus on standard materials can be found in *Pimienta et al.* [2015a] and *Pimienta et al.* [2015b]. With this apparatus, two types of stress oscillations can be achieved: hydrostatic (Figure 1a) to measure the bulk modulus (K) and axial (Figure 1b) to measure the Young's modulus (E) and the Poisson's ratio (ν). To investigate the effect of the fluid's viscosity, the sample's properties were measured under dry, glycerin-saturated and finally water-saturated conditions. At room temperature (22° C), the viscosity of pure glycerin and water is, respectively, $\eta_{gly} = 1$ Pa s and $\eta_{water} = 10^{-3}$ Pa s [*Segur and Oberstar*, 1951] . We also studied the effect of the boundary conditions on the measured elastic properties, with two different configurations for the drainage system: (1) open (drained conditions) and (2) closed (undrained for the system {*sample* + *dead volumes*}) (Figure 1a). *Pimienta et al.* [2016b] demonstrated that the effect of the dead volumes on the measured properties depends upon the ratio of the storage capacities of the sample and the drainage system. In the drained frequency range, the measured properties would tend to their undrained value if the dead volumes tend to zero. The dead volumes of the closed drainage system (second case) were measured at about $V_d = 3.3$ mL for the top and bottom end platens [*Pimienta et al.*, 2016b]. *Pimienta et al.* [2016b] showed that if the dead volumes are greater than $10V_d$, the measured properties converge to the fully drained values. For our experiments, when the drainage system is open (first case), the dead volumes are in fact much larger and correspond to the volume of all the hydraulic tubings added to the volume of fluid in the Quizix pumps (~60 mL). During the stress oscillations, the pore pressure pumps are shut off, to avoid a fluid-induced response back to the sample.

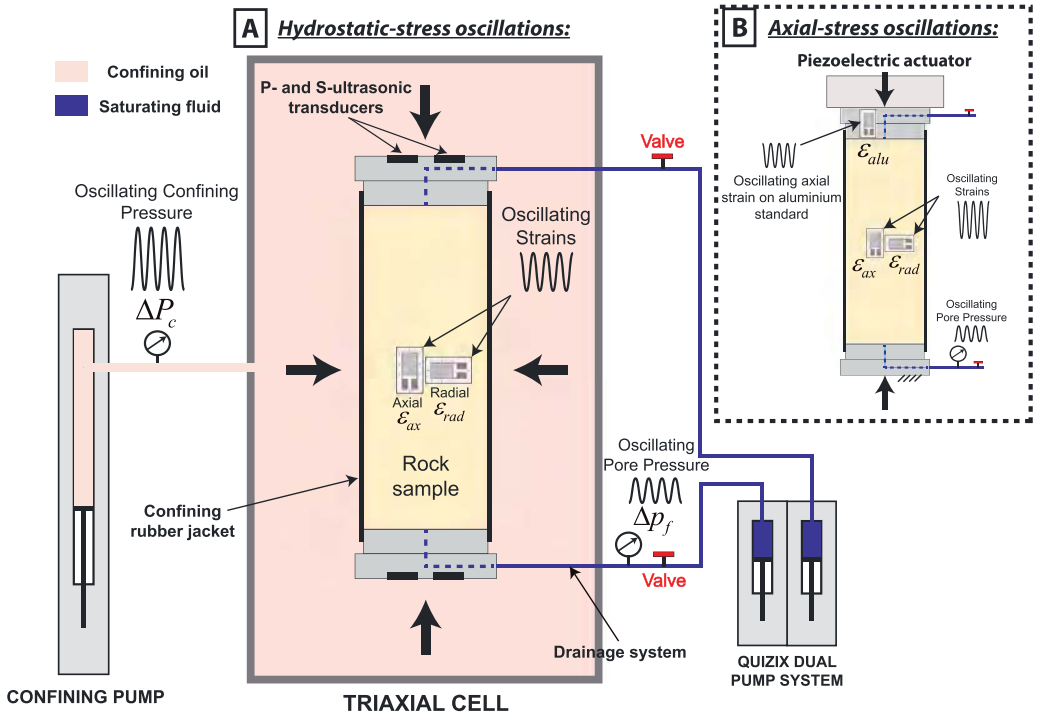

Figure 1. Schematics of the experimental setup for (a) hydrostatic oscillations and (b) axial oscillations, in the triaxial cell at the ENS of Paris. The hydrostatic oscillations were imposed by the confining pump, in the frequency range of [0.004; 0.4] Hz. The axial oscillations were imposed by a piezoelectric actuator mounted over the top end platen, in the frequency range of [0.01; 10] Hz. Strains are measured by axial and radial strain gauges bonded on the sample at midheight. Ultrasonic transducers are settled in the end platens to obtain the *P* and *S* wave velocities at 1 MHz.

The sample is 8 cm long and 4 cm diameter cylinder. To measure the strains, four pairs of 350Ω metal foil strain gauges with axial and radial orientations are glued at midheight all around the lateral surface (Figure 1). Axial strain (ε_{ax}) and radial strain (ε_{rad}) are averaged from all the strain gauges. The sample is under a rubber jacket that separates the pore pressure (p_f) from the confining pressure (P_c) (Figure 1a). When the sample is fluid saturated, the pore pressure is controlled by a Quizix dual pump system connected to the top and bottom of the sample through a drainage circuit (Figure 1a). Throughout all the measurements, the pore pressure was maintained at 2 MPa. Measurements at different differential pressures ($P_{diff} = P_c - p_f$) were done, in a range below the pore-collapse pressure (P^*) of the sample.

2.1. Hydrostatic Stress Oscillations—Bulk Modulus

The hydrostatic stress oscillations give a direct measurement of the bulk modulus K_{hyd} [*Pimienta et al.*, 2015a]. The oscillations are obtained from the confining pressure ΔP_c that oscillates with an amplitude of 0.2 MPa around a mean value P_c (Figure 1a). This amplitude value has been calibrated in order to obtain small strains on the sample ($\varepsilon \sim 10^{-6}$) to remain in the linear elastic domain (Figure 2a) [*Winkler and Murphy*, 1995]. The frequency of these hydrostatic oscillations is between 4×10^{-3} Hz and 4×10^{-1} Hz. The induced volumetric strain signal (ε_{vol}) is calculated by $\varepsilon_{vol} = \varepsilon_{ax} + 2\varepsilon_{rad}$. Thus, the bulk modulus K_{hyd} is obtained from the measured stress ΔP_c and the measured strain ε_{vol} such that

$$K_{hyd} = \frac{-\Delta P_c}{\varepsilon_{vol}}, \tag{3}$$

with the convention $\Delta P_c = -\sigma_{ii}/3$. A linear regression of the stress signal versus the strain signal is then processed to calculate K_{hyd} (Figure 2b).

2.2. Axial Stress Oscillations—Young's Modulus and Poisson's Ratio

In order to perform axial stress oscillations [e.g., *Batzle et al.*, 2006; *Mikhaltsevitch et al.*, 2014; *Tisato and Madonna*, 2012; *Madonna and Tisato*, 2013; *Pimienta et al.*, 2015b; *Szewczyk et al.*, 2016], we used a piezoelectric actuator that is mounted between the axial piston of the triaxial cell and the top end platen (Figure 1b).

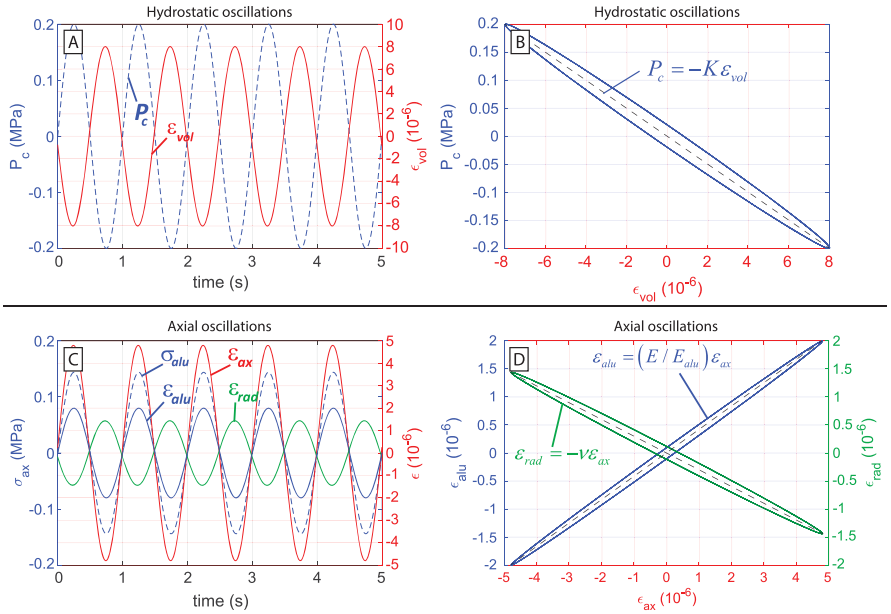

Figure 2. Example of stress and strain versus time recordings during (a, b) hydrostatic oscillations and (c, d) axial oscillations. The elastic moduli are calculated from the linear regressions of the stress versus strain curves (Figures 2b–2d). The ellipse shapes (hysteresis) result from the phase shift between stress and strain when dispersion occurs, similarly to viscoelastic materials.

A small deviatoric stress of 1 MPa is maintained on the assemblage in order to have a good contact. The frequency range of the oscillations applied on the Lavoux sample is 10^{-2} Hz to 10 Hz. The top end platen is made out of AU4G aluminum and is bonded with two axial strain gauges acting as a axial stress sensor (Figure 1b). During the measurements, the two axial strains are averaged (ε_{alu}) and the axial stress is computed from $\sigma_{ax} = E_{alu}.\varepsilon_{alu}$ (Figure 2c), where E_{alu} is the Young's modulus of AU4G (E_{alu}=72 GPa). With the measurements of the axial strain (ε_{ax}) and the radial strain (ε_{rad}) of the sample (Figure 2c), we can directly obtain the Young's modulus (E) and the Poisson's ratio (ν) of the sample:

$$E = \frac{\sigma_{ax}}{\varepsilon_{ax}} \quad \text{and} \quad \nu = -\frac{\varepsilon_{rad}}{\varepsilon_{ax}}. \tag{4}$$

E and ν are determined by linear regression of the signals, respectively, σ_{ax} over ε_{ax} and $-\varepsilon_{rad}$ over ε_{ax} (Figure 2d). A bulk modulus (K_{ax}) and a shear modulus (G_{ax}) are calculated, with the assumption of an isotropic medium:

$$K_{ax} = \frac{E}{3(1-2\nu)} \quad \text{and} \quad G_{ax} = \frac{E}{2(1+\nu)}. \tag{5}$$

K_{ax} can then be compared to the bulk modulus K_{hyd} obtained from the hydrostatic oscillations to validate the assumption of isotropy and to check the consistency of the results.

2.3. Attenuation — Q^{-1} Measurements

The factor Q^{-1} measures the elastic energy dissipation within the sample. When this dissipation occurs, the rheology of the medium is similar to a viscoelastic material [*O'Connell and Budiansky*, 1977]. The stress-strain curve presents an elliptic shape that clearly highlights the nonelastic behavior (e.g., Figures 2b and 2d). This results from the phase shift between the stress and the strain (equation (2)). During a dynamic oscillation of frequency f, the complex stress can be expressed as $\bar{\sigma} = \sigma e^{i(2\pi ft+\phi_\sigma)}$ and the resulting complex strain $\bar{\varepsilon} = \varepsilon e^{i(2\pi ft+\phi_\varepsilon)}$, where ϕ_σ and ϕ_ε are the phases of $\bar{\sigma}$ and $\bar{\varepsilon}$. For each elastic modulus, the calculation of the Q^{-1} factor is based on the causality principle, where the complex modulus $\bar{M}$ relates the stress $\bar{\sigma}$ to its resulting strain $\bar{\varepsilon}$:

$$\bar{\sigma} = \bar{M}\bar{\varepsilon}. \tag{6}$$

The factor Q_M^{-1} of the modulus $\bar{M}$ is then defined as follows [*O'Connell and Budiansky*, 1978]:

$$Q_M^{-1} = \frac{\mathrm{Im}(\bar{M})}{\mathrm{Re}(\bar{M})} = \frac{\mathrm{Im}\left(\bar{\sigma}/\bar{\varepsilon}\right)}{\mathrm{Im}\left(\bar{\sigma}/\bar{\varepsilon}\right)} = \tan\left(\phi_\sigma - \phi_\varepsilon\right), \tag{7}$$

In the case of the bulk modulus measured from hydrostatic oscillations, $Q_{K_{\mathrm{hyd}}}^{-1}$ is deduced from the phase shift between the hydrostatic stress $-\Delta P_c$, with the convention $\Delta P_c = -\sigma_{ii}/3$, and the volumetric strain $\varepsilon_{\mathrm{vol}}$. With the combination of equations (3) and (7), we obtain the following:

$$Q_{K_{\mathrm{hyd}}}^{-1} = \tan\left(\phi_{-\Delta P_c} - \phi_{\varepsilon_{\mathrm{vol}}}\right). \tag{8}$$

The Young's modulus and Poisson's ratio factors Q_E^{-1} and Q_ν^{-1} are deduced from equations (4) and (7):

$$Q_E^{-1} = \tan\left(\phi_{\sigma_{\mathrm{ax}}} - \phi_{\varepsilon_{\mathrm{ax}}}\right) \quad \text{and} \quad Q_\nu^{-1} = \tan\left(\phi_{\varepsilon_{\mathrm{ax}}} - \phi_{\varepsilon_{\mathrm{rad}}}\right). \tag{9}$$

To derive Q^{-1} for K_{ax} and G_{ax}, with the assumptions of isotropy and small strains, we combine equations (4) and (5) as follows:

$$K_{\mathrm{ax}} = \frac{1}{3}.\frac{\sigma_{\mathrm{ax}}}{\varepsilon_{\mathrm{ax}} + 2\varepsilon_{\mathrm{rad}}} \quad \text{and} \quad G_{\mathrm{ax}} = \frac{1}{2}.\frac{\sigma_{\mathrm{ax}}}{\varepsilon_{\mathrm{ax}} - \varepsilon_{\mathrm{rad}}}. \tag{10}$$

For both K_{ax} and G_{ax} the stress is σ_{ax} and the resulting strains are, respectively, $\varepsilon_{\mathrm{ax}} + 2\varepsilon_{\mathrm{rad}}$ and $\varepsilon_{\mathrm{ax}} - \varepsilon_{\mathrm{rad}}$. After combining equations (7) and (10), the related attenuations are as follows:

$$Q_{K_{\mathrm{ax}}}^{-1} = \tan\left(\phi_{\sigma_{\mathrm{ax}}} - \phi_{\varepsilon_{\mathrm{ax}}+2\varepsilon_{\mathrm{rad}}}\right) \quad \text{and} \quad Q_{G_{\mathrm{ax}}}^{-1} = \tan\left(\phi_{\sigma_{\mathrm{ax}}} - \phi_{\varepsilon_{\mathrm{ax}}-\varepsilon_{\mathrm{rad}}}\right) \tag{11}$$

Three different methods can be used to calculate the Q^{-1} factors [e.g., *Tisato and Madonna*, 2012]. The first method consists of fitting two sine functions $y = A\sin(2\pi f + \phi)$ through the stress and strain signals and extract ϕ from each signal to calculate the phase shift $\phi_\sigma - \phi_\varepsilon$. The second method consists in extracting the phases from a Fourier analysis of the signals. For this purpose a fast Fourier transform (FFT) algorithm is applied on the stress and strain signals. And finally, the last method is based on the definition of Q^{-1} factor that relates Q^{-1} to the dissipated elastic energy (ΔE) during a stress-strain cycle and to the average elastic energy stored (E_m) as follows [*O'Connell and Budiansky*, 1978]:

$$Q^{-1} = \frac{\Delta E}{4\pi E_m}. \tag{12}$$

When viscous dissipation occurs in the fluid, the stress-strain curve presents an elliptic shape, similarly to viscoelastic materials (e.g., Figures 2b and 2d). The dissipated energy ΔE is equal to the surface of this ellipse, and E_m is equal to the average surface under the stress-strain curve. The surfaces that represent ΔE and E_m can be calculated from the stress versus strain curve by numerical integration [*Tisato and Madonna*, 2012]:

$$\Delta E = \sum_{n=1}^{N-1} \frac{\left(\sigma_{n+1} + \sigma_n\right)\left(\varepsilon_{n+1} - \varepsilon_n\right)}{2N_c} \quad \text{and} \quad E_m = \sum_{n=1}^{N} \frac{\sigma_n \varepsilon_n}{2N}, \tag{13}$$

where σ_n and ε_n are all the data points of, respectively, $\bar{\sigma}$ and $\bar{\varepsilon}$ signals during one recording, N is the total number of sampled data and $N_c = f.t_{\mathrm{tot}}$ is the number of cycles, f being the frequency of the oscillation, and t_{tot} the total time of the sequence. For simplicity, the three methods presented above are, respectively, denominated as "Sines," "FFT," and "Ellipse" methods in the following text. The experimental measurements presented later in the results section were calculated from the Ellipse method, and comparison between the three methods will be provided for the axial oscillations.

The relation between the dispersion and the attenuation of the complex modulus, $\bar{M}$, arises from the causality principle between the stress and strain that is expressed through the Kramers-Kronig equations [*Mikhaltsevitch et al.*, 2016b]. If $\bar{M} = M_R + iM_I$, with i the imaginary unit, M_R the real part, and M_I the imaginary part of $\bar{M}$, an approximation of the Kramers-Kronig equations was found by *O'Donnell et al.* [1981]:

$$M_I(\omega) = \frac{\pi}{2}\omega\frac{dM_R(\omega)}{d\omega}, \tag{14}$$

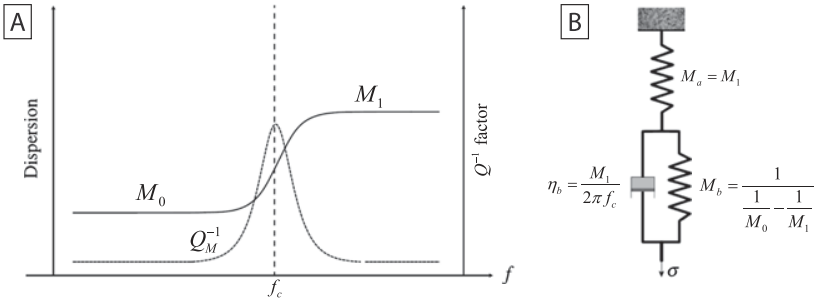

Figure 3. Zener's viscoelastic model used to calculate the attenuation from the dispersion. (a) Model applied to the dispersion of the modulus M of relaxed value M_0 and unrelaxed value M_1. (b) Spring-damper representation of Zener's model, with the relationships between the springs elastic moduli (M_a and M_b) and dispersion's relaxed and unrelaxed values (M_0 and M_1). The viscosity (η_b) of the damper is a function of M_1 and the cutoff frequency f_c: $\eta_b = M_1/2\pi f_c$.

where $\omega = 2\pi f$. The major drawback of applying equation (14) to experimental data is that an accurate calculation of the derivative $dM_R/d\omega$ by finite difference requires a good resolution in ω.

Because our experimental measurements did not necessarily have a proper resolution in ω, the consistency between the measured dispersion and attenuation was verified instead with a Zener viscoelastic model [*Pimienta et al.*, 2015a]. The equivalent spring-damper model is represented in Figure 3b, and its transfer function $\bar{M}$ can be expressed with the viscoelastic parameters of the system:

$$\bar{M} = \frac{1 + i\omega\tau}{\left(\frac{1}{M_a} + \frac{1}{M_b}\right) + \frac{i\omega\tau}{M_a}}, \tag{15}$$

where M_a and M_b are the moduli of the two springs and $\tau = \eta_b/M_b$ where η_b is the viscosity of the dashpot element (Figure 3b). This model follows the assumption that only one viscous dissipation mechanism is involved. With the approximation $M_a \ll M_b$, equations (7) and (15) give the following:

$$Q_M^{-1} \simeq \frac{\omega\tau}{1 + \omega^2\tau^2}\frac{M_a}{M_b}. \tag{16}$$

If we consider a dispersive transition where the sample's modulus ($\bar{M}$) varies from M_0 to M_1 around the cutoff frequency f_c (Figure 3a), the elastic parameters of the Zener model become $M_a = M_1$ and ${M_b}^{-1} = {M_0}^{-1} - {M_1}^{-1}$, and the viscosity of the dashpot becomes $\eta_b = M_1/2\pi f_c$ (Figure 3b). Therefore, only three parameters are required to calculate the Q^{-1} factor from Zener's model: the moduli M_0 and M_1 and the cutoff frequency f_c. It is to note here that if the dispersion is related to the global flow, M_0 and M_1 would be the drained and undrained (isobaric) moduli. If the dispersion is related to squirt flow, M_0 and M_1 would be the undrained (isobaric) and unrelaxed (isolated) moduli.

2.4. Ultrasonic Measurements

In addition to the stress-strain oscillations, the apparatus enables the measurement of ultrasonic (~ 1 MHz) moduli from *P* and *S* wave transducers, glued in the end platens at both ends on the sample (Figure 1a). *P* and *S* wave velocities V_P and V_S are inferred from the traveltime (Δt) of the ultrasonic waves through the sample's length ($L = 80$ mm), after correction of the traveltime through the end platens. The arrival times of the *P* and *S* waves are handpicked with a maximum error of $\pm 0.1\mu$s. The velocity (V) is then calculated by $V = L/\Delta t$. With a maximum error on L of ± 0.01 mm, the relative uncertainty on the velocities is about $\Delta V/V = 0.5\%$. The high-frequency moduli K_{HF} and G_{HF} are obtained by the well-known formulas:

$$K_{HF} = \rho\left({V_P}^2 - \frac{4}{3}{V_S}^2\right) \quad \text{and} \quad G_{HF} = \rho{V_S}^2, \tag{17}$$

where ρ_{sample} is the density of the medium, calculated from the density of the dry sample $\rho_{dry} = 2160$ kg m^{-3}, the density of the saturating fluid ρ_{fluid}, and the porosity ϕ by $\rho_{sample} = \rho_{dry} + \phi.\rho_{fluid}$. The densities of glycerin and water are, respectively, $\rho_{gly} = 1250$ kg/m^3 and $\rho_{water} = 1000$ kg/m^3 [*Bosart and Snoddy*, 1927]. With a relative uncertainty on ρ estimated around 1%, the relative uncertainty of the product ρV^2 is about 2%. From this we can deduce the relative uncertainties $\Delta K_{HF}/K_{HF} \simeq 4\%$ and $\Delta G_{HF}/G_{HF} \simeq 2$ for, respectively, the ultrasonic

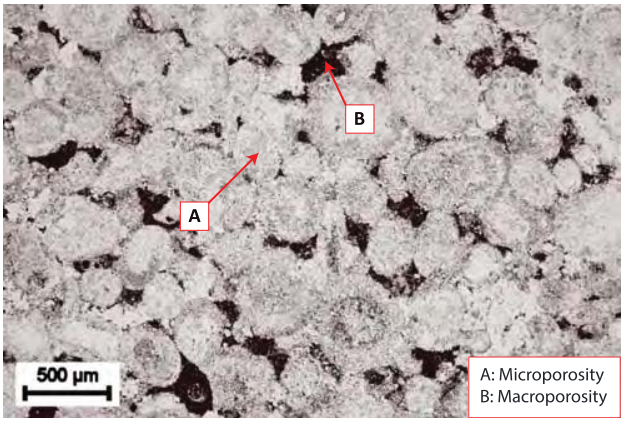

Figure 4. SEM photomicrograph of the Lavoux sample. The sample is a pure calcite grainstone composed of microporous oolites (marker A), surrounded by macropores (marker B). The average size of the oolites is around 300µm.

bulk and shear modulus. Before measuring the traveltimes of the elastic waves in the sample, an aluminum standard (2007A/AU4G) of 80 mm length was measured to calibrate the traveltimes in the top and bottom end platens.

3. Sample Description

The studied sample is a Lavoux limestone that was quarried in Paris Basin and was extensively studied in the literature [e.g., *Fabre and Gustkiewicz*, 1997; *Rasolofosaon and Zinszner*, 2002; *Youssef et al.*, 2008; *Bemer and Lombard*, 2010; *Vincent et al.*, 2011; *Zinsmeister*, 2013]. It is from Dogger age and is considered as an analogue to the White Oolitic Formation of Paris Basin [*Bemer and Lombard*, 2010]. It is a pure calcite oolitic grainstone with intergranular macroporosity and intragranular microporosity (Figure 4). Mercury porosimetry measurements from *Zinsmeister* [2013] or *Vincent et al.* [2011] confirm the presence of a connected bimodal porosity distribution with pore entry diameters around 0.6 µm and 20 µm, which corresponds, respectively, to the intra-oolite micropores and the interoolite macropores. Moreover, the NMR unimodal distribution results from *Vincent et al.* [2011] were interpreted as indicating a good connectivity between the intragranular-micropore network and the intergranular-macropore network.

The porosity was measured around 23% from the triple-weight method, where the sample's mass is measured under three different conditions: dry, fluid saturated, and suspended in the saturant. Image analysis of the SEM photomicrograph enables to evaluate the proportion of macroporosity in the total porosity. A threshold was applied on the gray scale of the photomicrograph to turn it into a binary image showing solely the macropores (Figure 5). The macropores' proportion in the binary image, combined with the previous

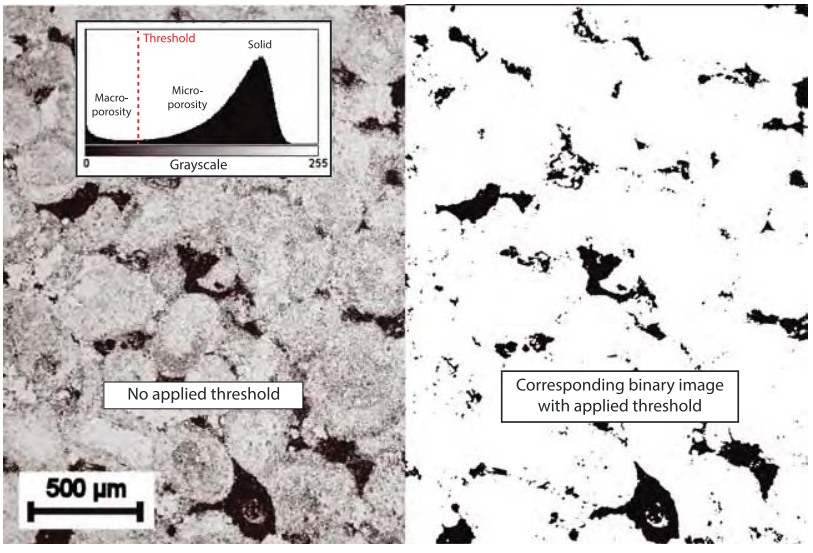

Figure 5. Determination of the proportion macroporosity/microporosity in the sample from the gray scale analysis of the SEM photomicrograph. A threshold is applied on the initial photomicrograph (left), to create a binary image representing solely the macropores (right). The porosity of the macropores is calculated from the number of black pixels over the total number of pixels of the image, evaluated at 10.35%. With a total porosity of 23% measured experimentally, the proportion of macroporosity over microporsity is therefore around 45/55.

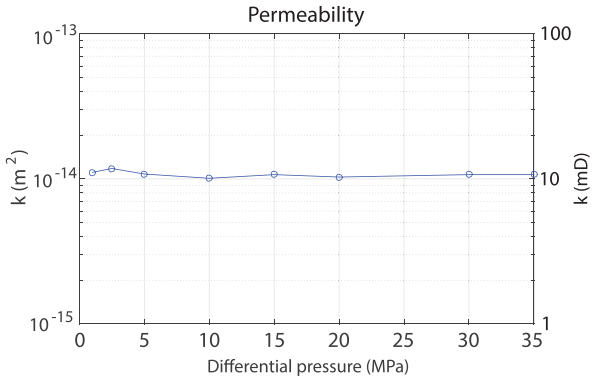

Figure 6. Intrinsic permeability of the Lavoux sample as a function of differential pressure. The measurements were obtained by Darcy's law under water-saturated conditions. The results show no dependence to the effective pressure.

experimental porosity, gives a contribution to the total porosity of 45% and 55% for the macroporosity and the microporosity, respectively. The permeability was measured to be around 10 mD, under water-saturated conditions, and shows no dependence to differential pressure (Figure 6).

4. Results

4.1. Pressure Dependence of the Sample's Elastic Properties

Ultrasonic measurements and the axial oscillations have been performed at differential pressures from 2.5 MPa to 20 MPa, to check the pressure dependence of the elastic moduli. The traveltimes measured for the Lavoux limestone are reported in Table 1, along with the deduced *P* wave and *S* wave velocities and high-frequency moduli K_{HF} and G_{HF} (equation (17)). K_{HF} and G_{HF} for dry-, water-, and glycerin-saturated conditions as a function of differential pressure are represented in Figure 7. No variation in pressure is to be noted. K_{HF} is constant at about 14.5 GPa, 21.5 GPa, and 25.5 GPa, respectively, for the dry-, water-, and glycerin-saturated conditions. We can see that the fluid nature strongly affects the high-frequency bulk moduli. On the other hand, G_{HF} remains constant at 9.5 GPa, with no sensitivity to the fluid nature.

For the axial oscillations at different pressures, the Young's modulus (E) and Poisson's ratio (ν) results measured at 5×10^{-2} Hz, 10^{-1} Hz, and 5 Hz are presented in Figure 8. Again, no dependence to differential pressure is observed, either for Young's modulus (Figure 8a) or Poisson's ratio (Figure 8b). Under dry conditions, no dependence to f is observed. Under glycerin-saturated conditions, nearly no dependence to f is observed on E (Figure 8a), but a large one is observed on ν (Figure 8b).

We can conclude that, similarly to the permeability, the elastic properties of the Lavoux limestone seem to not depend on the differential pressure. Therefore, in the following, all the results will be presented solely for a differential pressure of 2.5 MPa and can be considered as independent of differential pressure.

4.2. Axial Stress Oscillations Results at $P_{diff} = 2.5$ MPa

The dispersion and attenuation results from the axial and the hydrostatic oscillations under dry-, water-, and glycerin-saturated conditions are presented in Figures 9–11. The results are represented as a function of an

Table 1. Ultrasonic Measurements (1 MHz) on the Lavoux Limestone Under Dry-, Water-, and Glycerin-Saturated Conditions[a]

Saturating Fluid	P_{diff} (MPa)	t_P (μs)	t_S (μs)	V_P (m s^{-1})	V_S (m s^{-1})	K_{HF} (GPa)	G_{HF} (GPa)
	2.5	23.0	38.5	3520	2103	14.0	9.6
Dry	5	22.4	38.0	3614	2131	15.4	9.8
$\rho_{sample} = 2160$ kg m^{-3}	10	23.0	38.0	3520	2131	13.7	9.8
	15	22.4	38.0	3614	2131	15.1	9.8
	20	22.5	38.0	3598	2131	14.9	9.8
Water	2.5	21.4	40.8	3783	1984	21.7	9.4
$\rho_{sample} = 2391$ kg m^{-3}	10	21.5	40.6	3766	1994	21.2	9.5
	2.5	20.6	42.3	3930	1914	25.9	9.0
Glycerin	5	20.4	42.2	3969	1918	26.5	9.0
$\rho_{sample} = 2448$ kg m^{-3}	10	20.8	42.0	3892	1928	25.0	9.1
	15	20.7	41.6	3911	1946	25.1	9.3
	20	20.6	41.4	3930	1956	25.3	9.4

[a]The traveltimes t_P and t_S were corrected from the traveltimes in the end platens. The length of the sample is 80 mm. K_{HF} and G_{HF} are deduced from equation (17).

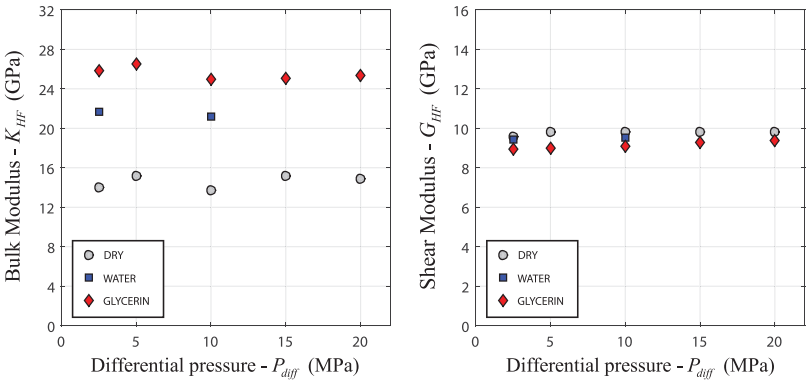

Figure 7. Ultrasonic results (1 MHz) at different differential pressures ($P_{diff} = P_c - p_f$) for (left) the bulk modulus (K_{HF}) and (right) the shear modulus (G_{HF}), for dry-, water-, and glycerin-saturated conditions.

apparent frequency $f^* = f.(\eta_{fluid}/\eta_{water})$ to take into account the effect of the fluid's viscosity, with water as the reference fluid ($\eta_{water} = 10^{-3}$ Pa s). For dry conditions, the viscosity of air is considered at about $\eta_{air} = 10^{-5}$ Pa s. The Q^{-1} factor results are calculated from the Ellipse method and are systematically compared to Zener's viscoelastic model. The measurements are done with the valves of the drainage circuit open (Figure 1a), i.e., in drained boundary conditions, with a pore pressure of $p_f = 2$ MPa.

The Young's modulus and Poisson's ratio dispersion and attenuation results from the axial oscillations at $P_{diff} = 2.5$ MPa are presented in Figure 9. The Young's modulus (E) is constant around 22.5 GPa between 10^{-3} Hz and 10^2 Hz, with a good agreement between the dry, water, and glycerin saturations (Figure 9a). Then, E increases slightly between 10^2 Hz and 10^3 Hz from 22.5 GPa to 24 GPa (Figure 9a). The factor Q_E^{-1} results are consistent with the dispersion data: no attenuation under 10^2 Hz, a small peak around $Q_E^{-1} = 0.025$ at 3×10^2 Hz, and no more attenuation beyond 10^3 Hz (Figure 9b). Moreover, the results are in good agreement with Zener's model, using the parameters $M_0 = 22.5$ GPa, $M_1 = 24$ GPa, and $f_c = 220$ Hz (Figure 3).

Similarly to E, the Poisson's ratio (ν) below 10^2 Hz shows no dispersion, but a slight disagreement subsists between the dry- ($\nu = 0.25$) and the water- and glycerin-saturated results ($\nu = 0.275$) (Figure 9c). Then ν increases from 0.275 to 0.35 between 5×10^1 Hz and 10^3 Hz (Figure 9c), in correlation with a Q_ν^{-1} peak of 0.08 at around 3×10^2 Hz (Figure 9d). For this case, Zener's model seems to overpredict the attenuation. The Zener peak is around 0.13 at 3×10^2 Hz, with the parameters $M_0 = 0.275$ and $M_1 = 0.35$. (Figure 9d).

Assuming isotropic conditions, the dispersion and attenuation results of the bulk modulus and the shear modulus, deduced from E and ν, are presented in Figure 10. The bulk modulus deduced from the axial oscillations (K_{ax}) shows a large dispersion from 16 GPa to 26 GPa between $f^* = 5 \times 10^1$ Hz and $f^* = 10^3$ Hz, visible under glycerin-saturated conditions (Figure 10a). The corresponding attenuation peak reaches $Q_{K_{ax}}^{-1} = 0.225$ around $f^* = 3 \times 10^2$ Hz with a good fit with Zener's model with the parameters $M_0 = 16$ GPa and $M_1 = 26$ GPa. The shear

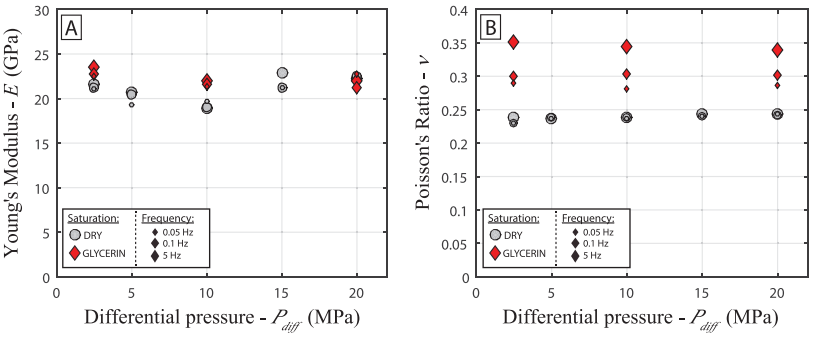

Figure 8. Axial oscillations results at different differential pressures ($P_{diff} = P_c - p_f$) for (a) Young's modulus (E) and (b) Poisson's ratio (ν). The results for dry- and glycerin-saturated conditions are presented, for 0.05 Hz, 0.1 Hz, and 5 Hz.

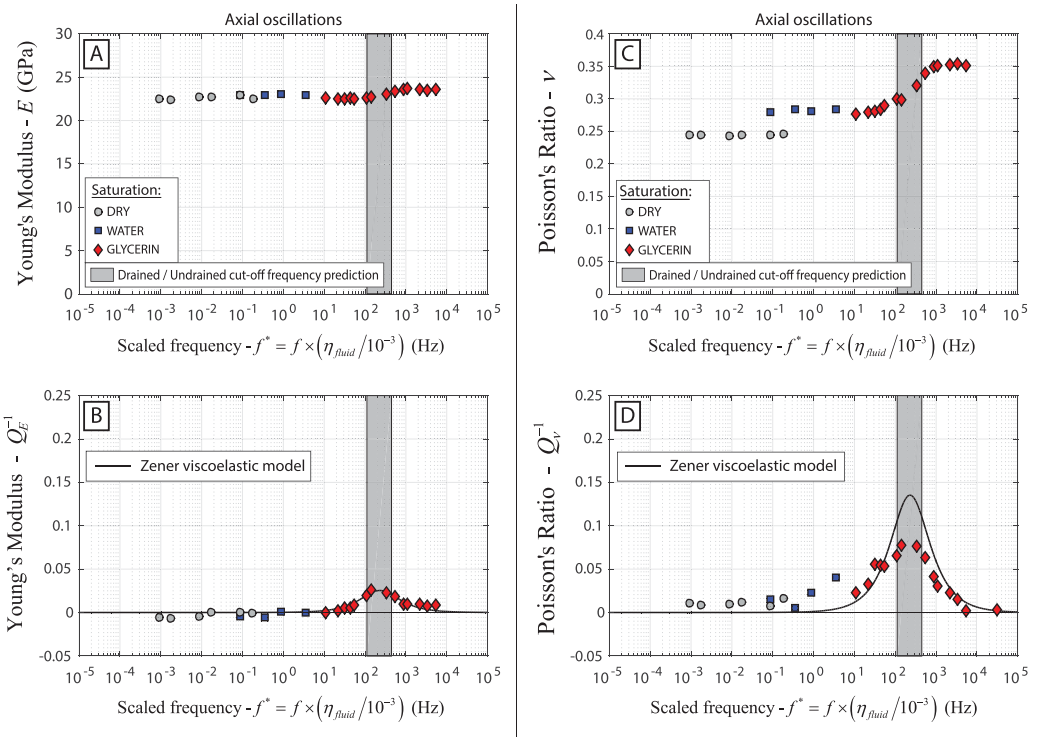

Figure 9. (a) Young's modulus E, (b) Q_E^{-1}, (c) Poisson's ratio ν, and (d) Q_ν^{-1} resulting from the axial oscillations at $P_{diff} = 2.5$ MPa, under dry-, water-, and glycerin-saturated conditions. The frequency is scaled with the viscosity of the saturating fluid η_{fluid}. The factors Q_E^{-1} and Q_ν^{-1} are compared to Zener's model. The range for the drained/undrained cutoff frequency f_1^* is represented by the gray area.

modulus G_{ax} shows no dispersion at all, with a constant value around $G_{ax} = 9$ GPa (Figure 10c). Consistently, the related attenuation $Q_{G_{ax}}^{-1}$ is nil throughout the whole frequency range (Figure 10d).

4.3. Hydrostatic Oscillations Results at $P_{diff} = 2.5$ MPa

The results of the purely hydrostatic oscillations at $P_{diff} = 2.5$ MPa are presented in Figure 11. The measured bulk modulus K_{hyd} shows a dispersion from 16 GPa to 25 GPa between $f^* = 2\times10^1$ Hz and $f^* = 4\times10^2$Hz, visible under glycerin-saturated conditions (Figure 11a). The related factor $Q_{K_{hyd}}^{-1}$ has a peak at about $Q_{K_{hyd}}^{-1} = 0.22$ around $f^* = 2 \times 10^2$ Hz and is nil elsewhere (Figure 11b). The attenuation seems to compare well with Zener's model with the parameters used previously for K_{ax} ($M_0 = 16$ GPa, $M_1 = 26$ GPa) (Figure 11b).

4.4. Uncertainty Analysis

For the hydrostatic oscillations, the uncertainty on the bulk modulus measurements (δK) depends on the confining pressure uncertainty (δP) and the uncertainty of the strain measurements ($\delta\varepsilon$). From equation (3), the relative uncertainty on K is given by:

$$\frac{\delta K_{hyd}}{K_{hyd}} = \frac{\delta P}{P} + \frac{\delta\varepsilon}{\varepsilon}. \tag{18}$$

The pressure sensor of the confining cell is capable to measure pressure with a resolution of $\delta P = 0.001$ MPa. The amplitude of the confining pressure oscillations being around 0.2 MPa, the relative uncertainty on pressure becomes $\delta P/P = 0.005$, which can be considered negligible. Therefore, the uncertainty on the bulk modulus highly depends on the quality of the strain measurement. The higher the number of strain gauges, the lower this uncertainty becomes. A total of $n = 8$ strain gauges was used (four axial and four radial). When proceeding with the oscillations, the amplitude of the strain gauges may vary slightly from one another. These variations could be related to the quality of the contact between the strain gauge and the sample or to small heterogeneities in the sample despite being considered perfectly homogeneous. Although the orientation of the strain gauges relatively to the vertical and horizontal axis can be determinant for axial oscillations, it is

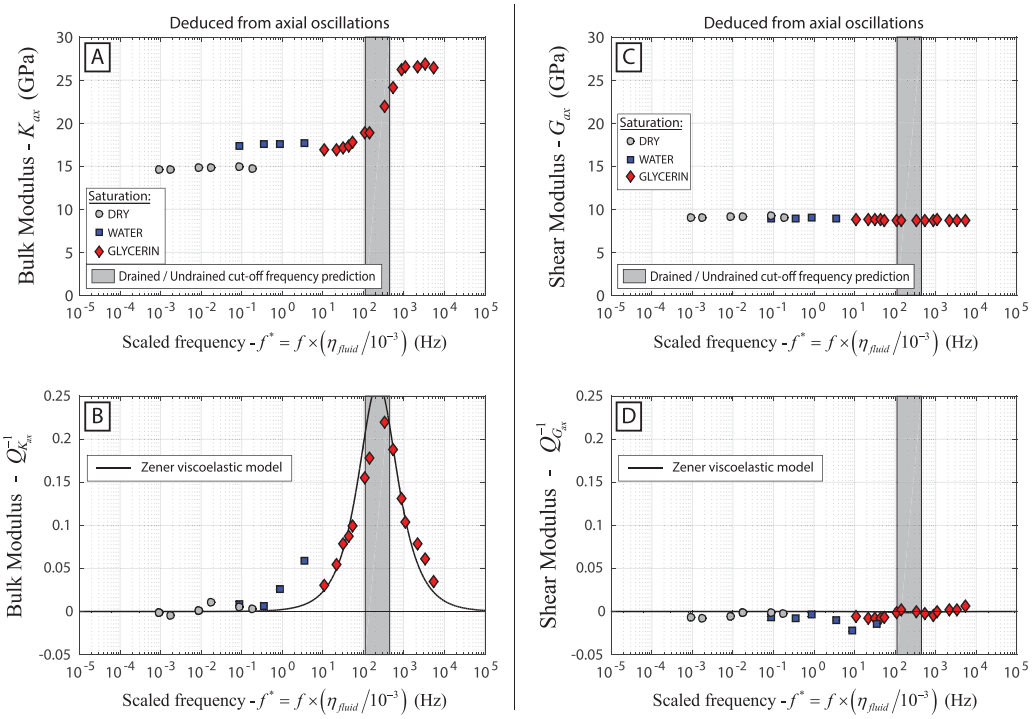

Figure 10. (a) Bulk modulus K_{ax}, (b) $Q^{-1}_{K_{ax}}$, (c) shear modulus G_{ax}, and (d) $Q^{-1}_{G_{ax}}$ deduced from the results of the axial oscillations (Figure 9). K_{ax} and G_{ax} are deduced from E and ν (equation (5)) under the assumption of an isotropic medium. $Q^{-1}_{K_{ax}}$ and $Q^{-1}_{G_{ax}}$, deduced from equations (10) and (11), are compared to Zener's model. The frequency is scaled with the viscosity of the saturating fluid η_{fluid}. The range for the drained/undrained cutoff frequency f_1^* is represented by the gray area.

irrelevant for hydrostatic oscillations on an isotropic medium. For the hydrostatic oscillations at $f = 0.004$ Hz and $P_{diff} = 2.5$ MPa, the average of the eight measured strain was $\varepsilon = 2.22$ μm/m, with a standard deviation of $std = 0.266$ μm/m. The error on the average strain ($\delta\varepsilon$) can be calculated from $\delta\varepsilon = std/\sqrt{n} = 0.094$ μm/m. From equation (18), we deduce the relative uncertainty on K_{hyd} for the hydrostatic oscillations: $\delta K_{hyd}/K_{hyd} = 4.2\%$. This corresponds to an error of about ± 0.3 GPa for K_{hyd}.

The similar approach can be done to calculate the uncertainties for the axial oscillations results. From equation (4), we can deduce the following:

$$\frac{\delta E}{E} = \frac{\delta\varepsilon_{alu}}{\varepsilon_{alu}} + \frac{\delta\varepsilon_{ax}}{\varepsilon_{ax}} \quad \text{and} \quad \frac{\delta\nu}{\nu} = \frac{\delta\varepsilon_{rad}}{\varepsilon_{rad}} + \frac{\delta\varepsilon_{ax}}{\varepsilon_{ax}}. \tag{19}$$

With two strain gauges measuring ε_{alu}, four measuring ε_{ax}, and four measuring ε_{rad}, the relative uncertainties on E and ν were found to be $\delta E/E = 12\%$ and $\delta\nu/\nu = 8\%$. These uncertainties correspond to errors of ± 1.3 GPa for E and ± 0.01 for ν. We can then use equation (5) to propagate the error to K_{ax} and G_{ax}. This gives an error of ± 1.5 GPa for K_{ax} and ± 0.6 GPa for G_{ax}.

4.5. Comparison of the Three Methods Used to Infer Q^{-1}

Q^{-1} factors of all the elastic properties deduced from the axial oscillations at $P_{diff} = 2.5$ MPa under glycerin-saturated conditions were also calculated using the Sines and the FFT method. Those are compared to the previously presented results from the Ellipse method (Figure 12). For E, K_{ax}, and G_{ax} (respectively Figures 12a, 12c, and 12d) the three methods compare well over the experimental frequency range $f \in [2 \times 10^{-2}\ ;\ 5]$ Hz. In case of ν (Figure 12b), the FFT and Ellipse methods are consistent with each other but not with the Sines method. The results obtained with the Sines method for ν are unstable and give erratic results with data points off the chart (Figure 12b). The Sines method shows also some slight inconsistencies with the other methods at 10^{-2} Hz for E and K_{ax} (Figures 12a and 12c). We can therefore conclude that only the Ellipse and FFT methods are reliable to calculate Q^{-1} in our case.

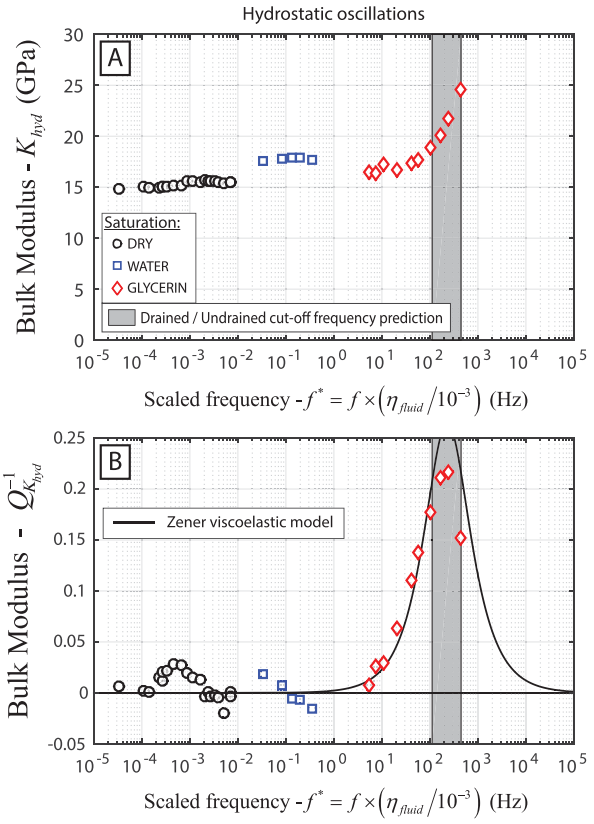

Figure 11. (a) Bulk modulus K_{hyd} and (b) $Q^{-1}_{K_{hyd}}$ resulting from the hydrostatic oscillations at $P_{diff} = 2.5$MPa, under dry-, water-, and glycerin-saturated conditions. The frequency is scaled with the viscosity of the saturating fluid η_{fluid}. The factor $Q^{-1}_{K_{hyd}}$ is compared with Zener's model. The range for the drained/undrained cutoff frequency f_1^* is represented by the gray area.

5. Discussion

5.1. The Drained and Undrained Regimes

With respect to the cutoff frequencies (equation (1)), and especially the drained/undrained cutoff frequency, a viscosity contrast for the fluid results in a shift in frequency of the transition. The results presented with the three different saturating fluids show a good continuity in scaled frequency (Figure 13). A slight discrepancy exists between the dry- and water-saturated conditions, the dry bulk modulus being about 2.5 GPa lower than the water-saturated bulk modulus (Figure 13a). This discrepancy is seen in both the hydrostatic and axial oscillations and seems larger than the uncertainties of the measurements (Figure 13a). It is possible that the sample was not fully dry during the measurements, with the presence of moisture that would induce a weakening effect. Although this effect is known to be important in sandstones and rather negligible in limestones [*Clark et al.*, 1980; *Pimienta et al.*, 2014], measurements on a Leuders limestone from *Clark et al.* [1980] still show an increase of about 5 GPa for K and 0.04 for ν when going from a relative humidity of 35% (ambient room) to a vacuum state.

The drained/undrained cutoff frequency (f_1) was experimentally measured around 2×10^{-1} Hz in glycerin-saturated conditions, which is a frequency that is equivalent to 2×10^{2} Hz in water-saturated conditions. Therefore, when studying dispersion and attenuation phenomenon related to diffusion processes at different scales, the experimental frequencies can be scaled by the dynamic viscosity of the fluid η [*Pimienta et al.*, 2015a, 2015b, 2016a; *Spencer and Shine*, 2016]. This has the major advantage to increase the apparent frequency range reachable by the experimental setup up, in our case for the axial oscillations from $10^{-2} - 10^{1}$ Hz to $10^{-4} - 10^{4}$ Hz, and therefore characterize the dispersion of the sample over a much larger frequency band.

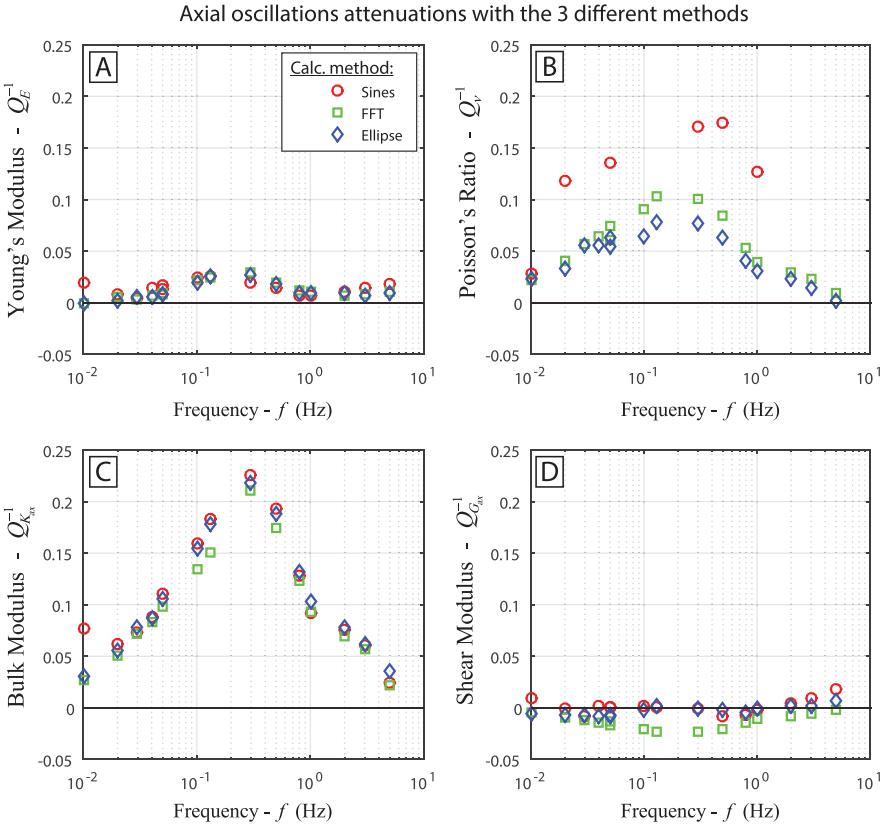

Figure 12. Comparison of the three methods used to calculate Q^{-1}: Sines, FFT, and Ellipse methods. Example for the axial oscillations at P_{diff} = 2.5 MPa under glycerin-saturated conditions, for (a) Young's modulus, (b) Poisson's ratio, (c) bulk modulus, and (d) the shear modulus.

5.1.1. Elastic Moduli

The common elastic modulus we can extract from the hydrostatic and axial oscillations is the bulk modulus, respectively, K_{hyd} and K_{ax} (deduced from E and ν). The comparison between the dispersion and Q^{-1} of both moduli at P_{diff} =2.5 MPa is presented in Figure 13. The hydrostatic and axial results compare well over their overlapping frequencies, both for the dispersion (Figure 13a) and for Q^{-1} (Figure 13b). This tends to validate our hypothesis of an isotropic medium and shows a good consistency between both stress-strain methods for the drained and undrained regimes.

Using the measured permeability value (i.e., $\kappa = 10^{-14}$ m^2) and the dry bulk modulus (i.e., K_d=15 GPa) and assuming a diffusion length L in the sample between 40 mm and 80 mm, the expected cutoff frequency f_1^* for the drained/undrained transition (equation (1)) is between 10^2 Hz and 4×10^2 Hz. All the previous dispersions and Q^{-1} results are in agreement with this frequency transition (Figures 9–11, and 13). The maximum Q^{-1} peaks for E, ν, K_{ax}, and K_{hyd}, and the dispersion slopes of the elastic moduli are systematically in the expected range of f_1^* (Figures 9–11, and 13).

The undrained elastic properties of a rock are generally deduced from the drained (or dry) properties using Biot-Gassmann relations [*Gassmann*, 1951]:

$$K_u = K_d + \frac{K_f\left(1-\frac{K_d}{K_S}\right)^2}{\Phi + \left(\left(1-\frac{K_d}{K_S}\right)-\Phi\right)\frac{K_f}{K_S}} \quad \text{and} \quad G_u = G_d, \tag{20}$$

where K_d and G_d are, respectively, the drained bulk modulus and shear modulus, Φ the porosity, K_f the saturating fluid's bulk modulus, K_S the skeleton bulk modulus, and K_u and G_u, respectively, the undrained bulk modulus and shear modulus. The Biot-Gassmann predictions for the bulk modulus with water- and glycerin-saturated conditions are presented in Figure 13a, using the parameters K_d = 15 GPa, Φ = 23%,

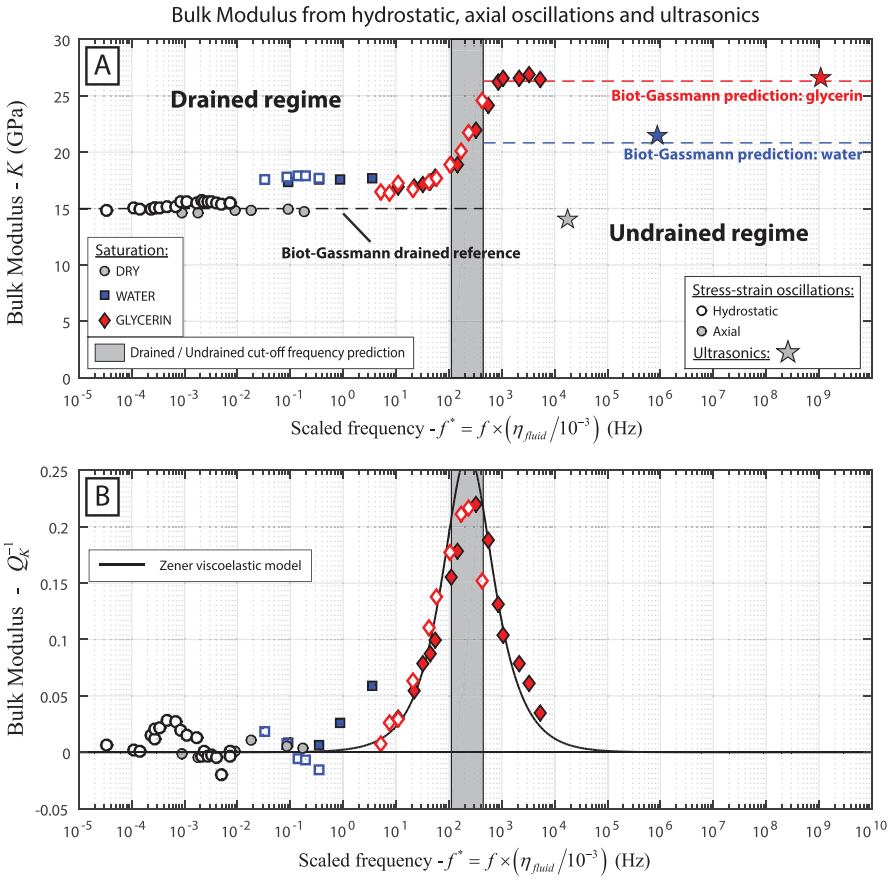

Figure 13. (a) Comparison of the hydrostatic, the axial, and the ultrasonic measurements for the bulk modulus and (b) the bulk modulus Q^{-1} factor deduced from the hydrostatic and axial oscillations for dry-, water-, and glycerin-saturated conditions at P_{diff} = 2.5 MPa. Biot-Gassmann's predictions for water and glycerin are represented for the undrained regime in addition to the ultrasonic results (Figure 13a). The frequency is scaled with the viscosities of the saturating fluids.

$K_{f-water}$ =2.21 GPa, $K_{f-glycerin}$ =4.36 GPa [*Bridgman*, 1931], and K_S = 77 GPa, which is the bulk modulus of calcite [*Mavko et al.*, 2009]. The predictions give an undrained bulk modulus with water of K_{u-wat} = 20.8 GPa and with glycerin K_{u-gly} = 25.8 GPa. These results are consistent with the bulk modulus results independently obtained from the stress-strain oscillations under glycerin-saturated conditions (Figure 13a). Moreover, the shear modulus G_{ax} deduced from the axial oscillations is constant over the frequency range of the drained/undrained transition (Figure 10c), which is again consistent with Biot-Gassmann's theory.

5.1.2. Q^{-1} Factors

The Zener viscoelastic model (Figure 3), used to calculate Q^{-1} from the modulus' dispersion, gives accurate results for the Young's modulus (Figure 9b), the bulk modulus (Figures 10b and 11b), and the shear modulus (Figure 10d). However, the model seems to overpredict Q^{-1} for the Poisson's ratio (Figure 9d), with a peak value of 0.13 instead of 0.09. These results, added to similar observations in Fontainebleau sandstones [*Pimienta et al.*, 2015a], show the general good applicability of Zener's model to the drained/undrained transition.

In an isotropic medium, we previously showed that the bulk modulus and the shear modulus can be deduced from axial solicitations and that the bulk modulus gives consistent results with the hydrostatic measurements in the drained and undrained regimes. Therefore, the axial oscillations allow to measure all the moduli if we measure the axial and radial strains. The Young's modulus Q_E^{-1} and Poisson's ratio Q_ν^{-1} are directly measured from the phase shifts between the output signals σ_{ax}, ε_{ax} and ε_{rad} (equation (9)). We presented a method to deduce the bulk modulus $Q_{K_{ax}}^{-1}$ and the shear modulus $Q_{G_{ax}}^{-1}$ from different combinations of the previous output signals (equation (11)). It is therefore of great interest to check the consistency of these Q^{-1} values with existing equations that give relationships between Q^{-1} of all the different moduli. Our aim is to calculate

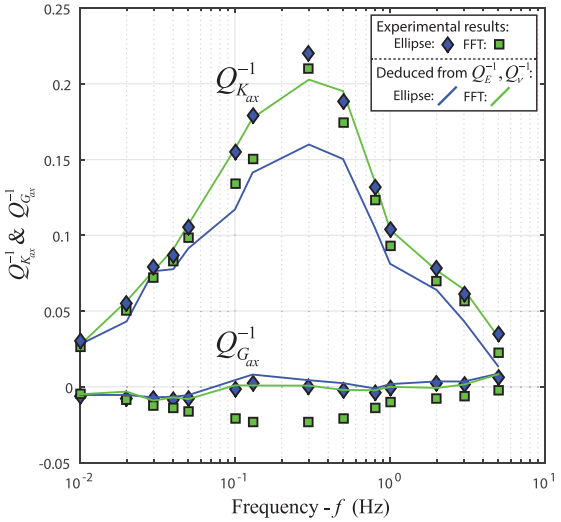

Figure 14. Comparison between $Q_{K_{ax}}^{-1}$ and $Q_{G_{ax}}^{-1}$ obtained experimentally (equation (11)) with the FFT and the Ellipse methods for the drained/undrained transition under glycerin-saturated conditions at $P_{diff} = 2.5$ MPa (Figures 12c and 12d) and the same factors deduced from Q_E^{-1}, Q_ν^{-1}, and ν (equations (22) and (23)).

Q_K^{-1} and Q_G^{-1} from the measured Q_E^{-1} and Q_ν^{-1}. Such relationships have been given by *Winkler and Nur* [1979] but with the hypothesis of a constant Poisson's ratio ν. *Pimienta et al.* [2016c] introduced a dispersive ν into *Winkler and Nur*'s [1979] equations and obtained the following relationship between ν, Q_ν^{-1}, Q_E^{-1}, and Q_G^{-1}:

$$Q_\nu^{-1}\left[\nu + Q_G^{-1}\left((1+\nu)\,Q_E^{-1} - Q_G^{-1}\right)\right] = (1+\nu)\,Q_E^{-1} - (1+\nu)\,Q_G^{-1}. \tag{21}$$

For our purpose, the previous equation can be turned into a second-order polynomial on Q_G^{-1}:

$$-Q_\nu^{-1}\left[Q_G^{-1}\right]^2 + (1+\nu)\left(1 + Q_\nu^{-1}Q_E^{-1}\right)\left[Q_G^{-1}\right] + \left(\nu Q_\nu^{-1} - (1+\nu)\,Q_E^{-1}\right) = 0, \tag{22}$$

which admits two solutions that can be numerically calculated. The order of magnitudes of these two solutions is around $Q_G^{-1} \sim 0.01$ and $Q_G^{-1} \sim 10$. The second solution being unrealistic as it would give a phase shift between the stress and the strain of nearly $\pi/2$, we keep only the first one. We then calculate the bulk modulus attenuation Q_K^{-1} with the relationship from *Winkler and Nur* [1979]:

$$Q_K^{-1} = \frac{3}{1-2\nu}Q_E^{-1} - \frac{2(1+\nu)}{1-2\nu}Q_G^{-1}. \tag{23}$$

For the axial oscillations, in the frequency range of the drained/undrained transition under glycerin-saturated conditions at $P_{diff} = 2.5$ MPa, the results for Q_K^{-1} and Q_G^{-1} deduced from equations (22) and (23) are reported in Figure 14, along with $Q_{K_{ax}}^{-1}$ and $Q_{G_{ax}}^{-1}$ obtained experimentally from the output signals with the FFT and the Ellipse method (equation (11) and Figures 12c and 12d). The results show a general good match between the two methods to calculate Q_K^{-1} and Q_G^{-1}. Q_K^{-1} as deduced from $Q_{E_{Ellipse}}^{-1}$ and $Q_{\nu_{Ellipse}}^{-1}$ through equations (22) and (23), seems to be a bit lower than the direct experimental result, with a value of 0.15 instead of 0.22 at $f = 0.3$ Hz (Figure 14). This error is solely related to the small difference that was measured between $Q_{\nu_{Ellipse}}^{-1}$ and $Q_{\nu_{FFT}}^{-1}$ (Figure 12b). Note that $Q_{E_{Ellipse}}^{-1} = Q_{E_{FFT}}^{-1}$ (Figure 12a). We can therefore conclude that, in an isotropic medium and for the drained/undrained transition, the axial oscillations allow to measure all moduli and their respective Q^{-1} factors, directly calculated either from σ_{ax}, ε_{ax}, and ε_{rad} (equation (11)) or from the relationships relating ν, Q_E^{-1}, Q_ν^{-1}, Q_K^{-1}, and Q_G^{-1} (equations (22) and (23)).

5.2. Absence of Dispersion at Higher Frequencies

Once the drained and undrained properties of the rock are clearly identified, one can investigate the possible existence of other dispersive transitions at higher frequencies. This concerns a possible unrelaxed (saturated isolated) regime.

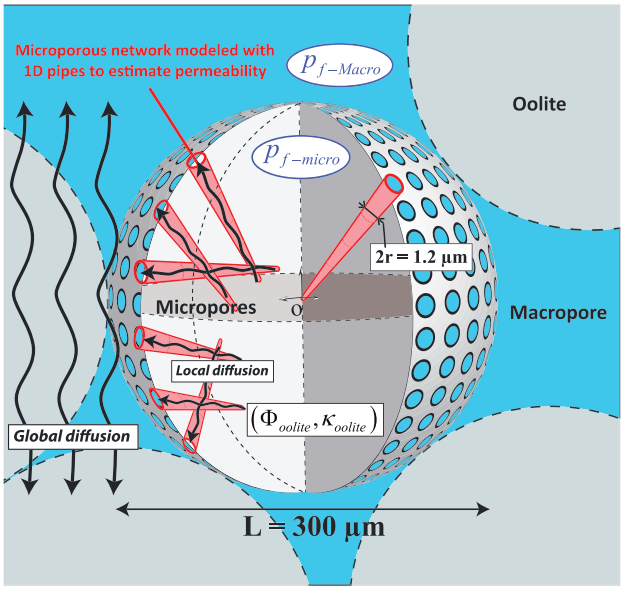

Figure 15. Model of the Lavoux, composed of spherical microporous oolites surrounded by macropores. The global diffusion within the REV and the local diffusion in the oolites are represented. The oolites' porosity (ϕ_{oolite}) is deduced from the experimental total porosity (23%) and from the ratio macroporosity/microporosity (45/55), calculated from the photomicrograph's analysis (Figure 5). A 1-D pipe model (equation (24)) is used to calculate the local permeability of the oolites (κ_{oolite}). The obtained results are $\phi_{oolite} = 14.2\%$ and $\kappa_{oolite} = 1.6 \times 10^{-15}$ m^2. The calculated local permeability of the micropores (κ_{oolite}) is smaller than the sample's permeability measured experimentally ($\kappa = 10^{-14}$ m^2).

5.2.1. No Squirt Flow—Absence of Cracks

Undrained/unrelaxed transitions can exist when local flows occur within the REV in the undrained regime, for instance, squirt flows from compliant cracks to rounded pores [*Mavko and Jizba*, 1991]. The only high-frequency properties available to us in this study are the ultrasonic results (1 MHz) reported Table 1. The high-frequency bulk modulus K_{HF} for dry-, water-, and glycerin-saturated conditions are reported in Figure 13a. In dry conditions, the ultrasonic result corresponds clearly to the drained properties. For water- and glycerin-saturated conditions, the ultrasonic results show a good correspondence with the undrained properties or the Biot-Gassmann's predictions (Figure 13a). We can conclude that no distinct unrelaxed regime is expected beyond the drained/undrained transition for this dual-porosity limestone. In the Lavoux limestone, the elastic moduli are independent of the differential pressure (Figures 7 and 8), suggesting the absence of cracks. Consistently, no squirt flow is thus possible between cracks or from cracks to rounded pores. This is corroborated by the sample's permeability that is also independent of differential pressure (Figure 6) [*Gueguen et al.*, 2011].

5.2.2. No Local Diffusion Between the Microporosity and the Macroporosity

In a bimodal porosity medium, question rises whether there could be a local diffusion between the macroporosity and the microporosity, delayed relative to the global diffusion, due to a lower permeability of the micropores contained in the oolites. The macroporosity of the Lavoux limestone being connected independently of the microporosity, we can model this grainstone as a pile of spherical microporous oolites, of diameters 100 µm to 500 µm, solely surrounded by macropores (Figure 15). The REV of the Lavoux would be a volume containing a few oolites separated by macropores, as no heterogeneity larger than the oolites seems to exist (Figure 4). At $f = 1$ MHz in saturated conditions, the ultrasonic velocities of both the *P* and *S* waves are greater than 1914 m s^{-1} (Table 1) corresponding to a minimum wavelength of approximately 2 mm. This wavelength represents a square area similar to half the area of the photomicrograph presented in Figure 4, containing at least a dozen of oolites. Thus, we can safely assume that, during the propagation of the ultrasonic *P* and *S* waves, the volume of the oscillating stress field is much larger than the limestone's REV. In the undrained regime, the pore pressure is isobaric in the REV [*Gassmann*, 1951], meaning that the fluid's pressure in the macropores ($p_{f-Macro}$) is equal to the fluid's pressure in the oolites' micropores ($p_{f-micro}$) (Figure 15).

Similar to the drained/undrained transition characterized by the cutoff frequency f_1^* that concerns the global fluid flow, a local cutoff frequency $f^*_{1\ oolite}$ could characterize the fluid flow occurring locally from the oolites to

the macropores. The permeability of the oolites κ_{oolite} should be lower than the total permeability of the sample because of a much smaller pore entry radius compared to the macropores (Figure 4). A 1-D permeability model from *Gueguen and Dienes* [1989] can be used to have an estimation of κ_{oolite}. The oolite's microporous network is modeled as a set of pipes of variable radii r and lengths λ, isotropically distributed (Figure 15). If we assume that all the pipes are connected, with respect to the definition of percolation theory, *Gueguen and Dienes* [1989] showed that the permeability of the medium can be given by:

$$\kappa_{\text{oolite}} = \frac{\bar{r}^2}{32}\Phi_{\text{oolite}}. \tag{24}$$

The porosity of the oolite Φ_{oolite} is calculated from the proportion of microporosity in the total porosity, which was deduced from the SEM image analysis at about 55% (Figure 5), and the total porosity measured experimentally at about 23%. If we consider all the microporosity to be in the oolites and the total volume $V_{\text{tot}} = V_{\text{Macropores}} + V_{\text{oolites}}$, we can deduce $\Phi_{\text{oolite}} = 14.2\%$. The average radius $\bar{r}$ is taken as the pore entry radius of the micropores measured from the porosimetry measurements from *Zinsmeister* [2013], and corroborated with the SEM photomicrograph (Figure 4), at about $\bar{r} = 0.6$ µm. Therefore, equation (24) gives a permeability of $\kappa_{\text{oolite}} = 1.6 \times 10^{-15}$ m^2, which is smaller than the sample's global permeability ($\kappa = 10^{-14}$ m^2). Now if we apply the drained/undrained cutoff frequency (equation (1)) to the oolite, with a diffusion length L of about 300µ m (Figure 15) and a drained bulk modulus K_d taken as 15 GPa, we obtain $f^*_{1\ \text{oolite}} = 10^6$ Hz in scaled frequency, which is far above the cutoff frequency of the global diffusion ($f^*_1 = 2 \times 10^2$ Hz). This frequency measures the minimum timescale that allows total diffusion in the oolite and therefore to equilibrate the inner pore pressure $p_{f-\text{micro}}$ and the surrounding pore pressure $p_{f-\text{Macro}}$ (Figure 15). Above $f^*_{1\ \text{oolite}}$, no fluid exchange by diffusion is possible between the oolites and the macropores.

The only measurement we have above $f^*_{1\ \text{oolite}}$ is the ultrasonic measurement in glycerin-saturated conditions ($f^* = 10^9$ Hz). The bulk modulus and shear modulus $K_{\text{HF}-\text{gly}}$ and $G_{\text{HF}-\text{gly}}$ of the sample were found to be equal to their respective undrained values (Table 1 and Figures 10a and 10c). Therefore, no dispersion is visible around $f^*_{1\ \text{oolite}}$, which suggests that there is no flow between the oolites and the macropores in the undrained regime ($f^* > f^*_1$). This is consistent with the idea that the micropores and the macropores have similar aspect ratios ($\xi = 1$), implying no pressure gradients to relax, and that the fluid is isobaric in the REV because the sample is already in the undrained regime. If $f^*_{1\ \text{oolite}}$ had been less than f^*_1, one could imagine a "partially undrained" regime, for a frequency between $f^*_{1\ \text{oolite}}$ and f^*_1, where the oolites are undrained while the macropores are still drained. A local transition around $f^*_{1\ \text{oolite}}$ could then be expected with dispersion and attenuation.

5.3. Effect of the Boundary Conditions — 1-D Diffusion Model for the Drained and Undrained Regimes

The effect of the boundary conditions on the elastic properties has been studied, with two different configurations for the drainage system: (1) open (drained conditions) and (2) closed (undrained conditions for the system sample + dead volumes) (Figure 1a). We recall that all the results presented previously were obtained in the first configuration. Because the dead volumes are very large in that case (~ 60 mL), the boundary conditions can be assimilated to drained boundary conditions [*Pimienta et al.*, 2016b]. Analogue measurements, using axial and hydrostatic oscillations for a glycerin-saturated sample, have been performed in the closed configuration, with dead volumes of 3.3 mL. The results for the bulk modulus at $P_{\text{diff}} = 2.5$ MPa are reported in Figure 16b, along with the previous results obtained with fully drained conditions (Figure 16a). With dead volumes, the drained/undrained transition is visible around the same cutoff frequency as in the first case, but the dispersion is smaller (Figure 16b). In the drained frequency range, the bulk modulus measured in the second case is higher than in fully drained conditions. Its value is 22 GPa (Figure 16b) instead of 16 GPa (Figure 16a). In the undrained frequency range, the bulk modulus of the sample is independent of the boundary conditions, with a value of 26 GPa in both configurations (Figures 16a and 16b), which is consistent with the definition of the undrained regime.

In the second configuration, the pore pressure in the drainage circuit ($p_f{}^*$) was monitored during the stress oscillations. In order to have a nonzero measurement, $p_f{}^*$ has to be measured in a closed volume to allow for pressure buildup when fluid drains out of the sample. The volumetric strain (ε_{vol}), induced by hydrostatic stress oscillations ($\sigma_{ii}/3$), generates a flux of fluid going in and out of the sample, into the dead volumes. This volumetric strain is defined as follows:

$$\varepsilon_{\text{vol}} = \frac{1}{K}\left(\frac{\sigma_{ii}}{3} - \alpha\Delta p_f\right), \tag{25}$$

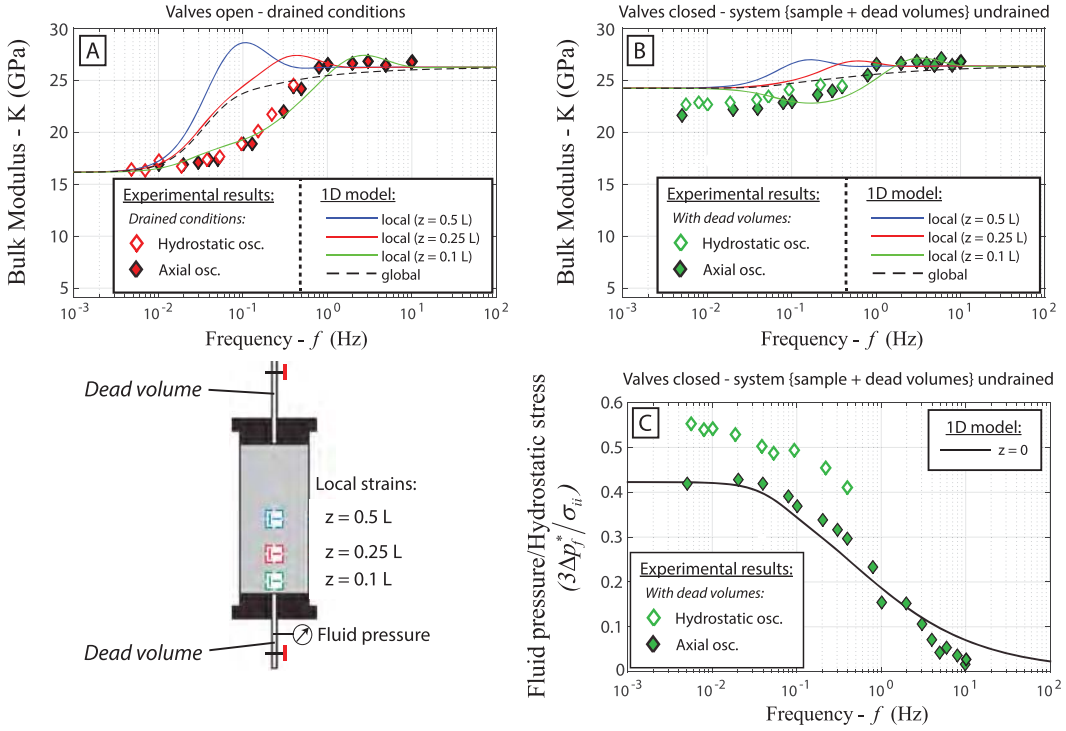

Figure 16. Effect of the two types of experimental boundary conditions on the measured bulk modulus and comparison with the 1-D diffusion model: (a) drained conditions and (b) system sample + dead volumes undrained. The experimental results are from the hydrostatic and axial oscillations in glycerin-saturated conditions at P_{diff} = 2.5 MPa. The model is calculated from local strains at different positions (0.5 *L*, 0.25 *L*, and 0.1 *L*) and from global strain. The experimental results are from strains measured at $z = 0.5\,L$. (c) Measurements of the ratio pore pressure over hydrostatic stress ($3p_f^*/\sigma_{ii}$) in the second type of boundary conditions are compared to the 1-D model, at the limit $z = 0$. For the hydrostatic oscillations $\sigma_{ii}/3 = \Delta P_c$ and for the axial oscillations $\sigma_{ii}/3 = \sigma_{ax}/3$.

where α is the Biot coefficient and Δp_f is the oscillation amplitude of the pore pressure in the medium. Experimentally, when we apply the hydrostatic oscillations on the sample, we have $\sigma_{ii}/3 = \Delta P_c$. This pressure induces the volumetric strain ϵ_{vol}. On the other hand, when we apply the axial oscillations in an isotropic medium, the equivalent hydrostatic stress to obtain the same volumetric strain ϵ_{vol} is $\sigma_{ii}/3 = \sigma_{ax}/3$ (equation (25)). Here we assume that the stress σ is positive in compression and represents the amplitude of oscillation and that the radial stress is constant during the axial stress oscillations ($\sigma_{rad} = 0$). For both stress oscillations at $P_{diff} = 2.5$ MPa on glycerin-saturated sample, the ratio between the amplitude of the oscillating fluid pressure $\Delta p_f{}^*$ and the amplitude of the equivalent hydrostatic stress oscillation $\sigma_{ii}/3$ is equal to $3\Delta p_f{}^*/\sigma_{ii}$. This ratio is reported in Figure 16c as a function of frequency. For both hydrostatic and axial oscillations, the ratio tends to zero as the frequency crosses the drained/undrained transition range ($[5 \times 10^{-2}; 1]$ Hz). In the drained frequency range ($f < 5 \times 10^{-2}$ Hz), the ratio measured with hydrostatic measurements is slightly higher than with the axial oscillation, respectively, 0.55 and 0.41 (Figure 16c). This ratio was defined as the "pseudo-Skempton" coefficient $B^* = \Delta p_f{}^*/\Delta P_c$ by *Pimienta et al.* [2015a] in the case of hydrostatic oscillations or the "pseudo-consolidation" parameter $\gamma^* = \Delta p_f{}^*/\sigma_{ax}$ in case of axial oscillations in *Pimienta et al.* [2015b]. This hydraulic parameter cannot be considered as the real Skempton coefficient (*B*) of the sample, because *B* is solely defined for an undrained REV, and $p_f{}^*$ does not measure the pore pressure p_f inside the sample, unless the sample is fully drained.

A 1-D diffusion model has been developed by *Pimienta et al.* [2016b] to take into account these effects of the boundary conditions and has been compared to the previous experimental results (Figure 16). The principle of the model is to find the steady state solution of the diffusion equation for the pore pressure p_f, when the sample undergoes hydrostatic pressure oscillations P_c. Because the lateral surface of the sample is jacketed and the drainage system acts on the top and bottom faces (Figure 1), it was proposed by *Pimienta et al.* [2016b] to solve only the 1-D diffusion along the vertical axis (*z*) of the sample. For the sake of simplicity, $p_f = p_f(z, t) - \bar{p}_f$ and $P_c = P_c(t) - \bar{P}_c$, where $\bar{p}_f$ and $\bar{P}_c$ are the mean pressures during the oscillations, such that $P_{diff} = \bar{P}_c - \bar{p}_f$.

The 1-D diffusion equation writes as follows:

$$\frac{\partial p_f}{\partial t} = \frac{\kappa}{\eta S_s}\frac{\partial^2 p_f}{\partial z^2} + B\frac{\partial P_c}{\partial t}, \tag{26}$$

where S_s is the storage coefficient of the sample, B the Skempton coefficient, and κ the permeability. According to the poroelastic relationships provided by *Kumpel* [1991], $B=(1/K_d-1/K_u)/(1/K_d-1/K_S)$ and $S_s=\alpha/BK_d$. For the model, K_u is deduced from Biot-Gassmann's relationship (equation (20)) to limit the number of adjustment parameters. The applied stress $P_c(t)$ is supposed to be of sinusoidal form such that $P_c(t)=\Delta P_c e^{i\omega t}$. For a sample of length L, *Pimienta et al.* [2016b] give the steady state solution of equation (26) for drained boundary conditions ($p_f(0,t)=p_f(L,t)=0$):

$$p_f(z,t) = B\Delta P_c e^{i\omega t}\left[1 - \frac{\sinh(a(L-z)) + \sinh(az)}{\sinh(aL)}\right], \tag{27}$$

with $a = (1+i)\sqrt{\omega\eta S_s/2\kappa}$. With symmetric dead volumes on top and bottom of the sample, the solution becomes [*Pimienta et al.*, 2016b]:

$$p_f(z,t) = B\Delta P_c e^{i\omega t}\left[1 - \frac{cosh\left(a\left(\frac{L}{2}-z\right)\right)}{b.\sinh\left(a\frac{L}{2}\right) + \cosh\left(a\frac{L}{2}\right)}\right], \tag{28}$$

with $b = (1-i)A\left(S_s/S\right)\sqrt{2\kappa/\omega\eta S_s}$, A being the cross-sectional area of the sample, and $S = V_{\text{dead vol.}}/K_f$ the storage capacity of the dead volumes. Then, the local volumetric strain is obtained from $\varepsilon_{\text{vol}}(z,t) = K_d^{-1}\left(P_c(t) - \alpha p_f(z,t)\right)$, which is a local result. A global volumetric strain can be calculated from $\bar{\varepsilon}_{\text{vol}}(t) = \frac{1}{L}\int_0^L \varepsilon_{\text{vol}}(z,t)dz$ and can be used to calculate a global bulk modulus. For local or global strain, the bulk modulus is deduced from $K_{model} = -\left|P_c\right| / \left|\bar{\varepsilon}_{\text{vol}}\right|$. Thanks to the model, the ratio fluid pressure over hydrostatic stress ($3p_f/\sigma_{ii}$) could be calculated along the z axis of sample, but for the comparison with the fluid's pressure measured in the dead volumes ($p_f{}^*$), the ratio is evaluated for $z = 0$, i.e., $(3p_f{}^*/\sigma_{ii})_{\text{model}} = \left|p_f(0,t)\right| / \left|P_c(t)\right|$. Here we assume that the pore pressure at the boundary is the fluid pressure in the dead volume.

The model's predictions in both configurations for a glycerin-saturated sample are presented in Figure 16. The model has been calculated for local strains at three different positions (0.5 L, 0.25 L, and 0.1 L) and for the global strain. We recall that the experimental results are deduced from local strains measured at $z = 0.5\,L$. The parameters used for the model predictions were $L = 80$ mm, $A = \pi(40)^2 = 5027$ mm^2, $K_d = 16$ GPa, K_S=77 GPa, $K_f = 4.36$ GPa, $\eta = 1.083$ Pa s, $\Phi = 24\%$, $\kappa = 10^{-14}$ m^2, and $V_{\text{dead vol.}} = 3.3$ mL. Concerning the bulk modulus in the drained frequency range, the model predicts $K_{\text{model}} = 24$ GPa for the second configuration (Figure 16b). This is slightly above the experimental result of 23 GPa (Figure 16b). The bulk modulus K_{model} is 16 GPa in fully drained conditions (Figure 16a). In the undrained frequency range, the model predicts $K_{\text{model}} = 26$ GPa (Figure 16a), which by construction of the model corresponds to Biot-Gassmann's prediction. For the ratio $3p_f{}^*/\sigma_{ii}$, the model predicts a value of 0.41 in the drained frequency range, which corresponds to the experimental measurement done with axial oscillations (Figure 16c). For the drained/undrained transition, the ratio $(3p_f{}^*/\sigma_{ii})_{\text{model}}$ decreases down to 0 consistently with the axial experimental results (Figure 16c).

When comparing the model and the experimental results both deduced from local strain at z=0.5 L, we can see a frequency shift of nearly 1 order of magnitude (Figures 16a and 16b). The predicted cutoff frequency is around 0.04 Hz for the model, and the experimental value is 0.2 Hz (Figures 16a and 16b). The model calculated from local strain at $z = 0.1\,L$ seems to fit better the experimental results. However, no shift in frequency appears for the ratio $(3p_f{}^*/\sigma_{ii})$ (Figure 16c). The position of the local strain mainly affects the measured cutoff frequency of the transition: the closer to the boundary, the higher the cutoff frequency. In other words, when the frequency of the stress oscillations increases, the REVs at the center of the sample become undrained before the REVs close to the open boundaries. However, the amplitude of the dispersion is unchanged. *Pimienta et al.* [2016b] compared the model to experimental results on Fontainebleau sandstones and found that the cutoff frequency of the bulk modulus was in their case consistent with the experimental results. However, in their case, it was the ratio $3\Delta p_f{}^*/\sigma_{ii}$ that had a frequency shift of 1 order of magnitude compared to the experimental results. Therefore, there seems to be a systematic frequency shift between the bulk modulus and the

ratio $3\Delta p_f^*/\sigma_{ii}$ predicted by the model. This could be due to the limitation to a 1-D diffusion. Experimentally, radial diffusion may occur near the end platens because of the sample's cross section being much larger than the exit holes for the fluid.

6. Conclusion

The elastic moduli (E, ν, K, and G) dispersion and their associated Q^{-1} factors have been measured on a Lavoux limestone, using stress-strain oscillations and ultrasonic measurements in a triaxial cell. The sample was measured under dry-, water-, and glycerin-saturated conditions, which enabled to extend the apparent frequency range of our measurements. Two types of stress oscillations were performed: axial and hydrostatic.

The bulk modulus obtained from both the axial and hydrostatic oscillations compared well over their mutual frequency range, confirming the consistency of both methods when applied on an isotropic material in the drained and undrained regimes. Therefore, the axial oscillations enable to calculate all the moduli and Q^{-1} factors. The formalized relationships between the Q^{-1} factors [*Winkler and Nur*, 1979; *Pimienta et al.*, 2016c] are in agreement with the experimental results, with the condition of a dispersive Poisson's ratio.

The drained/undrained transition has been successfully characterized, with a dispersive effect on all the elastic moduli except for the shear modulus. The Q^{-1} factors were also measured and correlate well with the measured dispersions. The dispersion on K and G is consistent with Biot-Gassmann's theory, either in the water-saturated sample or the glycerin-saturated sample. Experimentally, the boundary conditions around the sample were either drained or undrained for the system sample + dead volumes. A 1-D diffusion model was used to successfully take into account the effect of these boundary conditions on the measured drained moduli.

No other dispersive transitions are detected above the drained/undrained cutoff frequency. We interpret this as an absence of squirt flow due to the absence of cracks. This is corroborated by the fact that the elastic properties and the permeability are independent of effective pressure. We conclude that both the intragranular micropores and intergranular macropores are rounded pores ($\xi_{\text{Macro}} = \xi_{\text{micro}} = 1$). The sample has a bimodal porosity distribution. Local diffusion between the oolites' micropores and the surrounding macropores is however faster than the global diffusion. In other words, the cutoff frequency of the global flow (drained/undrained transition) f_1^* is lower than the theoretical cutoff frequency of the local flow in the oolites $f_{1\,\text{oolite}}^*$.

The drained/undrained transition is measurable in the laboratory. Its critical frequency concerns a global diffusion process on a small length scale, which in our case is the size of the sample L. In the field, with seismic or sonic logs, the global diffusion process would occur within the scale of the wavelength, which is far larger than L for frequencies under 10^5 Hz. Therefore, at the seismic and sonic frequencies, the medium would always be in the undrained regime and be nondispersive. This would not be the case if an open, or drained, boundary condition would exist, for example, a permeable fault.

Acknowledgments
The authors wish to thank D. Deldicque for his expertise on SEM photomicrographs. The authors would also like to thank L. Adam and I. Jackson for their constructive comments. This work has been supported by TOTAL, under project FR00007429. We would like to thank TOTAL for allowing publication of these results. The data for this paper are available by contacting the corresponding author at borgomano@geologie.ens.fr.

References

Adam, L., M. Batzle, and I. Brevik (2006), Gassmann's fluid substitution and shear modulus variability in carbonates at laboratory seismic and ultrasonic frequencies, *Geophysics*, *71*(6), F173–F183, doi:10.1190/1.2358494.

Adam, L., M. Batzle, K. T. Lewallen, and K. van Wijk (2009), Seismic wave attenuation in carbonates, *J. Geophys. Res.*, *114*, B06208, doi:10.1029/2008JB005890.

Adelinet, M., J. Fortin, Y. Guéguen, A. Schubnel, and L. Geoffroy (2010), Frequency and fluid effects on elastic properties of basalt: Experimental investigations, *Geophys. Res. Lett.*, *37*, L02303, doi:10.1029/2009GL041660.

Adelinet, M., J. Fortin, and Y. Gueguen (2011), Dispersion of elastic moduli in a porous-cracked rock: Theoretical predictions for squirt-flow, *Tectonophysics*, *503*(1-2), 173–181, doi:10.1016/j.tecto.2010.10.012.

Anselmetti, F. S., and G. P. Eberli (1993), Controls on sonic velocity in carbonates, *Pure Appl. Geophys.*, *141*(2-4), 287–323.

Baechle, G. T., G. P. Eberli, R. J. Weger, and J. L. Massaferro (2009), Changes in dynamic shear moduli of carbonate rocks with fluid substitution, *Geophysics*, *74*(3), E135–E147, doi:10.1190/1.3111063.

Batzle, M. L., D.-H. Han, and R. Hofmann (2006), Fluid mobility and frequency-dependent seismic velocity—Direct measurements, *Geophysics*, *71*(1), N1–N9.

Bemer, E., and J. Lombard (2010), From injectivity to integrity studies of CO_2 geological storage: Chemical alteration effects on carbonates petrophysical and geomechanical properties, *Oil Gas Sci. Technol. – Revue de l'Inst. Francais du Pet.*, *65*(3), 445–459, doi:10.2516/ogst/2009028.

Bosart, L., and A. Snoddy (1927), New glycerol tables, *Ind. Eng. Chem.*, *19*(4), 506–510.

Bridgman, P. W. (1931), The volume of eighteen liquids as a function of pressure and temperature, *Proc. Am. Acad. Arts Sci.*, *66*(5), 185–233, doi:10.2307/20026332.

Clark, V. A., B. R. Tittmann, and T. W. Spencer (1980), Effect of volatiles on attenuation (Q^{-1}) and velocity in sedimentary rocks, *J. Geophys. Res.*, *85*(B10), 5190–5198, doi:10.1029/JB085iB10p05190.

Cleary, M. P. (1978), Elastic and dynamic response regimes of fluid-impregnated solids with diverse microstructures, *Int. J. Solids Struct.*, *14*(10), 795–819, doi:10.1016/0020-7683(78)90072-0.
David, E. C., J. Fortin, A. Schubnel, Y. Gueguen, and R. W. Zimmerman (2013), Laboratory measurements of low-and high-frequency elastic moduli in Fontainebleau sandstone, *Geophysics*, *78*(5), D369–D379.
Dvorkin, J., G. Mavko, and A. Nur (1995), Squirt flow in fully saturated rocks, *Geophysics*, *60*(1), 97–107, doi:10.1190/1.1443767.
Eberli, G. P., G. T. Baechle, F. S. Anselmetti, and M. L. Incze (2003), Factors controlling elastic properties in carbonate sediments and rocks, *Leading Edge*, *22*(7), 654–660.
Fabre, D., and J. Gustkiewicz (1997), Poroelastic properties of limestones and sandstones under hydrostatic conditions, *Int. J. Rock Mech. Min. Sci.*, *34*(1), 127–134, doi:10.1016/S1365-1609(97)80038-X.
Fabricius, I. L., G. T. Bächle, and G. P. Eberli (2010), Elastic moduli of dry and water-saturated carbonates—Effect of depositional texture, porosity, and permeability, *Geophysics*, *75*(3), N65–N78, doi:10.1190/1.3374690.
Fortin, J., A. Schubnel, and Y. Gueguen (2005), Elastic wave velocities and permeability evolution during compaction of Bleurswiller sandstone, *Int. J. Rock Mech. Min. Sci.*, *42*(7-8), 873–889, doi:10.1016/j.ijrmms.2005.05.002.
Fortin, J., L. Pimienta, Y. Guéguen, A. Schubnel, E. C. David, and M. Adelinet (2014), Experimental results on the combined effects of frequency and pressure on the dispersion of elastic waves in porous rocks, *Leading Edge*, *33*(6), 648–654.
Fournier, F., and J. Borgomano (2009), Critical porosity and elastic properties of microporous mixed carbonate-siliciclastic rocks, *Geophysics*, *74*(2), E93–E109, doi:10.1190/1.3043727.
Gassmann, F. (1951), Elasticity of porous media, *Vierteljahrsschrder Naturforschenden Gesselschaft*, *96*, 1–23.
Gueguen, Y., and J. Dienes (1989), Transport properties of rocks from statistics and percolation, *Math. Geol.*, *21*(1), 1–13.
Gueguen, Y., M. Adelinet, A. Ougier-Simonin, J. Fortin, and A. Schubnel (2011), How cracks modify permeability and introduce velocity dispersion: Examples of glass and basalt, *Leading Edge*, *30*(12), 1392–1398.
Kumpel, H.-J. (1991), Poroelasticity: Parameters reviewed, *Geophys. J. Int.*, *105*(3), 783–799, doi:10.1111/j.1365-246X.1991.tb00813.x.
Lucia, F. J. (1995), Rock-fabric/petrophysical classification of carbonate pore space for reservoir characterization, *Am. Assoc. Pet. Geol. Bull.*, *79*(9), 1275–1300.
Madonna, C., and N. Tisato (2013), A new seismic wave attenuation module to experimentally measure low-frequency attenuation in extensional mode, *Geophys. Prospect.*, *61*(2), 302–314.
Mavko, G., and D. Jizba (1991), Estimating grain-scale fluid effects on velocity dispersion in rocks, *Geophysics*, *56*(12), 1940–1949, doi:10.1190/1.1443005.
Mavko, G., T. Mukerji, and J. Dvorkin (2009), *The Rock Physics Handbook: Tools for Seismic Analysis of Porous Media*, 460 pp., Cambridge Univ. Press, Cambridge, U. K.
Mikhaltsevitch, V., M. Lebedev, and B. Gurevich (2014), A laboratory study of low-frequency wave dispersion and attenuation in water-saturated sandstones, *Leading Edge*, *33*(6), 616–622.
Mikhaltsevitch, V., M. Lebedev, and B. Gurevich (2016a), Laboratory measurements of the effect of fluid saturation on elastic properties of carbonates at seismic frequencies: Effect of fluid saturation on carbonates, *Geophys. Prospect.*, *64*(4), 799–809, doi:10.1111/1365-2478.12404.
Mikhaltsevitch, V., M. Lebedev, and B. Gurevich (2016b), Validation of the laboratory measurements at seismic frequencies using the Kramers-Kronig relationship, *Geophys. Res. Lett.*, *43*, 4986–4991, doi:10.1002/2016GL069269.
Muller, T. M., B. Gurevich, and M. Lebedev (2010), Seismic wave attenuation and dispersion resulting from wave-induced flow in porous rocks—A review, *Geophysics*, *75*(5), 75A147–75A164.
O'Connell, R. J., and B. Budiansky (1977), Viscoelastic properties of fluid-saturated cracked solids, *J. Geophys. Res.*, *82*(36), 5719–5735, doi:10.1029/JB082i036p05719.
O'Connell, R. J., and B. Budiansky (1978), Measures of dissipation in viscoelastic media, *Geophys. Res. Lett.*, *5*(1), 5–8, doi:10.1029/GL005i001p00005.
O'Donnell, M., E. Jaynes, and J. Miller (1981), Kramers-Kronig relationship between ultrasonic attenuation and phase velocity, *J. Acoust. Soc. Am.*, *69*(3), 696–701.
Pimienta, L., J. Fortin, and Y. Gueguen (2014), Investigation of elastic weakening in limestone and sandstone samples from moisture adsorption, *Geophys. J. Int.*, *199*(1), 335–347, doi:10.1093/gji/ggu257.
Pimienta, L., J. Fortin, and Y. Gueguen (2015a), Bulk modulus dispersion and attenuation in sandstones, *Geophysics*, *80*(2), D111–D127, doi:10.1190/geo2014-0335.1.
Pimienta, L., J. Fortin, and Y. Gueguen (2015b), Experimental study of Young's modulus dispersion and attenuation in fully saturated sandstones, *Geophysics*, *80*(5), L57–L72, doi:10.1190/geo2014-0532.1.
Pimienta, L., J. Fortin, J. V. M. Borgomano, and Y. Gueguen (2016a), Dispersions and attenuations in a fully saturated sandstone: Experimental evidence for fluid flows at different scales, *Leading Edge*, *35*(6), 495–501, doi:10.1190/tle35060495.1.
Pimienta, L., J. V. M. Borgomano, J. Fortin, and Y. Gueguen (2016b), Modelling the drained/undrained transition: Effect of the measuring method and the boundary conditions: Modelling drained/undrained transition, *Geophys. Prospect.*, *64*(4), 1098–1111, doi:10.1111/1365-2478.12390.
Pimienta, L., J. Fortin, and Y. Gueguen (2016c), Effect of fluids and frequencies on Poisson's ratio of sandstone samples, *Geophysics*, *81*(2), D183–D195, doi:10.1190/geo2015-0310.1.
Rasolofosaon, P., and B. Zinszner (2002), Vérification expérimentale de la formule de Gassmann dans les calcaires poreux, *Oil Gas Sci. Technol.*, *57*(2), 129–138.
Sarout, J. (2012), Impact of pore space topology on permeability, cut-off frequencies and validity of wave propagation theories: Pore space topology and wave propagation, *Geophys. J. Int.*, *189*(1), 481–492, doi:10.1111/j.1365-246X.2011.05329.x.
Segur, J. B., and H. E. Oberstar (1951), Viscosity of glycerol and its aqueous solutions, *Ind. Eng. Chem.*, *43*(9), 2117–2120, doi:10.1021/ie50501a040.
Shafiro, B., and M. Kachanov (1997), Materials with fluid-filled pores of various shapes: Effective elastic properties and fluid pressure polarization, *Int. J. Solids Struct.*, *34*(27), 3517–3540, doi:10.1016/S0020-7683(96)00185-0.
Spencer, J. W., and J. Shine (2016), Seismic wave attenuation and modulus dispersion in sandstones, *Geophysics*, *81*(3), D211–D231, doi:10.1190/geo2015-0342.1.
Szewczyk, D., A. Bauer, and R. M. Holt (2016), A new laboratory apparatus for the measurement of seismic dispersion under deviatoric stress conditions: Apparatus for seismic dispersion, *Geophys. Prospect.*, *64*(4), 789–798, doi:10.1111/1365-2478.12425.
Tisato, N., and C. Madonna (2012), Attenuation at low seismic frequencies in partially saturated rocks: Measurements and description of a new apparatus, *J. Appl. Geophys.*, *86*, 44–53, doi:10.1016/j.jappgeo.2012.07.008.

Verwer, K., G. Eberli, G. Baechle, and R. Weger (2010), Effect of carbonate pore structure on dynamic shear moduli, *Geophysics*, *75*(1), E1–E8, doi:10.1190/1.3280225.

Vincent, B., M. Fleury, Y. Santerre, and B. Brigaud (2011), NMR relaxation of neritic carbonates: An integrated petrophysical and petrographical approach, *J. Appl. Geophys.*, *74*(1), 38–58, doi:10.1016/j.jappgeo.2011.03.002.

Winkler, K., and A. Nur (1979), Pore fluids and seismic attenuation in rocks, *Geophys. Res. Lett.*, *6*(1), 1–4, doi:10.1029/GL006i001p00001.

Winkler, K. W., and W. F. Murphy (1995), Acoustic velocity and attenuation in porous rocks, in *Rock Physics and Phase Relations: A Handbook of Physical Constants*, pp. 20–34, AGU, Washington, D. C.

Youssef, S., M. Han, D. Bauer, E. Rosenberg, S. Bekri, M. Fleury, and O. Vizika (2008), High resolution μCT combined to numerical models to assess electrical properties of bimodal carbonates, UAE, Abu Dhabi, 29 Oct.–2 Nov.

Zinsmeister, L. (2013), Study of the hydromechanical evolution of a carbonate after chemical alteration. Application of the 2D and 3D digital image correlation during mechanical loading at different scales, Thesis, Ecole Polytechnique X, Palaiseau, France. [Available at https://pastel.archives-ouvertes.fr/pastel-00955351.]

Appendix B

Elastic dispersion and attenuation in fully-saturated sandstones: Role of mineral content, porosity and pressures.

Article accepted in **Journal of Geophysical Research: Solid Earth**.

Pimienta, L., J.V.M. Borgomano, J. Fortin and Y. Guéguen.

Accepted September 2017

Elastic dispersion and attenuation in fully-saturated sandstones: Role of mineral content, porosity and pressures.

Lucas Pimienta[1,2], Jan V.M. Borgomano[1], Jérôme Fortin[1], and Yves Guéguen[1]

KEY POINTS:

1. Dispersion and Attenuation over seismic frequency range in fluid-saturated sandstones.
2. Clear observation of the drained/undrained transition for all samples.
3. Different behavior in the high frequency range for the different sandstones.

Corresponding author: L. Pimienta, Laboratory of Experimental Rock Mechanics, ENAC-EPFL, Lausanne, Switzerland. (lucas.pimienta@epfl.ch)

[1]laboratoire de Géologie de l'ENS - PSL Research University - UMR8538 du CNRS.

[2]Laboratory of Experimental Rock Mechanics, Ecole Polytechnique Fédérale de Lausanne, Station 18, CH-1015, Lausanne, Switzerland.

Abstract.

Because measuring the frequency dependence of elastic properties in the laboratory is a technical challenge, not enough experimental data exist to test the existing theories. We report measurements of three fluid-saturated sandstones over a broad frequency band: Wilkenson, Berea and Bentheim sandstones. Those sandstones samples, chosen for their variable porosities and mineral content, are saturated by fluids of varying viscosities. The samples elastic response (Young's modulus and Poisson's ratio) and hydraulic response (fluid flow out of the sample) are measured as a function of frequency. Large dispersion and attenuation phenomena are observed over the investigated frequency range.

For all samples, the variation at lowest frequency relates to a large fluid flow directly measured out of the rock samples. These are the cause (i.e. fluid flow) and consequence (i.e. dispersion/attenuation) of the transition between drained and undrained regimes. Consistently, the characteristic frequency correlates with permeability for each sandstone. Beyond this frequency, a second variation is observed for all samples, but the rocks behave differently. For Berea sandstone, an onset of dispersion/attenuation is expected from both Young's modulus and Poisson's ratio at highest frequency. For Bentheim and Wilkenson sandstones, however, only Young's modulus shows dispersion/attenuation phenomena. For Wilkenson sandstone, the viscoelastic-like dispersion/attenuation response is interpreted as squirt-flow. For Bentheim sandstone, the second effect does not fully follow such response, which could be due to a lower accuracy in the measured attenuation.

1. Introduction

When interpreting seismic data obtained at the field scale, accounting for the frequency dependence of the elastic wave velocities is a major challenge. Indeed, porous crustal rocks are known to be dispersive media. Their elastic properties are frequency dependent. In the upper crust, elastic dispersion and attenuation in fluid-saturated sedimentary rocks is expected to originate from fluid flow at different scales [*Biot*, 1941; *O'Connell and Budiansky*, 1977; *Cleary*, 1978; *Mavko et al.*, 1979; *Müller et al.*, 2010]. As detailed in *Müller et al.* [2010], various theories have been developed to describe those different mechanisms. In partially-saturated rocks, several mechanisms are expected to occur [e.g., *Müller et al.*, 2010; *Tisato et al.*, 2015; *Chapman et al.*, 2016; *Papageorgiou et al.*, 2016; *Amalokwu et al.*, 2017]. In fully saturated homogeneous rocks, only two mechanisms [*Gardner*, 1962; *O'Connell and Budiansky*, 1977; *Cleary*, 1978; *Mavko et al.*, 1979] are expected to occur over the allowed frequency range [e.g., *Adelinet et al.*, 2010; *Sarout*, 2012; *Fortin et al.*, 2014]: the drained/undrained and undrained/unrelaxed (or "squirt flow") transitions, which separate the three distinct drained, undrained and unrelaxed elastic regimes. Yet, such conclusion relies on a very limited amount of data acquired on very few rock types.

Despite the technical complexity of measuring such effects in the laboratory, different teams aimed at investigating the frequency dependence of elastic properties in rocks using different methodologies (see *Subramaniyan et al.* [2014], and references therein). Under the lead of *Spencer* [1981], *Jackson and Paterson* [1987] and *Batzle et al.* [2001], the forced oscillation method, allowing measurements over a wide frequency range and under varying confining pressure, was shown promising and faced important technical advances over the last decade [e.g.,

Adelinet et al., 2010; *Tisato and Madonna*, 2012; *Madonna and Tisato*, 2013; *Fortin et al.*, 2014; *Mikhaltsevitch et al.*, 2014; *Szewczyk et al.*, 2016; *Pimienta et al.*, 2016a; *Spencer and Shine*, 2016]. The aim of most teams was in particular to investigate the squirt-flow phenomenon [*O'Connell and Budiansky*, 1977; *Mavko et al.*, 1979], responsible for inducing a transition from the undrained to the unrelaxed regime. For this purpose, most teams applied experimental undrained condition on the rock sample in order to investigate effects beyond the undrained regime. Several authors [e.g., *Mikhaltsevitch et al.*, 2014; *Pimienta et al.*, 2015a; *Subramaniyan et al.*, 2015; *Mikhaltsevitch et al.*, 2015, 2016a; *Pimienta et al.*, 2016b, a; *Spencer and Shine*, 2016] interpreted the measured dispersion and attenuation in terms of squirt flow. Consistent with squirt-flow theory, the observed dispersion/attenuation effect depends both on frequency and fluid viscosity.

Several experimental artifacts need however to be accounted for [e.g., *Gardner*, 1962; *Dunn*, 1987; *Pimienta et al.*, 2016c]. In the experimental methodology usually chosen [e.g., *Batzle et al.*, 2006; *Tisato and Madonna*, 2012; *Madonna and Tisato*, 2013; *Mikhaltsevitch et al.*, 2014], a valve is placed at the nearest of the rock sample to obtain experimental undrained conditions. However, a pure nil dead volume can seldom be achieved experimentally. As discussed by *Pimienta et al.* [2016c], the existence of a small but non-zero dead volume implies that the sample will not be purely undrained. In that case, the measured effect could be the Biot-Gardner effect (i.e. drained/undrained transition). This observation has long-reaching consequences when interpreting laboratory data on dispersion and attenuation in fluid-saturated rocks. To counter this limit, a new methodology has been designed at ENS [*Pimienta et al.*, 2015b] in which a large dead volume is maintained at both ends of the sample. Using this approach, the drained/undrained transition has been evidenced [*Pimienta et al.*, 2015b, a, 2016a].

When a second frequency effect is measured at higher frequencies, with no fluid flow out of the sample, it can be safely interpreted as the undrained/unrelaxed transition [*Pimienta et al.*, 2015a, 2016b].

Those two transitions were documented in two quartz-pure Fontainebleau sandstones of low porosity [e.g., *Pimienta et al.*, 2016a]. As sandstones found in the nature are seldom clean (i.e. quartz pure) and can cover a broad range in porosity, this work reports measurement of dispersion and attenuation in three sandstone samples ranging in porosity and mineral content. First, the experimental method, and the samples mineralogy and microstructure are described. Then, the frequency dependent properties are reported for different effective confining pressures. Ultimately, comparing this dataset with previous ones, interpretations are suggested and discussed.

2. Experimental set-up & rock samples

2.1. Experimental set-up

The experimental set-up used for the study is a oil confining cell equipped of a maneuverable axial piston, allowing to apply pure confining pressures up to $P_c = 300$ MPa and deviatoric stress up to $\sigma_{ax} = 1000$ MPa [*Fortin et al.*, 2007]. Two set-ups can be used: (i) Bulk modulus and its intrinsic dissipation are measured from pure hydrostatic oscillations by lifting the piston [*Adelinet et al.*, 2010; *David et al.*, 2013; *Pimienta et al.*, 2015b; *Borgomano et al.*, 2017]; (2) Young's modulus and Poisson's ratio (and their intrinsic dissipations) are measured from axial stress oscillations by shifting down the piston [*Pimienta et al.*, 2015a, 2016b; *Riviere et al.*, 2016; *Borgomano et al.*, 2017]. The piston is equipped with a piezo-electric actuator ***PI piezo-ceramics*** able to apply small axial stress oscillations at frequencies from 1 mHz up to 100 Hz. All rock samples are equipped with three couples of radial and axial strain gages. The gages

are glued on the cylindrical surface, at the sample center. For this study, the confining pressure range chosen did not exceed $P_c = 32$ MPa that is the blocking pressure for the actuator. Axial stress was kept to a minimum in order to avoid an effect of pressure-induced anisotropy on the measurements [*Pimienta et al.*, 2015a]. In the present contribution, Young's modulus E and Poisson's ratio ν as well as their related dissipation coefficients are investigated. E and ν are obtained from linear regression between axial stress and axial strain and between radial strain and axial strain, respectively. Their related dissipations, Q_E^{-1} and Q_ν^{-1}, are obtained from the tangent of the signal phase of those two end-members [e.g., *Pimienta et al.*, 2015a, 2016b; *Borgomano et al.*, 2017].

The pore fluid set-up and procedure has been described in *Pimienta et al.* [2015b]. The fluid tubing is linked to a ***Quizix*** pump, able to deliver pressures in the range of $[0; 10]$ MPa. The fluid line can be either opened (i.e. drained conditions) or closed (i.e. experimentally undrained conditions) thanks to two valves situated at both sides of the sample. The total dead volume, at both ends of the sample has been measured to be 6.6 mL. A pore pressure sensor is introduced in this dead volume. When changing confining pressures, the valves are opened to maintain a constant pore fluid pressure, and the sample is drained. When the measurement begins, the valves are closed and pore pressure variations are measured.

All samples are measured under both dry and liquid-saturated conditions. However, the liquid chosen differs for the rock samples: (i) Bentheim sandstone is measured under glycerine saturation; (ii) Wilkenson sandstone is measured under water saturation; and (iii) Berea sandstone is measured under saturation of glycerine and a water-glycerine mixture. To ascertain the repeatability of the measurements under water-glycerine saturation and investigate boundary effects, the sample is measured twice, i.e. it is water-saturated and dried after the first measurement,

then saturated again by the water-glycerine mixture. For the second measurement, the sample is equipped differently. Two strain gages are glued at the sample center, and two strain gages are glued near the bottom end-platen to investigate boundary effects. More information is given in the discussion section.

2.2. Rock samples

The three sandstones investigated are Wilkenson, Bentheim and Berea sandstone. Wilkenson sandstone is a low porosity (about $9\,\%$ porosity) sandstone, with a quartz content of about $50\,\%$ [*Duda and Renner*, 2013]. Berea sandstone is a reference in the rock mechanics and rock physics community [e.g. *Christensen and Wang*, 1985; *Sayers et al.*, 1990; *Tao et al.*, 1995; *Prasad and Manghnani*, 1997; *Pagoulatos and Sondergeld*, 2004; *Hart and Wang*, 2010; *Mavko and Vanorio*, 2010; *Pimienta et al.*, 2016c; *Spencer and Shine*, 2016]. Samples from this rock have porosities ranging from $17\,\%$ to $23\,\%$, and a quartz content ranging from $75\,\%$ to $95\,\%$ [*Pimienta et al.*, 2014]. Bentheim sandstone is a quartz-rich sandstone also used as a reference rock [e.g. *Klein et al.*, 2001; *Vajdova et al.*, 2004; *Louis et al.*, 2005; *Blöcher et al.*, 2014; *Pimienta et al.*, 2017], which porosity is in the range of $20\,\%$ up to $25\,\%$. All three rock samples are documented to be isotropic and homogeneous at the sample scale, thus allowing for a good applicability of the method tested in this contribution.

As qualitatively shown from the SEM images (Fig. 1), the selected samples cover a large porosity range (i.e. from about $10\,\%$ up to $25\,\%$) and a wide range in mineral content (i.e. from about $50\,\%$ up to $98\,\%$ in quartz). Fig. (1) shows the variability from one sample to the other: (i) Bentheim sandstone is almost quartz-pure, showing only traces of feldspars; (ii) Berea sandstone shows presence of feldspars, present as inclusions in a quartz-dominated rock matrix; and (iii) Wilkenson sandstone shows a large quantity of feldspars and alumino-silicate

minerals. From processing the various images acquired using ***ImageJ*** free software allows to infer the approximate mineral content (Table 1). From the thin section, Wilkenson, Berea and Bentheim sandstone samples have respectively (i) a quartz content of about $51\,\%$, $82\,\%$ and $98\,\%$; and (ii) a porosity of about $10\,\%$, $22\,\%$ and $25\,\%$. A good consistency is obtained with literature data and with the three weighting method, leading to porosities of $9.1\,\%$, $19.2\,\%$ and $24.8\,\%$, respectively.

3. Results

3.1. Physical properties of the sandstones

3.1.1. Permeability and elastic properties

For the three rock samples, permeability is measured as a function of Terzaghi effective pressure (P_{eff}). Moreover, the variation in volumetric strain of the sample is also recorded for characterization purposes. For comparison, we also report the permeability and volumetric strain on the two Fontainebleau sandstones investigated in *Pimienta et al.* [2015a]. The dependence of these two properties on P_{eff} is reported in Fig. (3).

The samples permeability (Fig. 3a) range over five orders of magnitude, from about $10^{-18}\,m^2$ for Wilkenson sandstone up to $2\,10^{-13}\,m^2$ for Bentheim sandstone, and exhibit varying dependences to confining pressure. The less permeable Wilkenson sandstone has a permeability that decreases from about $5\,10^{-18}\,m^2$ down to $1\,10^{-18}\,m^2$ as P_{eff} increases from 1 to 30 MPa. The permeabilities of Berea sandstone (i.e. $2\,10^{-14}\,m^2$) and Bentheim (i.e. $5\,10^{-13}\,m^2$) sandstones are constant with pressure. The two Fontainebleau sandstones from *Pimienta et al.* [2015a] appear to be in between these two extremes, with permeabilities of about $5\,10^{-15}\,m^2$ and $1\,10^{-14}\,m^2$, and with a slight dependence on P_{eff}.

Comparing the volumetric strain variations (Fig. 3b), all samples exhibit a transition from non-linear variations at low P_{eff} up to linear variations at higher P_{eff}. However, the characteristic pressure for the change of slope and the magnitude of variations differ from one rock to the other. Bentheim, Berea and Wilkenson sandstones have very similar magnitudes of variations over the pressure range. Those variations have larger magnitudes than the ones of the Fontainebleau samples. It directly implies smaller stiffnesses (i.e. elastic moduli) than those of the Fontainebleau samples. In case of Wilkenson sandstone, as highlighted by the slope at higher pressures, the static bulk modulus reaches $30\,$GPa at $P_{eff} = 30\,$MPa.

3.1.2. Elastic dispersion at 1 MPa effective pressure

Owing to the range in permeability observed for the different sandstone samples, a specific fluid is chosen to saturate each of the rock samples. The reason is that the critical frequency for the drained/undrained transition (i.e. Biot-Gardner flow) varies as κ/η [e.g., *Cleary*, 1978]. To account for the viscosity effect [e.g., *Batzle et al.*, 2006; *Spencer and Shine*, 2016], we define an apparent frequency $f^* = f(\eta/\eta_0)$, with $\eta_0 = 10^{-3}\,$Pa.s [e.g., *Pimienta et al.*, 2015b]. The properties of the high permeability Bentheim sandstone are investigated under glycerine saturation (i.e. high viscosity fluid). The properties of the lower permeability Berea sandstone are investigated under saturation of both glycerine and a water-glycerine mixture. The properties of the low permeability Wilkenson sandstone are investigated under water saturation (i.e. low viscosity) only. The samples properties are reported as a function of apparent frequency [e.g., *Pimienta et al.*, 2015b] at lowest Terzaghi effective pressure of $P_{eff} = 1\,$MPa (Fig. 4). The elastic properties measured are (i) Young's modulus E; (ii) Poisson's ratio ν; (iii) Young's modulus dissipation Q_E^{-1}; and (iv) Poisson's ratio dissipation Q_ν^{-1}. The hydraulic property, ad-

dressed here as "fluid flow parameter", refers to the frequency-dependent pseudo-consolidation parameter [e.g., *Pimienta et al.*, 2015b, 2016a], an in-situ proxy of fluid flow out of the sample.

For all sandstone samples, both Young's modulus and Poisson's ratio show an increase with increasing apparent frequency. Yet, different trends are observed for Young's modulus and Poisson's ratio. Young's modulus of Wilkenson sandstone slightly increases but remains in the range of $[16, 18]$ GPa for frequencies below $f^* = 10$ Hz (Fig. 4b). Beyond this frequency, a steep increase is observed, up to about $E = 27$ GPa at 100 Hz. In case of Berea sandstone, a slow increase from $E = 20$ GPa to $E = 30$ GPa is observed over the frequency range of measurement (i.e. $f^* = [1; 3.10^4]$ Hz). For this rock, measurements under glycerine saturation are slightly shifted up as compared to the water-glycerine saturation. Young's modulus of Bentheim sandstone shows the largest increase, from $E = 31$ GPa up to $E = 52$ GPa. Similar to Wilkenson sandstone, a slow increase is observed at frequencies below $f^* = 2 - 5$ kHz. Beyond this frequency, a steep increase is observed.

For all rocks, Poisson's ratio increases with the measuring frequency (Fig. 4b). The largest variation is observed for Wilkenson sandstone, i.e. from $\nu = 0.24$ up to $\nu = 0.37$ as frequency increases. Beyond $f^* = 10$ Hz, a plateau is reached and Poisson's ratio remains constant. Berea sandstone Poisson's ratio also shows a large increase, from $\nu = 0.25$ up to $\nu = 0.34$, at frequencies below $f^* = 1$ kHz. The values remain relatively constant in the range of $f^* = [1; 10]$ kHz, and then decrease slightly beyond $f^* = 20$ kHz. For Bentheim sandstone, an increase up to $\nu = 0.35$ is observed at $f^* = 10$ kHz. Beyond this frequency, ν remains constant.

Overall, the variations in E and ν correlate with the measured dissipations (Figs. 4c & 4d). The Q_ν^{-1} peaks are consistent with the monotonous variations in ν. For Wilkenson and Bentheim sandstones, large increases in E and ν correlate with large peaks in Q_E^{-1} and Q_ν^{-1}. Consistently

206 also, the almost linear increase in Berea sandstone Young's modulus correlates to a constant
207 $Q_E^{-1} \sim 0.05$ over the frequency range. From the sample hydraulic response, a large frequency-
208 dependent decrease in fluid flow is observed for all samples (Fig. 4e). This indicates that, for f^*
209 beyond 10 Hz, 100 Hz and 1 kHz respectively, the Wilkenson, Berea and Bentheim sandstones
210 are undrained.

3.2. Role of effective confining pressure

211 Different frequency dependences of Young's modulus and Poisson's ratio are observed for the
212 different sandstones. For Bentheim and Wilkenson sandstones, E and Q_E^{-1} data are consistent
213 with two distincts transitions in frequency. But, this not the case for ν and Q_ν^{-1} for which
214 only one transition seems to exist. Moreover, large variations in E and ν are observed over the
215 frequency range. In the following, the pressure effect on these transitions is examined for the
216 two rocks.

217 3.2.1. Bentheim sandstone

218 Elastic and hydraulic properties of the Bentheim sandstone sample under glycerine saturation
219 are measured as a function of frequency for different effective pressures in the range of $P_{eff} =$
220 $[1; 10]$ MPa (Fig. 5). For all values of P_{eff}, an increase in E (Fig. 5a) and ν (Fig. 5b) is
221 observed with increasing frequency. These increase in elastic properties correlate to Q_E^{-1} (Fig.
222 5c) and Q_ν^{-1} (Fig. 5d) peaks. Two peaks are observed on Q_E^{-1} at $f_1 = 3$ Hz and $f_2 = 50$ Hz, and
223 one for Q_ν^{-1} at $f_1 = 3$ Hz. For all pressures, consistently with E, the first peak is of much lower
224 magnitude than the second, and the characteristic frequencies remain the same. By reporting
225 the characteristic frequencies for the two Q_E^{-1} peaks in all graphs, one notes that the Q_ν^{-1} peak
226 occurs at f_1.

The fluid flow parameter (Fig. 5e) shows a large frequency dependent decrease, down to 0 beyond 10 Hz. Consistently, this value of 10 Hz corresponds to the frequency at which a change of slope is observed on E, and a plateau is reached for ν. Interestingly, no effect of pressure on the fluid flow is observed. In terms of pressure dependence, E and ν differ. Beyond 10 Hz, the dependence of E to effective pressure is very small. A large dependence of ν to P_{eff} is observed over the whole frequency range.

3.2.2. Wilkenson sandstone

Wilkenson sandstone properties are measured as a function of frequency for pressures in the range of $P_{eff} = [1; 20]$ MPa (Fig. 6). For all P_{eff}, two Q_E^{-1} peaks and one Q_ν^{-1} peak are again observed, which correlates with the variations in E and ν. Similar to variations for the Bentheim sandstone, the first Q_E^{-1} peak (at $f_1 = 0.2$ Hz) is much smaller than the second one (at $f_2 = 40$ Hz). The Q_ν^{-1} peak occurs again at the frequency f_1, and no variation is observed at f_2.

As for Bentheim sandstone, P_{eff} affects differently the frequency dependence of E (Fig. 6a) and ν (Fig. 6b). Consistently with the first Q_E^{-1} peak, E is shifted to higher values as P_{eff} increases, so that dispersion decreases, yet the frequency dependence remains apparently unaffected by pressure. The second peak (i.e. at f_2) decreases down to half its initial value as P_{eff} increases. Poisson's ratio decrease with P_{eff}, but the magnitude of dispersion (Fig. 6b) and attenuation (Fig. 6d) remain constant. Consistently, the amount of fluid flow decreases as P_{eff} increases.

4. Interpretation : Dispersion/Attenuation in sandstones over the frequency range

Different effects are observed in the three different sandstones. In the following, to better investigate those variations, measurements are first compared to previous results on two

Fontainebleau sandstones [*Pimienta et al.*, 2015a, 2016b] to attain a larger overview of frequency effects in sandstones. While different authors reported results on sandstones [e.g., *Spencer and Shine*, 2016], because the role of the measuring method was shown to be of major importance [e.g., *Pimienta et al.*, 2016c], only measurements using the same apparatus and procedure are used in this part. A comparison between the different measurements methods is then discussed.

4.1. Variability of frequency effects in sandstones: Microstructural control

4.1.1. Measured frequency effects in five sandstones

The frequency-dependent elastic properties of up to five sandstones samples can be compared over the frequency range (Fig. 7). Note that two different porosities are investigated: (i) the two Fontainebleau and the Wilkenson sandstones have similar porosities in the range of $\phi = [7; 9]\,\%$, and (ii) the Bentheim and Berea sandstones have a similar porosity of $\phi = [20; 25]\,\%$. Overall, a large variability can be observed between the five different sandstones. Very different characteristic frequencies are observed (Fig. 7). Table (2) reviews the samples properties as well as the observed frequency of the variations for the different sandstone samples. The variability between the characteristic frequencies observed does not directly correlate to the sample porosity or mineral content.

In the available frequency range, two distinct fluid flow phenomena are expected to occur [e.g., *Pimienta et al.*, 2016a]: (i) Biot-Gardner flow (i.e. drained/undrained transition), separating the drained and the undrained regimes, and (ii) squirt-flow (i.e. undrained/unrelaxed transition), separating the undrained and the unrelaxed regimes. Both Fontainebleau sandstone samples [*Pimienta et al.*, 2015a, 2016b] were shown to exhibit both the Biot-Gardner (i.e. drained/undrained) and squirt-flow (i.e. undrained/unrelaxed) transitions, leading to dis-

persion/attenuation on both Young's modulus and Poisson's ratio. But, although of similar porosity (i.e. about $7\,\%$ and $8\,\%$), the two samples showed evidence of very different behaviors. For the $7\,\%$ porosity Fontainebleau sample, two large dispersion/attenuation effects were measured on both Young's modulus and Poisson's ratio. For the $8\,\%$ porosity Fontainebleau sample, both critical frequencies overlapped, leading to a single transition from the drained to the unrelaxed regime.

For the three sandstones examined in this work, a dispersion/attenuation effect is observed on both Young's modulus and Poisson's ratio in the low frequency range. At higher frequency, very different behaviors are observed for the three rocks. From the slope change in E and ν at highest frequency, the beginning of a second frequency-dependent dispersion/attenuation phenomena is observed for Berea sandstone. For Wilkenson and Bentheim sandstones, a second frequency effect is clearly observed. For both rocks, only Young's modulus and its dissipation seem to be affected by the second effect.

4.1.2. Fluid flow theories: Apparent frequency vs microstructure

According to *Cleary* [1978] and *O'Connell and Budiansky* [1977], the two transitions relate to a characteristic frequency that depends on microstructural variables of the rock sample. The Biot-Gardner flow (i.e. drained/undrained transition) separates the drained regime (i.e. flow out of a volume) and the undrained regime (i.e. fluid pressurization in the volume). As shown by *Cleary* [1978], this transition is proportional to the rock hydraulic conductivity (i.e. κ/η) and a fluid diffusion length L such that:

$$f_1 = \frac{4\kappa K_d}{\eta L^2}. \tag{1}$$

Where η is the fluid viscosity and K_d and κ are respectively the drained bulk modulus and the permeability of the investigated rock sample. In the experimental conditions, L is a length as-

sociated to the rock sample size [e.g., *Adelinet et al.*, 2011]. L is expected to be between the sample length and half of it, i.e. $L \in [40; 80]$ mm. At higher frequencies, fluid has no more time to equilibrate in the REV (Representative Elementary Volume) so that a third flow regime is present that is called "unrelaxed". Since, in general, a porous rock contains inclusions of different shapes (i.e. pores and microcracks), fluid can flow from a compliant microcrack to a neighbouring less compliant pore [*O'Connell and Budiansky*, 1977]. This squirt-flow phenomenon is associated with a critical frequency that depends on the skeleton bulk modulus (i.e. K_s), on the microcrack aspect ratio ξ and on the fluid viscosity η such that [*O'Connell and Budiansky*, 1977]:

$$f_2 = \frac{\xi^3 K_s}{\eta}. \tag{2}$$

Using realistic parameters (i.e. $K_d \in [5; 15]$ GPa, $L \in [40; 80]$ mm, $K_s \in [35, 40]$ GPa), range of values can be predicted for f_1 (Eq. 1) and f_2 (Eq. 2). Fig. (8) compares the observed characteristic frequencies f for the different attenuation peaks to the predicted ranges for f_1 and f_2. In case of Biot-Gardner flow, the theory predicts an increase in the cut-off frequency as permeability increases or as fluid viscosity decreases. The two parameters being measured directly and with accuracy, it is possible to compare directly measurements and prediction (Fig. 8a). Overall, a good fit is observed for all rock samples and all saturating fluids. In case of squirt-flow (Fig. 8b), the characteristic frequency is controlled by the aspect ratio of microcracks, a parameter not measurable directly with accuracy in rocks. Comparing the predicted and observed critical frequency, a range of aspect ratio is assessed for all rock samples: About $\xi = 10^{-4}$ in both the Wilkenson sandstone and in Fo8, a slightly higher value of about $\xi = 5\,10^{-4}$ for Fo7, and larger values of $\xi = 1 - 3\,10^{-3}$ for Bentheim and Berea sandstones. These aspect ratio values are realistic for sandstones [e.g., *Walsh*, 1965; *Fortin et al.*, 2007; *David et al.*, 2013; *Fortin et al.*,

298 2014], and could be inferred from different methods [e.g., *De Paula et al.*, 2012]. Ultimately
299 comparing the results of Fig. (8) with the ones of Table (2), different dependences to the perme-
300 ability, porosity and mineral content are observed: (i) consistent with Eq. (1), the first transition
301 correlate to permeability, which in turn is dependent on porosity and mineral content. For sim-
302 ilar porosities, permeability decreases as the content in clay mineral increases. (ii) as expected
303 from Eq. (2), the frequency for the second transition is independent of the rock permeability.

Note finally that the first transition correlates with a fluid flow out of the sample (Fig. 4e). Consistent with results on the two Fontainebleau sandstones [*Pimienta et al.*, 2016b], the much larger dispersion/attenuation in Poisson's ratio than Young's modulus for this transition is expected. Following Biot-Gassmann theory, the rock shear modulus G is expected to be constant for this transition. From linear elasticity in an isotropic medium:

$$E = 2G(1+\nu). \tag{3}$$

Assuming linear viscoelasticity, one gets:

$$\frac{\Delta E}{E} = \frac{\Delta \nu}{\nu}\frac{\nu}{(1+\nu)} \approx 0.3\,\frac{\Delta \nu}{\nu}. \tag{4}$$

304 Hence, the small effect on Young's modulus is consistent. These additional information confirm
305 that the first dispersion/attenuation phenomenon is caused by the transition from drained to
306 undrained regime.

4.2. Zener rheological model : Fluid flow in the high frequency range ?

307 Large dispersion/attenuation on Young's modulus are observed at high frequencies in Ben-
308 theim and Wilkenson sandstones, when no flow out of the sample occurs anymore. Are the
309 observed variations in modulus and dissipation consistent with a linear viscoelastic behavior ?
310 Indeed, viscoelasticity is a robust way to test the measured variations in modulus and the mea-

sured dissipation [e.g., *Pimienta et al.*, 2015b; *Mikhaltsevitch et al.*, 2016a; *Borgomano et al.*, 2017]. Kramers-Kronig equations, expressing the causality principle between dispersion and dissipation, could be used [e.g., *Mikhaltsevitch et al.*, 2016a]. A simpler approach is to use Zener rheological model [e.g., *Pimienta et al.*, 2015a; *Borgomano et al.*, 2017], which follows Kramers-Kronig principle but assumes only a single relaxation time. This assumption may not be valid if, for instance, there is a broad spectrum of crack aspect ratio. Consistent with what has been already described in other works [e.g., *Pimienta et al.*, 2015b, a; *Borgomano et al.*, 2017], the first transition can be shown to follow Kramer-Kronig causality principle for all samples. This is expected as quasi-static poroelasticity fits the viscoelastic framework [e.g., *Rubino et al.*, 2008]. This should theoretically be the case also for the squirt-flow effect [e.g., *Carcione and Gurevich*, 2011; *De Paula et al.*, 2012]. It is thus of interest to investigate the links between measurements and viscoelasticity for this second transition.

For the two Fontainebleau sandstones, it was also shown to be true but one sample did not follow the Zener-like frequency dependence [e.g., *Pimienta et al.*, 2015a, 2016b]. For Wilkenson sandstone (Figs. 9b & 9d), an excellent fit is observed between data and Zener model predictions. Because both the amplitude and the band-width of the peak fit, it further implies that only one relaxation time, i.e. only one single family of aspect ratio, is observed in this frequency range. Combining with the results of Fig. (8b), the cracks family has an inferred average aspect ratio of $\xi = 10^{-4}$. For Bentheim sandstone, however, the E variations and the Q_E^{-1} peak do not fit (Figs. 9a & 9c). Fitting Zener model to the E variations, the predicted attenuation peak is of 0.20, higher than the data that indicates a maximum of $Q_E^{-1} = 0.15$. Moreover, the peak band-width is not consistent with a Zener-like model. Such effect could be due to either (i) a lower accuracy on Q_E^{-1}; or (ii) the existence of phenomenon that deviates from viscoelasticity.

A possible low accuracy in the measurement of Q_E^{-1} is likely and cannot be ruled out at this point. However, could another physical effect be the cause of an uncoupling between dispersion and attenuation ? Interestingly, out of the sandstones studied, Bentheim sandstone is the most porous (i.e. $\phi = 24\,\%$) and permeable (i.e. $\kappa = 5\,10^{-13}$ m^2).

5. Discussion: Other datasets & Effect of the measuring method

In section 4, no comparison was made with other datasets as very different experimental methods have been used by other authors. However, it is important to compare the results to other published data in order to gain a better insight on on the effects, independently of the measuring set-up and conditions.

5.1. Previous measurements on Berea sandstone

In comparison with other sandstones (e.g. Fontainebleau sandstone) showing large variabilities, elastic properties for different Berea sandstone samples are similar [e.g., *Pimienta et al.*, 2014]. In the framework of the investigation of the frequency dependence of elastic properties, samples of this rock were measured by *Tisato and Madonna* [2012], *Chapman et al.* [2016], *Mikhaltsevitch et al.* [2016b], *Spencer and Shine* [2016] and in this study. *Tisato and Madonna* [2012] and *Chapman et al.* [2016] investigated mainly effects under partial saturation conditions. As in this work, *Mikhaltsevitch et al.* [2016b] and *Spencer and Shine* [2016] measured a Berea sandstone under full saturation by fluids of varying viscosity. As shown in Table (3), porosity is relatively similar for all samples but variable permeabilities are observed in the samples. The sample used by *Spencer and Shine* [2016] has a permeability two orders of magnitudes larger than the one used in this study. The sample used by *Mikhaltsevitch et al.* [2016b] is similar to that of this study. Interestingly, one observes a good correlation between permeability and

cut-off frequency observed by the authors: the effect for *Spencer and Shine* [2016] occurs at frequency $f^* = 40\,\text{kHz}$, that is two orders of magnitude higher than $f^* = 0.3 - 0.5\,\text{kHz}$ found in this study and in *Mikhaltsevitch et al.* [2016b]. Moreover, comparing results on Young's modulus and Poisson's ratio by *Mikhaltsevitch et al.* [2016b] with the ones in this study, a very good fit is observed in both magnitude and frequency dependence of the effects.

Mikhaltsevitch et al. [2016b] and *Spencer and Shine* [2016] interpreted the measured dispersion/attenuation as induced by squirt-flow phenomena. The present paper reports also the hydraulic response that was not measured with other set-ups. This confirms in our case that the observed transition is the transition between drained and undrained elastic regimes. It is possible that they measured also the Biot-Gardner flow: a transition from partially-drained [*Pimienta et al.*, 2016c] to undrained regime. The same possibility holds for the data of *Spencer and Shine* [2016]. It could be also that *Spencer and Shine* [2016] measured an effect that is a combination of the two transitions, similar to what was observed on the Fo8 sample by *Pimienta et al.* [2015b].

5.2. Role of the measuring method over the frequency range

Pimienta et al. [2016c] showed theoretically that "global" or "local" measurements, or "local" measurements in different localisations, would lead to different apparent behaviors of the rock sample. To investigate this effect, the second experiment on the Berea sample reported in Figs. (4b & 4d) was measured with a different set-up. Strain gages were glued at different axial positions on the sample, i.e. at the middle length (i.e. dark-green symbols in Fig. 10) and near the end-platen (i.e. light-green symbols in Fig. 10). Moreover, the effect of changing the fluid pressure on the measurement was also tested. The dispersion/attenuation measurements on the sample under dry and fluid-saturated conditions are reported in Fig. (10). Under dry conditions,

consistently, no frequency dependence is observed, and no differentiation is made between the strain gages positions. Under saturation by the water-glycerine mixture, large deviations are observed depending on the strain gage positions.

For the strain gage positioned in the middle of the sample (i.e. dark-green symbols), results are the same as those previously obtained (Figs. 4b & 4d). At lowest frequency, because the rock is partially undrained [*Pimienta et al.*, 2016b, c], Poisson's ratio is much larger than under dry conditions (Fig. 10b). At very low pore fluid pressure (i.e. $p_f = 0.1\,\text{MPa}$), because it gets more difficult for fluid to pressurise in the dead volume and oppose the sample strain, values are initially much lower and then strongly increase with frequency to reach the same value in the undrained regime. For all p_f values, the effect occurs in approximately the same frequency range of $f \in [10^{-1}, 10^{1}]\,\text{Hz}$. In case of the strain gauge located near the end platen (i.e. light-green symbols), the values initially fit with the ones under dry conditions. Then, as frequency increases beyond $f = 10\,\text{Hz}$, a dramatic increase is measured, leading to values close to the previous ones (Fig. 10b). Interestingly, in this case, no effect of p_f is observed. Note further that, in both cases, dispersion (Figs. 10a & 10b) and attenuation (Figs. 10c & 10d) fit with Zener models. The effects are also consistent with predictions from the model *Pimienta et al.* [2016c].

Hence, the measuring position appears to lead to very different results. *Spencer and Shine* [2016] used capacitive displacement sensors, a set-up measuring the "global" response of the sample, a response expected to average all "local" measurements across the sample length [*Pimienta et al.*, 2016c]. Then, the results should be in-between the two responses in Figs. (10b) & (10d), with a transition spanning several orders of magnitude in frequency. Note that *Spencer and Shine* [2016] data show dispersion/attenuation phenomena over more than four or-

399 ders of magnitude in frequency. *Mikhaltsevitch et al.* [2016b] used a "local" method, as in our
400 study, which is consistent with the very similar response in terms of frequency range and mag-
401 nitude of the effect. Note finally that squirt-flow phenomena are not expected to be dependent
402 on the measured location, provided that the sample is homogeneous, i.e. that each REV of the
403 sample are the same.

6. Conclusion

404 Young's modulus and Poisson's ratio of different sandstones, saturated by different fluids,
405 have been measured as a function of frequency. Large frequency dependent variations are ob-
406 served for all sandstones. The measured transitions differ in the characteristic frequency of
407 occurence, magnitude or amount of elastic constants involved. Further comparing with pub-
408 lished data, two different effects are observed for all samples over the allowed frequency range.
409 Overall, the drained/undrained transition is observed for all samples. The characteristic fre-
410 quency for this effect is consistent with the measured permeabilities. At higher frequency, a
411 second effect is also observed that is however more difficult to assess. Interpreting this second
412 transition in terms of squirt-flow effect yields very realistic aspect ratio families for all rock
413 samples.

414 For the second effect, large dispersions and attenuation are measured for Wilkenson and Ben-
415 theim sandstones. In case of Bentheim sandstone, the measured dispersion and attenuation do
416 not fit with Zener-like variations. This implies either that the measured dissipation is not ac-
417 curate or that another physical effect is here observed. Noting that the sample is much more
418 permeable than the others, its large pore entry diameters could be a cause for this effect. Ul-
419 timately, Berea sandstone is used as a comparison mean with published data by other teams.
420 Very consistent results are observed. Experimental evidence of a strong control by the measur-

ing method and conditions is highlighted in case of the drained to undrained transition. In case of squirt-flow, no effect is expected.

Acknowledgments. This work has been supported by TOTAL, under project no.FR00007429. The first author wishes to thank Damien Deldicque and Dr. Alexandre Schubnel for their help in using the SEM-EDS cartography set-up, an analytical tool bought thanks to the European Research Council under the grant REALism. The presented datasets are available upon request.

References

Adelinet, M., J. Fortin, Y. Guéguen, A. Schubnel, and L. Geoffroy (2010), Frequency and fluid effects on elastic properties of basalt: Experimental investigations, *Geophysical Research Letters*, *37(2)*(2), L02,303, doi:10.1029/2009GL041660.

Adelinet, M., J. Fortin, and Y. Guéguen (2011), Dispersion of elastic moduli in a porous-cracked rock: Theoretical predictions for squirt-flow, *Tectonophysics*, *503*(1), 173–181.

Amalokwu, K., G. Papageorgiou, M. Chapman, and A. I. Best (2017), Modelling ultrasonic laboratory measurements of the saturation dependence of elastic modulus: New insights and implications for wave propagation mechanisms, *International Journal of Greenhouse Gas Control*, *59*, 148–159.

Batzle, M., R. Hofmann, D.-H. Han, and J. Castagna (2001), Fluids and frequency dependent seismic velocity of rocks, *The Leading Edge*, *20*(2), 168–171.

Batzle, M. L., D.-H. Han, and R. Hofmann (2006), Fluid mobility and frequency-dependent seismic velocitydirect measurements, *Geophysics*, *71*(1), N1–N9.

Biot, M. A. (1941), General theory of three-dimensional consolidation, *Journal of applied physics*, *12*(2), 155–164.

Blöcher, G., T. Reinsch, A. Hassanzadegan, H. Milsch, and G. Zimmermann (2014), Direct and indirect laboratory measurements of poroelastic properties of two consolidated sandstones, *International Journal of Rock Mechanics and Mining Sciences*, *67*, 191–201.

Borgomano, J. V. M., L. Pimienta, J. Fortin, and Y. Guéguen (2017), Dispersion and attenuation measurements of the elastic moduli of a bimodal-porosity limestone, *Journal of Geophysical Research*, *accepted*.

448 Carcione, J. M., and B. Gurevich (2011), Differential form and numerical implementation of
449 biots poroelasticity equations with squirt dissipation, *Geophysics*, *76*, N55–N64.
450 Chapman, S., N. Tisato, B. Quintal, and K. Holliger (2016), Seismic attenuation in partially
451 saturated berea sandstone submitted to a range of confining pressures, *Journal of Geophysical*
452 *Research: Solid Earth*, *121*(3), 1664–1676.
453 Christensen, N., and H. Wang (1985), The influence of pore pressure and confining pressure on
454 dynamic elastic properties of berea sandstone, *Geophysics*, *50*(2), 207.
455 Cleary, M. P. (1978), Elastic and dynamic response regimes of fluid-impregnated solids with
456 diverse microstructures, *International Journal of Solids and Structures*, *14*(10), 795–819.
457 David, E. C., J. Fortin, A. Schubnel, Y. Guéguen, and R. W. Zimmerman (2013), Laboratory
458 measurements of low-and high-frequency elastic moduli in fontainebleau sandstone, *Geo-*
459 *physics*, *78*(5), D369–D379.
460 De Paula, O. B., M. Pervukhina, D. Makarynska, and B. Gurevich (2012), Modeling squirt dis-
461 persion and attenuation in fluid-saturated rocks using pressure dependency of dry ultrasonic
462 velocities, *Geophysics*, *77*(3), WA157–WA168.
463 Duda, M., and J. Renner (2013), The weakening effect of water on the brittle failure strength of
464 sandstone, *Geophysical Journal International*, *192*(3), 1091–1108.
465 Dunn, K.-J. (1987), Sample boundary effect in acoustic attenuation of fluid-saturated porous
466 cylinders, *The Journal of the Acoustical Society of America*, *81*, 1259.
467 Fortin, J., Y. Guéguen, and A. Schubnel (2007), Effects of pore collapse and grain crushing on
468 ultrasonic velocities and vp/vs, *Journal of Geophysical Research: Solid Earth (1978–2012)*,
469 *112(B8)*(B8).

Fortin, J., L. Pimienta, Y. Guéguen, A. Schubnel, E. David, and M. Adelinet (2014), Experimental results on the combined effects of frequency and pressure on the dispersion of elastic waves in porous rocks, *The Leading Edge*, *33*(6), 648–654.

Gardner, G. (1962), Extensional waves in fluid-saturated porous cylinders, *The Journal of the Acoustical Society of America*, *34*(1), 36–40.

Hart, D., and H. Wang (2010), Variation of unjacketed pore compressibility using gassmann's equation and an overdetermined set of volumetric poroelastic measurements, *Geophysics*, *75*(1), N9–N18.

Jackson, I., and M. Paterson (1987), Shear modulus and internal friction of calcite rocks at seismic frequencies: pressure, frequency and grain size dependence, *Physics of the earth and planetary interiors*, *45*(4), 349–367.

Klein, E., P. Baud, T. Reuschlé, and T. Wong (2001), Mechanical behaviour and failure mode of bentheim sandstone under triaxial compression, *Physics and Chemistry of the Earth, Part A: Solid Earth and Geodesy*, *26*(1), 21–25.

Louis, L., C. David, V. Metz, P. Robion, B. Menendez, and C. Kissel (2005), Microstructural control on the anisotropy of elastic and transport properties in undeformed sandstones, *International journal of rock mechanics and mining sciences*, *42*(7), 911–923.

Madonna, C., and N. Tisato (2013), A new seismic wave attenuation module to experimentally measure low-frequency attenuation in extensional mode, *Geophysical Prospecting*, *61*(2), 302–314.

Mavko, G., and T. Vanorio (2010), The influence of pore fluids and frequency on apparent effective stress behavior of seismic velocities, *Geophysics*, *75*(1), N1.

Mavko, G., E. Kjartansson, and K. Winkler (1979), Seismic wave attenuation in rocks, *Reviews of Geophysics*, *17*(6), 1155–1164.

Mikhaltsevitch, V., M. Lebedev, and B. Gurevich (2014), A laboratory study of low-frequency wave dispersion and attenuation in water-saturated sandstones, *The Leading Edge*, *33*(6), 616–622.

Mikhaltsevitch, V., M. Lebedev*, and B. Gurevich (2015), A laboratory study of attenuation and dispersion effects in glycerol-saturated Berea sandstone at seismic frequencies, in *proceedings of SEG 85th Annual Meeting*, pp. 3085–3089, Society of Exploration Geophysicists.

Mikhaltsevitch, V., M. Lebedev, and B. Gurevich (2016a), Validation of the laboratory measurements at seismic frequencies using the kramers-kronig relationship, *Geophysical Research Letters*, *43*(10), 4986–4991.

Mikhaltsevitch, V., M. Lebedev, and B. Gurevich (2016b), An experimental evidence of the squirt-flow effect in glycerol-saturated berea sandstone at seismic frequencies, in *proceedings of the 78th EAGE Conference and Exhibition*, doi:10.3997/2214-4609.201600675.

Müller, T. M., B. Gurevich, and M. Lebedev (2010), Seismic wave attenuation and dispersion resulting from wave-induced flow in porous rocksa review, *Geophysics*, *75*(5), 75A147–75A164.

O'Connell, R. J., and B. Budiansky (1977), Viscoelastic properties of fluid-saturated cracked solids, *Journal of Geophysical Research*, *82*(36), 5719–5735.

Pagoulatos, A., and C. Sondergeld (2004), Evaluation of multistage triaxial testing on berea sandstone, Master's thesis, University of Oklahoma.

Papageorgiou, G., K. Amalokwu, and M. Chapman (2016), Theoretical derivation of a brie-like fluid mixing law, *Geophysical Prospecting*, *64*(4), 1048–1053.

Pimienta, L., J. Sarout, L. Esteban, and C. Delle Piane (2014), Prediction of rocks thermal conductivity from elastic wave velocities, mineralogy and microstructure, *Geophysical Journal International*, *197*(2), 860–874, doi:10.1093/gji/ggu034.

Pimienta, L., J. Fortin, and Y. Guéguen (2015a), Experimental study of youngs modulus dispersion and attenuation in fully saturated sandstones, *Geophysics*, *80*(5), L57–L72, doi:10.1190/geo2014-0532.1.

Pimienta, L., J. Fortin, and Y. Guéguen (2015b), Bulk modulus dispersion and attenuation in sandstones, *Geophysics*, *80*(2), D111–D127, doi:10.1190/geo2014-0335.1.

Pimienta, L., J. Fortin, J. V. Borgomano, and Y. Guéguen (2016a), Dispersions and attenuations in a fully saturated sandstone: Experimental evidence for fluid flows at different scales, *The Leading Edge*, *35*(6), 495–501.

Pimienta, L., J. Fortin, and Y. Guéguen (2016b), Effect of fluids and frequencies on poissons ratio of sandstone samples, *Geophysics*, *81*(2), D183–D195, doi:10.1190/geo2015-0310.1.

Pimienta, L., J. Borgomano, J. Fortin, and Y. Guéguen (2016c), Modelling the drained/undrained transition: effect of the measuring method and the boundary conditions, *Geophysical Prospecting*, *64*(4), 1098–1111, doi:10.1111/1365-2478.12390.

Pimienta, L., J. Fortin, and Y. Guéguen (2017), New method for measuring compressibility & poroelasticity coefficients in porous and permeable rocks., *Journal of Geophysical Research: Solid Earth*, doi:10.1002/2016jb013791.

Prasad, M., and M. Manghnani (1997), Effects of pore and differential pressure on compressional wave velocity and quality factor in berea and michigan sandstones, *Geophysics*, *62*(4), 1163.

Riviere, J., L. Pimienta, M. Scuderi, T. Candela, P. Shokouhi, J. Fortin, A. Schubnel, C. Marone, and P. A. Johnson (2016), Frequency, pressure, and strain dependence of nonlinear elasticity in berea sandstone, *Geophysical Research Letters*, *43*(7), 3226–3236.

Rubino, J. G., C. L. Ravazzoli, and J. E. Santos (2008), Equivalent viscoelastic solids for heterogeneous fluid-saturated porous rocks, *Geophysics*, *74*(1), N1–N13.

Sarout, J. (2012), Impact of pore space topology pn permeability, cut-off frequencies and validity of wave propagation theories, *Geophysical Journal International*, *189*, 481–492.

Sayers, C., J. Van Munster, and M. King (1990), Stress-induced ultrasonic anisotrophy in berea sandstone, in *International Journal of Rock Mechanics and Mining Sciences & Geomechanics Abstracts*, vol. 27, pp. 429–436, Elsevier.

Spencer, J. (1981), Stress relaxations at low frequencies in fluid-saturated rocks: Attenuation and modulus dispersion, *Journal of Geophysical Research*, *86*(B3), 1803–1812.

Spencer, J. W., and J. Shine (2016), Seismic wave attenuation and modulus dispersion in sandstones, *Geophysics*, *81*(3), D211–D231.

Subramaniyan, S., B. Quintal, N. Tisato, E. H. Saenger, and C. Madonna (2014), An overview of laboratory apparatuses to measure seismic attenuation in reservoir rocks, *Geophysical Prospecting*, *62(6)*, 1211–1223.

Subramaniyan, S., B. Quintal, C. Madonna, and E. H. Saenger (2015), Laboratory-based seismic attenuation in fontainebleau sandstone: Evidence of squirt flow, *Journal of Geophysical Research: Solid Earth*, *120*(11), 7526–7535.

Szewczyk, D., A. Bauer, and R. M. Holt (2016), A new laboratory apparatus for the measurement of seismic dispersion under deviatoric stress conditions, *Geophysical Prospecting*, *64*(4), 789–798.

560 Tao, G., M. King, and M. Nabi-Bidhendi (1995), Ultrasonic wave propagation in dry and brine-
561 saturated sandstones as a function of effective stress: laboratory measurements and mod-
562 elling1, *Geophysical Prospecting*, *43*(3), 299–327.

563 Tisato, N., and C. Madonna (2012), Attenuation at low seismic frequencies in partially saturated
564 rocks: Measurements and description of a new apparatus, *Journal of Applied Geophysics*, *86*,
565 44–53.

566 Tisato, N., B. Quintal, S. Chapman, Y. Podladchikov, and J.-P. Burg (2015), Bubbles attenu-
567 ate elastic waves at seismic frequencies: First experimental evidence, *Geophysical Research*
568 *Letters*, *42*(10), 3880–3887.

569 Vajdova, V., P. Baud, and T. Wong (2004), Compaction, dilatancy, and failure in porous carbon-
570 ate rocks, *Journal of geophysical research*, *109*(B5), B05,204.

571 Walsh, J. B. (1965), The effect of cracks on the compressibility of rocks, *Journal of Geophysical*
572 *Research*, *71*, 2591–2599.

Table 1. Grain size, porosity and content in elements from the SEM-EDS images. Average grain size is qualitatively deduced from the image. Porosity and elements content are quantatively obtained using ***ImageJ*** processing software, by applying thresholds on the different mineralogy images. From the content in silicium, assuming that no amorphous silica are present, the quartz (i.e. $Si0_2$) content is directly inferred. Combining contents in aluminium (Al) and potassium (K) or sodium (Na) elements, content in feldspars minerals can be inferred.

Sandstone	Grain size (μm)	$\phi(\%)$	Quartz $(\%)$	Al $(\%)$	Ca $(\%)$	Fe $(\%)$	K $(\%)$	Mg $(\%)$	Na $(\%)$
Bentheim	150	25.09	97.87	2.88	0.02	0.05	1.13	0.07	0.17
Berea	100	21.69	81.71	9.35	0.27	0.54	6.18	2.88	1.81
Wilkenson	400	10.08	51.09	19.51	0.94	3.54	12.01	2.22	11.47

Figures

Table 2. Properties measured for the five rock samples at an effective pressure of $P_{eff} \sim 1$ MPa. Porosity and quartz content are from SEM-EDS images. Permeability and bulk modulus are measured at $P_{eff} \sim 1$ MPa. Frequency is picked from the Q_E^{-1} peaks. Results on the Fontainebleau are from *Pimienta et al.* [2015b, a, 2016c].

Sample ♯	Fo7	Fo8	WilkS	BeS	BhS
Porosity (ϕ)	$7.2\,\%$	$8.7\,\%$	$9.1\,\%$	$19.2\,\%$	$24.8\,\%$
Quartz content	$99.9\,\%$	$99.9\,\%$	$51.1\,\%$	$81.7\,\%$	$97.9\,\%$
Permeability (κ in m^2)	$4\,10^{-15}$	$1\,10^{-14}$	$3\,10^{-18}$	$2\,10^{-14}$	$5\,10^{-13}$
Drained Bulk modulus (K_d)	7 GPa	25 GPa	7 GPa	5 GPa	5 GPa
Frequency (f^*_{obs1})	10 Hz	20 Hz	0.3 Hz	$30 - 300$ Hz	1 kHz
Frequency (f^*_{obs2})	1 kHz	–	30 Hz	$20 - 40$ kHz	10 kHz

Table 3. Comparison of measured physical properties (i.e. porosity, quartz content and permeability) by different teams on Berea sandstone: [1] this study, [2] *Mikhaltsevitch et al.* [2016b] and [3] *Spencer and Shine* [2016]. For the three studies, the sample is measured under glycerin full saturation. The reported frequency is the one corresponding to the Q_E^{-1} peak in the different studies, by normalising by the fluid viscosity to obtain f^*.

Study ♯	[1]	[2]	[3]
Porosity (ϕ)	$19.2\,\%$	$19\,\%$	$24.4\,\%$
Quartz content	$81.7\,\%$	$80\,\%$	–
Permeability (κ in m^2)	$2\,10^{-14}$	$7.1\,10^{-14}$	$1.3\,10^{-12}$
Drained Bulk modulus (K_d)	5 GPa	–	–
Frequency ($f^* = f(\eta/\eta_0)$)	0.3 kHz	0.5 kHz	40 kHz

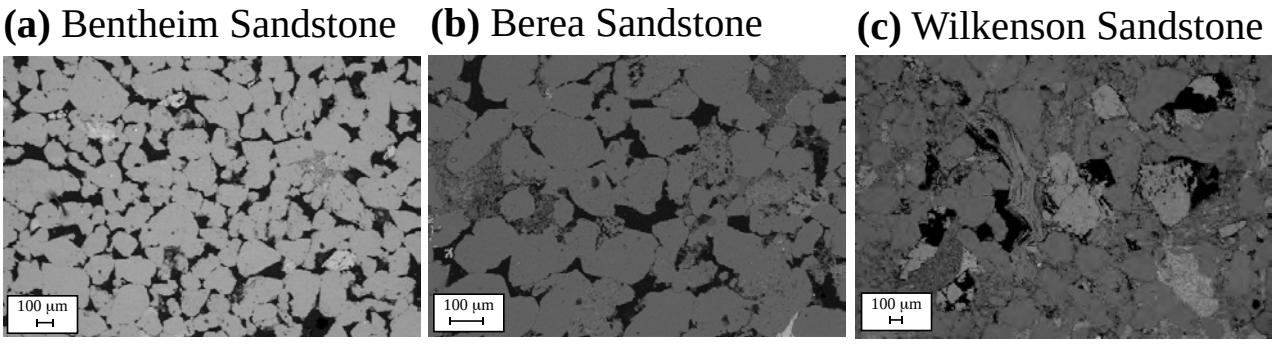

Figure 1. Scanning Electron Microscopy (SEM) images of thin sections of the (a) Bentheim sandstone, (b) Berea sandstone, and (c) Wilkenson sandstone. From the different grey levels, the denser materials are brighter as compared to the less dense ones. Quartz crystals dominantly appear as bright grains. For Berea and Bentheim sandstones, open grain contacts are observed. For Wilkenson sandstone, microcracked grains are also observed.

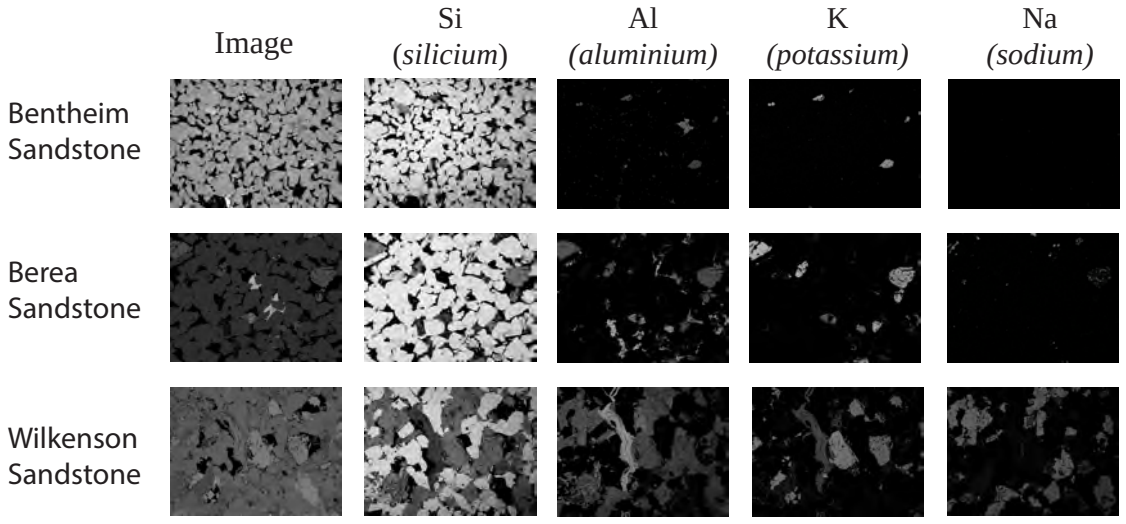

Figure 2. Energy Dispersion Spectrometry (EDS-SEM) image on the same thin sections as in Fig. (1), showing the different atoms and their localisation in the thin section of the rock sample.

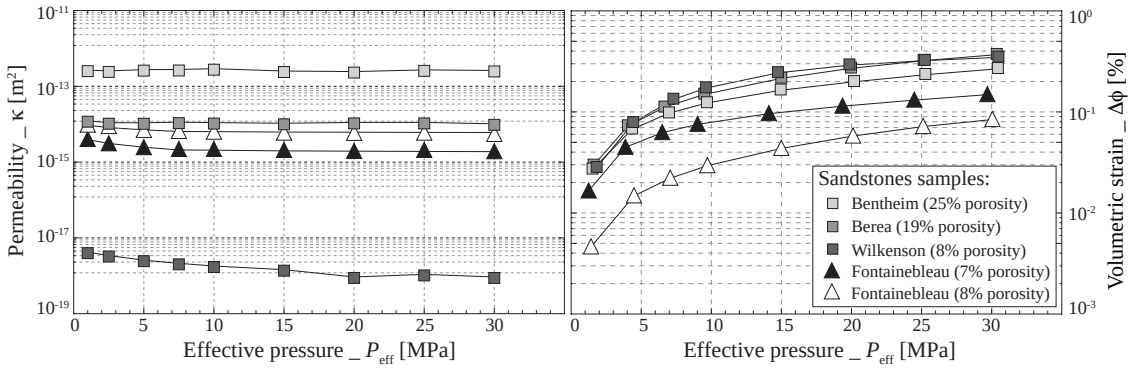

Figure 3. Measured physical properties of the sandstones investigated: (a) Permeability of the water-saturated rocks as a function of confining pressure; (b) Young's modulus of the dry rocks; Poisson's ratio of the dry rocks. The measurement from *Pimienta et al.* [2015a] on a 7 % porosity Fontainebleau sandstone sample are reported for comparison.

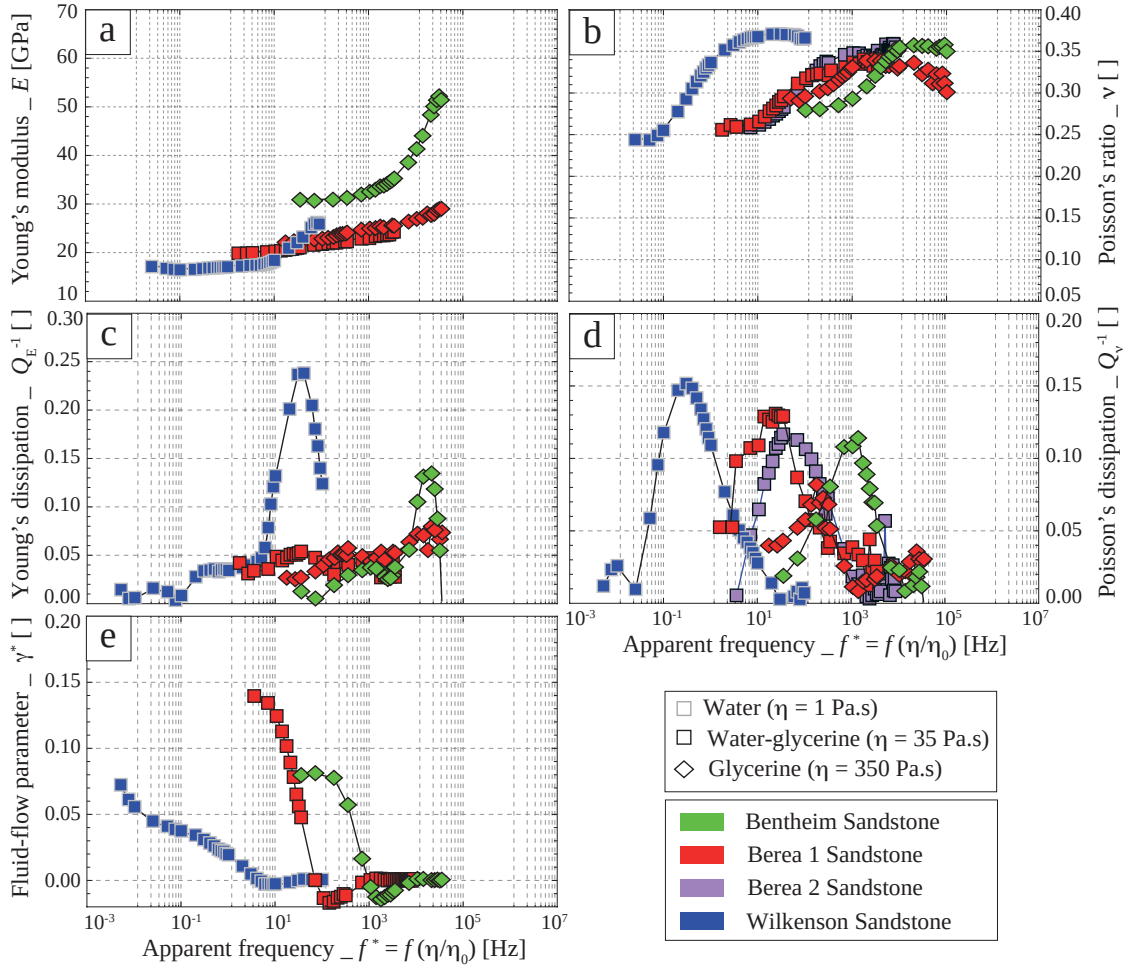

Figure 4. Measured (a) Young's modulus and (b) Poisson's ratio as a function of apparent frequency in the fluid-saturated samples for an effective pressure of $P_{eff} = 1$ MPa. The samples studied are a water-saturated Wilkenson sandstone, a glycerine-saturated Bentheim sandstone and a Berea sandstone under either glycerine or water-glycerine saturation. The Poisson's ratio of the Berea sandstone is measured twice under water-glycerine saturation. The in-situ liquid viscosity (η) used to determine the apparent frequency (f^*) is obtained from the measured hydraulic diffusivity for the different samples.

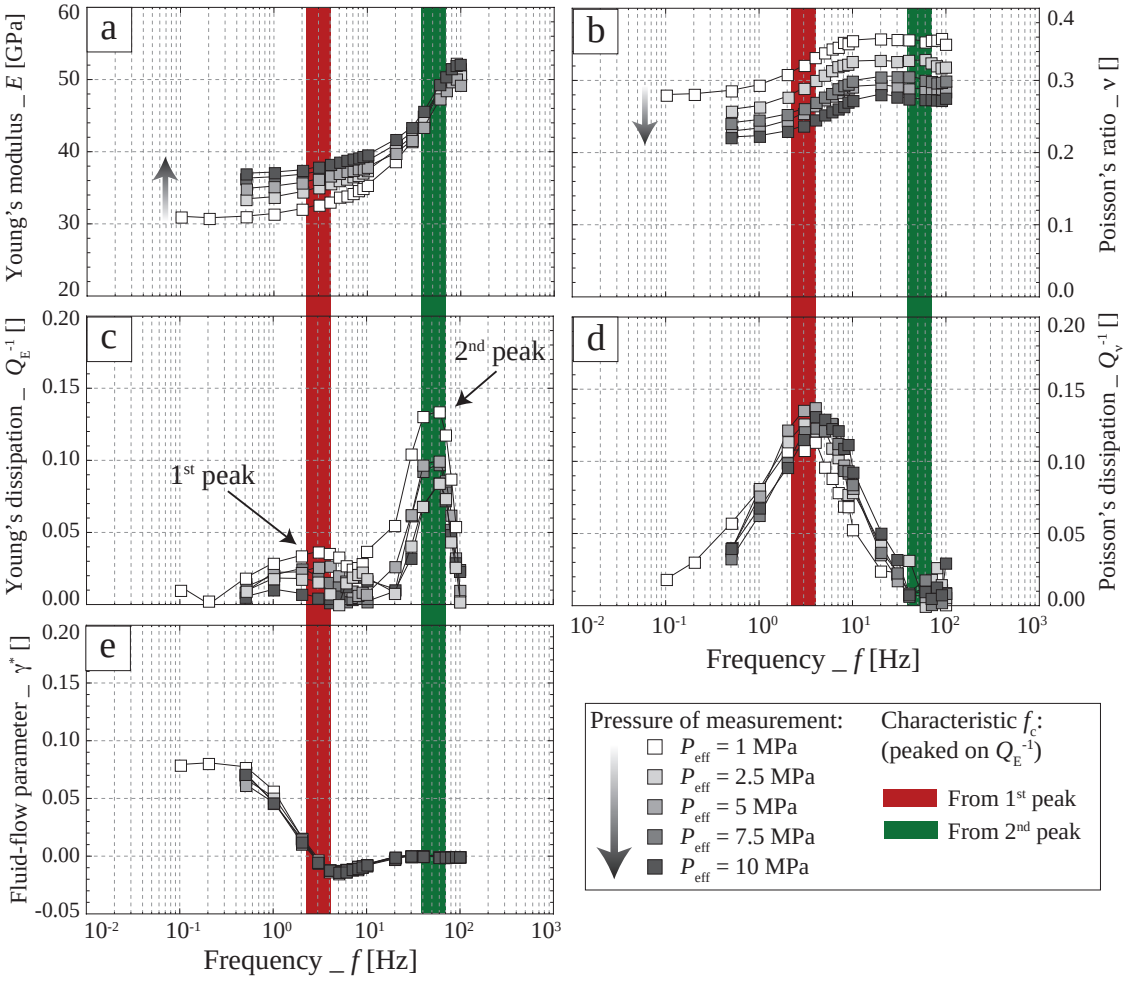

Figure 5. Measured frequency dependence of all available properties on a glycerine-saturated Bentheim sandstone for varying effective pressures in the range of $[1; 10]$ MPa. The properties measured are (a) Young's modulus; (b) Poisson's ratio (c) Young's modulus associated dissipation (i.e. addressed as Young's attenuation); (d) Poisson's ratio associated dissipation (i.e. addressed as Poisson's attenuation); and (e) Pseudo-consolidation parameter γ^*, direct indication of fluid flow out of the sample.

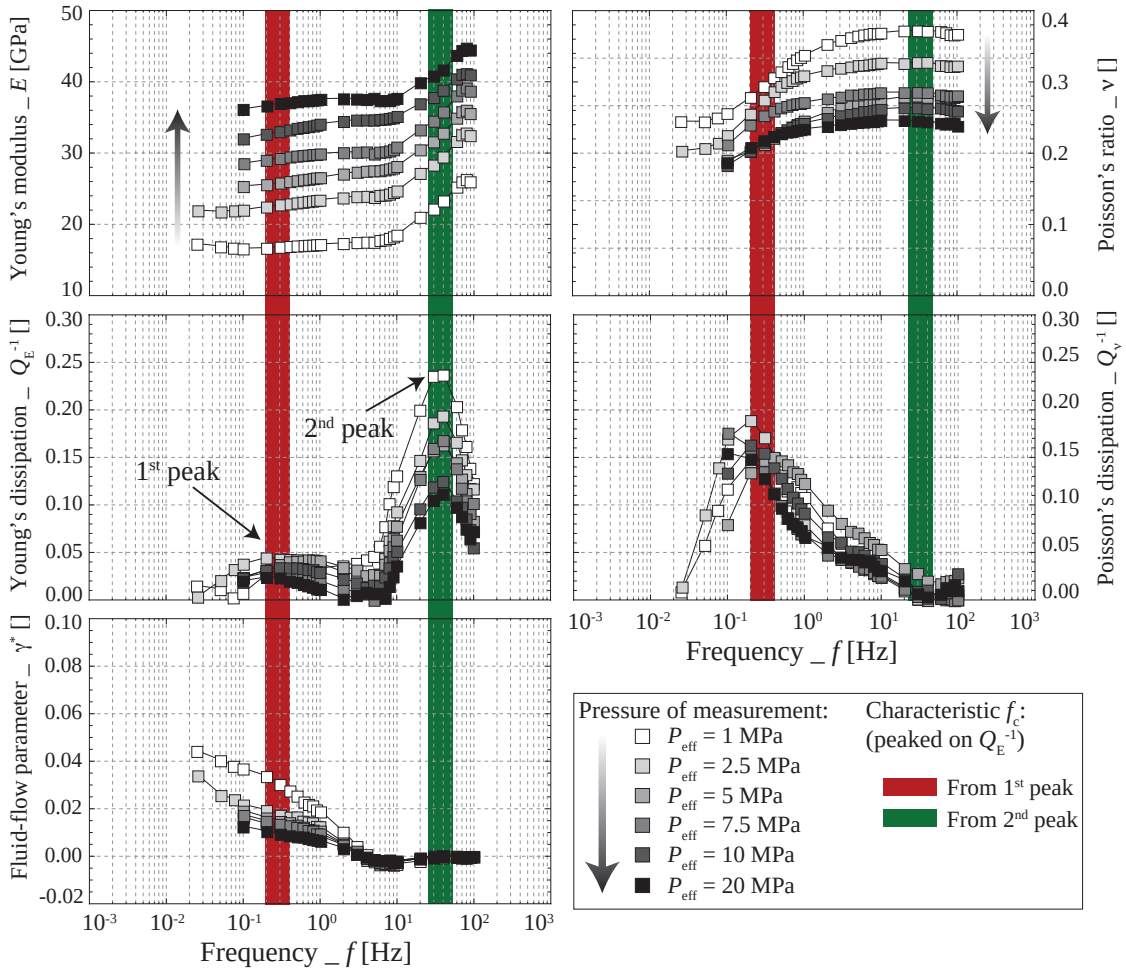

Figure 6. Measured frequency dependence of all available properties on a water-saturated Wilkenson sandstone for varying effective pressures in the range of $[1; 10]$ MPa. The properties measured are (a) Young's modulus; (b) Poisson's ratio (c) Young's modulus associated dissipation (i.e. addressed as Young's attenuation); (d) Poisson's ratio associated dissipation (i.e. addressed as Poisson's attenuation); and (e) Pseudo-consolidation parameter γ^*, direct indication of fluid flow out of the sample.

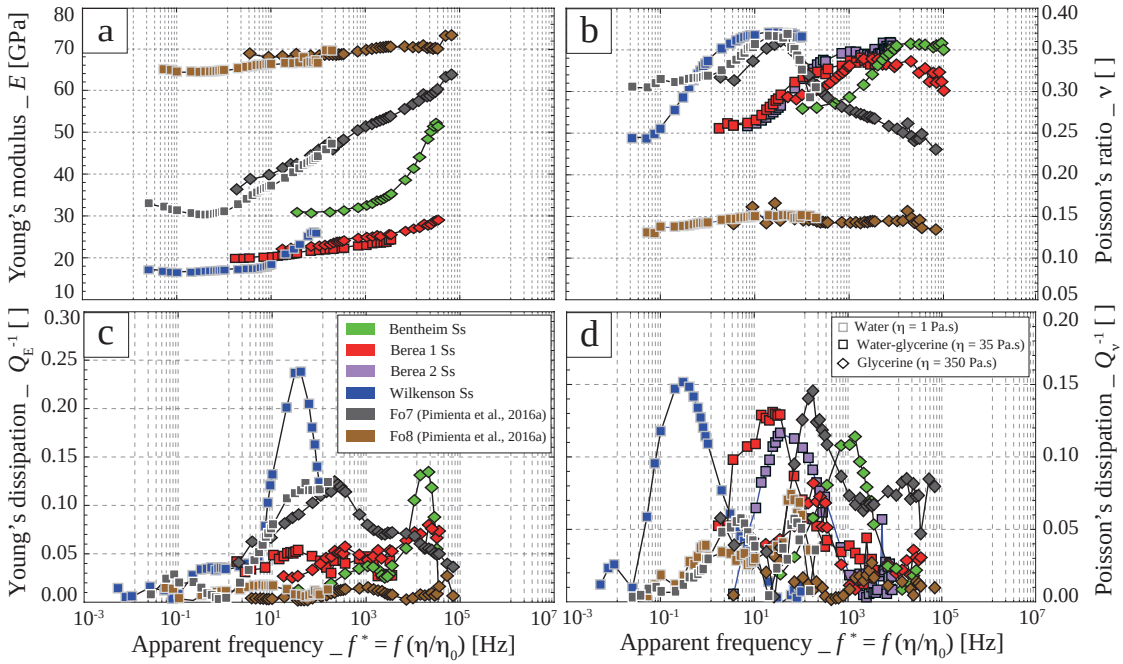

Figure 7. Comparison of the (a-b) Young's modulus E and Q_E^{-1}, and (c-d) Poisson's ratio ν and Q_ν^{-1} as a function of apparent frequency for the five sandstone samples saturated by either water (i.e. gray squares), glycerine (i.e. diamonds) and a water-glycerine mixture (i.e. black squares). In addition to the three sandstones studied, the Fontainebleau sandstone samples from *Pimienta et al.* [2015a, 2016b] are reported for comparison.

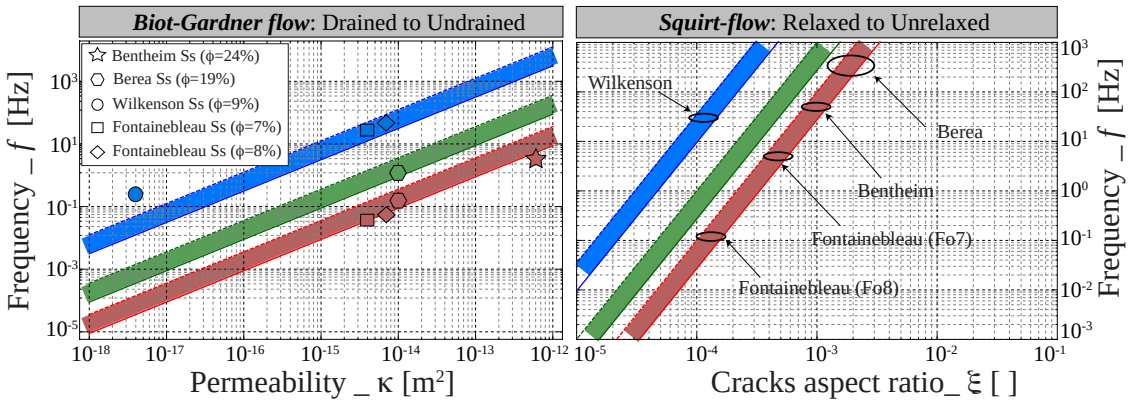

Figure 8. Comparison plot of the predicted characteristic frequency for the (a) Biot-Gardner flow and (b) squirt-flow phenomena. The frequency is calculated from Eqs. (1) and (2) using three different fluid viscosities (i.e. blue for water, green for the water-glycerine mixture and red for glycerine). For the two transitions, domains of realistic of frequency values are drawn by using a range of realistic parameters (i.e. $K_d = [5, 15]$ GPa, $L = [40, 80]$ mm and $K_s = [35, 40]$ GPa).

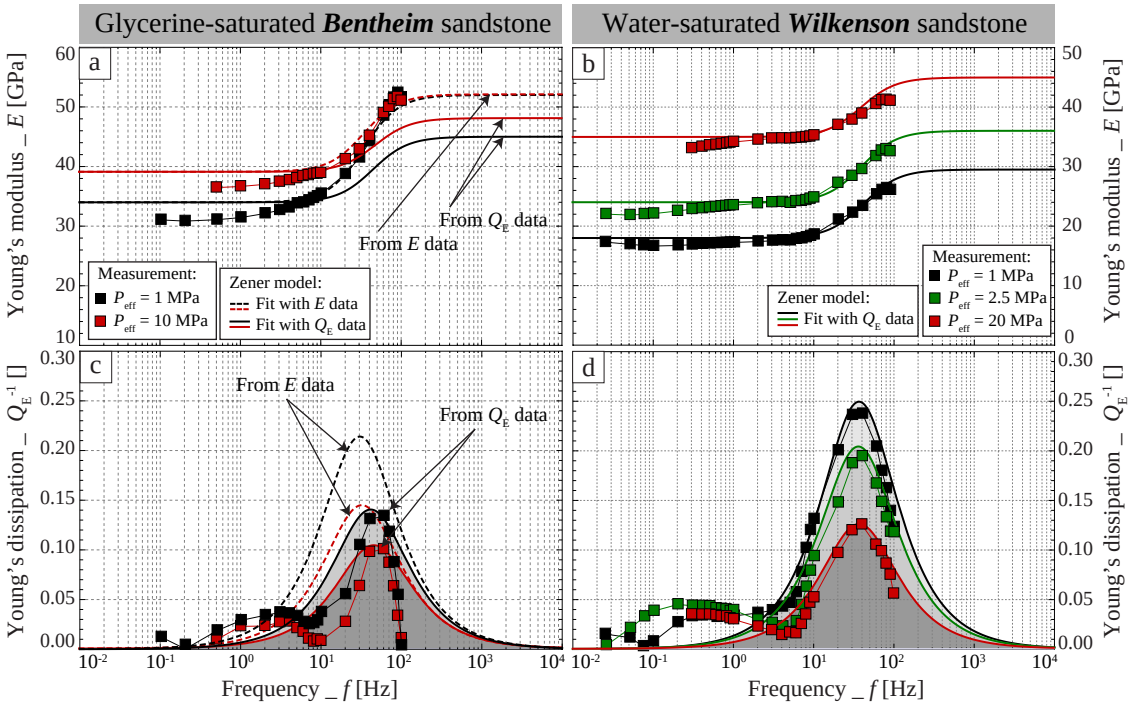

Figure 9. Comparison between measured (a-b) Young's modulus E and its related (c-d) Young's dissipation for the second frequency-dependent variation using Zener rheological models. Only the magnitude of the effect is of interest here, and the dashpot viscosity is adjusted to fit the frequency dependence. For the glycerine-saturated Bentheim sandstone, two comparisons are tested, from using either the data of E (i.e. dashed lines) or of Q_E^{-1} (i.e. continuous lines).

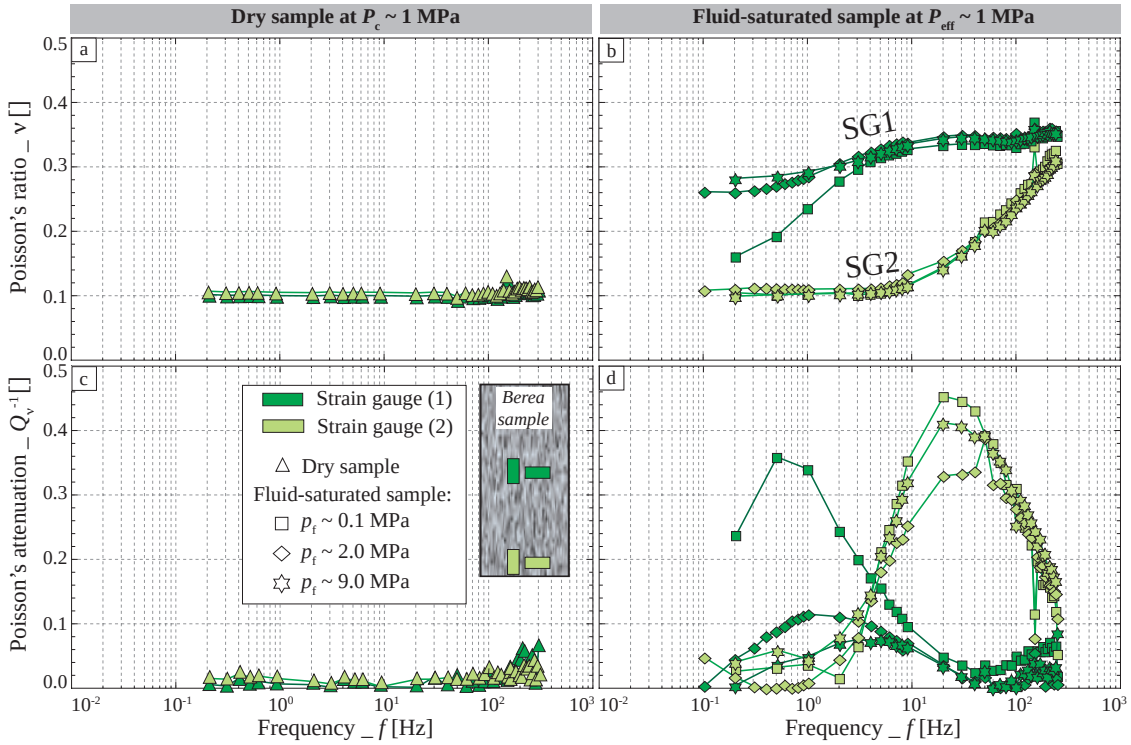

Figure 10. Measured frequency dependence of (a-b) Poisson's ratio and (c-d) its associated dissipation in a Berea sandstone sample at a Terzaghi effective pressure of $P_{eff} = 1$ MPa. The sample is either (a-c) dry or (b-d) saturated by a water-glycerine mixture. Under both dry and liquid-saturated conditions, the role of the measuring position is tested from the measuring the strains at sample's half-length (i.e. dark-green) or near the sample's bottom (i.e. light-green). Under liquid-saturated conditions, the role of pore fluid pressure is tested while keeping a Terzaghi effective pressure of $P_{eff} = 1$ MPa.

Appendix C

Laboratory measurements of seismic attenuation and stiffness moduli dispersion in glycerine-saturated Berea sandstone.

Article submitted in **Geophysical Prospecting**.

Chapman, S., J. Fortin, J.V.M. Borgomano, H. Yin, and B. Quintal.

Submitted October 2017.

Laboratory measurements of seismic attenuation and stiffness moduli dispersion in glycerine-saturated Berea sandstone

Samuel Chapman[1] (samuel.chapman@unil.ch), Jerome Fortin[2], Jan V. M. Borgomano[2], Hanjun Yin[2,3], and Beatriz Quintal[1]

1) Institute of Earth Sciences, University of Lausanne, Lausanne, Switzerland.

2) Laboratoire de Geologie de L'ENS, PSL Research University, Paris, France.

3) State Key Laboratory of Petroleum Resources and Prospecting, China University of Petroleum-Beijing, Beijing, China.

Abstract

We performed forced hydrostatic and axial oscillation experiments on dry and fully glycerine saturated Berea sandstone samples to determine their dynamic stiffness moduli and attenuation at micro-seismic and seismic frequencies (0.004 – 30 Hz). In a sample (BS-H3) with pronounced horizontal bedding layers with respect to its vertical axis we observe an attenuation peak at 0.07 – 0.1 Hz with corresponding bulk modulus dispersion, associated with the pore pressure diffusion from the sample into the pore fluid lines. By reducing the volume of the pore fluid lines the attenuation magnitude is reduced. In a second sample (BS-V5) with poorly defined vertical bedding layers a good agreement is observed between the bulk modulus and corresponding attenuation determined from the hydrostatic and axial oscillations, suggesting that the sample is approximately isotropic. For the glycerine saturated sample two transitions are observed in the frequency dependent bulk and Young's moduli, with corresponding attenuation peaks. The first attenuation peak at 0.1 – 0.2 Hz is again associated with the diffusion of pore pressure from the sample into the fluid lines. A second,

partial, attenuation peak is observed beginning at ~5 Hz and is likely in response to squirt flow. The later is supported by the observation that the shear modulus and attenuation become increasingly frequency dependent above 1 Hz, while negligible shear attenuation is observed at lower frequencies.

Key Words

- Attenuation
- Rock physics

1. Introduction

Porous rocks saturated with fluids can strongly attenuate seismic waves. Different forms of wave-induced fluid flow (WIFF) are thought to be the primary intrinsic mechanism for seismic wave attenuation (e.g. Pride *et al.* 2004). Fluid flow arises predominantly from contrasts in compressibility either in the solid matrix of the rock, for instance between compliant grain contacts and stiff pores, or in the saturating fluids, such as a heterogeneous distribution of water and gas. In response to such compressibility contrasts, seismic waves induce pressure gradients, resulting in viscous fluid flow and the conversion of the waves' mechanical energy into heat. The frequency dependence of the associated seismic attenuation depends strongly on the spatial distribution of the heterogeneities in the rock matrix and/or the saturating fluids (Masson and Pride 2007, 2011; Müller *et al.* 2008). A direct consequence of the frequency dependent attenuation is that the corresponding stiffness modulus of the rock will also be frequency dependent.

Much focus has been given to squirt flow, pressure diffusion arising from microscopic compressibility heterogeneities in the rock, as one of the dominant mechanism for wave attenuation in fluid saturated rocks. Numerous theoretical models (e.g. O'Connell and Budiansky 1977; Mavko and Jizba 1991; Chapman *et al.* 2002; Gurevich *et al.* 2010; Adelinet *et al.* 2011) have been developed to try to explain laboratory observations at sonic and ultrasonic frequencies. More recently, with the progress made in using the forced oscillation method (e.g. McKavanagh and Stacey 1974), squirt flow has been studied also at seismic frequencies by using high viscosity fluids such as glycerine. On a Fontainebleau sandstone sample saturated with glycerine, Pimienta *et al.* (2015a) observe an extensional mode attenuation peak at 1 to 10 Hz, which was reduced in amplitude with increasing effective stress. Subramanyian *et al.* (2015) also measured the extensional mode attenuation and Young's modulus in Fontainebleau sandstone with similar properties, in this case varying the fluid viscosity by mixing water and glycerine. For the sample fully saturated by glycerine they observe an attenuation peak in a similar frequency range and with similar amplitude, supporting the observation of Pimienta et al. (2015a). Subramanyian et al. (2015) used Gurevich *et al.'s* (2010) analytical solution of squirt flow to interpret their observations, however the analytical solution consistently underestimated the attenuation magnitude measured in the laboratory. The broad attenuation peaks observed are possibly related to a distribution of crack aspect ratios (Subramanyian *et al.* 2015). Mikhaltsevtich *et al.* (2015; 2016) measured the dynamic Young's modulus and Poisson ratio of a glycerine saturated Berea sandstone, from which they inferred the bulk and shear moduli as well as the corresponding attenuation modes. By performing measurements at temperatures from 31 to 23 °C, they observe a shift of the extensional-mode attenuation peak from ~ 2 to ~ 0.4 Hz, associated with the reduction of the glycerine viscosity. Mikhaltsevtich *et al.* (2015) interpreted the attenuation as being caused by squirt flow. All these laboratory observations

appear to confirm that squirt flow can be a significant source of attenuation at seismic frequencies in those two types of sandstone, for fluids of high viscosity. Following on these observations it seems reasonable that bedding plane orientation, which at ultrasonic frequencies cause significant anisotropy (Prasad and Manghnani 1997), and deviatoric stresses (Collet and Gurevich 2016) could influence the crack aspect ratio distribution, which could in turn affect the frequency dependence of the attenuation measured in the laboratory.

In the laboratory, the boundary conditions of the experiment can be an additional source of frequency dependent moduli dispersion and attenuation. Fluid pressure diffusion across the lateral boundary of the sample was theoretically shown to produce strong modulus dispersion and attenuation by Gardner (1962) and Dunn (1987), and experimentally at seismic frequencies by Mörig and Burkhardt (1989). By sealing the lateral boundary this effect can be mitigated. However, fluid pressure diffusion can also occur from the sample into the pore fluid lines. Pimienta *et al.* (2015b) studied this effect, referring to it as the drained-undrained transition, and later provided a simple analytical solution for the 1D fluid pressure diffusion (Pimienta *et al.* 2016) in response to hydrostatic compression. They show that the amplitude of the attenuation and modulus dispersion is dependent on the ratio between the storage capacity of the sample and the storage capacity of the pore fluid lines. One way to mitigate the influence of this boundary effect is to strongly reduce the volume of the pore fluid lines relative to the pore volume of the sample, for example, by placing mechanical valves in the pore fluid lines close as to as possible to the sample (Batzle *et al.* 2006). However, even when the volume in the pore fluid lines is considerably reduced, the influence of the pore pressure diffusion from the sample to the pore fluid lines can still be significant in low porosity rocks, meriting further study and quantification.

In the following sections we will present the results of forced hydrostatic and axial oscillation experiments on Berea sandstone samples, complemented with ultrasonic P- and S- wave measurements. The experiments where performed on the dry and fully glycerine saturated samples for a range of effective stresses and static axial loadings. We will provide a description of the samples used and how they were prepared, as well as the experimental set-up and conditions used. Following the presentation of the results we will briefly discuss the results and provide our conclusions.

2. Samples and experimental methodology

2.1 Sample description

A total of six cylindrical samples, 4 cm in diameter and 8 cm in length, were cored from two different Berea sandstones blocks. Three of the samples have poorly defined bedding planes parallel to the vertical axis (Figure 1a, BS-V4 to BS-V6) and the other three have pronounced bedding planes perpendicular to the vertical axis (Figure 1b, BS-H1 to BS-H3). Besides the variation in bedding orientation, the samples are similar with respect to glycerine permeability, porosity and dry bulk density (Table 1). The permeability is determined from applying a pressure gradient across the sample and measuring the associated fluid flow. For effective stresses, here defined as the difference between the confining and fluid pressure, $\sigma_{eff} = P_c - P_f$, of 2.5 to 25 MPa, the permeability of sample BS-H3 was moderately stress dependent, which is why we provide the permeability in Table 1 as range. The permeability provided for BS-V5 is the mean permeability for a range of flow rates at 2.5 MPa effective stress. The porosity was determined with a pyknometer, using subsections of samples BS-H1

and BS-V6. The dry density is the mean density determined from the dry masses and dimensions of the two sets of samples.

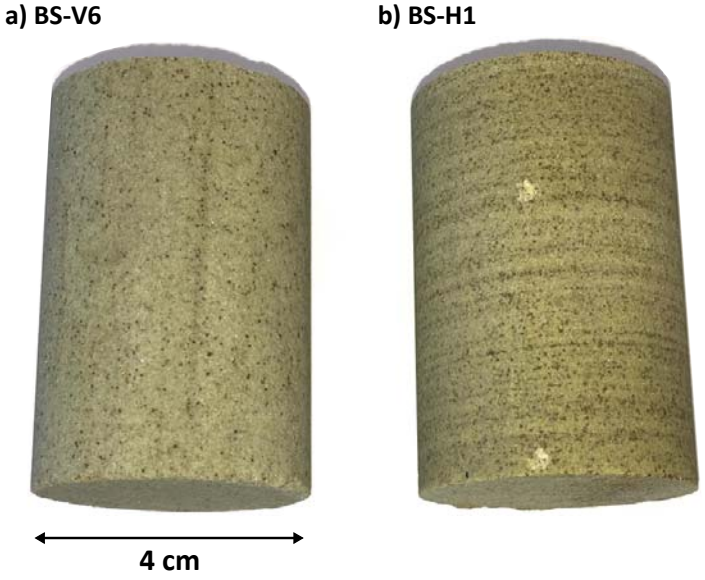

Figure 1. Photograph of samples a) BS-V6 with poorly defined bedding planes parallel to the vertical axis and b) BS-H1 with pronounced bedding planes perpendicular to the vertical axis. The data presented in this article are from experiments performed on samples cored form the same source blocks as BS-V6 and BS-H1.

2.2 Sample preparation

After coring and cutting the samples, they were fixed in a cylindrical steel holder and mounted on a lathe. A diamond-studded grinder was then used to parallelize the sample ends. Four pairs of radial and axial strain gauges were glued at approximately 90 degrees to each other and centred on the lateral surface of the samples. The strain gauges on BS-H3 were glued directly on the sample, with the result of them being forced into the sample's pores at high effective stresses, breaking their circuits and causing the failure of a number of strain gauges. To avoid the failure of strain gauges on BS-V5, a thin layer of epoxy was first applied to fill the pores near the sample's surface. The epoxy layer was polished down until the grains

came through the epoxy. The strain gauges were then glued onto these polished surfaces. The samples where placed in a rubber jacket, with epoxy sealed feed-throughs for the wires connected to the strain gauges, to isolate the samples from the confining oil.

Table 1. Sample properties

	BS-H1 to BS-H3	BS-V4 to BS-V6
Glycerine Permeability (mD)	25.5 – 32.0*	58.7 ± 1.14**
Porosity (%)	21.1	22.15
Dry Density (kg/m^3)	2144 ±12.8	2087 ± 6.55

* Measured at 25 and 2.5 MPa effective stress. ** Measured at 2.5 MPa effective stress.

2.3 Experimental setup - dynamic moduli and attenuation modes

Forced oscillation and ultrasonic measurements were performed in a tri-axial cell at ENS Paris. Borgomano *et al.* (2017) provide a detailed description of the experimental setup, data processing and uncertainty analysis of the measurements. Pimienta *et al.* (2015a,b) provide further details on the calibration of the apparatus with standard materials. We will briefly list the governing relations used to determine the various moduli and associated attenuation modes.

Two types of stress oscillation on the sample, producing strains on the order of ~10^{-6}, can be performed in this cell: hydrostatic and axial. The hydrostatic oscillation (4×10^{-3} to ~1 Hz) is induced by the confining pressure pump (Adelinet *et al.* 2010; David *et al.* 2013) and allows for directly measuring the sample's dynamic bulk modulus from the confining pressure oscillation $\Delta P_c = -\sigma_{ii}/3$, where σ_{ii} (i = 1,2,3) are the principal stresses, and the associated average volumetric strain ε_{vol} as follows:

$$K_{hyd} = \frac{-\Delta P_c}{\varepsilon_{vol}}. \quad (1)$$

The axial oscillation (1×10^{-1} to 30 Hz) is induced by a piezo-electric actuator placed between the sample and the axial piston of the cell and allows for measuring the sample's Poisson ratio ν and Young's modulus E:

$$\nu = -\frac{\varepsilon_{rad}}{\varepsilon_{ax}} \text{ and } E = \frac{\sigma_{ax}}{\varepsilon_{ax}}, \quad (2)$$

where the axial stress σ_{ax}, is determined from the deformation of the aluminium end plate of known Young's modulus, and ε_{rad} and ε_{ax} are the average radial and axial strains on the sample. Given the Poisson ratio and Young's modulus, the axial bulk K_{ax} and shear G_{ax} moduli can be inferred as follows:

$$K_{ax} = \frac{E}{3(1-2\nu)} \text{ and } G_{ax} = \frac{E}{2(1+\nu)}. \quad (3)$$

For each mode of deformation, the attenuation can be determined from the phase shift between the applied stress and resulting strain ($\Delta\phi = \phi_{stress} - \phi_{strain}$) (O'Connell and Budiansky 1978). The bulk attenuation for the hydrostatic oscillation can be determined from the phase shift between the hydrostatic stress ΔP_c and the volumetric strain ε_{vol}, such that:

$$\Delta\phi = \phi_{-\Delta P_c} - \phi_{\varepsilon_{vol}}. \quad (4)$$

The extensional mode attenuation is in turn determined from the phase shift between the axial stress σ_{ax} and strain ε_{ax}, such that:

$$\Delta\phi_{extensional} = \phi_{\sigma_{ax}} - \phi_{\varepsilon_{ax}}. \quad (5)$$

Assuming that the sample is isotropic, the bulk and shear attenuation can be inferred from the phase shift between the axial stress σ_{ax} and the axial and radial strains ε_{ax} and ε_{rad} (Borgomano *et al.* 2017):

$$\Delta\phi_{bulk} = \phi_{\sigma_{ax}} - \phi_{\varepsilon_{ax}+2\varepsilon_{rad}} \text{ and } \Delta\phi_{shear} = \phi_{\sigma_{ax}} - \phi_{\varepsilon_{ax}-\varepsilon_{rad}}, \quad (6)$$

where the phases of $\varepsilon_{ax} + 2\varepsilon_{rad}$ and $\varepsilon_{ax} - \varepsilon_{rad}$ are derived from combining equations 2 and 3. The attenuation corresponding to each deformation mode can be calculated as (O'Connell and Budiansky 1978):

$$Q^{-1} = \tan\left(\Delta\phi\right). \quad (7)$$

2.4 Experimental conditions

Axial and hydrostatic oscillations, as well as ultrasonic measurements, were performed on the dry and glycerine saturated samples BS-H3 and BS-V5. Axial oscillations and ultrasonic measurements were performed at effective stresses between 2.5 and 25 MPa, with additional axial static loads of 2, 4 and 6 MPa. The hydrostatic oscillations were performed for the same range of effective stresses, while the axial piston was raised off of the sample. Additional ultrasonic measurements were also performed on the dry samples BS-H2 and BS-V4 for effective stresses up to 39 MPa. Before saturating each sample with glycerine, a vacuum pump was used to remove air from the sample and the pore fluid lines. Glycerine was then pumped into the sample using two Quizix pumps that subsequently regulated the fluid pressure at 4 MPa.

3. Results

3.1 Ultrasonic and hydrostatic measurements - dry samples

Figure 2 presents the variation of the ultrasonic P- and S-wave velocities with effective stress in the dry samples, BS-H2 and BS-V4. Below 20 MPa effective stress the P- and S-wave

velocities rapidly increase with effective stress, though the increase is more gradual for BS-H2 (Figure 2a) than for BS-V4 (Figure 2b). Above 20 MPa effective stress the velocities are comparable for both samples, and gradually increase with effective stress. The evolution of the velocities under hydrostatic conditions suggests that the bedding only minimally influences the samples compressibility and that for effective stresses above 20 MPa the majority of cracks and grain contacts are likely closed (e.g. Johnston *et al.* 1979).

Figure 3 shows the attenuation and bulk modulus determined from the hydrostatic oscillation as a function of frequency at effective stress up to 20 MPa for samples BS-H3 and BS-V5. As with the ultrasonic measurements the bulk modulus determined from the hydrostatic oscillation is dependent on the effective stress. Moreover, it is frequency independent. As a first approximation we assume that the samples are isotropic so that, from the ultrasonic velocity measurements and the samples density ρ, we can infer the bulk K_{HF} and shear G_{HF} moduli:

$$K_{HF} = \rho\left(V_p^2 - \frac{4}{3}V_s^2\right) \text{ and } G_{HF} = \rho V_s^2, \tag{8}$$

where, the subscript HF denotes the high frequency measurement. The results for selected effective stresses are provided in Table 2. For both samples the ultrasonic bulk modulus is generally consistent with that determined from the hydrostatic oscillations for the corresponding samples.

Table 2. Ultrasonic measurements (1 MHz) of travel time t_p and t_s on the dry samples BS-H2 and BS-V4, the corresponding p-wave and s-wave velocities V_p and V_s and the derived bulk K_{HF} and shear G_{HF} moduli (equation 8) for selected effective stresses σ_{eff}.

	σ_{eff} (MPa)	t_p (µs)	t_s (µs)	V_p (m/s)	V_s (m/s)	K_{HF} (GPa)	G_{HF} (GPa)
BS-V4	2	30.4	46.2	2738	1801	6.6	6.8
	4	28.3	42.1	2914	1977	7.2	8.2
	14	23.6	36.4	3527	2286	11.4	10.9
	18	22.8	35.3	3651	2357	12.4	11.6
BS-H2	5	27.5	43.4	3039	1924	9.2	7.9
	14	24.2	40.3	3447	2070	13.2	9.2
	20	23.3	38.4	3580	2175	14.0	10.1

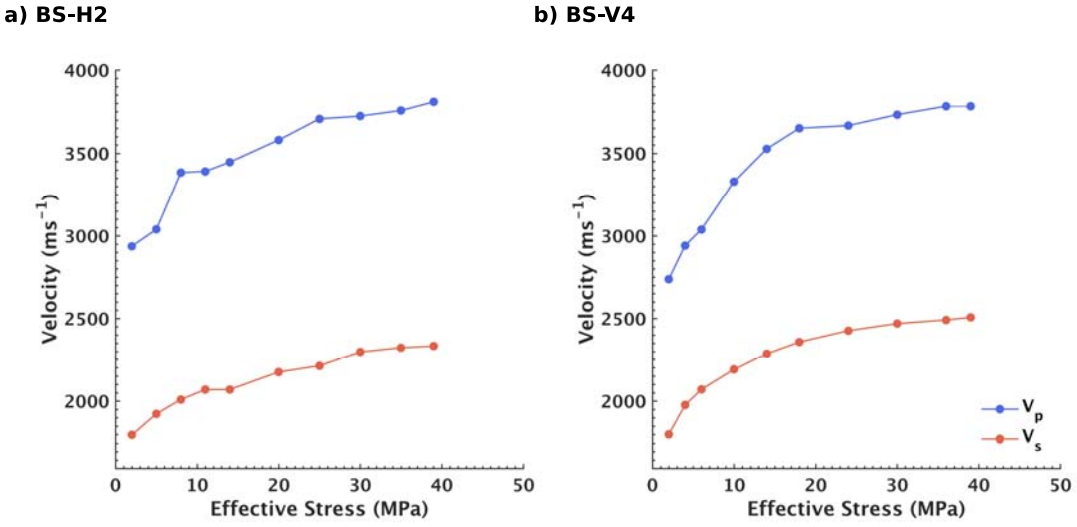

Figure 2. P- and S-wave velocities V_p and V_s versus effective stress for the dry samples BS-H2 a) and BS-V4 b).

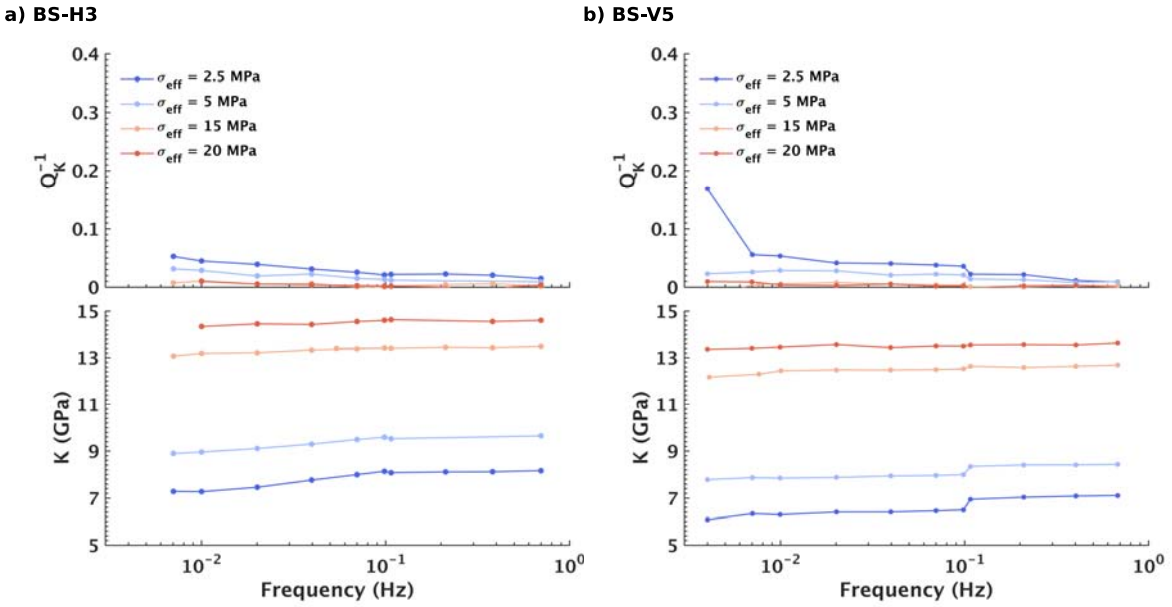

Figure 3. Bulk modulus K and attenuation Q_K^{-1} of the dry samples BS-H3 a) and BS-V5 b) determined from the hydrostatic oscillation of the confining pressure. The legend provides the applied effective stress σ_{eff}.

3.2 Hydrostatic measurements - glycerine saturation and dead volume

The drained-undrained transition is a boundary condition problem of fluid saturated samples. In the laboratory this generally means that the data is representative not only of the properties of the sample and saturating fluids, but also the properties of the measuring device. In the case of the drained-undrained transition it is predicted that the volume of the pore fluid lines, or dead volume, is a primary control of the amplitude of the attenuation and modulus dispersion (Pimienta *et al.* 2016). For our experiments, we increased the dead volume by essentially lengthening the pore fluid lines. The total volume of the pore fluid lines for the large dead volume was 26 millilitres, while the small dead volume was 11 millilitres.

These experiments were performed on sample BS-H3 using hydrostatic oscillations. In Figure 4 we show the bulk modulus and attenuation from the glycerine saturated sample, for the small and large dead volumes. For the larger dead volume (Figure 4a) we observe a significantly larger attenuation peak than for the smaller dead volume (Figure 4b), which in both cases is reduced as the effective stress is raised. For the bulk modulus we observe a similar high frequency limit for all effective stresses, but for the larger dead volume the sample is significantly more compressible at low frequencies.

The influence of the dead volume is also noticeable in the pseudo-skempton coefficient, defined as (Pimienta *et al.* 2015b):

$$B^* = \frac{\Delta p_f}{\Delta P_c}, \tag{10}$$

where Δp_f is the fluid pressure amplitude measured in the pore fluid line and ΔP_c is the confining pressure amplitude. For both dead volumes the pseudo-skempton coefficient is elevated at low frequencies, indicating that the glycerine had enough time to flow in response to the confining pressure oscillation and raise the pressure in the pore fluid lines (Figure 4). At low frequencies (0.01 Hz) the sample can therefore be considered partially drained. The pseudo-skempton coefficient drops off as the frequency of the confining pressure oscillation increases, because the fluid no longer has the time to diffuse form the sample and raise the pressure in the pore fluid lines. At high frequencies (1 Hz) the sample is therefore undrained. When approximately the same fluid volume is expelled from the sample during the forced oscillation, increasing the dead volume results in smaller pressure amplitude in the pore fluid lines, because of the compressibility of glycerine, and consequently resulting in a smaller pseudo-skempton coefficient. Increasing the effective stress increases the sample stiffness, which means that a larger portion of the load is carried by the sample's frame and not

transferred to the fluid. The consequence of increasing the effective stress is that the pseudo-skempton coefficient is also reduced, which is consistent with the observations of Hart and Wang (1999) for variation of the Skempton's coefficient with effective stress for Berea sandstone.

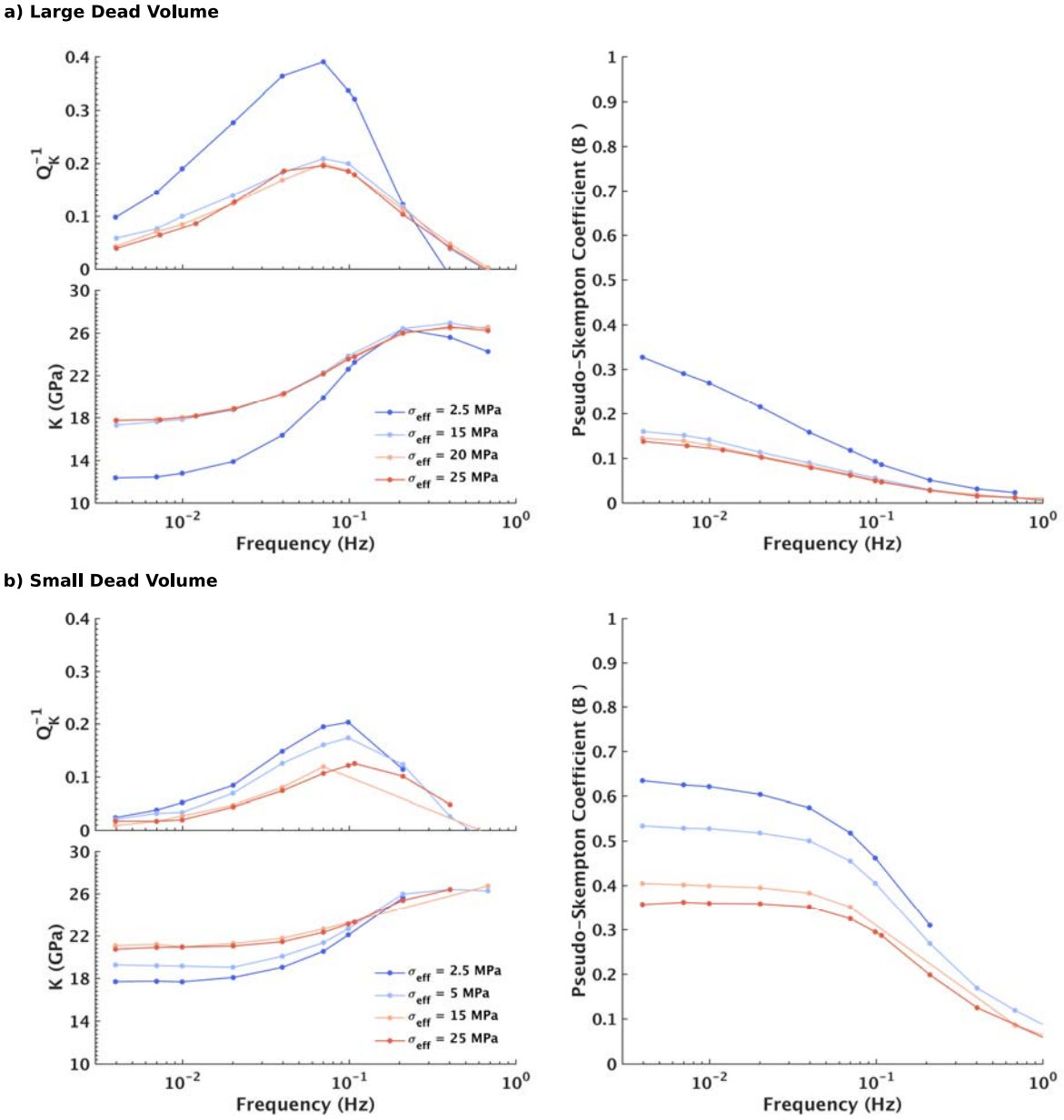

Figure 4. Bulk modulus K and attenuation Q_K^{-1} as well as the Pseudo-Skempton coefficient B^* of the glycerine saturated sample BS-H3 determined from the hydrostatic oscillation of the confining pressure. a) large dead volume (26 millilitres) and b) small dead volume (11

millilitres) achieved by varying the length of the pore fluid lines. The legend provides the range of applied effective stress σ_{eff}.

3.3 Axial and hydrostatic measurements - dry and glycerine saturation

From the axial oscillation the Young's modulus and Poisson ratio are determined, which allow for inferring the bulk and shear moduli and the corresponding attenuation modes. For the dry sample BS-V5 the extensional (Figure 5a), bulk (Figure 5c) and shear attenuation (Figure 5d) modes show no frequency dependence and are only moderately influenced by the increase in effective stress. The various moduli have also no frequency dependence and increase with increasing effective stress. The Poisson ratio (Figure 5b) is frequency independent and increases moderately with increasing effective stress. For all axial oscillations measurements presented in this section the sample was subjected to a static axial stress of 2 MPa.

When the sample is glycerine saturated (Figure 6) all modes show significant frequency dependent attenuation. For the extensional and bulk attenuation (Figure 6a and c) two peaks are observed: one at ~0.1 Hz and another beginning at ~5 Hz and above. For the shear attenuation (Figure 6d) however only the attenuation peak at higher frequencies is observed. The attenuation peak at ~0.1 Hz is reduced in amplitude as the effective stress is increased, but is still observed at 25 MPa effective stress. The second partial peak at higher frequencies is likewise reduced in amplitude, however at 25 MPa effective stress the measured attenuation is comparable in amplitude to the attenuation measured for the dry sample.

As with the attenuation the various stiffness moduli are frequency dependent once the sample was glycerine saturated (Figure 6). The overall increase in the sample's stiffness is particularly observed in the Young's and bulk moduli (Figure 6a and 6c). The shear modulus (Figure 6d) at low frequencies is on the order of the shear modulus of the dry sample (Figure 5d). Towards higher frequencies the shear modulus shows some dispersion. The Young's and bulk moduli are dispersive at both ~0.1 Hz and again beginning at ~5 Hz. Overall the moduli become less dispersive with increasing effective stress. At high frequencies the bulk modulus possibly converges to a common limit. The Poisson ratio (Figure 6b) is significantly increased with respect to the Poisson ratio measured in the dry sample (Figure 5b) and is frequency dependent. For the saturated sample, with increasing effective stress the Poisson ratio is reduced and at high frequencies it is nearly frequency independent.

In Table 3 we provide results of the ultrasonic measurements for the dry and glycerine saturated sample to complement the axial measurements. The high frequency bulk K_{HF} and shear moduli G_{HF} are inferred using Equations 8. The density of the glycerine saturated sample ρ_{sat} is approximated from the dry sample density ρ_{dry}, the sample's porosity ϕ and fluid density ρ_{fluid} ($\rho_{glycerine}$ = 1250 kg/m^3) as:

$$\rho_{sat} = \rho_{dry} + \phi\rho_{fluid}. \qquad (11)$$

For the dry measurements the inferred high frequency bulk moduli (Table 3) are moderately elevated compared to the bulk moduli determined from the axial oscillations (Figure 5a), while the inferred high frequency shear moduli are in good agreement with the shear moduli determined from the axial oscillations (Figure 5d). Under glycerine saturation the high frequency bulk modulus corresponds well with the bulk moduli of the axial oscillations at ~30 Hz, while the high frequency shear modulus is slightly higher than the shear modulus deduced from the axial oscillations (Figure 6d).

Because the stress applied to the sample for the hydrostatic oscillation is determined from a pressure transducer close to the sample in the confining oil, while for the axial oscillation the stress it is determined from the deformation of the aluminium end plate on which the sample is placed, the bulk modulus and attenuation can be measured independently by these two methods. If the sample BS-V5 is in fact isotropic then the bulk modulus and attenuation measured by these two methods should be the same. In Figure 7 we show the bulk modulus and attenuation determined from both the hydrostatic and axial oscillations for the dry and glycerine saturated sample BS-V5, at different effective stresses. We observe for both the dry (Figure 7a) and glycerine saturated (Figure 7b) states, that the bulk modulus and attenuation is generally independent of the measurement type. However as the effective stress is increased the hydrostatic measurements do show a slightly higher bulk modulus than the axial measurements, seen for both the dry and glycerine saturated states.

Table 3. Ultrasonic measurements (1 MHz) of travel times t_p and t_s, on the dry and glycerine saturated sample BS-V5 and the corresponding p- and s-wave velocities V_p and V_s and the bulk K_{HF} and shear G_{HF} moduli for selected effective stresses. The axial stress is 2.5 MPa.

	σ_{eff} (MPa)	t_p (μs)	t_s (μs)	V_p (m/s)	V_s (m/s)	K_{HF} (GPa)	G_{HF} (GPa)
Dry	2.5	27.8	46.0	3000	1813	9.6	6.9
	5	25.3	42.0	3296	1985	11.7	8.2
	15	23.1	36.0	3610	2315	12.3	11.2
	25	22.3	33.9	3740	2459	12.4	12.6
Glycerine Saturated	2.5	20.4	36.3	4088	2297	22.9	12.5
	5	20.5	35.3	4068	2362	21.5	13.2
	15	20.1	33.4	4149	2496	21.1	14.7
	25	19.9	33.0	4191	2526	21.4	15.1

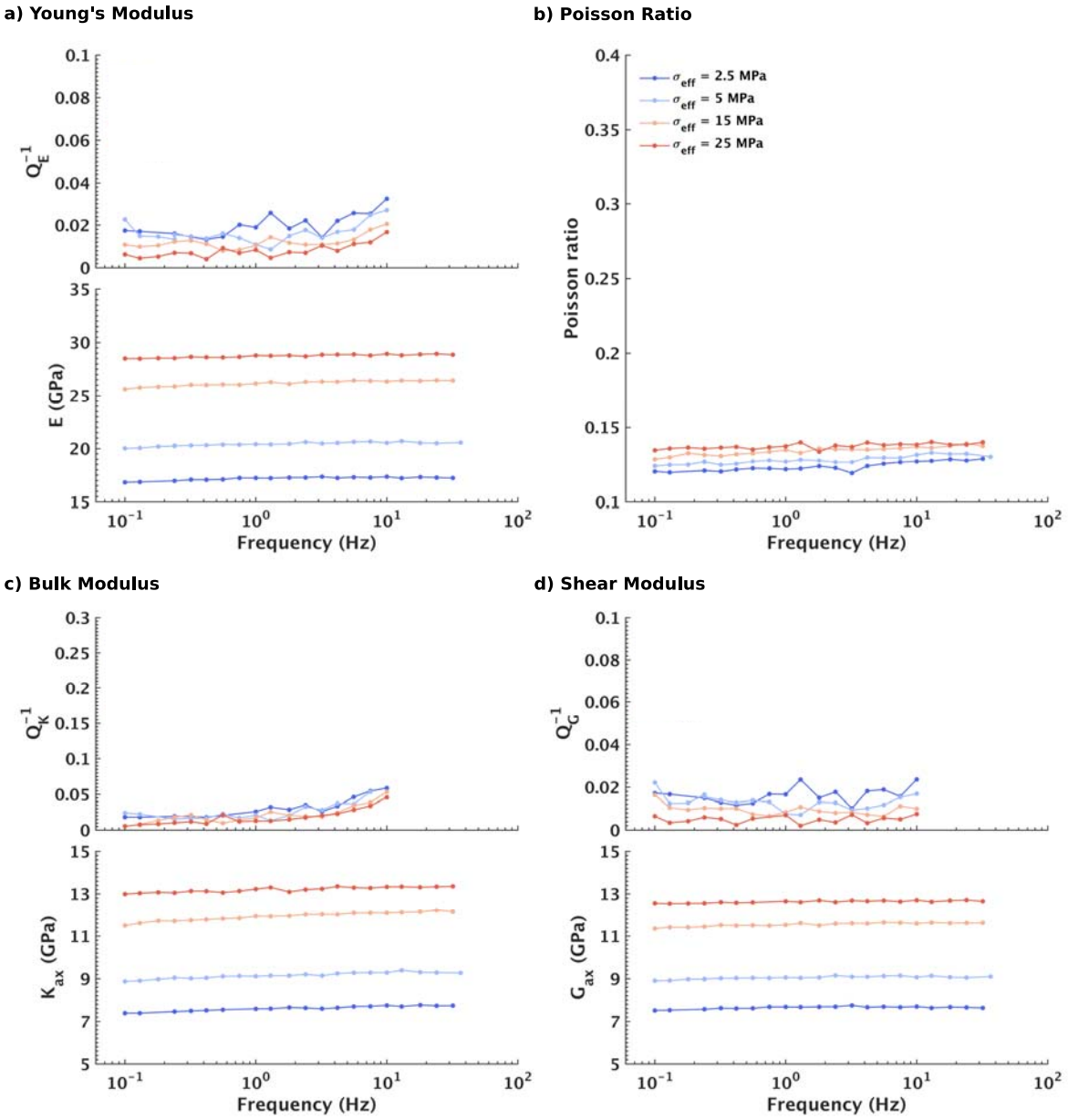

Figure 5. a) Extensional attenuation Q_E^{-1} and Young's modulus E, b) Poisson ratio, c) bulk modulus K_{ax} and attenuation Q_K^{-1}, and d) shear modulus G_{ax} and attenuation Q_G^{-1} of the dry sample BS-V5 determined from the forced axial oscillations. The sample was subjected to a static axial stress of 2 MPa. The legend provides the range of applied effective stresses σ_{eff}.

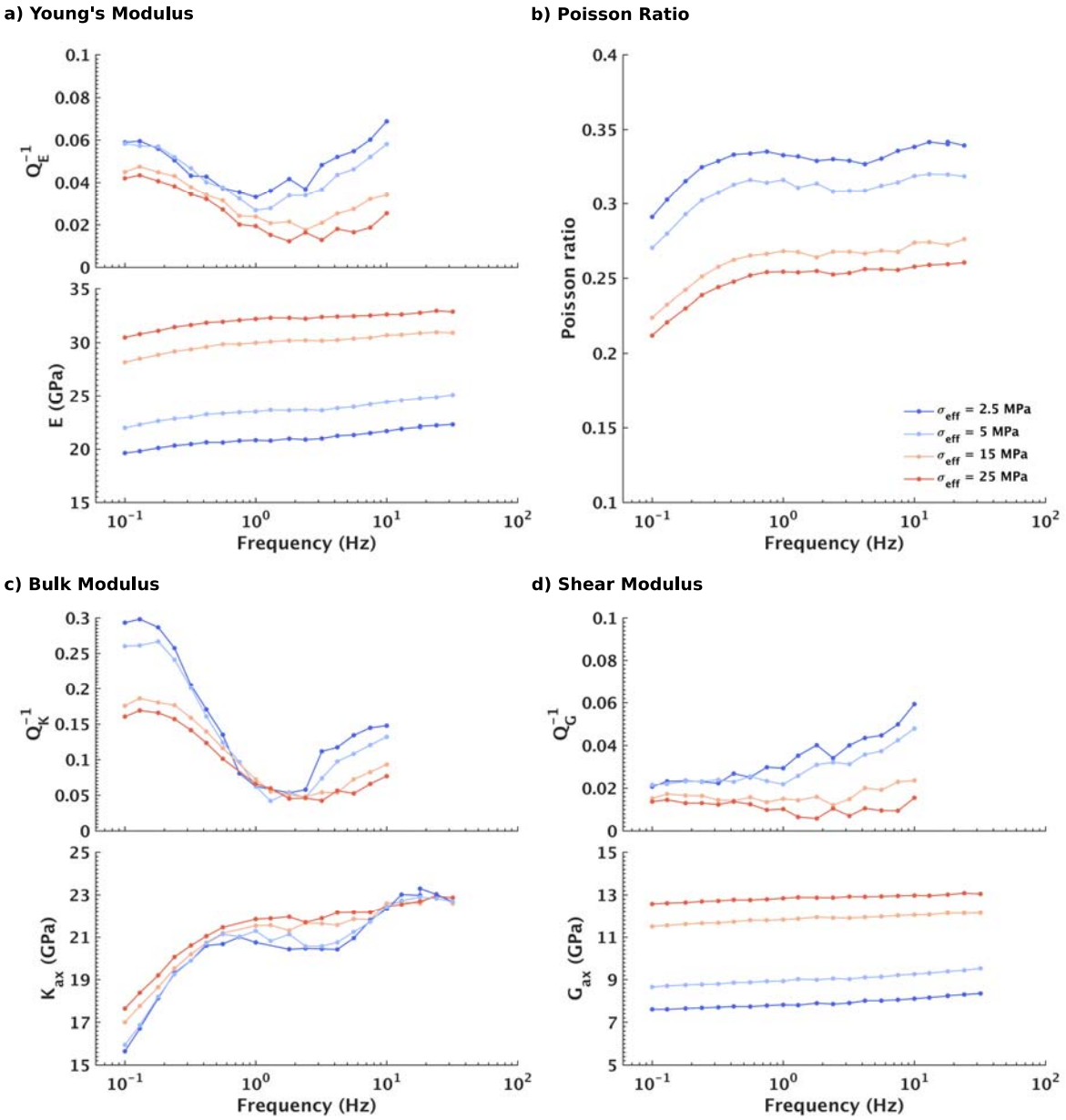

Figure 6. a) Extensional attenuation Q_E^{-1} and Young's modulus E, b) Poisson ratio, c) bulk modulus K_{ax} and attenuation Q_K^{-1}, and d) shear modulus G_{ax} and attenuation Q_G^{-1} of the glycerine saturated sample BS-V5 determined from the forced axial oscillations. The sample was subjected to a static axial stress of 2 MPa. The legend provides the range of applied effective stresses.

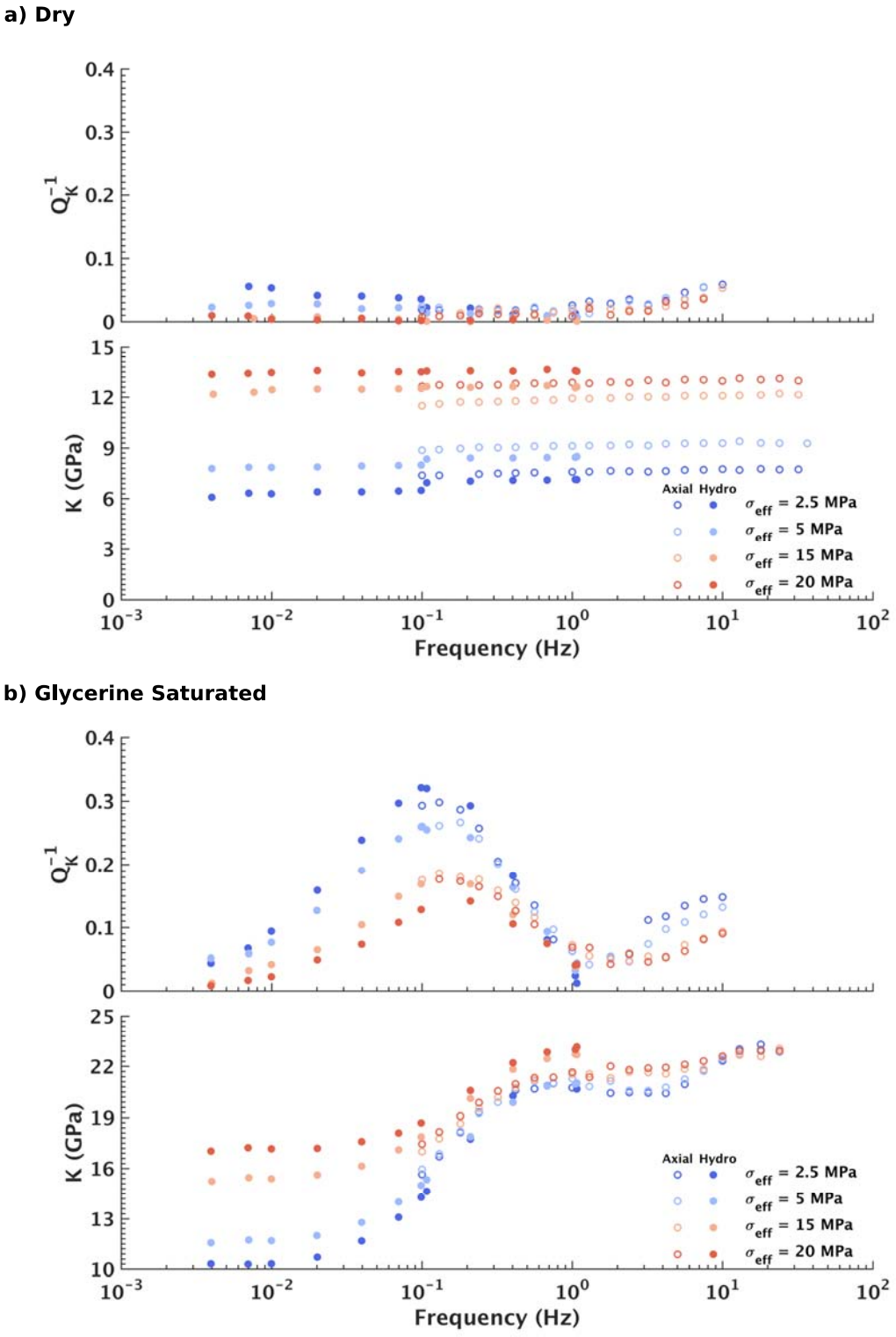

Figure 7. Bulk modulus K and attenuation Q_K^{-1} of the dry a) and glycerine b) saturated sample BS-V5 determined from the forced axial and hydrostatic oscillations. For the axial oscillations the sample was subjected to a static axial stress of 2 MPa. The legend provides the range of applied effective stress σ_{eff}.

3.4 Ultrasonic and axial measurements with static axial stress - dry and glycerine saturation

One of the controlling parameters of squirt flow is the aspect ratio of the micro cracks and grain contacts (O'Connell and Budiansky 1977). When planning our experiments, one idea was to investigate if the attenuation and modulus dispersion in response to squirt flow could be sensitive to the applied axial stress. To investigate this, the sample BS-V5 was subjected to static axial stresses of 2, 4 and 6 MPa.

The ultrasonic P-wave velocity of the dry sample shows some sensitivity to the applied static axial stress (Figure 8). At low effective stress, increasing the static axial stress resulted in a small increase of the P-wave velocity. For example, at 2.5 MPa effective stress the P-wave velocity increased by 200 m/s for an increase in the static axial stress from 2 to 6 MPa. With increasing effective stress the sensitivity to the static axial stress of the P-wave velocity becomes negligible. This is to be expected given that the relative importance of the static axial stress decreases as the effective stress is increased because of a reduction in the deviatoric stress. The S-wave velocity is less sensitive to the static axial stress. For the saturated samples, neither the P- or S-wave velocity is sensitive to the static axial stress.

In Figure 9 we show the different moduli and corresponding attenuation for the dry and glycerine saturated sample BS-V5, for static axial stresses of 2, 4 and 6 MPa. Given that the static axial stress has more influence at low effective stresses (Figure 8), we only show the results at 2.5 MPa effective stress. Both for the dry and saturated sample, increasing the static axial stress results in a moderate increase in the bulk and Young's moduli and corresponding decrease in the attenuation amplitude. On the other hand the shear modulus of the saturated sample decreases moderately with respect to the shear modulus of the dry sample as the static

axial stress is increased (Figure 9d). The Poisson ratio of the dry sample increases with increasing static axial stress and the reverse is observed for the saturated sample (Figure 9b). Since the attenuation peak beginning at ~5 Hz lies predominately outside the investigate frequency range it is not clear whether the scaling of the attenuation with respect to frequency is influenced by changes in the axial stress. Overall the variation in the stiffness moduli is on the order of the measurement uncertainty (Borgomano *et al.* 2017), making the impact of the applied static axial stress approximately negligible.

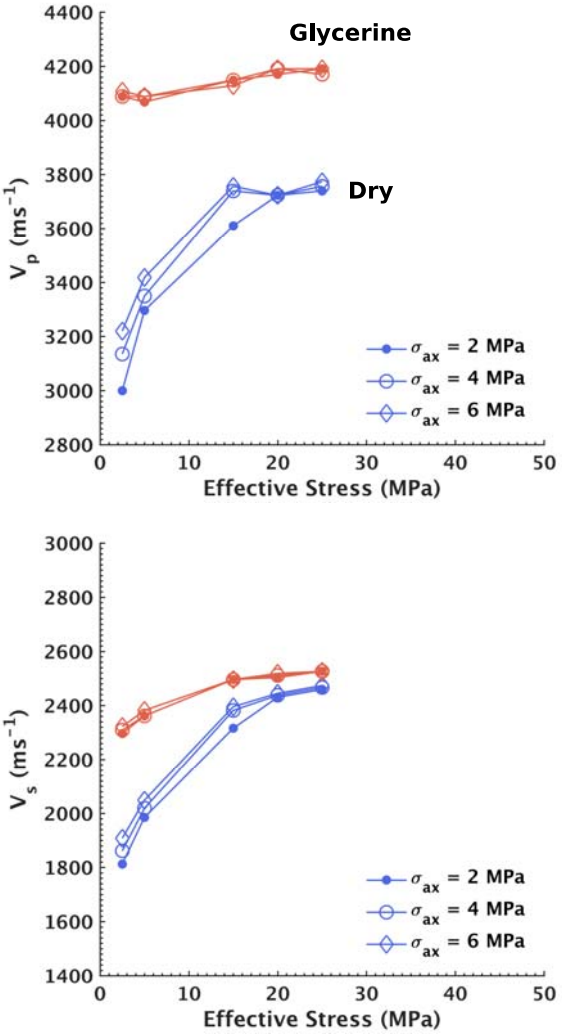

Figure 8. P- and S-wave velocities V_p and V_s versus effective stress for the dry and glycerine saturated sample BS-V5. The legend provides the applied axial stresses σ_{ax}.

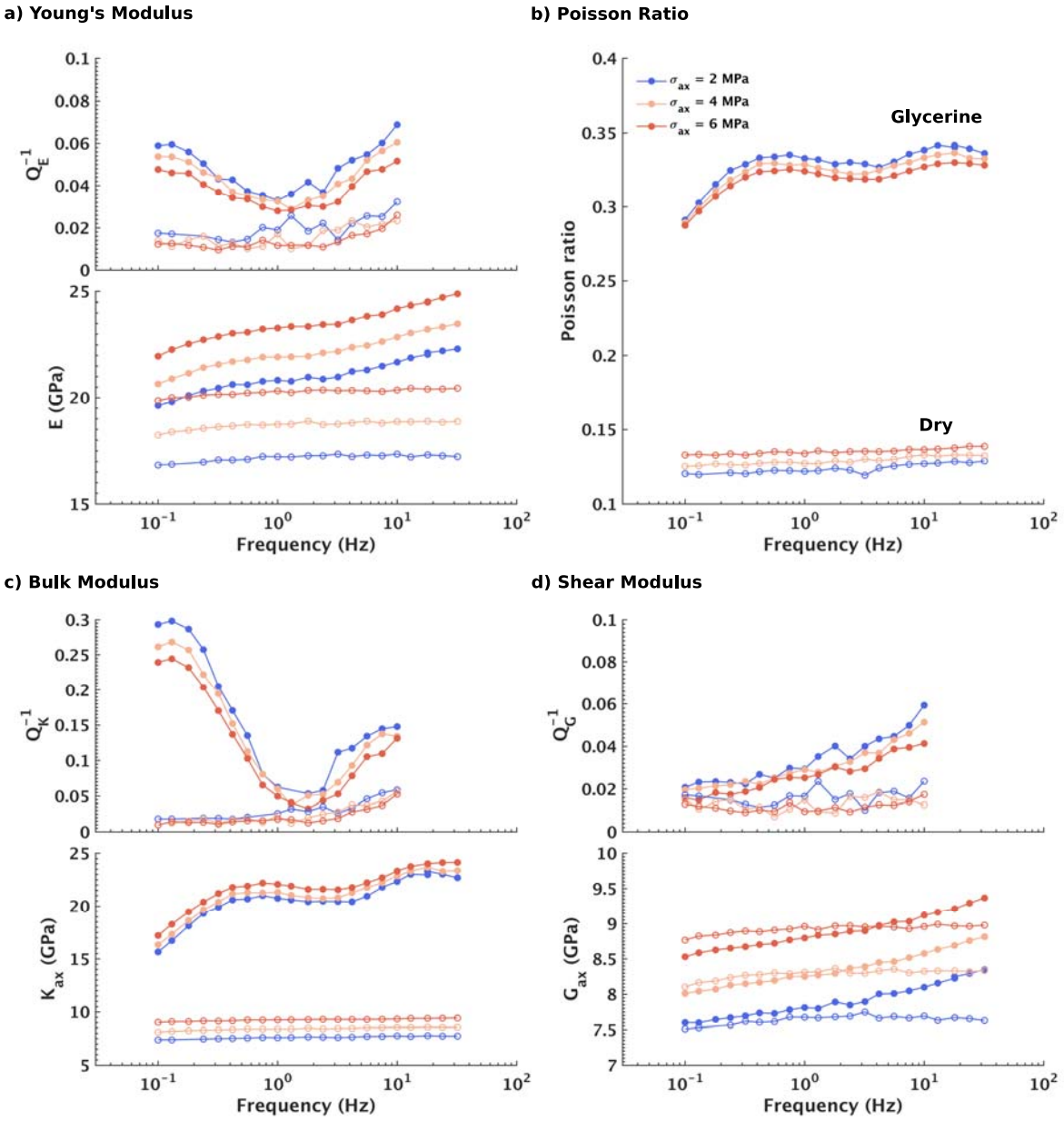

Figure 9. a) Extensional attenuation Q_E^{-1} and Young's modulus E, b) Poisson ratio, c) bulk modulus K_{ax} and attenuation Q_K^{-1}, and d) shear modulus G_{ax} and attenuation Q_G^{-1} of the dry (open circles) and glycerine saturated (closed circles) sample BS-V5 determined from the forced axial oscillations. The sample was subjected to an effective stress of 2.5 MPa. The legend provides the range of applied axial stresses σ_{ax}.

4. Discussion

For the drained-undrained transition Pimienta *et al.* (2016) derived a 1-D analytical solution for the fluid pressure diffusion along the vertical axis of a sample subjected to a hydrostatic pressure oscillation. The analytical solution makes a number of predictions for the response of the measured attenuation and modulus dispersion to changes in the experimental conditions that we observe in our data. Among these are the reduction of the measured attenuation when the dead volume is reduced and the increasing partially-drained bulk modulus with increasing effective stress (Figure 4). Another key observation that indicates that the attenuation peak measured at low frequencies for both samples is in response to the drained-undrained transition are the frequency dependent pseudo-Skempton coefficient (Figure 4). Furthermore because the sample frame is homogenous, the shear modulus is not dispersive (Figures 6d and 9d). These observations are consistent with those of Borgomano *et al.* (2017) for limestone. The frequency dependent pseudo-Skempton coefficient is the primary indicator for the drained-undrained transition because it shows a direct response of the pressure diffusion from the sample into the pore fluid lines. Although qualitatively our observations are entirely consistent with the analytical solution's predictions for the drained-undrained transition, our measured undrained limit of the bulk modulus is higher than that predicted by Gassmann's (1951) fluid substitution. As consequence, Pimienta *et al.'* (2016) analytical solution underestimates the amplitude of the bulk modulus dispersion and corresponding attenuation measured in the laboratory.

There are also a number of analytical solutions that have been developed to explain modulus dispersion and attenuation related to squirt flow (e.g. Mavko and Jizba 1991; Chapman *et al.* 2002; Gurevich *et al.* 2010). A number of predictions of these models are also observed in our data for the second attenuation peak that occurs above ~5 Hz. Among these is a dispersive shear modulus and associated shear attenuation (Figure 6d and 9d). The transition frequency

for squirt flow in this glycerine saturated sample is likely above the highest measured frequency (Figure 9c and 9d). The broad shear attenuation curve, when compared to the bulk attenuation, possibly suggests a distribution of crack aspect ratios. We made use of Gurevich *et al.*'s (2010) analytical solution for squirt flow to analyse the observed bulk modulus dispersion and attenuation in sample BS-V5 at 2.5 MPa effective stress. However, again the analytical solution underestimated the amplitude of the measured bulk modulus dispersion and attenuation. Subramanyian *et al.* (2015) also used Gurevich *et al.'s* (2010) squirt flow model and observed elevated attenuation compared to the analytical solution.

Of interest is also how our measurements compare to those of other studies that interpret their results as in response to squirt flow. The most appropriate comparison is to Mikhaltsevitch *et al.* (2015; 2016), who performed forced axial oscillation experiments on a glycerine-saturated Berea sandstone sample with a permeability of 71 mD and 19 % porosity. Both of these properties are similar to those of the samples used in this study. Mikhaltsevitch *et al.* (2015) saturated their sample by pumping five pore volumes of glycerine through the sample and then maintaining a 13 MPa confining pressure and 3 MPa fluid pressure to achieve an effective stress of 10 MPa on the sample, as well as maintaining a temperature of 23 °C. Under these conditions they observed a single attenuation peak at ~0.4 Hz with a magnitude of Q_E^{-1} ~0.055. In addition to the Young's modulus they also measured the Poisson ratio, which they use to infer the shear and bulk moduli. Both of which are dispersive, with the shear modulus having a transition frequency at higher frequencies than the bulk modulus. While the dispersion amplitude in the Young's and shear moduli are comparable to our measurements, the bulk modulus measured by Mikhaltsevitch *et al.* (2015) is significantly more dispersive than in our measurements. In the study of Mikhaltsevitch *et al.* (2015) the transition peak attributed to squirt flow in the extensional attenuation and Young's modulus is

at a frequency almost two orders of magnitude lower to the one observed here, which suggests that even if the two Berea sample have the same porosity and permeability, they do not contain the same pre-existing cracks.

We hoped that it would be possible to detect an impact of either the orientation of the bedding planes or the induced applied static axial stress on the measured attenuation related to squirt flow. However, in the case of BS-H3, which had pronounced horizontal bedding planes (e.g. Figure 1b), some of the strain gauges were lost during the experiments and we subsequently decided to not show the results of the axial oscillation. On the other hand sample BS-V5 only had very poorly defined bedding planes (e.g. Figure 1a), which proved to be approximately isotropic as seen in the good match of the bulk modulus and attenuation from the axial and hydrostatic oscillations (Figure 7). Given these circumstances we cannot draw any conclusions on the impact of the bedding plane orientation as it relates to squirt flow. As noted in the results the impact of the axial stress is also largely negligible as the variation is near the uncertainty limit of our measurements. Furthermore we only partially resolve the attenuation peak that we interpret as in response to squirt flow and therefore cannot draw any conclusion about the variation in scaling of the attenuation with frequency either. The applied static axial stress did not exceed 6 MPa in order to not damage the piezo-electric actuator, which applied the axial oscillations.

5. Conclusions

We performed hydrostatic and axial forced oscillations experiments on dry and glycerine saturated Berea sandstone samples subjected to effective stresses up to 25 MPa. For the sample with poorly defined bedding layers we found a good agreement between the bulk

attenuation and modulus directly measured from the hydrostatic oscillations and those inferred from the axial and radial strains measured during the axial oscillations. In the glycerine saturated sample the measured attenuation is frequency dependent with an attenuation peak at ~0.1 Hz and a second, partial, peak beginning at ~5 Hz. Both of these attenuation peaks are also observed in the extensional mode, while in the shear attenuation is only frequency dependent above 1 Hz. The first attenuation peak is in response to fluid pressure diffusion from the sample into the pore fluid lines, referred to as the drained-undrained transition. The second partial attenuation peak is likely in response to squirt flow, resulting from microscopic heterogeneities in compressibility of the sample matrix. Reducing the volume of the pore fluid lines lowers the attenuation and modulus dispersion related to the drained-undrained transition. The applied static axial stress on the sample appears to induce negligible anisotropy in the sample.

Acknowledgments

This work is supported by a grant from the Swiss National Science Foundation. We thank Marie Violay for access to the EPFL Laboratory of Experimental Rock Mechanics, Laurent Gastaldo for coring the samples from the source blocks and Lucas Pimienta for doing the porosity measurements. We thank Jean-Pierre Burg for access to the ETH Zurich Rock Deformation Laboratory and Claudio Madonna for helping with the sample preparation. The data for this paper are available by contacting the corresponding author at samuel.chapman@unil.ch.

References

Adelinet M., Fortin J., Gueguen Y., Schubnel A. and Geoffroy L. 2010. Frequency and fluid effects on elastic properties of basalt: Experimental investigations. Geophysical Research Letters, 37, L02303.

Adelinet M., Fortin J. and Gueguen Y. 2011. Dispersion of elastic moduli in a porous-cracked rock: Theoretical predictions for squirt-flow. Tectonophysics, 503, 173-181.

Batzle M. L., Han D.-H. and Hofmann R. 2006. Fluid mobility and frequency-dependent seismic velocity - Direct measurements. Geophysics, 71, N1-N9.

Borgomano J. V. M., Pimienta L., Fortin J. and Gueguen Y. 2017. Dispersion and attenuation measurements of elastic moduli of a dual-porosity limestone. Journal of Geophysical Research: Solid Earth, 122, doi:10.1002/2016JB013816.

Chapman M., Zatspin S. V. and Crampin S. 2002. Derivation of a microstructural poroelastic model. Geophysical Journal International, 151, 427-451.

Collet O. and Gurevich B. 2016. Frequency dependence of anisotropy in fluid saturated rocks – Part II: Stress-induced anisotropy case. Geophysical Prospecting, 64, 1085-1097.

David E. C., Fortin J., Schubnel A., Gueguen Y. and Zimmerman R. W. 2013. Laboratory measurements of low- and high-frequency elastic moduli in Fontainebleau sandstone. Geophysics, 78, D369-D379.

Dunn K.-J. 1987. Sample boundary effect in acoustic attenuation of fluid-saturated porous cylinders. Journal of the Acoustical Society of America, 81, 1259-1266.

Gardner G. H. F. 1962. Extensional waves in fluid-saturated porous cylinders. Journal of the Acoustical Society of America, 34, 36-40.

Gassmann F. 1951. Über die Elastizität poröser Medien: Vierteljahrsschrift der Naturforschenden Gesellschaft in Zürich, 96, 1-23.

Gurevich B., Makaryska D., de Paula O. S. and Pervukhina M. 2010. A simple model for squirt-flow dispersion and attenuation in fluid-saturated granular rocks. Geophysics, 75, 6.

Hart D. J. and Wang H. F. 1999. Pore pressure and confining stress dependence of poroelastic linear compressibilities and Skempton's B coefficient for Berea sandstone. American Rock Mechanics Association, 37th US Rock Mechanics Symposium.

Johnston D. H., Toksöz M. N. and Timur A. 1979. Attenuation of seismic waves in dry and saturated rocks: II. Mechanisms. Geophysics, 44, 691-711.

Masson Y. J. and Pride S. R. 2007. Poroelastic finite difference modeling of seismic attenuation and dispersion due to mesoscopic-scale heterogeneity. Journal of Geophysical Research, 112, B03204, doi:10.1029/2006JB004592.

Masson Y. J. and Pride S. R. 2011. Seismic attenuation due to patchy saturation. Journal of Geophysical Research, 116, B03206, doi:10.1029/2010JB007983.

Mavko G. and Jizba D. 1991. Estimating grain-scale fluid effects on velocity dispersion in rocks. Geophysics, 56, 1940-1949.

McKavanagh B. and Stacey F.D. 1974. Mechanical hysteresis in rocks at low strain amplitudes and seismic frequencies. Physics of the Earth and Planetary Interiors, 8, 246–250.

Mikhaltsevitch V., Lebedev M. and Gurevich B. 2015. A laboratory study of attenuation and dispersion effects in glycerol-saturated Berea sandstone at seismic frequencies. SEG, doi: http://dx.doi.org/10.1190/segam2015-5898429.1.

Mikhaltsevitch V., Lebedev M. and Gurevich B. 2016. Validation of the laboratory measurements at seismic frequencies using the Kramers-Kronig relationship. Geophysical Research Letters, 43, 4986-4991.

Mörig R. and Burkhardt H. 1989. Experimental evidence for the Biot-Gardner theory. Geophysics, 54, 524-527.

Müller T. M., Toms-Stewart J. and Wenzlau F. 2008. Velocity-saturation relation for partially saturated rocks with fractal pore fluid distribution. Geophysical Research Letters, 35, L09306.

Müller T. M., Gurevich B. and Lebedev M. 2010. Seismic wave attenuation and dispersion resulting from wave-induced flow in porous rocks – A review. Geophysics, 75, A147-A164

O'Connell R. J. and Budiansky B. 1977. Viscoelastic Properties of Fluid-Saturated Cracked Solids. Journal of Geophysical Research, 5719-5735.

O'Connell R. J. and Budiansky B. 1978. Measures of dissipation in viscoelastic media. Geophysical Research Letters, 5, 5-8.

Pimienta L., Fortin J. and Guéguen Y. 2015a. Experimental study of Young's modulus dispersion and attenuation in fully saturated sandstones. Geophysics, 80, L57-L72.

Pimienta L., Fortin J. and Guéguen Y. 2015b. Bulk modulus dispersion and attenuation in sandstones. Geophysics, 80(2), D111-D127, doi: 10.1190/geo2014-0335.1.

Pimienta L., Borgomano J. V. M., Fortin J. and Guéguen Y. 2016. Modelling the drained/undrained transition: effect of the measuring method and the boundary conditions. Geophysical Prospecting, 64, 1098-1111.

Prasad M. and Manghnani M. H. 1997. Effects of pore and differential pressure on compressional wave velocity and quality factor in Berea and Michigan sandstones. Geophysics, 62, 1163-1176.

Pride S. R., Berryman J. G. and Harris J. M. 2004. Seismic attenuation due to wave-induced flow. Journal of Geophysical Research, 109, B01201.

Subramaniyan S., Quintal B., Madonna C. and Saenger E. H. 2015. Laboratory-based seismic attenuation in Fontainebleau sandstone: Evidence of squirt flow. Journal of Geophysical Research, 120.

Appendix D

Script code for the numerical modelling of the drained/undrained transition in 2D and 3D using GetDP solveur.

Input file (.PRO) for GetDP.

```
/*======================
  Constants definitions
======================*/
// OSCILLATIONS
DefineConstant[f     =     {1e-3,     Name
"Frequency",  Choices  {1e-3,2e-3,4e-3,7e-
3,1e-2,2e-2,4e-2,7e-2,1e-1,2e-1,4e-1,7e-
1,1,2,4,7}} ];

deltaP = 0.2; // MPa

// ROCK
Kd = 16.2*1e9;   //PA
Ks = 77.*1e9;   //PA
poro = 23.8; // (%) !
k = 1.1e-14;  //  m2

// FLUID + Dead Volume
eta = 1.087; // Pa.s
Kfl = 4.36*1e9;   //PA
Vu = 3.3; // mL : volume of dead volume
(hyp = for upper and lower)

// Calculations
B  =  (1/Kd  -  1/Ks)/(1/Kd  -  1/Ks  +
poro*0.01*(1/Kfl - 1/Ks));
alpha = 1 - Kd/Ks;
D = 1e6*k*B*Kd/(eta*alpha); // mm2/s

/*======================
  Geometrical Entities
======================*/
Group {
  Sample = Region[ 85 ];
  VolUp = Region[ 86 ];
  VolDown = Region[ 87 ];
  Drainage = Region[{VolDown,VolUp}];
  AllOmega                                =
Region[{Sample,VolDown,VolUp}];
}
/*======================
Functions
======================*/
Function {
  // Initial State
   InitialState[AllOmega] = 0.;

  // control oscillations
  osc[] = deltaP* 1e6 * B * 2.*Pi*f *
Cos[2.*Pi*f*$Time];

  // time discretisation
  t0 = 0.; // t_ini
   T = 4*(1./f); // t_max
  dt = T/600.;

  // type of scheme // see crank nicolson
on the manual
   gamma = 1;
}
/*==============================
  Constraints and Initial State
==============================*/
Constraint {
  // initial state
  { Name InitialData; Type Init;
     Case {
        {    Region    AllOmega;    Value
InitialState[];}
     }
  }
  // boundary condition "drained"
  { Name Drained ; Type Assign;
   Case {
      { Region Drainage ; Value 0. ; }
    }
  }
}
/*====================
  Functional Spaces
====================*/
FunctionSpace{
  { Name Vh; Type Form0;
    BasisFunction{
      {Name  wn;  NameOfCoef  vn;  Function
BF_Node;
    Support        AllOmega;        Entity
NodesOf[All];}
    }
    Constraint {
    { NameOfCoef vn; EntityType NodesOf;
         NameOfConstraint Drained; }
    { NameOfCoef vn; EntityType NodesOf;
         NameOfConstraint InitialData; }
    }
  }
}
/*====================
    Jacobian
====================*/
Jacobian {
  { Name JVol ;
    Case {
      { Region All ; Jacobian Vol ; }
    }
  }
  { Name JSur ;
    Case {
      { Region All ; Jacobian Sur ; }
    }
  }
```

```
  { Name JLin ;
    Case {
      { Region All ; Jacobian Lin ; }
    }
  }
}
/*======================
   Integral Parameters
======================*/
Integration {
  { Name I1 ;
    Case {
      { Type Gauss ;
        Case {
          {     GeoElement     Point     ;
NumberOfPoints  1 ; }
          {     GeoElement     Line      ;
NumberOfPoints  4 ; }
          {    GeoElement    Triangle    ;
NumberOfPoints  6 ; }
          {   GeoElement   Quadrangle    ;
NumberOfPoints 7 ; }
          {   GeoElement   Tetrahedron   ;
NumberOfPoints 15 ; }
          {   GeoElement   Hexahedron    ;
NumberOfPoints 34 ; }
        }
      }
    }
  }
}
/*======================
  Weak formulations
======================*/
Formulation{
  {Name Diffusion; Type FemEquation;
    Quantity{
      {Name  phi;  Type  Local;  NameOfSpace
Vh;}
    }
    Equation{
      Galerkin{ DtDof[ Dof{phi}, {phi} ];
        In    Sample;    Jacobian    JVol;
Integration I1;}

      Galerkin{  [D*Dof{Grad  phi},  {Grad
phi}];
        In    Sample;    Jacobian    JVol;
Integration I1;}

      Galerkin{ [-osc[$TimeStep], {phi}];
        In    Sample;    Jacobian    JVol;
Integration I1;}
    }
  }
}
/*======================
  Resolution
======================*/
Resolution{
  {Name DiffusionSolver;

    System{
      {Name                  SysDiffusion;
NameOfFormulation Diffusion;}
    }
  Operation{
      // initialisation
      InitSolution[SysDiffusion];
SaveSolution[SysDiffusion];

      // computation on [t0 + dt,T]
      TimeLoopTheta[t0, T, dt, gamma] {
              //IterativeLoop[  80  ,  1e-4
, 1 ] {
          Generate[SysDiffusion];
Solve[SysDiffusion];
GenerateJac[SysDiffusion];
SolveJac[SysDiffusion];
              //}
       SaveSolution[SysDiffusion];
      }
    }
  }
}
/*==============
Post Processing
==============*/
PostProcessing {
   {         Name         DiffusionSolver;
NameOfFormulation  Diffusion;  NameOfSystem
SysDiffusion;
      Quantity{
         {    Name    Pressure_MPa;    Value
{Local{[{phi}*10^(-6)];    In    AllOmega;
Jacobian JVol; }}}
      }
   }
}
/*=============
Post Operation
=============*/
PostOperation {
   {Name                      Map_Pressure;
NameOfPostProcessing DiffusionSolver;
      Operation{
         Print[Pressure_MPa,  OnElementsOf
AllOmega, File "PressureResults.pos"];

      }
   }
}
```

Appendix E: Model results of E, ν and G compared to the axial oscillations results for the Indiana, Rustrel and Coquina samples.

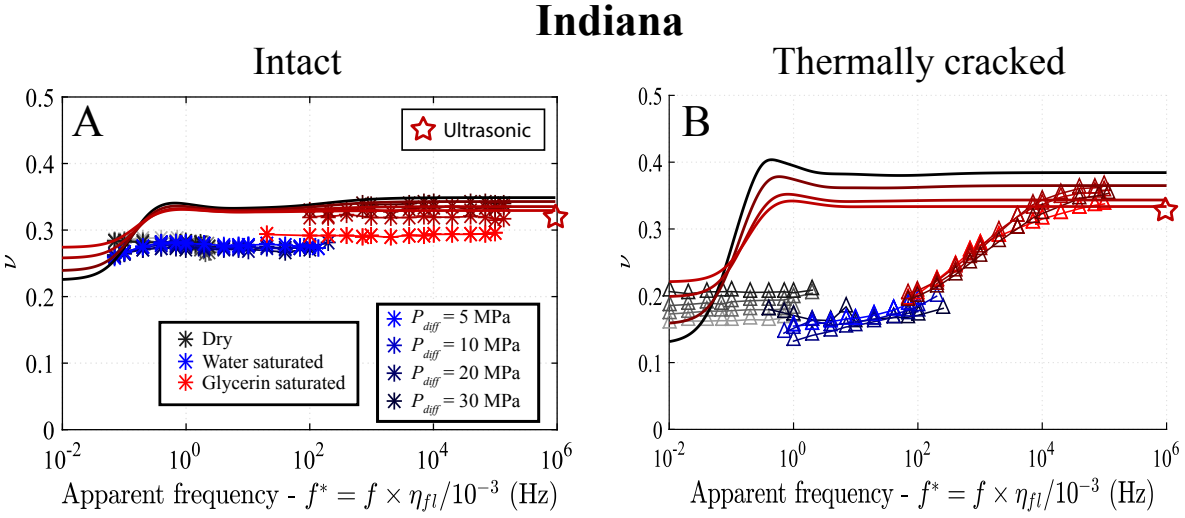

Figure 15: Model prediction of the Poisson's ratio compared to the axial oscillations and ultrasonic results for the Indiana limestone, intact (a), and after thermal cracking (b). The model is calculated for glycerin-saturated conditions.

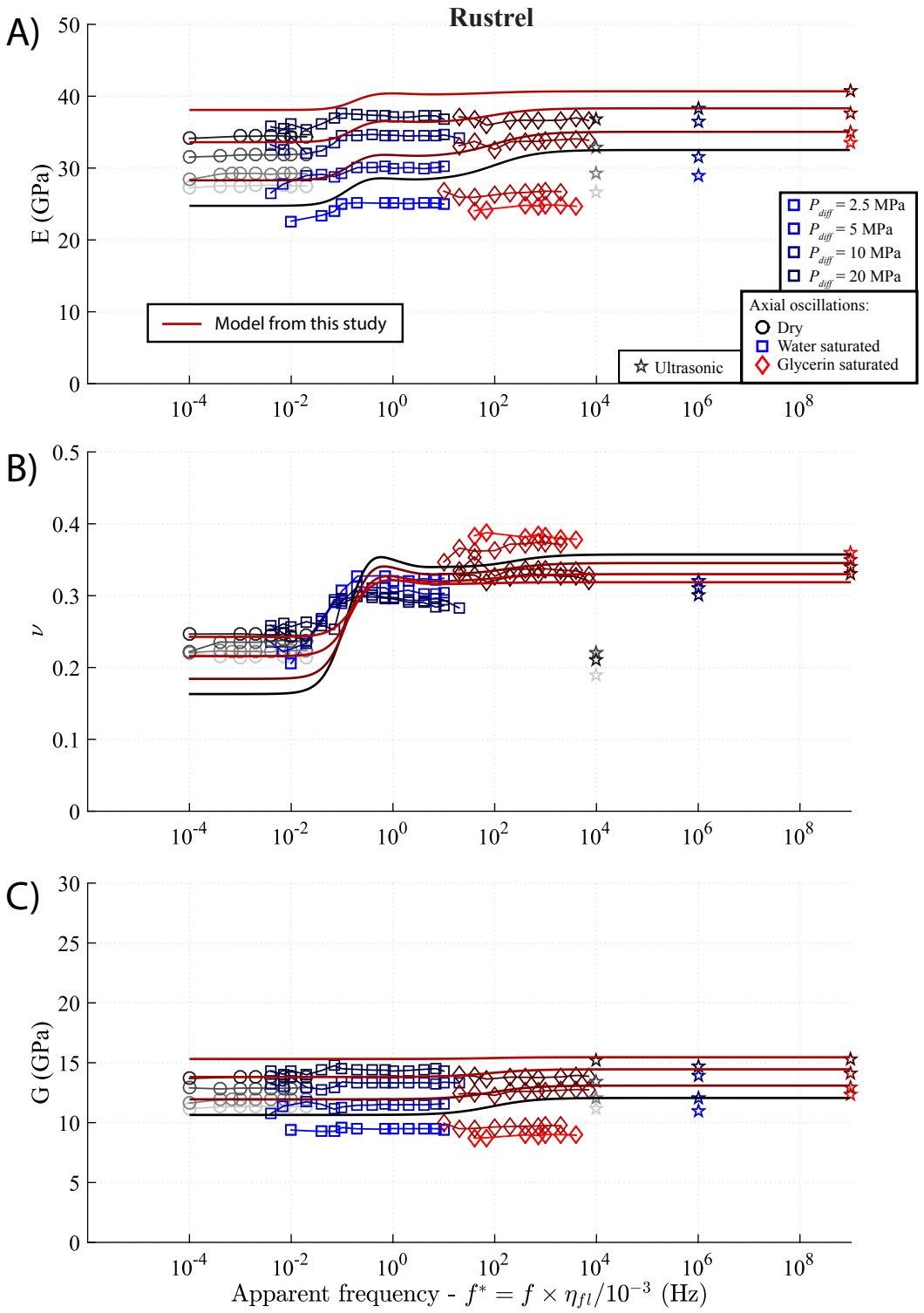

Figure 16: Model prediction of the E (a), ν (b) and G (c) compared to the axial oscillations and ultrasonic results for the Rustrel sample. The model is calculated for glycerin-saturated conditions.

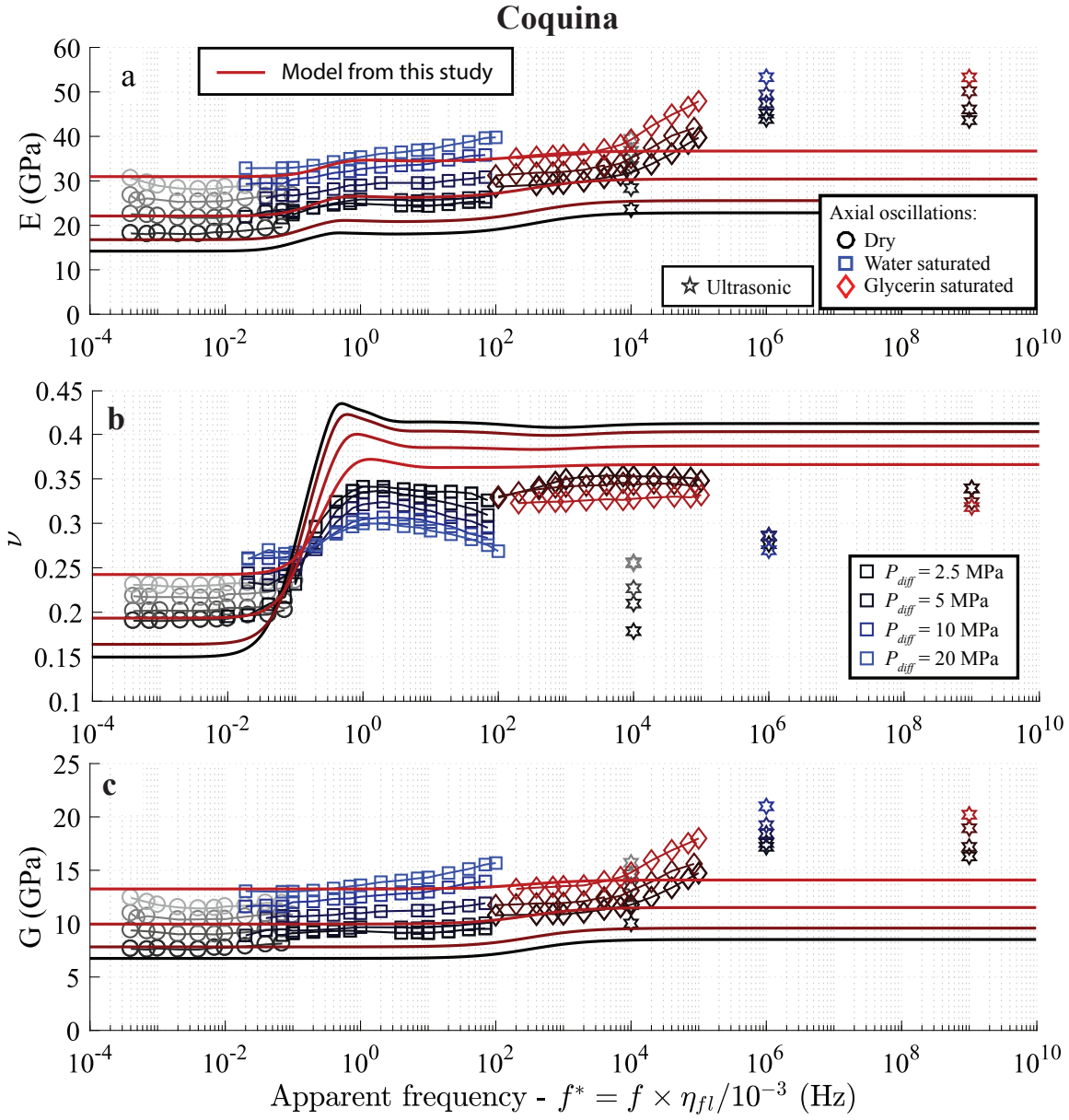

Figure 17: Model prediction of the E (a), ν (b) and G (c) compared to the axial oscillations and ultrasonic results for the Coquina sample. The model is calculated for glycerin-saturated conditions.

BIBLIOGRAPHY

Adam, L., M. Batzle, and I. Brevik (2006), Gassmann's fluid substitution and shear modulus variability in carbonates at laboratory seismic and ultrasonic frequencies, *Geophysics*, *71*(6), F173–F183.

Adam, L., M. Batzle, K. T. Lewallen, and K. van Wijk (2009), Seismic wave attenuation in carbonates, *Journal of Geophysical Research: Solid Earth*, *114*(B6), B06,208.

Adelinet, M., J. Fortin, Y. Guéguen, A. Schubnel, and L. Geoffroy (2010), Frequency and fluid effects on elastic properties of basalt: Experimental investigations, *Geophysical Research Letters*, *37*(2), n/a–n/a.

Adelinet, M., J. Fortin, and Y. Guéguen (2011), Dispersion of elastic moduli in a porous-cracked rock: Theoretical predictions for squirt-flow, *Tectonophysics*, *503*(1-2), 173–181.

Alsharhan, A. S., and A. E. M. Nairn (1997), *Sedimentary Basins and Petroleum Geology of the Middle East*, Elsevier, google-Books-ID: 0Ug0GdmopWMC.

Anderson, J. E., J. Cartwright, S. J. Drysdall, and N. Vivian (2000), Controls on turbidite sand deposition during gravity-driven extension of a passive margin: examples from Miocene sediments in Block 4, Angola, *Marine and Petroleum Geology*, *17*(10), 1165–1203.

Anselmetti, F. S., and G. P. Eberli (1993), Controls on sonic velocity in carbonates, *Pure and Applied Geophysics*, *141*(2-4), 287–323.

Avseth, P., T. Mukerji, G. Mavko, and Q. S. Interpretation (2005), *Quantitative Seismic Interpretation: Applying Rock Physics Tools to Reduce Interpretation Risk*, Cambridge University Press.

Baechle, G. T., G. P. Eberli, R. J. Weger, and J. L. Massaferro (2009), Changes in dynamic shear moduli of carbonate rocks with fluid substitution, *Geophysics*, *74*(3), E135–E147.

Batzle, M. L., D.-H. Han, and R. Hofmann (2006a), Fluid mobility and frequency-dependent seismic velocity—Direct measurements, *Geophysics*, *71*(1), N1–N9.

Batzle, M. L., D.-H. Han, and R. Hofmann (2006b), Fluid mobility and frequency-dependent seismic velocity—direct measurements, *Geophysics*, *71*(1), N1–N9.

Bemer, E., and J. Lombard (2010), From Injectivity to Integrity Studies of CO $_2$ Geological Storage: Chemical Alteration Effects on Carbonates Petrophysical and Geomechanical Properties, *Oil & Gas Science and Technology – Revue de l'Institut Français du Pétrole*, *65*(3), 445–459.

Berryman, J. G. (1980), Long-wavelength propagation in composite elastic media II. Ellipsoidal inclusions, *The Journal of the Acoustical Society of America*, *68*(6), 1820–1831.

Berryman, J. G. (1995), Mixture theory for rock properties, in *AGU Handbook of Physical Constants*, pp. 205–228.

Biot, M. A. (1956a), Theory of propagation of elastic waves in a fluid-saturated porous solid. I. Low-frequency range, *The Journal of the Acoustical Society of America*, *28*(2), 168–178.

Biot, M. A. (1956b), Theory of propagation of elastic waves in a fluid-saturated porous solid. ii. higher frequency range, *The Journal of the Acoustical Society of America*, *28*, 179.

Borgomano, J., J.-P. Masse, and S. Al Maskiry (2002), The lower Aptian Shuaiba carbonate outcrops in Jebel Akhdar, northern Oman: Impact on static modeling for Shuaiba petroleum reservoirs, *AAPG bulletin*, *86*(9), 1513–1529.

Borgomano, J., J.-P. Masse, M. Fenerci-Masse, and F. Fournier (2013), Petrophysics of Lower Cretaceous platform carbonate outcrops in Provence (SE France): implications for carbonate reservoir characterisation, *Journal of Petroleum Geology*, *36*(1), 5–41.

Borgomano, J. V. M., L. Pimienta, J. Fortin, and Y. Guéguen (2017), Dispersion and attenuation measurements of the elastic moduli of a dual-porosity limestone, *Journal of Geophysical Research: Solid Earth*, pp. n/a–n/a.

Born, W. T. (1941), the Attenuation Constant of Earth Materials, *Geophysics*, *6*(2), 132–148.

Bosart, L., and A. Snoddy (1927), New Glycerol Tables, *Industrial & Engineering Chemistry*, *19*(4), 506–510.

Bourbie, T., and B. Zinszner (1985), Hydraulic and acoustic properties as a function of porosity in Fontainebleau Sandstone, *Journal of Geophysical Research: Solid Earth*, *90*(B13), 11,524–11,532.

Brace, W. F., and D. K. Riley (1972), Static uniaxial deformation of 15 rocks to 30 kb, *International Journal of Rock Mechanics and Mining Sciences & Geomechanics Abstracts*, *9*(2), 271–288.

Brace, W. F., J. B. Walsh, and W. T. Frangos (1968), Permeability of granite under high pressure, *Journal of Geophysical Research*, *73*(6), 2225–2236.

Bridgman, P. W. (1931), The Volume of Eighteen Liquids as a Function of Pressure and Temperature, *Proceedings of the American Academy of Arts and Sciences*, *66*(5), 185.

Brown, R. J., and J. Korringa (1975), On the dependence of the elastic properties of a porous rock on the compressibility of the pore fluid, *Geophysics*, *40*(4), 608–616.

Chapman, M. (2003), Frequency-dependent anisotropy due to meso-scale fractures in the presence of equant porosity, *Geophysical Prospecting*, *51*(5), 369–379.

Chapman, M. (2009), Modeling the effect of multiple sets of mesoscale fractures in porous rock on frequency-dependent anisotropy, *Geophysics*, *74*(6), D97–D103.

Chapman, M., S. V. Zatsepin, and S. Crampin (2002), Derivation of a microstructural poroelastic model, *Geophysical Journal International*, *151*(2), 427–451.

Chapman, S., N. Tisato, B. Quintal, and K. Holliger (2016), Seismic attenuation in partially saturated Berea sandstone submitted to a range of confining pressures, *Journal of Geophysical Research: Solid Earth*, *121*(3), 1664–1676.

Chapman, S. A. (2017), Experimental characterization and analysis of fluid related seismic attenuation mechanisms in porous materials par.

Cheng, C. H., and D. H. Johnston (1981), Dynamic and static moduli, *Geophysical Research Letters*, *8*(1), 39–42.

Christensen, N., and H. Wang (1985), The influence of pore pressure and confining pressure on dynamic elastic properties of berea sandstone, *Geophysics*, *50*(2), 207.

Cleary, M. P. (1978), Elastic and dynamic response regimes of fluid-impregnated solids with diverse microstructures, *International Journal of Solids and Structures*, *14*(10), 795–819.

Cole, K. S., and R. H. Cole (1941), Dispersion and Absorption in Dielectrics I. Alternating Current Characteristics, *The Journal of Chemical Physics*, *9*(4), 341–351.

Collet, O., and B. Gurevich (2016), Frequency dependence of anisotropy in fluid saturated rocks – Part I: aligned cracks case, *Geophysical Prospecting*, *64*(4), 1067–1084.

Das, A., and M. Batzle (2008), Modeling studies of heavy oil—in between solid and fluid properties, *The Leading Edge*, *27*(September), 1116.

David, E., N. Brantut, A. Schubnel, and R. Zimmerman (2012), Sliding crack model for nonlinearity and hysteresis in the uniaxial stress–strain curve of rock, *International Journal of Rock Mechanics and Mining Sciences*, *52*, 9–17.

David, E. C., and R. W. Zimmerman (2012), Pore structure model for elastic wave velocities in fluid-saturated sandstones, *Journal of Geophysical Research*, *117*(B7).

David, E. C., J. Fortin, A. Schubnel, Y. Guéguen, and R. W. Zimmerman (2013), Laboratory measurements of low-and high-frequency elastic moduli in Fontainebleau sandstone, *Geophysics*, *78*(5), D369–D379.

De Paula, O. B., M. Pervukhina, D. Makarynska, and B. Gurevich (2012), Modeling squirt dispersion and attenuation in fluid-saturated rocks using pressure dependency of dry ultrasonic velocities, *Geophysics*, *77*(3), WA157–WA168.

Detournay, E., and A. H.-D. Cheng (1993), *Fundamentals of Poroelasticity, Vol. 2: Analysis and Design Method, pp. 113 - 171*, Pergamon Press.

Digby, P. (1981), The effective elastic moduli of porous granular rocks, *Journal of Applied Mechanics*, *48*(4), 803–808.

Dular, P., C. Geuzaine, F. Henrotte, and W. Legros (1998), A general environment for the treatment of discrete problems and its application to the finite element method, *IEEE Transactions on Magnetics*, *34*(5), 3395–3398.

Dunn, K.-J. (1986), Acoustic attenuation in fluid-saturated porous cylinders at low frequencies, *The Journal of the Acoustical Society of America*, *79(6)*(6), 1709–1721.

Dunn, K.-J. (1987), Sample boundary effect in acoustic attenuation of fluid-saturated porous cylinders, *The Journal of the Acoustical Society of America*, *81(5)*, 1259–1266.

Dutta, N., and H. Odé (1979), Attenuation and dispersion of compressional waves in fluid-filled porous rocks with partial gas saturation (white model)-part i: Biot theory, *Geophysics*, *44*(11), 1777–1788.

Dvorkin, J., G. Mavko, and A. Nur (1995), Squirt flow in fully saturated rocks, *Geophysics*, *60*(1), 97–107.

Eberli, G. P., G. T. Baechle, F. S. Anselmetti, and M. L. Incze (2003), Factors controlling elastic properties in carbonate sediments and rocks, *The Leading Edge*, *22*(7), 654–660.

Endres, A. L., and R. J. Knight (1997), Incorporating pore geometry and fluid pressure communication into modeling the elastic behavior of porous rocks, *Geophysics*, *62*(1), 106–117.

Eshelby, J. D. (1957), The determination of the elastic field of an ellipsoidal inclusion, and related problems, *Proceedings of the Royal Society of London. Series A. Mathematical and Physical Sciences*, *241*(1226), 376–396.

Evans, A. G. (1978), Microfracture from thermal expansion anisotropyâ€"I. Single phase systems, *Acta Metallurgica*, *26*(12), 1845 – 1853.

Fabre, D., and J. Gustkiewicz (1997), Poroelastic properties of limestones and sandstones under hydrostatic conditions, *International Journal of Rock Mechanics and Mining Sciences*, *34*(1), 127–134.

Fabricius, I., G. T. Bächle, and G. P. Eberli (2010), Elastic moduli of dry and water-saturated carbonates — Effect of depositional texture, porosity, and permeability, *Geophysics*, *75*(3), N65–N78.

Fjær, E. (2009), Static and dynamic moduli of a weak sandstone, *GEOPHYSICS*, *74*(2), WA103–WA112.

Fortin, J. (2005), Compaction homogène et compaction localisée des roches poreuses. Étude expérimentale et théorique, Ph.D. thesis, Université Pierre et Marie Curie-Paris VI.

Fortin, J., A. Schubnel, and Y. Guéguen (2005), Elastic wave velocities and permeability evolution during compaction of Bleurswiller sandstone, *International Journal of Rock Mechanics and Mining Sciences*, *42*(7–8), 873–889.

Fortin, J., Y. Guéguen, and A. Schubnel (2007), Effects of pore collapse and grain crushing on ultrasonic velocities and Vp/Vs, *Journal of Geophysical Research*, *112*(B8).

Fortin, J., L. Pimienta, Y. Guéguen, A. Schubnel, E. C. David, and M. Adelinet (2014), Experimental results on the combined effects of frequency and pressure on the dispersion of elastic waves in porous rocks, *The Leading Edge*, *33*(6), 648–654.

Fossum, A. F., P. E. Senseny, T. W. Pfeifle, and K. D. Mellegard (1995), Experimental determination of probability distributions for parameters of a salem limestone cap plasticity model, *Mechanics of Materials*, *21*(2), 119–137.

Fournier, F., and J. Borgomano (2009), Critical porosity and elastic properties of microporous mixed carbonate-siliciclastic rocks, *Geophysics*, *74*(2), E93–E109.

Fournier, F., P. Leonide, K. Biscarrat, A. Gallois, J. Borgomano, and A. Foubert (2011), Elastic properties of microporous cemented grainstones, *Geophysics*, *76*(6), E211–E226.

Fournier, F., P. Léonide, L. Kleipool, R. Toullec, J. J. Reijmer, J. Borgomano, T. Klootwijk, and J. Van Der Molen (2014), Pore space evolution and elastic properties of platform carbonates (Urgonian limestone, Barremian–Aptian, SE France), *Sedimentary Geology*, *308*, 1–17.

Fredrich, J. T., and T.-f. Wong (1986), Micromechanics of thermally induced cracking in three crustal rocks, *Journal of Geophysical Research: Solid Earth*, *91*(B12), 12,743–12,764.

Gassmann, F. (1951), Elasticity of porous media, *Vierteljahrsschrder Naturforschenden Gesselschaft*, *96*, 1–23.

Geuzaine, C., and J.-F. Remacle (2009), Gmsh: A 3-D finite element mesh generator with built-in pre- and post-processing facilities, *International Journal for Numerical Methods in Engineering*, *79*(11), 1309–1331.

Ghabezloo, S., and J. Sulem (2009), Stress dependent thermal pressurization of a fluid-saturated rock, *Rock Mechanics and Rock Engineering*, *42*(1), 1–24.

Ghabezloo, S., and J. Sulem (2010), Effect of the volume of the drainage system on the measurement of undrained thermo-poro-elastic parameters, *International Journal of Rock Mechanics and Mining Sciences*, *47*(1), 60–68.

Guéguen, Y., and M. Boutéca (2004), *Mechanics of fluid-saturated rocks*, vol. 89, Academic Press.

Guéguen, Y., and J. Dienes (1989), Transport properties of rocks from statistics and percolation, *Mathematical geology*, *21*(1), 1–13.

Guéguen, Y., and J. Sarout (2009), Crack-induced anisotropy in crustal rocks: Predicted dry and fluid-saturated Thomsen's parameters, *Physics of the Earth and Planetary Interiors*, *172*(1-2), 116–124.

Guéguen, Y., and J. Sarout (2011), Characteristics of anisotropy and dispersion in cracked medium, *Tectonophysics*, *503*(1-2), 165–172.

Guéguen, Y., T. Chelidze, and M. Le Ravalec (1997), Microstructures, percolation thresholds, and rock physical properties, *Tectonophysics*, *279*(1), 23–35.

Guéguen, Y., M. Adelinet, A. Ougier-Simonin, J. Fortin, and A. Schubnel (2011), How cracks modify permeability and introduce velocity dispersion: Examples of glass and basalt, *The Leading Edge*, *30*(12), 1392–1398.

Gurevich, B., D. Makarynska, O. B. de Paula, and M. Pervukhina (2010), A simple model for squirt-flow dispersion and attenuation in fluid-saturated granular rocks, *Geophysics*, *75*(6), N109–N120.

Hart, D. J., and H. F. Wang (1995), Laboratory measurements of a complete set of poroelastic moduli for berea sandstone and indiana limestone, *Journal of Geophysical Research: Solid Earth*, *100*(B9), 17,741–17,751.

Hashin, Z., and S. Shtrikman (1963), A variational approach to the theory of the elastic behaviour of multiphase materials, *Journal of the Mechanics and Physics of Solids*, *11*(2), 127–140.

Hill, R. (1952), The Elastic Behaviour of a Crystalline Aggregate, *Proceedings of the Physical Society. Section A*, *65*(5), 349–354.

Homand-Etienne, F., and J.-P. Troalen (1984), Behaviour of granites and limestones subjected to slow and homogeneous temperature changes, *Engineering Geology*, *20*(3), 219 – 233.

Hsieh, P., J. Tracy, C. Neuzil, J. Bredehoeft, and S. Silliman (1981), A transient laboratory method for determining the hydraulic properties of 'tight'rocks—i. theory, in *International Journal of Rock Mechanics and Mining Sciences & Geomechanics Abstracts*, vol. 18, pp. 245–252, Elsevier.

Ide, J. M. (1936), Comparison of statically and dynamically determined Young's modulus of rocks, *Proceedings of the National Academy of Sciences*, *22*(2), 81–92.

Jackson, I., and M. Paterson (1987), Shear modulus and internal friction of calcite rocks at seismic frequencies: pressure, frequency and grain size dependence, *Physics of the earth and planetary interiors*, *45*(4), 349–367.

Jackson, I., and M. S. Paterson (1993), A high-pressure, high-temperature apparatus for studies of seismic wave dispersion and attenuation, *Pure and Applied Geophysics PAGEOPH*, *141*(2-4), 445–466.

Jaeger, J. C., N. G. Cook, and R. Zimmerman (2009), *Fundamentals of rock mechanics*, John Wiley & Sons.

Jakobsen, M. (2004), The interacting inclusion model of wave-induced fluid flow, *Geophysical Journal International*, *158*(3), 1168–1176.

Jakobsen, M., and M. Chapman (2009), Unified theory of global flow and squirt flow in cracked porous media, *Geophysics*, *74*(2), WA65–WA76.

Jakobsen, M., T. A. Johansen, and C. McCann (2003), The acoustic signature of fluid flow in complex porous media, *Journal of applied Geophysics*, *54*(3-4), 219–246.

Ji, Y., P. Baud, V. Vajdova, and T.-f. Wong (2012), Characterization of Pore Geometry of Indiana Limestone in Relation to Mechanical Compaction, *Oil & Gas Science and Technology – Revue d'IFP Energies nouvelles*, *67*(5), 753–775.

Johnston, D. H., and M. N. Toksöz (1980), Thermal cracking and amplitude dependent attenuation, *Journal of Geophysical Research: Solid Earth*, *85*(B2), 937–942.

Johnston, D. H., M. N. Toksoz, and A. Timur (1979), Attenuation of seismic waves in dry and saturated rocks; II, Mechanisms, *Geophysics*, *44*(4), 691–711.

Jones, T. D. (1986), Pore fluids and frequency-dependent wave propagation in rocks, *Geophysics*, *51*(10), 1939–1953.

Kachanov, M. (1993), Elastic solids with many cracks and related problems, *Advances in applied mechanics*, *30*, 259–445.

King, M. S. (1969), Static And Dynamic Elastic Moduli Of Rocks Under Pressure, American Rock Mechanics Association.

Kümpel, H.-J. (1991), Poroelasticity: parameters reviewed, *Geophysical Journal International*, *105*(3), 783–799.

Laws, N., and J. C. Lee (1989), Microcracking in polycrystalline ceramics : Elastic isotropy and thermal anisotropy, *Journal of the Mechanics and Physics of Solids*, *37*(5), 603–618.

Le Ravalec, M. L., and Y. Guéguen (1996), High- and low-frequency elastic moduli for a saturated porous/cracked rock-Differential self-consistent and poroelastic theories, *Geophysics*, *61*(4), 1080–1094.

Lebedev, M., J. Toms-Stewart, B. Clennell, M. Pervukhina, V. Shulakova, L. Paterson, T. M. Müller, B. Gurevich, and F. Wenzlau (2009), Direct laboratory observation of patchy saturation and its effects on ultrasonic velocities, *The Leading Edge*, *28*(1), 24–27.

Leonide, P., J. Borgomano, J.-P. Masse, and S. Doublet (2012), Relation between stratigraphic architecture and multi-scale heterogeneities in carbonate platforms: The Barremian–lower Aptian of the Monts de Vaucluse, SE France, *Sedimentary Geology*, *265-266*, 87–109.

Lienert, B. R., and M. H. Manghnani (1990), The relationship between Q_E^{-1} and dispersion in extensional modulus E, *Geophysical Research Letters*, *17*(6), 677–680.

Lin, W. (1977), Compressible fluid flow through rocks of variable permeability, *Tech. rep.*, California Univ., Livermore (USA). Lawrence Livermore Lab.

Lion, M., F. Skoczylas, and B. Ledésert (2005), Effects of heating on the hydraulic and poroelastic properties of bourgogne limestone, *International Journal of Rock Mechanics and Mining Sciences*, *42*(4), 508–520.

Léonide, P., F. Fournier, J. J. Reijmer, H. Vonhof, J. Borgomano, J. Dijk, M. Rosenthal, M. van Goethem, J. Cochard, and K. Meulenaars (2014), Diagenetic patterns and pore space distribution along a platform to outer-shelf transect (Urgonian limestone, Barremian–Aptian, SE France), *Sedimentary Geology*, *306*, 1–23.

Lu, C., and I. Jackson (1996), Seismic-frequency laboratory measurements of shear mode viscoelasticity in crustal rocks I: competition between cracking and plastic flow in thermally cycled Carrara marble, *Physics of the earth and planetary interiors*, *94*(1-2), 105–119.

Lucet, N., P. N. J. Rasolofosaon, and B. Zinszner (1991), Sonic properties of rocks under confining pressure using the resonant bar technique, *The Journal of the Acoustical Society of America*, *89*(3), 980–990.

Lucia, F. J. (1995), Rock-Fabric/Petrophysical Classification of Carbonate Pore Space for Reservoir Characterization, *AAPG Bulletin*, *79*(9), 1275–1300.

Madonna, C., and N. Tisato (2013), A new Seismic Wave Attenuation Module to experimentally measure low-frequency attenuation in extensional mode, *Geophysical Prospecting*, *61*(2), 302–314.

Mallet, C. (2014), Etude de la fissuration des verres de stockage: comportement en condition de stockage géologique, Ph.D. thesis, Ecole normale supérieure-ENS PARIS.

Marton, L., G. C. Tari, and C. T. Lehmann (2000), Evolution of the Angolan Passive Margin, West Africa, With Emphasis on Post-Salt Structural Styles, *Atlantic rifts and continental margins*, pp. 129–149.

Mavko, G., and D. Jizba (1991), Estimating grain-scale fluid effects on velocity dispersion in rocks, *Geophysics*, *56*(12), 1940–1949.

Mavko, G., and A. Nur (1975), Melt squirt in the asthenosphere, *Journal of Geophysical Research*, *80*(11), 1444–1448.

Mavko, G., T. Mukerji, and J. Dvorkin (2009), *The rock physics handbook: Tools for seismic analysis of porous media*, Cambridge university press.

Mavko, G. M., and A. Nur (1979), Wave attenuation in partially saturated rocks, *Geophysics*, *44*(2), 161–178.

Michalopoulos, L. P., and G. E. Triandafilidis (1976), Influence of Water on Hardness, Strength and Compressibility of Rock, *BULL ASSOC ENG GEOL*, *xiii*(1), 1–22.

Mikhaltsevitch, V., M. Lebedev, and B. Gurevich (2014), A laboratory study of low-frequency wave dispersion and attenuation in water-saturated sandstones, *The Leading Edge*, *33*(6), 616–622.

Mikhaltsevitch, V., M. Lebedev, and B. Gurevich (2016a), Laboratory measurements of the effect of fluid saturation on elastic properties of carbonates at seismic frequencies: Effect of fluid saturation on carbonates, *Geophysical Prospecting*, *64*(4), 799–809.

Mikhaltsevitch, V., M. Lebedev, and B. Gurevich (2016b), Validation of the laboratory measurements at seismic frequencies using the Kramers-Kronig relationship, *Geophysical Research Letters*, p. 2016GL069269.

Müller, T. M., B. Gurevich, and M. Lebedev (2010), Seismic wave attenuation and dispersion resulting from wave-induced flow in porous rocks—A review, *Geophysics*, *75*(5), 75A147–75A164.

Morlier, P. (1971), Description de l'etat de fissuration d'une roche a partir d'essais non-destructifs simples, *Rock Mechanics and Rock Engineering*, *3*(3), 125–138.

Murphy III, W. F. (1982), Effects of partial water saturation on attenuation in massilon sandstone and vycor porous glass, *The Journal of the Acoustical Society of America*, *71*, 1458.

Murphy III, W. F., K. W. Winkler, and R. L. Kleinberg (1986), Acoustic relaxation in sedimentary rocks: Dependence on grain contacts and fluid saturation, *Geophysics*, *51*(3), 757–766.

Nakagawa, S. (2011), Split Hopkinson resonant bar test for sonic-frequency acoustic velocity and attenuation measurements of small, isotropic geological samples, *Review of Scientific Instruments*, *82*(4).

Nakagawa, S., T. J. Kneafsey, T. M. Daley, B. M. Freifeld, and E. V. Rees (2013), Laboratory seismic monitoring of supercritical CO2 flooding in sandstone cores using the Split Hopkinson Resonant Bar technique with concurrent x-ray Computed Tomography imaging, *Geophysical Prospecting*, *61*(2), 254–269.

O'Connell, R. J., and B. Budiansky (1974), Seismic velocities in dry and saturated cracked solids, *Journal of Geophysical Research*, *79*(35), 5412–5426.

O'Connell, R. J., and B. Budiansky (1977), Viscoelastic properties of fluid-saturated cracked solids, *Journal of Geophysical Research*, *82*(36), 5719–5735.

O'Connell, R. J., and B. Budiansky (1978), Measures of dissipation in viscoelastic media, *Geophysical Research Letters*, *5*(1), 5–8.

O'Donnell, M., E. Jaynes, and J. Miller (1981), Kramers–Kronig relationship between ultrasonic attenuation and phase velocity, *The Journal of the Acoustical Society of America*, *69*(3), 696–701.

Ougier-Simonin, A., Y. Guéguen, J. Fortin, A. Schubnel, and F. Bouyer (2011), Permeability and elastic properties of cracked glass under pressure, *Journal of Geophysical Research*, *116*(B7).

Paffenholz, J., and H. Burkhardt (1989), Absorption and modulus measurements in the seismic frequency and strain range on partially saturated sedimentary rocks, *Journal of Geophysical Research: Solid Earth (1978–2012)*, *94*(B7), 9493–9507.

Palmer, I., and M. Traviolia (1980), Attenuation by squirt flow in undersaturated gas sands, *Geophysics*, *45*(12), 1780–1792.

Pimienta, L., J. Fortin, and Guéguen (2014a), Evidence of a drained to undrained frequency dependent transition from elastic and hydraulic diffusion properties on a fontainebleau sandstone., *Proceedings of the 84th SEG Annual meeting*, pp. 2969–2972.

Pimienta, L., J. Fortin, and Y. Guéguen (2014b), Investigation of elastic weakening in limestone and sandstone samples from moisture adsorption, *Geophysical Journal International*, *199*(1), 335–347.

Pimienta, L., J. Sarout, L. Esteban, and C. Delle Piane (2014c), Prediction of rocks thermal conductivity from elastic wave velocities, mineralogy and microstructure, *Geophysical Journal International*, *197(2)*, 860–874.

Pimienta, L., J. Fortin, and Y. Guéguen (2015a), Bulk modulus dispersion and attenuation in sandstones, *Geophysics*, *80*(2), D111–D127.

Pimienta, L., J. Fortin, and Y. Guéguen (2015b), Experimental study of Young's modulus dispersion and attenuation in fully saturated sandstones, *Geophysics*, *80*(5), L57–L72.

Pimienta, L., J. Fortin, and Y. Guéguen (2016a), Effect of fluids and frequencies on Poisson's ratio of sandstone samples, *Geophysics*, *81*(2), D183–D195.

Pimienta, L., J. Borgomano, J. Fortin, and Y. Guéguen (2016b), Modelling the drained/undrained transition: effect of the measuring method and the boundary conditions, *Geophysical Prospecting*, *64*(4), 1098–1111.

Pimienta, L., J. Fortin, J. V. M. Borgomano, and Y. Guéguen (2016c), Dispersions and attenuations in a fully saturated sandstone: Experimental evidence for fluid flows at different scales, *The Leading Edge*, *35*(6), 495–501.

Prasad, M., and M. Manghnani (1997), Effects of pore and differential pressure on compressional wave velocity and quality factor in Berea and Michigan sandstones, *Geophysics*, *62*(4), 1163.

Pride, S. R., and J. G. Berryman (2003), Linear dynamics of double-porosity dual-permeability materials. I. Governing equations and acoustic attenuation, *Physical Review E*, *68*(3), 036,603.

Pride, S. R., J. G. Berryman, and J. M. Harris (2004), Seismic attenuation due to wave-induced flow, *Journal of Geophysical Research: Solid Earth*, *109*(B1).

Quintal, B., H. Steeb, M. Frehner, S. M. Schmalholz, and E. H. Saenger (2012), Pore fluid effects on S-wave attenuation caused by wave-induced fluid flow, *Geophysics*, *77*(3), L13–L23.

Quintal, B., R. Jänicke, J. G. Rubino, H. Steeb, and K. Holliger (2014), Sensitivity of S-wave attenuation to the connectivity of fractures in fluid-saturated rocks, *Geophysics*, *79*(5), WB15–WB24.

Quintal, B., J. G. Rubino, E. Caspari, and K. Holliger (2016), A simple hydromechanical approach for simulating squirt-type flow, *Geophysics*, *81*(4), D335–D344.

Rasolofosaon, P., and B. Zinszner (2002), Vérification expérimentale de la formule de Gassmann dans les calcaires poreux, *Oil & Gas Science and Technology*, *57*(2), 129–138.

Reuss, A. (1929), Berechnung der Fließgrenze von Mischkristallen auf Grund der Plastizitätsbedingung für Einkristalle ., *ZAMM - Journal of Applied Mathematics and Mechanics / Zeitschrift für Angewandte Mathematik und Mechanik*, *9*(1), 49–58.

Rice, J. R., and M. P. Cleary (1976), Some basic stress diffusion solutions for fluid-saturated elastic porous media with compressible constituents, *Reviews of Geophysics*, *14*(2), 227–241.

Rodriguez-Navarro, C., E. Ruiz-Agudo, A. Luque, A. B. Rodriguez-Navarro, and M. Ortega-Huertas (2009), Thermal decomposition of calcite: Mechanisms of formation and textural evolution of CaO nanocrystals, *American Mineralogist*, *94*(4), 578–593.

Rubino, J. G., T. M. Müller, M. Milani, and K. Holliger (2014), Seismic attenuation and velocity dispersion in fractured rocks: The role played by fracture contact areas, *Geophysical Prospecting*, *62*(6), 1278–1296.

Sarout, J. (2012), Impact of pore space topology on permeability, cut-off frequencies and validity of wave propagation theories: Pore space topology and wave propagation, *Geophysical Journal International*, *189*(1), 481–492.

Savoye, B., N. Babonneau, B. Dennielou, and M. Bez (2009), Geological overview of the Angola–Congo margin, the Congo deep-sea fan and its submarine valleys, *Deep Sea Research Part II: Topical Studies in Oceanography*, *56*(23), 2169–2182.

Sayers, C., J. Van Munster, and M. King (1990), Stress-induced ultrasonic anisotrophy in berea sandstone, in *International Journal of Rock Mechanics and Mining Sciences & Geomechanics Abstracts*, vol. 27, pp. 429–436, Elsevier.

Sayers, C. M., and M. Kachanov (1995), Microcrack-induced elastic wave anisotropy of brittle rocks, *Journal of Geophysical Research: Solid Earth*, *100*(B3), 4149–4156.

Schubnel, A., and Y. Guéguen (2003), Dispersion and anisotropy of elastic waves in cracked rocks, *Journal of Geophysical Research: Solid Earth*, *108*(B2), 2101.

Segur, J. B., and H. E. Oberstar (1951), Viscosity of Glycerol and Its Aqueous Solutions, *Industrial & Engineering Chemistry*, *43*(9), 2117–2120.

Seipold, U., H. Mueller, and P. Tuisku (1998), Principle differences in the pressure dependence of thermal and elastic properties of crystalline rocks, *Physics and Chemistry of the Earth*, *23*(3), 357–360.

Shafiro, B., and M. Kachanov (1997), Materials with fluid-filled pores of various shapes: Effective elastic properties and fluid pressure polarization, *International Journal of Solids and Structures*, *34*(27), 3517–3540.

Shapiro, S. A. (2003), Elastic piezosensitivity of porous and fractured rocks, *Geophysics*, *68*(2), 482–486.

Simmons, G., and W. F. Brace (1965), Comparison of static and dynamic measurements of compressibility of rocks, *Journal of Geophysical Research*, *70*(22), 5649–5656.

Solazzi, S. G., J. G. Rubino, T. M. Müller, M. Milani, L. Guarracino, and K. Holliger (2016), An energy-based approach to estimate seismic attenuation due to wave-induced fluid flow in heterogeneous poroelastic media, *Geophysical Journal International*, *207*(2), 823–832.

Song, I., and J. Renner (2006), Linear pressurization method for determining hydraulic permeability and specific storage of a rock sample, *Geophysical Journal International*, *164*(3), 685–696.

Song, I., and J. Renner (2007), Analysis of oscillatory fluid flow through rock samples, *Geophysical Journal International*, *170*(1), 195–204.

Spencer, J. W. (1981), Stress Relations at Low Frequencies in Fluid Saturated Rocks: Attenuation and Modulus Dispersion, *Journal of Geophysical Research*, *86*(80), 1803–1812.

Spencer, J. W., and J. Shine (2016), Seismic wave attenuation and modulus dispersion in sandstones, *Geophysics*, *81*(3), D211–D231.

Subramaniyan, S., B. Quintal, N. Tisato, E. H. Saenger, and C. Madonna (2014), An overview of laboratory apparatuses to measure seismic attenuation in reservoir rocks: Apparatuses to measure seismic attenuation, *Geophysical Prospecting*, *62*(6), 1211–1223.

Szewczyk, D., A. Bauer, and R. M. Holt (2016), A new laboratory apparatus for the measurement of seismic dispersion under deviatoric stress conditions: Apparatus for seismic dispersion, *Geophysical Prospecting*, *64*(4), 789–798.

Takei, Y., K. Fujisawa, and C. McCarthy (2011), Experimental study of attenuation and dispersion over a broad frequency range: 1. the apparatus, *Journal of Geophysical Research: Solid Earth (1978–2012)*, *116(B9)*(B9).

Thompson, D. L., J. D. Stilwell, and M. Hall (2015), Lacustrine carbonate reservoirs from Early Cretaceous rift lakes of Western Gondwana: Pre-Salt coquinas of Brazil and West Africa, *Gondwana Research*, *28*(1), 26–51.

Thomsen, L. (1986), Weak elastic anisotropy, *GEOPHYSICS*, *51*(10), 1954–1966.

Tisato, N., and C. Madonna (2012), Attenuation at low seismic frequencies in partially saturated rocks: Measurements and description of a new apparatus, *Journal of Applied Geophysics*, *86*, 44–53.

Toms, J., T. M. Müller, and B. Gurevich (2007), Seismic attenuation in porous rocks with random patchy saturation, in *Geophysical Prospecting*, vol. 55, pp. 671–678.

Vajdova, V., P. Baud, and T.-f. Wong (2004), Compaction, dilatancy, and failure in porous carbonate rocks, *Journal of Geophysical Research: Solid Earth*, *109*(B5), B05,204.

Verwer, K., G. Eberli, G. Baechle, and R. Weger (2010), Effect of carbonate pore structure on dynamic shear moduli, *Geophysics*, *75*(1), E1–E8.

Vincent, B., M. Fleury, Y. Santerre, and B. Brigaud (2011), NMR relaxation of neritic carbonates: An integrated petrophysical and petrographical approach, *Journal of Applied Geophysics*, *74*(1), 38–58.

Voigt, W. (1889), Ueber die Beziehung zwischen den beiden Elasticitätsconstanten isotroper Körper, *Annalen der Physik*, *274*(12), 573–587.

Walsh, J. B. (1965), The effect of cracks on the compressibility of rocks, *Journal of Geophysical Research*, *70*(2), 381–389.

Wang, H. F. (2000), Theory of linear poroelasticity, *Princeton Series in Geophysics, Princeton University Press, Princeton, NJ*.

White, J. (1975), Computed seismic speeds and attenuation in rocks with partial gas saturation, *Geophysics*, *40*(2), 224–232.

Winkler, K. (1985), Dispersion analysis of velocity and attenuation in berea sandstone, *J. geophys. Res*, *90*(6), 793–6.

Winkler, K., and A. Nur (1979), Pore fluids and seismic attenuation in rocks, *Geophysical Research Letters*, *6*(1), 1–4.

Winkler, K. W. (1983), Contact stiffness in granular porous materials: Comparison between theory and experiment, *Geophysical Research Letters*, *10*(11), 1073–1076.

Winkler, K. W., and W. F. Murphy III (1995), Acoustic velocity and attenuation in porous rocks, in *Rock Physics and Phase Relations, A Handbook of Physical Constants, AGU Refrence Shelf 3*, American Geophysical Union.

Wonham, J. P., M. Cyrot, T. Nguyen, J. Louhouamou, and O. Ruau (2010), Integrated approach to geomodelling and dynamic simulation in a complex mixed siliciclastic–carbonate reservoir, N'Kossa field, Offshore Congo, *Geological Society, London, Special Publications*, *347*(1), 133–163.

Youssef, S., M. Han, D. Bauer, E. Rosenberg, S. Bekri, M. Fleury, and O. Vizika (2008), High resolution µCT combined to numerical models to assess electrical properties of bimodal carbonates, *Abu Dhabi, UAE*, *29*.

Zhu, W., P. Baud, and T.-f. Wong (2010), Micromechanics of cataclastic pore collapse in limestone, *Journal of Geophysical Research: Solid Earth*, *115*(B4), B04,405.

Zimmerman, R. (2000), Coupling in poroelasticity and thermoelasticity, *International Journal of Rock Mechanics and Mining Sciences*, *37*(1-2), 79–87.

Zinsmeister, L. (2013), Study of the hydromechanical evolution of a carbonate after chemical alteration. Application of the 2d and 3d digital image correlation during mechanical loading at different scales., Theses, Ecole Polytechnique X.

Résumé

Pour les roches saturées, la comparaison entre les mesures ultrasoniques (1 MHz) au laboratoire et les mesures sismiques (100 Hz) ou de diagraphie (10 kHz) sur le terrain n'est pas directe à cause de la dispersion des vitesses des ondes. Les mécanismes impliqués dans la dépendance en fréquence sont les écoulements de fluides à différentes échelles provoqués par le passage de l'onde. La dispersion et l'atténuation des modules élastiques de roches carbonatées ont été étudiées expérimentalement. Les calcaires étudiés sont : un Lavoux, un Indiana intact et craqué thermiquement, un calcaire Urgonien de Provence (Rustrel), et un coquina pré-sel du Congo. Les mesures ont été faites sur une large gamme de fréquence, en combinant les techniques d'oscillations forcées (10^{-3} to 10^{2} Hz) et ultrasoniques (1 MHz) dans une presse triaxiale, pour différentes pressions effectives. Le forçage peut être hydrostatique pour mesurer un module d'incompressibilité, ou axial pour mesurer le module de Young et le coefficient de Poisson. Pour étudier l'effet de la viscosité, les mesures ont été faites en condition sèche, puis saturée en glycérine et en eau. Le drainage global et le mécanisme d'écoulement crack-pore ont été caractérisés, en termes d'amplitude de dispersion, d'atténuation viscoélastique, et de fréquence de coupure. Pour nos échantillons, la théorie de Biot-Gassmann s'est montrée valide pour les fréquences sismiques (10-100 Hz) sauf pour l'Indiana craqué thermiquement. La dispersion liée à des écoulements cracks-pores a été observée pour tous les échantillons sauf le Lavoux. Les fréquences de coupures de ceux-ci sont toutes dans la gamme des fréquences des diagraphies (10 kHz) pour des conditions de saturation en eau. Un modèle simple, combinant poroélasticité et milieux effectifs, a été développé pour prédire la dispersion des modules sur toute la gamme de fréquence, et s'est montré généralement en accord avec les résultats expérimentaux.

Mots Clés

Dispersion, atténuation, carbonate, modules élastiques, statique-dynamique, oscillations forcées, ultrasons, élasticité, viscoélasticité, poroélasticité, milieux effectifs, calcaire, Lavoux, Indiana, Rustrel, pré-sel coquina.

Abstract

For fluid-saturated rocks, comparing ultrasonic measurements (1 MHz) in the laboratory and seismic (100 Hz) or logging (10 kHz) measurements in the field is not straightforward due to dispersion of the body-wave velocities. The frequency-dependent mechanisms involved are wave-induced fluid flows that occur at different scales. The dispersion and the attenuation of the elastic moduli of four fluid-saturated carbonate rocks have been studied experimentally. The selected limestones were a Lavoux, an intact and thermally cracked Indiana, a Urgonian limestone from Provence (Rustrel), and a pre-salt coquina from offshore Congo. Measurements were done over a large-frequency range, by the combination of forced oscillations (10^{-3} to 10^{2} Hz) and ultrasonic measurements (1 MHz) in a triaxial cell, at various effective pressures. The forced oscillations were either hydrostatic to deduce the bulk modulus, or axial to deduce Young's modulus and Poisson's ratio. The measurements were done in dry-, glycerin- and water-saturated conditions to investigate the effect of viscosity. For all our samples, the global drainage and the squirt-flow mechanisms were characterized experimentally, in terms of amplitude of dispersion, amount of viscoelastic attenuation, and cut-off frequencies. Biot-Gassmann's theory was found to be valid at seismic frequencies (10-100 Hz) for all the samples except the thermally cracked Indiana. Squirt-flow transitions were observed for all the samples, except the Lavoux. The cut-off frequencies were all in the range of logging frequencies (10 kHz), for water-saturated conditions. A simple model, combining poroelasticity and the non-interaction approximation effective medium, was developed to predict the dispersion of the moduli over the whole frequency range, and was generally in agreement with the experimental results.

Keywords

Dispersion, attenuation, carbonate, elastic moduli, static-dynamic, forced oscillations, ultrasonic, elasticity, viscoelasticity, poroelasticity, effective medium, limestone, Lavoux, Indiana, Rustrel, pre-salt coquina.